ADD443213

Proceedings of Damping'89

8-10 February 1989
West Palm Beach, Florida

(Pages AAB-1 through DCD-11)

November 1989

Final Report for Period Feb 86 to Feb 89

19960611 157

Approved for public release; distribution is unlimited.

Sponsored by:

Flight Dynamics Laboratory
of the Air Force
Wright Aeronautical Laboratories

DTIC QUALITY INSPECTED 3

S

DISCLAIMER NOTICE

UNCLASSIFIED
Technical
Report

DEFENSE
TECHNICAL
INFORMATION
CENTER

DTIC   Acquiring Information
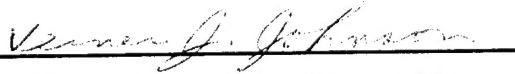Imparting Knowledge

DEFENSE LOGISTICS

UNCLASSIFIED
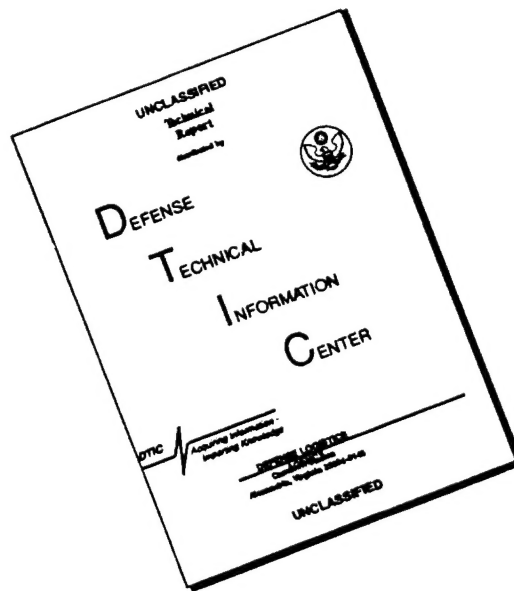
THIS DOCUMENT IS BEST QUALITY AVAILABLE. THE COPY FURNISHED TO DTIC CONTAINED A SIGNIFICANT NUMBER OF PAGES WHICH DO NOT REPRODUCE LEGIBLY.
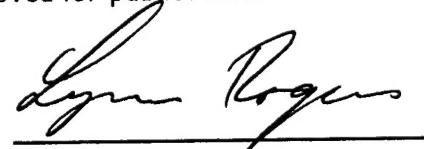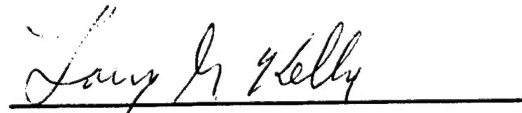
NOTICE

When Government drawings, specifications, or other data are used for any purpose other than in connection with a definitely Government-related procurement, the United States Government incurs no responsibility or any obligation whatsoever. The fact that the Government may have formulated or in any way supplied the said drawings, specifications, or other data, is not to be regarded by implication, or otherwise as in any manner, as licensing the holder or any other person or corporation; or as conveying any rights or permission to manufacture, use, or sell any patented invention that may in any way be related thereto.

This report is has been reviewed by the Office of Public Affairs (ASD/PA) and is releasable to the National Technical Information Service (NTIS). At NTIS, it will be available to the general public, including foreign nations.

This technical report has been reviewed and is approved for publication.

VERNER J. JOHNSON, Program Manager
Advanced Metallic Structures ADPO
Structures ADP Branch

LYNN ROGERS, PhD
Advanced Metallic Structures ADP

LARRY G. KELLY, Chief
Structures ADP Branch
Structures Division

"If your address has changed, if you wish to be removed from our mailing list, or if the addressee is no longer employed by your organization please notify WRDC/FIBAA, WPAFB, OH 45433-6553 to help us maintain a current mailing list".

Copies of this report should not be returned unless return is required by security considerations, contractual obligations, or notice on a specific document.

ADD443213
(ADD 443214 - ADD 443217)

REPORT DOCUMENTATION PAGE

Form Approved
OMB No. 0704-0188

1a. REPORT SECURITY CLASSIFICATION Unclassified	1b. RESTRICTIVE MARKINGS
2a. SECURITY CLASSIFICATION AUTHORITY	3. DISTRIBUTION/AVAILABILITY OF REPORT
2b. DECLASSIFICATION/DOWNGRADING SCHEDULE	Approved for public release; distribution unlimited.

4. PERFORMING ORGANIZATION REPORT NUMBER(S) WRDC-TR-89-3116, Vol I	5. MONITORING ORGANIZATION REPORT NUMBER(S)

6a. NAME OF PERFORMING ORGANIZATION Advanced Metallic Structures Adv Development Prog Office	6b. OFFICE SYMBOL (If applicable) WRDC/FIBAA	7a. NAME OF MONITORING ORGANIZATION

6c. ADDRESS (City, State, and ZIP Code) Wright-Patterson Air Force Base OH 45433-6553	7b. ADDRESS (City, State, and ZIP Code)

8a. NAME OF FUNDING/SPONSORING ORGANIZATION Flight Dynamics Lab. Wright Research Dev. Ctr.	8b. OFFICE SYMBOL (If applicable) WRDC/FIBA	9. PROCUREMENT INSTRUMENT IDENTIFICATION NUMBER

8c. ADDRESS (City, State, and ZIP Code)	10. SOURCE OF FUNDING NUMBERS			
	PROGRAM ELEMENT NO. 63211F	PROJECT NO. 486U	TASK NO. 11	WORK UNIT ACCESSION NO. 02

11. TITLE (Include Security Classification)

Damping 1989 Proceedings

12. PERSONAL AUTHOR(S)

13a. TYPE OF REPORT Final	13b. TIME COVERED FROM Feb 86 TO Feb 89	14. DATE OF REPORT (Year, Month, Day) 1989 November	15. PAGE COUNT 497

16. SUPPLEMENTARY NOTATION

Pages AAB-1 through DCD-11

17. COSATI CODES			18. SUBJECT TERMS (Continue on reverse if necessary and identify by block number)
FIELD	GROUP	SUB-GROUP	Vibration damping, controls/structure interaction.

19. ABSTRACT (Continue on reverse if necessary and identify by block number)

Individual papers of Damping 89 held 8-10 February 1989 in West Palm Beach FL are presented. The subjects included: mechanical properties of polymers, experimental methods, damping in metal matrix composites, friction damping, design of damping structure, modal damping values, and applications of damping, etc.

20. DISTRIBUTION/AVAILABILITY OF ABSTRACT ☒ UNCLASSIFIED/UNLIMITED ☐ SAME AS RPT. ☐ DTIC USERS	21. ABSTRACT SECURITY CLASSIFICATION Unclassified
22a. NAME OF RESPONSIBLE INDIVIDUAL Dr Lynn Rogers	22b. TELEPHONE (Include Area Code) (513)255-6622	22c. OFFICE SYMBOL WRDC/FIBAA

DD Form 1473, JUN 86 Previous editions are obsolete.

Workshop Administration

Director

Dr. Lynn Rogers
Flight Dynamics Laboratory of the Air Force
Wright Aeronautical Laboratories

Administrative Chairman

Mrs. Melissa Arrajj
Martin Marietta Astronautics Group

Assistant Administrative Chairman

Ms. Jo Ellen Dunn
CSA Engineering, Incorporated

Session Chairmen

Dr. M. Aswani, Aerospace Corporation
LTC R. L. Bagley, Air Force Institute of Technology Wright Patterson AFB
Mr. S. D. Bigelow, Boeing Aerospace Company
Dr. A. J. Bronowicki, TRW Space and Technology Group
Dr. D. I. G. Jones, Materials Laboratory, AFWAL
Dr. M. A. Cutchins, Auburn University
Mr. M. L. Drake, University of Dayton Research Institute
Mr. P. G. Gauthier, Naval Sea Systems
Mr. R. N. Gehling, Martin Marietta Astronautics Group
Dr. J. L. Gubser, McDonnell Douglas Astronautics Company
Dr. J. P. Henderson, Materials Laboratory, AFWAL
Mr. W. Hoskins, Lockheed Missiles & Space Company
Dr. R. Ikegami, Boeing Aerospace Company
Dr. C. D. Johnson, CSA Engineering, Incorporated
Mr. L. Kelly, Flight Dynamics Laboratory, AFWAL
Dr. E. M. Kerwin, BBN
Dr. R. LeMaster, W. J. Schaffer, Association
Dr. Y. P. Lu, DTNSRDC
Mr. D. R. Morgenthaler, Martin Marietta Astronautics Group
Mr. A. D. Nashif, Anatrol Corporation
Dr. T. S. Nishimoto, Rockwell International – SSD
Mr. M. L. Parin, Anatrol Corporation
Dr. K. E. Richards, Jr., Martin Marietta Astronautics Group
Dr. S. S. Sattinger, Westinghouse R&D Center
Dr. T. D. Scharton, Jet Propulsion Laboratory
Dr. J. Soovere, Lockheed – California Company
Mr. C. V. Stahle, Jr., General Electric Company
Mr. J. A. Staley, General Electric Company
Mr. S. J. Starr, LTV Aerospace – Aircraft Products
Dr. R. C. Stroud, Synergistic Technology, Incorporated
Dr. J. Unruh, Southwest Research Institute
Mr. H. Wolfe, Flight Dynamics Laboratory, AFWAL

FOREWORD

This publication includes the individual papers of DAMPING '89 held 8-10 February 1989, West Palm Beach, Florida. The Workshop was sponsored by the Air Force Wright Aeronautical Laboratories through the Advanced Metallic Structures Advanced Development Program Office (AFWAL/FIBAA).

It is desired to transfer vibration damping technology in a timely manner within the aerospace community, thereby, stimulating research, development and applications.

iv

TABLE OF CONTENTS

*Not available for publication.

TABLE OF CONTENTS (Continued)

*Not available for publication.

TABLE OF CONTENTS (Continued)

*Not available for publication.

TABLE OF CONTENTS (Continued)

*Not available for publication.

*Not available for publication.

*Not available for publication.

*Not available for publication.

TABLE OF CONTENTS (Continued)

*Not available for publication.

*Not available for publication.

*Not available for publication.

TABLE OF CONTENTS (Concluded)

*Not available for publication.

DAMPING - A KEY TO MORE, FASTER, FARTHER, HIGHER

Major General Thomas R. Ferguson, Jr.
Deputy Chief of Staff for Technology
and Requirements Planning
Headquarters Air Force Systems Command
Andrews Air Force Base, Maryland

Vibration is everywhere. And where there is vibration, there is damping. Most often, vibration is bad and damping is good. There are exceptions, but since this conference is about damping, we will leave the undamping crowd to their own devices.

After getting my primer on this subject, I was reminded that damping is a complicated subject. In simple terms, vibratory response can lead to cracked structure, defocused optics, or other types of degraded performance. Historically, the damping in a vibratory system has been "take what you get", called intrinsic damping. Only in the last few years has damping been a design parameter. So let's begin with a scramble: start the engines...on take off, light the burner. In my flying experience with the B-52, it was be sure all eight were running and start the Hound-Dogs on the roll...there's a lot of noise coming out of these engines. During take-off roll, there are two paths from the engine exhaust noise to the aft structure: one is direct, the other is reflected from the runway. Take-off is typically the highest acoustic environment the structure is exposed to. The skin panel responds to sound pressure level as does a microphone and it vibrates. It can vibrate enough to literally crack and break. The skin panel also re-radiates the sound into the interior. That's called "thru transmission." That's also the technical term for being able to hear people thru the motel wall, at least the motels government per diem can afford in places like Boston and Washington.

That aircraft skin panel also transmits vibratory energy into the substructure--the stringers, frames, and bulkheads. So internal equipment also gets hit with structural-borne vibratory energy at points like mounting brackets and with acoustic energy on their covers. Internal equipment can fail, malfunction or degrade to lower performance levels. As our pilot retracts the gear and accelerates, the dynamic pressure increases and the turbulent boundary layer, especially behind protuberances, can create very high sound pressure levels. At about mach 0.9, the oscillating shocks have the same effect. When we maneuver, especially transonically, the aeroacoustic levels on the leading and trailing edges (and external stores) reach high levels. When we open weapons bay doors, the open cavity acts like a giant whistle and the internal structure and stores can be subjected to tones of extremely large amplitude. Since we fly to fight, we carry weapons; we fly at ever-higher dynamic pressures and maneuver at transonic speeds to survive: This makes the vibroacoustics problem more severe. Today, to do our engineering right, structures-and-vibration-and-damping-engineers must participate in the original design of these modern flying machines.

Vibration is also no longer an earthly problem. It is becoming a design factor in satellites as well. Launch vibroacoustics typically cause the highest vibration levels and can break equipment. There are also more vibratory disturbances in orbit than you might think. There are always imbalances in reaction wheels, momentum wheels, and control moment gyros used for attitude control. Coolant flow, shifting solar arrays, liquid slosh, gravity gradient, particle impact, to name just a few, are all vibratory disturbances which, just for example, can degrade performance of sensitive optics.

I shouldn't have to convince this audience—we know that vibration is everywhere. Although the obvious is obvious to us, let's also acknowledge that damping is a highly specialized subject. A damping engineer is a specialist because he must first be a vibration engineer, who was probably a structures engineer to start with. So, right off, we have a specialty within a specialty within a specialty. The successful damping engineer must know more than damping. He'd better know systems integration and be very conversant about the operational environment. A prime example of this is the highly successful "Damping Wrap" for the inlet guide vanes on the engines used in the F-111F fighter. So many cracks were forming so quickly that the inlet guide vane case had to be refurbished after TOO few hours of service. Air coming into the engine is turned slightly by the inlet guide vanes to get best performance from the rotating first stage compressor. The IGV case consists of titanium inlet guide vanes welded to inner and outer rings. Vibration was suspected as the cause of the cracks which were forming in the heat affected zones of the welds. The intrinsic damping was extremely low, and in this case, the dynamic magnification factors at resonances were high. Obviously, the stage was set for a damping engineer to really impress his boss. Adding damping to the inlet guide vane was easy; developing a satisfactory damper wrap for a complex systems operational environment was not. Sophisticated bonding technology was used so that the damper wrap would adhere while exposed to the air flow. The wrap had to be thin to minimize inlet blockage area, since reduced air flow would affect engine performance. Engine stall characteristics, anti-icing effectiveness, erosion, corrosion, and durability were all investigated and proven satisfactory. The point being...this was a complex interdisciplinary problem—solved very successfully. This project has estimated cost avoidance savings to the Air Force of $50M. Spin-off damping applications in similar situations may well account for another $200 million. Other very recent demonstrations of vibration-caused structural failures fixed by damping are the A-7 center section leading edge flap, A-10 gun bay floor and side wall, and F-111 spoilers. Once again the logistics improvements in terms of dollars were significant. I should also add these improvements lower the heart rate for our maintainers.

For the most part, successful damping treatments have been of the add-on variety. The hardware has been designed and a vibration problem rears its ugly head. A damping treatment is designed and "added to" existing structure. Once the hardware exists, add-on damping may be an extremely cost effective solution. But it's better to avoid the problem altogether and that can be done with integral damping. Commercial examples are laminated valve covers, oil pans, and timing gear covers used in automobile and diesel engines.

Integral damping is also the key to longer life, more durable aircraft structure. The objective is increased sortie generation rate and reduced maintenance cost. Since we often learn more from our failures, there's no shame to admit there have been many unsuccessful attempts to design damping solutions. I'm told you don't have to be in this business very long to have been bit. In fact, you don't earn your damping wings until you've been humbled more than once. I don't want to focus on this aspect, but during breaks and at social opportunities it also pays to discuss the failures as well as the successes.

DAMPING '89 is put together to detail the state of the art, but the keynote role allows me latitude to summarize. A baseline of damping materials and manufacturing processes is established. We can measure properties of materials fairly well. Data banks on damping materials are also established. You can analyze simply supported beams in closed form and can perform finite element analysis of damped structure to predict modal frequencies and damping limits. You can experimentally measure the modal frequencies and damping of structure. There are a growing number of successful add-on and integral damping applications and you have quantified these successes in terms, pay-off terms, that management understands. Damping, in fact, is a hot, new tool in the engineer's kit bag. But it's good not to believe as the song goes "Oh Lord it's hard to be humble when you're perfect in every way." What we already know is just a glimpse of the future. There is still great opportunity. Therefore, it's important to make good investment decisions as we plan the future.

As in most technical disciplines, the explosion in computational power, coupled with advancements in damping technology, can greatly accelerate our knowledge. Better dynamic test techniques are needed; a greater range of materials properties should be measured and catalogued: and extensions to analytical methods would really expand the range of applications. With these wishes met, let's peer in the not too distant future and I'll make some predictions:

o   Measurement of the dynamic mechanical properties of viscoelastic damping materials will be more accurate, more efficient, and have less scatter.

o   Existing materials will be screened for toxicity, flammability, outgassing, corrosion, long-term environmental stability and others. These are properties which are mandatory for system application.

o   A fully computerized data clearing center will exist soon.

o   Wide-temperature range and low-temperature damping materials will be developed.

o   Approximate closed form analysis methods will come into use for structures like thin plates and shells, brackets, pipes and tubing.

o   Approximate finite element analysis models will be developed as preliminary design tools for damped structures such as satellite equipment support structures.

o   Computer aided design will yield optimum solutions by interacting finite element analysis of damped structure with a data base of damping materials.

o   Most aircraft sheet metal will be laminated, ditto for automobiles and household appliances.

o   Interest in damped composite structural materials will rise.

o   Housings and circuit boards of avionics equipment will be damped.

o   Logistics imperatives--maintainability and reliability--will dictate much more use of damping.

o   And, some of you who think you'll be millionaires exploiting these opportunities will probably go bankrupt because of Murphy. So, maximize the opportunity this conference offers.

o   Learn!!

o   Go home and apply the technology: Be passionate...become zealots for your work and the opportunity it presents.

o   Share your successes and failures with as wide a technical community as possible.

o   Think of yourselves as a team: Academia and practitioners in commercial and military applications. All must play their roles to see the most intelligent and widespread use of this technology.

I want to conclude with some non-damping thoughts. My boss, the AFSC Commander, General Randolph, just gave a talk at the AF Association's Tactical Air Warfare Symposium. He ok'd my use of some of his remarks because the message is so important for all of us. That message is about total quality management.

In the book, "A Passion for Excellence," Peters and Austin recall the management style of General Electric's aircraft engine pioneer, Gerhard Neumann when he worked with Claire Chennault's World War II Flying Tigers. Neumann wanted make sure his maintenance people fixed aircraft engines right...the first time. So each day he used to ask a few of his squadron mechanics to "volunteer" to test fly in the Single-Seat fighter they'd just repaired. The pilot would sit on the crew chief's lap, and neither could sit on a parachute because the cockpit wasn't big enough.

Well, improvements in workmanship were dramatic! In his book, "Herman the German," Neumann writes that each night, "Way past dinnertime, the airfield looked as if it were invaded by glowworms; the twinkling came from flashlights mechanics used to check--once more--the tightness of pipes or connections they had made in case Neumann might suggest that they 'Volunteer' to ride in their planes the next day."--Now there's a guy who knew how to motivate quality. TQM's an overdue sign of a national quality revolution. It's a buzzword you see in commercials, hear at symposiums, and notice in bookstores. But don't just dismiss TQM as yet another acronym that will die off. As a term, TQM might well change over time. However, as a philosophy TQM will last, as more companies and managers come to understand what continuous quality improvement means and what it can do. Affordable price tags, fair profits and high product quality will prove TQM's merits long after the trendiness of the buzzword disappears. It offers opportunities for every person involved in research, development, test, production and operations.

TQM--is BETTER QUALITY AT LOWER COST. It's the prerequisite to good performance. AFSC's senior people have been through training seminars with W. Edwards Deming, one of the best-known quality leaders in the world. Deming's philosophy is that 85 percent of quality problems are caused by the system; just 15 percent are caused by people. Just to be sure we're communicating--you're likely to be part of the 85 percent! If the products of U.S. industry are not well liked, loved, by the customer, you are involved because you're that 85 percent of the system that designs-in-problems the manufacturing work force can't correct.

General Randolph was challenged about his intensity on this subject of total quality management. The person said it sounds as if quality issues are a matter of life and death. He said no, they're much more important than that. Think about these statistics:

If the U.S. had service suppliers who did their jobs right 99.9 percent of the time, there would still be:

- 20,000 wrong prescriptions filled each year;

- Unsafe drinking water almost one hour each month;

- 2 long or short airplane landings a day (That's an accident) at Los Angeles and New York;

- And 2000 lost articles of mail per hour every day.

- In the defense arena, given 1 million grenades, you would have 999 duds—and 1 will go off in "0" seconds.

Where is your quality meter set?

General Randolph closed his talk with this story President Kennedy would tell and I'll do the same. It's about a retired French General whose hobby was gardening. He was a very cultured man with a deep sense of history. On his 80th birthday he bought a small shrub and instructed his gardener to plant it in the garden.

"But, Sir," the gardener protested, "that plant won't flower for a hundred years!" "Then by all means," the General said, "plant it now."

The total quality we plant in our work today is <u>FREEDOM FOR TOMORROW</u>. We need to plant more flowers.

GE Astro-Space

Pioneering Damping in Space

at GE Astro Space Division

Clyde Stahle
Damping 89
February 8, 1989

Outline

- Initial and current electronic component applications
- Acoustic cover
- Camera bracket
- Gimbal
- Satellite add-on panel damping
- RELSAT
- Lessons Learned
- Summary

> **Design, Analysis and Test Results Are Described for Damping Applications**

Purpose

- To highlight the maturing of damping technology through a review of GE-ASD projects

- To stimulate thinking by describing various applications where damping has effectively controlled vibration

- To emphasize basic considerations in effective use of damping

- To stimulate product improvement through future damping applications

> **GE-ASD Damping Has Spanned Two Decades**

Initial Application (1970)

- SMRD 100, developed as a space compatible sterilizable potting compound, was felt to have excellent damping properties

- Relay reliability on Landsat 1 provided impetus to damp relay panel

- Experimentally developed design using beam specimens with various materials

- Stiffner removed and replaced with foam/SMRD layer to maximize strain in viscoelastic material

- Maintained resonant frequency greater than 150 Hz and reduced amplification from 44 to 6

Highly Effective Damping Treatment Flown in Early 70's

Landsat PSM Relay Panel
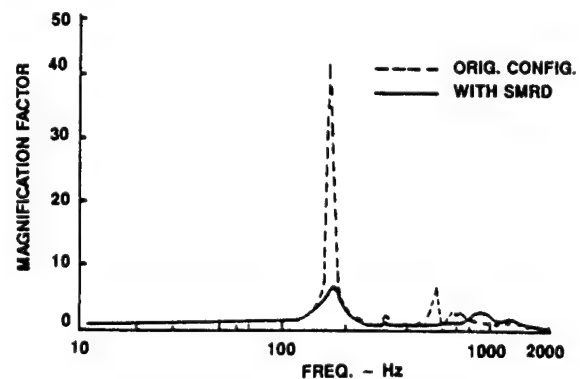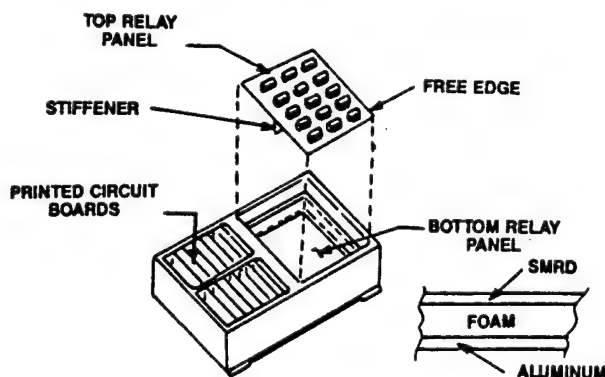
Offset Damping Layer Reduces Magnification from 44 to 6

Viking Lander (1973)

- Reliability for long duration interplanetary mission was motivation for reducing vibration of electronics parts

- SMRD damping strips with fiberglass constraining layers were designed with experimental parameter variations

- Damping strips applied between boards, on component side, or on printed circuit side

- Continuity of SMRD found to be unimportant – constraining layer was important

- Resonant amplification was reduced to less than 10 in most applications

- Damping felt to be the only way to reduce random vibration – stiffening increases G RMS

SMRD Damping Reduced Random Vibration by 50 Percent

Viking Lander (1973)
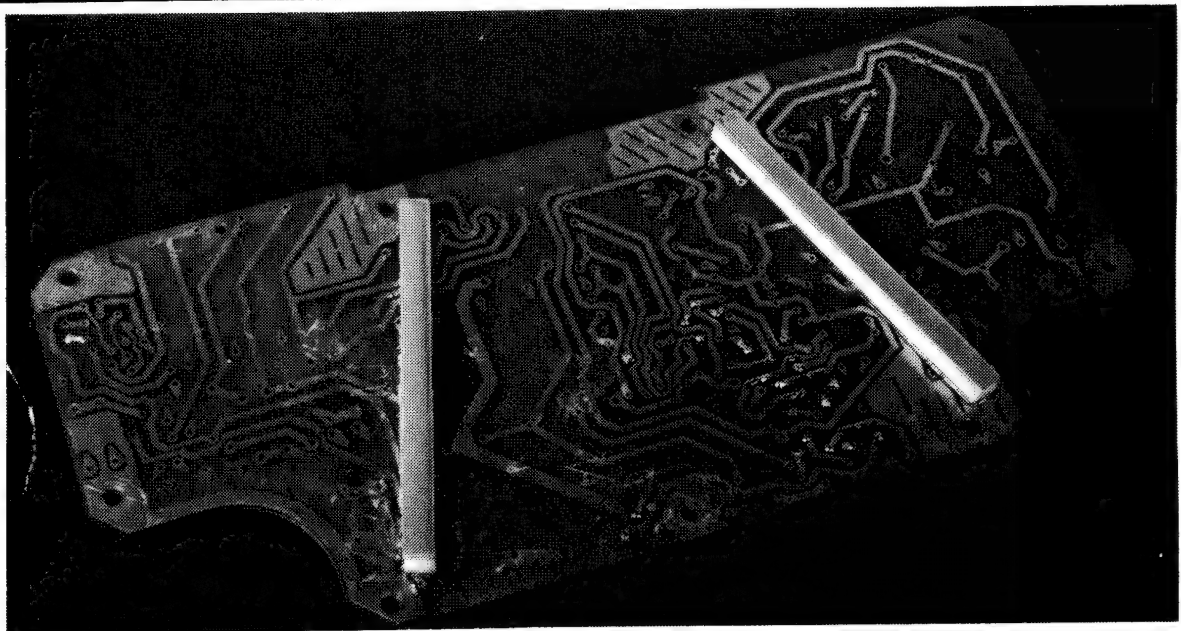
Damper on Printed Circuit Side

Viking Lander (1973)
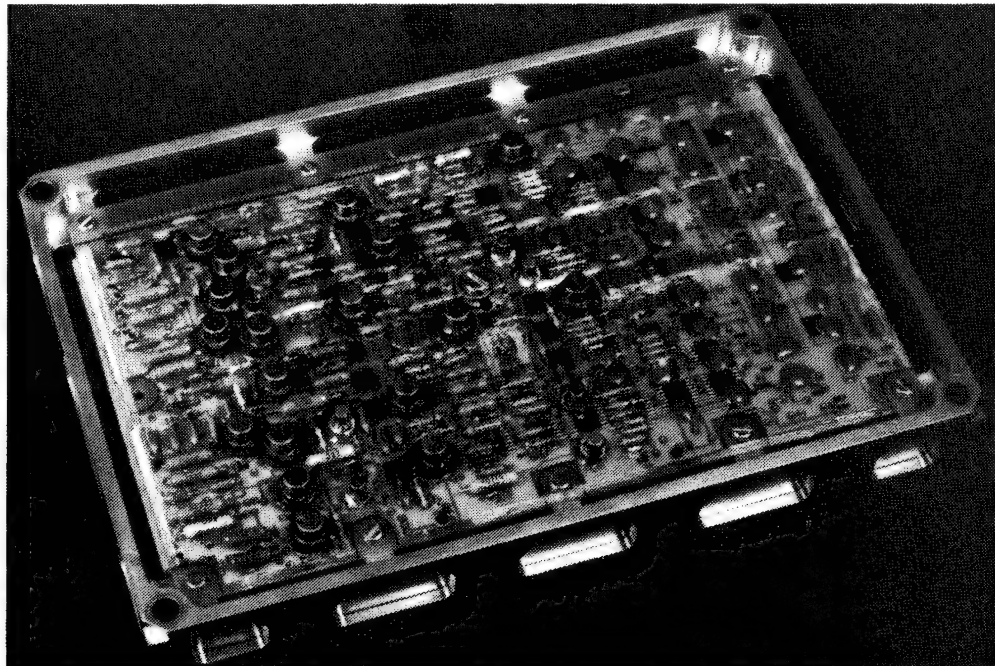
Damper Between Boards

Viking Lander (1973)
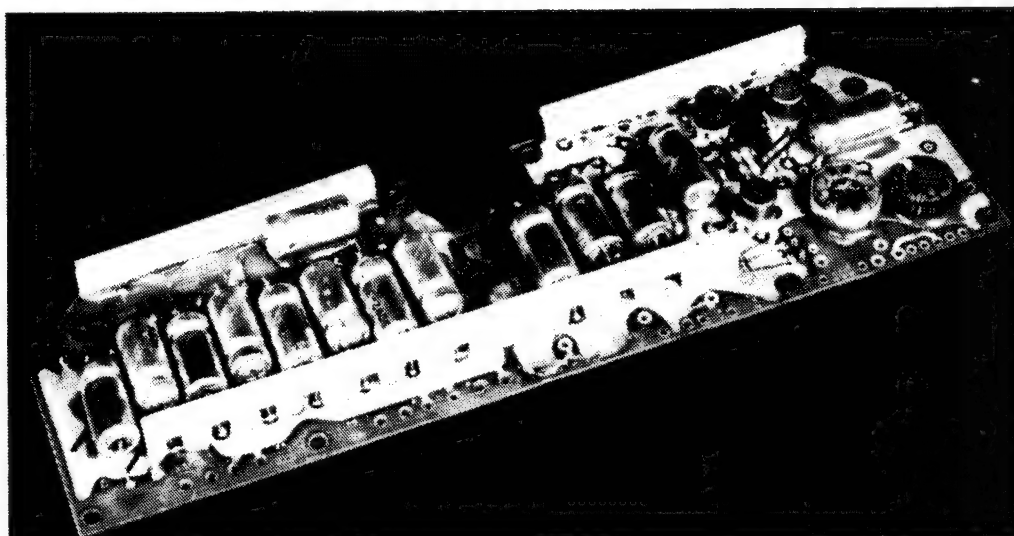
Discontinuous Damper on Part Side

Printed Wiring Board Damping Analysis

Early Analysis (1974)

- Initial SMRD properties were derived from resonant oberst beam tests using WLF relation to plot properties at room temperature

- Analysis used equivalent beam based on Kerwin-Ungar plate theory

Properties of SMRD 100F90

25°F ○   75°F ◊   125°F ▽
50°F ☐   100°F △   150°F ◔
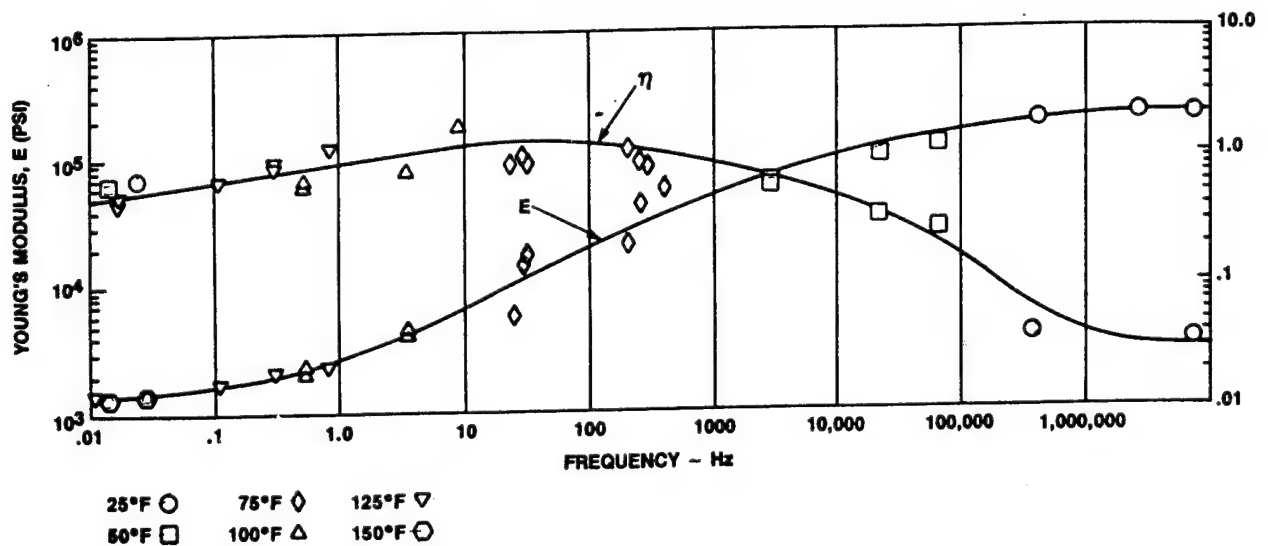
Temperature/Frequency Equivalence Used to Define Material Properties Over a Broad Frequency Range

Printed Wiring Board Damping Analysis

Current Analysis (1980's)

- Rogers–Jones International reduced temperature nomogram for material properties

- Nastran finite element models with modal strain energy used for predictions over range of operating temperatures

- SMRD strips with uniaxial graphite/epoxy constraining layers integrated into the design

- Risk graph based on deflection and acceleration limits developed for specified power spectral density

- Analysis agrees reasonably well with test results although boundary conditions cause errors

Finite Element Analysis is Used to Effectively Integrate Damping into the Design

Typical Damped PWB
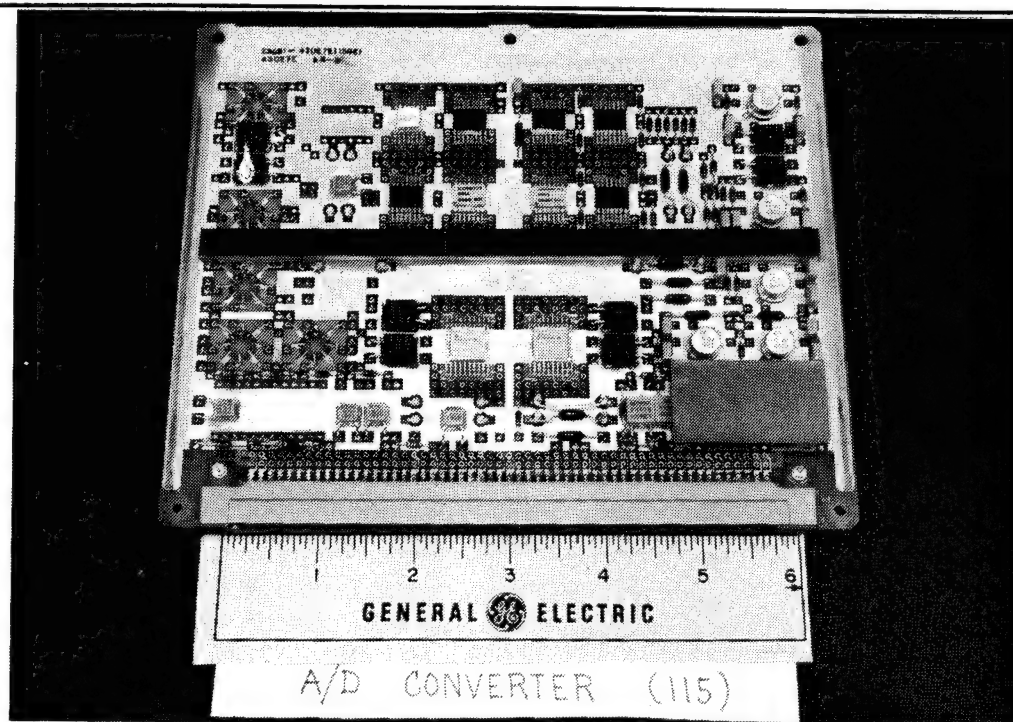
Damper Shown on Board Center

Rogers-Jones International Reduced Temperature Nomogram
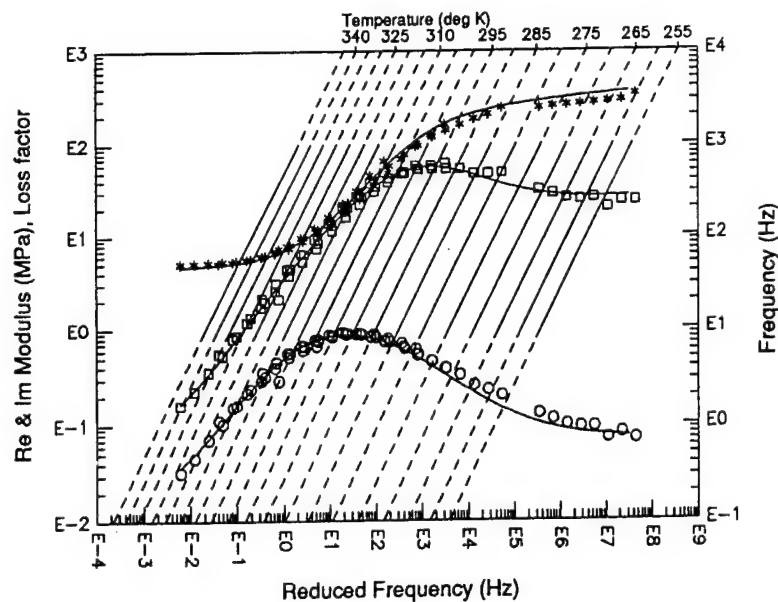
Applicable Range of Data is Shown by Solid Lines

Typical PWB Finite Element Model
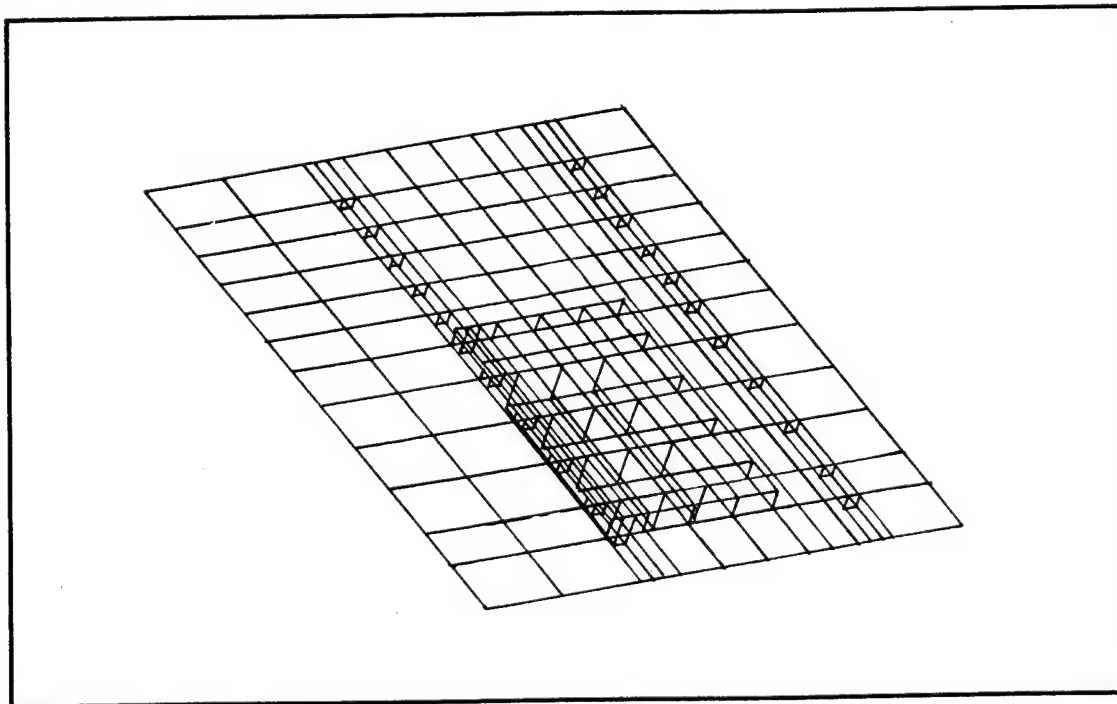
Nastran Models Board, Components and Dampers

Risk Graph

Predicted Loss Factor vs Frequency (Hz) risk graph showing regions: UNACCEPTABLE, MARGINAL, ADEQUATE, CONSERVATIVE, with curves labeled 0.25 MM, 0.123 MM, RMS, 0.75 MM, RELAYS, 110 RELAYS, and GRMS lines (15, 20, 25, 30, 40, 50, 100 GRMS).
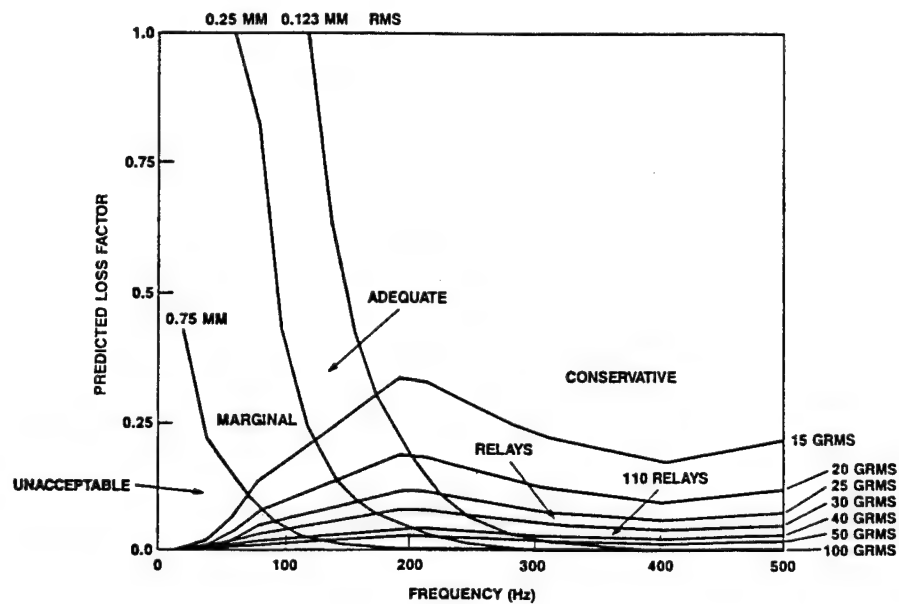
Design Adequacy Determined from Risk Graph

Vibration Test and Analysis Results

PWB	Test F_1	Test η_1	Test GRMS	Analysis F_1	Analysis η_1	$F_1 \dfrac{Analysis}{Test}$	$\eta_1 \dfrac{Analysis}{Test}$
5	189	.37	31.4	156	.31	.83	.84
6	178	.31	33.5	187	.32	1.05	1.03
7	202	.22	33.6	147	.22	.73	1.00
8	144	.25	28.6	153	.34	1.06	1.36
9	226	.23	35.6	229	.20	1.01	.87
10	243	.24	37.1	290	.19	1.19	.79
12	173	.13	27.4	147	.20	.85	1.54
13	127	.26	20.2	123	.21	.97	.81

Random Responses Are Limited to About 30 GRMS

NASA–GSFC Acoustic Cover (1974)

Purpose – To determine feasibility of protecting sensitive instruments from launch vehicle acoustic environment

Design – Lightweight cylindrical sandwich construction with viscoelastic (SMRD) strip core

Analysis – Used plate theory to optimize the design – 20 mil face sheets and half inch thick core using quarter inch SMRD strips in 5 inch square pattern

Results – Highly effective lightweight design having excellent low frequency acoustic attenuation

– Subsequent testing of square thermal canister showed about 6dB attenuation due to "add-on" damping strips

Viscoelastic Acoustic Covers Are Highly Effective

Acoustic Enclosure
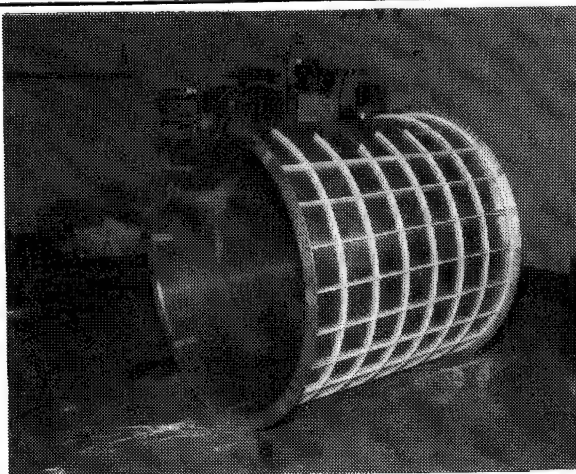
During Fabrication Without
Outer Face Sheet
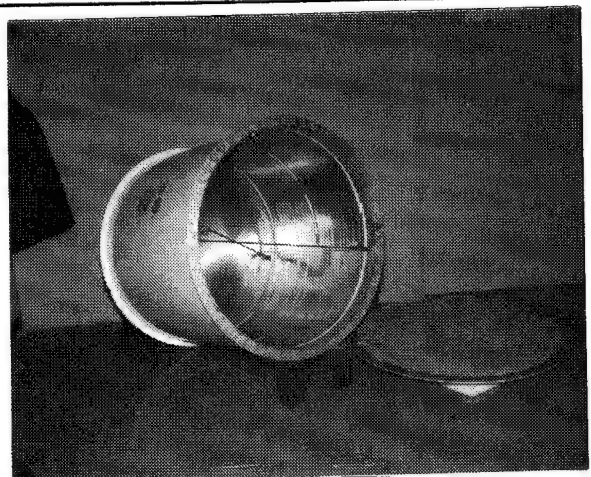
Completed 4 Foot
Cylindrical Enclosure

Sandwich with SMRD Core Provided
Highly Damped Stiff Design

Acoustic Cover Test Performance
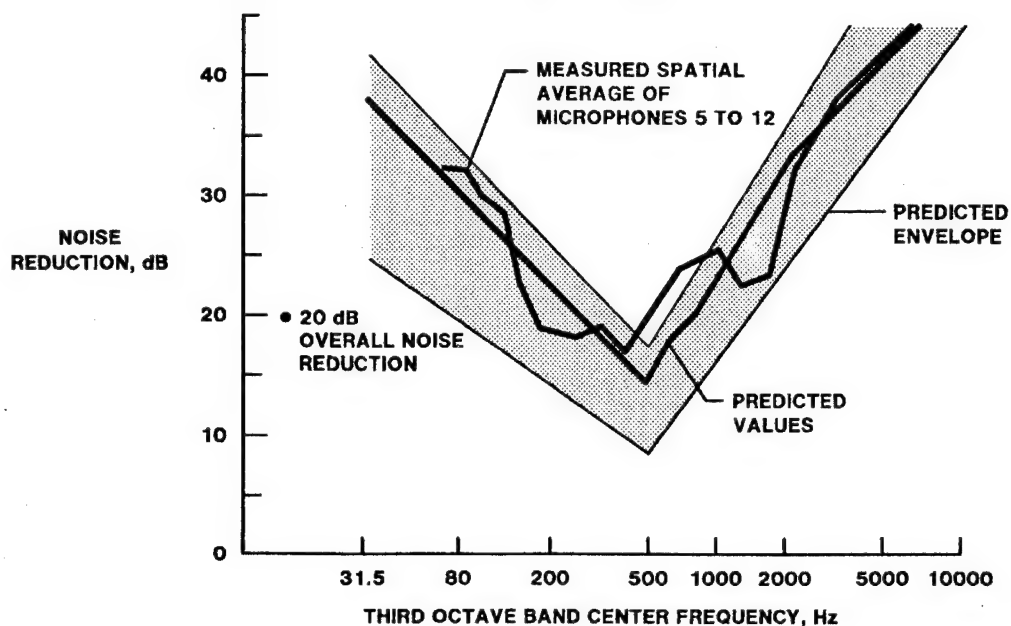
Test Measured an Order of Magnitude Noise Reudction

Acoustic Enclosure Comparison
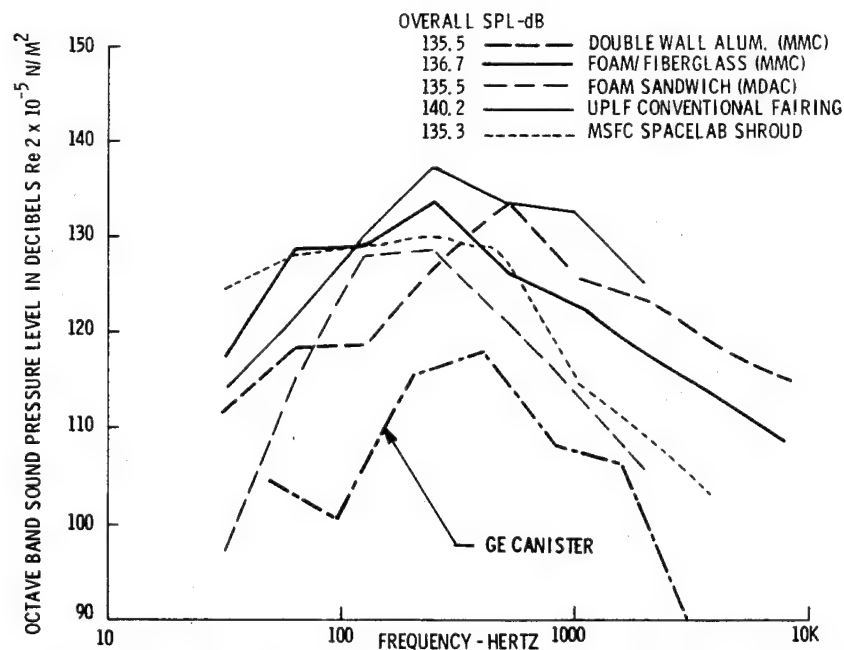
Viscoelastic Enclosure Performance is Excellent

NASA-GSFC Camera Bracket for IUE (1975)

Purpose - To prevent damage to camera from high deck vibroacoustic response

Design - Double picture frame mount with metal "dog-leg" springs and viscoelastic (SMRD) shear damping pads

- Isolate camera from deck and damp "dog-leg" resonance without elastomeric hysteresis

Analysis - Finite element analysis using modal strain energy sized damping pads for Q of 3

Results - Highly effective design with Q of about 4 due to outer frame twisting

- Flown on IUE secondary camera

SMRD Damped Design Using MSE Analysis Was Highly Effective

Damped Secondary Camera Bracket
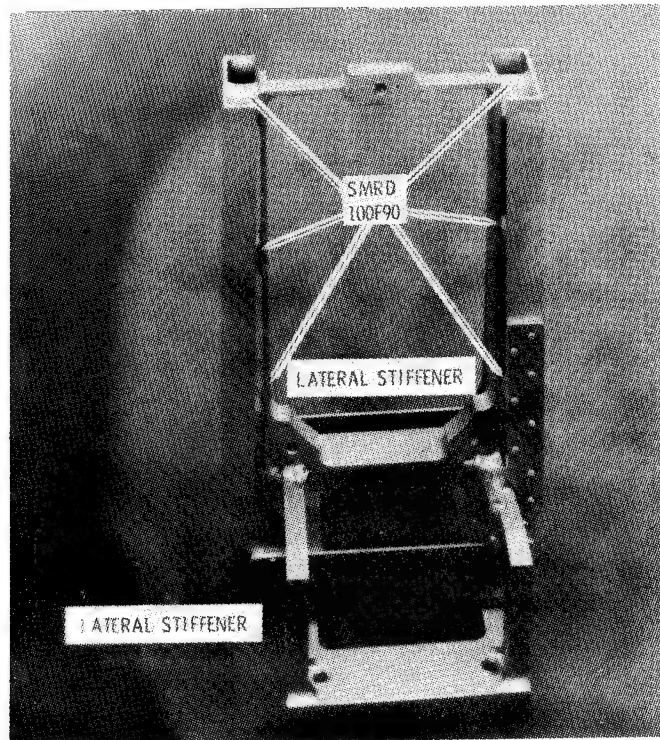
SAP Mode Shape
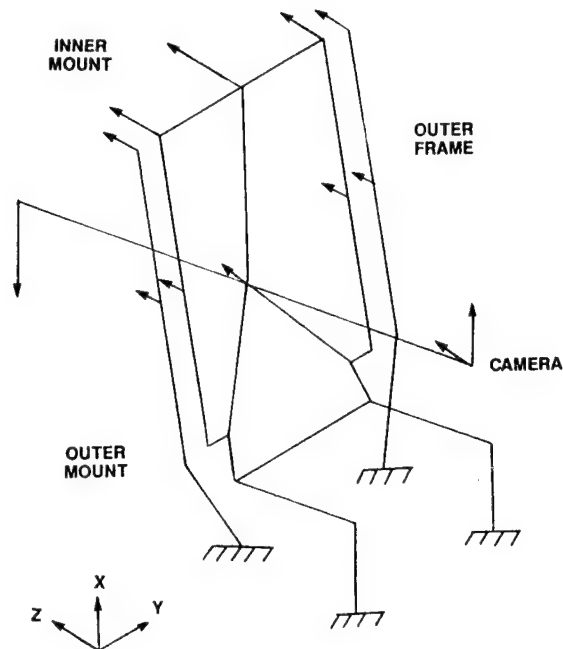
Camera Response on Hard-Mounted Damped Bracket
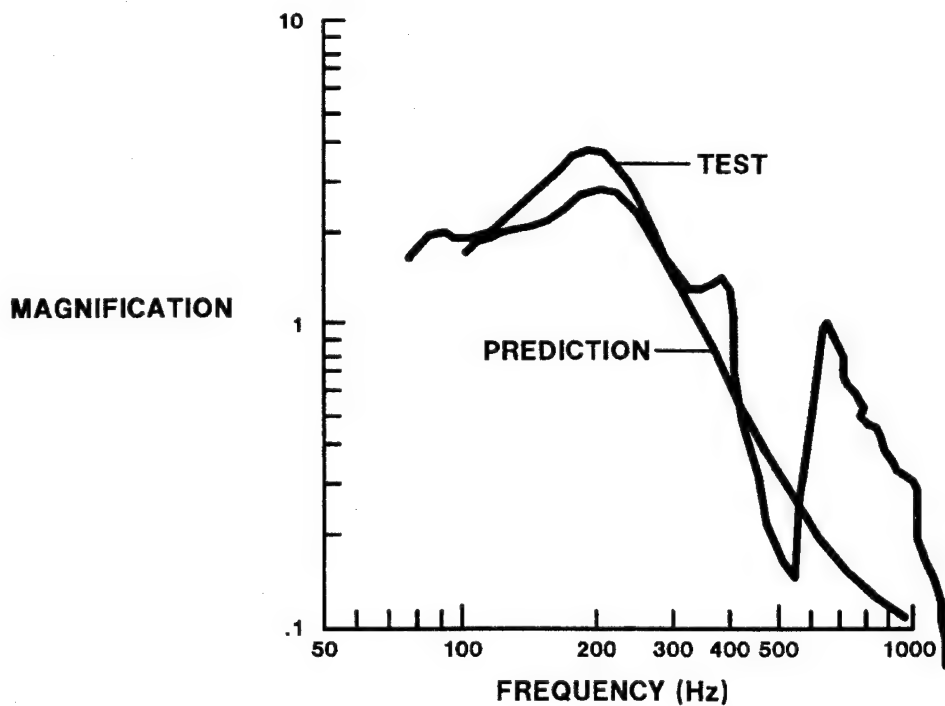
Good Agreement with Analytical Predictions

Gimbal Damping (1976)

Purpose – To provide lightweight gimbal design with amplification significantly less than original design (Q=40)

Design – Sperical sandwich construction with viscoelastic (SMRD) core strips

Analysis – SAP finite element analysis using modal strain energy post processor determined area coverage of SMRD

Results – Amplification reduced from 40 to 8

– Weight of gimbal reduced by 20 percent

Viscoelastic Design of Gimbal Was Highly Effective and Agreed Reasonably Well with Analysis

---

Standard Gimbal

Modified Gimbal Damping Approach
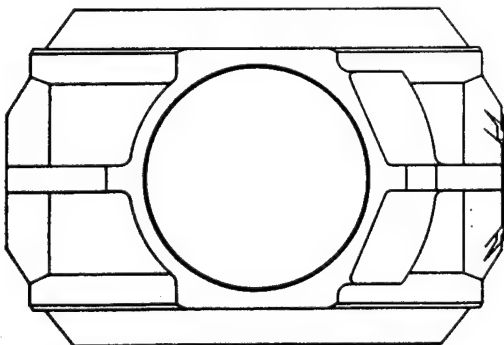
Standard Design Requires Thick Material and Rings for Stiffness and Strength
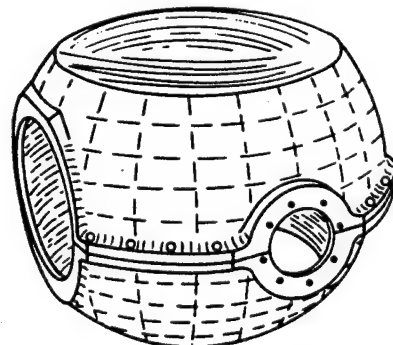
Sphericalized Gimbal Has Excess Material, Stiffness Removed

Damping Material Layout

1/2 GIMBAL WITH F90:
CONSTRAINING LAYER SHELL NOT SHOWN

GIMBAL
TYPICAL SECTION
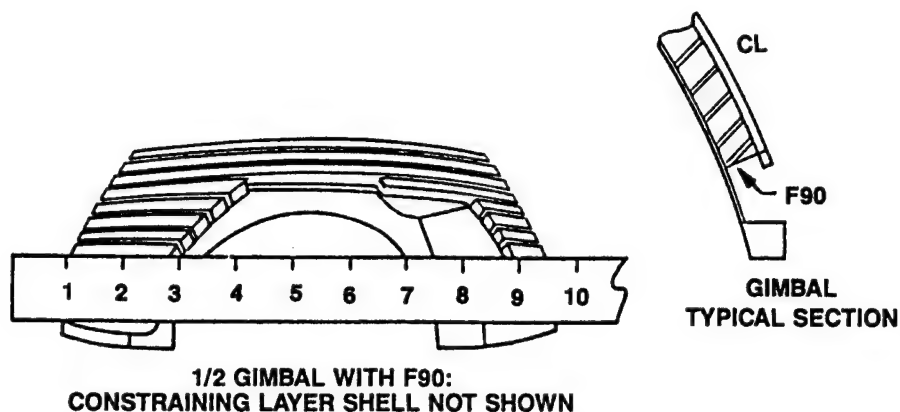
Constrained Layer Sandwich Cross Section
Provides Damping and Maintains Adequate Stiffness

Gimbal Vibration Response for 2G Input

STANDARD GIMBAL
Q = 40

RESPONSE G

DAMPED GIMBAL
Q = 8
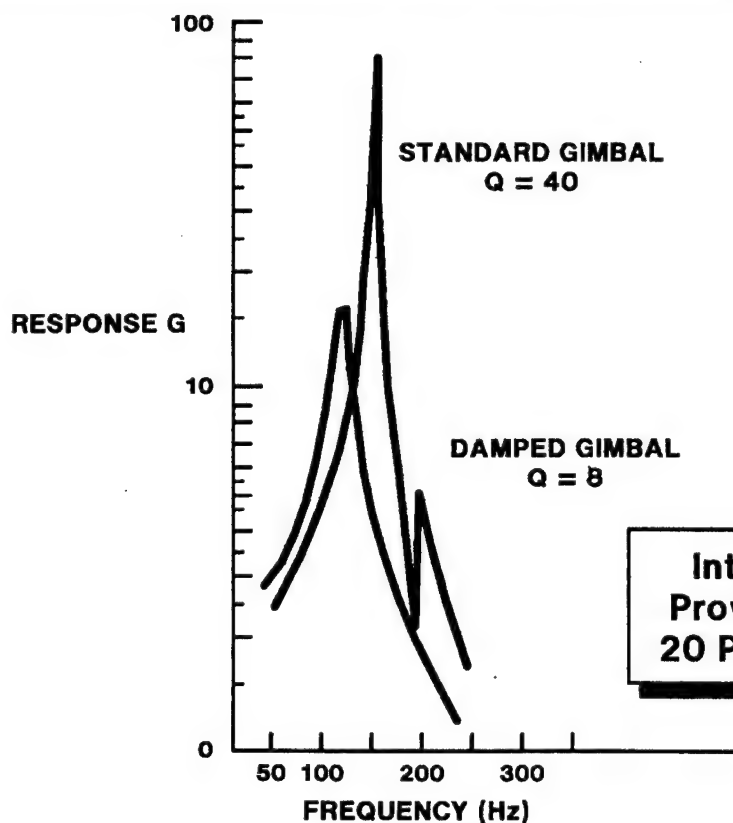
**Integrally Damped Design
Provides Low Response and
20 Percent Weight Reduction**

FREQUENCY (Hz)

AF Satellite Panel Damping (1978)

Purpose – To reduce vibroacoustic environment of a critical component to existing qualification levels

Design – Uniaxial graphite epoxy constrained layer SMRD damping strip added to structural panel supporting the component

Analysis – Nastran model using modal strain energy optimized strip dimensions for loss factor of 0.2 (Q=5)

Results – Vibroacoustic response of critical component reduced to existing specification levels

Damping Prevented Component Redesign And Preserved Heritage

Add-on Damper on Satellite Bulkhead Panel
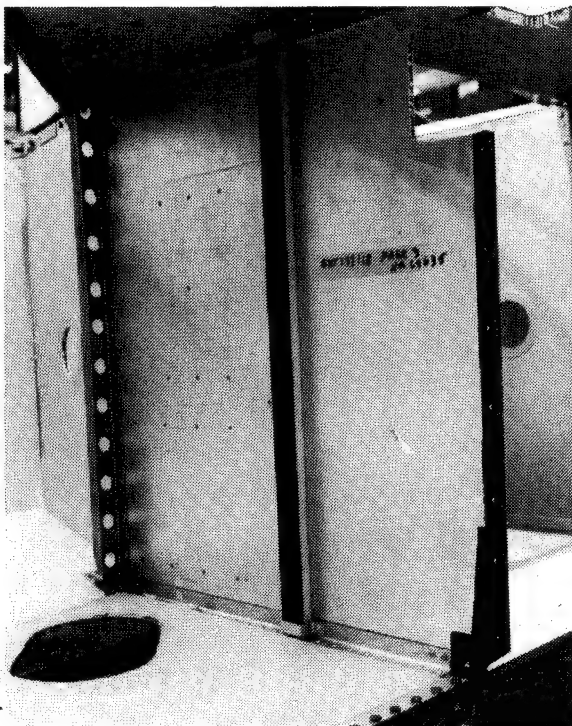
Robust Graphite/Epoxy Constrained Layer Damping Strip Was Designed

Analytical Approach

Nastran Model and First Mode Shape

CONSTRAINED LAYER DAMPER

CONSTRAINED LAYER DAMPER

COMPONENT CG
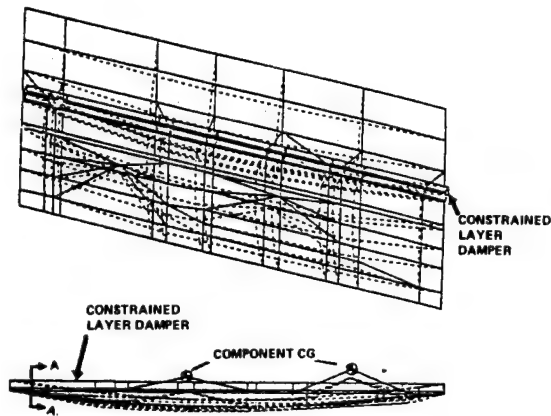
Nastran Parametric Optimization of Damper Design
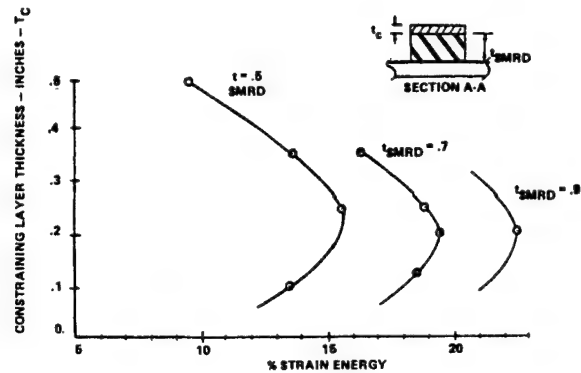
Optimization of Damping Treatment Used the Modal Strain Energy Method and Nastran

Panel Acoustic Response With and Without Damping Treatment

UNDAMPED

ACCEL. PSD (G^2/Hz)

DAMPED

FREQUENCY (Hz)
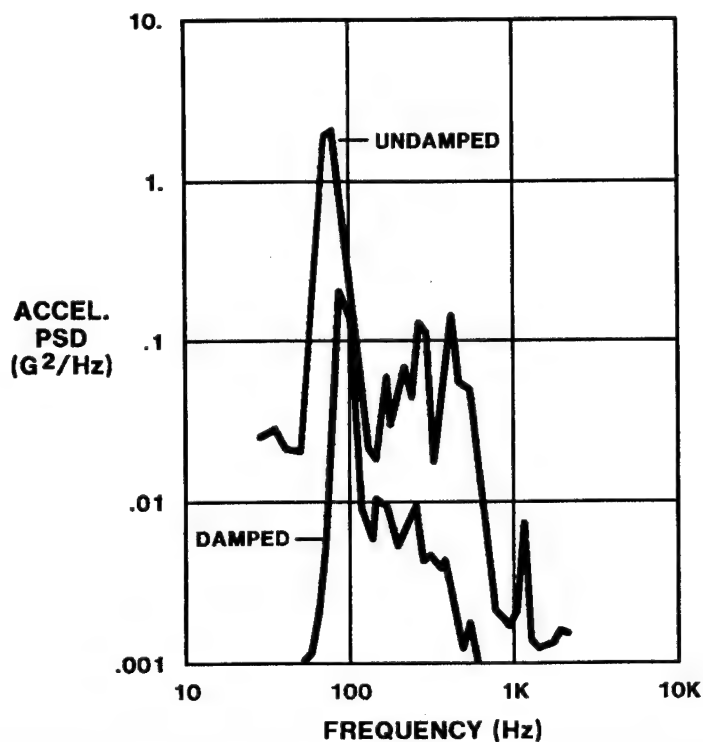
Damped Design Reduced Random Vibration to Specification Levels

AF-WRDC RELSAT Program (1983-1988)

Purpose – To demonstrate lightweight damping control of panel mounted component vibration

Design – Several integrally damped lightweight designs were developed including a highly effective damped stiffener using a graphite/epoxy honeycomb constraining layer

Analysis – Nastran models were studied parametrically to damp low frequency modes and minimize weight

– Reduced panel weight while adding damping

– Analysis predicted modal damping within approximately 20 percent

Results – Tests varied temperature to evaluate analysis

– Vibracoustic response reduced by 20 dB in low frequency range (two orders of magnitude PSD reduction)

– Specification levels reduced by 13 dB

RELSAT Demonstrated Highly Effective Lightweight Damped Designs

Damped Honeycomb Stiffener Panel

Nastran Panel Model – Honeycomb Stiffener/ SMRD 100F90
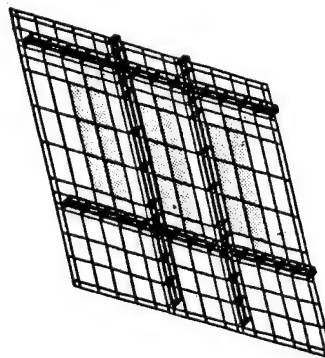
Nastran Was Used to Design an Integrally Damped Panel

Damped Panel Parametric Analysis

First Mode

Tcl (in.)
.25
.20
.15
.10

STRAIN ENERGY

DESIGN POINT

48.4 48.6 48.8 49.0 49.2
WT (lb.)

.3

.2

.1   .2   .3   .4
VEM THICKNESS (in.)
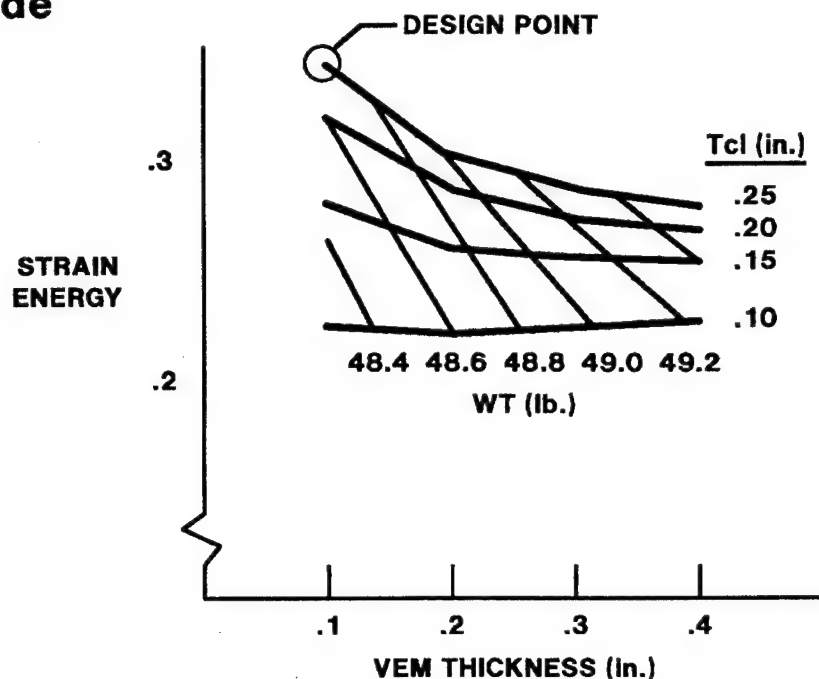
Minimum Weight Design Selected by Parametric Analysis

Test/Analysis Comparison

- ● TEST
- ▲ ANALYSIS WITH LAB A MATERIAL PROPERTIES
- ■ ANALYSIS WITH LAB B MATERIAL PROPERTIES

RESONANT FREQUENCY (Hz)

160
140
120
100
80
60

TEST W/O DAMPING

0   20   40   60   80   100   120
TEMPERATURE (°F)

LOSS FACTOR

.4
.3
.2
.1
0

0   20   40   60   80   100   120
TEMPERATURE (°F)
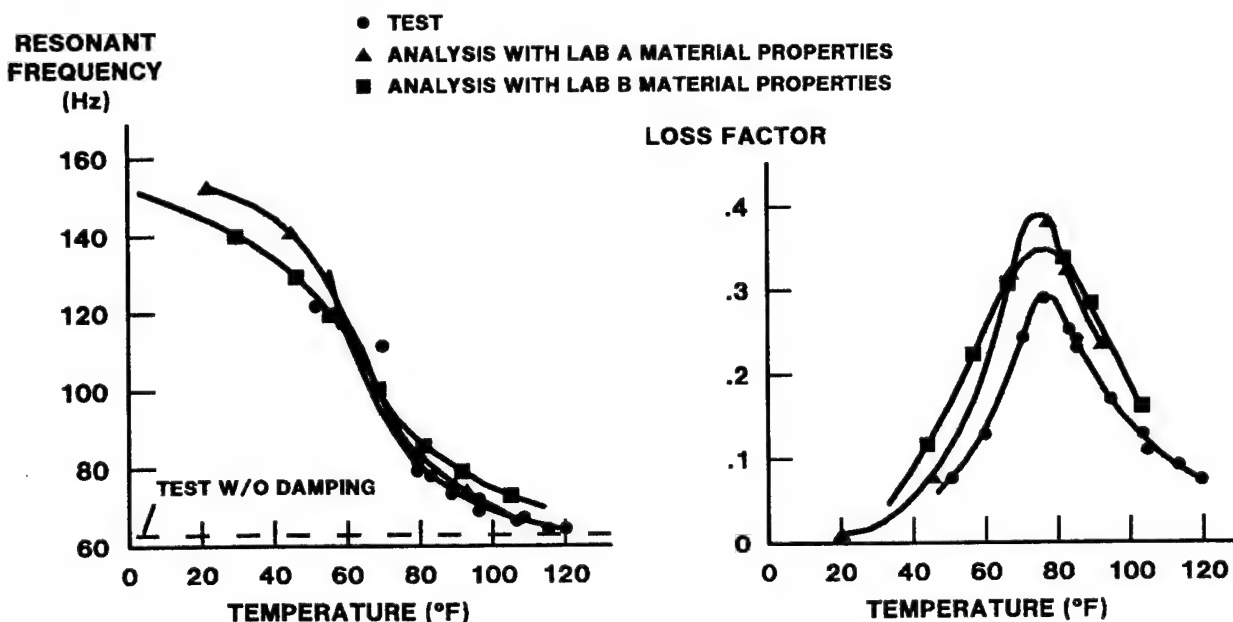
Controlled Temperature Variation is Essential to Evaluate Analysis

Vibroacoustic Response Out-of-Plane

95% Level at 72 Deg F Scaled to 145.3 dB Qual. Acoustic Level
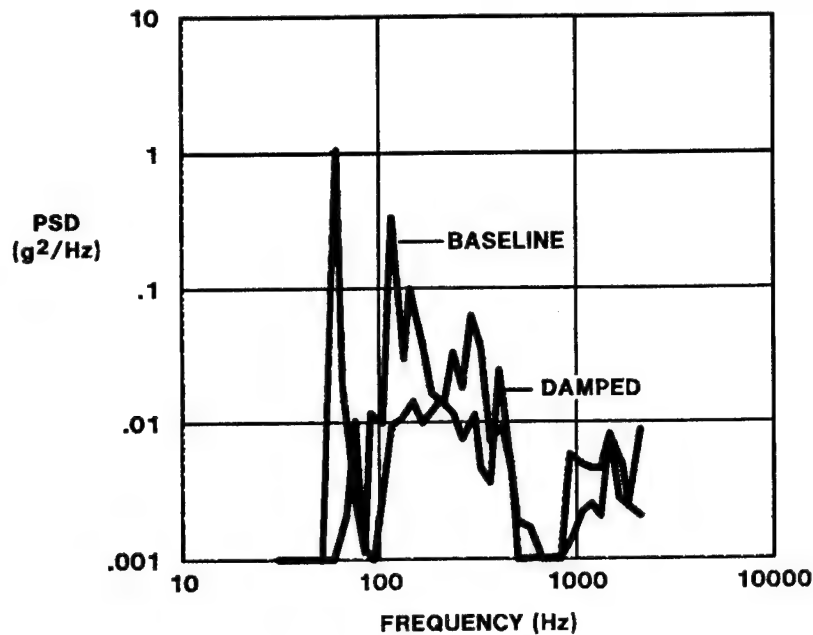
Damping Reduces Vibroacoustic Response by Up to 20 dB

DSCS Baseline & Damped Panel Qual Random Vibration Specs

Out-of-Plane Direction – Shuttle Launch at KSC

COMPONENT SPECS FOR BASELINE & DAMPED PANELS

RANDOM RESPONSE SPECTRA FOR BASELINE & DAMPED PANEL SPECS
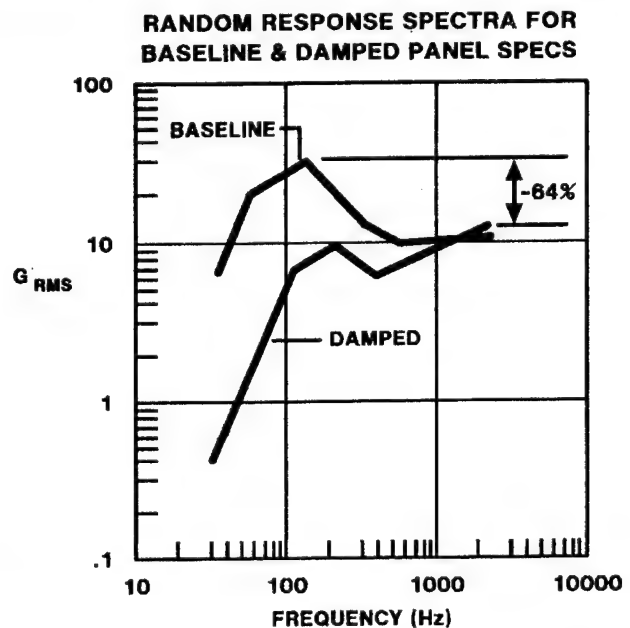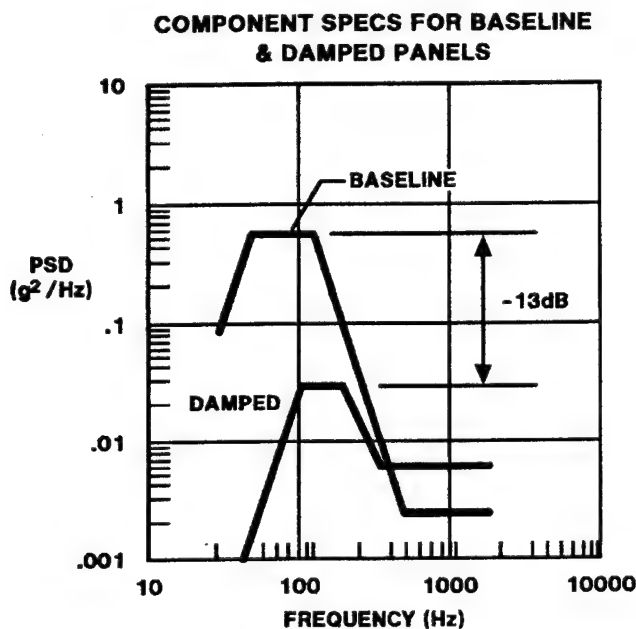
Damping Reduces Component Spec Level Significantly

Damping in Space

- SMRD damping material was used in printed wiring boards of modular attitude control subsystem (MACS)

- MACS was used on the Solar Max Mission (SMM) satellite

- Shuttle flight 41C recovered a MACS Unit from the SMM and returned it to earth for reuse

- Measured damping properties of the SMRD were found to agree with those of the original material after it had been in orbit for four years

> **SMRD Damping Materials Are Stable and Can Be Used in Orbital Applications**

Comparison of SMM SMRD 100F90 to Current Measurements by Lab B
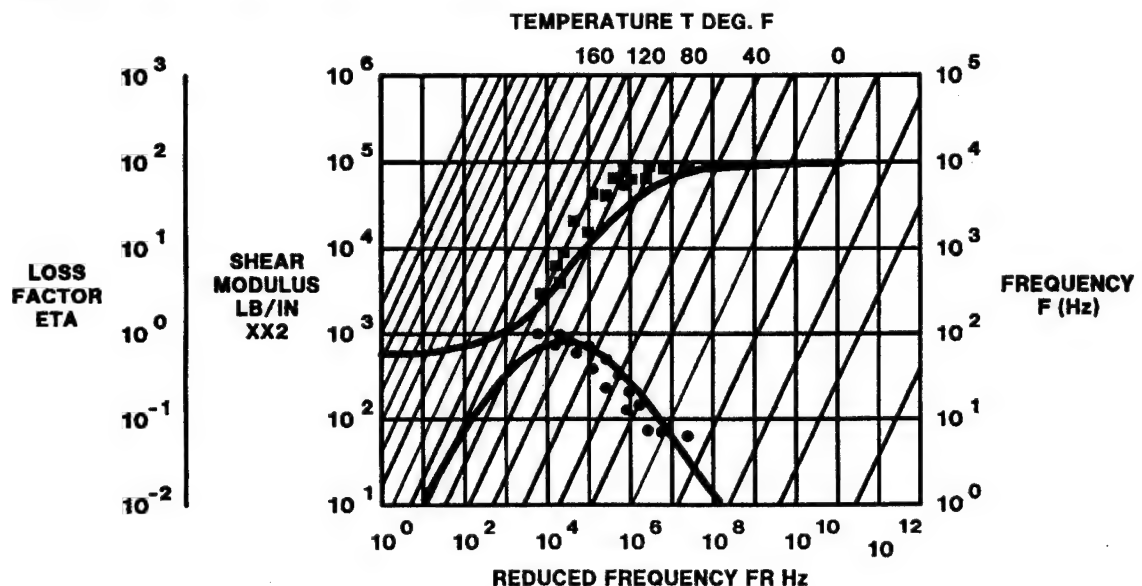
> **Good Damping Properties after 4 Years in Space**

Lessons Learned

- Design and analysis must show significant strain energy in the damping material for it to work
- Select or tailor a damping material to the specific application considering temperature, frequency, modulus and other requirements
- Integrate damping into the design to improve performance
- Temperature must be considered in determining damping material properties in addition to frequency
- Temperature should be controlled and varied to provide analytical correlation -- glassy and rubbery limits are helpful in assessing model adequacy
- Constrained layer damping configurations are one of the most effective designs
- Damping effect on loads should be considered to achieve weight reduction and more effective damping
- Finite analysis methods can be used to predict damped behavior with reasonable accuracy
- Stable damping materials (e.g. SMRD) are available which are space compatible

> **Damping Provides a Robust Design and Should Be Considered in Addition to Stiffening**

Summary

- Damping is maturing as a predictable means of controlling resonant vibration of large and small complex structures
  - Printed wiring boards
  - Acoustic cover
  - Camera bracket
  - Gimbal
  - Equipment panels

- Analysis methods are available using modal strain energy

- Designs that integrate damping into the configuration can improve performance and reduce weight

- Experimental results have confirmed analytical predictions and indicate viscoelastic material properties limit prediction accuracy

- GE Astro Space Division has integrated damping into satellite designs

AN AIRCRAFT MODAL SUPPRESSION YAW DAMPER SYSTEM

J.R. FULLER

BOEING COMMERCIAL AIRPLANES

SEATTLE, WASHINGTON

DAMPING '89

FEBRUARY 8-10, 1989

WEST PALM BEACH, FLORIDA

A CONFERENCE SPONSORED BY THE

FLIGHT DYNAMICS LABORATORY

AIR FORCE WRIGHT AERONAUTICAL LABORATORIES

WRIGHT-PATTERSON AIR FORCE BASE, OHIO

Objectives of Modal Suppression Yaw Damper

- Control Dutch Roll Response

- Provide Good Turn Coordination

- Suppress Flexible Body Modes

  - Improve Lateral Ride Comfort

747

PSD of the Lateral Acceleration at the Aft Galley

Peak at 0.007

PSD,
g²/rad/sec

Frequency, Hz
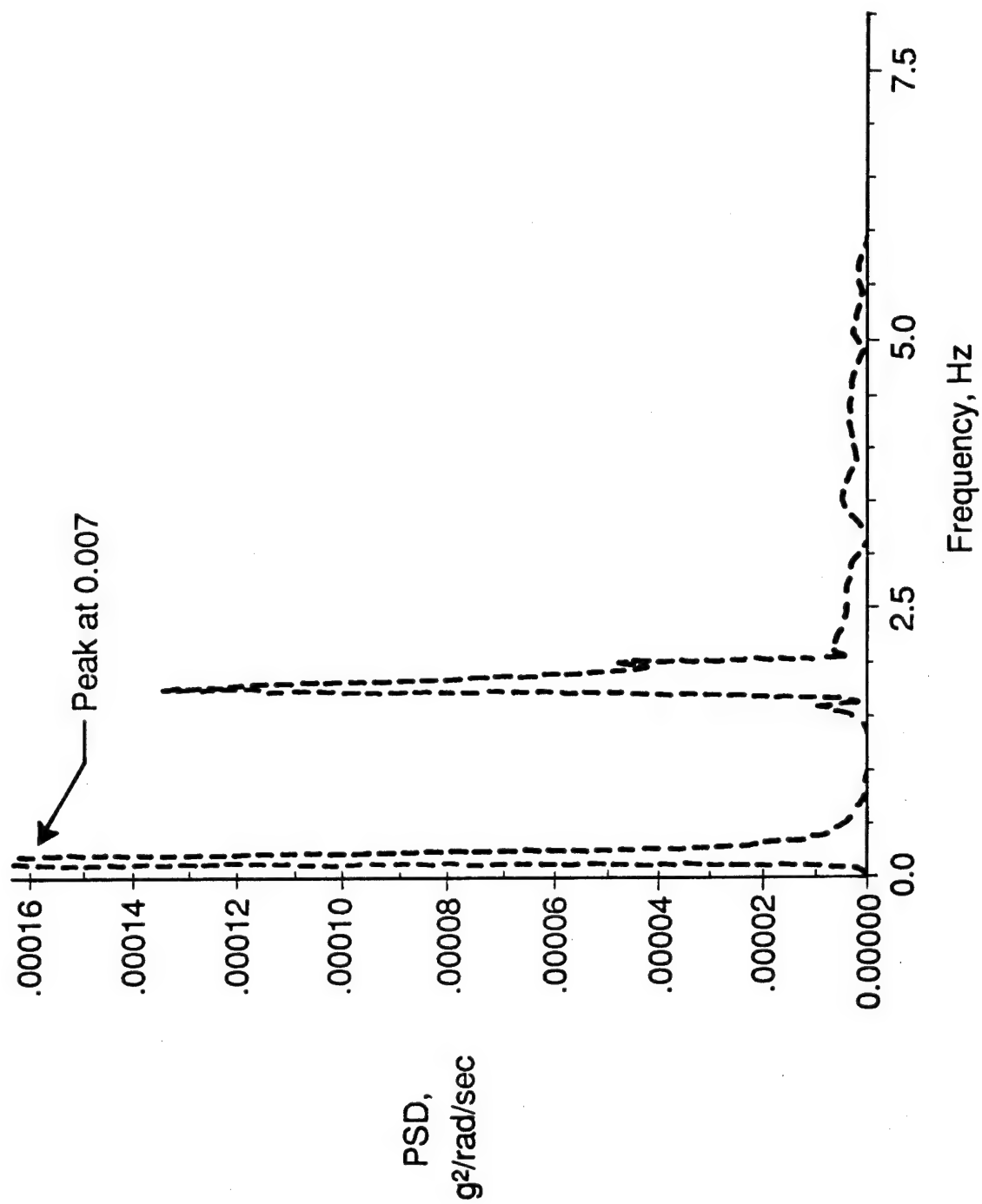
747
PSD of the Lateral Accleration at the Pilot Station

PSD,
g²/rad/sec

Frequency, Hz
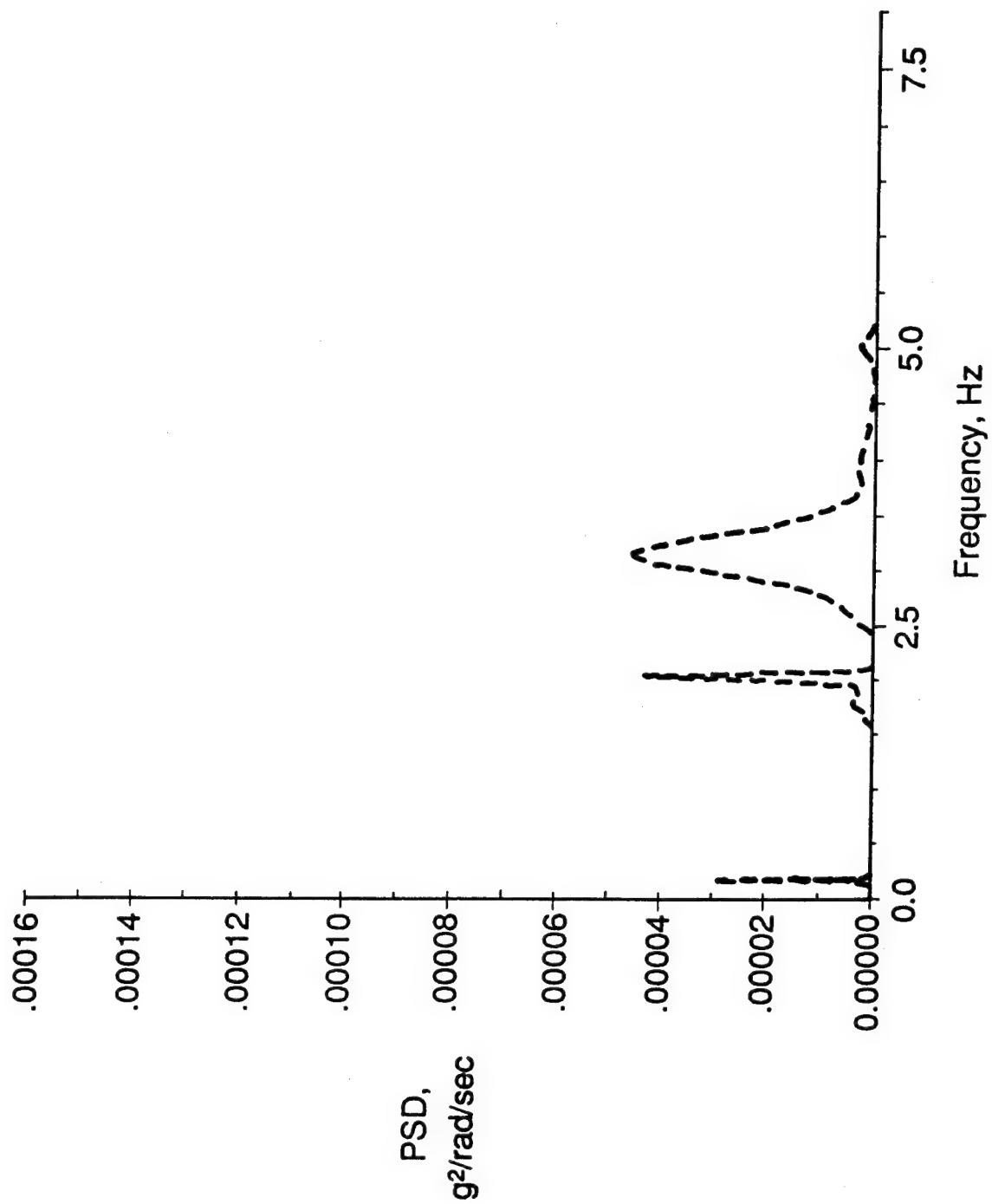
747
Plant Model for Aft Filter Design
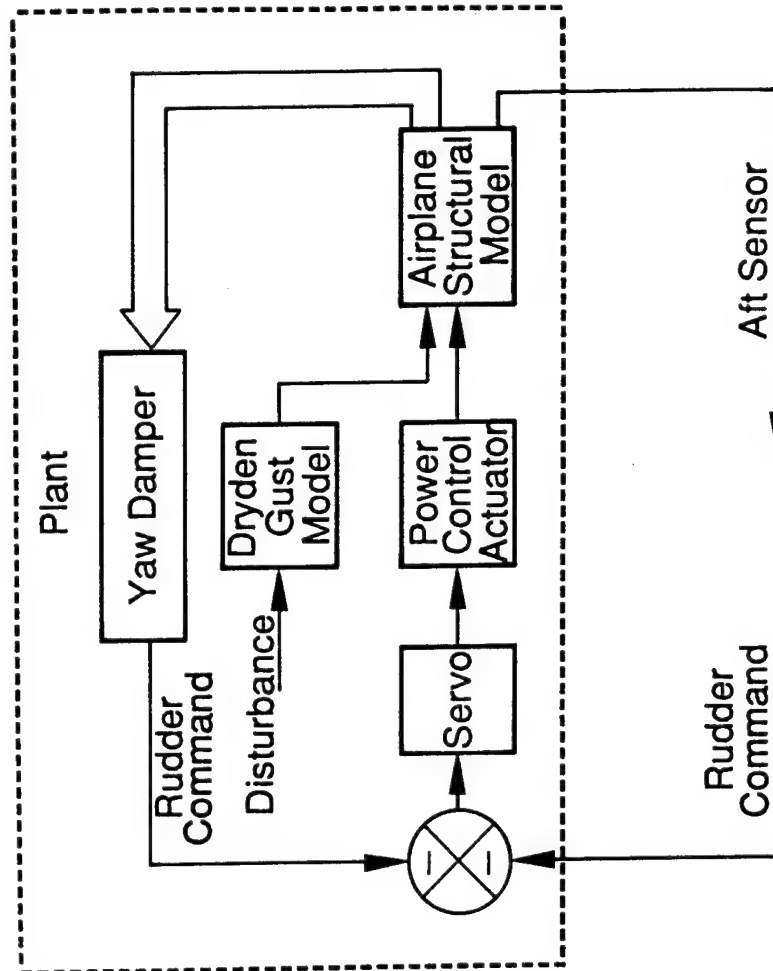
747
Transfer Function
Rudder Command to Aft Galley Sensor

Phase, degrees

Gain, dB

Frequency, Hz
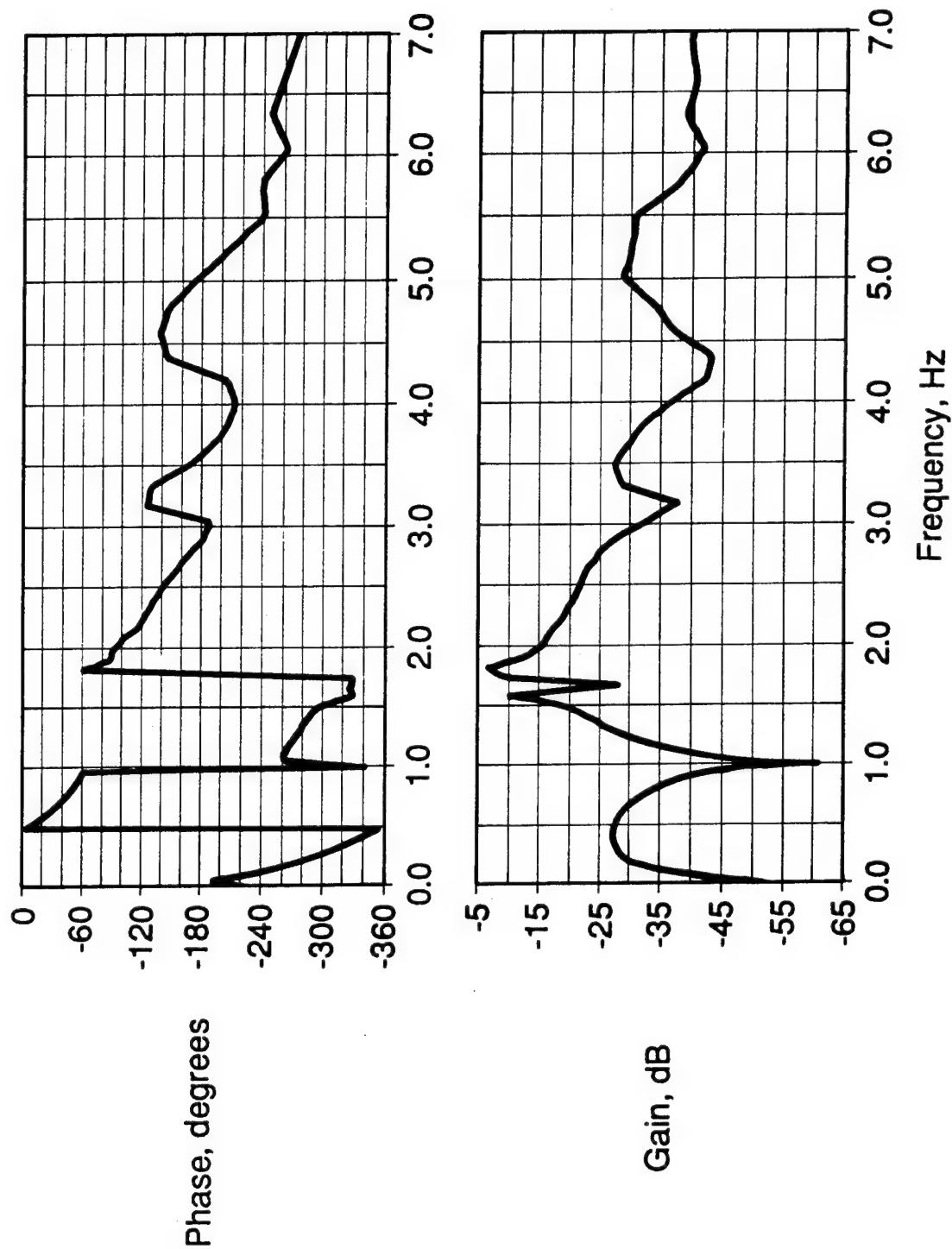
747
Transfer Function for the Aft Cabin Sensor Filter

Phase, degrees

Gain, dB

Frequency, Hz
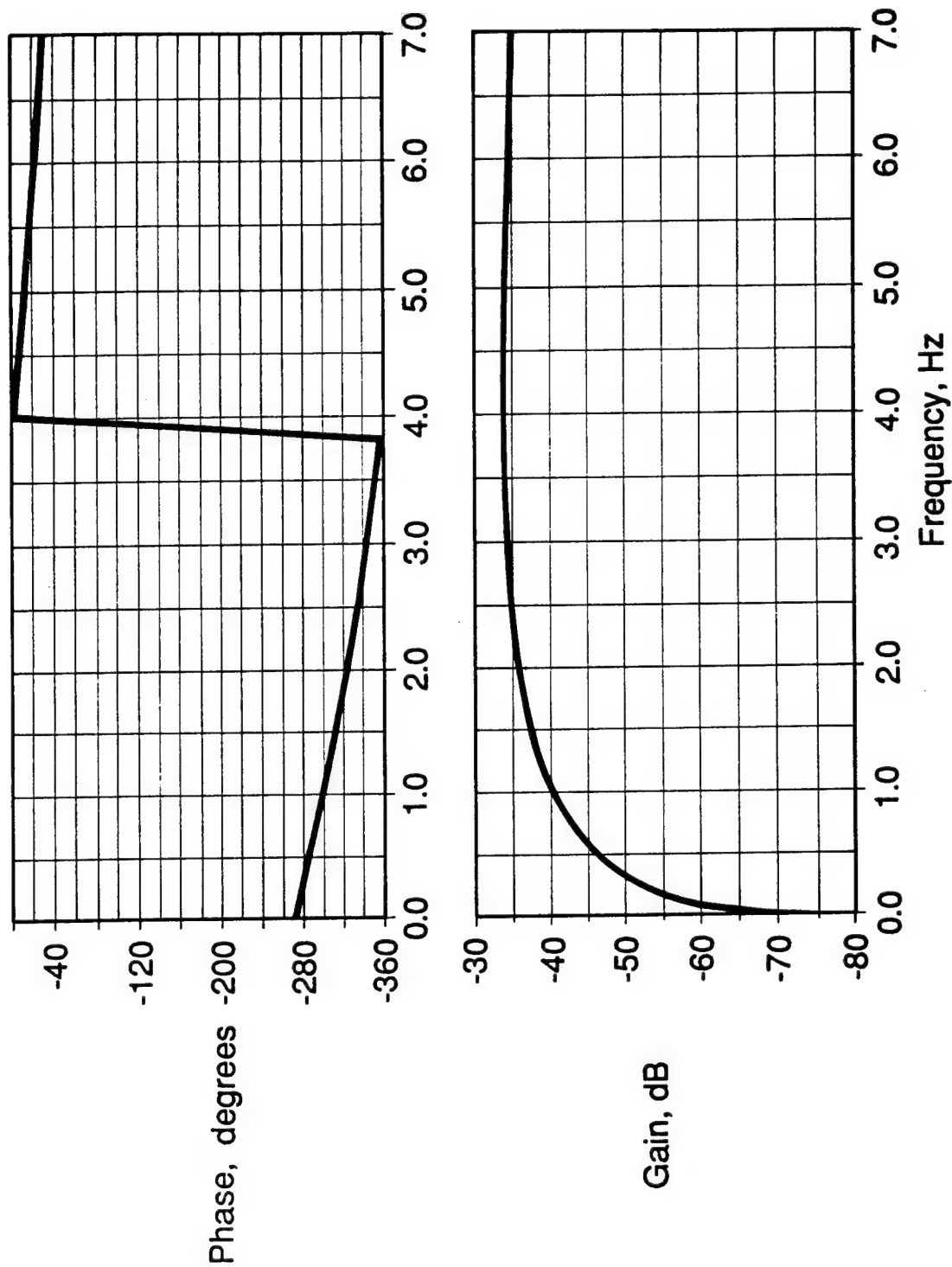
747
Plant Model for Pilot Station Filter Design

Plant

Yaw Damper

Dryden Gust Model

Power Control Actuator

Airplane Structural Model

Servo

Aft Filter

Aft Sensor

Front Sensor

Rudder Command

Disturbance

Rudder Command
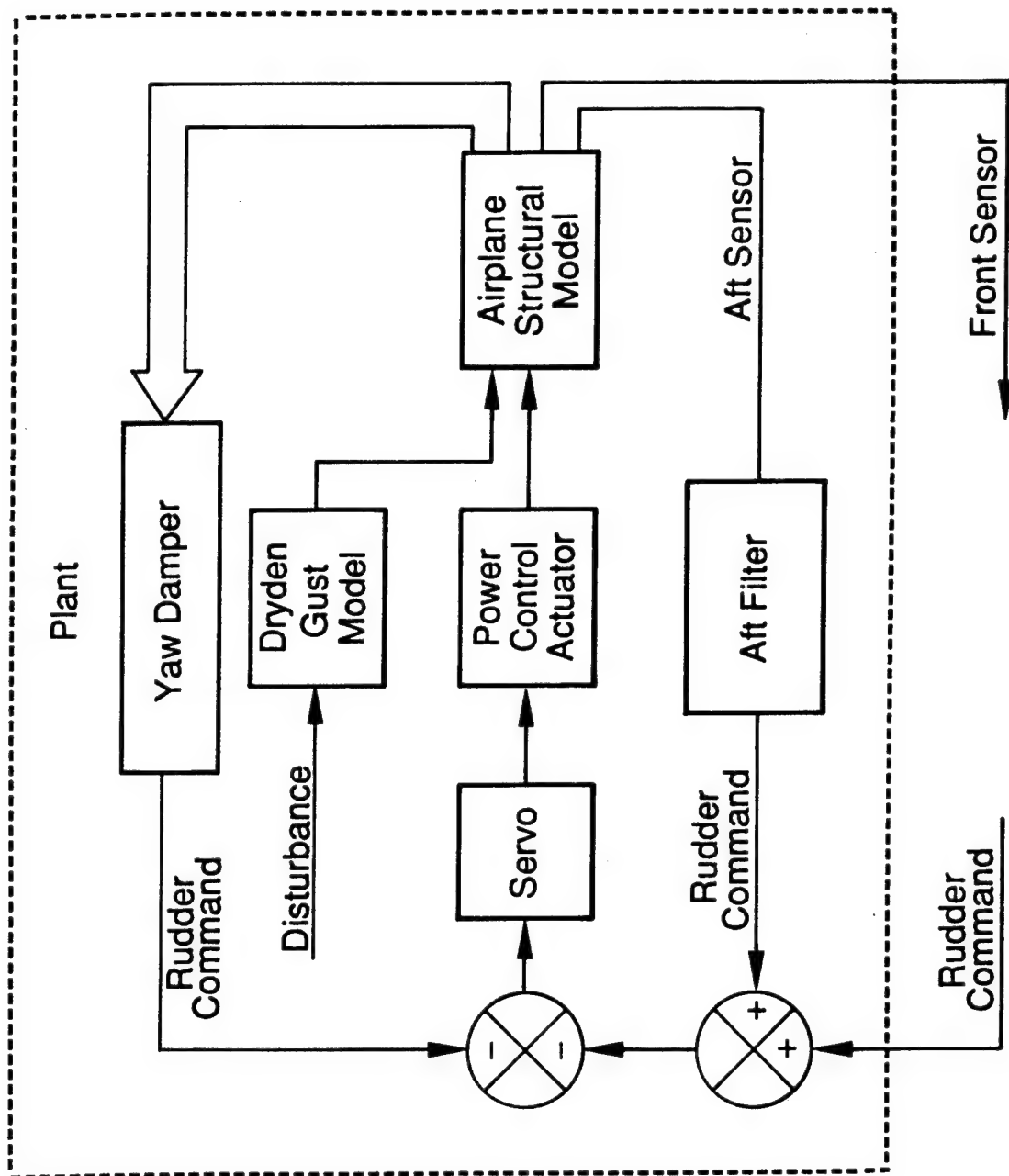
Rudder Command

747
Transfer Function
Rudder Command to Pilot Station Sensor
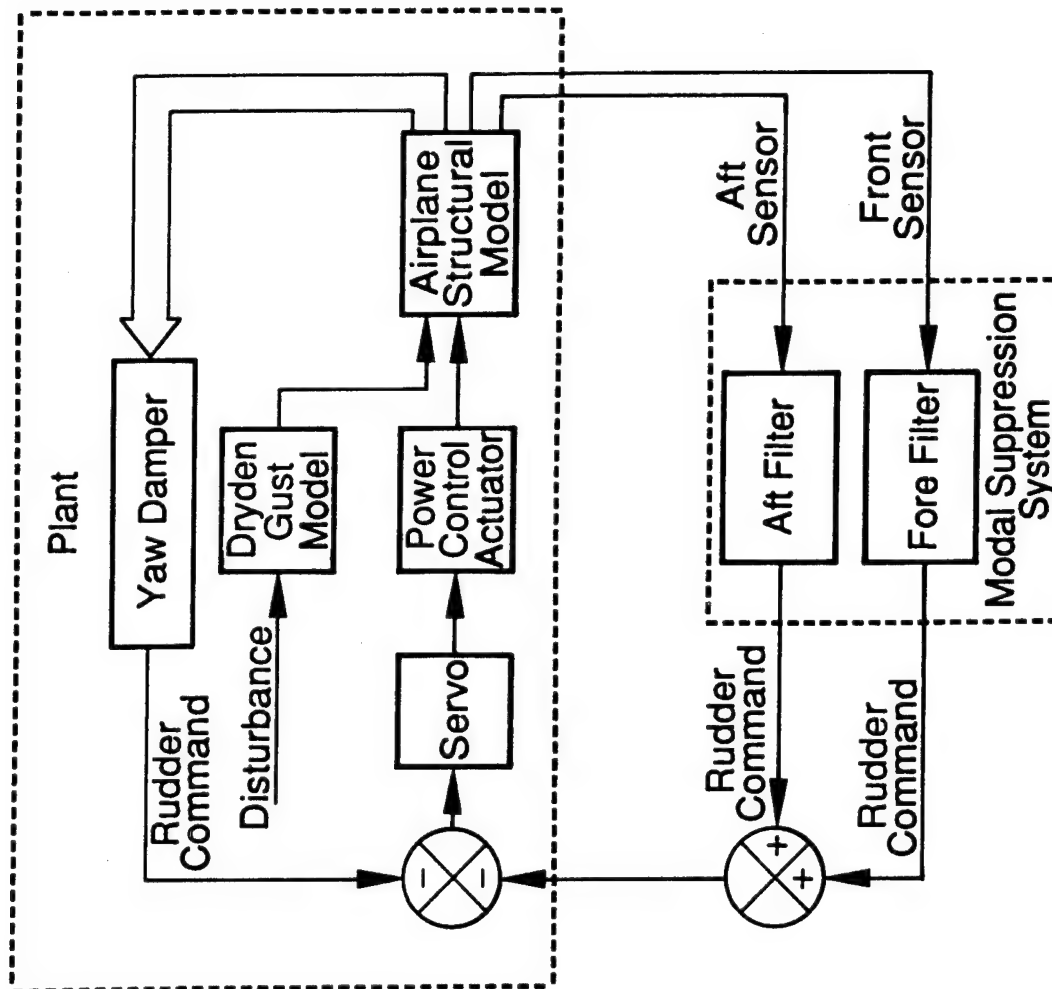
Phase, degrees

Gain, dB

Frequency, Hz

747
Closed-Loop System

747
PSD of the Lateral Acceleration at the Aft Galley

Closed-Loop Airplane
Basic Airplane

PSD,
g²/rad/sec

Frequency, Hz

0.0   2.5   5.0   7.5

.00016
.00014
.00012
.00010
.00008
.00006
.00004
.00002
0.00000
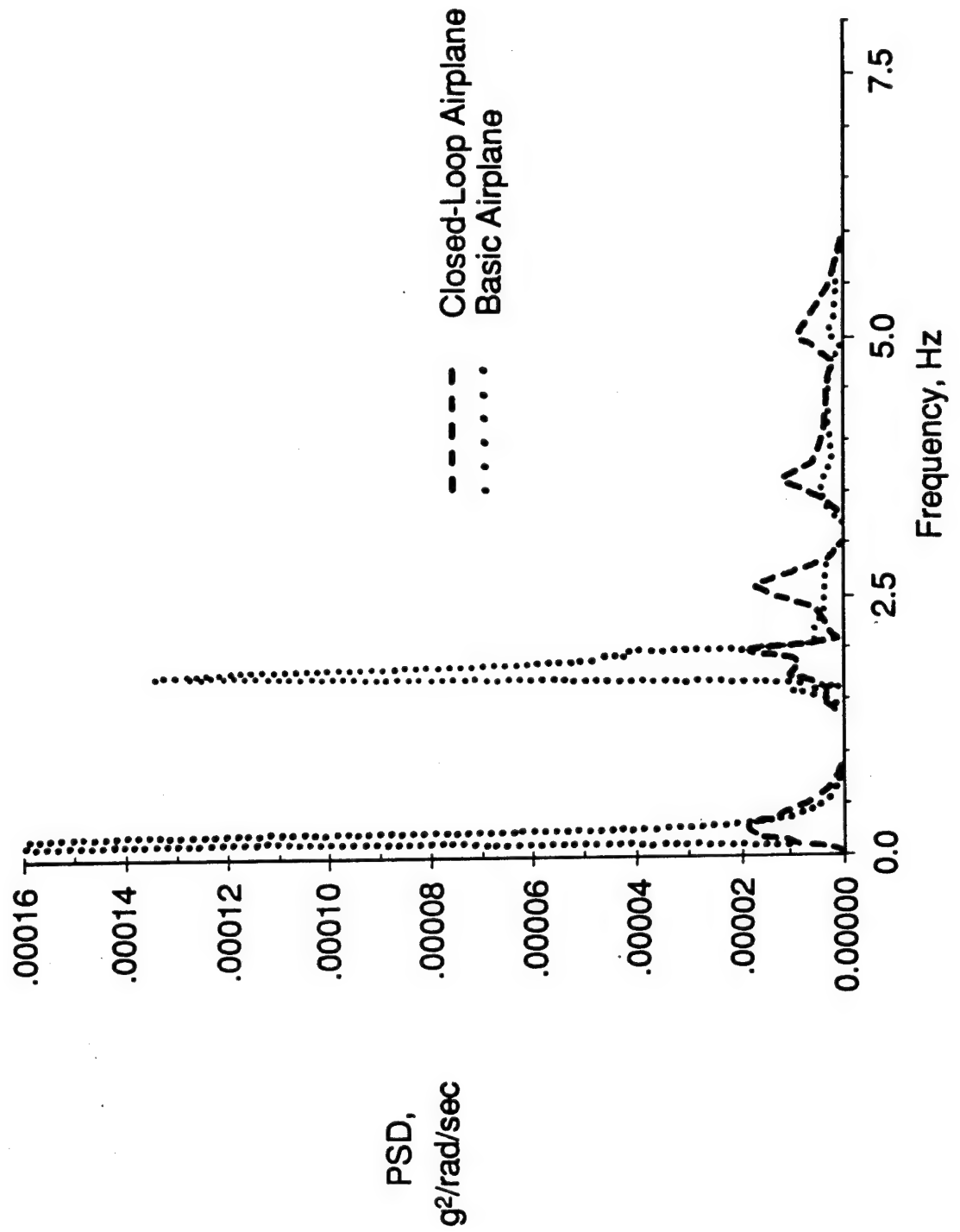
747
PSD of the Lateral Acceleration at Pilot Station

Closed-Loop Airplane

Basic Airplane

Frequency, Hz

PSD,
g²/rad/sec
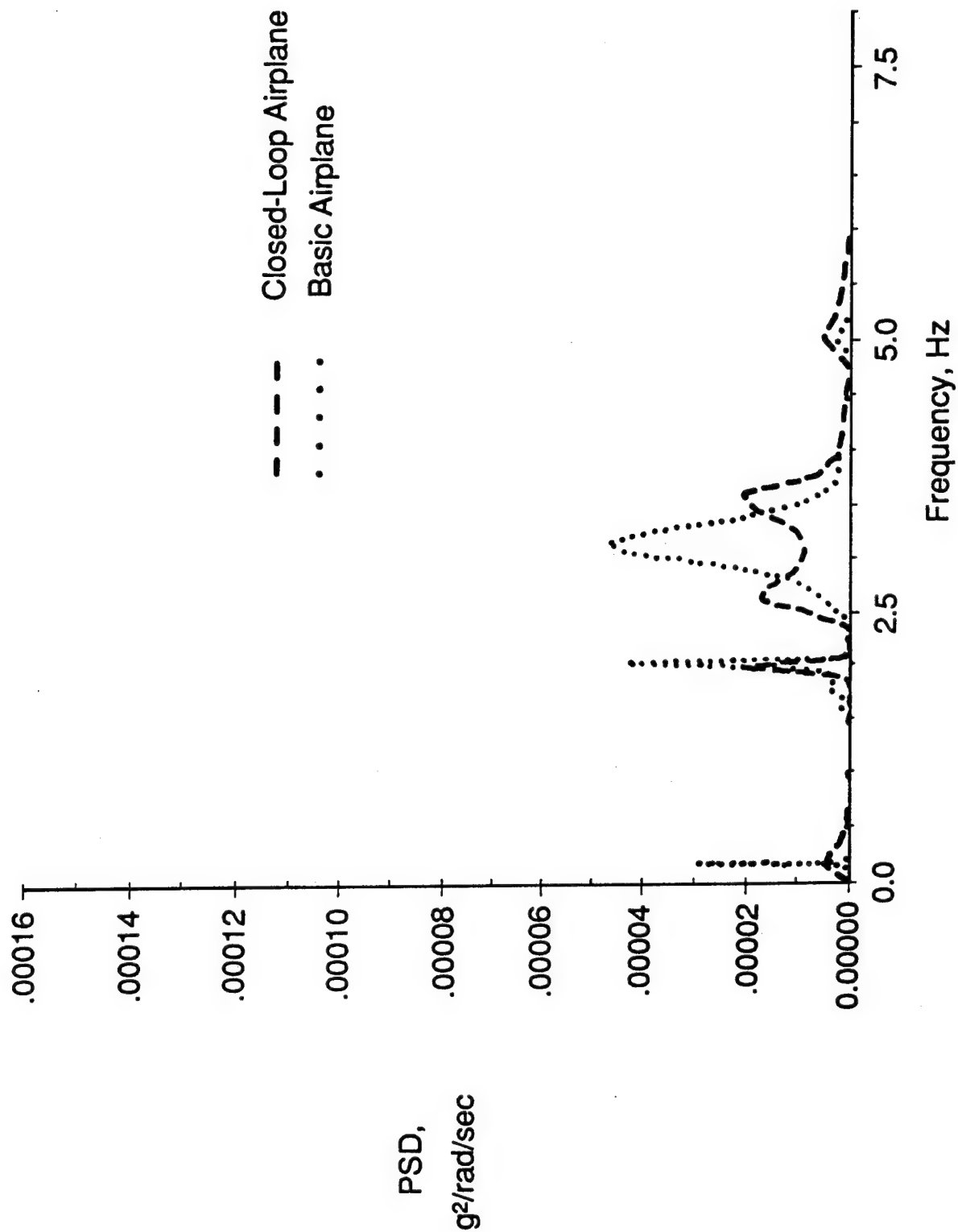
747-400 / PW4000 (RT401)
Modal Suppression Yaw Damper Flight Test 4-15
6 July 1988 (15:14:00)

- **Airplane Configuration**

  - **Typical Revenue Payload with FWD CG**

    - OEW   365.8 K   @   26.1 % MAC
    - ZFW   402.9 K   @   17.6 % MAC
    - T/O GW   685.0 K   @   10.0 % MAC
    - @ Test Condition 586.5 K   @   12.8 % MAC

  - **Fuel Loading**

	T/O (% Full)	Flight Condition (Approx.)
Center Wing	45	~45
Main #1	100	~100
Main #2	100	<50
Main #3	100	<50
Main #4	100	~100
Res #2	0	0
Res #3	0	0
Stabilizer	0	0

  - **Flight Condition** (Turbulence)

    $M = .45$

    $h = 8000$ ft

747-400
Power Spectrum
Vertical Acceleration - Right Wingtip

Power
Spectral
Density,
g²/Hz

Frequency, Hz

Modal
Suppression OFF

Modal
Suppression ON
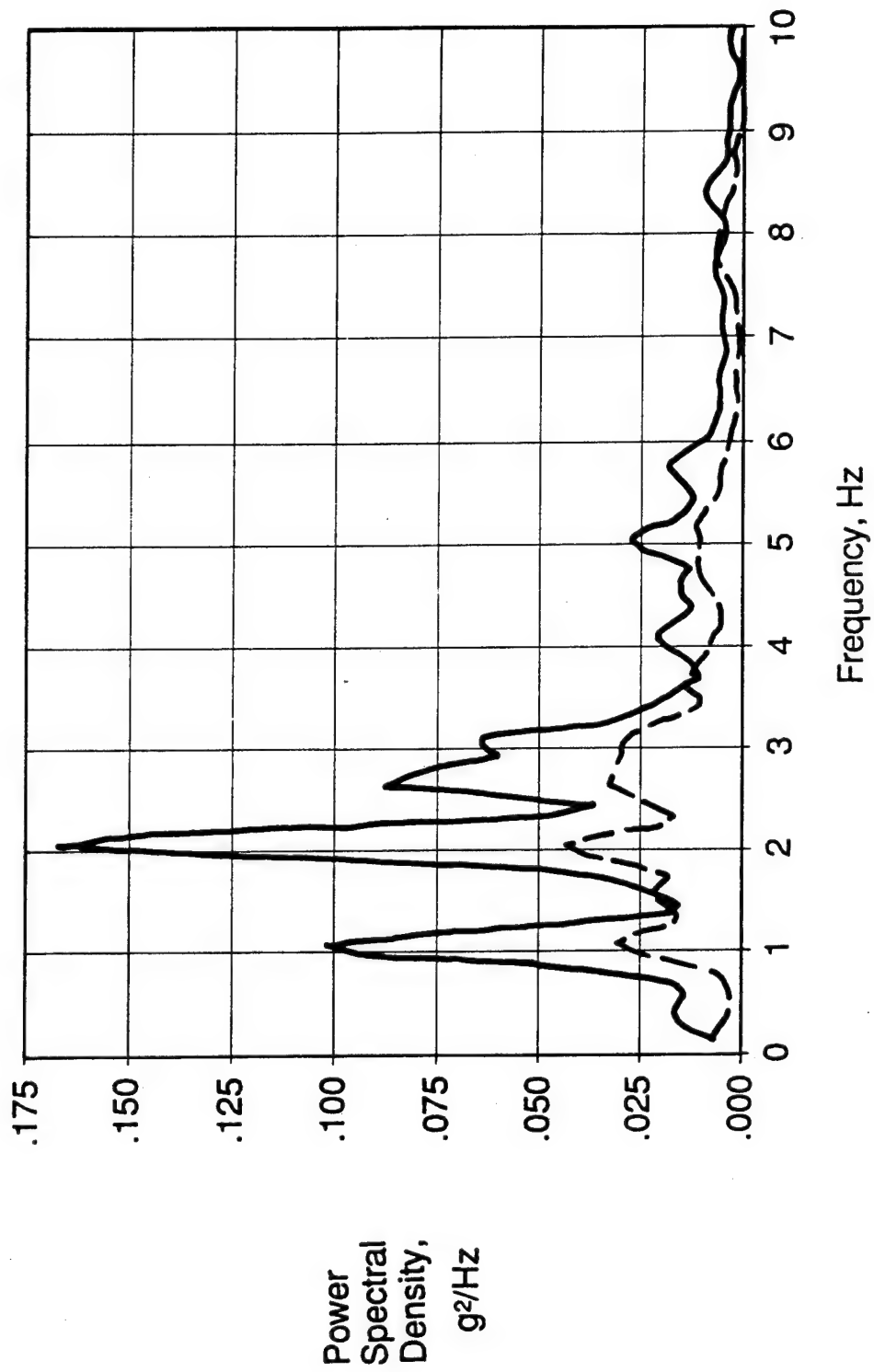
747-400
Power Spectrum
Vertical Acceleration - Left Wingtip

Power Spectral Density, g²/Hz

Frequency, Hz

Modal Suppression OFF

Modal Suppression ON
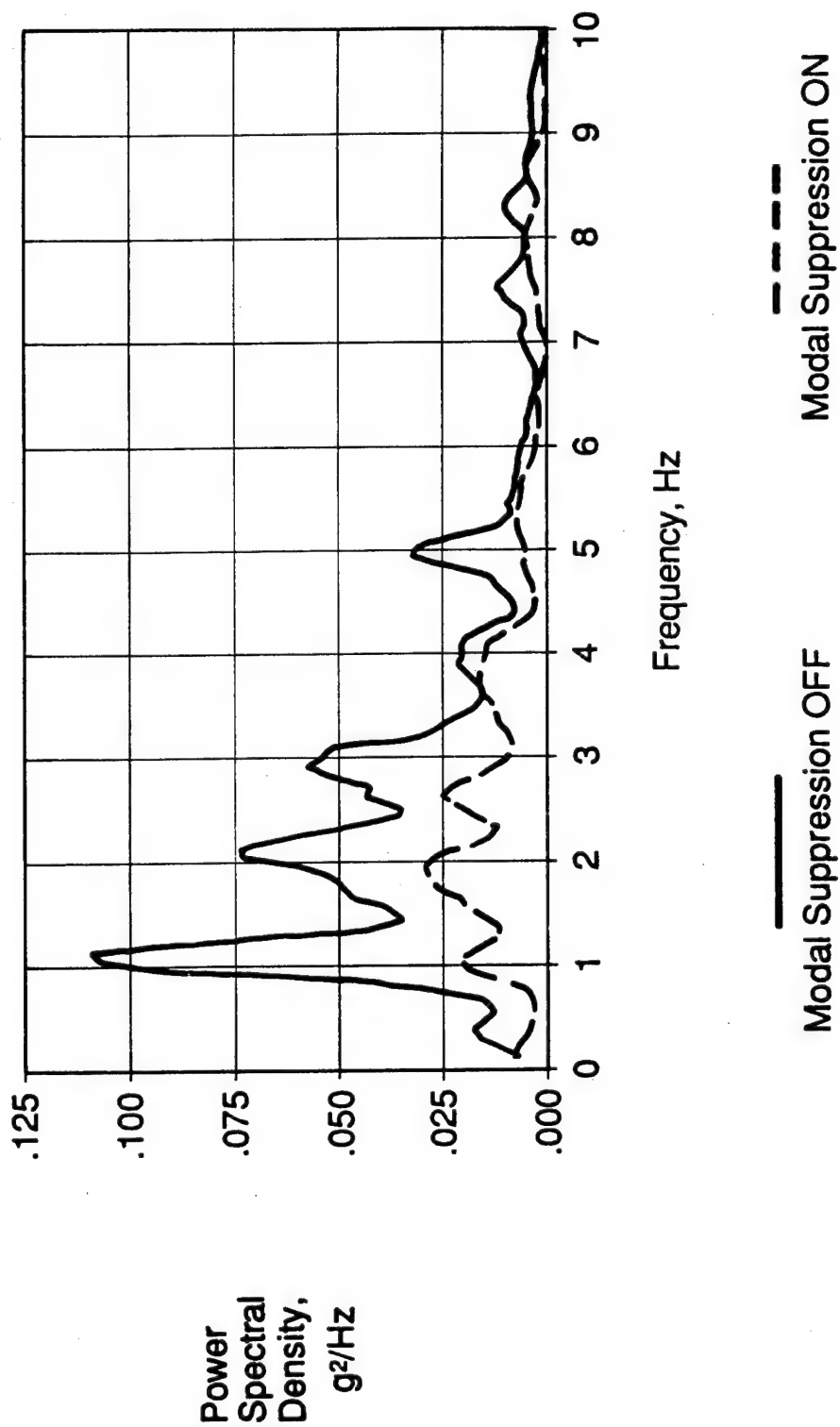
747-400
Power Spectrum
Lateral Acceleration - Fin Tip

Modal
Suppression OFF

Modal
Suppression ON

Power
Spectral
Density,
g²/Hz

Frequency, Hz
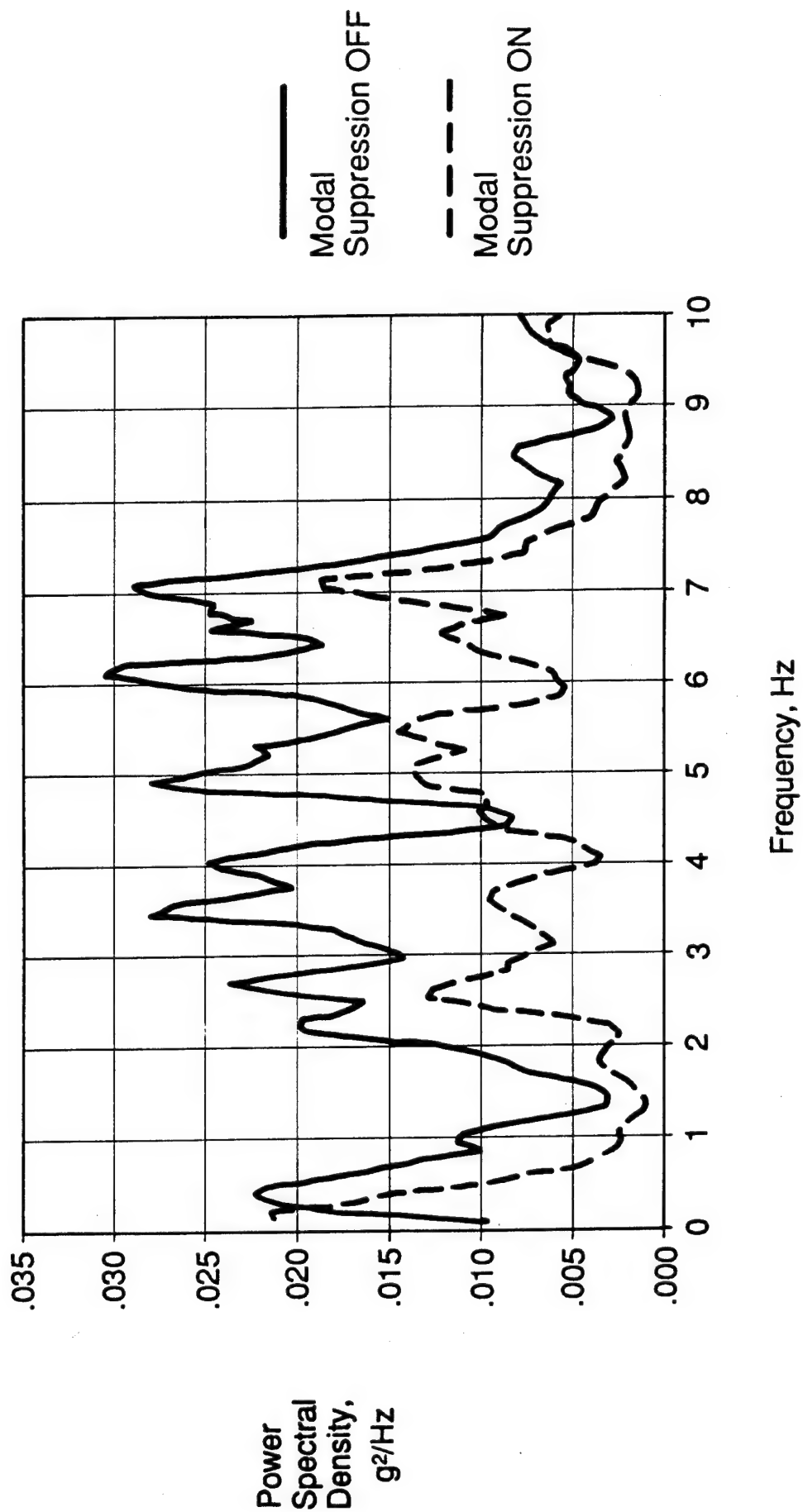
747-400
Power Spectrum
Vertical Acceleration - Left Stabilizer Tip
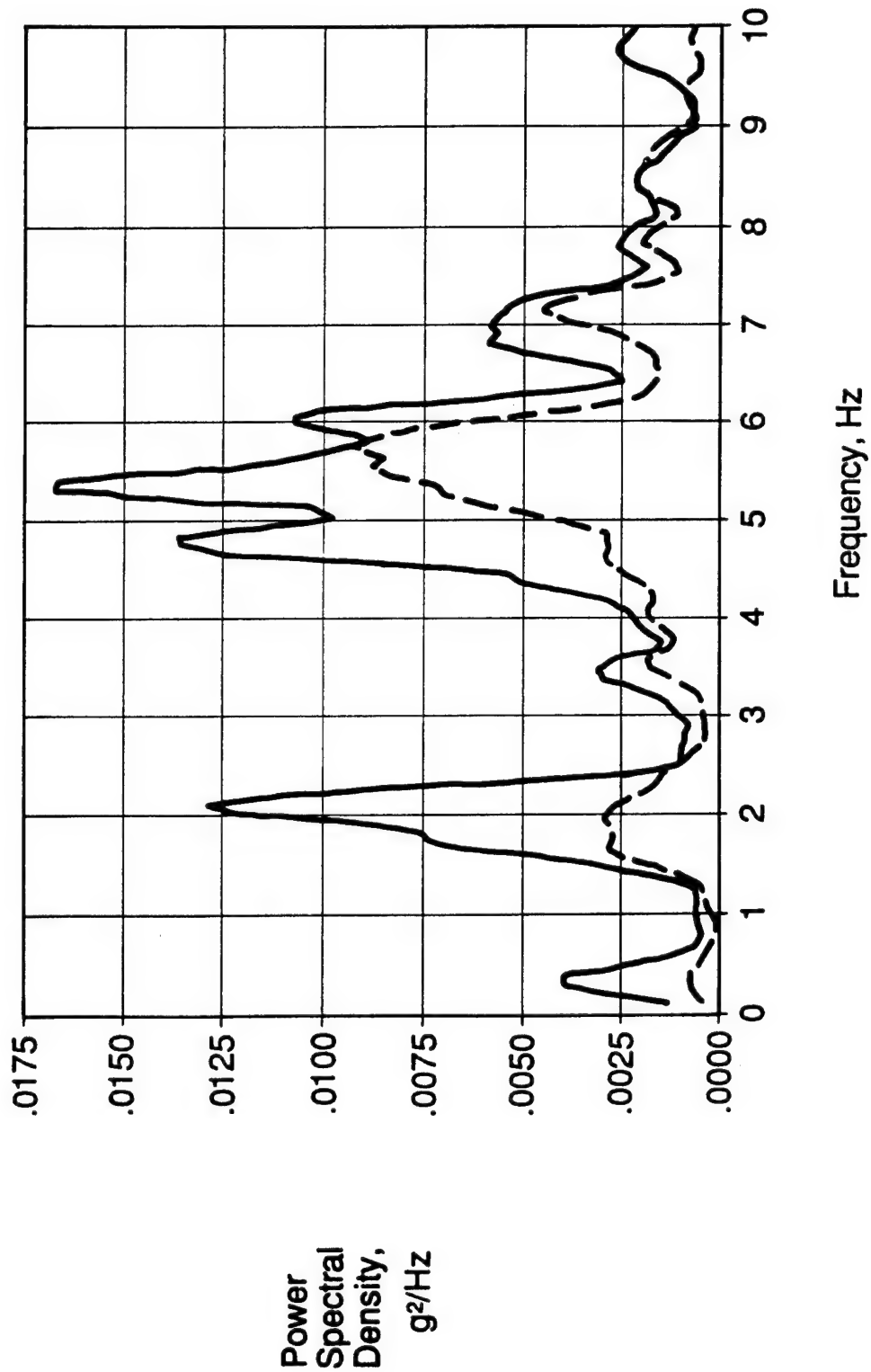
Power Spectral Density, g²/Hz

Frequency, Hz

Modal Suppression OFF

Modal Suppression ON

747-400
Power Spectrum
Lateral Acceleration at Pilots Seat

Modal Suppression OFF

Modal Suppression ON
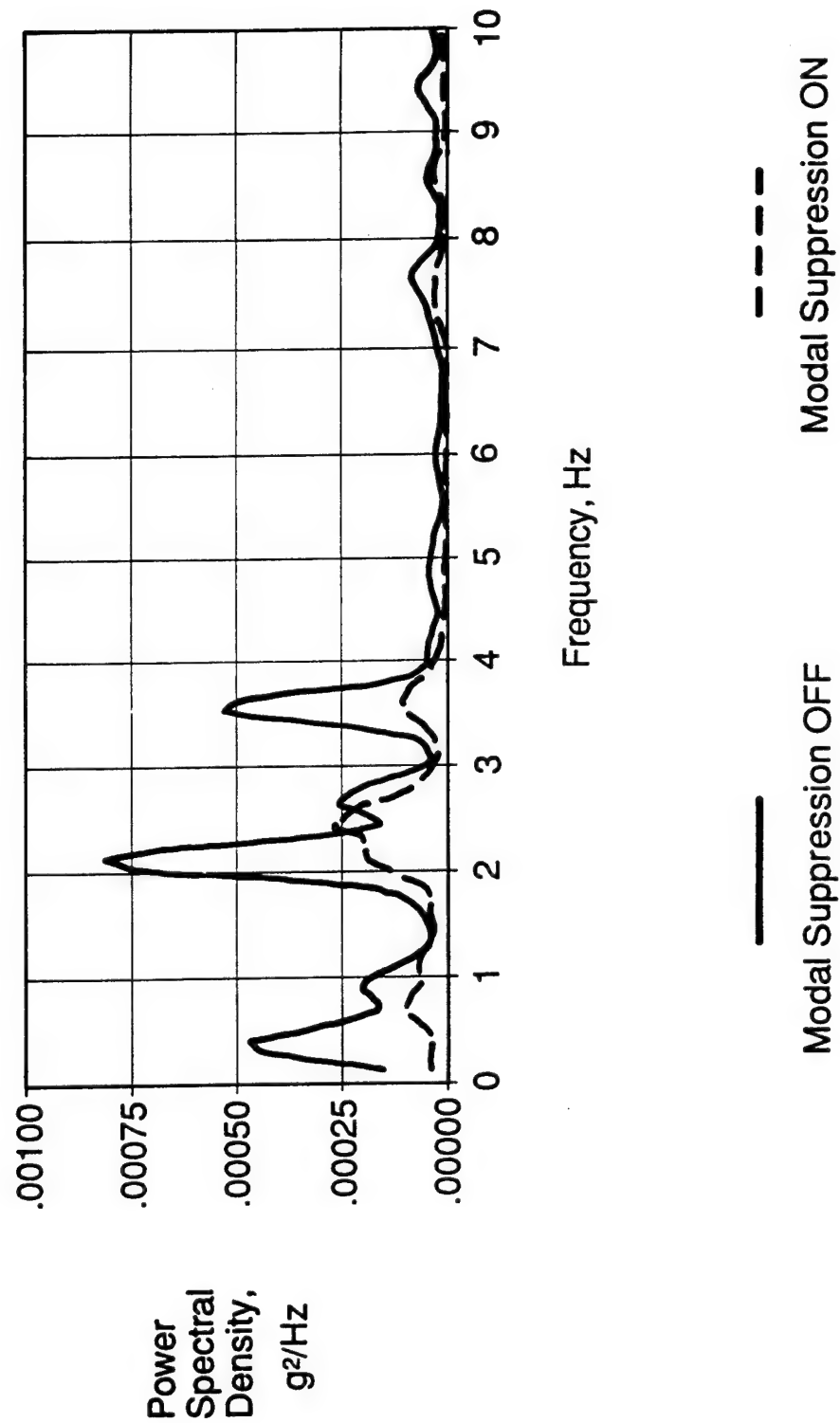
747-400
Power Spectrum
Lateral Acceleration at BS 2300

Modal Suppression OFF (solid line)

Modal Suppression ON (dashed line)

Power Spectral Density, g²/Hz (vertical axis: .00000, .00025, .00050, .00075, .00100, .00125, .00150, .00175, .00200)

Frequency, Hz (horizontal axis: 0, 1, 2, 3, 4, 5, 6, 7, 8, 9, 10)
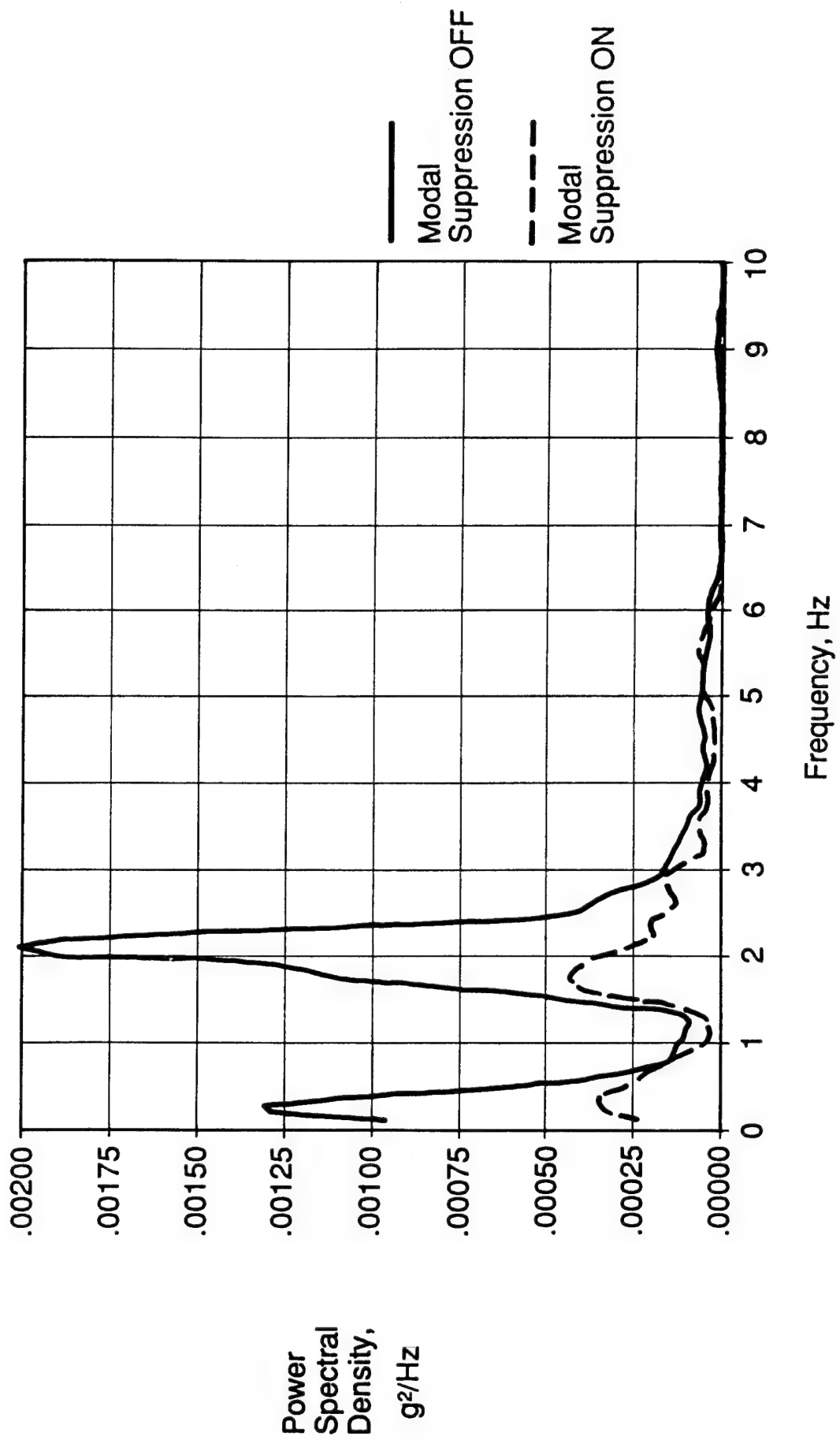
747-400
Power Spectrum
Rudder Position

Power Spectral Density, deg²/Hz

Frequency, Hz

Modal Suppression OFF

Modal Suppression ON

AAC-20
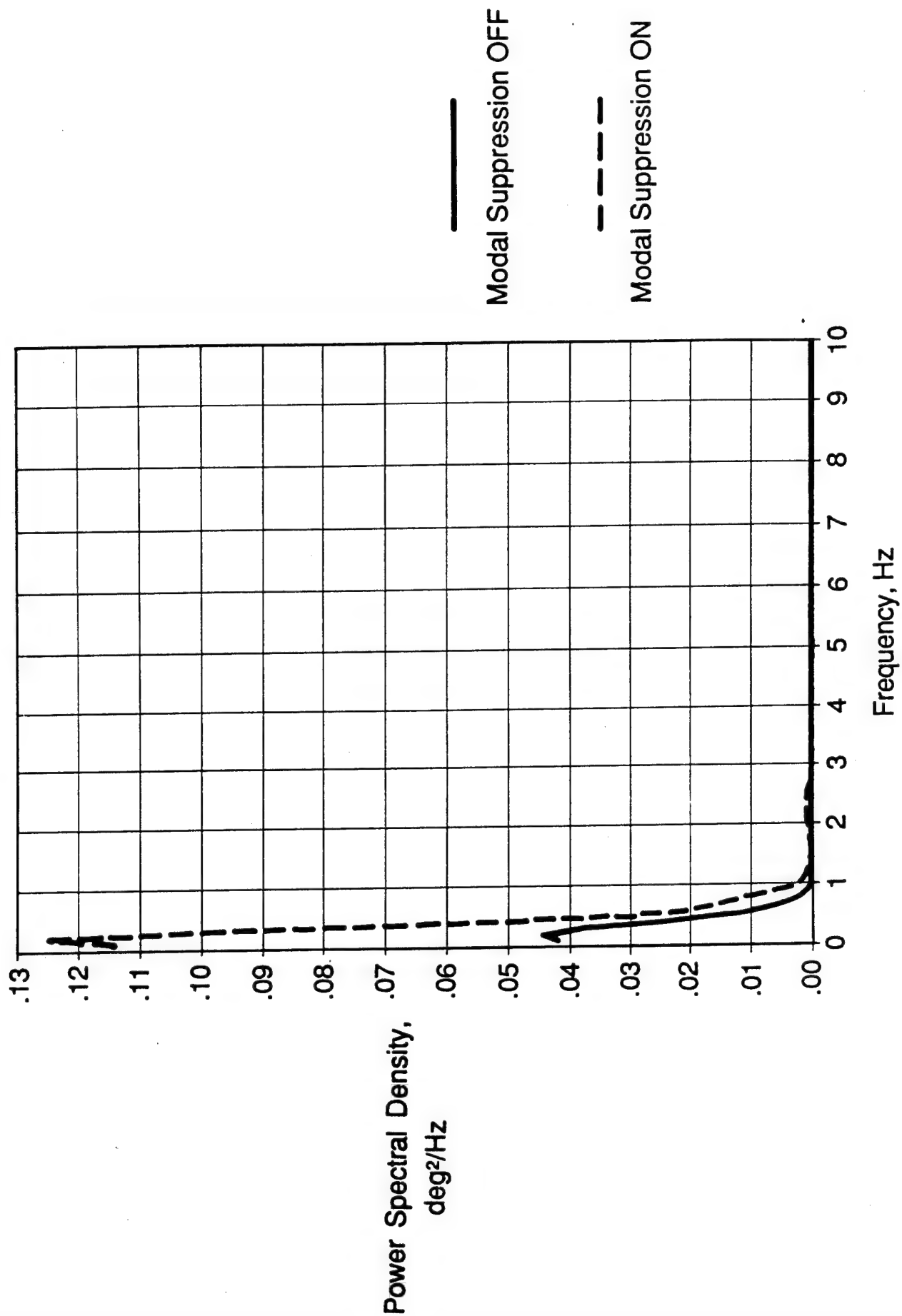
767-300
Modal SuppressionYaw Damper
15000 FT. MACH .60

Aft Body

PSD, g²/Hz

Frequency, Hz

- - - M/S OFF
—— M/S ON
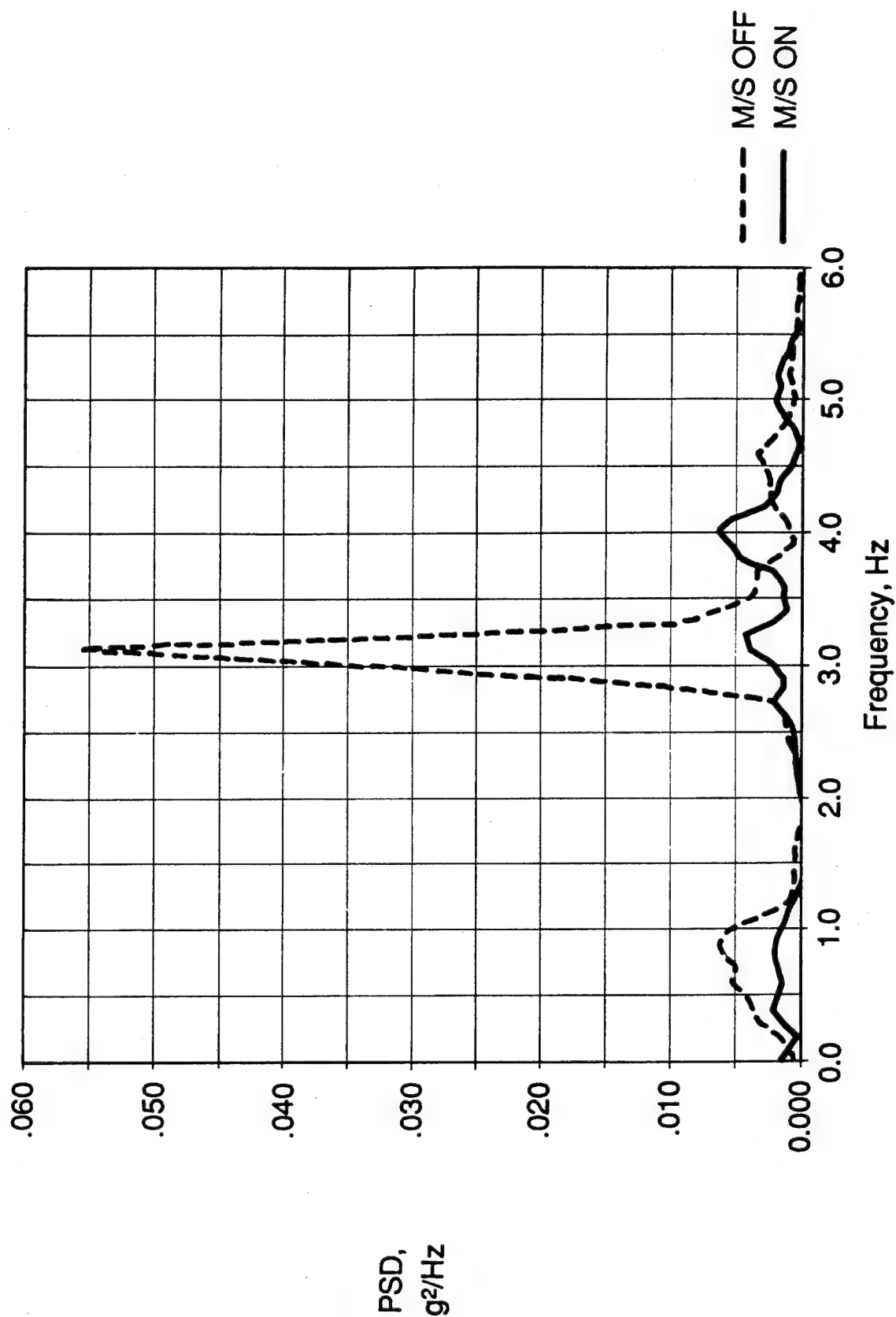
767-300
Power Spectrum
Fuselage Lateral Bending Moment
Aft Pressure Bulkhead BS 1714

Power Spectral Density,
1.0E16 (in-lb)^2/rad/in
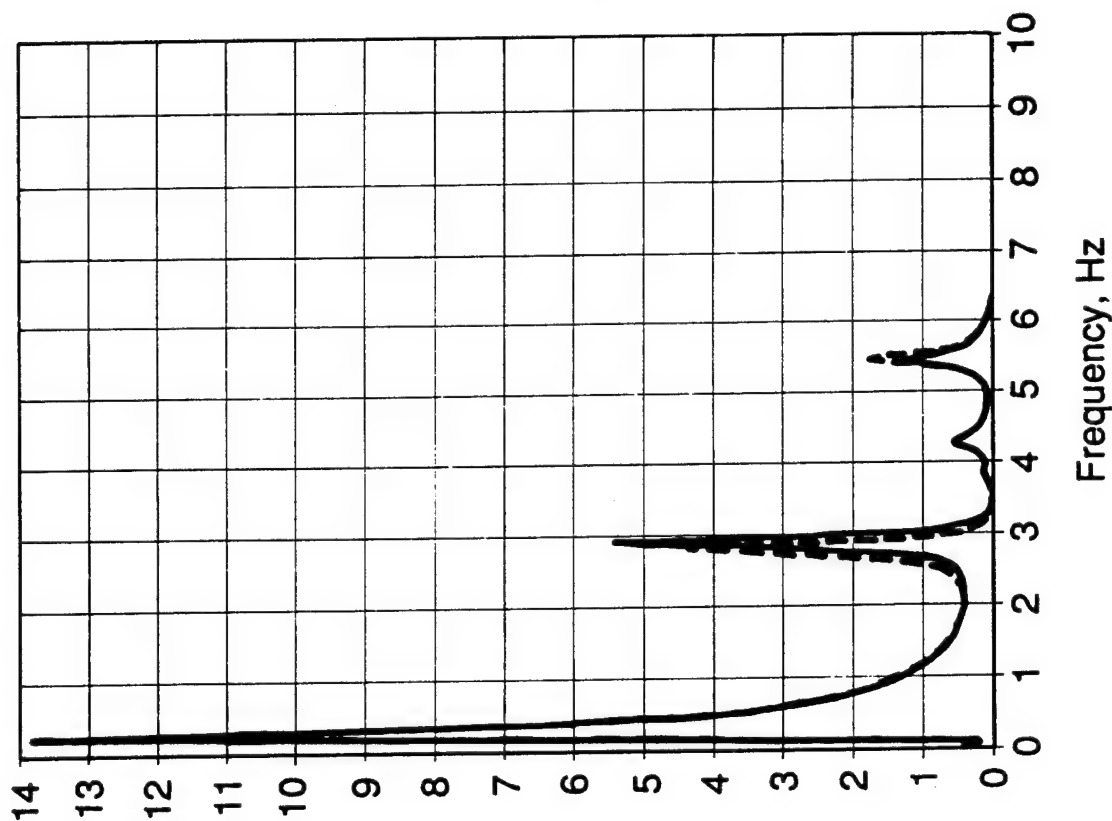
Frequency, Hz

—— Modal Suppression OFF

- - - Modal Suppression ON

One Yaw Damper ON
in both cases *

* Minimum Dispatch
Requirement

767-300
Lateral Gust Spectrum
Vertical Fin Root Bending Moment
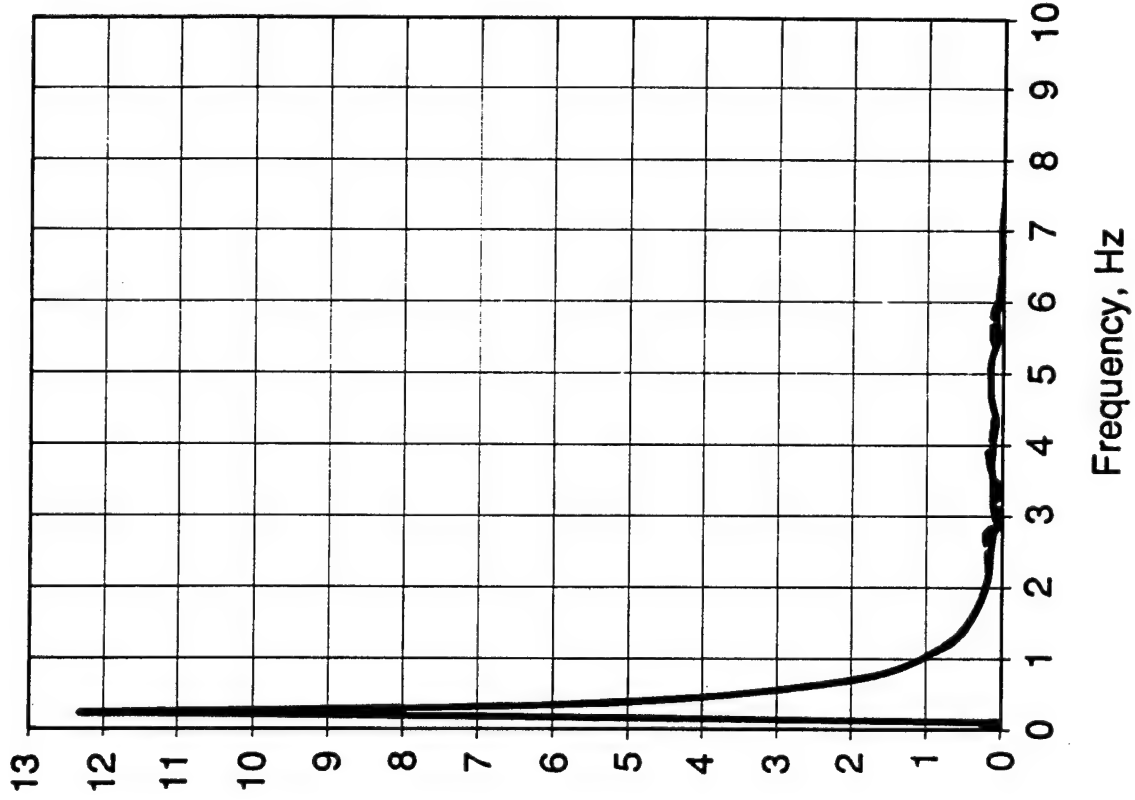
Power Spectral Density, 1.0E16 (in-lb)^2/rad/in

Frequency, Hz

—— Modal Suppression OFF

----- Modal Suppression ON

One Yaw Damper ON in both cases *

* Minimum Dispatch Requirement

Summary Comments

- The major contributor to lateral ride discomfort is the dutch roll mode which accounts for about 60 percent of the acceleration in the aft body.

- Sideslip Rate is used to control dutch roll. In addition, a fast frame time microprocessor, 15 msec, is used together with a wide bandwidth servo, 70/(s+70). The original yaw damper system, without modal suppression, used a 51 msec frame time and a low bandwidth servoactuator, 35/(s+35). The frame time and servo change was made to allow better phase adjustment for the dutch roll and the flexible mode filters.

- There are two (2) structural modes of importance at the Aft Galley location: 1.75 and 2.0 Hz.

- There is one mode of importance at the Pilot's Station: 3.2 Hz.

- The Aft Body filter was designed first: The phase required was +40 degrees at 1.8 Hz. The total phase of the airplane plus controller was made equal to 0 degrees.

- The Fore Body filter was designed next: The phase was -278 degrees at 3.2 Hz. The total phase of airplane plus controller again was made equal to 0 degrees.

- The Aft Body and Vertical Tail root bending moments are not significantly affected by the Modal Suppression System; therefore, there is essentially no degradation in fatigue life.

Credits

Anissipour, A. A.; Benson, R. A.; Coleman, E. E.: *Modeling and Control Systems Design and Analysis Tools for Flexible Structures*

Anissipour, A. A.; Benson, R. A.: *Modifying High-Order Aeroelastic Math Model of a Jet Transport Using Maximum Likelihood Estimation*

Goslin, T. J.; Ho, J. K.: *Structural Stability Augmentation System Design Using BODEDIRECT: A Quick and Accurate Approach*

Ho, J. K.; Cooper, S. R.; Tran, C. B.; Chakravarty, A.: *On the Design of Robust Compensators for Airplane Modal Control*

Ho, J. K.; Goslin, T. J.; Tran, C. B.: *Aircraft Modal Suppression System: Existing Design Approach and its Shortcomings*

Tran, C. B.; Goslin, T. J.; Ho, J. K.; Chakravarty, A.: *Aircraft Fore and Aft Modal Suppression System*

LOSS MODULUS AND DAMPING BEHAVIOR OF
POLY(VINYL METHYL ETHER)-POLYSTYRENE BLENDS AND IPN'S

J. J. Fay, C. J. Murphy[*], D. A. Thomas[**] and L. H. Sperling

Center for Polymer Science and Engineering
Materials Research Center
Department of Chemical Engineering
Whitaker Lab #5
Lehigh University
Bethlehem, PA 18015

* East Stroudsburg University, East Stroudsburg, PA 18301
** Department of Materials Science and Engineering

Abstract

Sequential full interpenetrating polymer networks, IPN's, were synthesized by crosslinking poly(vinyl methyl ether), PVME, with dicumyl peroxide, swelling in styrene, divinylbenzene and initiator and polymerizing in situ. The miscibility of PVME and polystyrene (PS) IPNs was examined by dynamic mechanical spectroscopy (DMS) and differential scanning calorimetry (DSC). DSC indicates an increase in the breadth of the glass transition region for midrange compositions in linear blends and IPNs. Similarly, DMS data shows a narrow glass transition region for a 70/30 weight composition PVME/PS IPN and increasingly broader regions for 50/50 and 30/70 PVME/PS IPNs. The broad transitions probably indicate a degree of microheterogeneous phase separation that may be dependent upon composition and degree of crosslinking. Various degrees of haziness or turbidity of a series of 50/50 PVME/PS samples indicates that the chemical blend is clear and miscible, while the semi-II, the semi-I and the full-IPN are phase separated. A cloud point curve was determined from PVME/PS physical blends by optical microscopy, confirming earlier studies and serving as a miscibility guideline.

Introduction

Polymers constitute useful noise and vibration damping materials near their glass transition temperature, Tg.[1,2] The onset of coordinated chain molecular motion in the Tg region can be used to convert vibrational energy into heat. Whereas homopolymers may be efficient dampers over a range of 30°C around Tg, interpenetrating polymer networks, IPN's, have been shown to exhibit damping over a broader range of temperatures.[3] An IPN may be defined as a combination of two polymers in network form.[4] Similar to other multicomponent polymer materials, the vast majority of IPN's are phase separated[5] and the introduction of crosslinks into each polymer limits the domain size.

The only single phase, miscible IPNs reported are the poly(2,6-dimethylphenylene oxide) (PPO) and polystyrene (PS) IPNs.[6] The corresponding blend of this system is miscible and does not undergo thermally induced phase separation before degradation.[7]

The phase separation behavior of the linear blend of poly(vinyl methyl ether) (PVME) and polystyrene (PS) has been characterized by small angle neutron scattering[8] and by other methods.[9,10] The phase diagram for this system has been developed indicating a lower critical solution temperature (LCST) which is dependent upon composition and molecular weight. Electron irradiation of the blends, which introduces random crosslinking, has been shown to increase the size of the single phase region of the phase diagram.[10] In this paper, PVME/PS IPNs and blends are synthesized and preliminary miscibility and damping behavior of the IPNs are examined by dynamic mechanical spectroscopy (DMS) and differential scanning calorimetry (DSC).

Previous Work

Research on sound and vibration damping began at Lehigh University in the early 1970's, under a contract from Aberdeen Proving Grounds. The objective was to prepare a two-layer constrained layer damping system in the form of a latex paint, based on interpenetrating polymer network technology.[11] The main advantage of the new material was its capability of damping over very broad temperature ranges, from −30 to 100°C.[2,12] The constraining layer was a filled epoxy composite material.

More recently, research at Lehigh centered about understanding the basic nature of the damping phenomenon itself. How were the polymer molecules actually absorbing the

energy? The result was a group contribution analysis, wherein each moiety in the polymer contributes to the loss modulus integral in the vicinity of the glass transition temperature.[13] By examining the area under the loss modulus-temperature curves, a quantitative analysis was developed based on the assumption of a weight fraction additive contribution of the structural units within the repeat unit to the total loss area. The basic equation for the LA group contribution analysis is[13]

$$LA = \sum_{i=1}^{n} \frac{(LA)_i M_i}{M} = \sum_{i=1}^{n} \frac{G_i}{M} \qquad (1)$$

where M_i is the molecular weight of the ith group in the repeating unit, M is the molecular weight of the whole mer, G_i is the molar loss constant for the ith group, $(LA)_i$ is the loss area contributed by the ith group, and n represents the number of moieties in the mer. As a corollary to eq. (1), an additive mixing rule can be written for use with copolymers and multicomponent polymer materials,[13]

$$LA = w_I (LA)_I + w_{II} (LA)_{II} + \cdots = \sum_{i=1}^{n} w_i (LA)_i \qquad (2)$$

where w_I, w_{II} ,... represent the weight fractions of the components in the material.

Table I summarizes loss areas, $(LA)_i$, and molar loss constants, G_i, for a number of moieties derived from group contribution analysis.[14] The group contribution analysis provides a predictive method for LA values via the structure of the polymer.
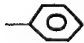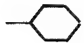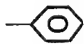
Experimental

Synthesis

Styrene monomer, Polysciences Inc., and divinyl benzene, Scientific Polymer Products, were cleaned by a column chromatographic technique using neutral alumina. Poly(vinyl methyl ether), Scientific Polymer Products, $Mw = 1.3 \times 10^5$ g/mole, was supplied as a 50 wt% toluene solution. Dicumyl peroxide, Phaltz and Bauer, benzoin, Adrich Chemical, and toluene, Fisher Chemical, were used as received.

Crosslinked PVME sheets were prepared in the following manner. Dicumyl peroxide was added to the PVME by a solution blending technique. After mixing the solution was placed in a teflon mold and the toluene was removed under vacuum at 100°C.

Table I. Summary of Group Contributions to LA[14]

Group	Group Location[a]	$(LA)_i$ (GPa°K)	G_i (GPa°K)(g/mol)
$\begin{array}{c} \text{H} \quad \text{H} \\ \mid \quad \mid \\ -\text{C}-\text{C}- \\ \mid \quad \mid \\ \text{H} \end{array}$	1	3.4	91.8
$-\text{O}-$	1	19.1	305.8*
$\begin{array}{c} \text{O} \\ \parallel \\ -\text{C}-\text{O}-(\ )- \quad \text{H} \end{array}$	2	20.8	936
$\begin{array}{c} \text{O} \\ \parallel \\ -\text{O}-\text{C}-(\ )- \quad \text{H} \end{array}$	2	20.1	905
$\begin{array}{c} \text{O} \\ \parallel \\ -\text{C}-\text{OH} \end{array}$	2	20.8	936
—⬡ (aromatic ring)	2	11.9	916
$-\text{CH}_3$	2	11.0	165
$-\text{OCH}_3$	2	21.7	674
$-\text{C}\equiv\text{N}$	2	23.2	603
$-\text{O}-\text{H}$	2	4.7	80
$-\text{Cl}$	2	9.2	327
—⬡ (cyclohexyl)	3	3.5	287
—⬡ (aromatic ring)	3	2.2	166
$\begin{array}{c} \text{CH}_3 \\ \mid \\ -\text{CH}_2-\text{CH}-\quad\text{CH}_3 \\ \mid \\ -\text{CH}- \end{array}$	3 / 3,4	-1.7 / 0.5	-98 / 7
$-\text{CH}_2-$	3	-3.0	-42
$-\text{C}\equiv\text{N}$	3	14.5	377
$-\text{Cl}$	3	15.7	556

[a]1: backbone; 2: side group attached to backbone directly; 3: side group not attached to backbone; 4: value derived from isobutyl side group.

*T. Hur, J. A. Manson and L. H. Sperling, to be published.

The resulting 2 mm thick sheet was then cured at 160°C for 60 mins. in a nitrogen atmosphere.

IPN's were prepared from the crosslinked PVME sheets by swelling in a mixture of styrene, divinyl benzene and benzoin. After equilibrium was achieved, swollen mass was then placed between Mylar sheets and glass plates. The mold was then sealed and placed in a UV box and photopolymerized for 72 hours. Semi-I IPN's, in which only the first component, PVME, is crosslinked, were synthesized by swelling in styrene and initiator, without crosslinker. Semi-II IPN's, in which the second component, PS, is crosslinked, were prepared by dissolving linear PVME in the styrene, divinyl benzene and benzoin solution. Synthesis of linear PS in the presence of linear PVME results in the formation of a chemical blend. UV photopolymerization was used in each case, similar to that for the full IPN case. Physical blends were prepared by synthesizing PS separately and solution blending to achieve the desired composition. Chemical blends differ from physical blends in that during the polymerization of the second component grafting may occur as the result of chain transfer to polymer.

Instrumental

A Mettler TA3000 system DSC30 (Mettler Instrument Co.) was used to obtain heat capacity thermograms. Ten mg samples were evaluated from -100 to 150°C at a heating rate of 10°C and a N_2 flow rate of 100 cc/min.

An Autovibron Dynamic Viscoelastometer (Rheovibron DDV-III-C; Toyo Baldwin Co., Ltd.) coupled with a computer and plotter (assembled by Imass, Inc.) was used to obtain the storage modulus, E', loss modulus, E", and the loss tangent, tan . The heating rate was approximately 1°C/min and the frequency was 110 Hz. The classical plots of the logarithmic loss modulus, E", were converted to the corresponding linear plots by a computer program.

The cloud point curve was determined using a Zeiss microscope (Opto-Systems Inc.) equipped with a microprocessor controlled hot stage at a heating rate of 2°C/min. Films were cast from toluene onto glass slides from 10 wt% polymer solutions. The films were then dried under vacuum at 100°C.

Results and Discussion

A series of 50/50 PVME/PS samples were synthesized and the miscibility of the components was evaluated. The chemical and physical blends were found to be clear while the semi-I, semi-II and the full-IPN were observed to be hazy. Such

haziness indicates a degree of heterogeneity, usually phase separation.

The cloud point diagram determined for the PVME/PS blends at varying compositions is shown in Fig. 1. The results are in accord with previously determined phase diagrams for the PVME/PS system excepting molecular weight differences.[10] Microscopic phase separation was observed with generally coarser morphology at increased PVME content. With annealing at lower temperatures, the phase separation was observed to be reversible, and clear films were obtained again.
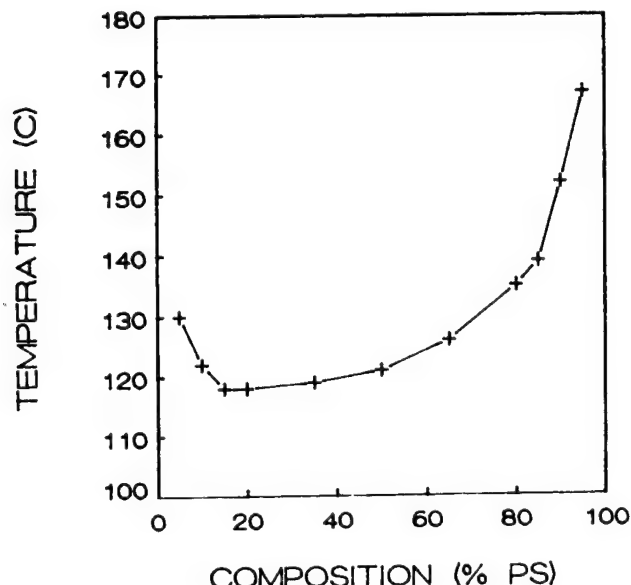
Fig. 1. The cloud point phase diagram for physical blends of PVME and PS, showing lower critical solution temperature, LCST, behavior.

Thermal analysis of PVME/PS IPN's indicates only one glass transition temperature located between the homopolymer Tg's. The position of the Tg is dependent upon composition but it does not follow the prediction of the Fox equation,[15] Table II.

Table II. Characterization of PVME/PS IPN's and Homopolymers.

% PVME	Loss Area (exper.)[†] GPa∗K	(calc.)	Loss Peak °C	Tg (DSC) °C	Fox Eqn. °C
100	8.9	13.2	−15	−24	−15
70	10.8	12.1	−4	−16	14
50	12.4	11.5	16	−8	38
30	11.6	10.7	(20) 67	20	65
0	9.4	9.7	117	93	117

Network	Crosslinker level	Mc (g/mol)
x−PVME	7.5 wt % dicumyl perox.	18,000
x−PS	1 mol % DVB	7,700

[†] based on $E' = 2.85 \times 10^{10}$ dynes/cm^2

The breadth of the transition also increases dramatically with increased PS content. The broad glass transition, resulting from the clustering of molecules near the lower critical solution temperature, is similar to broad transitions associated with microheterogeneous multicomponent polymer materials. Figure 2 compares the glass transition region of a physical blend, cast from toluene, and an IPN of the same composition. Both exhibit broad transitions, however, the IPN is significantly broader than the blend.
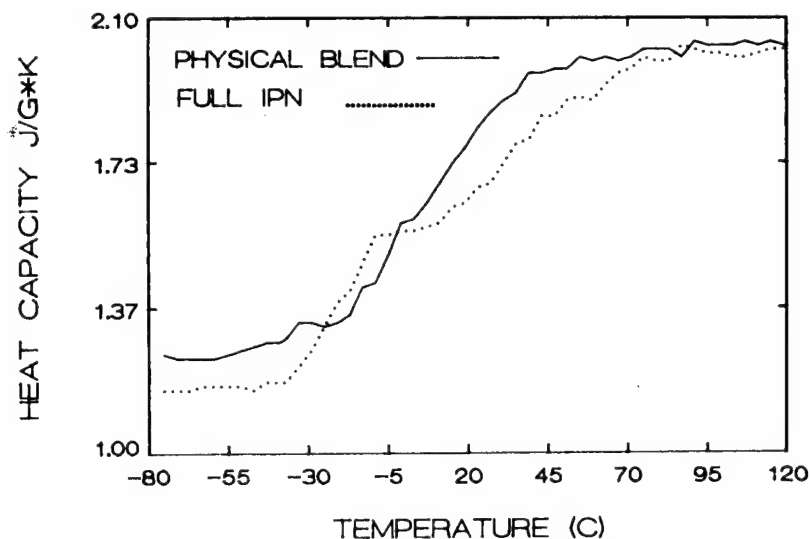
Figure 2. Differential Scanning Calorimetry of a PVME/PS physical blend and full-IPN. 50 wt % PS in each sample. Heating rate 10°C/min.

The dynamic mechanical spectra of a series of PVME/PS IPNs is shown in Fig. 3, illustrating the linear loss modulus plots. The homopolymers both show narrow, well defined loss peaks. The 70/30 PVME/PS IPN loss modulus curve is slightly broader than the PVME homopolymer peak. There is a dramatic change in the shape of the loss curve with increasing PS weight fraction as shown for the 50/50 and 30/70 IPNs. The loss modulus peak extends over a range of 100°C and in the 30/70 sample there is an observable shoulder on the low temperature end of the peak. The broad transitions indicate a degree of microheterogeneous phase separation that may be dependent on composition and the degree of crosslinking. Recently, Bauer et al. found that phase separation occured as the crosslink density of polystyrene was increased for semi-II IPNs, where only PS is crosslinked.[16] The IPNs synthesized in this lab have PS crosslinking levels corresponding to the crosslink level which resulted in phase separation of the semi-II IPNs in the work of Bauer et al.
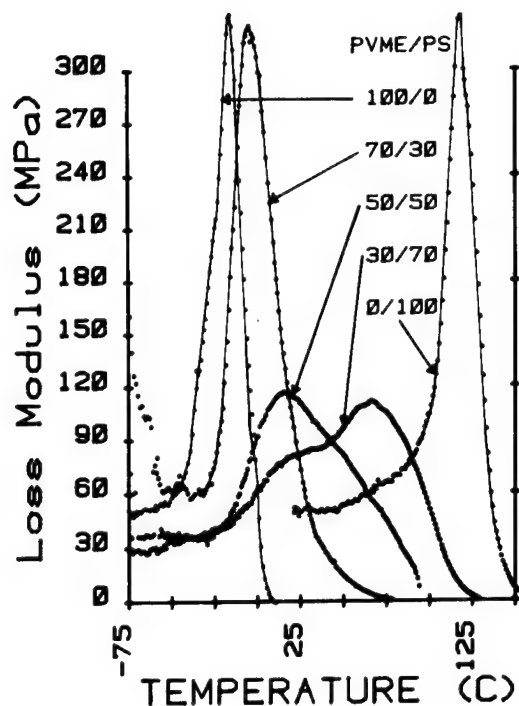
Fig. 3. Linear loss modulus versus temperature curves for PVME/PS full-IPN's and homopolymers. Rheovibron DDV-III dynamic mechanical spectroscopy at 110 Hz, heating rate 1°C/min.

The loss areas, LA's, obtained for the IPN's and homopolymers are compared with the values predicted from equation (2) and Table II. Except for the crosslinked PVME homopolymer, the LA values obtained by DMS are within 10% of the values predicted by the group contribution analysis. The large deviation in the LA value obtained for the crosslinked PVME homopolymer may be attributed to oxidation during sample preparation, as evidenced by sample discoloration, which was not observed in the IPN samples.

To examine the effect of phase separation on the loss modulus, a sample of a 50/50 chemical blend was phase separated at 130°C and and then evaluated by DMS, Fig. 4. Note that the 50/50 PVME/PS blend shows a broad transition indicative of clustering. This result is in accord with previous dynamic mechanical spectra of PVME/PS blends.[9] Comparatively, PPO/PS blends exhibit narrow loss moduli peaks that vary predictably over the entire range of composition.[6] Since the LCST for PPO/PS is significantly higher than the experimental temperatures employed, clustering does not occur, and narrow transitions are obtained. As compared to the untreated blend, the thermally treated PVME/PS blend shows a broader transition and also a larger loss area which may be attributed to a change in morphology. Similarly, the IPN shows a broader transition, however, the area is the same as the untreated blend, within experimental error. It should be noted that the phase separated blend has a milky white appearance whereas the IPN is slightly hazy. The degree of phase separation in the two cases is significantly different.
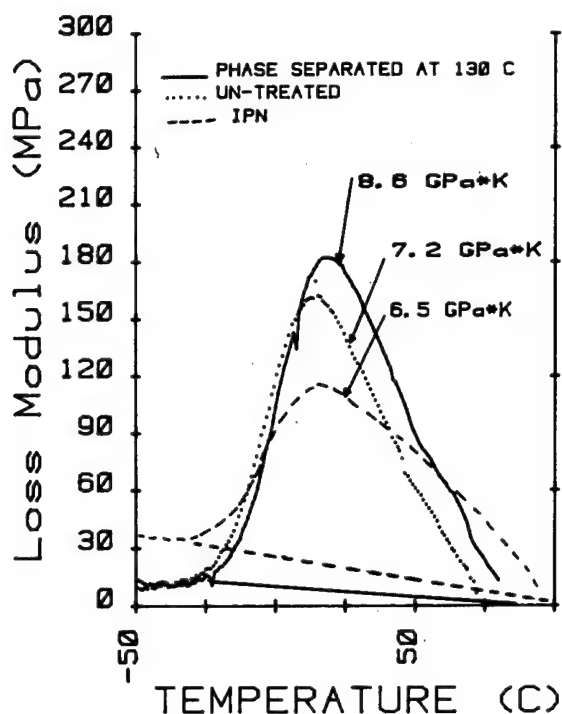
Fig. 4. Linear loss modulus curves for 50/50 PVME/PS chemical blends, under two different conditions, and a full-IPN. Baseline corrections are also shown.

Conclusions

The IPNs synthesized appear to be less miscible than the corresponding chemical and physical blends. The phase separated IPNs, having broader glass transition regions than the corresponding linear blends, enable damping over a broader temperature region.

Acknowledgement

References

1. L. E. Nielsen, "Mechanical Properties of Polymers and Composites," Vol. I, Marcel Dekker, Inc., New York, 1983
2. J. A. Grates, D. A. Thomas, E. C. Hickley and L. H. Sperling, J. Appl. Polym. Sci., 19, 1731 (1975).
3. L. H. Sperling, T. W. Chiu, and D. A. Thomas, J. Appl. Polym. Sci., 17, 2443 (1973).
4. L. H. Sperling, "Interpenetrating Polymer Networks and Related Materials," Plenum Press, New York, Chapter 8, 1981.

5. L. H. Sperling, in "Multicomponent Polymer Materials," D. R. Paul and L. H. Sperling, Eds., ACS Adv. Chem. Ser., 211, Chapter 2, 1986.

6. H. L. Frisch, D. Klempner, H. K. Yoon and K. C. Frisch, Macromolecules, 13, 1016 (1980).

7. W. J. Macknight, F. E. Karasz and J. R. Fried, "Polymer Blends," D. R. Paul and S. Newman, Eds., Academic Press, New York, 1978.

8. C. C. Han, M. Okada, Y. Muroga, B. J. Bauer and Q. Tran-Cong, Polym. Eng. Sci., 26(17), 1208, (1986).

9. D. J. Hourston and I. D. Hughes, Polymer, 19, 1181 (1978).

10. T. Nishi and T. K. Kwei, Polymer, 16, 285 (1975).

11. L. H. Sperling, V. Huelck and D. A. Thomas, in "Polymer Networks: Structural and Mechanical Properties," A. J. Chompff and S. Newman, Eds., Plenum, New York, 1971.

12. L. H. Sperling, T. -W. Chiu, R. G. Gramlich and D. A. Thomas, J. Paint. Technol., 46, 4 (1974); L. H. Sperling and D. A. Thomas, U. S. Pat. 3,833,404 (1974).

13. M. C. O. Chang, D. A. Thomas, and L. H. Sperling, J. Appl. Polym. Sci., 34, 409 (1987).

14. M. C. O. Chang, D. A. Thomas, and L. H. Sperling, J. Polym. Sci., Part B, Polym. Phys., 26, 1627 (1988).

15. T. G. Fox, Bull. Am. Phys. Soc., 1, 123 (1956).

16. B J. Bauer, R. M. Briber and C. C. Han, Private Communication

DEVELOPMENT OF A DAMPED A-10
ENGINE AIR INLET RING

BY

DAVID L. GIUNTO
&
STEVEN N. VACCA

LTV AIRCRAFT PRODUCTS GROUP
MILITARY AIRCRAFT DIVISION
P.O. BOX 655907
DALLAS, TX 75265-5907
(214)266-2559
(214)266-4784

ABSTRACT

A modern turbofan engine generates an intense acoustic environment which results in durability problems for the surrounding aircraft structure. Acoustic fatigue caused by jet engine noise is the principal origin of structural failures of A-10 engine air inlet extension rings. Many of these components exhibit failures in as few as a couple of hundred flight hours. This paper outlines the environments which cause these failures and presents the development of a damped A-10 inlet ring. The durability, cost, and weight of the re-designed component are compared to the baseline A-10 inlet ring. These comparisons demonstrate a significant improvement in the durability, weight, and life cycle cost through the incorporation of damping into an advanced inlet ring design.

INTRODUCTION

Many of the failures of secondary aircraft structures may be attributed to acoustic fatigue generated by modern turbofan engines. Engine inlets, nacelles, cowl doors, and surrounding structure are especially prone to these failures. While the failures themselves may not be catastrophic from the standpoint of an individual secondary component, potential foreign object damage to the turbofan engine could have a detrimental effect on the flight worthiness of the aircraft. Frequently recurring maintenance and repair of these structures adversely affects aircraft availability and operational costs. Recent Department of Defense directives rate operational availability equivalent to operational performance for the design of new aircraft. As a consequence, managers of future military system programs must incorporate advanced structural design and manufacturing technologies into those systems to ensure their reliability. The application of structural damping and careful structural design practices in areas subjected to high intensity acoustic excitation can reduce or eliminate the problems associated with the aforementioned secondary aircraft structures. LTV has established the viability of this technology through the re-design and manufacture of A-7 center section leading edge flaps, F-111 outboard spoilers, and A-10 engine air inlet rings.

This paper discusses the development and re-design of an inlet extension ring used on an A-10 attack aircraft. Work on this project was performed under the Structural Improvement of Operational Aircraft Program, Air Force Contract Number F33615-81-C-3219. The goals of this program were to develop advanced structural design and manufacturing technologies which would increase the durability and decrease the life cycle cost of secondary aircraft structures. These objectives were to be attained without a performance or weight penalty as compared to the baseline component. In pursuit of these goals, the failures plaguing the baseline inlet ring were identified and the causes established through a series of tests and analyses. An advanced inlet ring was then developed based on these design criteria, and its durability validated through the same analysis and laboratory test procedures used for the baseline inlet ring.

A schematic representation of the baseline inlet ring cross-section and its installation is depicted in Figure 1. This structure provides an aerodynamically smooth interface between the inner nacelle lip of the aircraft and the fan shroud of a TF34-GE-100 engine. The baseline inlet ring is approximately 42 inches in diameter and 9.25 inches wide. The materials used in its construction are conventional 2024 and 6061 aluminum alloys in various product forms and tempers. A laminated skin, composed of three 0.025" layers of aluminum, bonded with 3M's AF-126 modified epoxy film adhesive, is formed in 180° sections, and spliced in two locations to form the body of the baseline inlet ring. Aluminum angle stiffeners are employed at the forward and aft ends of the skin to add rigidity to the structure and provide attachment points for installation on the aircraft. The forward angle stiffener supports a floating forward flange which is attached via 24 discrete spring elements. This spring-loaded flange provides a flexible interface between the inlet ring and the inner nacelle lip of the aircraft. The adaptive nature of this interface ensures the ability to remove a damaged engine and/or inlet ring and replace it with an undamaged spare in a minimum amount of time. Figure 2 illustrates each of

INLET RING

42 IN.
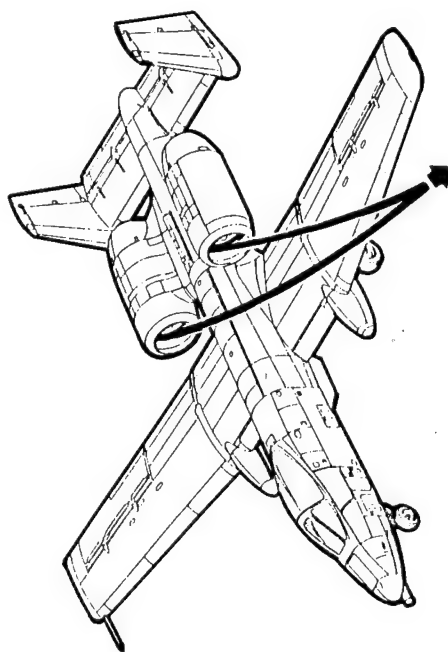
MECHANICALLY ATTACHED AFT RING
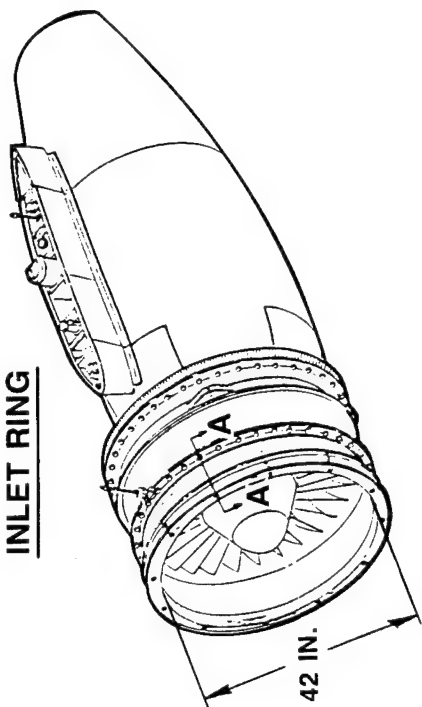
MECHANICALLY ATTACHED FLANGE

LAMINATED SKIN
– NOT DAMPED
– 2 PIECES WITH SPLICE PLATES

24 DISCRETE MECHANICAL SPRING SLIDERS
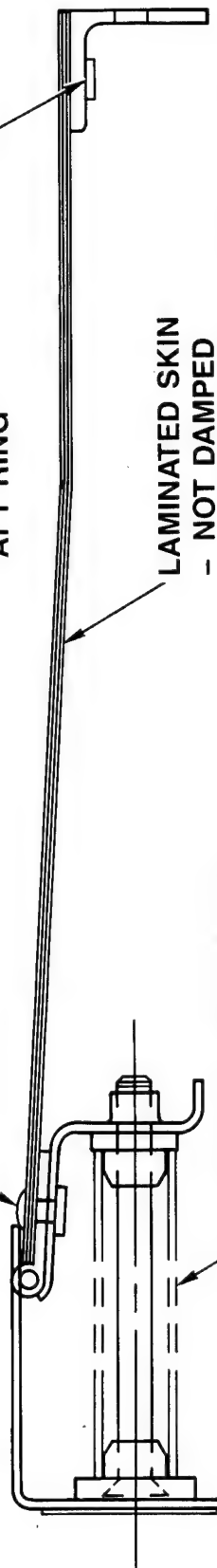
Figure 1 - Baseline Inlet Ring Cross-Section and Installation

Floating Fwd Flange

Fwd Angle Stiffener

Aft Angle Stiffener

Discrete Spring Element

Splice Plate
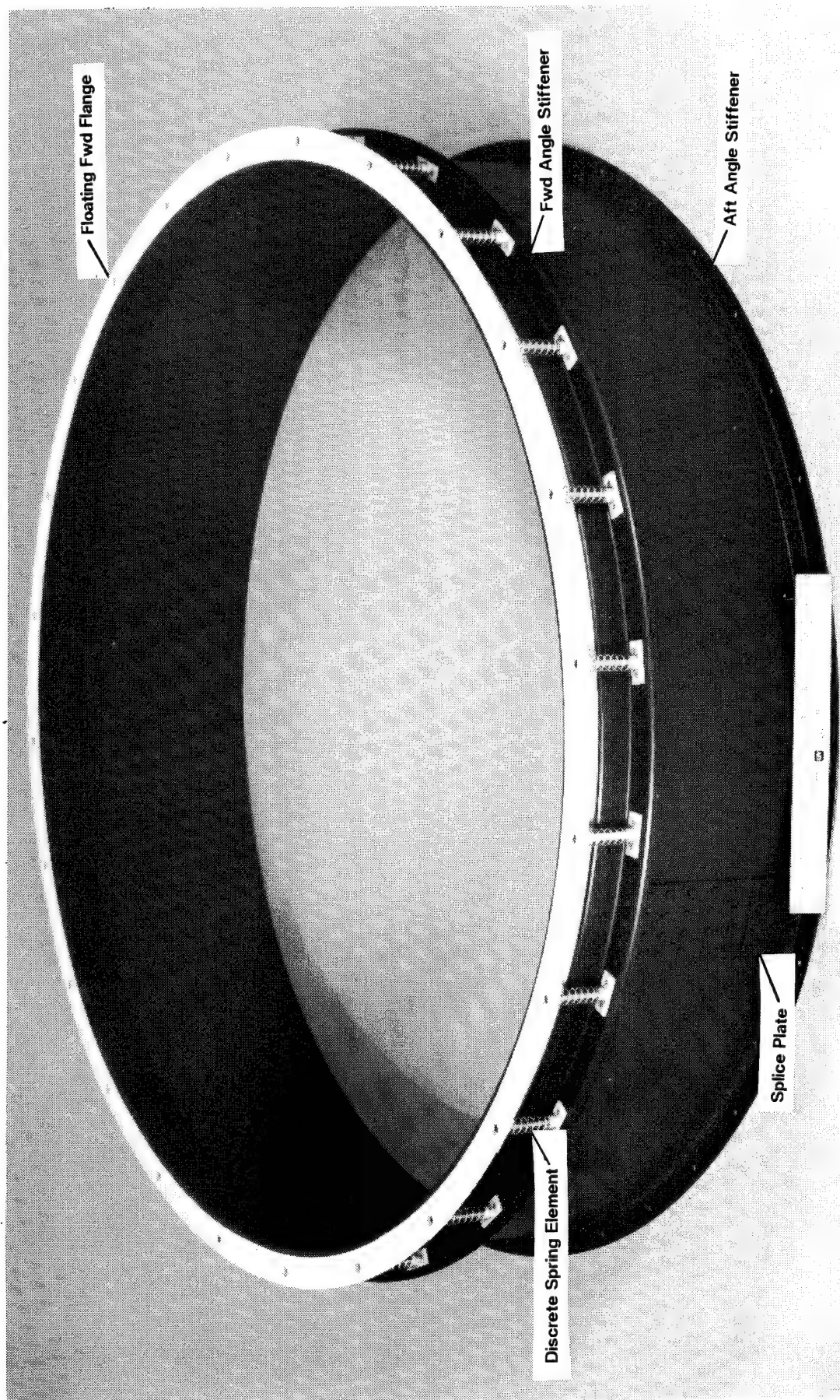
Figure 2 - Baseline A-10 Engine Air Inlet Extension Ring

the previously described elements of the baseline inlet ring and Figure 3 demonstrates how this component interfaces with the surrounding structure when installed in an aircraft.

A survey of baseline inlet rings in service identified a number of design shortcomings which induce unacceptable mean time between failure intervals for the component. The elements which exhibit durability problems include the rivets that attach the forward angle stiffener to the inlet skin, and the splice plates and splice angles which join the individual 180° segments of the inlet ring skin and angle stiffeners. Rivet failures occur at the forward angle stiffener in as few as 200 flight hours, with rivet head ingestion into the engine transpiring as a consequence of the failure. The deterioration of the rivet integrity may be attributed to an open shank condition which exists in the interface between the angle stiffener and the inlet skin. This situation is caused by the presence of an elastomeric seal between the skin and forward ring as illustrated in Figure 1. The lack of rigidity of the attachment at this interface is aggravated by an intense acoustic environment which produces circumferential bending and rocking modes of the forward ring. The discontinuous load application created by the discrete spring elements also enhances the severity of the problem. These effects contribute to the high cycle bending fatigue and eventual failure of the aluminum rivets. The failures associated with the splice plates and splice angles may be attributed to an abrupt change in the bending stiffness of the structure at these locations. When subjected to an acoustic environment, the inlet skin tends to deform about these stress raisers and the ensuing bending causes cracking of the splice plates. Finally, the flexible interface, at the forward end of the baseline inlet ring, provides little or no sealing to prevent blow-by and reduction of inlet ram pressure. This condition does not precipitate any structural failures, yet it prevents the inlet ring from completely and efficiently performing the function for which it was designed.

DESIGN CRITERIA

In order to effectively solve the problems associated with the baseline inlet ring, the reasons for the failures had to be identified. The establishment of the design criteria involved identifying the environments that the inlet ring encounters and verifying the failure mechanisms through analysis and laboratory test. Due to the inlet ring's proximity to the TF-34 engine, sonic fatigue caused by jet engine noise was surmised to be the principal cause of the baseline inlet ring failures. Acoustic fatigue of aircraft structures in the vicinity of modern jet engines is a well known phenomenon discussed extensively in the literature[1,2,3,4].

Predicated on these hypotheses, an engine ground run test was performed using an instrumented baseline inlet ring. The instrumentation included two microphones to monitor the sound pressure level at the interior of the inlet ring, and six accelerometers to assess the inlet ring response to the acoustic environment identified. Figures 4 and 5 illustrate the maximum sound pressure levels witnessed at the forward and aft ends of the inlet ring in a frequency range from 0 to 5000 Hertz. The most severe environments, based on maximum sound pressure level, occur in a
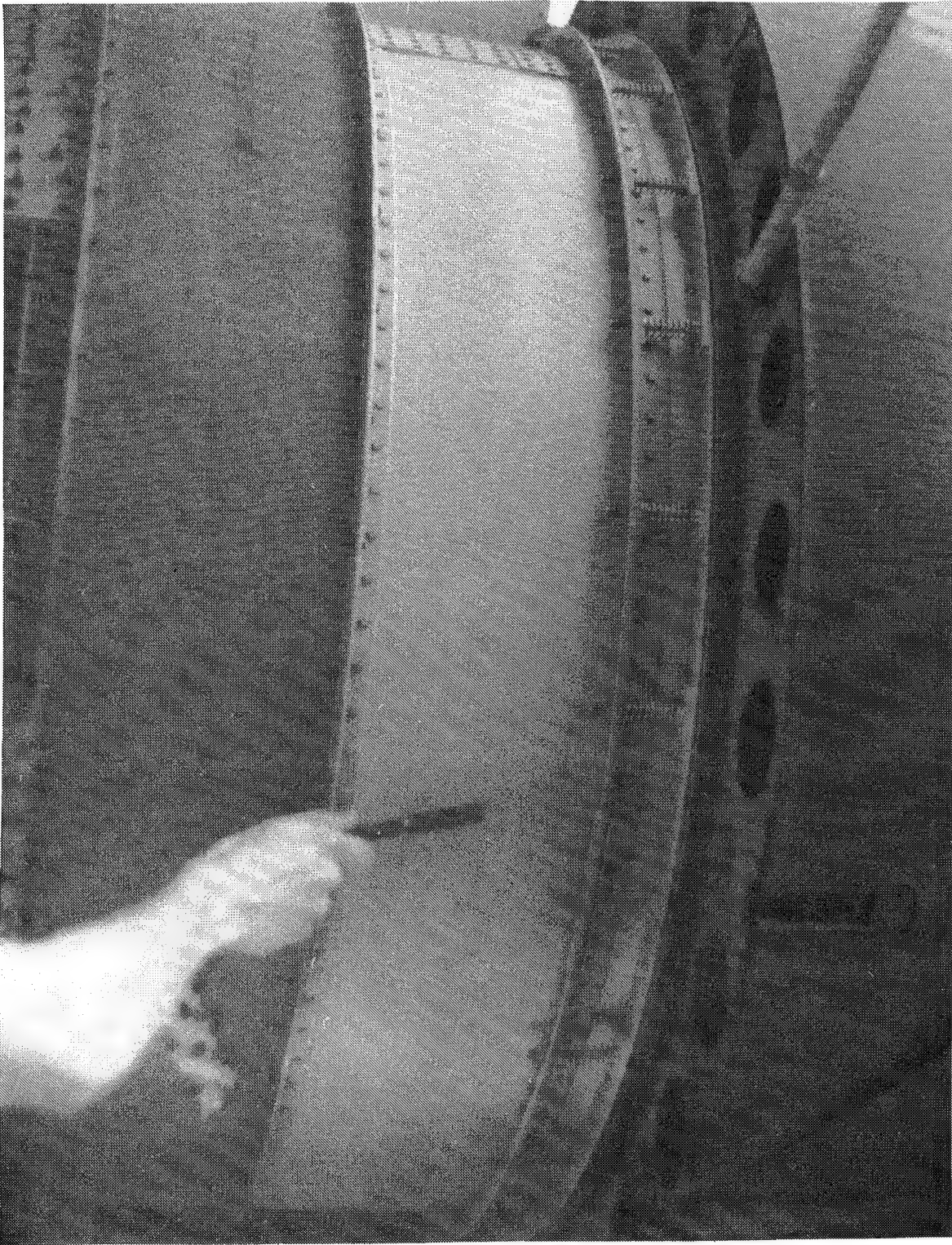
Figure 3 - Baseline A-10 Inlet Ring Installed in an Aircraft
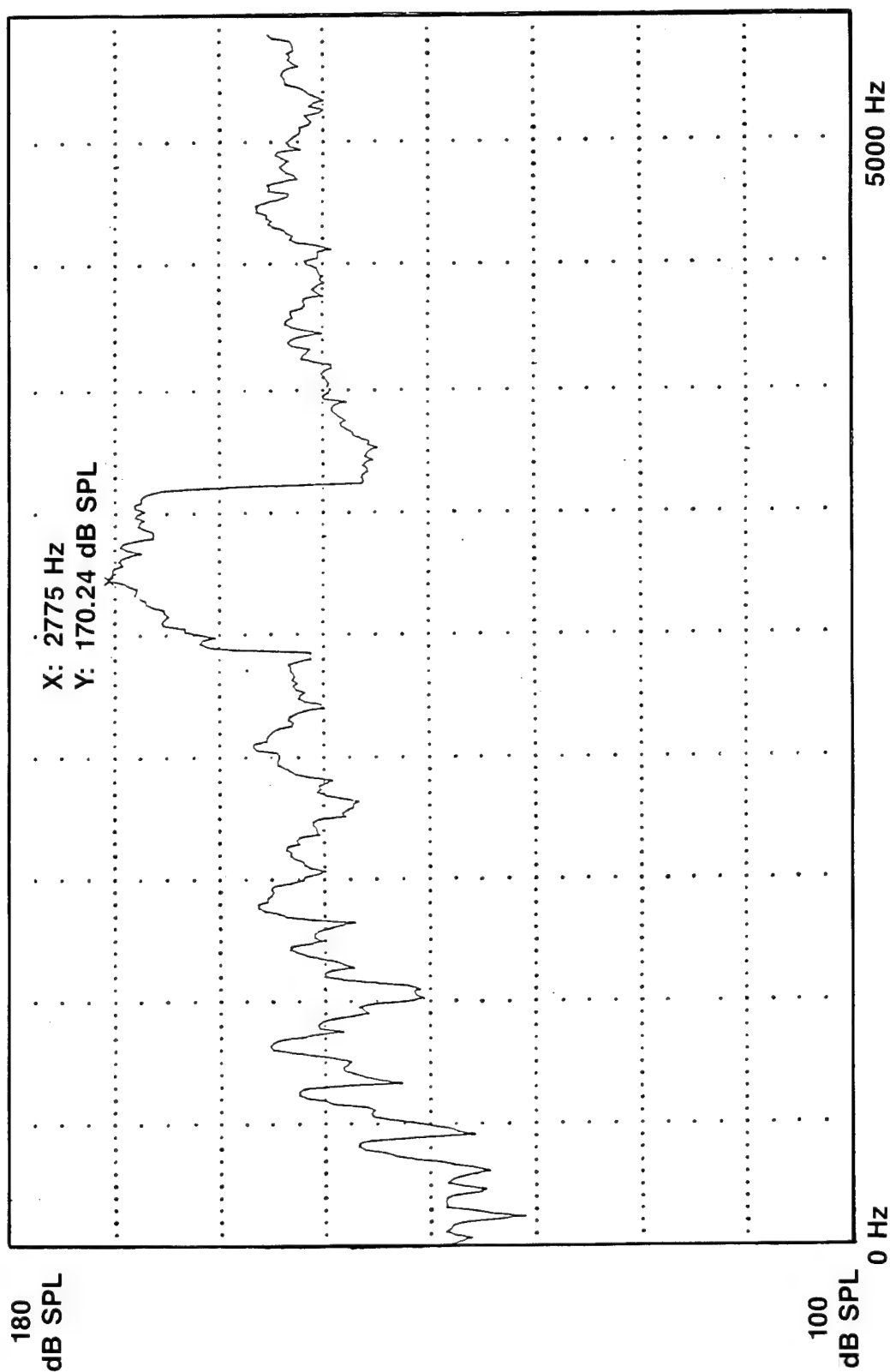
Figure 4 - Peak Hold Sound Pressure Level Data From Aft Mounted Microphone
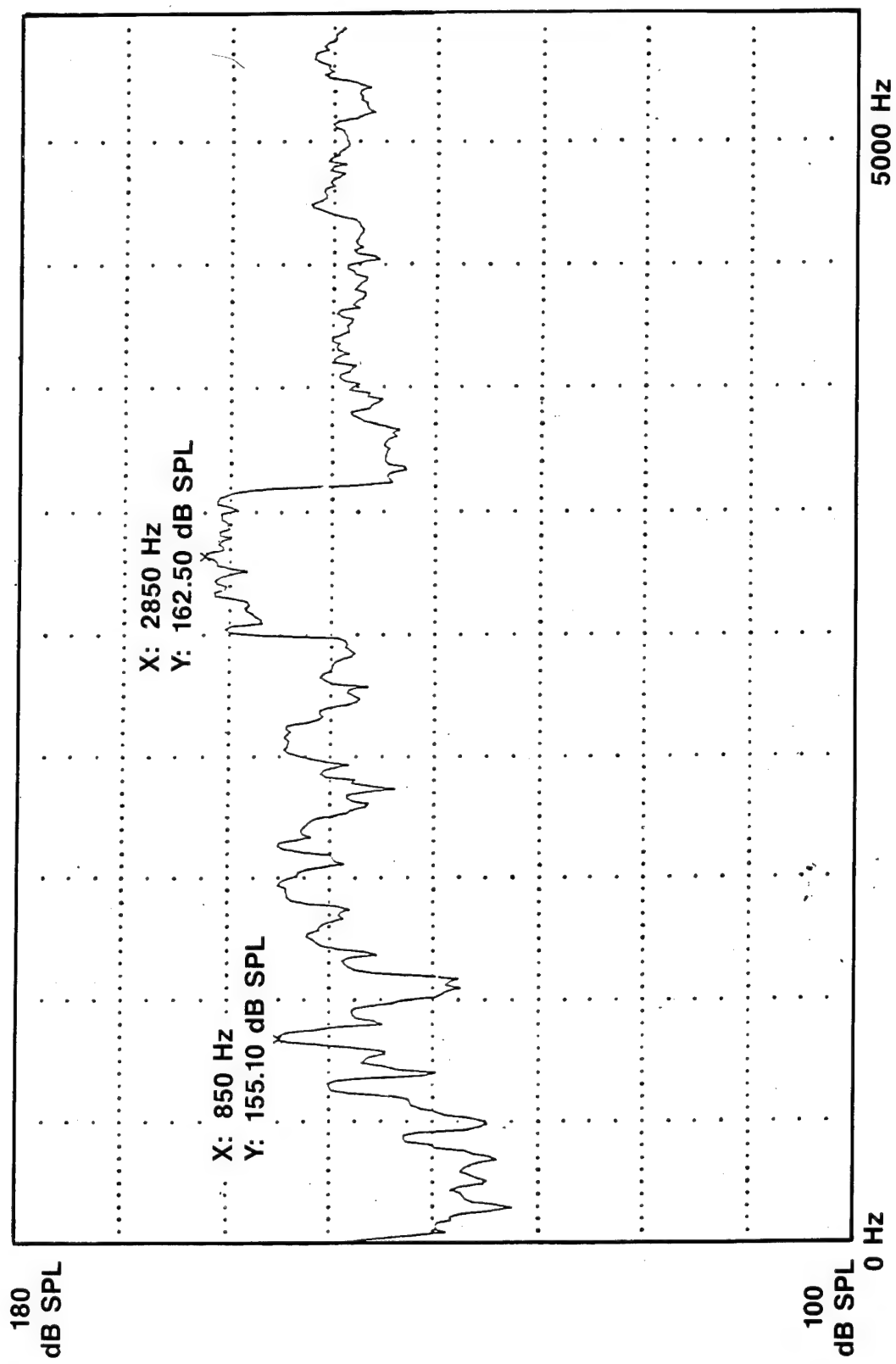
Figure 5 - Peak Hold Sound Pressure Level Data From Forward Mounted Microphone

X: 2850 Hz
Y: 162.50 dB SPL

X: 850 Hz
Y: 155.10 dB SPL

180 dB SPL

100 dB SPL

0 Hz

5000 Hz

range of frequencies from 800 to 1500 Hertz and 2500 to 3000 Hertz. The 2500 to 3000 Hertz regime is the result of fan blade passage and generates acoustic levels in excess of 170 dB (ref. 20 µPa). The other frequency range of interest, 800 to 1500 Hertz, produces maximum sound pressure levels of approximately 155 dB (ref. 20 µPa) in a range of engine speeds from 75 to 100 percent of maximum fan RPM. This multiple pure tone, or combination tone excitation, is caused by geometric and aeroelastic differences between successive fan blades which produces shock waves forward of the fan face. Phenomenon such as these have been characterized by various authors[1,3,4], and shown by Hancock[2] to be the cause of structural failures in another TF-34 installation.

With the environment information obtained in the literature and confirmed through engine ground run test, determining the amount of time that the inlet ring experiences this severe excitation was the only task that remained. It must first be realized that those environments identified through ground run testing will vary with atmospheric pressure and air density, and thus can change dramatically in flight. To assess these effects, an analysis of the the variation of sound pressure levels with climatic conditions and altitude was performed. Standard atmospheric conditions, outlined in MIL-STD-210A, were used for the purposes of this analysis. The study concluded that the multiple pure tone sound pressure levels remain significant to altitudes up to 8000 feet and the blade passage sound pressure levels remain meaningful to 12,000 feet. Using these altitude criteria and examining the A-10 mission profiles, the percentage of total flight time the aircraft operates within the severe excitation range of the two environments was determined. For the multiple pure tone excitation, the duty cycle equated to 10.2 percent of the total flight time, whereas the blade passage regime duty cycle was 22.9 percent of total flight time. The effects of these environments and duty cycles were further explored through finite element analysis and laboratory testing of the baseline structure.

An MSC/NASTRAN finite element model of the baseline design inlet ring was developed to determine the normal modes and response of the baseline structure. The two frequency regimes identified through the engine ground run test provided the bounds for this analysis. However, the frequency ranges used for analysis were somewhat narrower than the ranges over which maximum sound pressure levels were identified during the engine ground run test. Accelerometers mounted on the forward angle stiffener during this test showed significant response of this region between 800 and 1200 Hertz and also between 2800 and 3000 Hertz. Since this vibration was surmised to be the primary cause of the structural failures, the bandwidths used for analysis were decreased accordingly. Typical deformed shapes of this structure in the multiple pure tone and blade passage frequency bands are shown in Figures 6 and 7 respectively. Examination of these plots reveals the rocking and bending of the forward angle stiffener which causes rivet failure in this region. Because the excitation environments span the frequency ranges of 800-1200 Hertz and 2800-3000 Hertz, simply determining the stress associated with the inlet ring response at a single frequency does not fully characterize the stresses developed in the structure. In order to assess the stress generated by the random response of the inlet ring, Baranek[5] suggests the use of a root sum squared combination of the stresses determined from each individual mode. The difference in bandwidths of the two frequency regimes was taken into account by using an
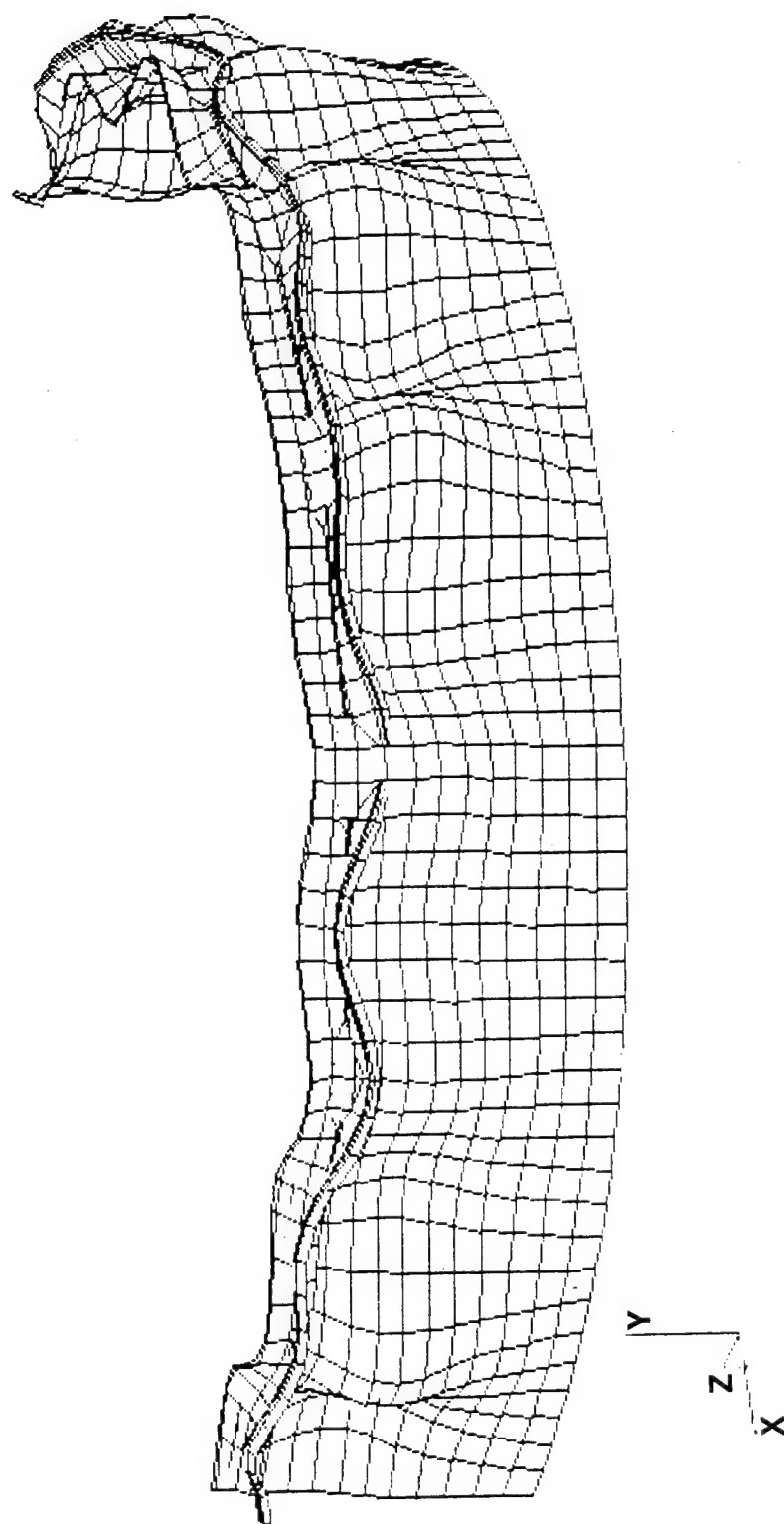
Figure 6 - Typical Deformed Shape Plot of the Baseline Finite Element Model in an 800-1200 Hz Environment
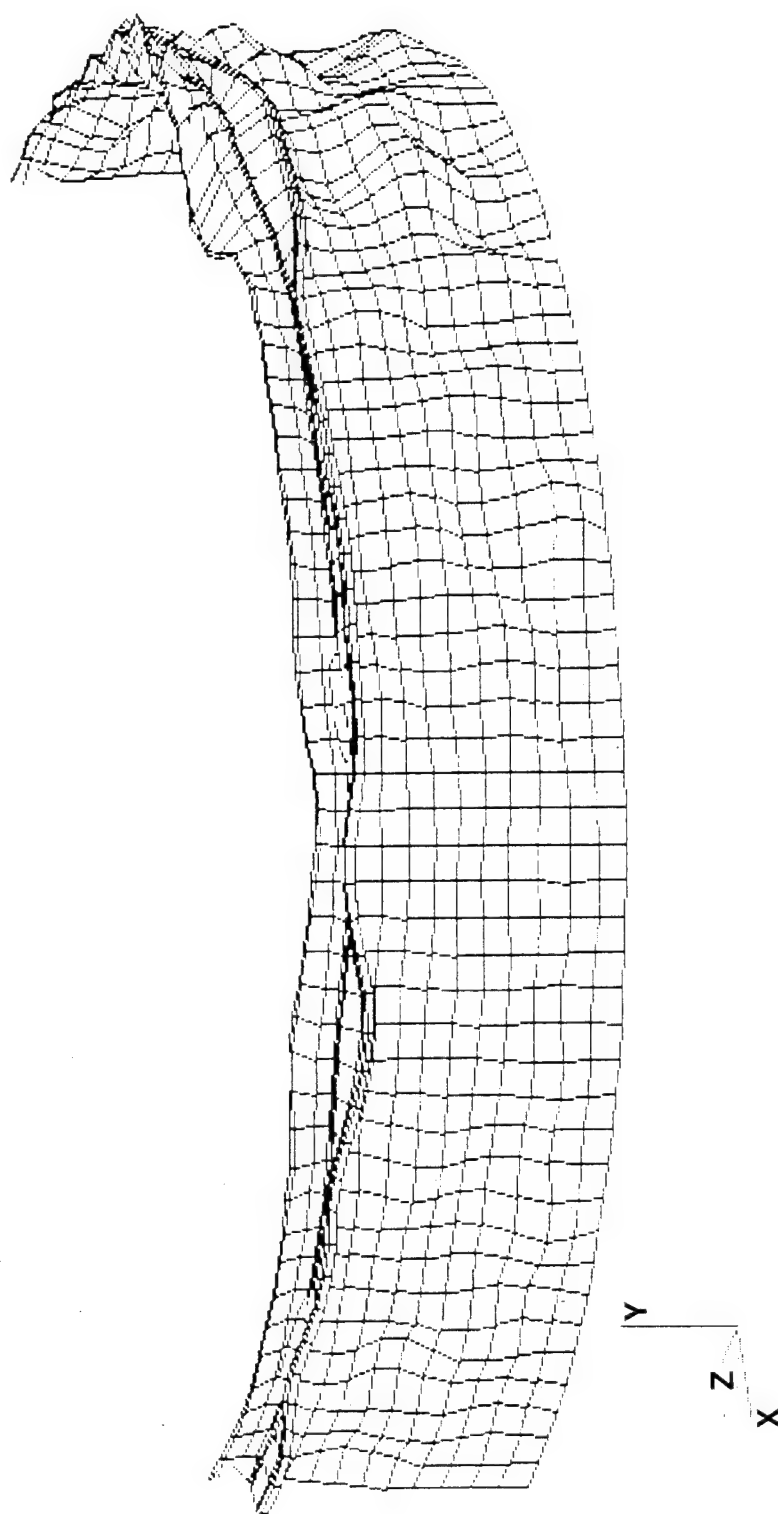
Figure 7 - Typical Deformed Shape Plot of the Baseline Finite Element Model in a 2800-3000 Hz Environment

equal number of the most severe modes from each bandwidth in this calculation. Upon calculating an equivalent stress for the frequency range, a constitutive relationship, derived from reference 6 for high cycle fatigue of monolithic aluminum, was applied to determine the life of various discrete structural elements of the baseline inlet ring. Applying the duty cycle information obtained previously yielded theoretical flight times to failure.

The results of the sonic stress analysis identified the rivets attaching the forward angle stiffener to the inlet skin as the most highly stressed region of the baseline inlet ring. Subsequent fatigue analysis, using the high cycle stress-life relationship described previously and Miner's Rule of cumulative damage, established a rivet life of 21.6 flight hours with the multiple pure tone environment contributing 99.8 percent of the fatigue damage. The significance of the multiple pure tone contribution based on analysis, coupled with the magnitude of the response witnessed during the engine ground run test, combine to substantiate this environment as the dominant fatigue mechanism. A good correlation between measured inlet ring response, and the response obtained through finite element analysis, served to further reinforce this hypothesis.

To substantiate the importance of the multiple pure tone regime in contributing to the failure of the baseline component, a series of laboratory tests were initiated. A modal analysis was performed on the baseline inlet ring to determine the modes of the actual structure and evaluate how these modes compare with those determined though finite element analysis. The inlet ring was mounted in a progressive wave tube and subjected to burst random excitation generated by two electro-pneumatic transducers attached to the front of the wave tube. This test setup is shown in Figure 8. A roving accelerometer was used to evaluate the response of the inlet ring at various points around its circumference. The data recorded from the roving accelerometer was then fed into a fast Fourier modal analyzer to determine the resonant modes of the structure. The structural modes of the baseline inlet ring were in good agreement with those established in the finite element analysis. Upon completion of the modal analysis testing, a sine sweep was performed. Since the duplication of the multiple pure tone environment required the use of a random excitation, and because the electro-pneumatic transducers could not produce this environment at sufficient sound pressure levels to duplicate the levels realized in service, a 45° section of the inlet ring was removed and mounted to an electro-dynamic shaker. Figure 9 illustrates this installation. A 45° segment was chosen as a result of the mode shapes of the structure identified from modal analysis. This segment provided a minimum of two wave lengths at the lowest frequencies, thus eliminating any adverse effects to the local structural response due to the clamped boundaries.

Sine sweeps of the segment confirmed the correlation of the response between the segment and the complete inlet ring. Validation of the similarity of the response led the way for the initiation of fatigue testing which duplicated the multiple pure tone environment. Dwell fatigue testing was initiated at 40g RMS in a bandwidth from 800-1500 Hz. The first rivet failure occurred after approximately 20 minutes of dwell testing. Total failure of the segment forward angle stiffener to skin joint was accomplished after 11 hours of dwell. When extrapolated to
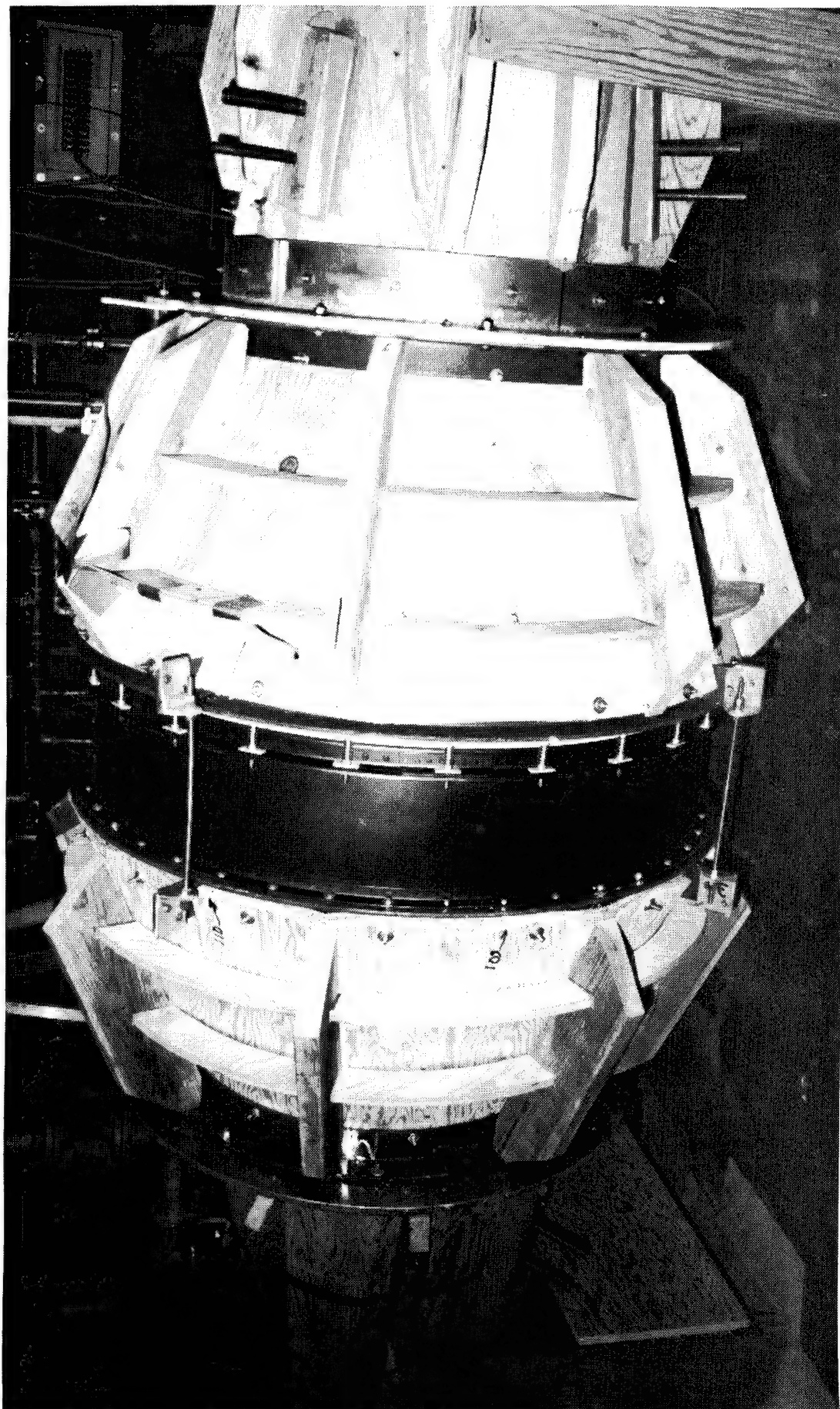
Figure 8 - Baseline Inlet Ring Installed in a Progressive Wave Tube
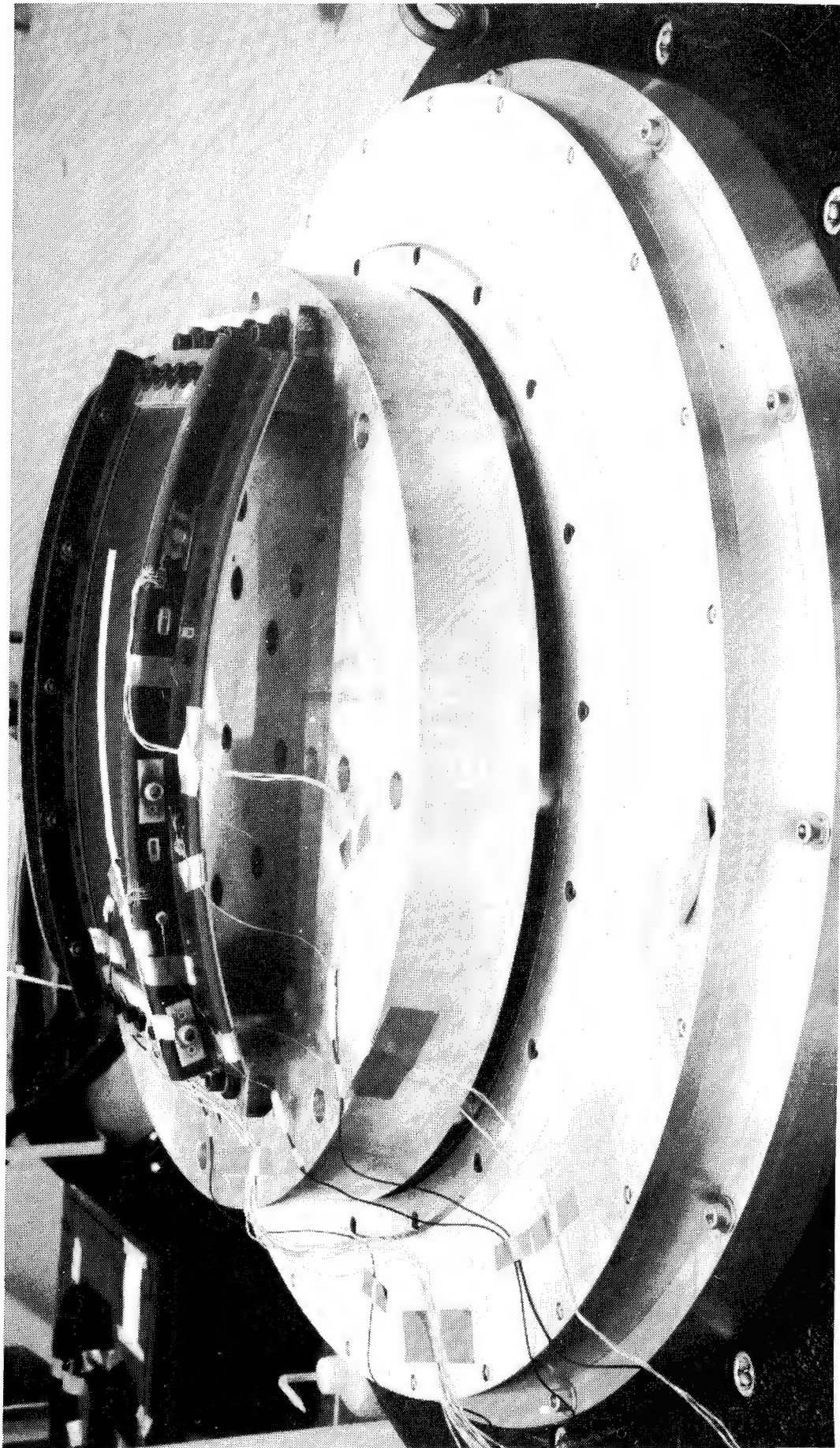
Figure 9 - Baseline Inlet Ring Segment Mounted to an Electro-Dynamic Shaker

flight times based on duty cycle, the failures that occurred in the laboratory testing were within the range of the failure times reported by Air Force maintenance personnel. By establishing the correlation between analysis, testing, and service experience, the foundation had been established for the design criteria, as well as providing a direct standard of comparison between the baseline and advanced designs during both analysis and test.

DESIGN DEVELOPMENT

Based on the environments identified when establishing the design criteria, the advanced inlet ring had to be designed to withstand a severe acoustic excitation. Guidelines utilized in the design of a structure subjected to high intensity acoustic excitation include providing continuous load paths, avoiding stiffness discontinuities, and incorporating structural damping where necessary. Many of the failures of the baseline inlet ring were the result of not adhering to these basic acoustic fatigue design principals. Therefore, other than the dimensional envelope dictated by the installation, the advanced inlet ring required a complete re-design. Some add-on fixes are available to provide acoustic fatigue resistance, but none of these treatments could remedy the inherent deficiencies of the baseline inlet ring. The elements of the baseline design which were eliminated from the advanced inlet ring include: 1) the riveted forward ring attachment, 2) the discontinuous splice configuration, and 3) the discrete spring elements. Improvements were also necessary in the area which forms a seal with the nacelle lip at the flexible forward interface. The design configuration created to satisfy these criteria is depicted in Figure 10.

Examining this cross-section reveals the elimination of the of the rivets at the forward flange by incorporating this element into the inlet skin. The discrete spring elements were replaced by a continuous elastomer spring which serves to evenly distribute the compression load when installed in an aircraft, as well as effecting a seal around the circumference. Figure 11 illustrates that by forming the nine individual skin plies simultaneously, and staggering the location at which each ply terminates, a continuous, spliceless skin can be produced. The laminated skin also serves as a method by which damping can be incorporated into the design. 3M's AF-32, a viscoelastic, nitrile phenolic adhesive, with proven damping properties, was used in this manner. Additionally, while no problems were recognized with the aft angle stiffener, its attachment method was modified to incorporate a rivet-bond procedure. The adhesive bond in this interface serves to provide a continuous path for load transfer and effectively reduces the stress concentration normally associated with a conventional riveted joint. This characteristic has proven to be especially advantageous on previous LTV programs, for detail attachment in structures subjected to severe acoustic excitation. Since the adhesive is the primary load carrying component of the joint, the number of rivets used in the aft ring attachment were reduced from the quantity used in the baseline inlet ring.

Upon completing the design development based upon the acoustic fatigue design practices outlined previously, analysis of the advanced inlet ring was initiated. The establishment of the baseline finite element model,

RIVET-BONDED AFT RING

DAMPED SKIN (NO SPLICE)

INTEGRAL FLANGE

ELASTOMER SPRING/SEAL
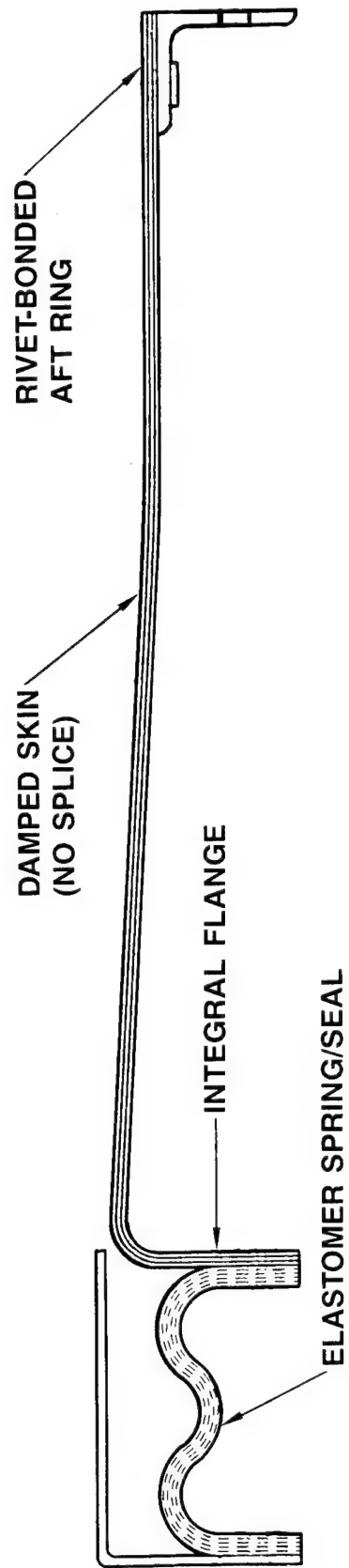
Figure 10 - Advanced Design Inlet Ring Cross-Section
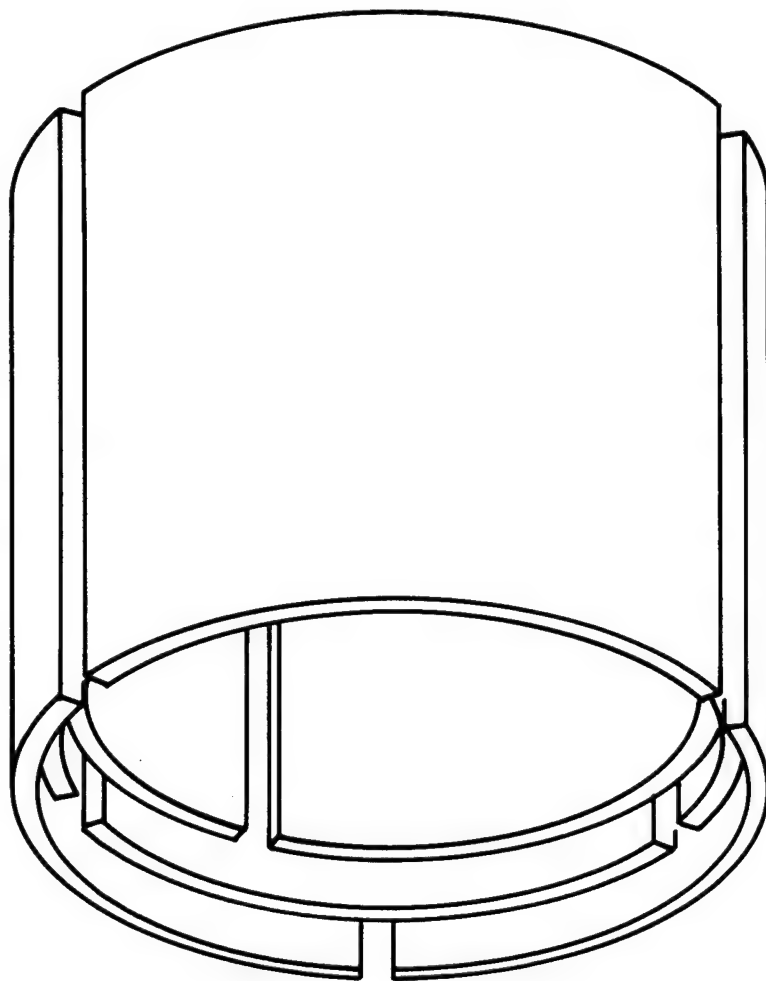
Figure 11 - Schematic of the Ply Nesting used in Production of the Advanced Inlet Ring Skin

with the results substantiated through laboratory and field test, provided the ground work for an advanced design finite element model which utilized similar assumptions. Consequently, the relative durabilities of the two components could be assessed prior to hardware production. An MSC/NASTRAN finite element model was constructed to evaluate the effects of the acoustic environment on the advanced inlet ring. Normal modes and response analyses were performed. Figure 12 illustrates a typical structural mode in the multiple pure tone frequency range and Figure 13 is indicative of modes occurring in the blade passage environment. Circumferential bending modes are also evident at the integral forward flange similar to those identified in the baseline inlet ring; however, the incorporation of damping reduces the stresses in this region to acceptable levels. The stress results from the frequency response analysis at discrete frequencies within the bandwidths of interest were combined using the same root sum squared procedure described for the baseline design analysis. The stresses which were identified in the various regions of the advanced inlet ring were, in all cases, much lower than those observed for the baseline design. Applying the same stress life relationship and duty cycle information utilized in the baseline design analysis, the projected total life, and life in flight hours based on duty cycle were obtained. This sonic fatigue analysis predicted a life greater than 6.9×10^5 flight hours for the advanced component.

The design development and analysis procedures were confirmed through segment and element testing of portions of the baseline and advanced design components. These tests provided a one-to-one durability comparison between the elements of each design before the advanced design inlet ring configuration was finalized and a full scale component produced. The tests also served to confirm analysis techniques and provide data where published data and analysis procedures were inadequate. The first of these series of tests compared the forward sections of each inlet ring design. Small straight sections representative of the forward ring area of both the baseline and advanced configurations were tested on an electro-dynamic shaker. The baseline segment exhibited rivet failure in three hours of dwell which was similar to those failures observed on the full scale baseline inlet ring. The advanced configuration was tested for the equivalent of 25 times that of the baseline segment, without failure, before the test was terminated. Acoustic test panels were used to confirm the advanced skin lap joint durability and compare that with the durability of the discrete splice plates used in the baseline design. The baseline panel, when mounted in a progressive wave tube and subjected to an acoustic environment, failed in four hours in a manner similar to that observed in inlet rings in service. The advanced panel was tested more than ten hours under the same environmental conditions without failure before testing was terminated. Other elements of the advanced design were tested simply to prove the proposed fabrication concept without a relevant comparison to the baseline inlet ring. These tests included the static and fatigue evaluation of the elastomer attachment method to the forward flange, and an abrasive wear test of a Teflon coating used to prevent metal-to-metal abrasion in the inlet skin radius.

The positive conclusions drawn from the development and analysis, combined with the confirmation of the design elements through segment and element testing, led the way for production of a full scale test component. The advanced inlet ring test article is shown in Figure 14. This inlet
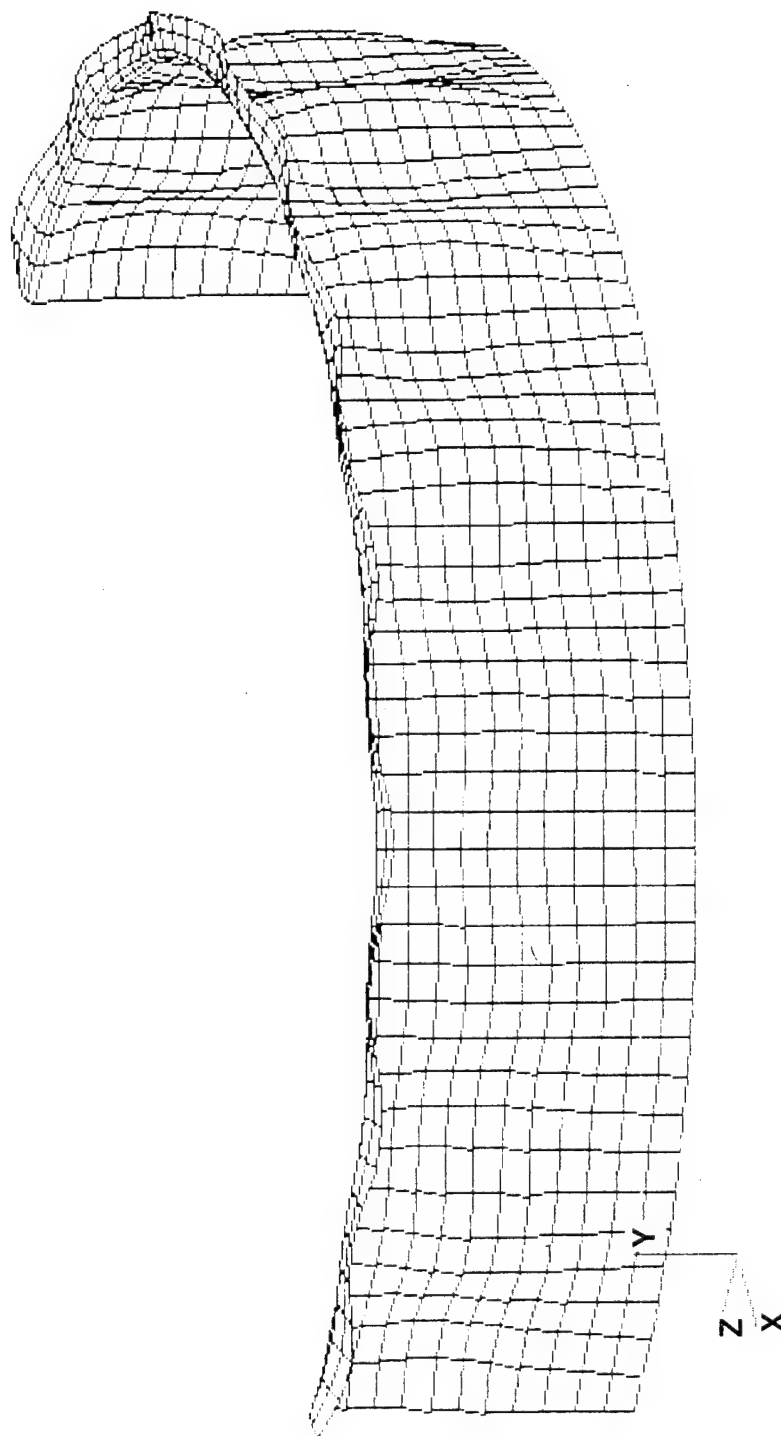
Figure 12 - Typical Deformed Shape Plot of the Advanced Finite Element Model in an 800-1200 Hz Environment
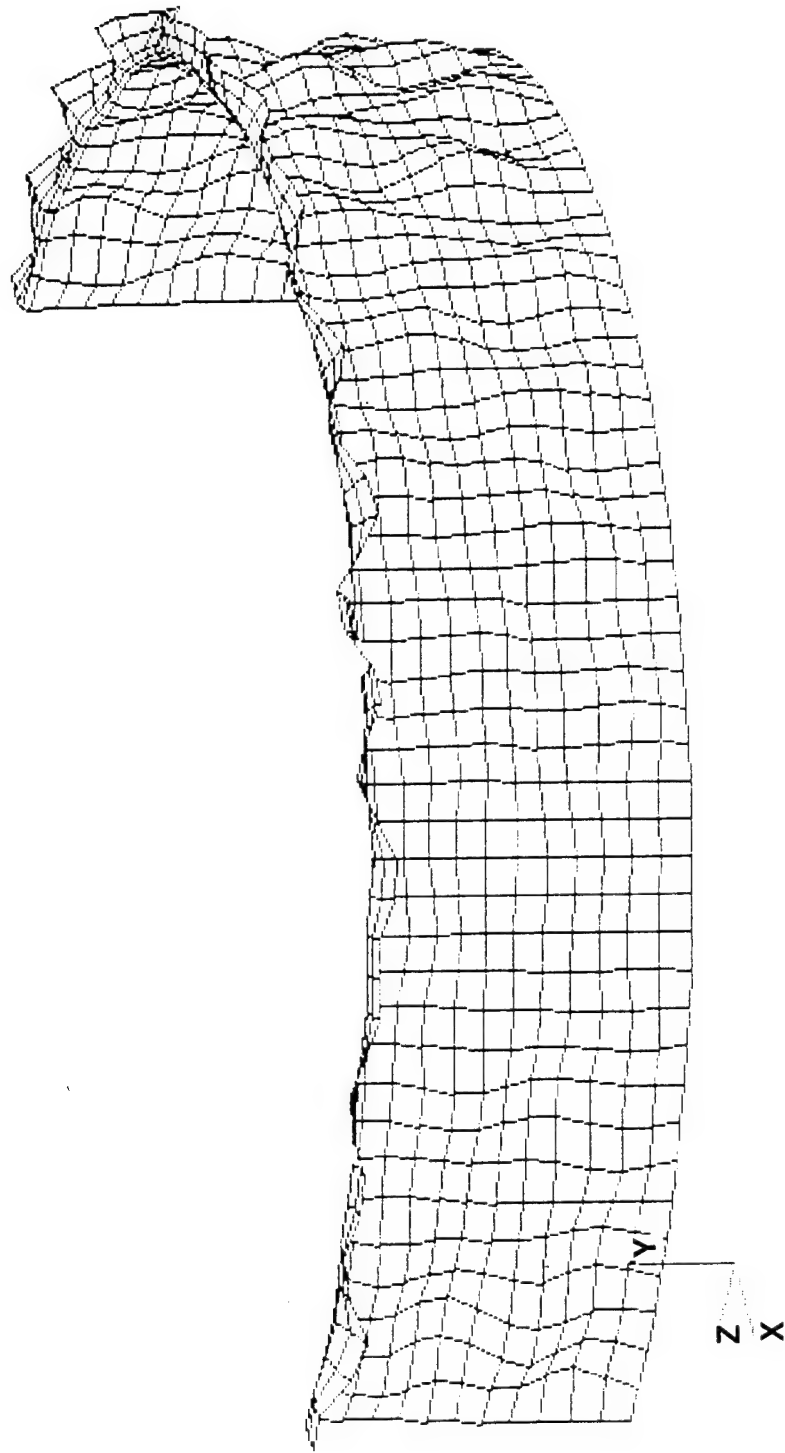
Figure 13 - Typical Deformed Shape Plot of the Advanced Finite Element Model in a 2800-3000 Hz Environment
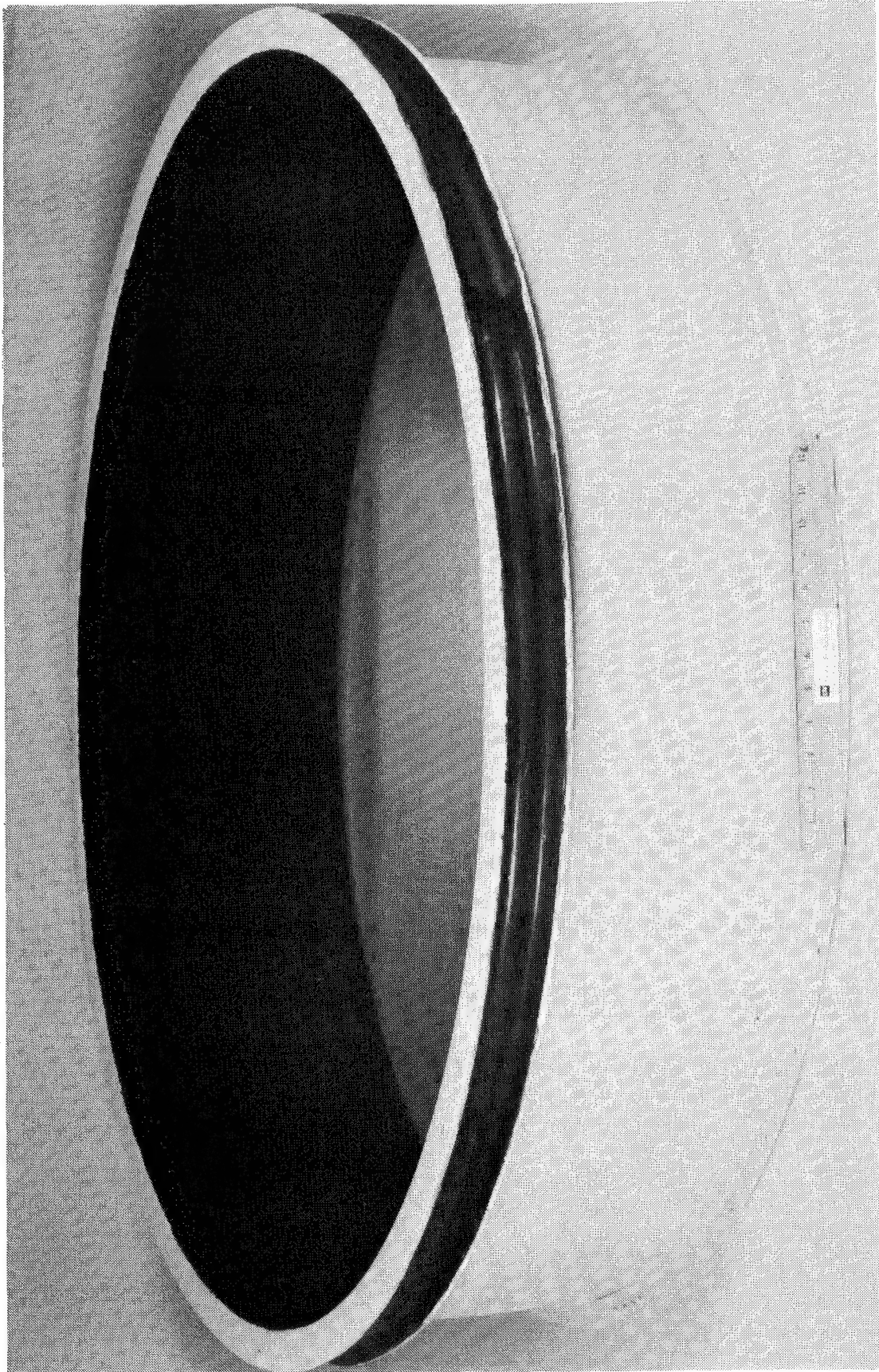
Figure 14 - Advanced Design Inlet Ring Test Article

ring was subjected to the same testing performed on the baseline inlet ring. First, a modal analysis was used to determine the resonant modes of the structure. Only four normal modes were extracted from the multiple pure tone frequency regime. Those modes that were obtained were ill defined and poorly correlated, which is indicative of a highly damped structure. A 45° segment was then removed from the inlet ring and mounted on an electro-dynamic shaker. Sine sweeps performed on this panel revealed broad peaks in the stress and acceleration versus frequency domain, which is also behavior typical of damped structure. Fatigue testing was initiated at 40g RMS from 800 to 1500 Hertz after the completion of the initial structural response testing. The advanced configuration was tested for 31 hours without failure before the level was increased to 50g RMS in the same frequency bandwidth. Six more hours of dwell were completed successfully before the testing was terminated.

DESIGN COMPARISON

The analysis and testing performed on the baseline and advanced design inlet rings provide a dramatic comparison between the relative durabilities of the two components. Analysis indicated that an 80 percent reduction in peak stress levels, and a durability increase of greater than a factor of 1000 could be expected for the advanced inlet ring. Full scale structural response and fatigue testing confirmed these predictions. Based on this testing, the advanced design exhibited less than half the number of modes in the multiple pure tone regime, demonstrated an 80 percent decrease in structural response, and was tested to greater than 500 times the life of baseline inlet ring without failure. As with any aircraft structure, durability alone is not the only consideration in assessing two functionally equivalent designs. The final structural weight and cost must also be evaluated to judge the effectiveness of the acoustic fatigue design practices outlined in this paper. Comparing these aspects of the baseline and advanced inlet rings reveals that the advanced component contains 86 percent fewer detailed parts, weighs 15 percent less, and has a preliminary projected cost reduction from the baseline inlet ring on the order of 25 percent. These comparisons highlight the effectiveness of the incorporation of integral damping as well as other other basic acoustic fatigue design principals in generating a lighter, more durable, and cost effective design.

CONCLUSION

The design of the advanced inlet ring was achieved through a systematic process of evaluation, analysis, design, and testing which validated the final configuration. First, potential causes of the baseline inlet ring failures were identified, and the installation environment was characterized through field testing. Once the potential causes of damage were recognized, the baseline structure was analytically modeled and tested in a controlled laboratory environment to confirm the failure modes exhibited in service. These activities served to pinpoint the most damaging acoustic environment. Having established the cause of the structural failures of the baseline component, detailed development and analysis of advanced design concepts were initiated. By adhering to acoustic fatigue design practices which suggest providing continuous load

paths, avoiding stiffness discontinuities, and incorporating damping, a final advanced design configuration was achieved. The final step of the process involved applying the same testing used for the baseline design to the advanced inlet ring. Extensive laboratory testing validated the development and analysis of the final advanced inlet ring configuration. Using this approach, an inlet ring which has demonstrated durabilities in excess of 500 times greater than the baseline component while also reducing overall detailed part count and total structural weight was achieved. These factors are expected to contribute to a decrease in the life cycle cost, and an improvement in operational availability of Air Force fleet aircraft. Demonstrating this technology on smaller secondary structure should also lead to the realization that this technology is a viable alternative for application to larger primary aircraft structures subjected to high intensity acoustic environments.

ACKNOWLEDGMENTS

REFERENCES

1) Thompson, A.G.R., et al, "Acoustic Fatigue Design Data, Part IV", Advisory Group for Aerospace Research and Development, AGARD-AG-162, London, England, November 1972.

2) Hancock, R. N., "Inlet Duct Sonic Fatigue Induced by the Multiple Pure Tones of a High Bypass Ratio Turbofan", Institute of Environmental Science Symposium, April 1973.

3) Kester, J. D., "Generation and Suppression of Combination Tone Noise from Turbofan Engines", Paper No. 19, Proceedings AGARD Fluid Dynamics Panel, Saint-Louis, France, May 1969.

4) Philpot, M. G., "The Buzz-Saw Noise Generated by a High Duty Transonic Compressor", ASME Paper No. 70-GT-54, May 1970, published in ASME Transactions, Journal of Engineering for Power, January 1971.

5) Beranek, Leo L., Noise and Vibration Control, McGraw Hill Book Company, New York, NY, 1971.

6) Thompson, A.G.R., et al, "Acoustic Fatigue Design Data, Part II", Advisory Group for Aerospace Research and Development, AGARD-AG-162, London, England, November 1972.

STATUS OF AIRCRAFT INTEGRAL DAMPING DEMONSTRATION

Carl L. Rupert*
Flight Dynamics Laboratory
WRDC/FIBG
Wright-Patterson AFB OH 45433-6523
and
Ralph E. Tate**
LTV-APG/MAD, M-S/194-26
P.O. Box 655907
Dallas TX 75265-5907

Abstract

The sound pressure levels generated by aircraft jet engines can result in sonic fatigue of structure and damage to sensitive, on-board electronic gear. The program objective is to develop the passive damping technology required to achieve sonic fatigue resistance at reduced weight and to suppress structural vibration within aircraft equipment bays. The approach is to incorporate constrained layer damping into the fuselage and equipment racks as an integral part of their design, rather than to use less effective add-on damping treatment after the structure has been manufactured. The aft equipment bay of the B-1B aircraft was selected as the baseline component with which to compare and demonstrate the technology developed in this program. The analyses and experimental testing accomplished during the preliminary design phase of this program are discussed. It is shown that integral damping can reduce vibration transmitted into equipment racks by 90 percent, and that the fuselage structure can be made sonic fatigue resistant at reduced weight.

Introduction

The skins and substructure of military aircraft are often exposed to intense vibroacoustic environments that can reduce structural fatigue life and cause equipment malfunction.

The usual design approach to reducing resonant response is to stiffen the structure, by increasing skin thickness for example, which results in a weight penalty. A need exists to develop lightweight aircraft structures that can withstand the severe environment while transmitting less vibration into equipment racks.

The use of add-on damping treatment is a common method of dealing with sonic fatigue and resonant vibration in aircraft skins and substructure. Previous exploratory development studies have shown that the most

cost-effective way to apply passive damping is to incorporate the viscoelastic material as an integral part of the structure during the design/fabrication process. This is a more efficient approach to reducing structural vibration than the addition of constrained layers of damping material, a method that characteristically requires more mass in order to be effective.

The purpose of the program described in this paper is to demonstrate that the use of advanced metallics can significantly reduce the weight and life-cycle cost of aircraft structures and equipment operating in a high vibroacoustic environment. This will be achieved by developing lightweight sonic fatigue-resistant aircraft structures incorporating passive damping. The validated technology that evolves from this program will provide generic guidance for the incorporation of new damping concepts and materials into the design of future aircraft. In addition, the technology will apply to the redesign of structural components on operational aircraft that have high maintenance costs. The program approach will be to redesign an existing aircraft structure that, because of its severe operational vibroacoustic environment, is especially vulnerable to damage from sonic fatigue, and whose interior equipment bays are subject to high vibration levels that adversely affect sensitive electronic gear. This baseline structure will be identified as the demonstration component.

Demonstration Component

The aft equipment bay (AEB) of the B-1B strategic bomber was selected as the baseline component for this program. It is considered the best of the candidate structures for several reasons. It is a major structural component, a 360 degree self-contained, retrofittable compartment that comprises part of the B-1B aft fuselage. The location of the AEB makes it an excellent baseline to demonstrate the objectives of this program (Fig. 1). It is located immediately aft and adjacent to the jet engine exhaust nozzles; as a result, the external surfaces of the AEB and the sensitive electronic gear within the bay are susceptible to damage from extended periods of exposure to the intense sound pressure levels (SPL) generated by the engines.

---

*Aerospace Engineer
**Engineering Specialist
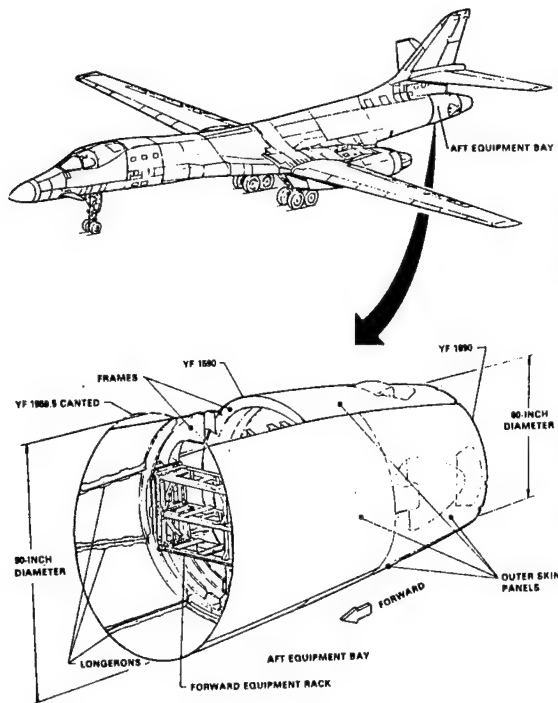
Fig. 1 Location of the Aft Equipment Bay on the B-1B Aircraft.

The AEB basic construction is conventional aluminum, stepped chem-milled skins riveted to a frame/longeron substructure. It contains two equipment rack assemblies, one forward and one aft, that are anchored to frame webs through cup-type vibration isolators. The AEB is 130 inches (3.30 m) long, with a 90 inch (2.29 m) forward diameter at station YF-1559, tapering down to 60 inches (1.52 m) at station YF1690. It weighs approximately 1350 lbs (612.9 kg) without avionics equipment installed. The AEB structure is sealed for pressurization above 8,000 ft (2440 m) altitude (Fig. 2 and 3).
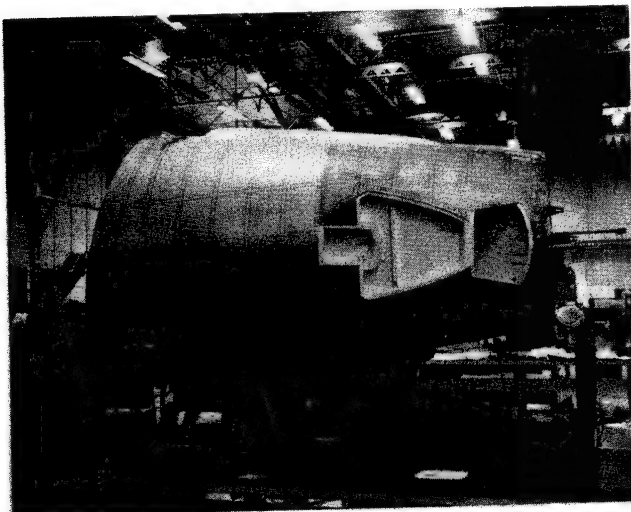
Fig. 2 Aft Equipment Bay (AEB).
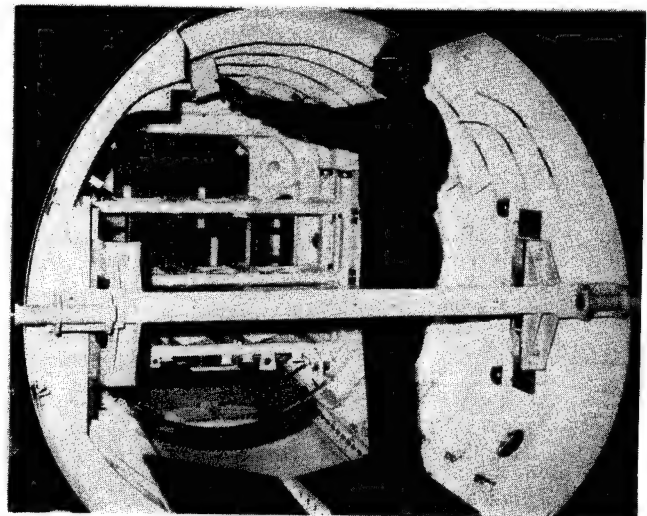
Fig. 3 View of the AEB Looking Aft.

Program Structure

The work described in this paper will be accomplished in three phases:

Phase I (Preliminary Analysis)

Baseline design criteria will be assembled and trade-off studies conducted of various viscoelastic materials and damping concepts. Coupon samples will be tested to evaluate candidate materials. Advanced design test panels will be fabricated for sonic fatigue and noise reduction tests. Advanced design features will be identified for the replacement AEB fuselage structure and equipment racks.

Phase II (Advanced Development Segment)

A full-scale structural segment of the replacement component will be fabricated using an advanced design based upon the results of Phase I. The segment will include internal structure that is integral to the segment, such as equipment racks, shelving, and shelving support structure. The instrumented segment will be used for modal response and acoustic fatigue tests and for noise reduction measurements. An assessment of the advanced segment performance will be made regarding its potential application in the design and construction of a complete full-scale component for future flight test demonstrations.

Phase III (Advanced Development Component)

The end product of this program will be a full-size, form-fit-and-function replacement structure that will be retrofittable in its entirety with the production baseline component. It will be designated as the advanced development component, designed on the basis of Phase I results and incorporating any modifications identified during the

advanced segment tests in Phase II. The advanced development component will be instrumented for static, dynamic and noise reduction tests. These tests will be performed in order to qualify the advanced development component for flight certification. Flight demonstrations of the advanced development component are planned for a future program.

Structural Analysis

Finite Element Model

The geometry of the baseline equipment racks, both fore and aft, is composed of a rigid system of shelving, braces and vertical rack supports interfacing the fuselage frames through an array of conventional cup-type vibration isolators. The forward equipment rack assembly is shown in Figures 4 and 5. At best, this arrangement presents a "stiff ride" for sensitive shelf-mounted equipment units in a severe vibroacoustic environment. Although most of the vibration is structurally transmitted into the racks, airborne noise within the AEB is a secondary source of excitation (Fig. 6).

Fig. 4   Sketch of Forward Equipment Rack Assembley.

To improve the vibroacoustic environment, a study was conducted to determine the best means of incorporating integral damping into the equipment rack structure. The approach taken was to conduct a modal analysis of the equipment rack structure using finite element modeling (FEM). Key rack components and structural joints, designated as Principal Design Features (PDFs), were selected for FEM analysis, both individually and as an assembly. The PDFs were: skin section, skin-to-frame joint, frame-to-rack interface,

rack-to-shelf interface, and shelf section. A finite element model of the baseline rack assembly is shown in Figure 7.

The rear access door of the AEB is constructed of graphite/epoxy skins bonded to a honeycomb core. In addition to the rack-related PDFs, the door also was modeled by FEM to investigate damping a composite component.

Analytical Results

The results from the equipment rack analysis are impressive. It was demonstrated by FEM that by using damped honeycomb shelves, each supported in a "floating beam" frame, the vertical end support posts and the vibration

Fig. 5   Forward Equipment Rack Mounted on Vibration Isolators (Without Center Post).

Fig. 6   Paths of Structural Vibration and Airborne Noise into the Equipment Rack.

isolators can be eliminated (Fig. 8 and 9). In their place, polymer "tension pads" will be used as an interface to independently anchor each shelf directly to the fuselage frames (Fig. 10). The tension pads also function as expansion joints during fuselage pressurization. The center support post of the rack structure will be retained. It is estimated that this "soft ride avionics" concept will reduce the total rack weight by over 50 percent and decrease vibration transmitted into equipment shelving by 90 percent.

Similarly, FEM analyses show that by using laminated skins/frames, sonic fatigue resistance of the fuselage structure can be achieved at a weight reduction of 20 to 25 percent.

Two concepts of damping the AEB composite access doors were examined by FEM. These are described in Acoustic Test Panels
It was shown that damping loss factors should be high enough to reduce the door weight by 5 percent.

Selection of Damping Adhesives

Different types of damping adhesives are required, each for a particular application, to incorporate damping into the various elements that comprise the advance design AEB skins and equipment racks. The expected resonant frequency responses and operational temperature ranges are the most important design parameters in adhesive selection. From previous screening, candidate adhesives were evaluated according to type for three particular applications; for use in laminated skins, rivet-bonding and graphite/epoxy structure.

Standard ASTM test specimens were used to characterize the strength and damping properties of the candidate adhesives. These included lap shear and creep coupons and vibrating reeds. From these tests nomographs were constructed showing how the loss factor and shear modulus of a particular adhesive vary for a given combination of temperature and frequency. An example is shown in Figure 11. The nomograph is entered horizontally from the right at the selected resonant frequency. Where that horizontal line intersects the temperature of interest, a vertical line is drawn. It, in turn will intersect the two plotted curves, giving the respective values of shear modulus and loss factor. The most promising of the candidate adhesives were identified for further evaluation.

Effective damping can be extended over a wider range of temperatures by using a "duplex system" of adhesives. This entails the use of two different adhesives, each with its own effective temperature range, in a back-to-back layup and single cure cycle.
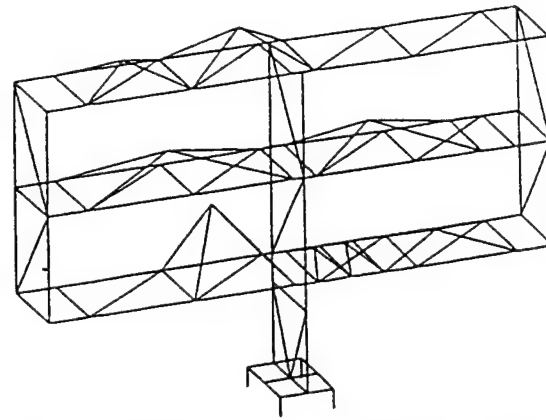
Fig. 7 Finite Element Model of the Baseline Forward Equipment Rack.
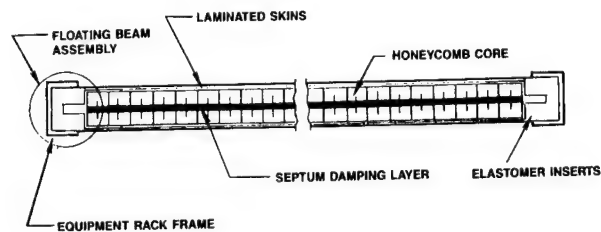
Fig. 8 Honeycomb Shelf with Laminated Skins and Damping Septum.
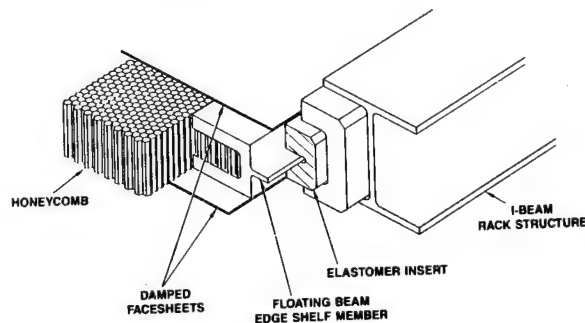
Fig. 9 Floating Beam Support for Equipment Rack Shelves.
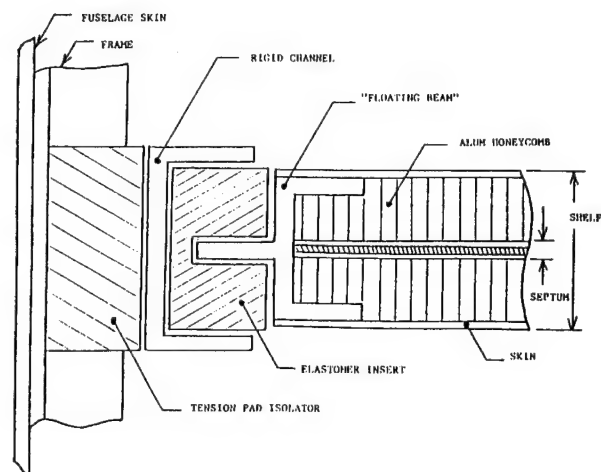
Fig. 10 Shelf Interface with Fuselage Frame.

BBC-4

Two duplex systems were selected for both metallic and Graphite/Epoxy laminates. They were AF-32/PM-2160 (film-film) and AF-32/EC-1838 (film-paste) (Fig. 12). AF-32 performed best at lower temperatures. Both the PM-2160 and the EC-1838 were selected for their high temperature properties and because their processing and cure characteristics were compatible with AF-32. Although paste adhesives are generally more difficult to work with, EC-1838 was included for comparison.

EC-3594 is the preferred adhesive for rivet bonding. It meets the room temperature cure requirement and has a pot life long enough to enable completion of assembly before it sets-up.

Acoustic Test Panels

Configurations

Nine curved acoustic test panels were fabricated to evaluate different skin laminates, using the damping adhesives previously identified. Each panel is curved to a 48 inch (1.22 m) radius, with a 50 inch (1.27 m) arc length and 30 inch (0.76 m) width. The features of each of the nine panels are listed in Table I.

Six of the panels are metallic, 9-bay configurations that represent the frame/longeron construction at Station YF 1610 on the B-1B AEB (Fig. 13). The six metallic panels are divided into two groups of three each; the first group (Concept 1.0) all have riveted skins; the second group (Concept 2.0) all have rivet-bonded skins. Concept 1.1 is the undamped baseline metallic with chem-milled lands. The remaining five metallic panels have laminated skins with bonded doublers. They vary within their own group only by the type of damping adhesive used in the laminates; the exception is Concept 2.3, which has damped frames in addition to laminated skins.

Table 1 Acoustic Test Panel Configurations

BASIC GROUP	CONCEPT	CONSTRUCTION	ADHESIVES
1.0 METALLIC	1.1	BASELINE	
	1.2	LAMINATED SKIN	DUPLEX (A) AF-32/EC-1838
RIVETED SKIN AND FRAMES	1.3	" "	DUPLEX (B) AF-32/PM-2160
2.0 METALLIC	2.1	" "	(A)
	2.2	" "	(B)
RIVET BONDED SKIN AND FRAMES (EC-3594)	2.3	LAMINATED SKIN AND FRAMES	(B)
3.0 COMPOSITE	3.1	BASELINE	
	3.2	LAMINATED SKINS OR DAMPING SEPTUM	(B)
GR/EP SKINS HONEYCOMB CORE (FM-300)	3.3	TUNED DAMPERS	PRC-1750 SILICONE
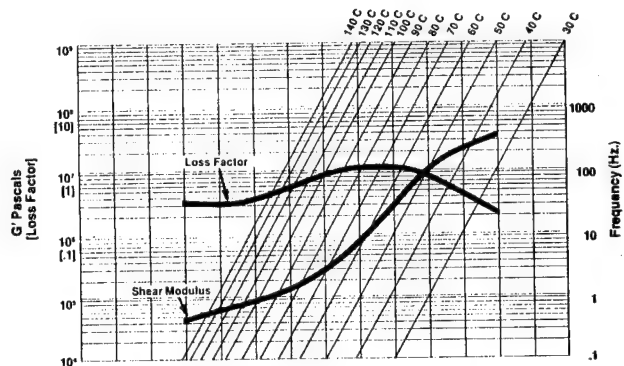
Fig. 11 Loss Factor and Shear Modulus of a Viscoelastic Material Related to Frequency and Temperature.
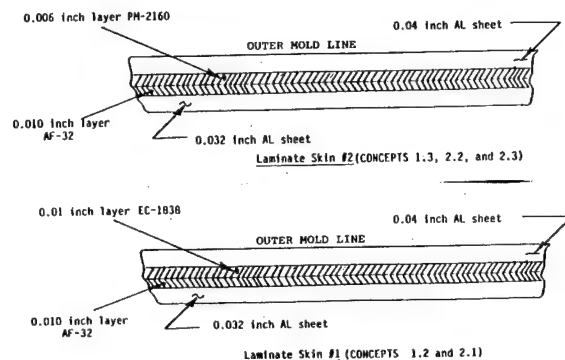
Fig. 12 Duplex Viscoelastic Damping Adhesives.
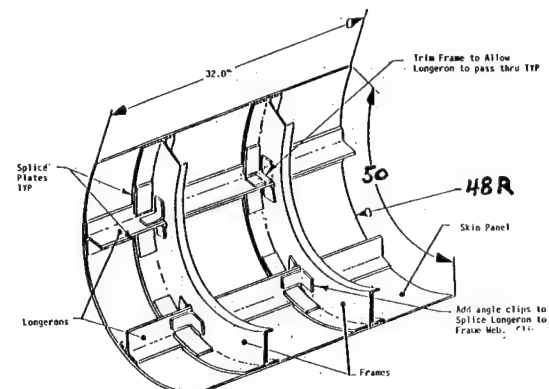
Fig. 13 Construction of Metallic 9-Bay Acoustic Test Panels.
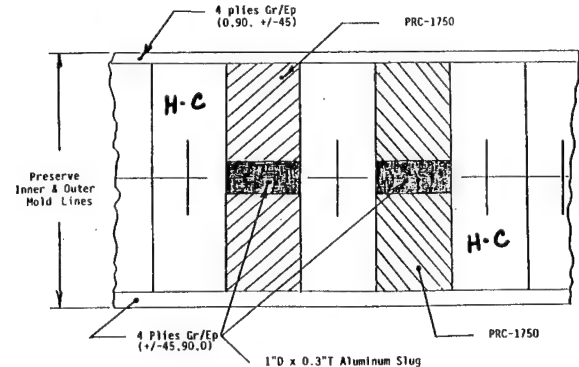
Fig. 14 Cross Section of Composite Panel Using Tuned Dampers.

The remaining three panels (Concept 3.0) are constructed with graphite/epoxy skins bonded to an aluminumin honeycomb core. Concept 3.1 is the baseline configuration with no damping.

Concept 3.2 will have either damped skins or a damping septum within the structure that divides the honeycomb core near the neutral axis. This configuration is similar to the damped honeycomb shelf shown in Figure 8.

Concept 3.3 uses a damping system composed of an array of "tuned-damper" aluminum slugs. As shown in Figure 14, each slug is suspended within the honeycomb core between two silicone inserts. This allows each slug to oscillate freely on an axis normal to the skins. The slugs are designed to oscillate at maximum amplitude when the panel is at its fundamental resonant frequency. In principle, this is the mechanism by which the vibration energy is dissipated.
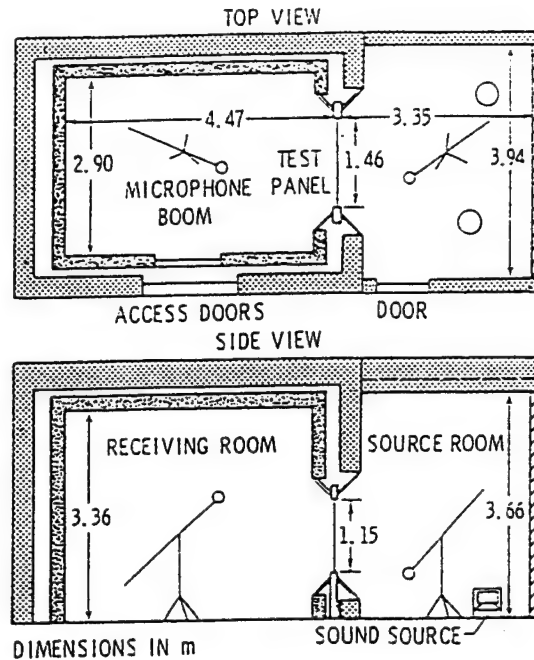
Fig. 15 NASA LaRC Noise Reduction Test Facility.

Test Conditions

A test plan was developed to evaluate the performance of the candidate damping adhesives and the damping concepts that are represented by the nine acoustic test panels. Experimental data will be obtained to determine the modal response, sound transmission loss and sonic fatigue resistance of each panel.

Response Tests

Modal response data will be recorded using two test methods, during which each panel is shaker-driven while mounted in a high-mass test fixture. The roving accelerometer method will be used first, followed by a holographic technique that enables mode shapes to be recorded on video tape or by still photography.

Additional modal response data will be recorded during frequency sweeps made with the panels mounted in a progressive wave test section and using electropneumatic noise generators as a source of acoustic excitation. All modal tests will be accomplished at the Flight Dynamics Laboratory's sonic fatigue test facility at Wright-Patterson AFB, OH.

Noise Reduction Tests

A sound transmission survey will be made to determine the noise loss through each of the nine panels. These tests will be conducted at the NASA Langley Research Center, Hampton VA. Their noise reduction test facility is composed of a "source" room and a "receiving" room (Fig. 15). Each of the panels will be installed in a rubber-mounted steel fixture that is built into the wall dividing the source and receiving rooms.

A random sound field is generated in the source room by two floor-standing centrifugal fans, reinforced by loudspeakers to obtain the required broadband spectrum over a frequency range of 100 Hz to 10 kHz.

Space- and time-average recordings of the SPL are made during a 32 second sampling in both rooms for each test condition. Panel temperatures are monitored using thermocouples, and accelerometer data are recorded from the center bay of each panel.

It is planned to test each panel at ambient temperature and at $180^{\circ}F$, first without and then with an acoustic/thermal material applied to the "receiving side" of the panel. A Fiberglas thermal blanket will be used on the two baseline panels. A sound absorbent polyurethane foam will be applied to each of the remaining seven advanced design panels. The test procedure for each panel in turn will be:

a) Install panel without treatment.

b) Conduct noise reduction test at ambient room temperature.

c) Heat panel until its "source side" temperature stabilizes at $190^{\circ}F \pm 10$ degrees, then conduct noise reduction test.

d) Install appropriate material on the receiving side of the panel.

e) Conduct noise reduction test at ambient room temperature.

f) Repeat (c).

Fatigue Tests

Acoustic tests will be conducted on each of the nine panels to evaluate their sonic fatigue resistance. Each panel will be installed in a 2 ft (0.61 m) wide x 6 ft (1.83 m) high x 8 ft (2.44 m) long progressive wave test section at the Flight Dynamics Laboratory's sonic fatigue test facility located at WPAFB OH. A sketch of the facility is shown in Figure 16. Three Wyle 30 kilowatt electropneumatic noise generators provide the noise source. They are controllable from 50 Hz to 500 Hz. The upper regions of the spectrum are filled in by the harmonics.
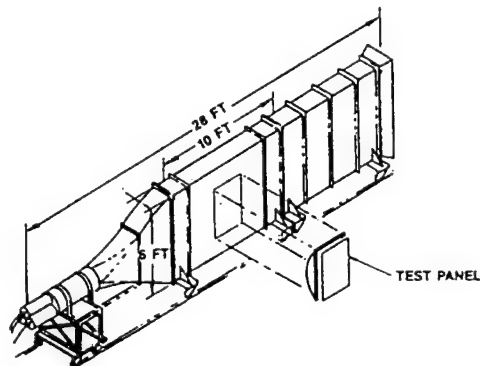
Fig. 16 Progressive Wave Test Section.

The qualification test conditions will be based upon measured flight data that show the AEB experiences 168-169 dB overall SPL at Station YF-1610 represented by the test panels (Fig. 17). Spectrum shaping will be accomplished by concentrating much of the acoustic power output into the 1/3 octave bands that contain the predominant response peaks that were identified during preliminary sine wave sweeps. The required test duration for each panel has been established at 21 hours. This figure is based on the predicted number of full-afterburner takeoffs that the B-1B aircraft will make during its projected 25 year life.
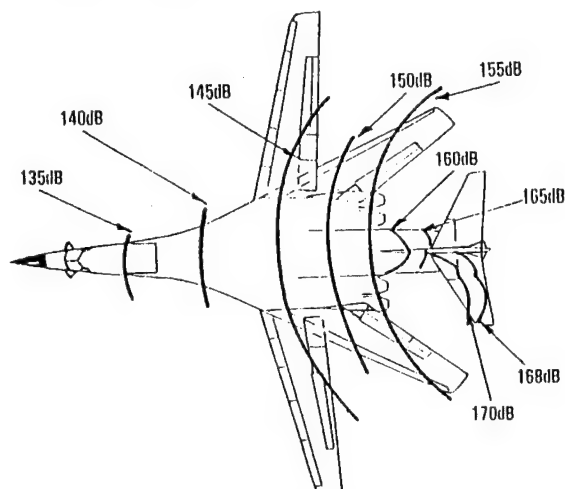
Fig. 17 SPL Contours on the B-1B Aircraft.

Summary

The results of the FEM study show that a less complex design of the equipment racks can be achieved by incorporating integral damping into the structure. This can be accomplished primarily by using damped honeycomb shelves with "floating beam" corner supports. These innovations would eliminate the need for the heavy vertical end posts and bulky vibration-isolators, resulting in a weight reduction of over 50 percent.

The results also show that the sonic fatigue resistance of the fuselage structure can be attained by using laminated skins rivet-bonded to the substructure while reducing weight by 20 to 25 percent.

In addition, it is estimated that the overall redesign of the aft equipment bay will result in a 90 percent reduction in the vibroacoustic environment currently experienced by shelf-mounted line equipment items in the baseline AEB.

BBC-7

Abstract
Damping in Metal Matrix Composites -An Overview

S. P. Rawal
J. H. Armstrong
M. S. Misra
Martin Marietta Space Systems, Denver, CO

S. G. Fishman
Office of Naval Research, Arlington, VA

Measurements of damping in metal matrix composites (MMC) have been conducted in flexural and extensional modes over a wide spectrum of frequency (1Hz - 80Hz) and strain amplitude (10^{-7}- 10^{-3} in/in) with various test techniques. Dynamic response of MMC can be described in terms of strain amplitude independent and dependent damping behavior. At very low strain amplitudes ($\sim 5 \times 10^{-5}$), damping is nearly independent of strain amplitude level, but varies with frequency showing a Zener relaxation peak. The total composite damping can be calculated from the modulus or strain energy weighted rule of mixtures. Average damping capacity (Ψ) of MMC is generally less than the Ψ value for matrix alloy because reinforcing fibers and whiskers have inherently very low damping. Beyond a critical strain amplitude level, the damping capacity of composite increases with increasing strain amplitude. This strain amplitude dependent response can be explained in terms of the Granato-Lucke theory which is based on a dislocation breakaway model. Also discussed are the efforts to improve damping in MMC by modifying the microstructural characteristics of fiber, matrix, and interfaces.[†] With enhanced damping contribution from MMC structural materials, the degree of additional passive and active controls required may be reduced for large precision space structures.

[†]   S. P. Rawal, J. H. Armstrong and M. S. Misra, "Interfaces and Damping in Metal Matrix Composites," Final Report No. MCR-86-684, prepared for Office of Naval Research, Arlington, VA.
M. S. Misra, S. P. Rawal and J. H. Armstrong, "Damping Characteristics of Metal Matrix Composites," Technical Report No. MCR-8-634, prepared for Office of Naval Research, Arlington, VA.

HIGHLY DAMPED GR/MG COMPOSITES FOR FLEXIBLE SPACE STRUCTURES

Uday Kashalikar
Joseph Boyce
Foster-Miller, Inc., Waltham, MA
(617) 890-3200

ABSTRACT

Structures for space-based weapons must possess a high vibrational damping for effective defense against a multiple missile threat. Development of an ultrastiff material ($E/\rho > 8 \times 10^8$ in.) with high inherent damping capacity ($\psi > 2$ percent) in the high frequency-low strain region will improve performance and reliability of the system, and reduce the need for active damping.

The Interfacial Slip Damping (ISD) mechanism consists of dissipating frictional energy at the fiber/matrix interface under external dynamic loading. In case of Gr/Mg composites, the fabrication residual stresses and the interface frictional coefficient must be reduced in order to promote energy dissipation by controlled interfacial slip rather than initiation and/or propagation of matrix cracks. The ISD phenomenon is effective even at low strain levels ($<10^{-5}$) which is essential for a fast decay of free structural vibrations to an acceptable amplitude. A 150 percent improvement in damping was achieved with P-55 Gr/Mg composite (from $\psi = 1.6$ percent to $\psi = 4$ percent), by promoting the ISD mechanism.

Advanced space structures will benefit from this technology in the following ways:

- Damping - Large improvements in strain-independent damping. A simplified model predicts that close to an order of magnitude improvement in damping is achievable with <5 percent reduction in stiffness of Gr/Mg metal matrix composite (MMC).

- Specific stiffness - High fiber content ($v_f > 60$ percent) will result in an outstanding specific stiffness ($>9 \times 10^8$ in. with 100-Msi reinforcement).

- Cost - Reduced requirement for active damping will lower structural cost.

INTRODUCTION

Continuous fiber-reinforced MMCs are well-suited for space structural applications because they typically possess a high specific stiffness, a near-zero coefficient of thermal expansion (CTE) and a good resistance to the space environment. In addition, flexible space structures such as the Space Based Laser (SBL) will require structural materials with a high inherent damping to achieve the requisite dynamic dimensional precision. The SBL is intended to destroy a large number of target missiles in a very brief period of time, which will require rapid retargeting and accurate firing capability. The short "readiness-to-fire" time for the SBL dictates that the vibrations induced under the inertial retarget loads must be damped quickly. As presented in Figure 1, the settling period of free vibrations will largely control the effectiveness of the SBL weapon. During this research, a significant improvement in the settling time was demonstrated in Gr/Mg MMCs through an innovative processing technique.

For a specified value of the acceptable amplitude, α_s, the settling period can be shortened by increasing:

- Material and structural damping

- Specific stiffness

- Natural frequency of the structure.
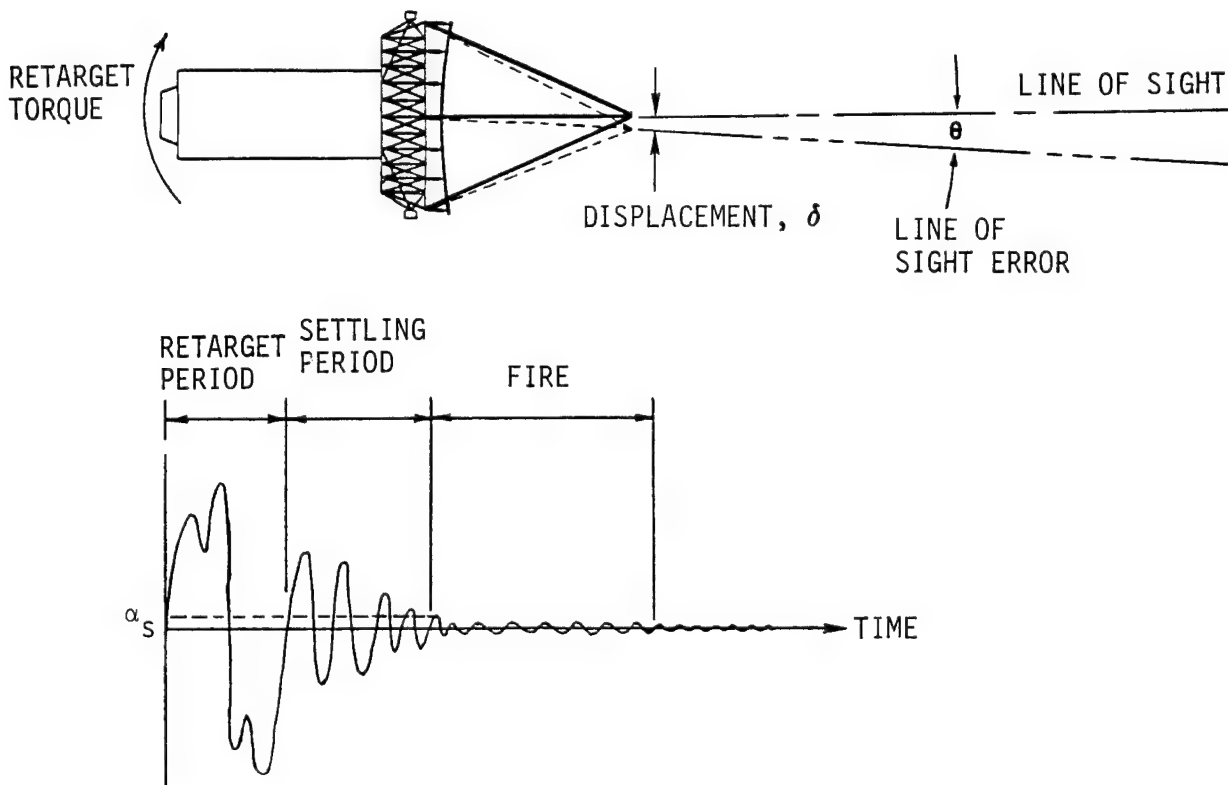
Figure 1. SBL Performance Simulation[1]

The damping behavior of continuous fiber MMCs has been reviewed by Timmerman,[2] Mishra,[3] and Steckel.[4] Various measures of damping have been reported such as loss factor (η), loss angle (ϕ), logarithmic decrement (δ), quality factor (Q), specific damping capacity (ψ) and damping ratio (ζ). In this paper, specific damping capacity, ψ, will be used as a measure of material damping. At low damping levels (i.e., $\eta < 1$), these damping parameters are interrelated by the following expression:

$$Q^{-1} = \eta = \tan\theta = \theta = E_I/E_R$$

$$= \delta/\pi = \psi/2\pi = \Delta W/2\pi W = 2\zeta$$

Damping properties of materials are a function of temperature, frequency, static preload and material strain. The effect of these parameters on damping in viscoelastic materials is described in Reference 5. Generally, at low stress or strain ($<10^{-6}$) levels, the damping behavior of a material is independent of stress amplitude, but depends on frequency and temperature. At intermediate stress or strain (10^{-6} to 10^{-3}) levels of engineering interest, polymeric materials still exhibit linear damping, but the damping capacity of metals and alloys increases with increasing stress amplitude and is independent of frequency and temperature. Various energy dissipation mechanisms at these stress levels involve movement of dislocations or interfaces such as magnetic domain walls, twin boundaries, or martensite invariants.

In the case of MMCs, the interface is a region of imperfections (voids, disbonds) and residual stresses. Most of the energy dissipation occurs in this region, and can be attributed to interaction between the constituents rather than the constituents themselves. This postulation is supported by the fact that damping in most MMCs is greater than the inherent damping in fiber and matrix phases.[3]

The effect of strain on damping in graphite fiber MMCs has been investigated by Martin Marietta[6], and the qualitative results are presented in Figure 2. The total damping capacity (ψ_{total}) of MMCs may be expressed as a sum of its strain-independent (ψ_i) and strain-dependent (ψ_H) components. While the linear strain-independent component exists at all strain levels, the nonlinear strain-dependent component is reduced to zero at low strain levels ($<10^{-5}$).

Strain-Independent Damping:

At low strain amplitude ($<10^{-5}$) where damping is independent of strain but depends on frequency, the energy dissipation is primarily a result of mechanisms involving atomic diffusion or Zener's thermoelastic effect.[7,8] In the case of composites, frictional energy can be dissipated due to relative motion between fiber and matrix phases. This is especially applicable to MMCs, where fiber/matrix bonding is mechanical rather than chemical. Interfacial slip can be promoted in MMCs by proper control of fabrication residual stresses and interface coefficient of friction, as demonstrated during this program. Strain-independence and frequency-dependence features of the ISD mechanism were verified during this research.
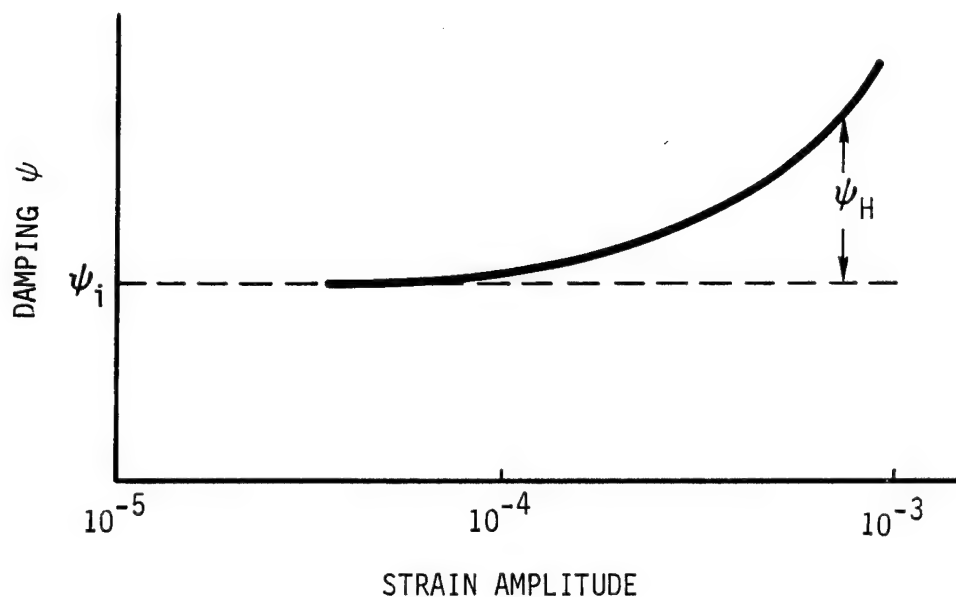
Figure 2. Strain-Dependence Behavior of MMC Damping[6]

Strain-Dependent Damping:

At intermediate strain levels (10^{-5} to 10^{-3}), the nonlinear strain-dependent damping (ψ_H) may involve hysteretic losses resulting from local yielding of the matrix under cyclic stress. At the microstructural level, the energy dissipation may involve a breakaway dislocation mechanism as envisioned by the Granato-Lucke (G-L) model.[2] Martin Marietta has researched the dislocation damping mechanism in Gr/Al[6], as well as Gr/Mg[9] composites, and has achieved significant improvement in strain-dependent damping by promoting this mechanism.

Table 1 presents the major characteristics of ISD and dislocation damping mechanisms. While dislocation damping offers higher payoffs at intermediate strains, interfacial slip enhances damping in the low strain region as well. Thus, effective application of both mechanisms is critical in improving dynamic dimensional precision of flexible space structures.

The objective of this research was to significantly shorten the settling period of free vibrations for Gr/Mg MMCs. This overall objective was to be achieved through:

• Enhanced material damping by promoting a controlled interfacial slip under external loading

• Increased specific stiffness.

Table 1. Primary Damping Mechanisms in MMCs

Characteristic	Interfacial Slip	Dislocation Damping
1. Effectiveness at low strain level ($<10^{-5}$)	Yes, $\psi = 4$ percent demonstrated	Not effective
2. Effectiveness at 10^{-5} to 10^{-3} strain	Yes, as above	More effective than interfacial slip[9]
3. Frequency, temperature dependency	Likely, must be investigated	None
4. Miscellaneous advantages (projections)	• Lower residual stresses will inhibit propagation of matrix cracks, hence improve fatigue strength, transverse strength • No limitations on choice of matrix alloy • Fiber coating can reduce stress concentration, hence increase transverse strength	• No interface wear
5. Miscellaneous concerns (projections)	• Wear at fiber/matrix • Effect of coating on longitudinal stiffness	• Limited to alloys with low σ_y (more dislocation prone) • High residual stresses (due to CTE mismatch) essential to form dislocations – Can promote matrix cracks, hence lower fatigue strength transverse strength

Conventional processing techniques produce Gr/Mg composites with high fabrication related interface residual stresses as a result of the mismatch in CTE of the two phases. The CTE of the magnesium alloy matrix is larger than the CTE of graphite fibers in the radial direction. Thus, as the composite cools down to room temperature, the matrix clamps down on the embedded graphite fibers. Compressive residual stresses in excess of 15 Ksi are predicted at the fiber/matrix interface.[10] Considering the coefficient of sliding fraction, μ to be 0.5 (typical for graphite on metal), interface tangential stresses close to 10^4 psi are required to overcome the frictional force and cause the fiber to slip. Until this stress level is attained, there is no fiber slippage, and the input energy must be stored as strain energy in the matrix. When the matrix cannot sustain any further strain energy, matrix cracks will be initiated. Thus, the stress level to permit interfacial slip will never develop in the MMC. Instead, the matrix cracks will propagate, leading to failure. Thus, the high interface frictional force is believed to result in low damping, low fatigue strength, low damage tolerance, and low toughness in MMCs. During this research, interface slip was promoted by lowering the residual stresses using a specialized processing technique.

RESEARCH AND RESULTS

Several P-55 Gr/Mg 10 Al specimens were fabricated using a proprietary pressure casting approach. Some of the MMC specimens are shown in Figure 3. The flat specimens consisted of control specimens and specially processed zirconia-dispersed specimens. The fine zirconia particulate dispersion was expected to reduce the residual stresses in the composite as a result of its low effective modulus. The MMC specimens were evaluated through microscopy, tensile tests and vibrational tests.
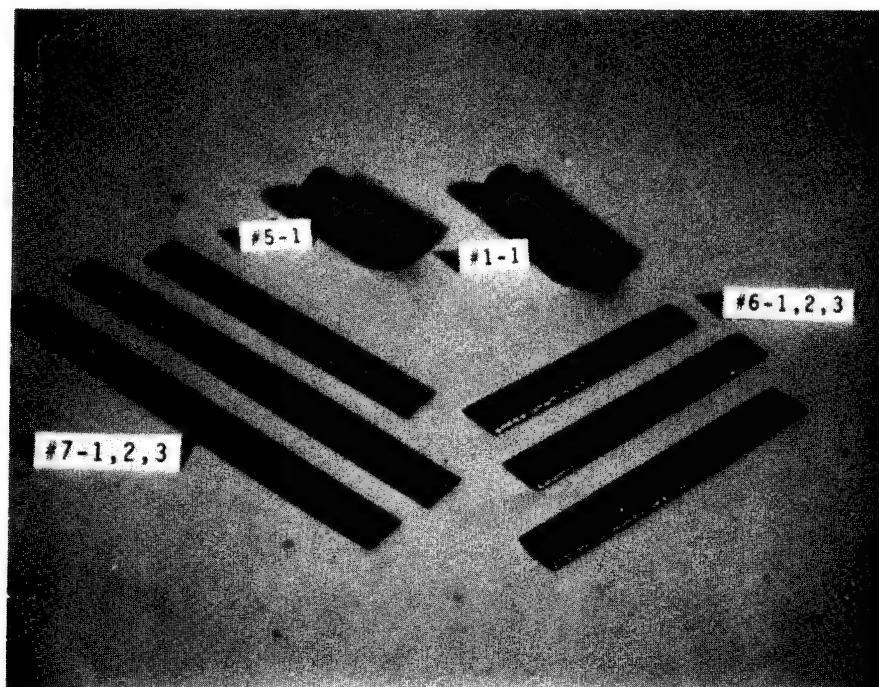
Figure 3. Tubular and Flat MMC Specimens

Microscopy Results:

Figure 4 is an optical micrograph showing a representative cross section of the control specimen. By areal measurement fiber content was estimated at 63 volume percent. The fiber distribution is uniform - "channeling" was avoided in all specimens through a high fiber content. Also evident is the excellent infiltration, as indicated by absence of voids in this specimen. Figure 5 presents scanning electron micrographs (SEMs) of the same specimen at a higher magnification (600 times). Again, the high fiber content can be noted. The micrograph in Figure 5 shows a few small (<1μ) voids present at fiber periphery. These voids appear to be shrinkage cavities (rather than uninfiltrated regions). The shrinkage cavities are a result of using a preheated fiber preform, which causes matrix solidification to occur last at the fiber surfaces. This problem can be reduced through improved directional solidification schemes and by reducing the preform temperature during infiltration.

Figure 6 is an SEM of a zirconia-dispersed Gr/Mg specimen. The ultrafine zirconia particles (0.15μ size) have coalesced into white zirconia regions around the graphite fibers. Zirconia particles have lodged between the graphite fibers, reducing the number of fiber-to-fiber contact points. This is expected to improve MMC transverse strength. Also, slip regions are evidenced at fiber matrix interface, promoted by reduced residual stresses in that region. In this case, the slip has occurred to relieve the compressive residual stresses along the fiber (due to negative fiber CTE). This is called the Bauschinger effect.
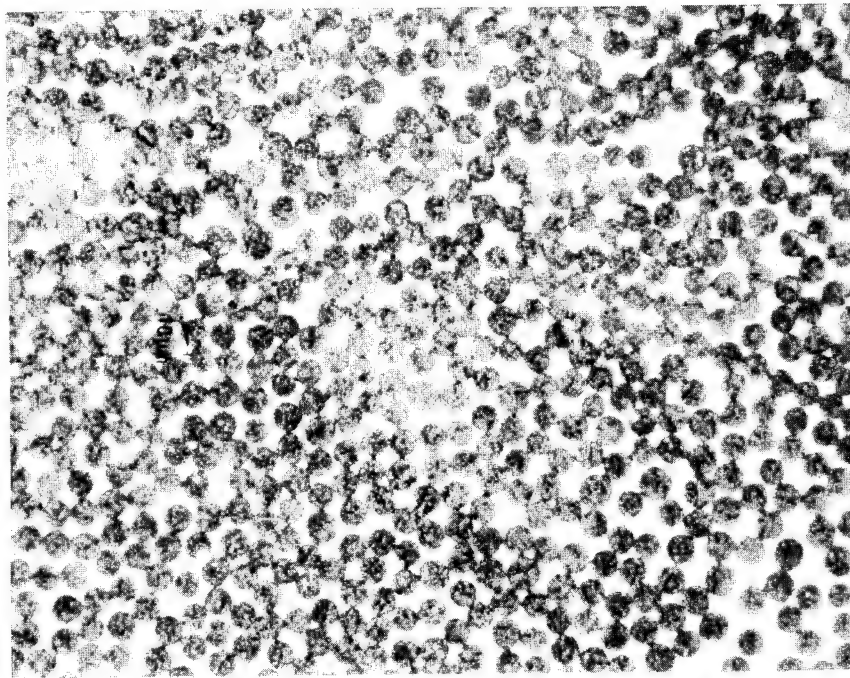
Figure 4. Cross Section of Control P-55 Gr/Mg Specimen
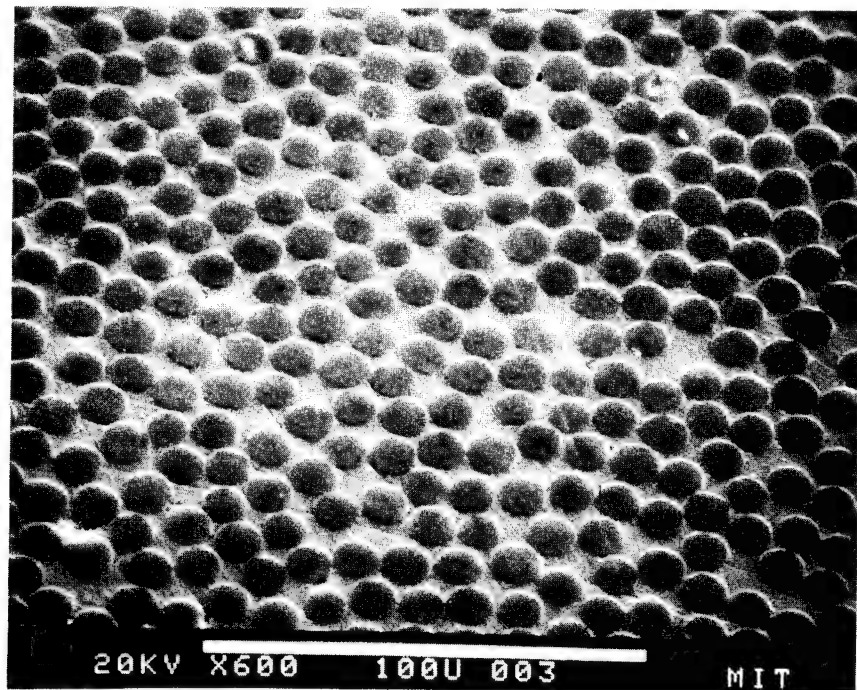
Figure 5.   SEM of Control P-55 Gr/Mg Specimen
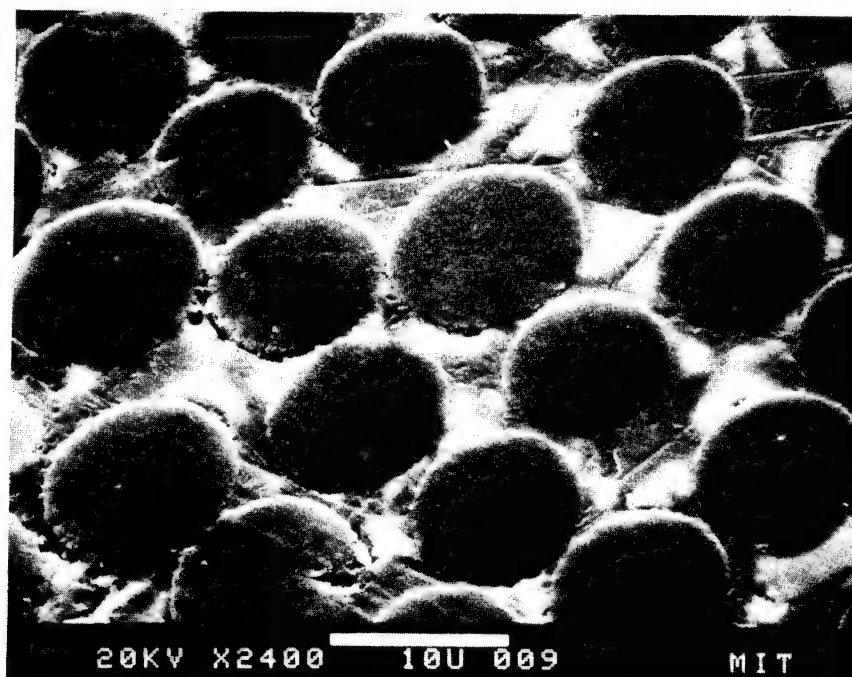
Figure 6.   Zirconia-Dispersed Gr/Mg Specimen

Tensile Test Results:

Unidirectional P-55 Gr/Mg specimens exhibited tensile modulus at 35 Msi with strengths over 100 Ksi. This indicates a fiber content around 60 volume percent with no apparent fiber degradation. This represents a significant advance over current MMC technology. The zirconia-dispersed specimens exhibited tensile modulus at 30 Msi with average strength at 70 Ksi. These specimens showed reduced fiber-to-fiber contact points and are expected to possess improved transverse tensile strength, which is a critical need of current MMC technology.

Two each of control and zirconia-dispersed P-55 Gr/Mg specimens were strain-gauged and tensile-tested to failure following ASTM standards. A low strain rate (ε = 0.03/min) was maintained to simulate a static, tensile loading. The stress-strain curve was linear to failure in every case – the tensile modulus and strength values measured are presented in Table 2.

The modulus of the zirconia-dispersed specimens is about 15 percent lower than that of the control specimens. This is a result of lower reinforcement content (about 5 to 10 volume percent) and increased compliance due to interfacial slip phenomenon. The same factors also contribute to the reduced tensile strength for the zirconia-dispersed specimens.

Vibrational Testing and Results:

Damping measurement tests were conducted on cantilever specimens placed in an evacuated bell jar to eliminate aerodynamic damping. Flexural vibrations were initiated in the specimen by a solenoid-operated striker plate. A noncontacting fiber optic probe was used to measure displacements of specimen surface, and the displacement history of the specimen surface recorded at a high scan rate. A schematic diagram of the experimental setup is presented in Figure 7. The Fotonic 1000 system produced by MTRI Instruments, Inc., Latham, NY was used to noninvasively monitor the decaying amplitude of vibration. The system was configured to measure submicron (<0.04 mils) target surface displacements. Displacement data was collected at a high scan rate (7,431 Hz – about 30 times the specimen natural frequency) and stored in memory to calculate specimen damping.

Table 2. Results of the Tensile Tests

Specimen Number	Type	Modulus (Msi)	Ultimate Strain (%)	Ultimate Strength (Ksi)
1-1	Control	34.97	0.276	94.55
3-1	Control	35.07	0.348	119.83
2-1	With ZrO_2	28.93	0.185	59.5
4-1	With ZrO_2	30.86	0.25	79.3
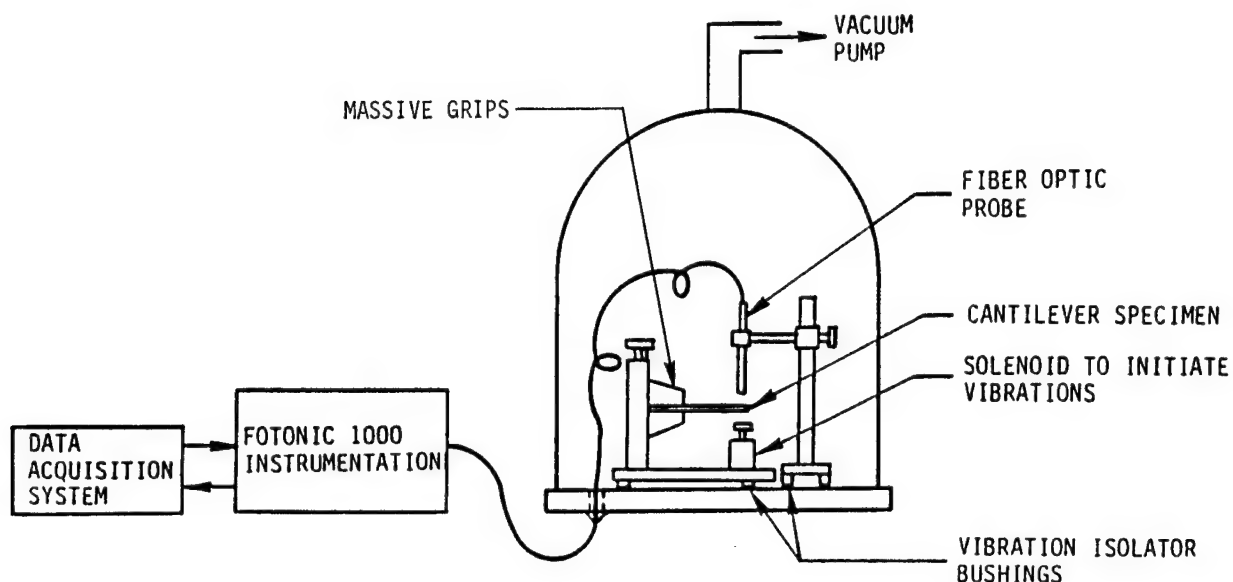
Figure 7. Schematic Representation of Test Setup

After initiation of vibrations, the specimens exhibited a decaying sinusoidal displacement response. The specific damping capacity ψ was calculated from amplitude decay over several hundred cycles using the relation

$$\psi = \frac{2}{j} \ell n \frac{\alpha_i}{a_{i+j}}$$

where, the amplitude decays from α_i to α_{i+j} over j consecutive cycles.

Six Gr/Mg specimens were tested to measure damping, with two specimens each of:

• Control – P-55/Mg, as-fabricated

• Annealed – P-55/Mg subsequently heat-treated

• Zirconia-dispersed – P-55/Mg with ~5 percent zirconia content.

In each case, electrical noise was controlled to a small fraction of the amplitude. Also, time-independence of the natural frequency was verified for each specimen. These displacement response curves were used to calculate specimen natural frequencies and strain levels using standard techniques – the results are presented in Table 3. Also, the specific damping capacity ψ was calculated using the procedure described earlier. Strain-dependence of damping for these specimens in the range 10^{-6} to 10^{-4} strain is illustrated in Figure 8.

Table 3. Summary of Vibration Characterization Test Results

Sample ID	Type	Natural Frequency, f_n (Hz)	Maximum Strain (ε_{max})	
			Initial	Final
1-1	Control	247.70	2.1×10^{-5}	4.5×10^{-6}
3-1	Control	206.42	2.6×10^{-5}	4.1×10^{-6}
3-3	Uncoated, annealed	206.42	1.9×10^{-5}	2.0×10^{-6}
3-2	Uncoated, annealed	206.42	1.6×10^{-5}	4.0×10^{-6}
4-1	With ZrO_2 dispersion	154.81	3.3×10^{-5}	2.7×10^{-6}
2-1	With ZrO_2 dispersion	195.55	2.5×10^{-5}	7.3×10^{-6}
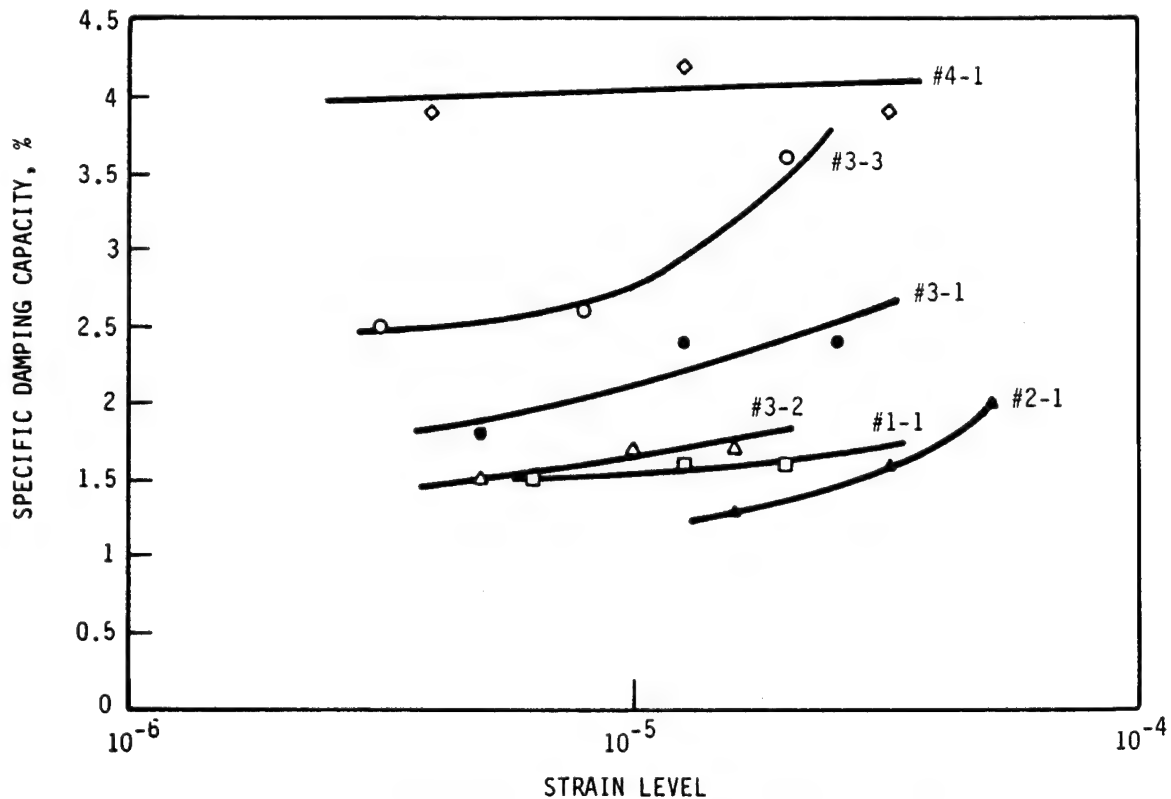
Figure 8. Strain-Dependence of Specific Damping Capacity for Various Specimens

The baseline damping value (strain-independent) for control specimens (No. 1-1, 3-1) is around 1.6 percent, which compares well with Martin Marietta data for Gr/Mg system.[9] The annealed specimens (No. 3-2, 3-3) show slight improvement in damping, with strain-independent damping close to 2.5 percent in specimen 3-3. The largest improvement in damping was exhibited by the zirconia-dispersed specimen (No. 4-1), with a strain-independent damping at 4 percent. The improvement in damping is expected to be the result of promoting interfacial slip through reduction in interface frictional coefficient and residual stresses. Unlike the dislocation damping mechanisms, the ISD mechanism improves damping at low strain levels ($<10^{-5}$), as seen in Figure 8. The other specimen in category (No. 2-1) did not exhibit interfacial slip mechanism, and consequently showed a strain-dependent damping similar to the control specimens. Thus, further work is necessary to promote ISD in MMCs with consistency. A parametric study must be conducted to understand the effect of fabrication process parameters, etc., on damping, followed by optimization of these parameters to maximize strain-independent damping. Also, the effect of vibration frequency and temperature on MMC damping must be characterized.

Settling Time Calculations:

Decay in amplitude of vibration for a freely vibrating component is obtained from the relation:

$$\alpha(t) = \alpha_0 \, e^{-\left(\frac{\psi \omega_n}{4\pi}\right)t}$$

where

$\alpha(t) \equiv$ amplitude as a function of time

$\alpha_0 \equiv$ amplitude at $t = 0$

$\psi \equiv$ specific damping capacity of material, assumed to be constant

$\omega_n \equiv$ natural frequency of component

$t \equiv$ time

Then, the settling time "t_s" is defined by the relation

$$t_s = \frac{4\pi}{\psi \omega_n} \ln \frac{\alpha_0}{\alpha_s}$$

where $\alpha_s \equiv$ acceptable amplitude of vibration in the component before firing.

These relations and the material properties measured were used to produce an amplitude decay representation for the flexural specimens after an impulse loading. In this calculation, only the strain-independent component of material damping was taken into consideration to represent low strain ($<10^{-5}$) behavior. Figure 9 presents the amplitude variation plots for Case 1 and Case 2. The decay in amplitude is much quicker for Case 2. To obtain a certain amplitude, α_s, was calculated using the same relation. Figure 10 presents the variation of (t_1/t_2) as a function of this acceptable amplitude, α_s. From this figure, a 75 to 90 percent reduction in settling time over current MMCs is projected, using the technology demonstrated during this research.

CONCLUSIONS

The strain-independent damping of Gr/Mg composites was improved by 150 percent by promoting the ISD mechanism. This was achieved through a zirconia dispersion with a low-effective modulus and specialized processing. The increased compliance resulted in a 5 to 50 percent reduction in the tensile modulus as compared to control specimens. Also, the reduced interface bond strength and stress concentrations caused by irregularly shaped zirconia regions were responsible for close to a 25 percent drop in the tensile strength as compared to control specimens. The drop in static mechanical properties can be reduced through a uniform compliant fiber coating.
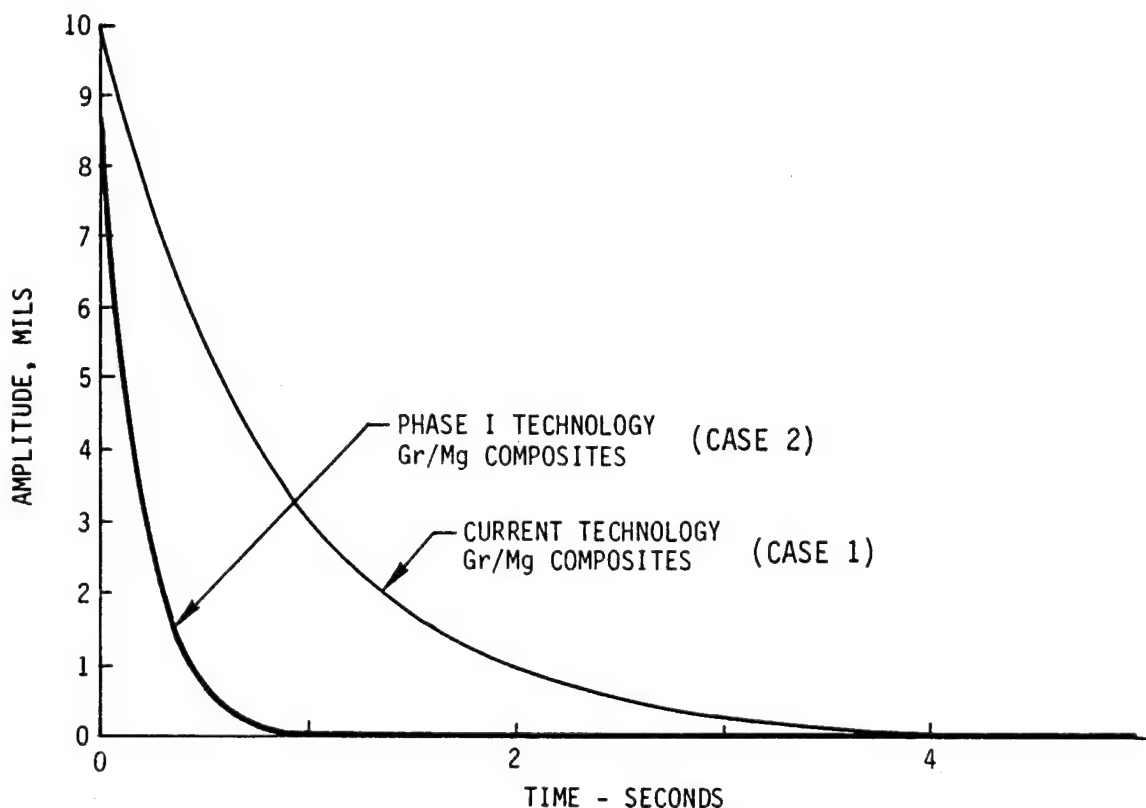
Figure 9. Amplitude Decay Representation in MMCs
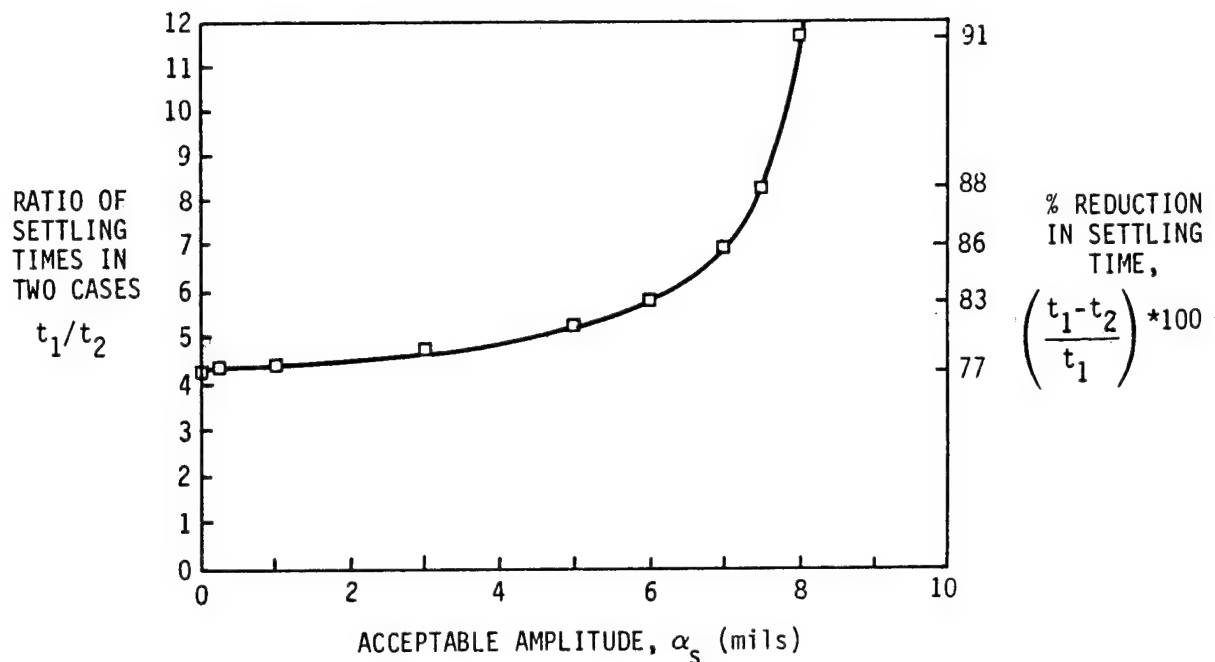
Figure 10. Reduction in Settling Time as a Function
of Acceptable Amplitude

The major advantages of the ISD mechanism over the dislocation damping
mechanism in MMCs are:

- ISD is effective in the low strain region ($<10^{-5}$) unlike dislocation
  damping.

- ISD is promoted by lowering residual stress in the MMC. This is
  expected to improve other dynamic properties, such as the fracture
  toughness and the fatigue strength. Dislocation damping is enhanced
  through high interface residual stresses which can deteriorate dynamic
  properties of the MMC.

- Dislocation damping is most effective in case of dislocation-prone
  matrix alloys which typically possess a low yield strength. This
  limitation will be reflected in the transverse properties of the MMC.

The interfacial slip mechanism needs to be researched further to obtain
predictable improvements in vibrational damping. A parametric study will
allow optimization of the process to minimize the deterioratory effect on
static properties. Further, the effect of temperature, frequency and service
time on the ISD mechanism must be characterized to develop suitable
applications.

REFERENCES

1. Garibotti, J.F., C.J. Northrup, and A. Gunderson, "Design Aspects of MMC in SDI Spacecraft," Proceedings of Seventh MMC Technology Conference, Silver Springs, MD, May 1987.

2. Timmerman, N. and J. Doherty, Loss Factors Measured in Metal Matrix Composite Materials, NTIS Report No. ADA143542, June 1984.

3. Rawal, S.P. and M.S. Misra, "Material Damping in Space Structures," Damping 1986 Proceedings, AFWAL-TR-86-3059, May 1986.

4. Steckel, G., Material Damping Behavior of Gr/Mg Composites, Aerospace Corporation, El Segundo, CA, ONR Report No. TOR-0084-A-5726-01(-1), October 1985.

5. Nashif, A., D. Jones, and J. Henderson, Vibration Damping, Wiley-Interscience Publication, 1985.

6. Rawal, S.P., J.H. Armstrong, and M.S. Misra, Interfaces and Damping in Metal Matrix Composites, Martin Marietta Denver Aerospace Report No. MCR-86-684, December 1986.

7. Lazan, B.J., Damping of Materials and Members in Structural Mechanics, Permagon Press, Oxford, 1968.

8. Zener, C., Elasticity and Anelasticity of Metals, University of Chicago Press, Chicago, 1948.

9. Dr. Suraj Rawal, Martin Marietta, Denver, CO, Telephone Conversation, April 1988.

10. Kashalikar, U., "Highly Damped Gr/Mg Composites for Space Structures," Final Report, Contract No. N60921-87-C-0258, July 1988.

MEASURED DAMPING AND MODULUS OF COMPOSITE CYLINDERS

J. B. Andriulli
Applied Technology Division
Oak Ridge National Laboratory*
Oak Ridge, Tennessee 37831-7294

ABSTRACT

Damping and moduli are measured on graphite and glass fiber/thermoset, thermoplastic, and metal matrix composite cylinders. Measurements are made by the impact-hammer modal-test method with the specimen suspended in the near free-free boundary condition. The axial and in-plane shear moduli are determined from the free-free axial and torsional vibration modes of the cylinder. Damping-loss factors for each of the associated modes are determined from the frequency-response function by the half-power point method or may also be determined by other curve-fitting methods. The effects on damping are presented for a number of different fiber/resin composites and for different lay-ups of the same fiber/resin material.

Cylinders are unique specimen configurations that permit simplified measurements of both the axial and in-plane shear (torsional) material properties from the same sample. The impact-hammer modal-test method provides a quick, inexpensive, small deformation, nondestructive estimate of the moduli and damping for the as-fabricated cylinders. After tests are completed, the cylinder can subsequently be used for its intended purpose. Details of the test method and procedure are described.

INTRODUCTION

Many composite structures are cylindrical shaped. When designing and fabricating composites, it is highly desirable to know the composition and material properties of the as-fabricated structure. It is common practice to cut coupon samples from an unneeded portion of the structure to submit to the laboratory for physical and mechanical property tests. These tests may include fiber volume fraction, matrix fraction, void, density, strength, modulus, and damping properties. Cutting and testing coupons can be expensive and time consuming. Also, the coupons are usually cut from one end of the composite structure and may not represent what the material properties are throughout the main structure.

Cylinders are unique specimen configurations that permit simplified measurements of both the axial and in-plane shear (torsional) material properties from the same sample. The impact hammer modal test method provides a quick, inexpensive, small-deformation, nondestructive estimate of the moduli and damping for the as-fabricated cylinders. This technique also applies to bar or rod samples to obtain axial modulus and associated damping. Damping values associated with cylindrical tube bending or rod bending are also provided by the impact-hammer modal-test method.

The cylinder and bar specimens are tested in the near free-free boundary condition. Therefore, no special specimen mount fixtures are needed to conduct the test. Specimens are simply suspended in soft rubber elastic or "bungee" cord. The instrumentation is minimal consisting of a force-gaged striker hammer, lightweight accelerometer, and a lightweight tangential striker block.

Knowing the specimen density, the axial, E_z, and shear, $G_{\theta z}$, moduli can be obtained from the axial and torsional resonances using the frequency formula for vibration of continuous media. The resonances are determined from a fast Fourier transform (FFT) analyzer using the frequency-response function. Damping associated with each mode is also determined from the frequency-response function by the half-power point method or some other suitable method.

This paper describes the test setup and the test method, including the use of the exponential window to avoid leakage errors, correcting damping for the exponential window, the effect of mass loading of light specimens due to the striker block and accelerometer, and the use of a noncontact microphone to avoid mass loading problems. The test method provides a pure estimate of axial modulus and torsional modulus because the axial resonance of the specimen is dominated primarily by the axial modulus and the torsional resonance of the specimen is dominated primarily by the in-plane shear modulus, $G_{\theta z}$. Likewise, axial and torsional damping estimates are also unencumbered by possible complex combined loading and deformation mechanisms. Other advantages of the test method are that (1) it is nondestructive on as-fabricated cylinders; (2) no coupons are necessary; (3) boundary conditions and air damping effects are minimized with free-free axial and torsional modes; and (4) the test method is quick and inexpensive.

APPLICABLE SPECIMENS

The axial and in-plane shear moduli are determined from the cylinder's free-free axial and torsional vibration modes, respectively. Any uniform cylindrical, tubular, or bar-shaped (axial only) specimen that approximates the long, slender, continuous media assumptions will provide reasonable data from the impact modal test method without conducting a complete modal test. Usually, it is easy to extract the modes of interest from specimens that are long, slender, thick walled, heavy, and have a high length-to-diameter (L/D) ratio. It is more difficult to identify the modes of interest of specimens that are short, of large diameter, thin walled, and lightweight because of the high modal density of the shell modes in the proximity of the axial and torsional modes.

The test method employed in these studies can accommodate quite a range in size, shape, and configuration of specimens. Examples of specimens tested are pictured in Fig. 1. Note the 1-ft rule in the lower lefthand corner of the photograph. Ranges of weight and dimensions of specimens tested are listed.

Weight	15 g to 210 lb
Outside diameter	1 to 17 in.
Wall thickness	0.030 to 1.5 in.
Length	5.0 to 109.0 in.
L/D	2.2 to 31.2

TEST DESCRIPTION

The test method employs standard modal test techniques using a force-gaged impact hammer for input and an accelerometer for response. Specimens are tested under near free-free boundary conditions for axial and torsional vibration modes to determine modulus of elasticity and damping-loss factor. The cylindrical or bar-shaped specimens are soft mounted using elastic bands, surgical tubing, or bungee cord depending on their weight. The axial and torsional modes of vibration are excited by impacting the specimen in the axial and tangential directions, respectively. Data are acquired on a dual channel FFT signal analyzer. The data are subsequently postprocessed, stored on disk, and plotted or printed using a microcomputer. A schematic of the test setup is shown in Fig. 2. A typical test is pictured in Fig. 3. Details of the axial and torsional test input and response are shown in Figs. 4 and 5, respectively.

The axial impact point at the edge of the cylinder, as indicated in Fig. 4, is eccentric to the cylinder's neutral axis and therefore excites bending as well as axial modes of vibration. The axially mounted accelerometer can respond to bending as well as axial modes. It is necessary to take enough data to be able to distinguish between modes. In some cases, it may be necessary to perform a full modal test. Some shortcut alternative mode identification techniques are discussed in the Results section.
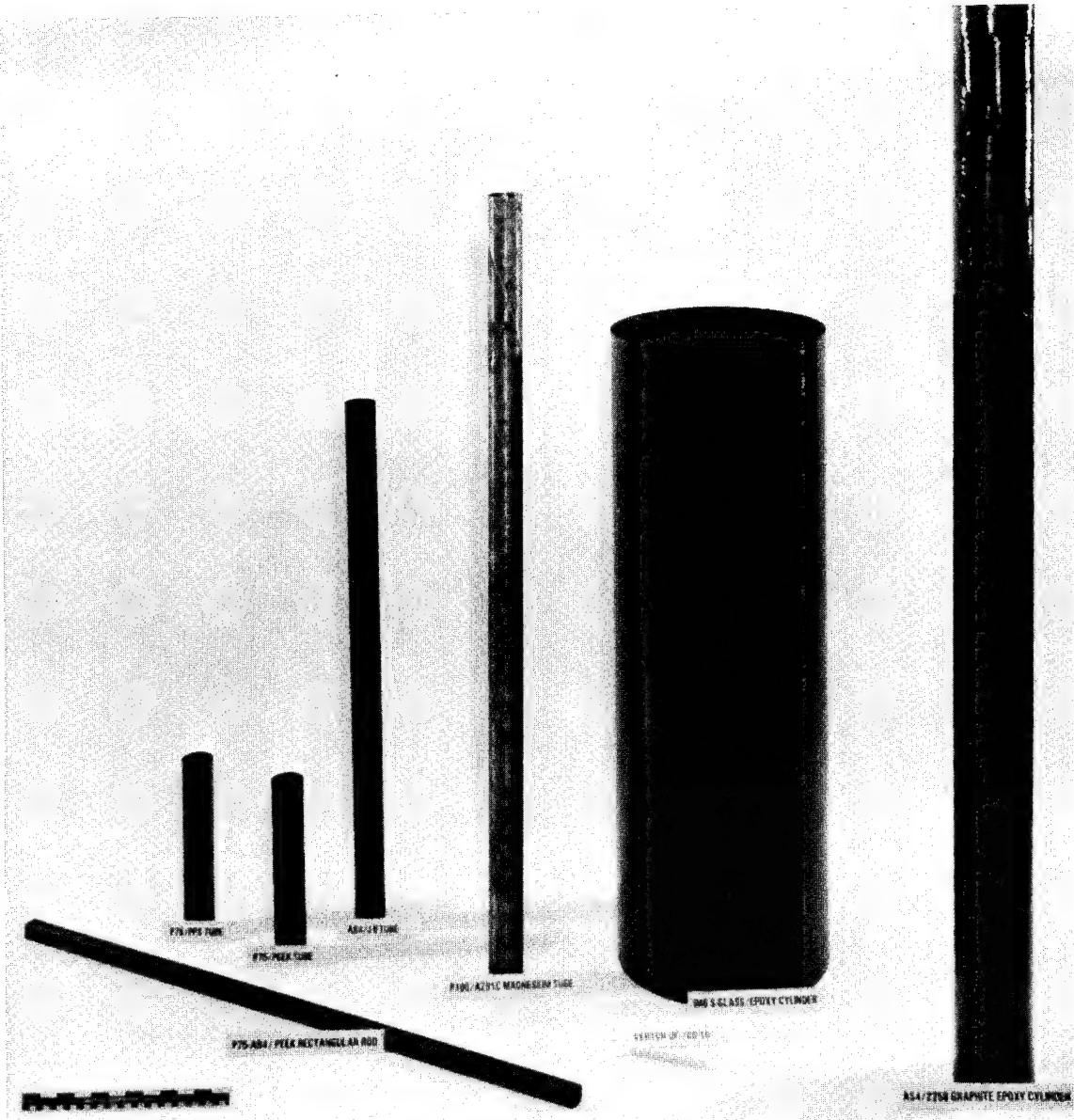
Fig. 1. Examples of cylindrical, tubular, and bar specimens.

DISK DRIVE

PLOTTER

PRINTER

HEWLETT-PACKARD
MODEL 217
SERIES 9000
MICROCOMPUTER

B&K TYPE 2032 DUAL-
CHANNEL FFT SIGNAL
ANALYZER

SIGNAL CONDITIONER,
PCB MODEL 480D06
POWER UNIT (TWO PLACES)

FORCE-GAGED HAMMER

FORCE-GAGE PCB MODEL 208A03

AXIAL INPUT

TORSIONAL INPUT

AXIAL ACCELEROMETER, PCB 303A03

CYLINDER SPECIMEN SUSPENDED ON
SOFT SURGICAL TUBING TO SIMULATE
FREE-FREE BOUNDARY CONDITIONS.

TORSIONAL ACCELEROMETER, PCB 303A03

ALUMINUM BLOCK FOR TORSIONAL INPUT HAMMER STRIKE

Fig. 2. Modal test schematic for axial and torsional free-free vibrations to determine modulus of elasticity and damping loss factor.

BCC-5
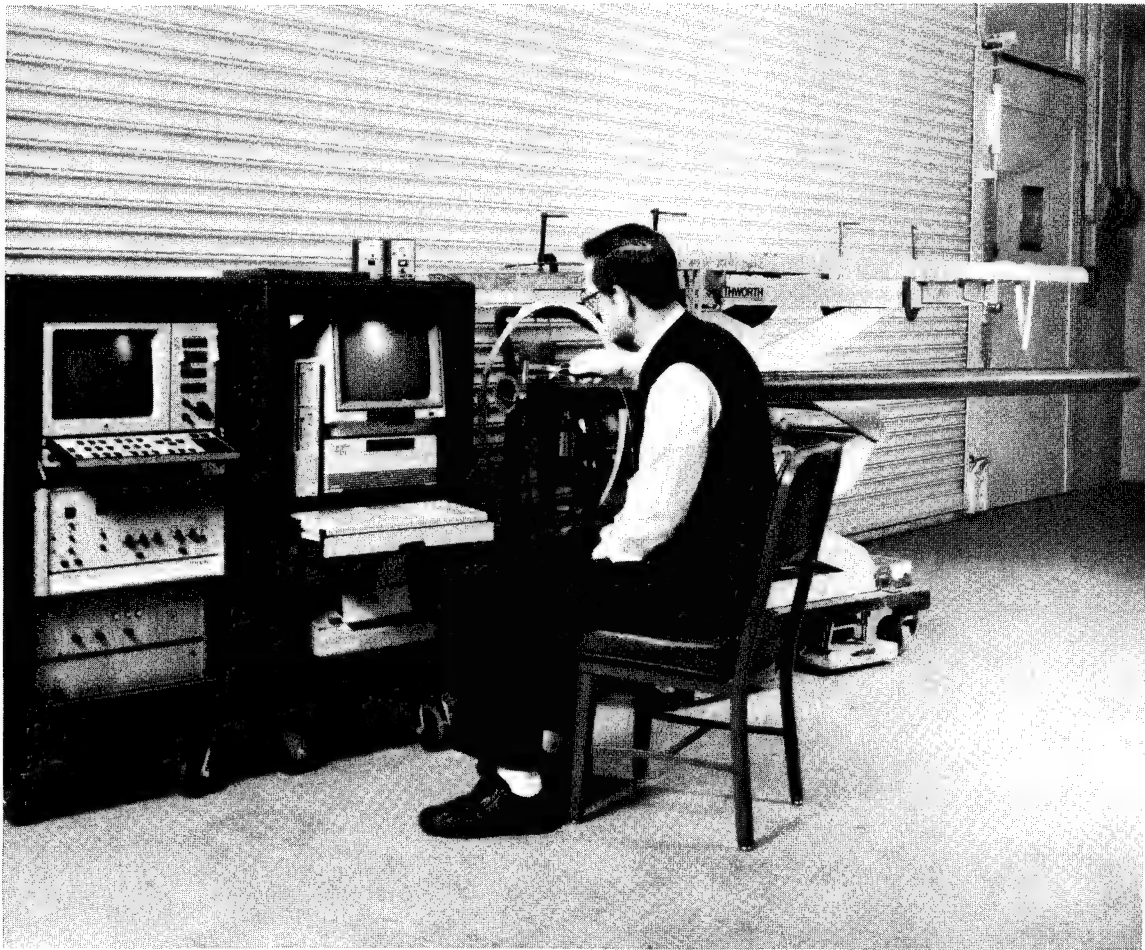
Fig. 3. Typical test setup.
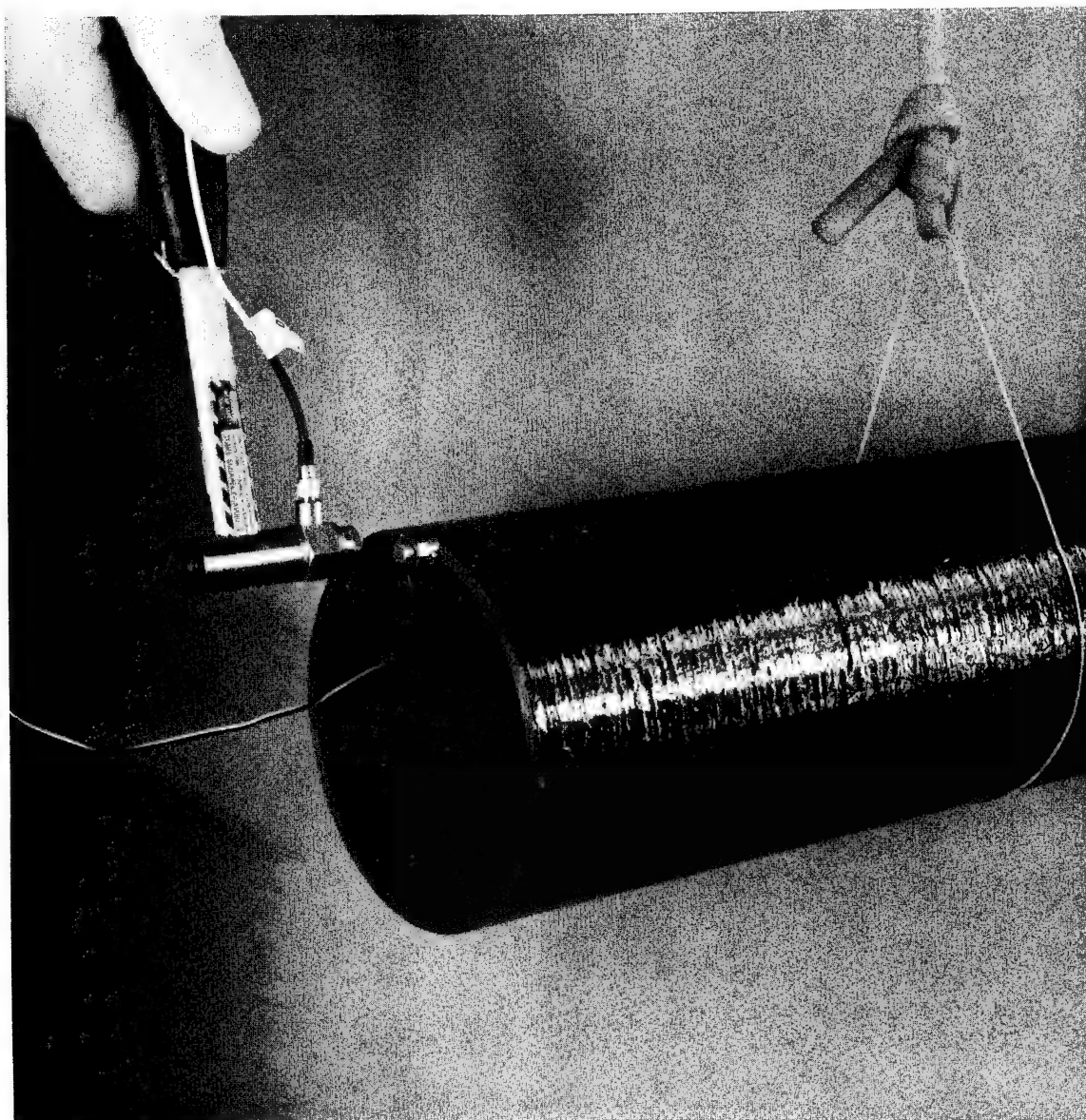
Fig. 4. Axial input and response.
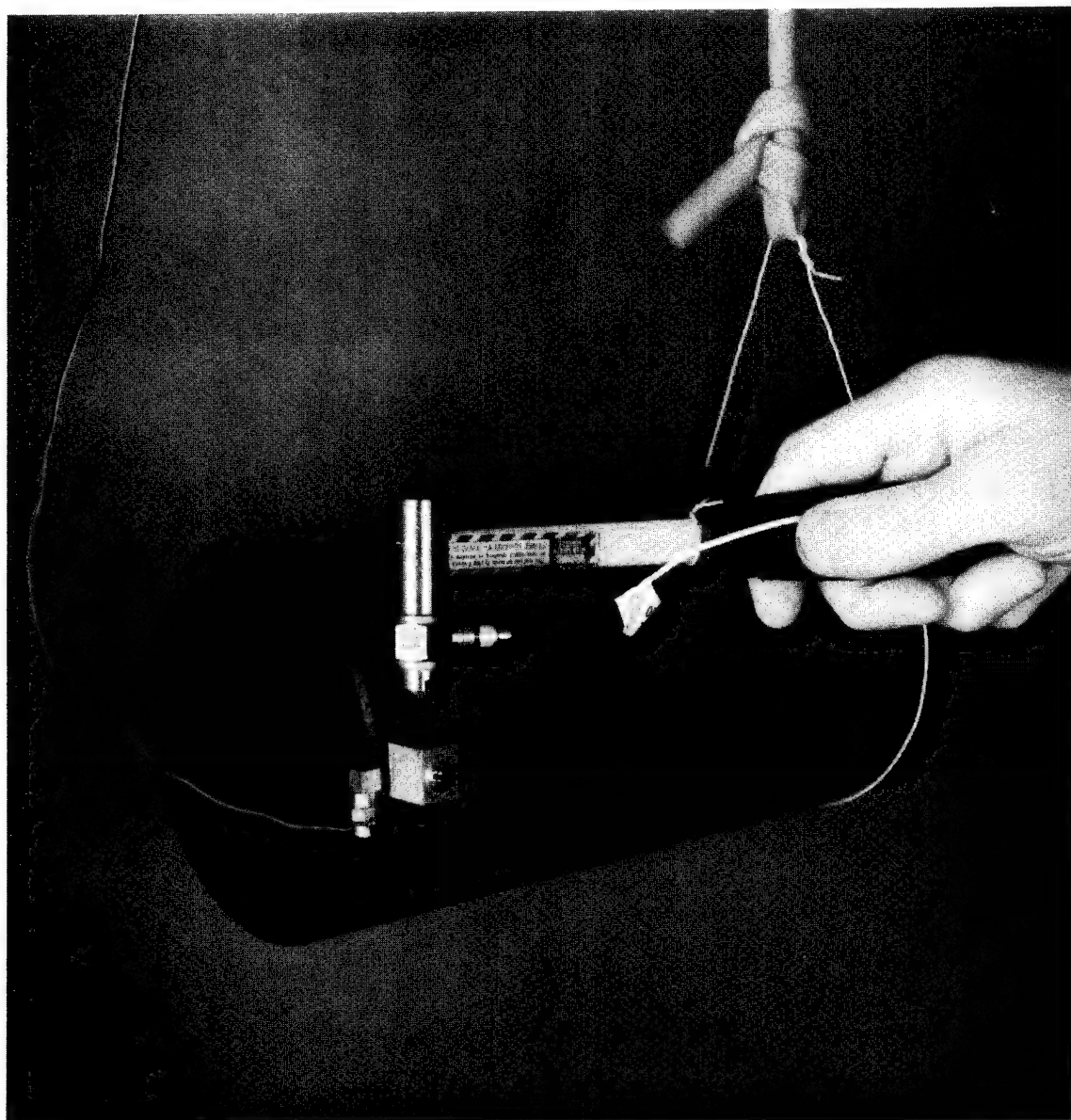
Fig. 5. Tangential (torsional) input and response.

Tangential force is transmitted into the specimen through a lightweight aluminum striker block bolted to the wall of the cylinder, as shown in Fig. 5. The block should be just big enough to apply the hammer blow and of low weight to minimize mass loading. Some effort should be made to match the striker block with the curvature of the cylinder. An exact match is not necessary. The same block has been used on cylinders from 2 to 20 in. in diameter, provided as the bolt is sufficiently tight to prevent rattle or slippage. In addition to the bolt, bee's wax has been used at the striker block/cylinder interface to compensate for slight differences in curvature and surface irregularities.

The tangential accelerometer is mounted as close as possible to the neutral axis of the shell surface, as shown in Fig. 5, to minimize sensitivity of the accelerometer to circumferential ring and shell modes. An alternative is to mount the accelerometer to the bottom of the striker block. On thick-wall specimens, this may be acceptable, but on thin-wall specimens, this alternative is not advisable because of prevalence and sensitivity to shell modes in proximity to the primary torsional modes of interest.

The axial modulus, E_z, and the shear modulus, $G_{\theta z}$, were determined from the free-free axial and torsional vibration modes using the frequency equation for prisms of continuous media, as shown in Fig. 6. Damping was measured using the half-power point method and corrected, as shown in Fig. 7, for artificially added damping due to the exponential window used to acquire the response accelerometer data. The exponential window was used to acquire response data to ensure that the assumption of periodicity employed in the FFT analyzer for the sample time history was not violated. Violating the FFT analyzer periodicity assumption results in leakage errors. Leakage errors introduce an "apparent" damping of an unknown quantity (wider peaks) in the frequency-response function. The exponential window can eliminate leakage errors, but it introduces damping of a known quantity. The decaying exponential window is a weighting function applied to the sampled response time history. The FFT analyzer processes the product of the measure-time history and the exponential window. The measured damping was subsequently corrected (see Fig. 7) for damping artificially added by the exponential window. A rule of thumb for selecting the time constant of the exponential window is that it should be about one-fourth of the sample time. For moderately damped materials, the response-time history decays to a negligible value within most test sample times. Therefore, an exponential window may not be necessary. For specimens with very high resonant frequency of interest and very low damping, the response signal may not decay to near-zero values within the test sample time. Therefore, the use of the exponential window is advisable.

The impact-modal method is applicable to composite rings as well as cylinders and rods. But one needs to use a combination of testing and finite element analysis to adjust the hoop modulus, E_θ, and shear modulus, $G_{R\theta}$, to match the first circumferential or ring resonance, as well as higher circumferential harmonics. For thin rings, adjusting for hoop modulus, E_θ, may be all that is necessary to match predicted and tested resonances. For thicker rings, it is necessary to adjust the hoop modulus, E_θ, and the shear modulus, $G_{R\theta}$, to obtain a reasonable match between tested and finite element-predicted resonances and harmonics.

AXIAL MODULUS $\quad E_{z,n} = \dfrac{4\ell^2 f_{A,n}^2\, \rho}{n^2 g}$

$E_z \quad = $ AXIAL MODULUS, lb/in.^{2}

$G_{\Theta z} = $ SHEAR MODULUS, lb/in.^{2}

$\ell \quad = $ CYLINDER LENGTH, in.

$f_{A,n} \quad = $ nth AXIAL FREE-FREE RESONANCE, Hz

$f_{T,n} \quad = $ nth TORSIONAL FREE-FREE RESONANCE, Hz

$n \quad = $ MODE NUMBER, 1, 2, ...

$\rho \quad = $ MATERIAL DENSITY, lb/in.^{3}

$g \quad = $ GRAVITATIONAL CONSTANT, 386.1 in./s^2

SHEAR MODULUS $\quad G_{\Theta z,n} = \dfrac{4\ell^2 f_{T,n}^2\, \rho}{n^2 g}$
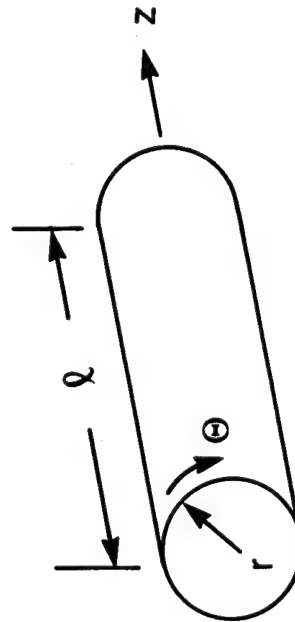
Fig. 6. Moduli are determined from free-free axial and torsional vibration modes.

BCC-10

HALF-POWER POINT OR 3-dB-DOWN METHOD TO COMPUTE LOSS FACTOR

MEASURED LOSS FACTOR $\eta_M = \dfrac{\Delta f_M}{f_M}$ INCLUDES ARTIFICAL EXPONENTIAL WINDOW DAMPING

CORRECTED LOSS FACTOR η $= \dfrac{\Delta f_M - \dfrac{1}{\pi \tau}}{f_M}$ CORRECTS FOR EXPONENTIAL WINDOW DAMPING

WHERE

Δf_M = MEASURED HALF-POWER POINT BANDWIDTH, Hz FROM FREQUENCY RESPONSE FUNCTION

f_M = MEASURED RESONANT FREQUENCY, Hz

τ = EXPONENTIAL WINDOW TIME CONSTANT s/RADIAN; TIME AT WHICH AMPLITUDE IS REDUCED BY THE FACTOR, 1/e

Fig. 7. Damping is measured by the half-power point method and corrected for artifically added damping by the exponential window.

EXAMPLE RESULTS

COMPOSITE DRIVE SHAFT (A LARGE SPECIMEN)

The composite drive shaft (shown as a typical test setup in Fig. 3) is described as follows.

Outside diameter	3.515 in.
Inside diameter	2.698 in.
Length	109.66 in.
Weight	27.14 lb
Density	~0.0621 lb/in.^{3}, ~1.719 specific gravity
Material	T-700 graphite fibers, OCF S-Glass, and 2258/m-phenylenediamine resin system

Material	Orientation	Fraction of thickness
S-Glass	Hoop	0.203
S-Glass	Helical ±45°	0.203
T-700	Helical ±45°	0.594
		1.000

Typical time histories of the axial forced input and acceleration response are shown in Fig. 8. About 140-lb force lasting a fraction of a millisecond is shown as input. The acceleration response at the input end of the cylinder is shown on the lower plot. In this example, the total sample time was 125 ms, about 31 ms of that sample is shown. The axial hammer input and the accelerometer installation are shown in Fig. 4. The 1.342-ms acceleration pulse time increment shown in Fig. 8, is the time required for the acceleration pulse to travel from the input end, reflect off the opposite end and return to the input end. The inverse of this time (~145 Hz) is approximately equal to the first axial resonance of the system (157 Hz) as determined from the frequency-response function (see Fig. 9). If observed, the acceleration pulse-time increment provides a good first estimate of the axial-resonant frequency, which aids in distinguishing this mode of interest from the other modes. Integrating the acceleration response time history of Fig. 8 twice yields a typical maximum axial displacement of 0.1 to 0.2 mils single amplitude (SA).

The first two axial modes are shown in the axial frequency-response function of Fig. 9. The first seven bending modes can also be observed in the axial frequency-response function because the input and response is eccentric to the neutral axis of the cylinder. The first axial mode of 756 Hz yields an axial modulus of ~4.43E6 psi. The loss factors for the first and second axial modes is 0.01022 and 0.01125, respectively. Note that the first two axial modes have about the same loss factor. The classical laminate code prediction for axial modulus for this cylinder is ~4.4E6 psi, which is very close to the measured value.
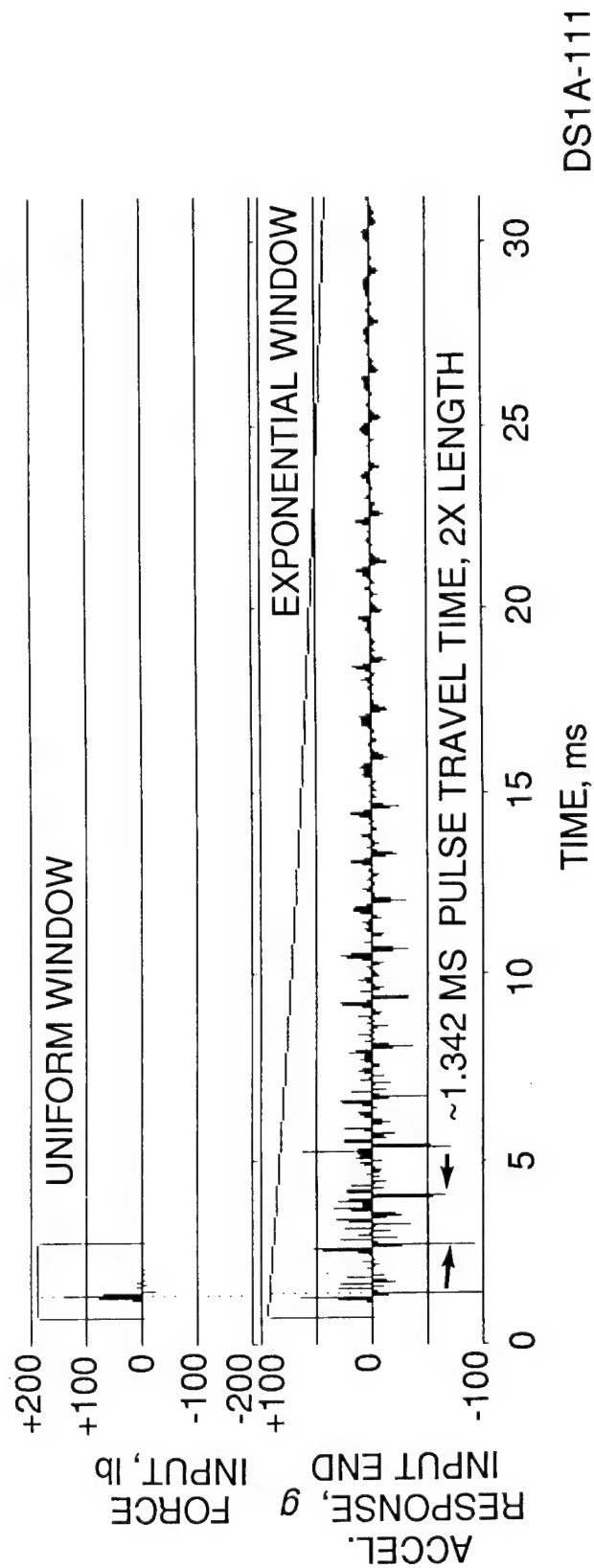
Fig. 8.   Composite drive shaft, typical time histories for axial input and response.

NOTE: TYPICAL MAXIMUM AXIAL DISPLACEMENT = 0.1 TO 0.2 mils SA.

DS1A-111

E = 4.43E6 psi

η = 0.01022
756 Hz

η = 0.01125
1514 Hz

BENDING MODES

AXIAL MODES

MAGNITUDE
INPUT END

A/F, g/lb
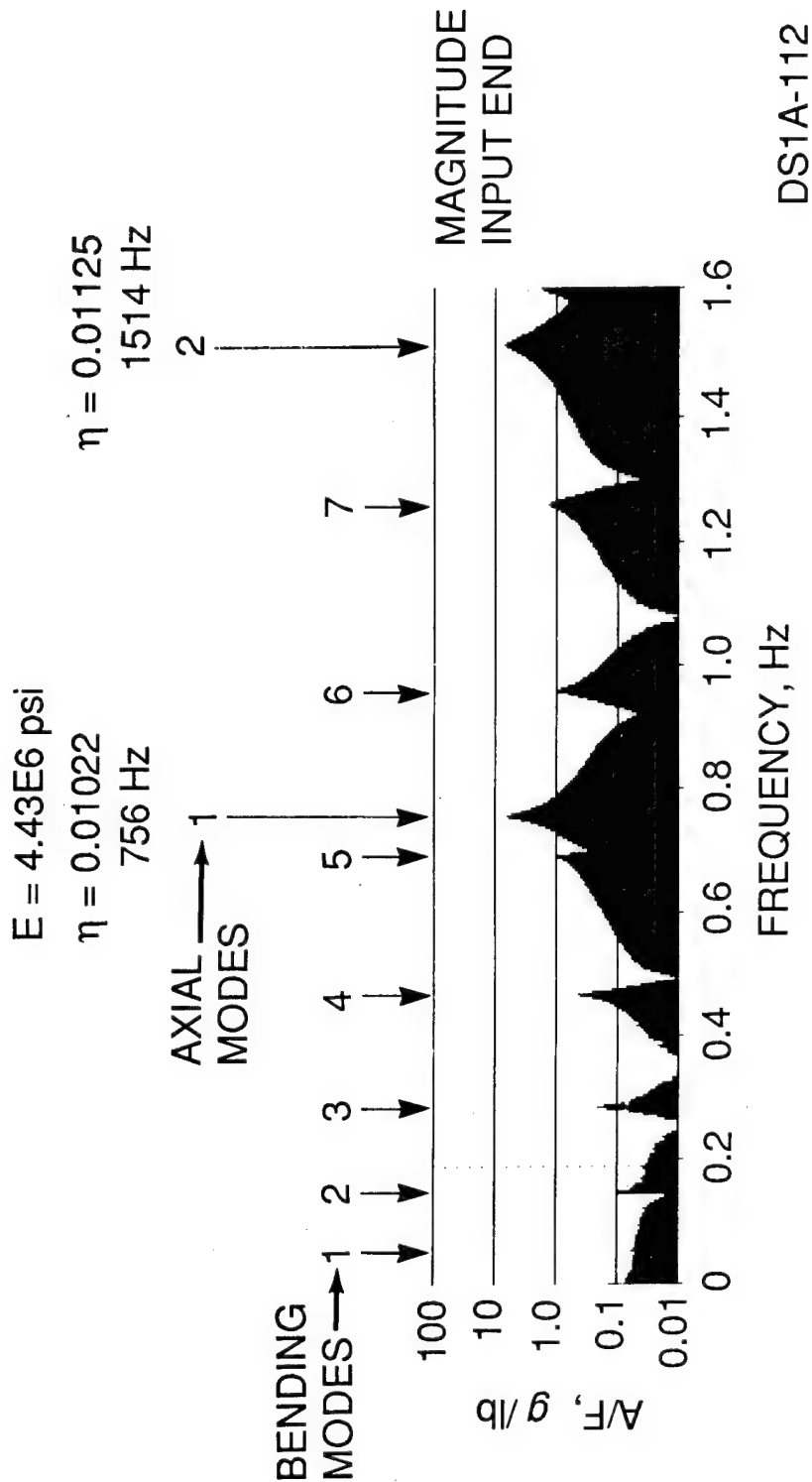
FREQUENCY, Hz

LAMINATE CODE PREDICTION E = 4.40E6 psi

TYPICAL MAXIMUM AXIAL DISPLACEMENT = 0.1 TO 0.2 mils SA.

DS1A-112

Fig. 9. Frequency-response function, A/F, measured with axial input and response, for a composite drive shaft.

Similarly, for tangential input and response, the first two torsional modes are observed as shown in the frequency-response curve of Fig. 10. The first torsional mode of 767 Hz yields a shear modulus of ~4.55E6 psi. Loss factor for the first and second modes is 0.00403 at 767 Hz and 0.00306 at 1537 Hz, respectively. The classical laminate code prediction for shear modulus of this specimen is 5.09E6 psi. Typical tangential displacement in this test was 3 to 4 mils SA.

The very small axial displacement of from 0.1 to 0.2 mils SA and tangential displacement of 3 to 4 mils SA are indications that the air damping for this specimen is probably negligible. According to Gibson's work,* where small flexure beam specimens were tested in both air and vacuum, it was found that air damping was negligible if beam displacements were equal to or less than the smallest cross-sectional dimension (thickness) of the flexure beam specimen. Consequently, air damping on the cylindrical specimens is expected to be very small because the response displacements are small compared with other dimensions of the specimen. Also, for axial motion, the edge surface area of the specimen doing the air pumping is extremely small. Likewise, resistance to torsional motion is drag of the air along the circumference of the cylinder, which is expected to be negligible.

One way to identify free-free axial and torsional modes of vibration from other modes is that axial and torsional harmonics are interger multiples of the first mode. This distinction helps to pick out these modes from the magnitude of the frequency-response function.

Another shortcut in determining vibration modes from modal test data is also illustrated in Fig. 10. The imaginary part of the frequency-response functions for tangential accelerometers mounted at opposite ends of the cylinder are shown in Fig. 10b and c. Because the real part of the free-free response function is zero at resonance, the imaginary part is essentially the total response of the specimen at resonance. The phase relationship of the ends of the cylinder can be determined from the imaginary part of the frequency-response function at resonance. For example, with the first torsional mode at 767 Hz, the imaginary part of the frequency-response function at the input and opposite ends have opposite signs indicating that the ends are out of phase, as would be expected for the first torsional mode. Likewise, for the second torsional mode at 1537 Hz, the imaginary part of the input and opposite ends have the same sign, indicating that the ends are in-phase as would be expected for the second free-free torsional mode shape. The same information can be determined for the bending modes. Note that the first bending mode has opposite ends of the cylinder in-phase, the second bending mode has opposite ends of the cylinder out of phase, and so on, as would be expected for the free-free bending mode shapes.

*R. F. Gibson et al., *Vibration Characteristics of Automotive Composite Materials*, ASTM STP 772, 133-150 (1982).
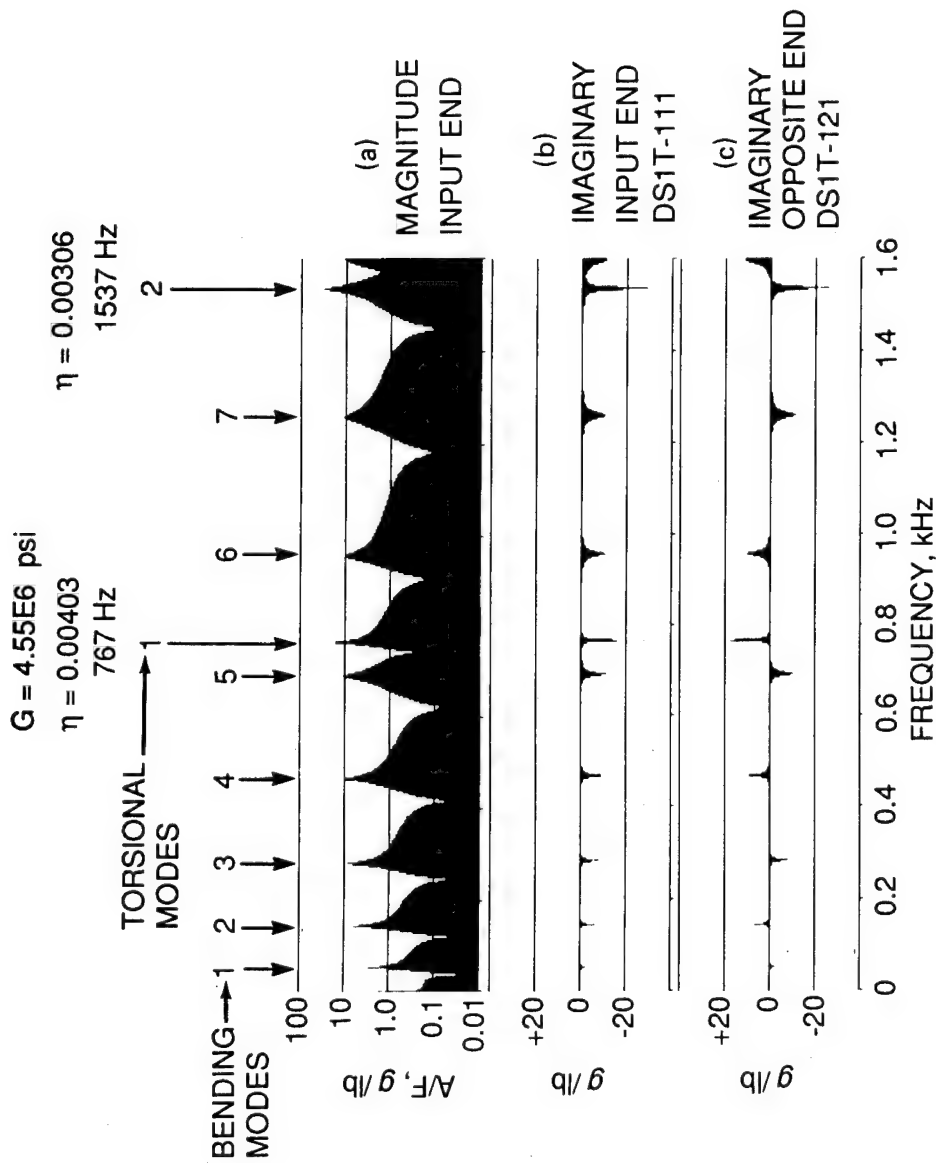
Fig. 10. Frequency-response function, A/F, measured with tangential (torsional) input and response, for a composite drive shaft.

INJECTION-MOLDED BAR (A SMALL SPECIMEN)

Another example of a specimen tested is shown in Fig. 11. It is a standard 5-in.-long flex-beam specimen made from long glass fiber-reinforced injection-molded nylon. The specimen weighs just over 15 g, and the accelerometer shown in the figure weighs 1 g. This example is shown to illustrate the effect of mass loading of very light specimens with the accelerometer and to illustrate the use of a microphone to measure the axial response and thereby eliminate the need and the effect of the accelerometer mass. In Fig. 12a, the axial acceleration frequency-response function shows a resonance at 11,000 Hz with a damping loss factor of 0.00870. In Fig. 12b, the frequency response is measured by a microphone with the accelerometer still attached to the specimen. It shows a resonance of ~10,995 Hz and a loss factor of 0.00880. Fig. 12c shows the frequency-response function measured by the microphone without the accelerometer attached, giving a resonance of 11,840 Hz and a loss factor of 0.0071. The resonance is higher because the accelerometer mass is removed from the specimen. The 11,840-Hz resonance yields an estimated modulus of 2.01E6 psi, which compares favorably with the vendor specification axial modulus of 2.22E6 psi from tensile tests and 2.00E6 psi from flexure tests. Note that the microphone shows more resonances than does the accelerometer. The reason is that the microphone is a omni-directional transducer and can measure noise resulting from many of the specimen modes, whereas the accelerometer is a single-direction transducer, and it will pick up motion, primarily in the direction that the accelerometer is oriented.

FREQUENCY RESOLUTION EFFECTS

A comparison of frequency-resolution effects on estimating damping is shown in Fig. 13. It is desirable to have the smallest frequency resolution in order to make a good estimate of damping using the half-power-point method. For the example trial-fabrication thin-walled composite cylinder, the axial resonance is determined by using base-band frequency analysis with a resolution of 8 Hz. A loss factor of 0.00231 was estimated at 4546-Hz axial resonance. By using zoom with frequency resolution of 2 Hz (see Fig. 13b), the loss factor for the first axial mode was 0.00219 at 4546 Hz. The axial modulus was estimated to be 24E6 psi, which compared well with the classical laminate code prediction of 27.3E6 psi. This example illustrates that there is very little difference in estimating the loss factor whether one uses zoom or a reasonable base band analysis as long as interpolation is used to estimate the half-power frequency width. When conducting tests on a large number of specimens, it is much easier and faster to conduct base-band frequency analyses than it is to conduct zoom analyses. As an initial test setup, it is recommended that one select a base-band frequency range so that the resonance of interest falls in the upper half of the frequency analysis range. Also, it is recommended that one use an interpolation method to estimate the half-power bandwidth.
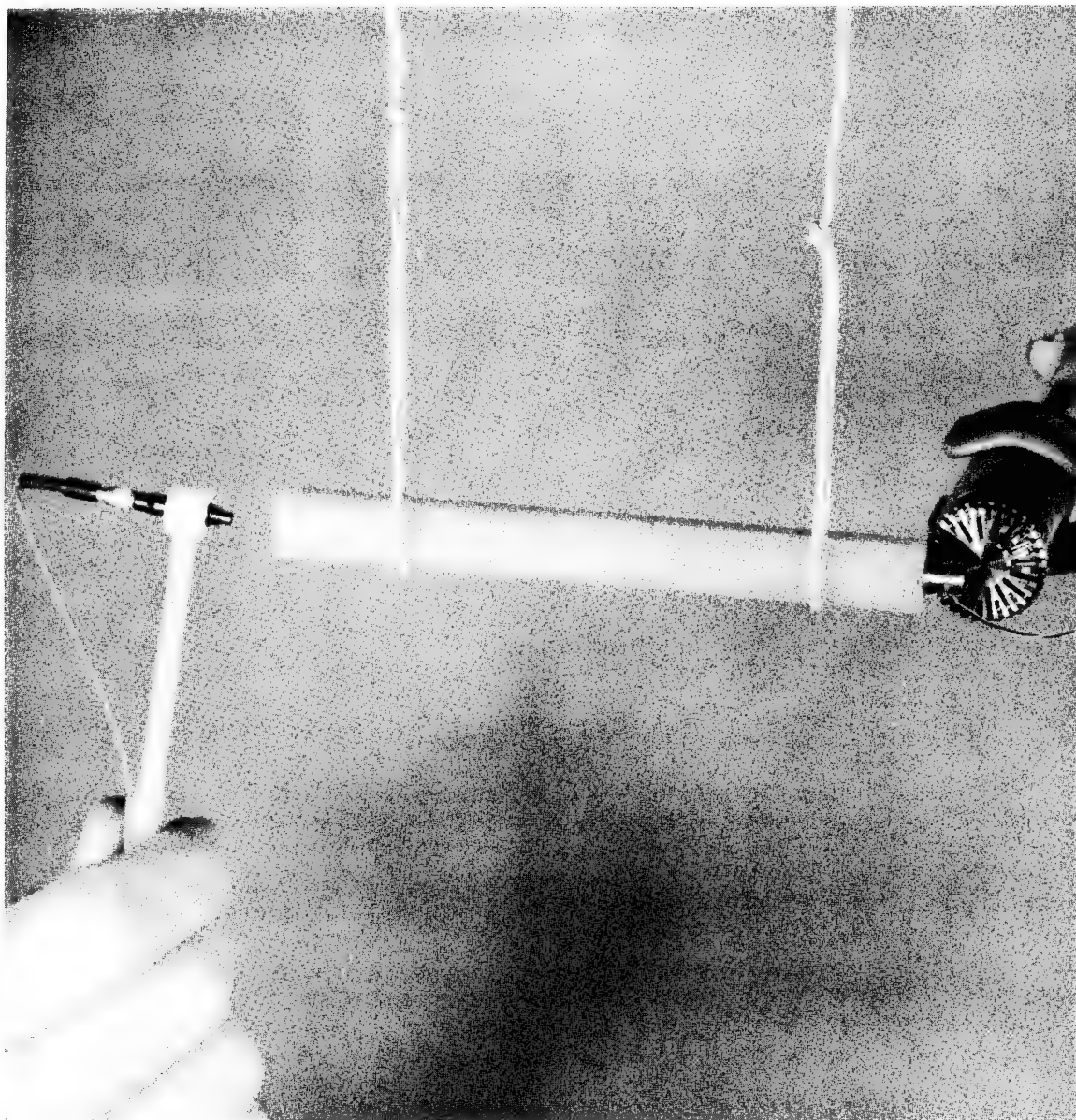
Fig. 11. Axial test of a small bar specimen.

INJECTION MOLDED FLEX BEAM
VERTON QF-700-10   0.25 x 0.50 x 5.00 in.
LONG-FIBER-REINFORCED NYLON 6/10   ICI/LNP

AXIAL INPUT AND RESPONSE   SPECIMEN MASS 15.2 g
FREQUENCY RESPONSE FUNCTION   ACCEL MASS   1.0 g

η = 0.00870 at 11000 Hz

(a)

AXIAL ACCEL.
RESPONSE
VTNA-122

η = 0.00880 at 10995 Hz

(b)

MICROPHONE
RESPONSE
w/ ACCEL.
ATTACHED
VTNA-123

E = 2.01E6 psi

η = 0.0071 at 11840 Hz

(c)

MICROPHONE
RESPONSE
w/o ACCEL.
ATTACHED
VTNA-125

VENDOR SPEC.   E TENSILE   = 2.22E6 psi
                   E FLEXURAL = 2.00E6 psi

Fig. 12. Accelerometer mass loading can be avoided.

BCC-19

14.02 in. OD, 41.73 in. LONG, ~0.062 in. WALL
79% P55 GRAPHITE AXIAL, 9% S-GLASS AXIAL, 13% S-GLASS HOOP

ERL 2258 EPOXY RESIN

AXIAL INPUT AND RESPONSE
FREQUENCY RESPONSE FUNCTION A/F g /lb

E = 24.0E6 psi

η = 0.00231 at 4546 Hz

(a)
BASEBAND
ΔF = 8 Hz
CMPS2-124

η = 0.00219 at 4546 Hz

(b)
ZOOM
ΔF = 2 Hz
CMPS2-123
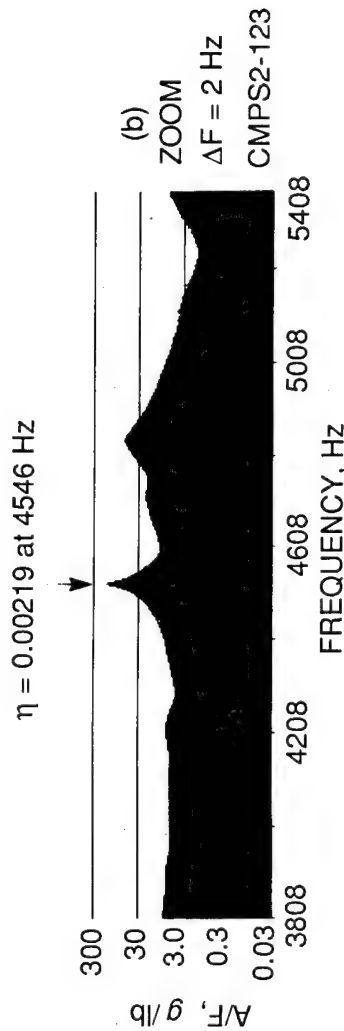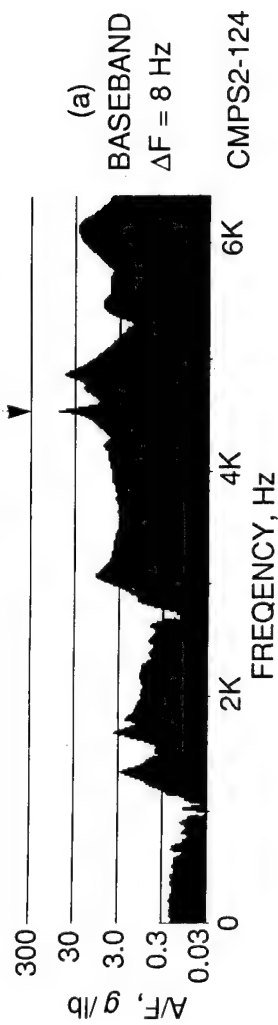
LAMINATE PREDICTED E = 27.3E6 psi

Fig. 13. Effect of zoom on damping measurement compulsator trial fabrication cylinder.

AN EXAMPLE OF THE EFFECT OF COMPOSITE LAY-UP ON DAMPING

An interesting set of axial and torsional damping loss factor data were taken on a dimensionally consistent set of cylinders made from various wet-wound composite lay-ups of AS4 graphite fiber/ERL-2258 epoxy matrix composite. Trial specimens were fabricated consisting of four different lay-ups, each with three different wall thicknesses. The inside diameter was ~4.40 in, the cylinder length varied from ~ 61 to 67 in., and the three nominal wall thicknesses were 0.125, 0.188, and 0.25 in. Table 1 shows the lay-up angle, the fraction of the total thickness at that angle, and the damping-loss factors for axial, torsional, and bending resonances. The 0° angle direction is axial, and the 90° direction is hoop. Because there was no significant difference in damping for various wall thicknesses, the average damping value for all three thickness is reported in Table 1.

Table 1. Axial and torsional damping loss factors for various cylinder lay-ups of AS4/2258 epoxy composite

| Lay-up angle,[a] fraction | Loss factor (normalized loss factor) | | |
	Axial	Torsional	Bending
0°, 0.5/90°, 0.5	0.00245 (1.00)	0.01749 (7.14)	0.00726 (2.96)
0°, 0.33/90°, 0.67	0.00355 (1.45)	0.01740 (7.10)	0.00688 (2.81)
0°, 0.25/90°, 0.25/±45°, 0.5	0.00456 (1.86)	0.00448 (1.83)	0.00744 (3.04)
±54° Helix	0.01653 (6.75)	0.00327 (1.34)	0.01632 (6.66)

[a] 0° = axial, 90° = hoop
Inside diameter, in. = 4.40
Nominal wall, in. = 0.125, 0.188, 0.25
Tube length, in. = 61.78 to 66.88

In the 0°/90° lay-up with the same amount of materials in the axial and hoop directions, the torsional loss factor is over seven times higher than that of the axial direction. This is because the torsional mode is dominated by the matrix material which provides a much higher damping than the fiber, whereas the axial mode is dominated by the fiber material. In the 0°/90° lay-up with twice as many hoops as axial, the torsional loss factor is likewise six to seven times higher than that of the axial loss factor. Again, this is due to the matrix dominance of the torsional motion and the fiber dominance of the axial motion.

For the 0°/90°/±45° quasi-isotropic composite lay-up, the torsional and axial damping loss factors are approximately equal as would be expected for a quasi-isotropic lay-up. Because the damping value for the quasi-isotropic lay-up is very close to that of the axial damping for the 0°/90° lay-up, one would conclude that both the torsional and axial modes of vibration for the quasi-isotropic lay-ups are fiber dominated.

For the ±54° helix lay-up, the axial loss factor is about five times greater than the torsional loss factor. This is true because, for the ±54° helix, the axial resonance is dominated by the matrix, and the torsional resonance is dominated by the fiber, which is opposite the case for the 0°/90° lay-up, as would be expected. Also, note that for the ±54° helix lay-up, the loss factor for bending is approximately the same as for axial. This should be expected because bending vibration involves the same axial strain energy loss mechanism as axial vibration.

In these data, it is also observed that the loss factor associated with bending for the 0°/90° lay-ups and the quasi-isotropic lay-ups are approximately two to three times higher than the axial loss factor. It is speculated that there could be two reasons for this. One is that beam bending involves some shear deformation. Consequently, matrix-dominated shear deformation in beam-bending vibration provides a supplemental damping mechanism to the fiber-dominated axial strain in beam bending. A second possibility is that additional apparent damping could be added to the free-free bending modes by the soft bungee cord or surgical tube suspension system. Additional work is planned to evaluate the significance of possible added damping from the soft suspension system by testing standard aluminum and steel (low damping material) in the same test setup under various test conditions including bending.

A similar set of data and conclusions can be drawn for a pair of specimens shown in Table 2. These data are for 7-in.-inside-diameter IM6 graphite/ERL-2258 epoxy composite cylinders--one with 0°/90° lay-up and one with quasi-isotropic 0°/90°/±45° lay-up. For the 0°/90° specimen, there is about eight times more damping for the matrix dominated torsional vibration than for the axial vibration. For the quasi-isotropic lay-up, there is about the same amount of damping in both the torsional and axial vibration modes.

ADVANTAGES OF THE TEST METHOD

The advantages of the impact modal test method are described as follows.

1. The modal impact test method provides nondestructive modulus and damping data on as-fabricated cylinders. There is no need to cut, fabricate, and test coupon samples.

2. The method applies to a wide variety of cylindrical or bar specimen sizes, weight, and configurations.

Table 2. Axial and shear moduli and damping loss factors for shear stiffened cylinders

Cylinder (material)	Fiber angle %	Fiber vol fraction	Modulus		Loss factor (frequency, Hz)		Normalized loss factor	
			Axial, E_z E6 psi	Shear, $G_{\theta z}$ E6 psi	Axial	Torsional	Axial	Torsional
SSC1[a] (IM6/2258 epoxy)	0°/33.5 90°/66.5	0.6659	8.90[b] [7.89][c] (9.68)[d]	1.07[b] (0.82)[d]	0.0035 (4034)	0.0293 (1397)	1.00	8.37
SSC2[e] (IM6/2258 epoxy)	0°/25 90°/25 ±45°/50	0.6217	8.21[b] [7.83][c] (9.18)[d]	3.42[b] (3.50)[d]	0.0053 (4468)	0.0051 (2883)	1.51	1.48

[a] SSC1 (SSC-2) 8.20 in. OD × 7.02 in. ID × 30.53 in. long, 11644 g, 25.67 lb.
[b] Data from modal tests.
[c] Data in [ ] are from strain gaged external pressure tests (i.e., compressive stress).
[d] Data in ( ) are from CLASS laminate code prediction.
[e] SSC2 (SSC-7) 8.31 in. OD × 7.02 in. ID × 26.65 in. long, 10311 g, 22.73 lb.

3. The near free-free boundary test condition requires no special fixturing. Also, the free-free test condition eliminates uncertainty in the resonant frequency and added damping which other constraining support mechanisms may introduce.

4. The pure axial and torsional modes provide data that are free of complex loading issues as might be encountered in a bending specimen that has both axial and shear deformation associated with bending vibration. Both axial and shear moduli and damping are obtained from the same specimen sample.

5. Air-damping effects are expected to be minimal because (a) displacements are small for axial and torsional modes compared with other dimensions of the specimen and (b) the pumping action normal to the moving surface area is negligible for axial modes of vibration and zero for torsional modes of vibration. For example, surface shear drag on the cylinder in torsional motion is expected to be negligible.

6. A noncontacting microphone can be used to detect resonances to avoid accelerometer mass loading of lightweight specimens. The use of a microphone has been demonstrated for detecting axial resonances. It is questionable as to whether it would detect torsional resonances.

7. Analyzer leakage errors can be eliminated by using exponential windows to acquire response time history data.

8. Tests are simple, quick, and inexpensive.

DISADVANTAGES OF THE TEST METHOD

The disadvantages of the impact modal test method include the following.

1. Data are limited to small deformations.

2. The modulus is associated with oscillatory stress--not one direction loading.

3. Modulus and damping are global--not local properties.

4. Data are associated with only specific specimen resonant frequencies unless steps are taken to alter them.

5. A variable, nonstandard specimen size and configuration may make it difficult to compare modulus and damping properties of similar material and composite lay-up.

6. Data may be difficult to obtain from specimens with low L/D ratios and with thin walls. High shell modal density or bending modes may obscure axial and torsional modes of interest. Acquiring meaningful data in a short period of time may be difficult or impossible under these conditions.

7. The accelerometer and tangential striker block can mass load and significantly alter resonances of relatively lightweight specimens. This is expected to affect the modulus measurement because of the lower resonant frequency but not to affect the damping measurement.

8. A noncontact displacement probe may be difficult to use on a free-free mounted specimen that is lightweight because high displacements after impact may move the specimen outside the range of the probe. This is less of a problem with heavy specimens that undergo small displacement under impact conditions.

9. There may be a question of the effect on axial resonance due to point excitation at the edge of a large-diameter cylinder instead of uniform loading distributed over the entire circumference.

ISSUES NEEDING ADDITIONAL WORK

To resolve some questions about the test methods, additional work in the following areas is recommended.

1. Investigate the effect on damping of the soft near free-free suspension system especially for vibration modes associated with beam bending. Dr. D. I. G. Jones of the Wright Research Development Center/Materials Laboratory recommended that this could be evaluated by testing specimens of known low-damping value, such as aluminum or steel, with the same near free-free soft suspension system.

2. Eliminate or compensate for the striker block and accelerometer mass loading affects on lightweight specimens in torsion.

3. Evaluate the use of a microphone as a noncontact transducer with other specimens.

4. Evaluate the affects of point vs uniform excitation on axial resonants of low L/D ratio cylindrical specimens.

SUMMARY

The impact modal test method on cylinders will provide a "pure" measurement of axial and in-plane shear moduli and associated damping. Since these are nondestructive tests on as-fabricated cylinders, no coupon tests are necessary. Boundary conditions and air-damping effects are minimized with free-free axial and torsional modes. For most specimens, the impact modal test method is a quick, inexpensive and nondestructive means of measuring moduli and damping of as-fabricated cylinders and rods.

Examples of damping data and modulus were shown for several sizes, configurations, and lay-ups of composites. Composite damping was shown to be

very sensitive to the applied principal stress relative to the fiber direction, even in the same specimen. In the composites illustrated, matrix-dominated deformation or motion provides ⑥ to ⑧ times more damping than fiber-dominated motion.

Axial and in-plane shear moduli determined from the impact modal test method of free-free cylinders compared well with expected values for most lay-ups.

Some helpful hints (short of a full-modal test) were described to distinguish axial and torsional modes of interest without performing a time-consuming, more costly full modal analyses including measured frequencies and mode shapes.

Careful selection of base-band analyses to ensure that resonances of interest are in the upper half of the frequency band, in many cases, will provide reasonable estimates of half-power points and damping loss factors. For many specimens, the use of time-consuming zoom analyses to increase frequency resolution can be avoided.

The effect on the bending-mode damping due to the soft, near free-free suspension system needs to be investigated. Difficulties may be encountered with low L/D, thin-walled, lightweight specimens because of the possible existence of high shell modal density in the vicinity of the primary axial or torsional modes of interest. Striker block and accelerometer mass loading of lightweight specimens may affect the estimate of modulus but is not expected to affect damping measurements.

THE USAGE OF ELECTRORHEOLOGICAL MATERIALS IN VISCOELASTIC LAYER DAMPING APPLICATIONS

John P. Coulter   Theodore G. Duclos   Debra N. Acker

Lord Corporation
Thomas Lord Research Center
Cary, North Carolina 27512, U.S.A.

ABSTRACT

For many years, viscoelastic material layers have been used as structural components to obtain desired levels of structural damping. In common applications, the viscoelastic material is either placed in a constrained position subjected to shear loading or in a free position subjected to extensional deformation. In such situations, the damping behavior of the overall structure can be related using well developed theories to the viscoelastic material properties of the constrained or free layers. Since most classical viscoelastic damping materials exhibit complex mechanical properties which cannot be controlled after fabrication, once a structure is designed and fabricated the damping characteristics of that structure are unchangeable. On the other hand, if the viscoelastic layer contains an electrorheological material having controllable viscoelastic material properties, then structures can be constructed with controllable damping behavior. This control of structural behavior would be very useful in many situations, examples of which are the vibration of robotic manipulators and space structures. In the present work, the classical viscoelastic theories are extended to constrained layers of electrorheological materials and experimental results demonstrating the controllable structural behavior concept are presented.

INTRODUCTION

Viscoelastic material layers have been utilized in structural damping applications for many years. In short, there are two classes of viscoelastic damping applications, one in which the viscoelastic material is placed in a state of tension, and the other in which the same material is put in shear. Both classes of structural damping were first conceived in the 1950s. Elongational viscoelastic damping was first reported in France by Lienard in 1951 and shortly thereafter in Germany by Oberst[1,2]. Following this, the concept of shear viscoelastic damping was developed in America and first reported in 1959 by Kerwin[3]. Kerwin and his co-workers developed a theory relating the material properties and geometrical arrangement of panels made up of viscoelastic and elastic layers to the overall flexural behavior of the composite structure. This theory, which has since become well accepted for certain applications and known as the Ross-Kerwin-Ungar (RKU) model, was initially presented in 1959[4]. The RKU model with its limitations is discussed in several contemporary vibration control texts, and is widely used to design for structural vibration behavior in many present day applications ranging from the vibration of robot arms and space structures to the motion of buildings exposed to wind[5,6]. Relatively speaking, high modulus viscoelastic materials are used in extensional damping applications and lower modulus viscoelastic materials are used in shear damping applications. In general, shear damping treatments are the most effective of the two types of damping layers, and only such treatments were considered during the present investigation.

The single most important component in the design of a shear damping treatment is the selection of the viscoelastic material or materials to be used. During the past few decades, the variety and quality of materials designed for such treatments have improved dramatically, but the materials available today still have several shortcomings. The most important of these is the limited temperature range over which any single material is effective as a shear damping layer. This limitation has been partially overcome in many instances by the usage of polymer blends of components with different ranges of temperature applicability and/or by the use of multiple constrained layers of several different damping materials, but an ideal solution to this complexity remains to be found. A second shortcoming of modern day viscoelastic damping materials is the lack of controllability of their material properties once they are installed in a selected application. The majority of design and analysis related to structural behavior control utilizing viscoelastic layers is based on the assumption that the properties of the viscoelastic materials being used remain constant with time, and these materials are placed within structures at strategic locations

so as to obtain a single invariable overall structural response to the proposed conditions which the structure is to be exposed. A possible exception to this is the recent use of piezoelectric polymers and ceramics[7-9] to vary structural response in a fully active manner. It would be desirable to have the capability to control structural response by varying the properties of viscoelastic damping materials encased within structural components, for having such a capability would allow for the in service tuning of the structure to avoid selected resonances and possibly accommodate temperature changes. A class of materials which may meet this need are electrorheological (ER) materials which exhibit viscoelastic properties that vary as a function of frequency and applied electric field. The potential usage of ER materials in viscoelastic layer shear damping applications is introduced in the present investigation.

ELECTRORHEOLOGICAL MATERIAL CHARACTERIZATION

Electrorheological materials are suspensions of very fine dielectric particles in insulating mediums which exhibit controllable rheological behavior in the presence of applied electric fields. The typical constitutive behavior of an ER material is shown in figure 1 where shear stress is plotted as a function of shear strain and shear rate respectively. As shown in figure 1a, ER material behavior can be divided into pre-yield and post-yield regions. The electrorheological effect was first observed by Winslow in 1947[10]. At that time, materials which behaved in this manner were labelled electroviscous fluids since from a macroscopic viewpoint the most notable change of a flowing ER suspension is a change in apparent or effective viscosity. Some years later, it was determined that the actual viscosity of the material, ν, remains relatively constant as the applied electric field is varied while the property that changes is τ_y, the yield stress of the Bingham plastic-like suspension. This is shown in figure 1b. The manifestation of this variable yield stress has proved very useful in devices where controllable post yield or flow properties are desired. Examples of electroactive devices in which this behavior has been used effectively include valves and clutches[11].
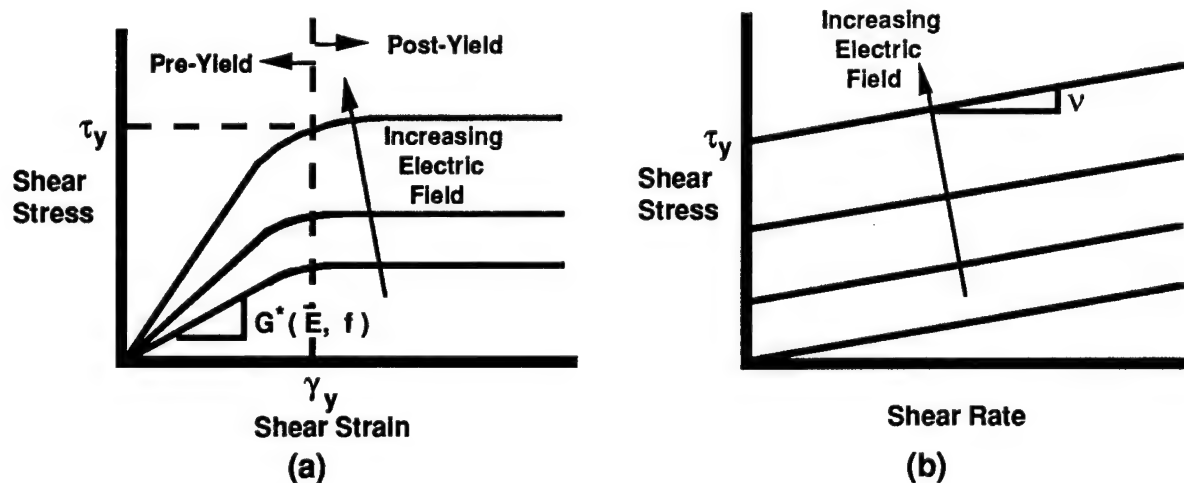
Figure 1: Typical rheological behavior of an ER material denoting the pre- and post-yield material behavior regions.

In comparison to the post-yield behavior, the controllable viscoelastic material behavior that ER materials exhibit while in the pre-yield phase remains virtually uninvestigated. As shown in figure 1a, this region is defined by a yield strain (γ_y), a yield stress (τ_y), and a complex shear modulus (G*). Since the yield stress in an ER material increases with increasing applied electric field and the yield strain normally remains at approximately 1% for all field strengths, the complex shear modulus increases with increasing electric field. The controllability of this pre-yield complex shear modulus and its usage to obtain controllable structural behavior was the focus of the present investigation.

The complex shear modulus can vary several orders in magnitude as a result of electric field strengths ranging between 0 and 4000 V/mm. A full analytical understanding of this phenomenon has not yet been obtained, but several workers including Adriani and Gast are pursuing this matter[12]. In the absence of this understanding, an experimental characterization of the pre-yield complex shear modulus of ER materials was undertaken. Many techniques exist for measuring the complex shear modulus of viscoelastic materials[13,14]. Of these, the best test method to use with ER materials has not yet been determined. Two methods, however, were selected for initial testing. These included a standardized resonating cantilever sandwich beam method, (ASTM G756-83) and a simplistic but as of yet non-standardized concentric cylinder annular pumping technique. In addition to the fact that it is a well accepted and widely used test method, the vibrating sandwich beam test was chosen for its inherent large frequency range capability and its direct relationship to distributed structural damping. Following some initial testing, however, the applicability of this technique was found to be questionable due to fact that present ER materials were found to have modulus values much lower than the materials commonly characterized using this method. Thus, for the purposes of the present study, the complex shear modulus of the chosen ER materials was determined using the concentric cylinder annular pumping technique. A diagram of the experimental apparatus used to accomplish this is shown in Figure 2.
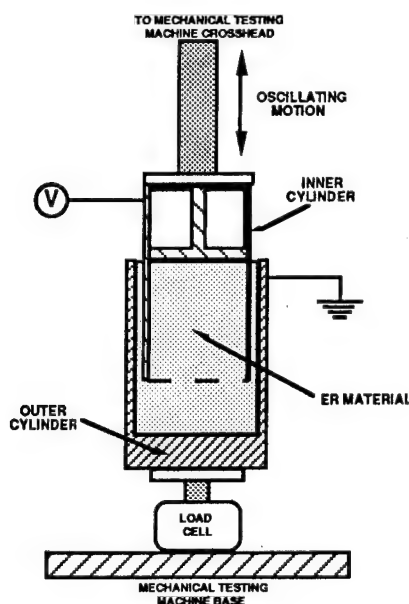
Figure 2: Cylindrical annular pumper apparatus used for complex shear modulus measurement.

A hollow aluminum cylinder having a thickness of 0.8 mm., an outside diameter of 44.5 mm., and a length of 47.6 mm. was connected to the actuator of a hydraulic mechanical testing machine. This cylinder was then lowered into an ER material filled stationary aluminum cup of thickness equal to 3.0 mm., inside diameter equal to 46.5 mm., and inside depth equal to 63.5 mm. This cup was connected to a load cell with a force range of 0-110 N. The depth of the cup was chosen to be much larger than the immersed length of the inner cylinder to minimize end effects and the diameters were chosen as stated to produce an ER material filled annulus with a thickness of 1.0 mm. An electric field was maintained in the gap between the cylinders by using the inner cylinder as a DC high voltage electrode and the outer cylinder as electrical ground. For each selected electric field, the inner cylinder was displaced vertically using band limited white noise with a bandwidth from 0 to 200 Hz. The frequency range was limited below 200 Hz. due to the capabilities of the mechanical testing machine. An amplitude of excitation was chosen so as to produce a maximum shear strain level of 1% within the ER material. The complex shear modulus was then deduced from the force and displacement waveforms resulting for each set of test conditions. All tests were performed at room temperature, and at electric field levels between 0 and 4000 V/mm.

The ER materials chosen for use in the present study were two proprietary materials developed over the past three years by Lord Corporation. The formulations are known as materials ERX-03-145 and 5501-21C respectively. The resultant pre-yield complex shear moduli for these two materials are presented as functions of frequency and applied electric field in figures 3 and 4. These results are presented in the form of shear storage modulus, G', and shear loss factor, η. The shear loss factor is related to the real and imaginary components of the complex shear modulus, G' and G" respectively by the relation

$$\eta = \frac{G''}{G'} \tag{1}$$

and was chosen for presentation due to its importance in viscoelastic damping applications. The shear modulus for material ERX-03-145 is presented in figure 3 and that for material 5503-21C in figure 4. Both materials exhibited storage modulus values that increased with applied electric field and frequency. For ERX-03-145 the magnitude of the storage modulus ranged from 0 up to 70 KPa. at the highest applied electric field and frequency tested while the corresponding range for 5503-21C only reached a level of 21 KPa. The shear loss factor for the two materials also increased with frequency but was generally found to decrease with applied electric field. This decrease, however, was less evident at the higher levels of electric field than it was at the lower levels where the material is more fluid-like in nature. Thus, for the 2000 to 4000 V/mm electric fields commonly applied in ER material applications, the shear loss factor of the two materials generally stayed between 0 and 4.0.

When comparing the properties of the ER materials discussed above with those of standard viscoelastic damping materials, it is immediately obvious that while the loss factor ranges are comparable, the storage modulus values of ER materials are several orders of magnitude less than those of present day shear damping treatment materials. The continued development of stronger ER materials along with their unique behavior, however, appropriates further discussion of their use in damping applications. The unique feature referred to is the controllability of the material properties within certain ranges. Examples of this are shown in figures 3 and 4. For each frequency value, the complex shear modulus can be controlled within the minimum and maximum values by the adjustment of applied electric field. This control can

be adjusted over time increments of several milliseconds, which is the response time of present day ER materials to changes in electric field levels. The capability for such control would be very useful to the structural damping industry.

Aside from the material property behavior discussed above, several other parameters are commonly considered when discussing ER materials. Two such parameters are current density and temperature dependence. The current density must be kept low to avoid large electrical power requirements at the high voltage levels required. For the materials presented, the current density is on the order of 0.1 μA/cm^2 at an electric field of 4000 V/mm The useful temperature range of both ERX-03-145 and 5501-21C is approximately 10-85°C. Within this range the pre-yield mechanical properties of the materials are relatively independent of temperature. The current density, however, does increase with temperature. Other factors worth mentioning are the stability and long term behavior of the materials. Some formulations of ER materials have shown a tendency of particle/carrier fluid separation over time. ERX-03-145 has exhibited this behavior in the past, while 5503-21C is much more stable. The long term behavior of both materials is presently being studied.
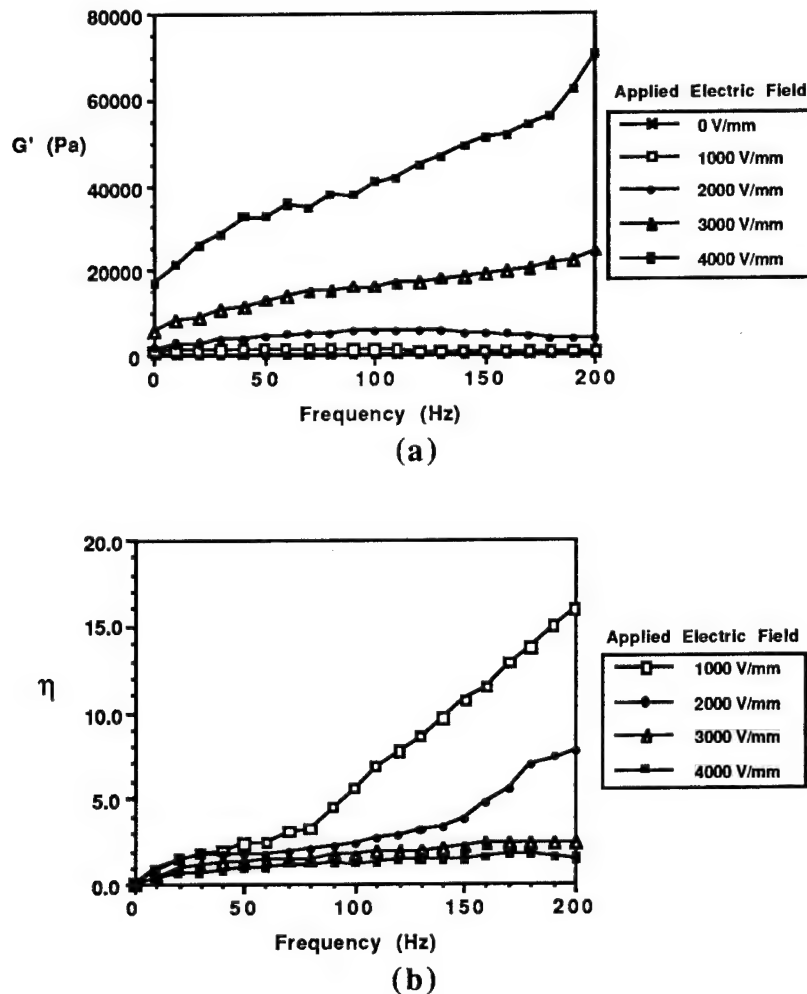
Figure 3: Complex shear modulus of electrorheological material ERX-03-145.
(a) Storage modulus, (b) Loss factor.
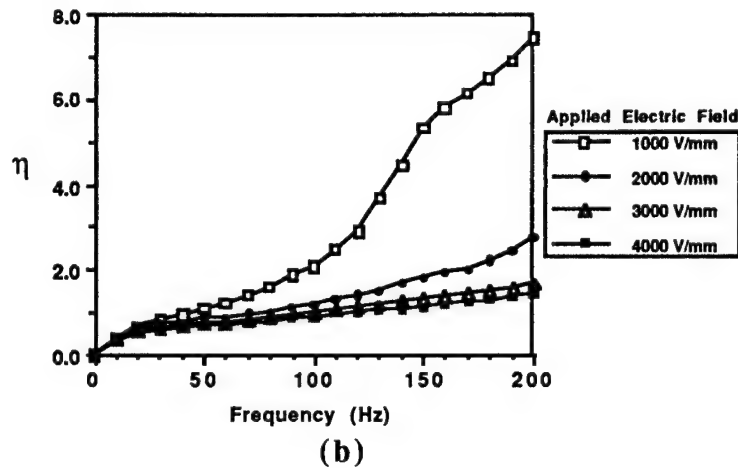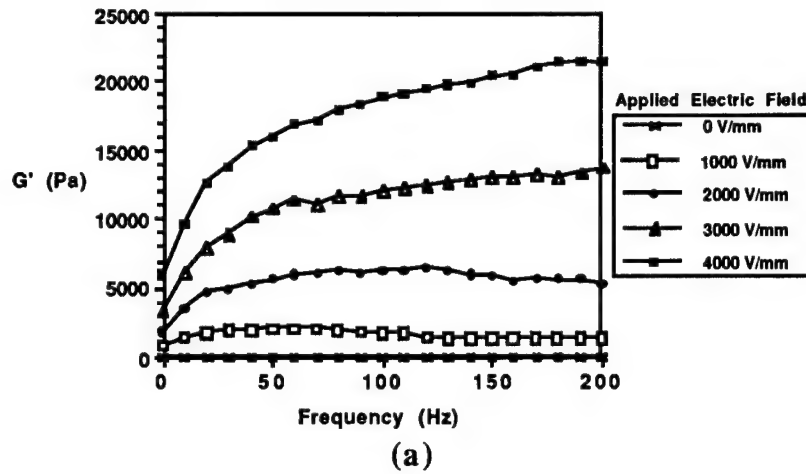
Figure 4: Complex shear modulus of electrorheological material 5503-21C. (a) Storage modulus, (b) Loss factor.

THEORETICAL BACKGROUND

As mentioned previously, the obtainment of structural damping using constrained viscoelastic layers in shear is common practice in the vibration control industry today. In many instances the Ross-Kerwin-Ungar model (RKU) is used in the design of structures. One of the purposes of the present study was to investigate whether or not this theory is applicable to structures containing ER materials as viscoelastic damping layers. A brief summary of the RKU model applied to shear damping treatments follows.

A sample shear damping configuration is shown in figure 5a. In such configurations, a viscoelastic material, denoted as material 2 in the figure, is sandwiched between two elastic material layers, which are shown in the figure as materials 1 and 3. Flexural deformation of the structure produces not only bending and extension but also shear, which occurs primarily in the

viscoelastic layer as shown in figure 5b. The strain energy associated with this shear tends to dominate the damping behavior of the overall structure.
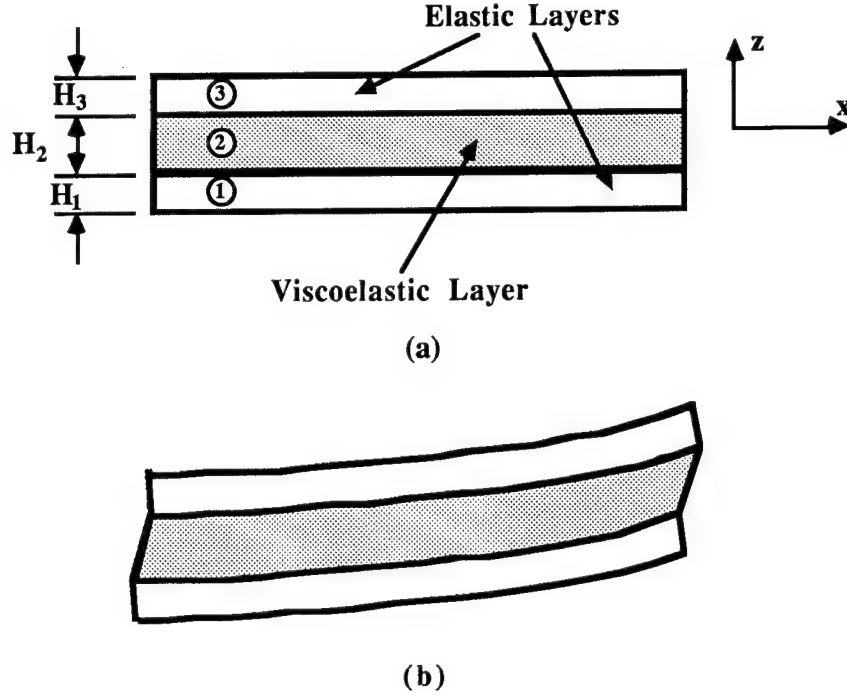
Figure 5: Typical section of a panel with a constrained viscoelastic layer.
(a) Undeformed, (b) Deformed.

Assuming that the extensional stiffness of the viscoelastic layer is small compared to that of the elastic materials, the loss factor of the entire structure is

$$\eta = \frac{\eta_2 \, Y \, X}{1 + (2 + Y) \, X + (1 + Y)(1 + \eta_2^2) \, X^2} \, . \tag{2}$$

In equation (2), η_2 is the loss factor in shear of the viscoelastic layer, $(\eta_2 = G'' / G')$, Y is a stiffness parameter, and X is a shear parameter. In its full form, the stiffness parameter, Y, is defined as

$$Y = \left[\frac{E_1 \, H_1^3 + E_3 \, H_3^3}{12 \, H_{31}^2} \left(\frac{1}{E_1 \, H_1} + \frac{1}{E_3 \, H_3} \right) \right]^{-1} \tag{3}$$

where E_i and H_i are the tensile modulus and thickness of the ith layer respectively and H_{31} is the distance between the mid-planes of the elastic constraining layers, ($H_{31} = H_2 + (H_1 + H_3) / 2$). For the present discussion, the elastic layers will be considered to be made of the same material

and to be of equal thickness, thus $E_1 = E_3$ and $H_1 = H_3$. With these assumptions, the stiffness parameter becomes simply a geometric parameter, which is

$$Y = 3 \left(\frac{H_{31}}{H_1} \right)^2 .$$ (4)

The shear parameter, X, is defined as

$$X = \frac{G_2'}{p^2 H_2} \left(\frac{1}{E_1 H_1} + \frac{1}{E_3 H_3} \right)$$ (5)

where p is the wavenumber, which for simply supported beams is related to the length of the beam, L, and mode of flexural vibration of the composite panel, n, by the relation $p = n\pi / L$. Thus, by choosing a viscoelastic material with a given complex shear modulus and designing a layer of this material into an otherwise elastic composite panel, one can determine the effective loss factor, and thereby the damping, of the overall structure.

In addition to dominating structural damping, the existence of a constrained viscoelastic material in a composite panel as shown in figure 5 also modifies the flexural rigidity of the structure. For the configuration shown, the real component of the effective complex flexural rigidity per unit depth of the structure is

$$B = (B_1 + B_3) \left\{ 1 + \left[\frac{XY + X^2 Y (1 + \eta_2^2)}{1 + 2X + X^2 (1 + \eta_2^2)} \right] \right\}$$ (6)

where

$$B_i = \frac{E_i H_i^3}{12}$$ (7)

This change in effective stiffness of composite panels due to the existence of a viscoelastic layer brings about a corresponding change in the resultant frequency of flexural vibration, f_n. For simple beam panels, this is evident through the relation

$$f_n = \frac{p^2}{2\pi} \sqrt{\frac{B}{\mu}}$$ (8)

in which μ is the mass per unit area of the panel. For three layer laminated composite beams, μ can be determined using the expression:

$$\mu = \sum_{i=1}^{3} \rho_i H_i$$ (9)

in which ρ_i is the mass density of the material of layer i. Thus, like the loss factor, the frequency of vibration of composite panel structures encompassing a viscoelastic layer changes with corresponding changes in the complex shear modulus of the viscoelastic material.

DESCRIPTION OF VIBRATION EXPERIMENTS

In order to test the usage of ER materials in distributed viscoelastic layer damping applications, small amplitude vibration experiments were performed with ER material filled symmetric sandwich beam specimens. A diagram of a specimen is shown in figure 6. As shown in the figure, sandwich beams were constructed with 0.53 mm thick aluminum face layers and 2.0 mm thick ER material filled cores. The total length and width of each beam was 0.254 m and 0.0254 m respectively. A constant core thickness throughout each beam was obtained by positioning small silicone rubber face plate separators of the desired thickness at the ends and center of each side of the beam. At the center of the beams, these separators were adhered to one side only while at the ends of each beam, the silicone was bonded to both the upper and lower face plates. The sides of the beams were sealed by the loose application of a 0.25 mm thick latex sheet material bonded to the outside surfaces of the face plates to create a sealed core. For the purpose of clarity, only one latex side skin is shown in figure 6. After the appropriate ER material was placed in the core, the ends of each beam were sealed with silicone rubber sealant. The application of an electric potential to each face plate was allowed for by the inclusion of small end tabs at one of the corners of each plate. Two such beams were fabricated, each containing one of the two ER materials previously discussed.
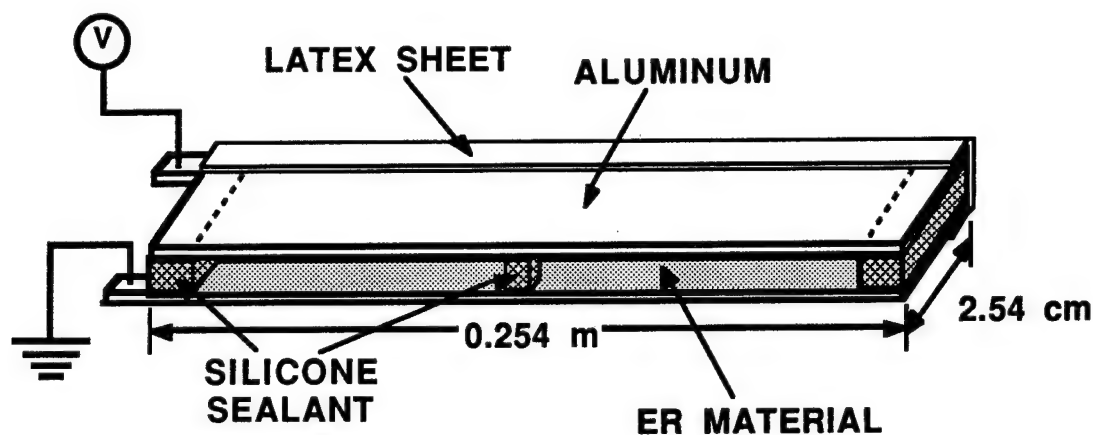
Figure 6: Configuration of ER material filled composite sandwich beam specimens.

During testing, each beam was positioned in a horizontal simply supported configuration as shown in figure 7. A non-contacting electromagnetic actuator was used to input a 0-200 Hz random vertical oscillating force on the beam at an axial position equal to one fourth of the length of the beam from one of the supports. Likewise, a non-contacting electromagnetic proximity probe was used at the other quarter length position to record the vertical displacement at that location as a function of time. Small steel targets were attached to the beam at the actuator and sensor locations to permit their use. The maximum amplitude of oscillation at any point along the beam was maintained at a level less than 0.5 mm. Controllable high voltage was applied by grounding one face plate of the beam and applying a DC voltage to the other face plate using a high voltage power supply. Voltage levels between 0 and 5000 volts were applied to the beam in 1000 volt increments. This resulted in electric field levels between 0 and 2500 V/mm. At each level of applied electric field, the natural frequency for each mode of vibration below 200 Hz was

determined from the spectral response of displacement at the proximity probe location. Corresponding structural loss factors were determined for each mode from the half power bandwidth of the frequency response.
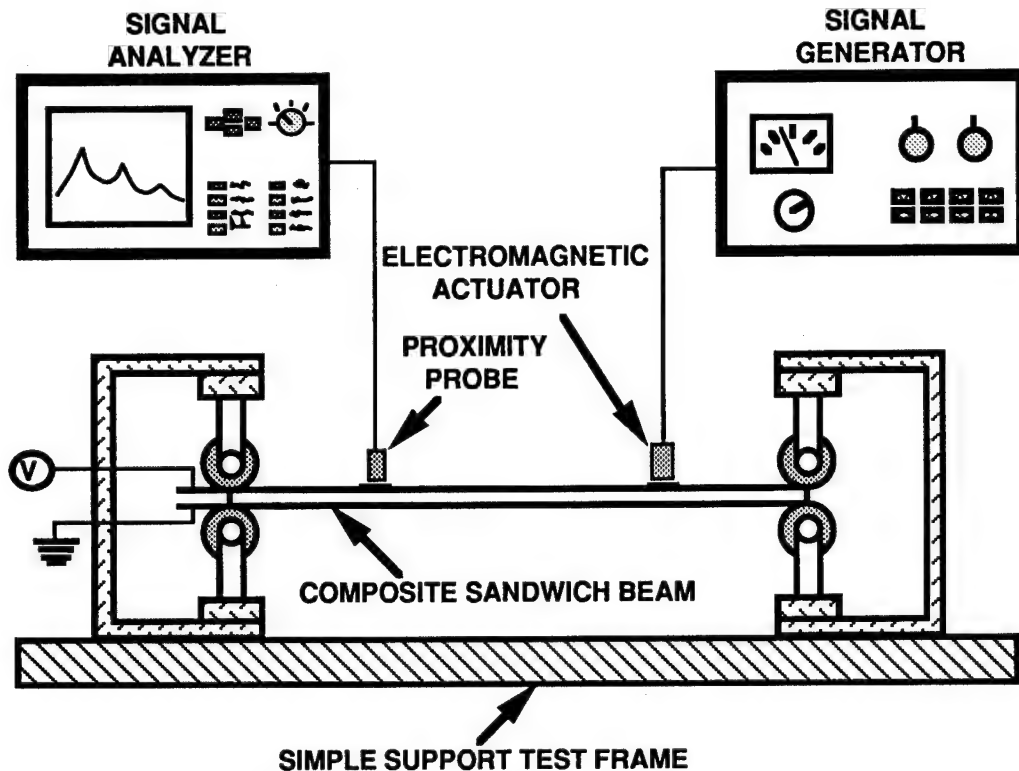
Figure 7: Experimental apparatus used during vibrational testing.

RESULTS AND DISCUSSION

For all but the lowest voltages applied during testing, only the first three flexural modes of vibration existed within the 0-200 Hz. range chosen. The resultant modal frequencies and corresponding loss factors observed for the two sandwich beams are presented as functions of electric field applied across the ER material in figures 8 and 9. As evident from figure 8a , the natural frequency of each of the three modes of the beam containing ER material ERX-03-145 increased significantly with applied electric field. Over the 0-2500 V/mm range tested, this increase was nearly linear, and the lines resulting from least squares analyses of the data are included in the figure. The change in modal frequency with applied electric field for modes 1 through 3, in units of Hz/(KV/mm), were 12.1, 13.0, and 18.6 respectively. All the curve fits yielded correlation coefficient values exceeding 0.97. The observed behavior in modal loss factor with applied electric field for the same beam, shown in figure 8b, was not as orderly as the frequency behavior. It can be concluded, however, that the modal loss factor was found to decrease with mode number and generally increase with applied electric field. Overall structural loss factor values ranging between 0.03 and 0.11 resulted.
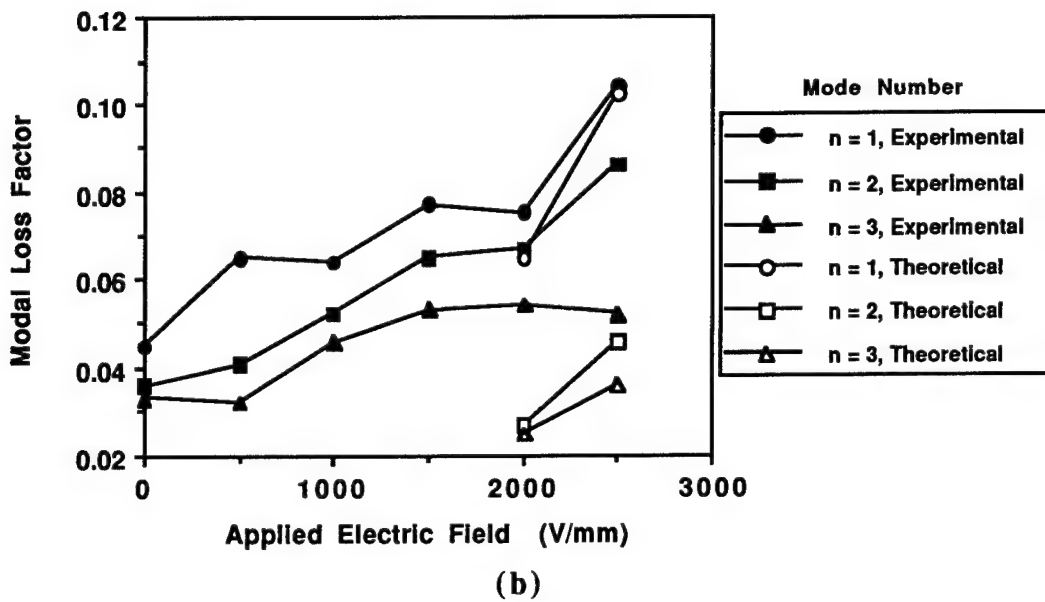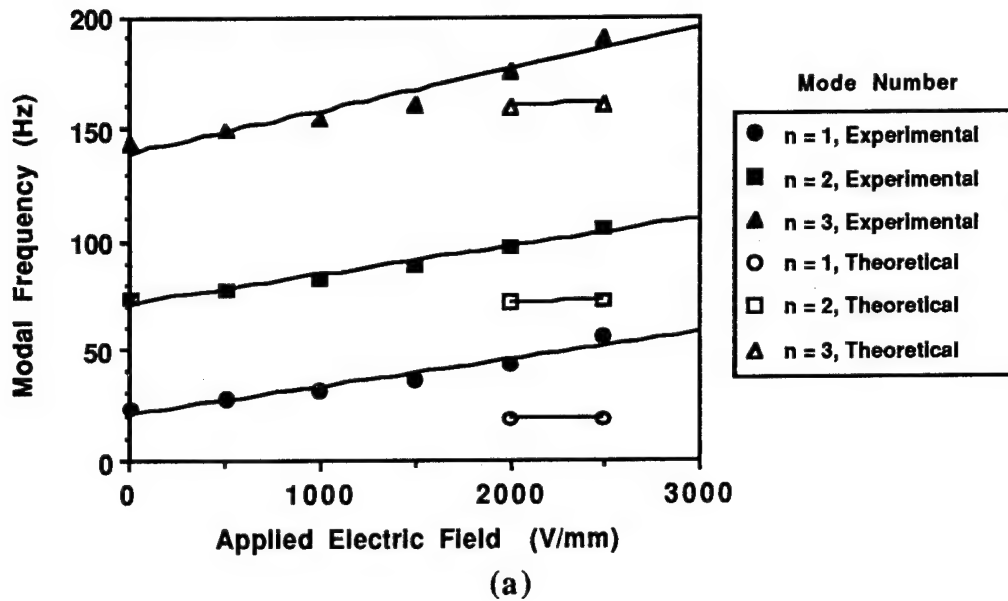
Figure 8: Observed dependence of beam modal frequency and loss factor
on applied electric field; ER material ERX-03-145.
(a) Modal frequency, (b) Modal loss factor.

The modal frequencies of the beam filled with ER material 5503-21C were also found to increase linearly with applied electric field. This is shown in figure 9a, and the resultant gradients of frequency with applied electric field were 8.2, 7.9, and 14.1 Hz/(KV/mm) for modes 1 through 3 respectively. The correlation coefficients of the curves all exceeded 0.98. The dependence of modal loss factor on applied electric field for this case, as shown in figure 9b, was again somewhat disordered. For modes 2 and 3 the loss factor followed the previously

mentioned pattern of generally increasing with applied electric field. For mode 1 however it was observed in this case that the loss factor increased with applied electric field for fields below 1500 V/mm and then decreased with electric field for field levels above this point. This behavior was seen consistently during repeated testing.
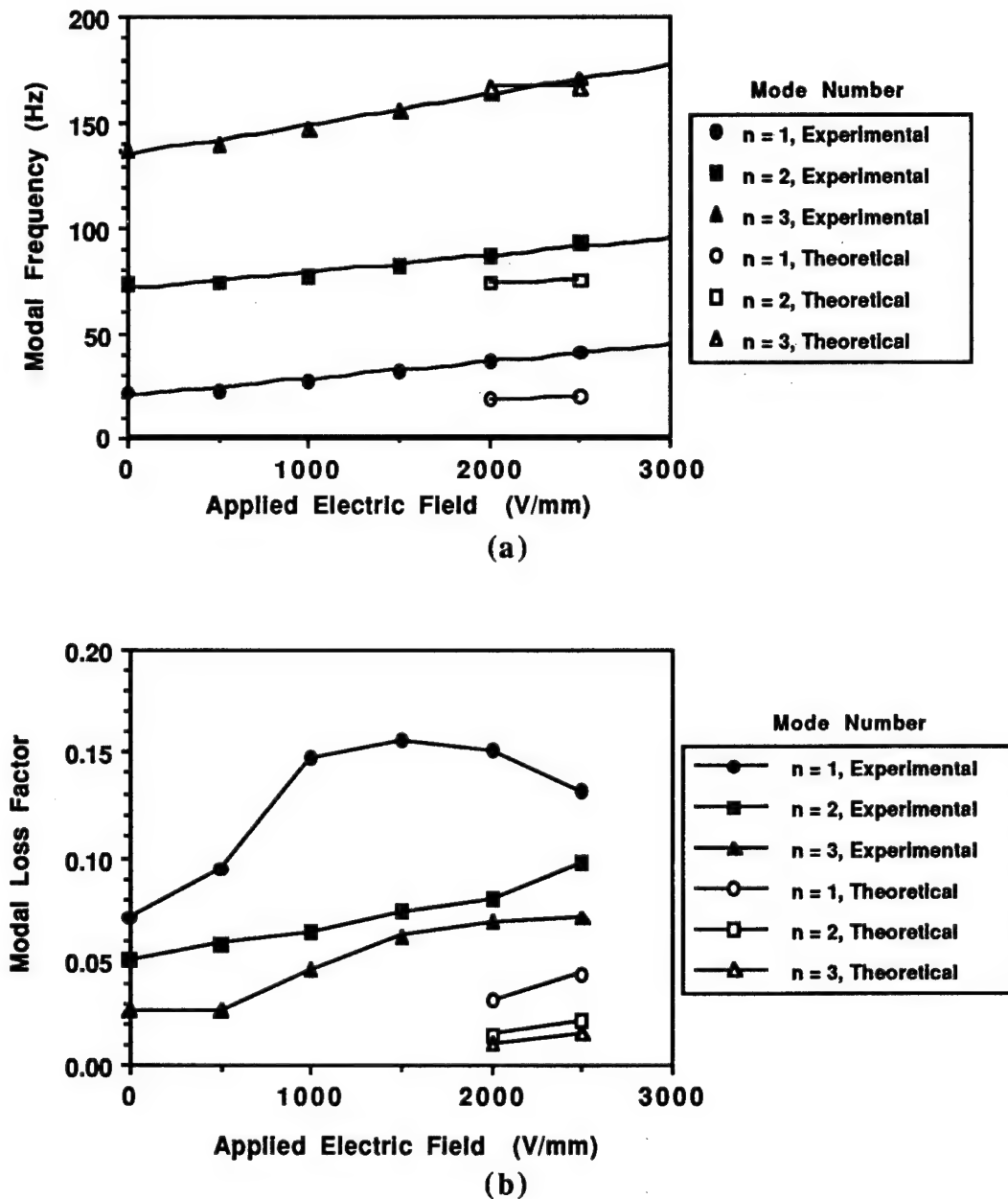
Figure 9: Observed dependence of beam modal frequency and loss factor
on applied electric field; ER material 5503-21C.
(a) Modal frequency, (b) Modal loss factor.

Following the obtainment of experimental results, an attempt was made to theoretically predict the observed behavior using the classical RKU theory. This was done by first obtaining appropriate ER material shear storage modulus and loss factor values at the observed frequencies of vibration and applied electric field levels using the data presented in figures 3 and 4. These values were used along with the density of the ER material, the properties of aluminum, and the geometry of the beams constructed to determine predicted structural modal frequencies and loss factors using equations (2) through (9). Initially, no effects of the silicone rubber or the latex were considered. The predicted modal frequencies and loss factors resulting from these calculations for the highest two electric field levels tested are included in figures 8 and 9. From figures 8a and 9a it can be concluded that the theory as applied generally underpredicted the vibrational modal frequencies observed. The degree of deviation from experimental observation ranged from practically none for mode three of the beam filled with ER material 5503-21C to as much as 63% for mode one of the beam filled with ER material ERX-03-145. The loss factor data shown in figures 8b and 9b reveal that although the loss factor was predicted to increase with applied electric field and mode number, the actual magnitudes of the theoretical loss factors calculated were much less than those observed. The only exception to this is the loss factor for the first mode of vibration of the beam filled with ERX-03-145.

In response to the above mentioned discrepancies in predicted and observed behavior, the possibility of accounting for the influence of the silicone sealant was investigated. The influence of the latex material was assumed to be minimal due to the loose manner in which it was purposefully installed. Since the silicone is believed to have a higher shear storage modulus than the ER materials, the beams constructed were probably stiffer than would be predicted by only considering the ER material between the face plates. This in turn would lead to the observation of higher than predicted frequencies of flexural vibration. To test this hypothesis, a volume weighted rule of mixtures component was added to the theoretical analysis and an effective complex shear modulus of the material occupying the core region of the beams was determined using the relationships

$$ G'_{eff} = \frac{G'_{Si} V_{Si} + G'_{ER} V_{ER}}{V_{TOT}} \tag{10} $$

and

$$ G''_{eff} = \frac{G''_{Si} V_{Si} + G''_{ER} V_{ER}}{V_{TOT}} \tag{11} $$

where the subscripts Si and ER refer to the silicone rubber and ER material respectively and V represents to volume of viscoelastic material in the beam. The resultant effective complex shear modulus values were then used throughout the remainder of the calculations to determine new structural modal frequency and loss factor values. Since the silicone occupied less than 10% of the viscoelastic material volume in the beams, however, this revised analysis did not lead to significant changes in the theoretical predictions. The possibility remains that the properties used for the silicone rubber were inaccurate since they were taken from the literature to be G'_{Si} = 69,000 Pa and G''_{Si} = 6,900 Pa. The actual properties of the silicone sealant used remain to be measured.

Another potential source of error in the calculations is inaccuracy in the values of the ER material complex shear modulus. During the material characterization phase of the study, the properties of the ER materials tested varied with time of continuous exposure to an electric field

and whether field levels were being increased or decreased. Although care was taken to obtain similar material property conditions during material characterization and structural testing, it is likely that the two situations did not exactly coincide. Further work is in progress to better quantify the rheological behavior of ER materials, and as this supporting work progresses it is likely that more accurate structural behavior predictions will also result.

Accepting the fact that further work is needed to more closely correlate theory and experimentation in this area, the controllable vibration observed remains a truly remarkable phenomenon which may be of significant utility in the vibration control industry. This can be seen by simply examining the linear behavior of structural modal frequency with applied electric field, as shown in figures 8a and 9a. A potential use of this technology is in the tuning of structural properties to avoid vibrational resonances. An example of this is shown in figure 10, where the observed structural response amplitude of one of the beams tested is plotted as a function of frequency for the two cases of no electric field and an electric field of 2500 V/mm. If one desired to avoid resonances over a given frequency range, the structure could be "tuned" by either applying or removing the electric field so that the response to a given frequency of excitation was minimized. If the excitation frequency for one reason or another changed, the structure could be adjusted in a matter of milliseconds to again produce a minimized response at the new frequency. This would result in a capability of obtaining a response amplitude spectrum equivalent to the shaded area in figure 10. Such a capability has not been obtainable using any other means of controllable passive damping to date.
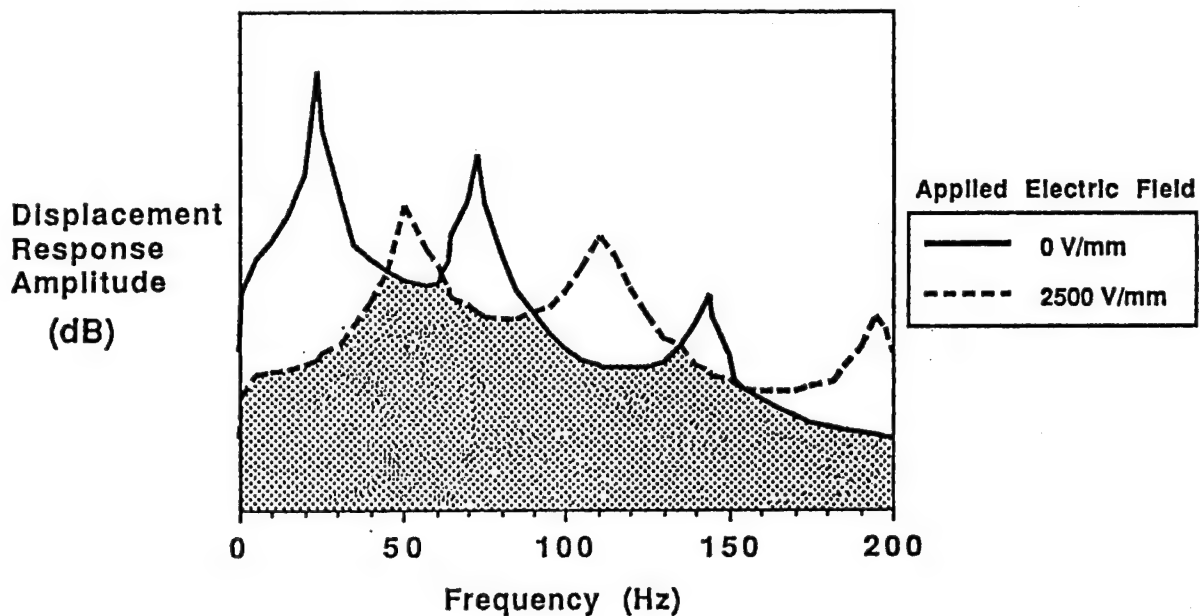
Figure 10: Structural response amplitude as a function of frequency for two states of an ER material filled composite beam.

CONCLUSIONS

The present study was among the first in which the controllable pre-yield properties of electrorheological materials were investigated as to their utility in distributed structural control applications. Although the pre-yield shear storage modulus values of present day ER materials were found to be much lower than those of conventional viscoelastic shear damping materials, composite sandwich beams were constructed encasing ER materials and demonstrated to exhibit controllable response to flexural vibration excitation. Most notably, a linear relationship was found to exist between modal response frequency and applied electric field for the beams tested. An attempt was made to predict this behavior using a classical constrained layer damping analysis, and it was concluded that further work was needed to more closely correlate theory and experimentation. Nevertheless, it was suggested that composite structures containing ER materials would have the unique capability of tunable vibrational response. This tuned passive approach to structural behavior is likely to be very useful in the vibration control industry in the years to come.

ACKNOWLEDGEMENTS

REFERENCES

1. Lienard, P., "Etude d'une Methode de Mesure du Frottement Interieur de Revetements Plastiques Travaillant en Flexion," *La Recherche Aeronautique*, Vol. 20, 1951, pp. 11-22.

2. Oberst, H., "Ueber die Dampfung der Biegeschwingungen dünner Bleche durch fest haftende Belage," *Acustica*, Vol. 2, Akustische Beihefte No. 4, 1952, pp. 181-194. (Translation by H. L. Blackford, Inc., 24 Commerce St., Newark, N.J.)

3. Kerwin, E. M. Jr., "Damping of Flexural Waves by a Constrained Visco-Elastic Layer," *Jour. Acoust. Soc. Am.*, Vol 31, July 1959.

4. Ross, D., Ungar, E. E., and Kerwin, E. M. Jr., "Damping of Plate Flexural Vibrations by Means of Viscoelastic Laminae," in J. E. Ruzicka (ed.), *Structural Damping*, Sec. 3, The American Society of Mechanical Engineers, New York, 1959.

5. Beranek, L. L. (ed.), *Noise and Vibration Control*, McGraw Hill, New York, 1971.

6. Nashif, A. D., Jones, D. I. G., and Henderson, J. P., *Vibration Damping*, John Wiley and Sons, New York, 1985.

7. Bailey, T. and Hubbard, J. E. Jr., "Distributed Piezoelectric-Polymer Active Vibration Control of a Cantilever Beam," *Journal of Guidance, Control, and Dynamics*, Vol. 8, No. 5, 1985, pp. 605-611.

8. Plump, J. M., Hubbard, J. E. Jr., and Bailey, T., "Nonlinear Control of a Distributed System: Simulation and Experimental Results," *Journal of Dynamic Systems, Measurement, and Control*, Vol. 109, 1987, pp. 133-139.

9. Hanagud, S., Obal, M. W., and Calise, A. G., "Piezoceramic Devices and PVDF Films as Sensors and Actuators for Intelligent Structures," in C. A. Rogers (ed.), *Smart Materials, Structures and Mathematical Issues*, Technomic Publishing Co., Lancaster, Pennsylvania, 1989.

10. Winslow, "Induced Fibration of Suspensions," *Journal of Applied Physics*, Vol. 20, 1949, pp. 1137-1140.

11. Duclos, T. G., "Design of Devices Using Electrorheological Fluids," *Society for Automotive Engineers Technical Paper 881134*, Warrendale, Pennsylvania, 1988.

12. Adriani, P. M. and Gast, A. P., "A microscopic model of electrorheology," *Physics of Fluids*, Vol. 31, No. 10, 1988, pp. 2757-2768.

13. Ferry, J. D., *Viscoelastic Properties of Polymers*, John Wiley and Sons, Inc., New York, 1961.

14. *Standard Method for Measuring Vibration-Damping Properties of Materials*, ASTM Standard E 756-83, The American Society for Testing Materials, Philadelphia, Pennsylvania, 1983.

ANALYSIS OF A MODIFIED PASSIVE HYDRAULIC DAMPER WITH VARIABLE DAMPING CHARACTERISTICS

Hong Su,   S. Rakheja and   T. S. Sankar

Department of Mechanical Engineering
Concordia University
1455 de Maisonneuve Blvd.   West
Monteal, Canada
H3G 1M8

ABSTRACT

Conventional hydraulic dampers, which are widely employed in mechanical vibration and shock isolation systems, exhibit inherent performance limitations due to the fixed orifice damping characteristics.   In this paper, a conventional hydraulic damper is modified to achieve variable damping via simple passive means.   The variable damping mechanism is realized passively by limiting the pressure differential across the hydraulic damper piston, using pressure relief valves.   The hydraulic damper is modelled as a nonlinear dynamical system incorporating the nonlinearities such as orifice damping, gas-spring and pressure relief mechanism.   The damping characteristics of both conventional and the modified dampers are discussed in view of vibration isolation performance.   The dynamic response of a vehicle suspension model employing the modified hydraulic damper is investigated via computer simulation.   The transmissibility characteristics of the vehicle suspension system are obtained to evaluate the vibration isolation performance of the proposed damper.   The shock isolation performance is evaluated in terms of its transient response to a road bump input.   The simulation results of the modified vehicle suspension are compared with that of the conventional hydraulic shock absorber system.   It is concluded that the vehicle ride performance can be improved considerably using the modified hydraulic damper.

INTRODUCTION

The selection of appropriate spring and damping mechnisms is one of the most important tasks in the design of vibration and shock isolation systems. Conventional passive hydraulic dampers are widely employed in mechanical vibration and shock isolation systems and offer a simple, inexpensive and reliable mean to protect the mechanical systems and human body from vibration and shock disturbances. However, it is well known that the passive vibration isolation systems exhibit inherent performance limitations due to the fixed orifice damping characteristics [1, 2]. A heavily damped passive vibration isolation system tends to reduce the amplitude of vibration response only when the frequency of the base disturbances is around the natural frequency of the system. While the vibration isolation performance of the passive system is deteriorated considerably at higher frequency range. On the other hand, a lightly damped vibration isolation system is desirable when the disturbance frequencies are beyond the natural frequency; however it yields a poor response at the resonance of the system. In order to overcome these inherent limitations of the passive vibration isolation systems, various vibration isolation systems with variable parameters have been proposed, such as active and semi-active vibration isolation systems.

In active vibration isolation systems, the controlled damping and stiffness parameters change with variations in excitation and response characteristics and thus provide superior isolation performance. However, active controlled damping mechanisms, proposed in the literature, require an external energy source, complex feedback control devices and sensors. Thus the general use of active shock and vibration isolation systems has been severely limited due to the associated high costs, complexities and poor reliability [3, 4].

Semi-active vibration isolation systems generate damping forces passively while the damping parameters are modulated using an active control system. Semi-active damping is often realized by modulating the orifice area of hydraulic dampers using various control schemes, such as skyhook [5, 6] and sequential or 'on-off' schemes [2]. Semi-active vibration isolation systems require only low level electrical power for necessary signal processing and can provide improved vibration and shock isolation performance compared with that of the passive vibration isolation systems. However, the semi-active vibration isolation systems still require a comprehensive instrumentation and control devices.

In this paper, a conventional hydraulic damper is modified to achieve a variable damping in vibration and shock isolation systems via simple passive means. The variable damping mechanism is realized passively by limiting the pressure differential across the hydraulic damper piston, using pressure relief valves. The hydraulic damper is modelled as a nonlinear dynamical system incorporating the nonlinearities, such as orifice damping, gas-spring and pressure limiting mechanism. The damping characteristics of both conventional and the

proposed dampers are discussed in view of their vibration isolation performance. The concept of the proposed modified hydraulic damper employing pressure limiting valves is discussed through the flow and force balance equations. The dynamic response of a vehicle suspension employing the modified hydraulic damper is investigated via computer simulation. The vibration isolation performance of the proposed damper is discussed in terms of the vibration transmissibility characteristics of the vehicle model. The shock isolation performance is established in terms of its transient response to a road bump input. The simulation results of the modified suspension system are compared with that of the conventioal hydraulic shock absorber system to demonstrate the improved vehicle ride performance of the proposed damper.

DEVELOPMENT OF ANALYTICAL MODEL

Fig. 1 presents the schematic of a conventional passive hydraulic damper. Neglecting leakage flows and seal friction, the total dynamic force f_D generated by the hydraulic damper due to pressure differential across the piston is expressed as:

$$f_D = (p_1 - p_0)A_P - (p_2 - p_0)(A_P + A_R) \tag{1}$$

where p_0 is the hydraulic pressure corresponding to the static equilibrium position, p_1 and p_2 are the instantaneous pressures in chambers I and II, respectively, A_P is the piston area, and A_R is the cross section area of the rod. By letting $p_{ij} = p_i - p_j$, equation (1) can be expressed as:

$$f_D = p_{12}A_P + p_{32}A_R - p_{30}A_R \tag{2}$$

where p_3 is the instantaneous pressure in chamber III. Assuming turbulent flow condition the pressure differentials p_{12} and p_{32} across the piston and cylinder orifices are expressed as [7]:

$$P_{12} = \frac{\rho}{2n^2 C_{d1}^2} \left(\frac{A_P}{a_1}\right)^2 |\dot{z}|\dot{z} \tag{3}$$

and

$$P_{32} = \frac{\rho}{2C_{d1}^2} \left(\frac{A_R}{a_2}\right)^2 |\dot{z}|\dot{z} \tag{4}$$

where z is the relative velocity across the damper, given by

$$\dot{z} = \dot{x} - \dot{x}_i$$

and n is the number of orifices on the piston, a_1 and a_2 are areas of orifices on the piston and cylinder, respectively, C_{d1} and C_{d2} are discharge coefficients, and ρ is the density of hydraulic fluid. The pressure differential in chamber III can be related to the relative compression/extension of gas column. Assuming polytropic process, the differential pressure P_{30} is be expressed as:

$$P_{30} = - \frac{[(V_0 + A_R z)^\gamma - V_0^\gamma]}{(V_0 + A_R z)^\gamma} P_0 \tag{5}$$

where V_0 is the initial gas volume corresponding to the static equilibrium position and γ is the polytropic constant. It is evident from equations (2) to (5) that the total dynamic force generated by the damper comprises of a damping force f_d due to the orifice flow and a restoring force f_a due to the pressurized gas column. The total dynamic force generated by the hydraulic damper can be expressed as:

$$f_D(t) = f_d(t) + f_a(t) \tag{6}$$

where

$$f_a(t) = - P_{30} A_R \tag{7}$$

$$f_d(t) = \alpha p_{12} \tag{8}$$

and

$$\alpha = A_P + \frac{P_{32}}{P_{12}} A_R \tag{9}$$

From equations (3) and (4), it is evident that the ratio of pressure differentials (p_{32}/p_{12}) can be expressed as a constant:

$$\frac{P_{32}}{P_{12}} = \left(\frac{C_{d1}}{C_{d2}}\right)^2 \left(\frac{na_1}{a_2}\right)^2 \left(\frac{A_R}{A_P}\right)^2 = \lambda \qquad (10)$$

From equations (3) and (8) it is clear that the pressure differential p_{12} and thus the damping force are dependent upon the square of relative velocity across the damper. The magnitude of the damping force becomes predominant at high excitation frequencies and thus yields poor vibration isolation performance. The magnitude of damping force at high excitation frequencies can be lowered in a manner similar to the sequential semi-active dampers by limiting the pressure differential across the piston. However, the pressure limiting and thus variable damping force can be realized via passive means using pressure relief valves. The pressure relief valves are selected to limit the magnitude of pressure differential across the piston to a preset value $(p_{12})_o$ by modulating the flow through compression and rebound relief valves across chambers I and II, as shown in Fig. 2. When the magnitude of the pressure differential p_{12} is less than a preset limiting value $(p_{12})_o$ of the relief valves, the relief valves remain closed and thus the damper acts as a conventional passive hydraulic damper. However, when the magnitude of the pressure p_{12} exceeds the preset value $(p_{12})_o$, the relief valve opens. The damping force is then reduced considerably by permitting the fluid flow pass through the opened relief valve. Neglecting dynamics of the relief valves, the sequential damping force due to the modified passive damper can be expressed as:

$$f_d = \begin{cases} \alpha p_{12}, & |p_{12}| < (p_{12})_o \\ \\ \alpha(p_{12})_o \mathrm{sgn}(p_{12}), & \text{otherwise} \end{cases} \qquad (11)$$

where

$$\mathrm{sgn}(*) = \begin{cases} +1, & (*) > 0 \\ -1, & (*) < 0 \end{cases}$$

The sequential damping via pressure limiting can be realized completely passively, and it does not require the instrumentation and control package and external power required by the active and semi-active systems.

DAMPING CHARACTERISTICS OF THE MODIFIED DAMPER

A damping parameter β is defined as the ratio of the damping force to the critical damping force of a viscously damped vibration isolation system:

$$\beta = f_d/(2\sqrt{mk}\ \dot{z}) \tag{12}$$

From equations (3), (8) and (12), the damping parameter of the conventional passive hydraulic damper is obtained as:

$$\beta = \frac{\alpha}{2\sqrt{mk}} \left(\frac{\rho}{2n^2 C_{d1}^2}\right) \left(\frac{A_P}{a_1}\right)^2 |\dot{z}| \tag{13}$$

It is obvious that the damping parameter of the conventional hydraulic damper is proportional to the magnitude of relative velocity across the damper. The damping parameter of the modified hydraulic damper can be obtained from equations (11) and (12):

$$\beta = \begin{cases} \dfrac{\alpha}{2\sqrt{mk}} \left(\dfrac{\rho}{2n^2 C_{d1}^2}\right) \left(\dfrac{A_P}{a_1}\right)^2 |\dot{z}|, & |p_{12}| < (p_{12})_o \\[4mm] \dfrac{\alpha(p_{12})_o}{2\sqrt{mk}|\dot{z}|}, & \text{otherwise} \end{cases} \tag{14}$$

Equation (14) reveals that for $|p_{12}| < (p_{12})_o$ the damping parameter of the modified damper is proportional to the magnitude of the relative velocity response as in the same case of the passive damper. However, the damping parameter is inversely proportional to the magnitude of the relative velocity response, when the pressure differential p_{12} exceeds the limiting value of $(p_{12})_o$.

In view of vibration isolation performance, it is desirable to achieve a high value of damping parameter around the resonant frequency so that the resonant peak can be appropriately controlled. On the other hand, a low value of damping parameter is desirable at high frequencies to achieve the improved vibration isolation performance. The modified hydraulic damper can provide the desirable damping characteristics expressed in equation (12) when $(p_{12})_o$ is appropriately selected. In order to control the resonant peak response, the minimum value of the limiting pressure is estimated by using the relationship of damping parameter and resonant amplitude of a linear vibration system [8]. A suitable value of the preset limiting pressure $(p_{12})_o$ is then expressed as:

$$(p_{12})_o = \nu(kX_i/\alpha) \tag{15}$$

where X_i is the amplitude of excitation, and ν is the pressure limiting factor of the modified hydraulic damper. The pressure differential characteristics of a base excited single degree-of-freedom mechanical system employing the modified damper is compared with that of the conventional damper as shown in Fig. 3. The pressure differential p_{12} across the conventional damper piston increases rapidly with the increase of the excitation frequency. However, the pressure differential p_{12} of the modified damper increases with the excitation frequency and then settles down to the preset value $(p_{12})_o$. The value of pressure differential p_{12} and thus the damping force at high excitation frequencies are dependent upon the limiting factor ν as shown in Fig. 3. The damping characteristics of the modified damper as well as the conventional hydraulic damper are presented in Fig. 4. It is observed that at low excitation frequencyies the damping parameter of the modified damper is identical to that of the conventional hydraulic damper. However, the damping parameter of the modified damper decreases at higher frequencies when p_{12} exceeds $(p_{12})_o$.

MODELLING OF A VEHICLE SUSPENSION WITH MODIFIED DAMPER

A vehicle suspension equipped with the modified hydraulic damper, as shown in Fig. 5, is modelled and analysed, in order to evaluate the vibration and shock isolation performance of the modified damper. The vehicle is modelled as a two-degree-of-freedom dynamic system, often refered to as 'quarter vehicle model' [9]. The vehicle mass is represented by a sprung mass m_s, and the wheel and axle assembly is modelled as an unsprung mass m_u. The primary vehicle suspension model comprises of a linear spring of stiffness k_s and a modified nonlinear hydraulic damper D. The total force generated by the modified damper includes a restoring force due to the gas-spring and a dissipative force due to the orifice flow. The tire is modelled as a linear spring of stiffness k_t, assuming point contact with the terrain. The hysteretic properties of the tire is assumed to be small. The equations of motion of the two-degree-of freedom vehicle model are expressed as:

$$m_s\ddot{x} + k_s z + f_a(t) + f_d(t) = 0 \tag{16}$$

$$m_u\ddot{x}_1 - k_s z - f_a(t) - f_d(t) + k_t x_1 = k_t x_i \tag{17}$$

where $z=x-x_1$, $f_a(t)$ is the gas-spring force derived in equations (5) and (7), and $f_d(t)$ is the modified damping force expressed in equations (3) and (11).

The simulation parameters of the vehicle model and the modified hydraulic damper are selected as follows:

$m_s=240$ kg, $m_u=36$ kg, $k_s=16000$ N/m, $k_t=160000$ N/m, $\rho=797.18$ kg/m^3, $C_{d1}=0.7$, $C_{d2}=0.7$, $A_P=2.513\times10^{-3}$ m^2, $A_R=3.1416\times10^{-4}$ m^2, $\gamma=1.4$, $V_0=1.9\times10^{-4}$ m^3, $p_0=13.7\times10^5$ Pa, and $a_1=3.1416\times10^{-6}$ m^2, $a_2=3.1416\times10^{-6}$ m^2, and $X_i = 1.86\times10^{-3}$ m.

RESULTS AND DISCUSSION

The vehicle model incorporating nonlinearities due to gas-spring, orifice damping and pressure relief valve mechanism is simulated using the numerical integration technique. The dynamic ride performance of the vehicle suspension employing the modified damper is evaluated through the vibration and shock isolation characteristics. The vibration isolation characteristics of the modified hydraulic suspension are expressed in terms of vibration transmissibility of the suspension system. The shock isolation performance of the modified damper is evaluated in terms of its transient response to a road bump input.

Vibration Isolation Performance

The vibration isolation performance of the conventional and modified suspensions is evaluated for harmonic displacement excitations at the tire-road interface. The vibration transmissibility is obtained by computing the ratio of the steady state response amplitude to the excitation amplitude for each excitation frequency.

The velocity transmissibility response of the sprung mass of the vehicle employing modified and conventional passive dampers is shown in Fig. 6. The damper piston with two orifices is considered for the conventional as well as modified damper (n=2). A unit pressure limiting factor $\nu=1$ is selected for the modified hydraulic damper. It is observed that the transmissibility of the conventional hydraulic damper system yields two peaks corresponding to the resonant frequencies of the sprung and unsprung masses of the vehicle, respectively. The second peak corresponding to the resonance of the unsprung mass m_u, is mainly due to the high value of orifice damping produced by the conventional passive damper. The transmissibility characteristics of the vehicle model employing the modified hydraulic damper, is identical to that of the

conventional suspension system at low exciting frequency. The modified hydraulic damper continues to dissipate energy identical to that of the conventional damper around the first resonant frequency. However, as the excitation frequency and thus the relative velocity response increase, the pressure differential p_{12} is held around $(p_{12})_o$ by the pressure relief mechanism to reduce the damping force generated by the modified hydraulic damper. Thus the velocity transmissibility peak corresponding to the unsprung mass resonance is reduced significantly as shown in Fig. 6. A comparison of the transmissibility characteristics of the modified and conventional dampers reveals that the vibration isolation performance of the modified hydraulic damper system is considerably superior to that of the conventional damper at higher excitation frequencies.

The vibration transmissibility of the conventional passive damper, corresponding to the unsprung mass resonance, can be reduced considerably via increasing the number of orifices, as shown in Fig. 7. However, the peak transmissibility response, corresponding to the the sprung mass resonant frequency, increases considerably with light damping. A comparrison of the displacement transmissibility characteristics of the conventional dampers (n=2 and n=4) with the modified damper (n=2 and ν=1) reveals that the modified damper can provide an appropriate control of the peak response corresponding to the low as well as high frequencies. A comparison of velocity and displacement transmissibilities in figures 6 and 7 also confirms that for nonlinear dynamical systems the transmissibiities of velocity and displacment are no longer identical as in the case of linear systems.

The velocity transmissibility characteristics of the modified hydraulic dampers with different preset pressure limiting factors, ν= 0.7, 1.0 and 1.5, are shown in Fig. 8. The influence of limiting factor ν and thus the pressure limiting value $(p_{12})_o$ on the vibration transmissibility is observed by comparing the response due to the different ν values. A low value of pressure limiting factor ν yields a further improved vibration transmissibility at the higher excitation frequencies as compared with that of a higher value of ν factor. However, a lower value of ν factor with a lower preset pressure limiting value $(p_{12})_o$ results in a early opening of relief valves, that may produce a very large resonant peak due to the insufficient damping at the resonance. A higher value of ν factor results in a late opening of the relief valves and yields a higher transmissibility value at higher excitation frequency. It is obvious that the suspension system equipped with the modified hydraulic damper with the pressure limiting factor, $0.7 < \nu < 1.5$, exhibits superior vibration isolation performance.

Shock Isolation Performance

The shock isolation performance of the conventional as well as modified dampers is investigated for bump excitation, as shown in Fig. 9. The bump represent a half round obstacle of radius h. The vehicle is assumed to travel at a constant speed v. The instantaneous coordinate of the vehicle u(t) is expressed as:

$$u(t) = u_0 + vt \tag{18}$$

where t is the time, u_0 is the initial possition of the vehicle away from the centre point of the bump. The instantaneous excitation due to the road bump can be expressed as:

$$x_i = \begin{cases} \sqrt{h^2 - u^2}, & -h < u < h \\ 0, & \text{otherwise} \end{cases} \tag{19}$$

The shock isolation characteristics of the suspension system equipped with the modified hydraulic damper are established through computer simulation, with the following parameters: h=0.1524 m, u_0=−0.2524 m, and the vehicle speed is selected as v= 5 m/s.

The transient displacement response of the sprung mass m_s of the vehicle suspension system with a conventional passive damper and a modified hydraulic damper, together with the history of the input displacement x_i, is shown in Fig. 10. Where the total orifice areas of both conventional and modified hydraulic dampers are identical (n=2), and the pressure limiting factor for the modified damper is selected as ν= 1. Fig. 11 shows the transient velocity response of the sprung mass with the conventional and modified hydraulic damper systems. Figs. 10 and 11 reveal that the peak displacement and velocity response of the modified hydraulic damper are considerably smaller tant that of the conventional damper. Moreover, the transient response of the modified damper is less oscillatory than that of the conventional damper. The transient displacement response of the unsprung mass m_u, $x_1(t)$, for the same systems is shown in Fig. 12. The maximum transient response of the modified hydraulic damper is slightly larger than that of the conventional damper system, however it yields less oscilations than that of the conventional system. Since the main purpose of the suspension design is to reduce the oscilation of the sprung mass, the modified hydraulic damper can, therefore, be used to improve the ride performance.

The transient displacement response of the sprung mass m_s with a lightly damped suspension system ($n=6$) both the conventional and modified hydraulic dampers, together with the bump input history, is shown in Fig. 13. The conventional passive damper system with much small damping yields an improved transient response as compared with that of the conventional system with a higher damping in Fig. 10. The maximum amplitude of the response is slightly lower and the oscilations are much less than those of the highly damped system. However, the modified hydraulic damper yields a further improved transient response, in terms of both the maximum amplitude and the munber of oscillations, as compared with that of the lightly damped conventional system. Moreover, it should be pointed out that a lightly damped conventional system yields a high peak value of vibration transmissibility of the sprung mass at the resonance as shown in Fig. 7.

CONCLUSIONS

A conventional hydraulic damper is modified to achieve a variable damping in vibration and shock isolation systems. The damping characteristics of the modified hydraulic damper are discussed in view of the vibration isolation performance. A vehicle suspension model employing the modified hydraulic damper is analysed via computer simulation. The shock and vibration isolation performance of the suspension due to the modified passive hydraulic damper with the variable damping is evaluated and compared with that of the conventional hydraulic damper system. The vibration isolation performance of the modified damper is presented in terms of its transmissibility caharacteristics. The shock isolation performance is evaluated in terms of its transient response to a road bump input. From the results of both the vibration transmissibility and the transient respons, it is concluded that the vehicle ride performance can be improved considerably by using the modified hydraulic damper.

REFERENCES

1. Snowdon, J. C., "Vibration and Shock in Damped Mechanical Systems," New York, John Wiley and Sons, 1968.

2. Rakheja, S. and Sankar, S., "Vibration and Shock Isolation Performance of a Semi-active 'On-off' Damper," ASME, Journal of Vibration, Acoustics, Stress and Reliability in Design, Vol.107, 1985, pp.398-403.

3. Hall, B. B. and Gill, K. F., "Performance Evaluation of Motor Vehicle Active Suspension Systems," Proc. Instn. Mech. Engrs., Vol.201, No.D2, 1987, pp.135-148.

4. Crolla, D. A., Pitcher, R. H. and Lines, J. A., "Active Suspension Control for an Off-road Vehicle," Proc. Instn. Mech. Engrs., Vol.201, No.D1, 1987, pp.1-10.

5. Margolis, D. L., Tylee, J. L. and Hrovat, D., "Heave Mode Dynamics of Tracked ACV with Semi-active Airbag Secondary Suspension," ASME, Journal of Dynamic Systems, Measurement and Control, Vol.97, No.4, Dec., 1975, pp.399-407.

6. Karnopp. D., "Force Generation in Semi-active Suspensions using Modulated Dissipative Elements," Vehicle System Dynamics, Vol.16, 1987, pp.333-343.

7. Su, H., "Performance of a Pressure Limited Hydraulic Damper for Vehicle Suspensions," Technical Report, Dept. of Mechanical Engineering, Concordia University, 1987.

8. Thompson, W. T., Theory of Vibration with Applications, 2nd Ed., Prentice-Hall, Englewood Cliffs, N.J., 1981.

9. Chalasani, R. M., "Ride Performance Potential of Active Suspension Systems -- Part I: Simplified Analysis Based on a Quarter-car Model," Symposium on Simulation and Control of Ground Vehicles and Transportation Systems, Anaheim, Cal., Dec. 7-12, 1986, pp.187-204.
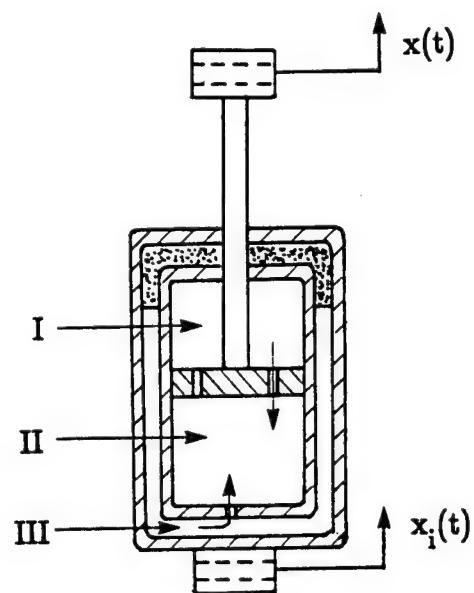
Fig.1 Schematic of a conventional hydraulic damper
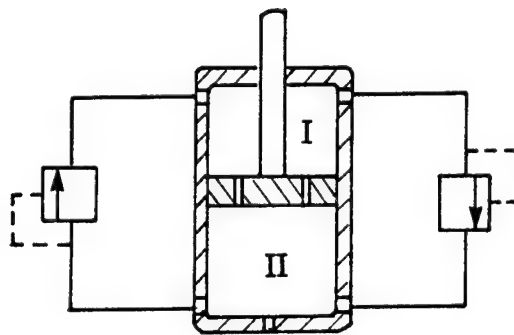
Fig.2 Schematic of a modified hydraulic damper with two relief valves
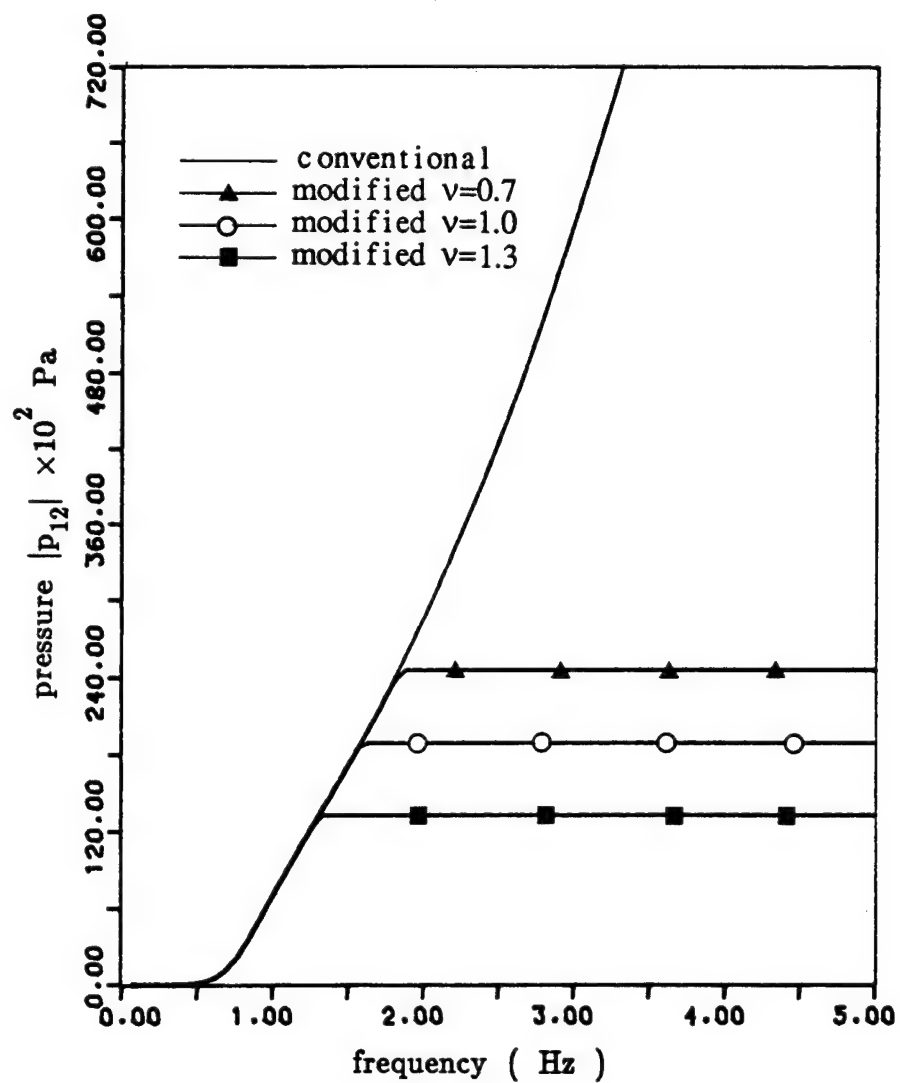
Fig.3 Pressure differential characteristics of the conventional and modified shock absorbers (ν = 0.7, 1.0 and 1.3)
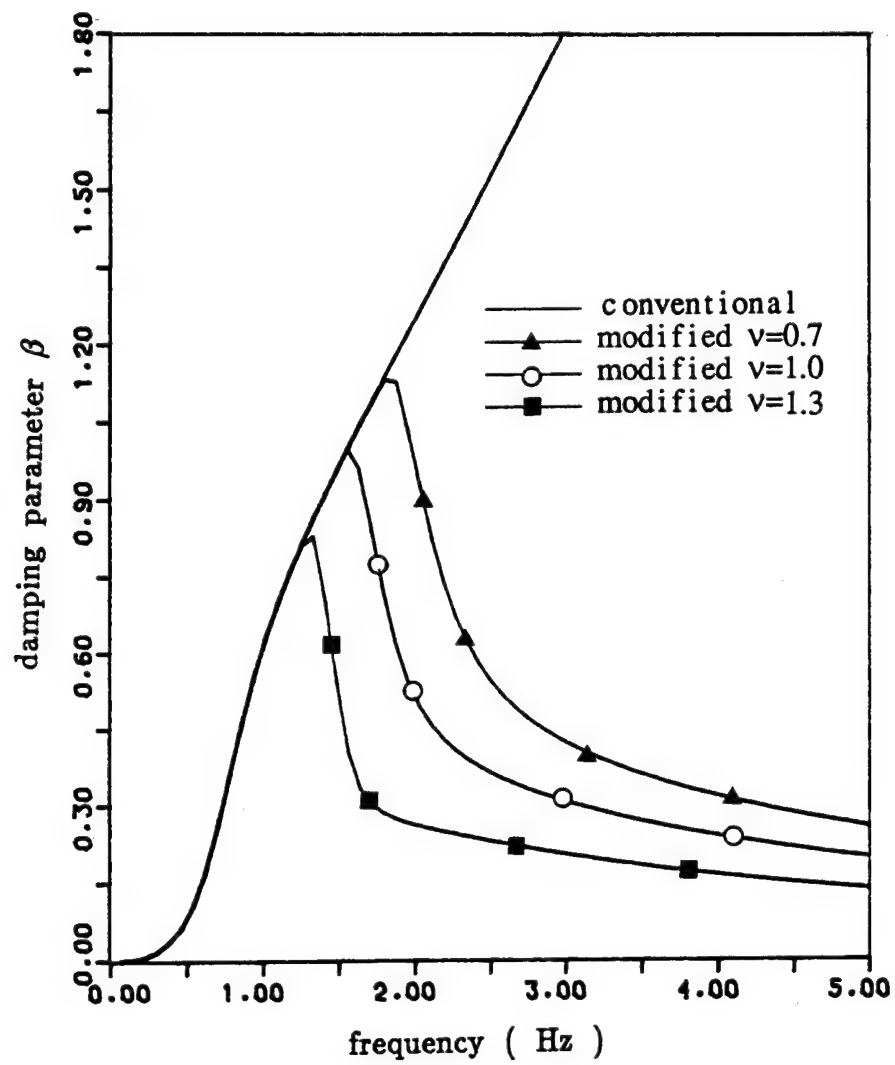
Fig.4 Damping characteristics of the conventional and modified shock absorbers (ν = 0.7, 1.0 and 1.3)
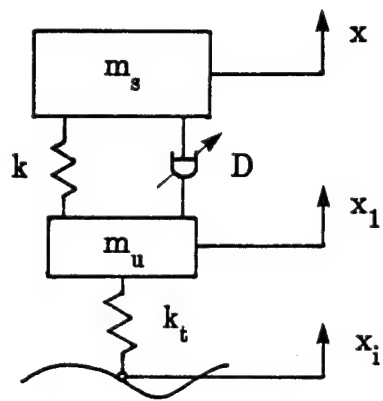
Fig.5   A quarter vehicle model
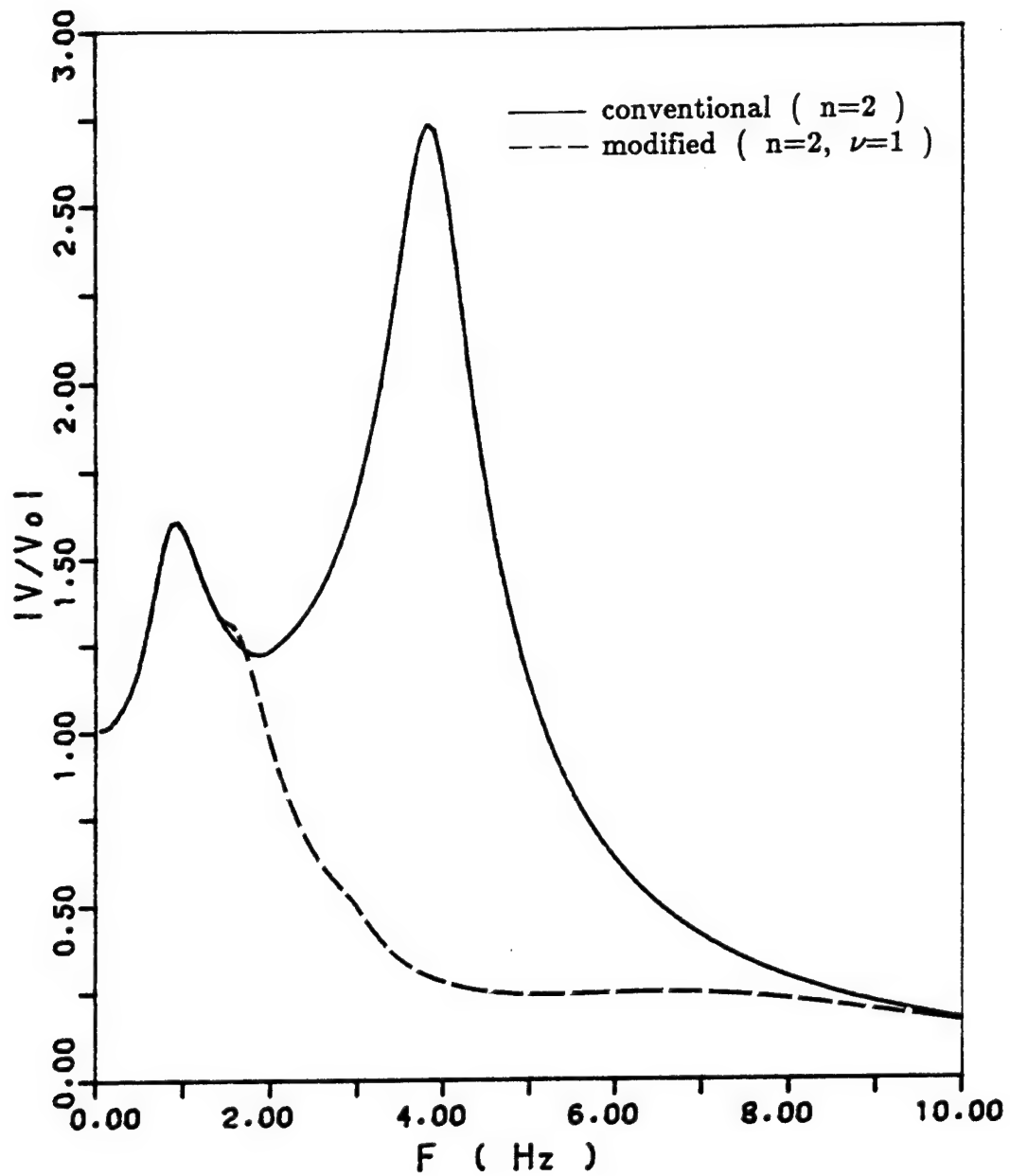
Fig.6 Velocity transmissibility characteristics of the vehicle
suspension with conventional and modified dampers
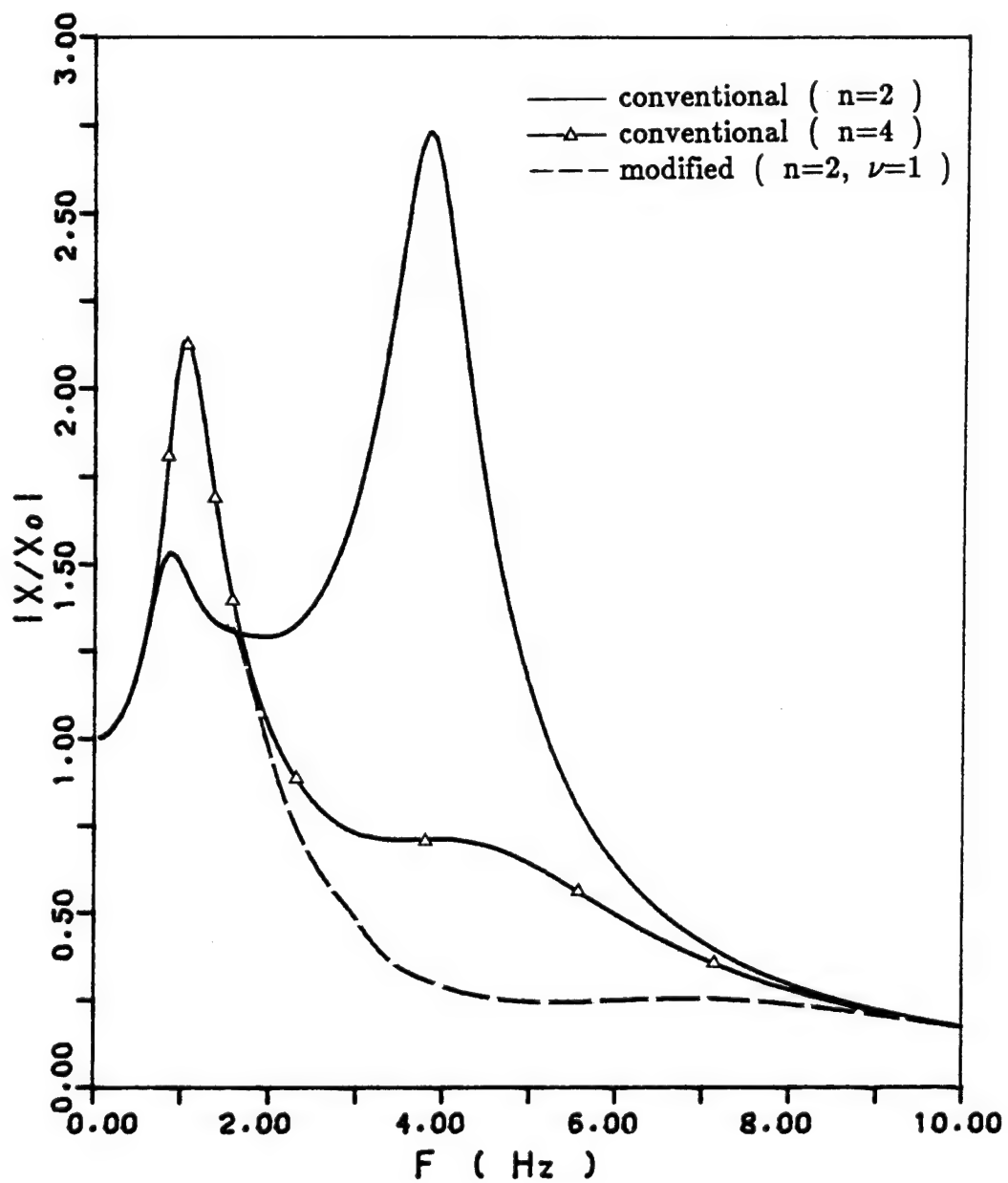
Fig.7 Displacement transmissibility characteristics of the vehicle suspension with two conventional dampers (n=2 and n=4) and a modified damper (n=2, ν=1)
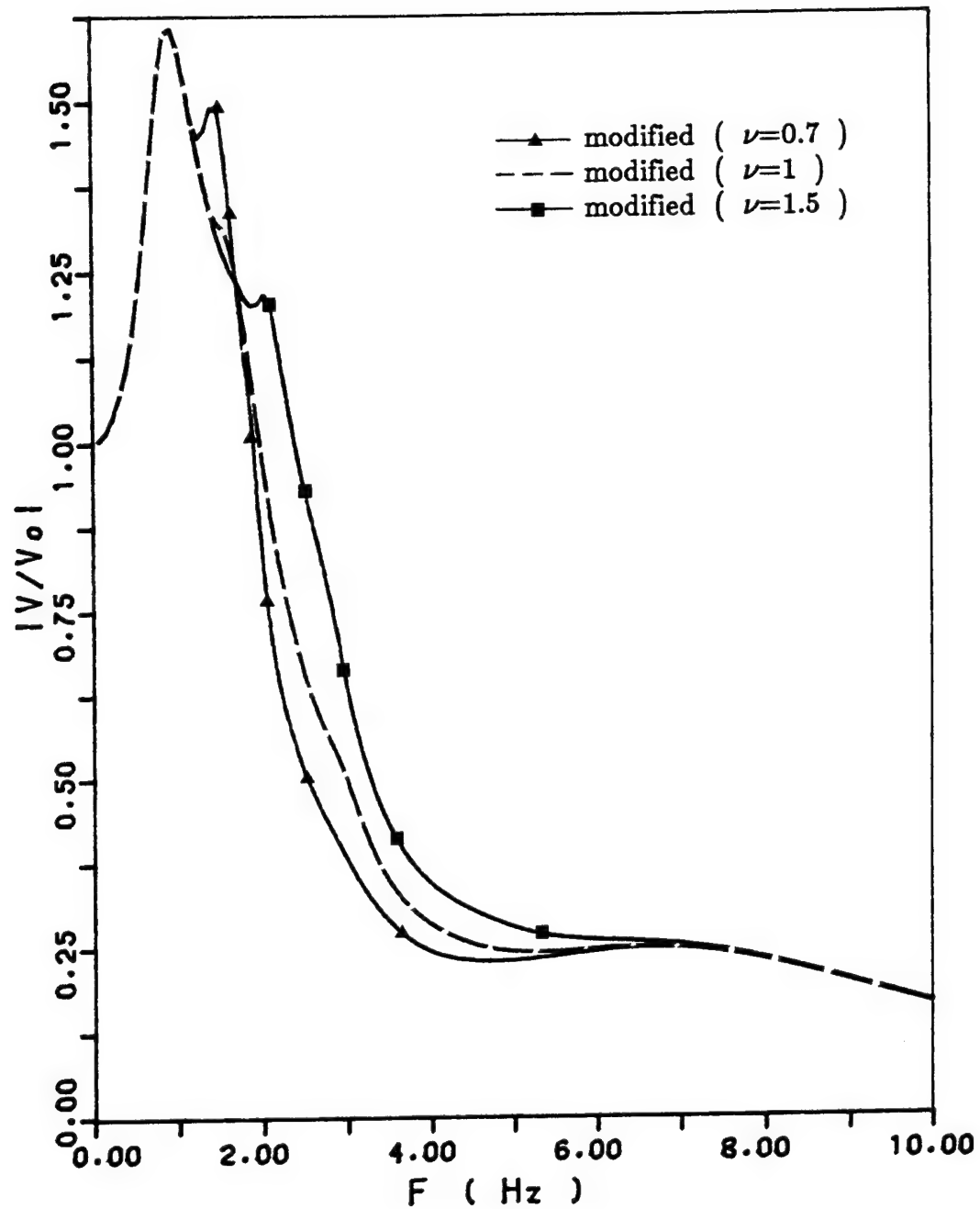
Fig.8   Velocity transmissibility characteristics of the vehicle
suspension with modified damper (n=2; v=0.7, 1.0 and 1.5)
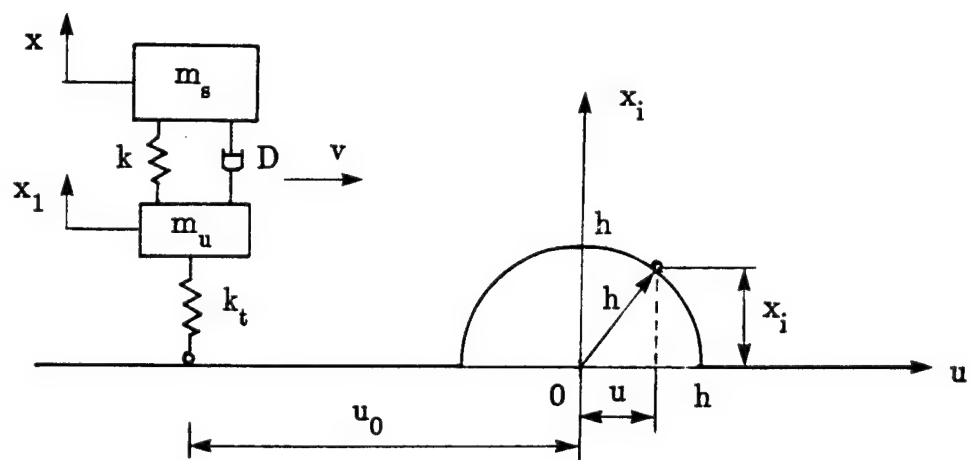
Fig.9 Representation of a bump input
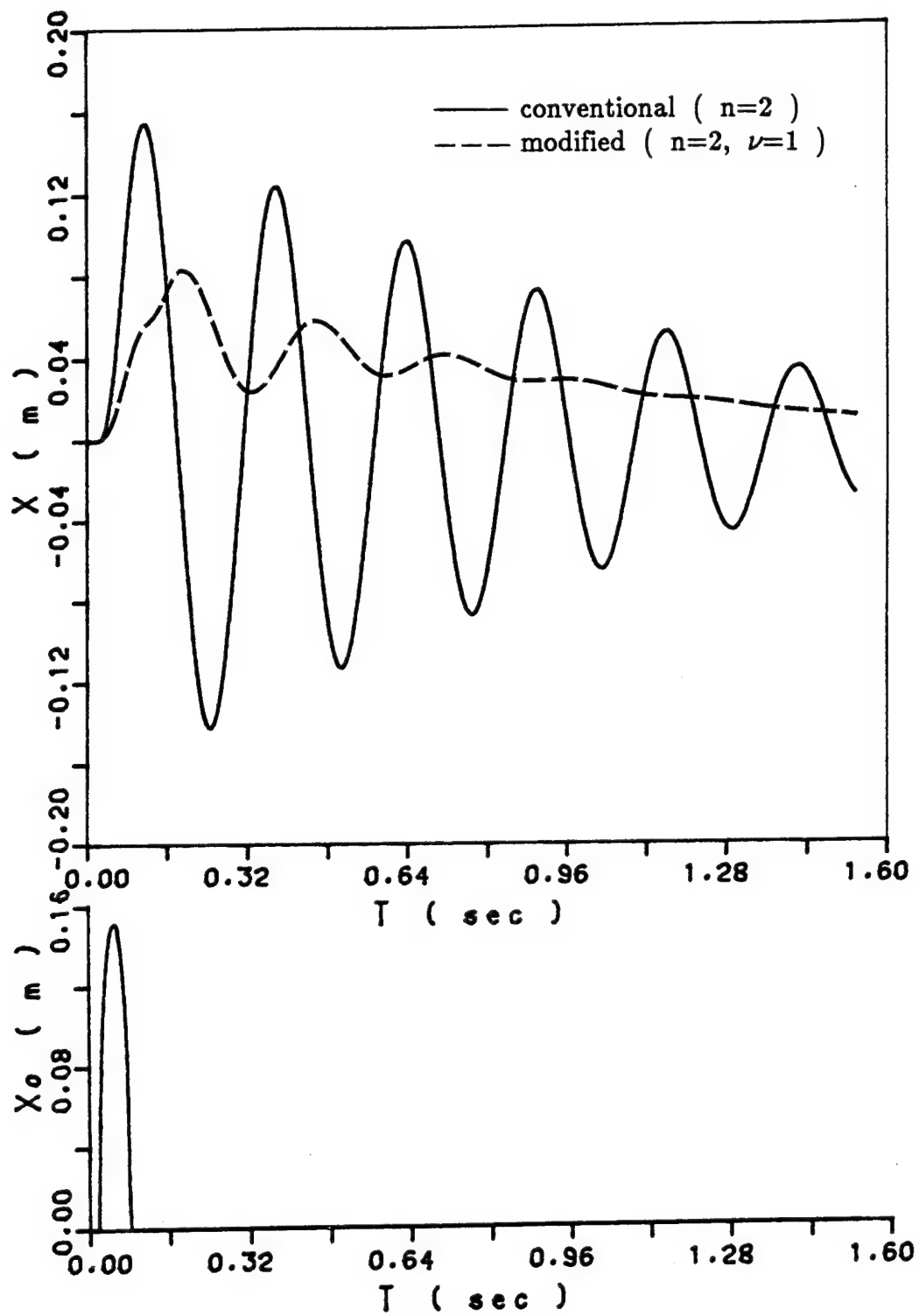
Fig.10 Transient displacement response of the sprung mass
with conventional and modified dampers
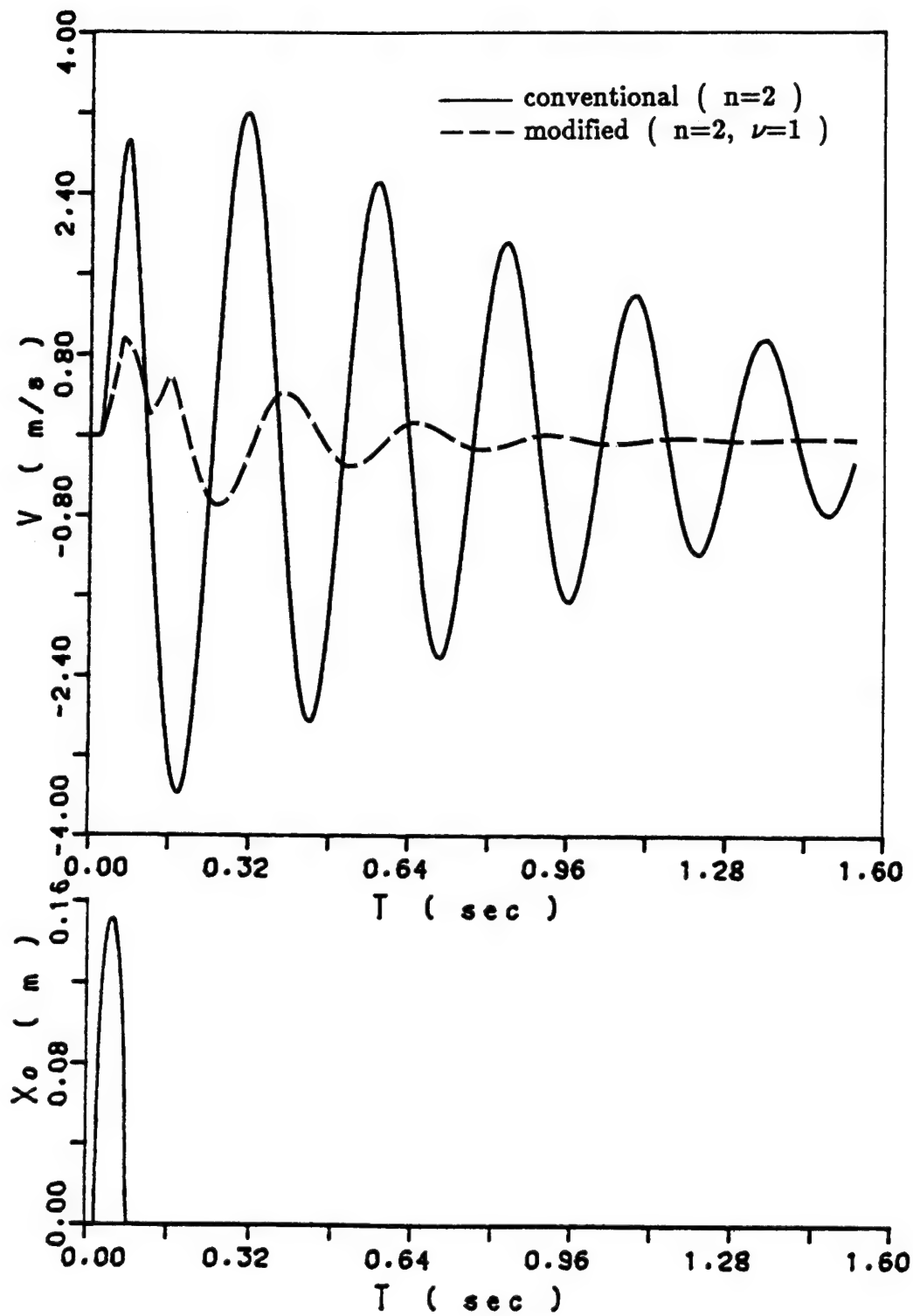
Fig.11 Transient velocity response of the sprung mass
with conventional and modified dampers
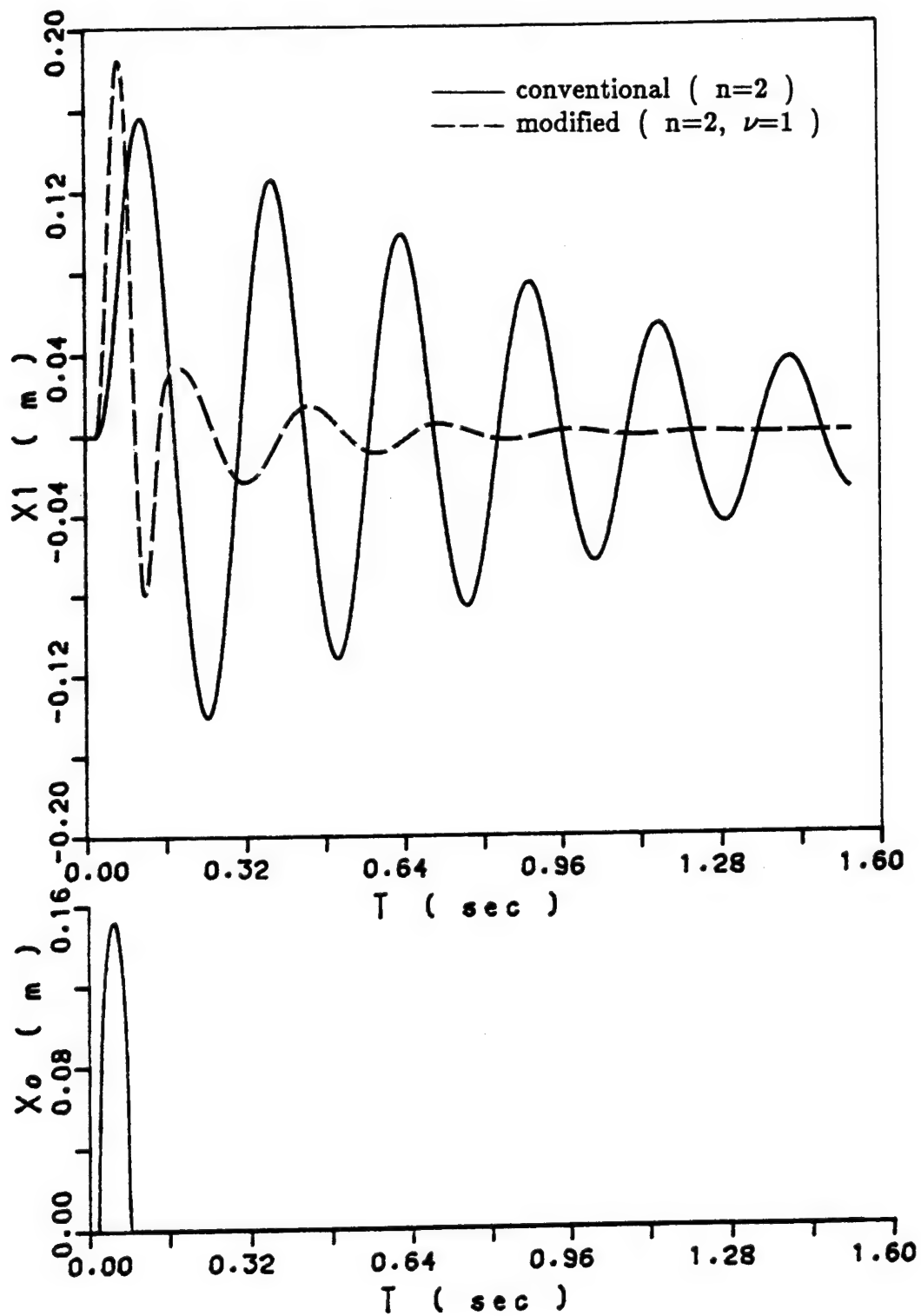
Fig.12 Transient displacement response of the unsprung mass
with conventional and modified dampers

CAB-24
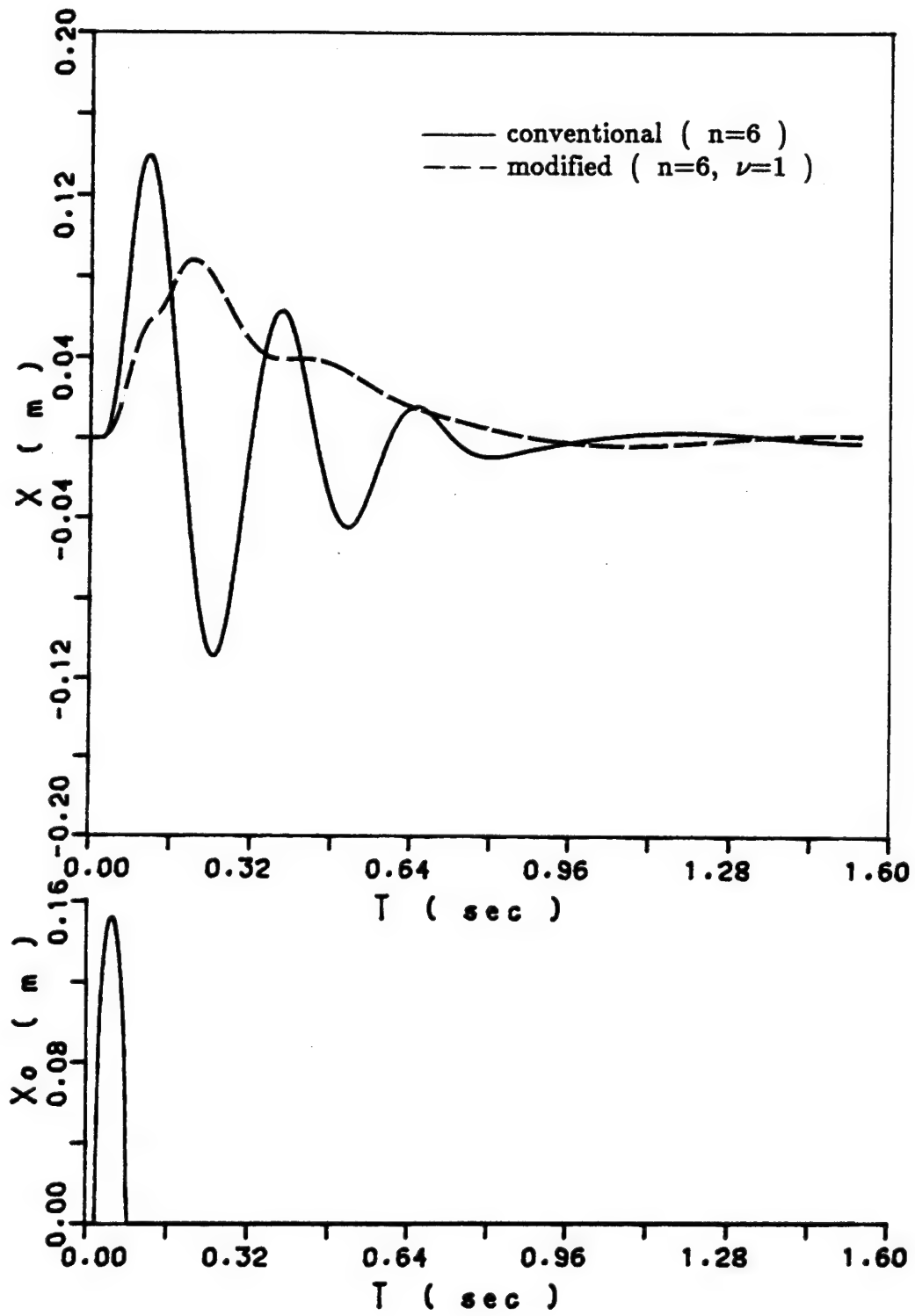
Fig.13 Transient displacement response of the sprung mass
with conventional and modified dampers (n=6)

AN EXPERIMENTAL INVESTIGATION ON THE ACTIVE-DAMPING CHARACTERISTICS OF A CLASS OF ULTRA-ADVANCED INTELLIGENT COMPOSITE MATERIALS FEATURING ELECTRO-RHEOLOGICAL FLUIDS

by

S.B. Choi[*], B.S. Thompson[+], and M.V. Gandhi[†]

Intelligent Materials and Structures Laboratory
Composite Materials and Structures Center
Michigan State University
East Lansing, MI 48824

[*](517) 355-9886,   [+](517) 355-2179,   [†](517) 355-1744

ABSTRACT

A new generation of revolutionary multi-functional, dynamically-tunable, intelligent, ultra-advanced composite materials featuring electro-rheological fluids is proposed herein for the active continuum vibrational-control of structural systems. This paper reports on a pioneering proof-of-concept experimental investigation focused on evaluating the elastodynamic transient response characteristics of cantilevered beams fabricated in this new class of materials. The results of this investigation clearly demonstrate the ability to dramatically change the vibrational characteristics of beam-like specimens fabricated in ultra-advanced composite materials by changing the electrical field imposed on the fluid domains. The capability of these materials to interface with modern solid-state electronics can be exploited by extending the fundamental phenomenological work presented herein by the successful incorporation of intelligent sensor technologies and modern control strategies in order to significantly accelerate the evolution of these composite materials for military and aerospace applications.

PREFACE: BACKGROUND ON ELECTRO-RHEOLOGICAL FLUIDS

Electro-rheological (ER) fluids are typically suspensions of micron-sized hydrophilic particles suspended in suitable hydrophobic carrier liquids, which undergo significant instantaneous reversible changes in material characteristics when subjected to electrical potentials. References [1-12] provide a flavor of the research activities in ER fluids. The most significant change in the material characteristics of an ER fluid is associated with the energy dissipation characteristics of the suspension which varies dramatically upon applying an electrical field to the fluid. The tailoring of this rheological property by the imposition of a suitable electrical potential can be usefully exploited in vibration-suppression applications.
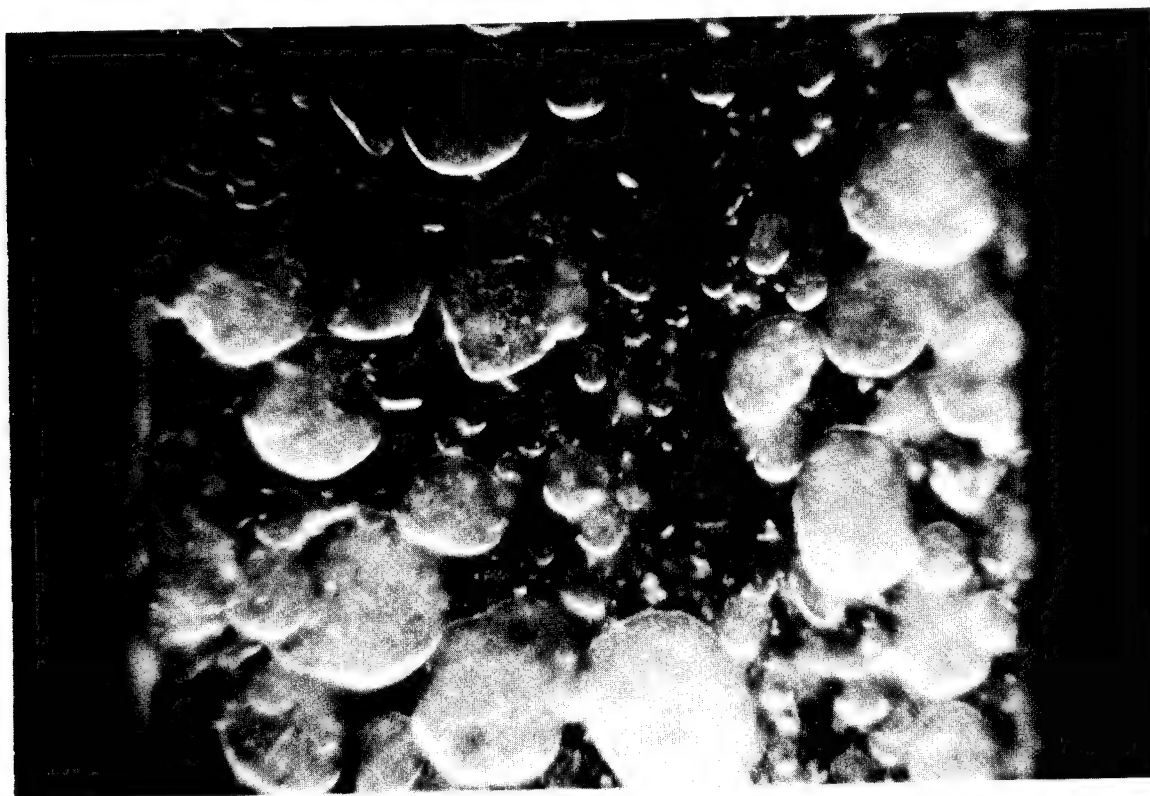
Figure 1.   Photomicrograph of an Electro-Rheological Fluid
with and Electric Field Strength of 0 kV/mm

Figures 1 and 2 present photomicrographs of an electro-rheological fluid subjected to electrical field intensities of 0 kV/mm and 2 kV/mm respectively.   The photomicrographs were taken in the Biothermal Sciences Laboratory at Michigan State University using a Zeiss universal phase-contrast microscope with a X40 magnification and a Chinon camera.   The black regions at the sides of the photographs are images of the electrodes employed to generate the electrical field in the ER fluid.   Figure 1 clearly shows the random structure of the suspension when a potential difference is

not generated between the electrodes. This structure imparts nominally isotropic global mechanical properties to the suspension. Figure 2 clearly shows the truly dramatic change in the structure of the suspension upon developing a potential difference between the electrodes of magnitude 2 kV/mm. Under these conditions, the particles in the suspension orientate themselves in relatively regular chain-like patterns to form a mixture with globally anisotropic mechanical properties. These columnar structures increase the energy-dissipation characteristics of the suspension, they increase the stiffness of the global suspension/electrode structure, and they are also responsible for re-orientation of the mass distribution of the suspension. Thus, by imposing an electric field upon an ER fluid, the mass, stiffness and energy-dissipation characteristics of the electro-viscous suspension are changed. When the field returns to a zero potential upon switching off the electrical energy supplied to the electrodes, the particles return to a state of random orientation in the carrier fluid as shown in Figure 1.
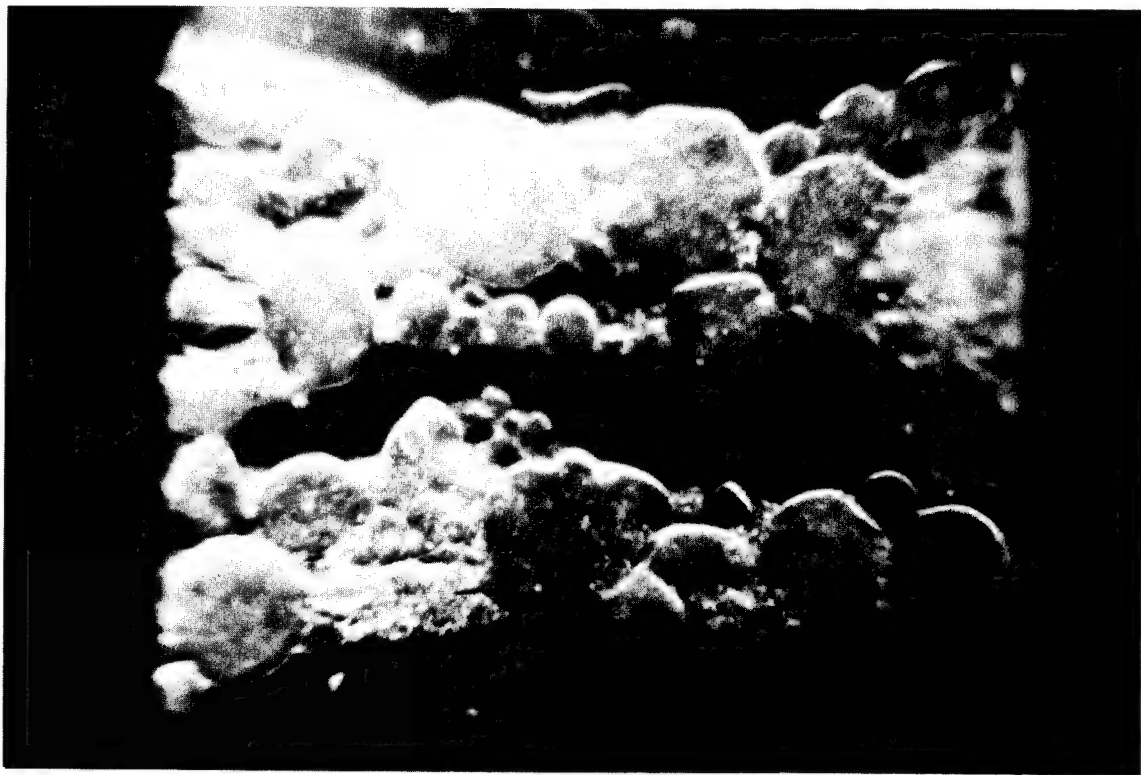
Figure 2. Photomicrograph of an Electro-Rheological Fluid
with an Electric Field Strength of 2 kV/mm

INTRODUCTION

The insatiable demand in the international marketplace for high-performance structural and mechanical systems for the aerospace and defense industries has triggered the evolution of advanced composite materials technologies. These diverse high-performance applications have mandated that designers tailor the materials and the material microstructural characteristics in order to provide optimal performance of the structural systems under various service conditions and unstructured environments. [13,14]

With traditional advanced composite materials, the optimization strategies result in an optimal design which is passive in nature and cannot respond to unstructured environments. For instance, the vibrational characteristics of a helicopter rotor fabricated in an advanced composite material are clearly dependent upon several factors such as the rotational speed, aerodynamic loading, payload and the ambient hygrothermal environment. An optimally-tailored rotor designed in a traditional advanced composite material is passive in the sense that it cannot actively respond to changes in the rotor speed and aerodynamic loading, for example. It is clearly evident, therefore, that the elastodynamic response of the rotor is sub-optimal for all service conditions except the one for which the rotor was optimally designed.

In order to overcome this limitation, a new generation of revolutionary, intelligent, ultra-advanced composite materials featuring ER fluids is proposed herein which will enable the response characteristics to be continuously varied in order to achieve the optimal performance under varying service conditions. These ultra-advanced composite materials capitalize on the superior characteristics of advanced composite materials which are interfaced with dynamically-tunable ER fluids contained in voids in the advanced composite structure. Changes in the electrical field imposed upon the ER fluids dramatically alter the rheological characteristics of the fluids and hence the global mass, stiffness and dissipative characteristics of the ultra-advanced composite structure. A methodology for synthesizing this class of smart materials is presented in Figure 3.

The instantaneous response-time of the ER fluids and the inherent ability of these materials to interface with solid-state electronics and modern control systems provides designers, for the first time, with a unique capability to synthesize ultra-advanced intelligent composite structures, whose continuum electro-elastodynamic response can be actively controlled in real-time. An application of this philosophy to control the vibrational response of an aircraft wing is schematically represented in Figure 4.
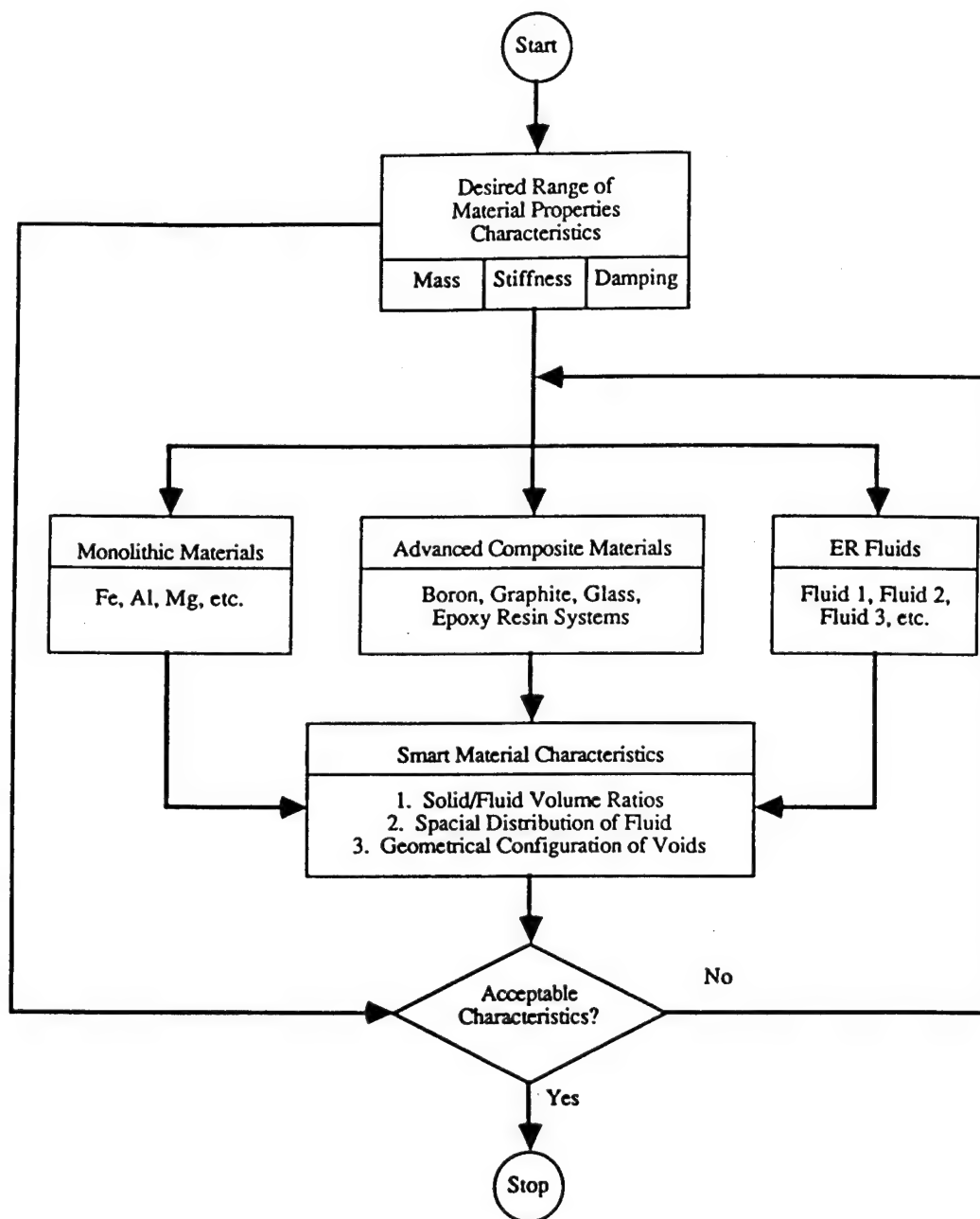
Figure 3.   A Methodology for Synthesizing Materials
Incorporating ER Fluids
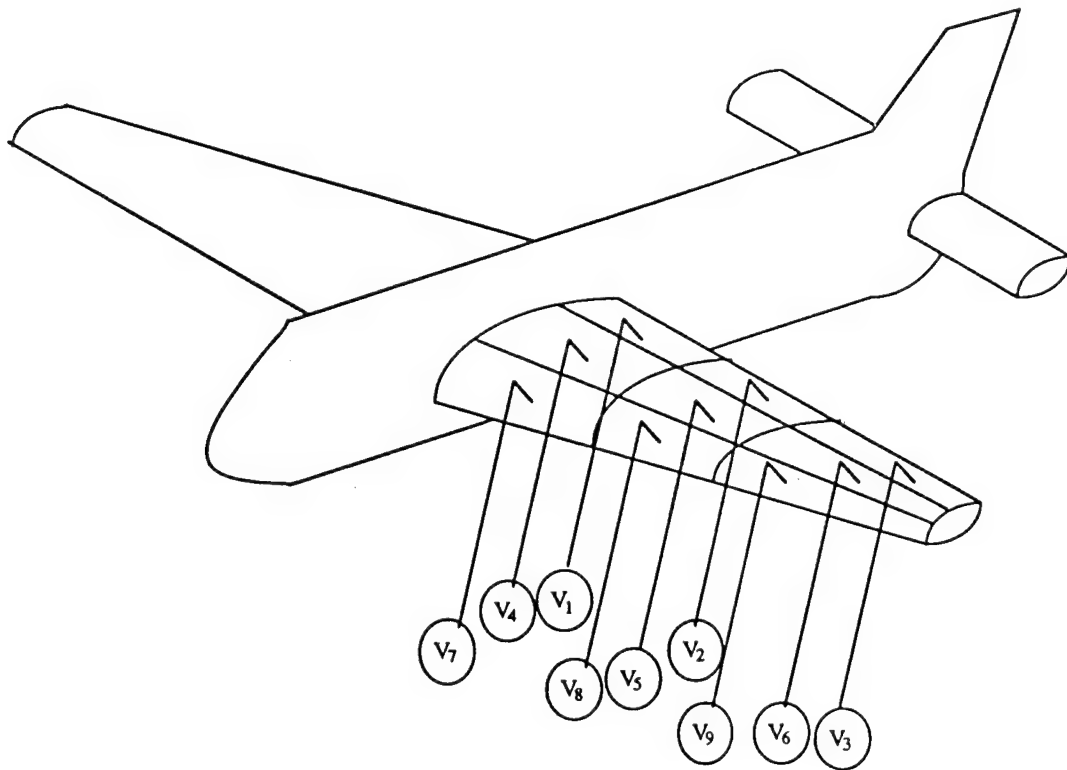
Figure 4. A Schematic Diagram of an Aircraft with a Wing Fabricated
from an Ultra-Advanced Intelligent Composite Material

       This class of innovative materials derive their intelligence from
the merger of sensors, built into the finite element control segments of the
ultra-advanced composite material continuum, microprocessors, and
dynamically-tunable electro-rheological fluids as shown schematically in
Figure 5. The sensors monitor the elastodynamic behavior of the ultra-
advanced composite structure, and the signals from the sensors are fed to
the appropriate microprocessor which evaluates the signals prior to
determining an appropriate control strategy in order to synthesize the
desired elastodynamic response characteristics. This is typically
accomplished by controlling the rheological characteristics of the ER fluid
domains in the finite element segment associated with the particular sensor.
This change in the rheological characteristics of the ER fluid in a typical
finite element control segment, in turn alters the global mass, stiffness,
and damping characteristics of the ultra-advanced composite structure in
order to achieve the desired vibrational response.
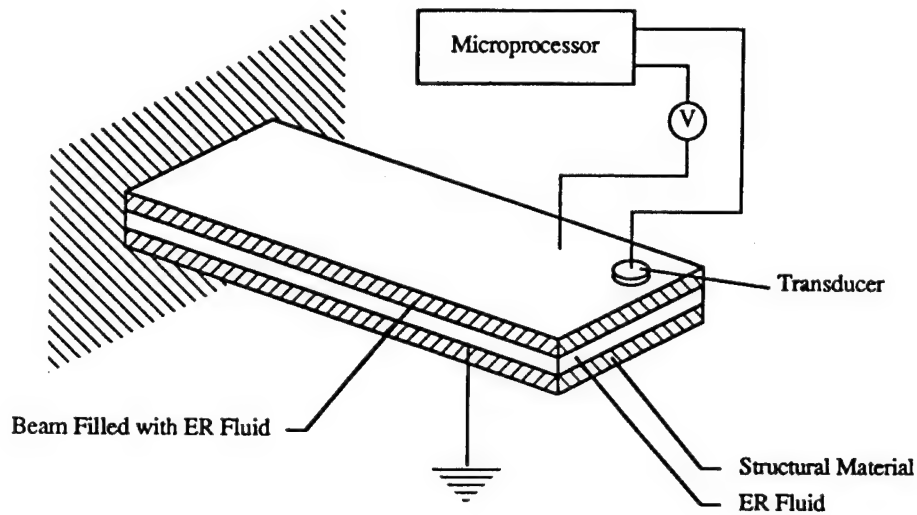
Figure 5.   Schematic of a Cantilevered Beam Fabricated in an Ultra-
            Advanced Intelligent Composite Material Showing Sensor and
            Date-Processing Components

This paper reports on a pioneering proof-of-concept experimental investigation focussed on evaluating the elastodynamic response of cantilevered beams fabricated from ultra-advanced intelligent composite materials. The preliminary results of this investigation clearly demonstrate the ability to dramatically change the transient elastodynamic response characteristics of beam-like specimens fabricated in the ultra-advanced composite materials by changing the electrical field imposed on the ER fluid domains.

EXPERIMENTAL PROGRAM

The objective of the experimental program was to investigate the transient response characteristics of various cantilevered beam specimens fabricated in smart ultra-advanced composite material in a variety of different operating conditions in order to provide a basis for evaluating the controllability of these structures in real-time. The experimental investigation focussed on evaluating the responses of AS4/3501-6 graphite-epoxy beams featuring various stacking sequences, and containing various ER fluids. The subsequent investigations focussed on evaluating the transient behavior of ultra-advanced composite beams subjected to sudden changes in the electrical field intensity as a first step towards evaluating the controllability of this innovative class of structures.
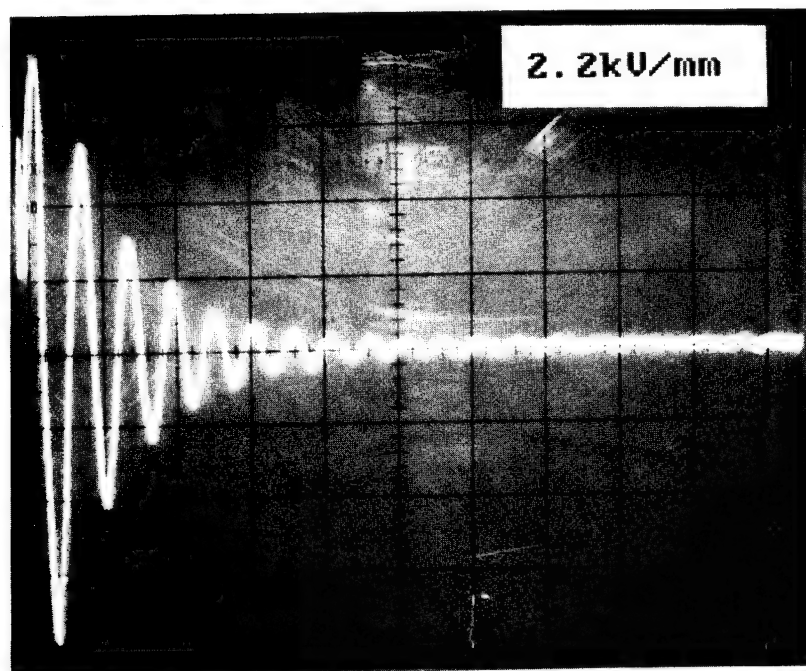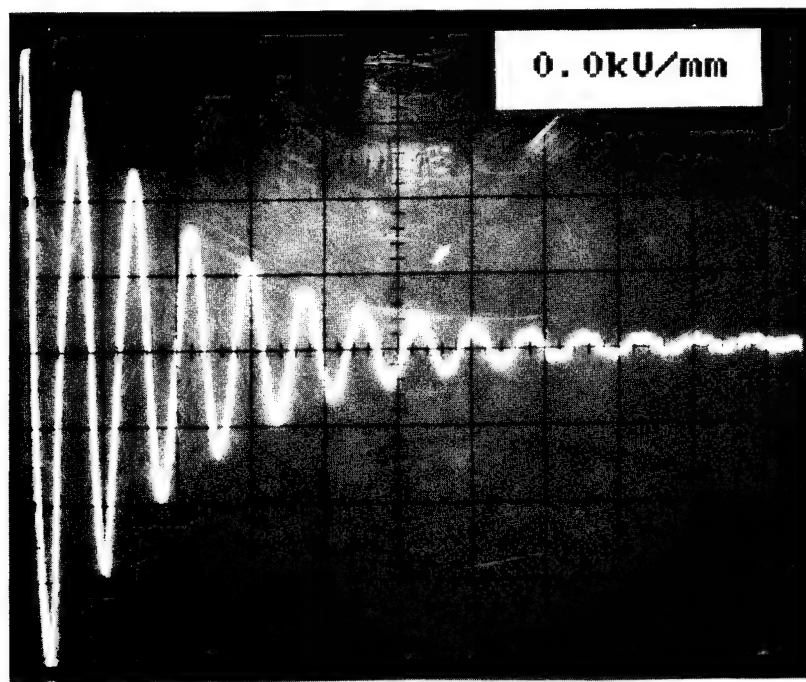
Figure 6. Transient Response of a Cantilever Beam Speciment With and Without Electric Field at Room Temperature

DISCUSSION OF EXPERIMENTAL RESULTS

Figure 6 presents polaroid photographs of the oscilloscope traces of the transient elastodynamic responses of a cantilever beam specimen at room temperature at two discrete, different, voltage stages. It is evident from these results that the frequency of the response and also the damping ratio of the signal are strongly dependent upon the voltage applied to the beam. Thus as the electrical field intensity increases, the damping increases monotonically and the fundamental natural frequency of the beam also increases.
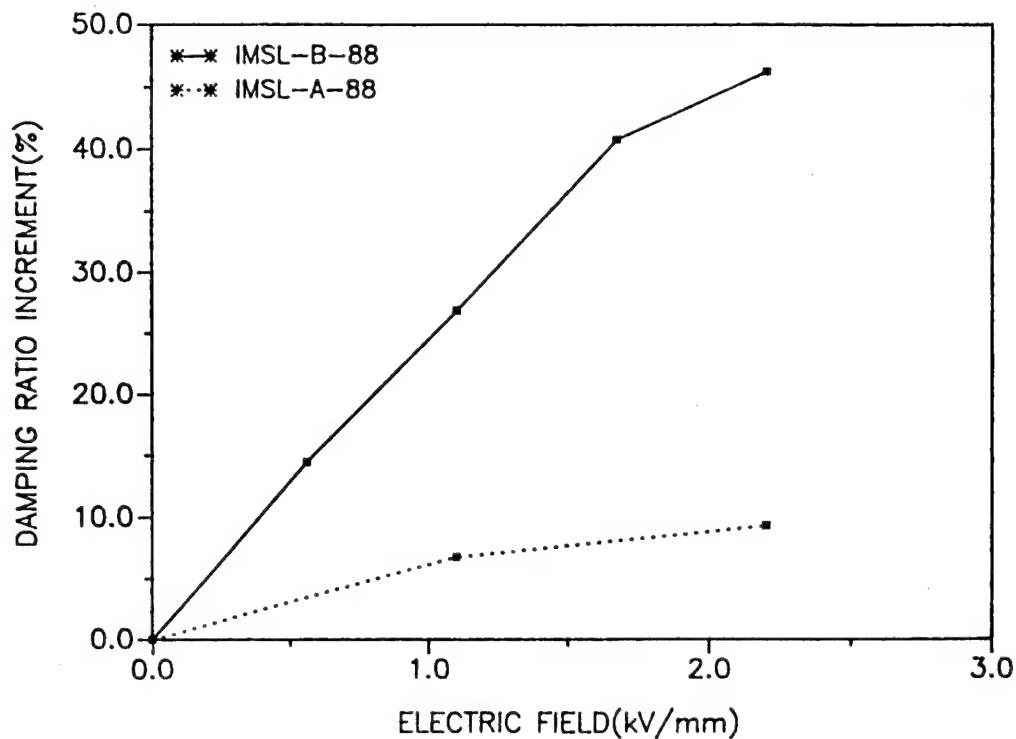
Figure 7. Comparison of the Relative Damping Ratio Increment Between AS4/3501-6 Specimens Featuring Different ER Fluids at Room Temperature

Figure 7 presents a comparison of the damping ratio increments between different specimen classifications as a function of the applied voltage. The relative increment in the damping ratio of each ultra-advanced composite beam specimen in the presence of an electric field is defined with respect to the corresponding magnitude in the absence of an electric field, which is employed as the datumn. Thus, in the context of Figure 7 and the damping ratio increment, when the fluid domain in the beam specimen is not subjected to an external voltage, the damping ratio increment is zero, however, the beam naturally has a non-zero damping ratio due to the energy-dissipation characteristics of the structural and fluid components of the ultra-advanced composite material. The results presented in Figure 7 were

obtained from specimens with the same structural properties and geometries but one specimen featured ER fluid type IMSL-B-88 and the other featured ER fluid type IMSL-A-88. These results indicate that the type of ER fluid has a major impact on the change in damping and hence controllability of the elastodynamic response of the material.

Figure 8 presents the experimental results for the damping ratio increment as a function of the applied electrical field for two classes of beam specimens. The specimens contained the same ER fluid and they were fabricated with identical geometries, but the layups of the graphite pre-preg AS4/3501-6 were different. A consequence of these different layups is that the stiffness and damping properties of the specimens are quite different, thus the properties of the ER fluid and the properties of the encasing structional material are crucial parameters in the synthesis of this class of dynamically-tunable smart materials.
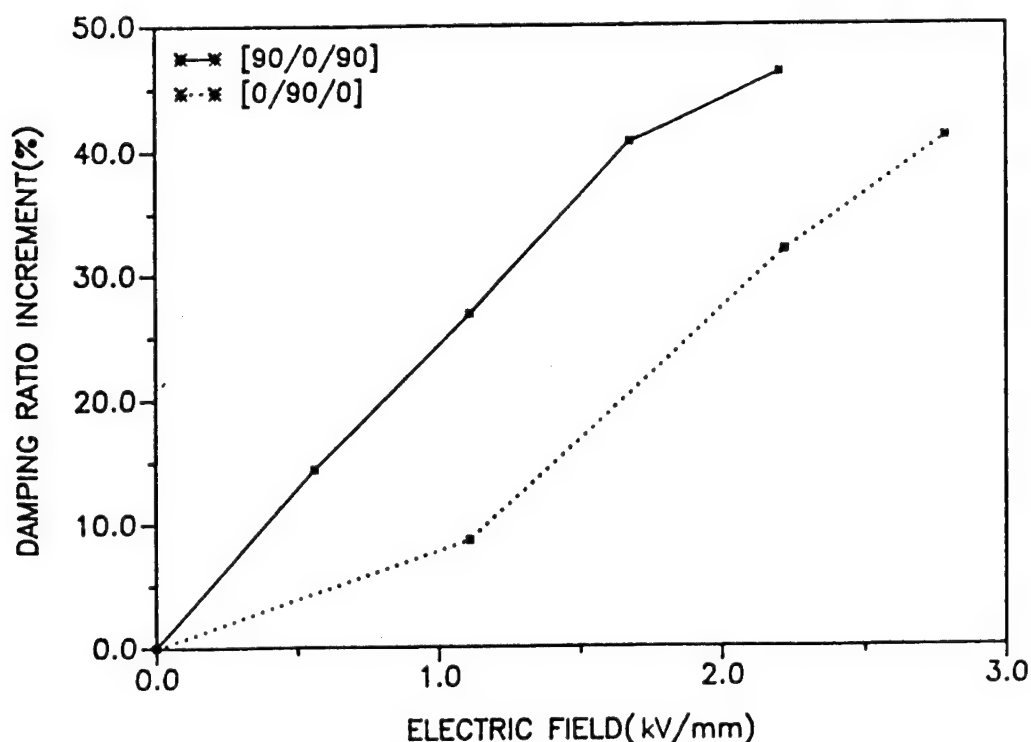
Figure 8. Comparison of the Relative Damping Ratio Increment Between Specimens Featuring Two Different Lay-ups of AS4/3501 at Room Temperature

Figure 9 presents the polaroid photographs of the oscilloscope traces of the controlled transient elastodynamic response of a cantilever beam specimen at room temperature. The transient response of the specimen for zero applied voltage is presented in Figure 9a). Figure 9b) presents the transient response of the identical specimen subjected to the same initial conditions, namely the same initial tip transverse deflection and an electrical field intensity of 0 kV/mm. This field intensity was maintained for the first 0.37 seconds of the response profile, prior to instantaneously generating a field intensity of 2.5 kV/mm. These two piecewise-constant discrete voltage inputs represent the active-control inputs based on a bang-bang control strategy. A cursory review of the response profiles presented
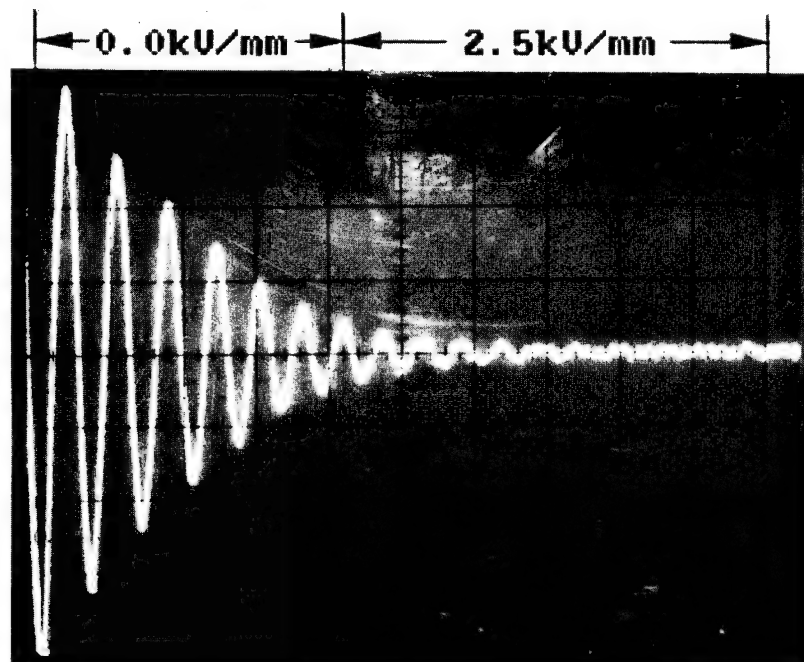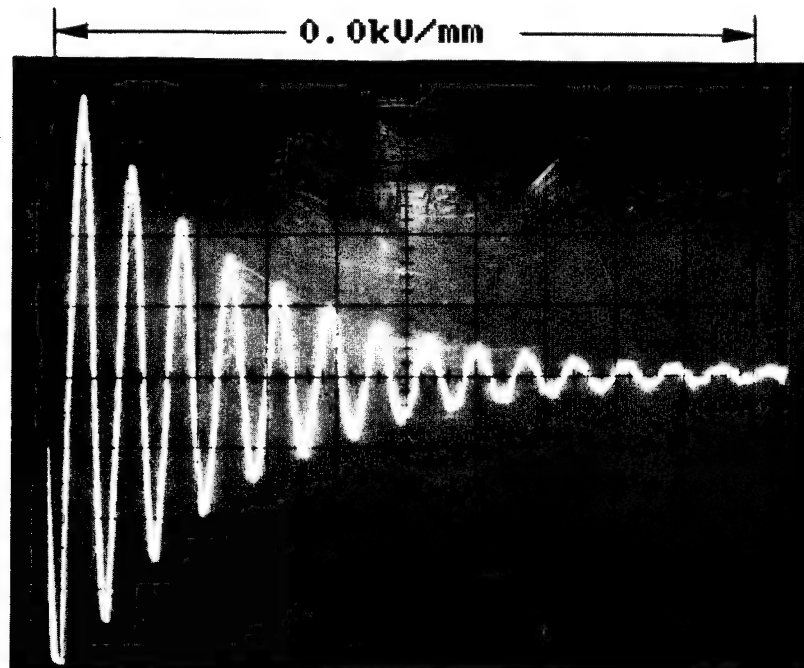
Figure 9. Controlled Transient Response of a Cantilever Beam Specimen
at Room Temperature

in Figures 9a) and 9b) clearly indicates that the amplitude of the vibrational response in the two profiles is identical for the first 0.37 seconds. Subsequently, the amplitude of vibration presented in Figure 9b) is substantially attenuated upon imposing the 2.5 kV/mm electrical field strength.

It is clearly evident from these proof-of-concept results that the elastodynamic response characteristics of structures fabricated from ultra-advanced composite materials can be actively controlled in real-time in order to obtain desired performance characteristics of the structure by altering the applied voltage. Naturally, advanced control algorithms and sensors must be employed to realistically implement this philosophy in practice.

CONCLUDING REMARKS

A new generation of innovative, ultra-advanced, intelligent composite materials featuring ER fluids has been proposed herein. A proof-of-concept investigation focussed on evaluating the elastodynamic response characteristics of beam-like specimens has been undertaken. The results of these investigations clearly demonstrate for the first time the feasibility of actively controlling in real-time the continuum vibrational characteristics of structures fabricated upon ultra-advanced composite materials by altering the voltage applied to the structure. It is anticipated that the successful integration of the fundamental phenomoneological work presented herein with modern control strategies and intelligent sensor technologies will significantly accelerate the evolution of a new generation of innovative ultra-advanced intelligent composite materials for the defense and aerospace industries.

ACKNOWLEDGEMENTS

REFERENCES

1. König, W., "Bestimmung einiger Reibungscoefficienten und versuche iber den Einfluss der Magnetisitung und Electrisinung auf die Reibungder Flussigleuten, <u>Annals of Physics</u>, Vol. 25, pp. 618-624 (1985).

2. Winslow, W.M., "Induced Fibration Suspensions," <u>Journal of Applied Physics</u>, Vol. 20, pp. 1137-1140 (1949).

3. Stangroom, J.E., "Electrorheological Fluids," <u>Journal of Physics Technology</u>, Vol. 14, pp. 290-296 (1983).

4. Makatun, V.N., Lapko, K.N., Matsepuro, A.D. and Tikavyi, V.F., "Characteristics of Charge Transport in the Disperse Phase of Electrorheological Suspensions," <u>Inzhenerno-Fizicheskii Zhurnal</u>, Vol. 45, pp. 597-602 (1983).

5. Bullough, W.A. and Peel, D.J., "Electrorheological Oil Hydraulics," <u>Japanese Hydraulic and Pneumatic Society</u>, Vol. 17, No. 7, pp. 510-526 (1986).

6. Shulman, Z.P., Gorodkin, R.G., Korobko, E.V., Gleb, V.K., "The Electrorheological Effect and its Possible Uses," <u>Journal of Non-Newtonian Fluid Mechanics</u>, Vol. 8, pp. 29-41 (1981).

7. Uejima, H., "Dielectric Mechanism and Rheological Properties of Electro-Fluids," <u>Japanese Journal of Applied Physics</u>, Vol. 11, No. 3, pp. 319-326 (1972).

8. Gorodkin, R.G., Korobko, Y.V., Blokh, G.M., Gleb, V.K., Sidorova, G.I. and Ragotnor, M.M., "Applications of the Electrorheological Effect in Engineering Practice," <u>Fluid Mechanics - Soviet Research</u>, Vol. 8 No. 4, pp. 48-61 (1979).

9. Gandhi, M.V., Thompson, B.S., Choi, S.B. and Shakir, S., "Electro-Rheological-Fluid-Based Articulating Robotic Systems," ASME Paper No. 87-DAC-55, published in Advances in Design Automotion - 1987: Volume Two, Robotics, Mechanisms, and Machine Systems, (S.S. Rao, ed.) DE-Vol. 10-2, pp. 1-10, and <u>ASME Journal of Mechanisms, Transmissions and Automation in Design</u> (in press).

10. Gandhi, M.V., Thompson, B.S. and Choi, S.B., "Ultra Advanced Composite Materials Incorporating Electro-Rheological Fluids," Proceedings of the 4th Japan-U.S. Conference on Composite Materials, Washington, DC, June 1988.

11. Gandhi, M.V. and Thompson, B.S., "A New Generation of Revolutionary Intelligent Composite Materials Featuring Electro-Rheological Fluids", Proceedings of the ARO Workshop on Smart Materials, Structures and Mathematical Issues, Blacksburg, VA, September, 1988.

12. Gandhi, M.V., Thompson, B.S. and Choi, S.B., "A New Generation of Innovative Ultra-Advanced Intelligent Composite Materials Featuring Electro-Rheological Fluids: An Experimental Investigation," <u>Journal of Composite Materials</u> (in press).

13. Sung, C.K., Thompson, B.S., Gandhi, M.V. and Lee, C.Y., "A Methodology for Synthesizing Symmetric Laminated Beams with Optimal Elastodynamic Response Characteristics," <u>International Journal of Mechanical Sciences</u>, Vol. 29, No. 12, pp. 821-830 (1987).

14. Adali, S., "Multiobjective Design of an Antisymmetric Angle-ply Laminate by Nonlinear Programming," <u>ASME Journal of Mechanisms, Transmissions, and Automation in Design</u>, Vol. 105, pp. 214-218 (1983).

Identification of System Parameters in a Slewing Control Experiment

Ephrahim Garcia
Graduate Research Fellow

Daniel J. Inman
Professor

State University of New York at Buffalo
Buffalo, New York

Abstract

Presented is a method for state space model improvement using measured free decay time histories of a dynamic system. This methodology is called the matrix exponential method (MEM). MEM assumes that some state space model exist for a dynamic system, and that the model's system matrix, $A(P)$, is a function of various parameters, P_i's. MEM uses a first order Taylor series expansion of the measurement time histories to determine what changes in the system parameters, ΔP_i's, are necessary such that the dynamic response of our model more closely resembles the measured response of the physical system. This paper will present the results of this parameter correction method to a control structure interaction problem, namely, a slewing control experiment. MEM will be used to correct some unknown, and often unpredictable, parameters, e.g., the angular viscous damping. Comparisons of the model's time histories and frequencies will be compared with measurements from the experiment.

I. Introduction

Arriving at a mathematical model that accurately reflects events that occur in physical systems can often be extremely difficult. In many instances certain parameters of a dynamic system can be measured and/or calculated precisely. For example, knowing the mass distribution and geometry of a rigid body allows dynamicists to obtain accurate values for the inertia of such bodies. Similarly, in elastic structures, the measurement of force to displacement yields precise information about stiffness, in the sense that the predicted inertia and stiffness for a system can be calculated and/or measured. Damping can be considered to be a dynamic parameter in that it can only be measured using the response of the system to some known force, or a free-decay from some initial condition.

Typically, models are developed based on our knowledge of a system's parameters. However, simulation results quite often do not correspond to the dynamic behavior of the physical system. In the finite element method, users often adjust models by using "equivalent lengths" or "equivalent mass" elements so that the eigenvalues of the FEM model and those of the physical system appear similar. The goal of MEM is simply to determine what changes in the system parameters, ΔP_i's, are necessary such that the model's response simulation results more closely resemble the measured response of the physical system.

The matrix exponential method(MEM) was developed by Tsen and Mook in Ref.1 and 2. Another time domain identification scheme[3] identifies entire system matrices, i.e., the mass, stiffness, and damping. However, this method assumes that all acceleration, velocity and displacement time histories are measurable. The MEM approach is different than other approaches because it simply determines which parameters in an existing model should be adjusted in order to improve a model's prediction of the physical system's dynamic response, rather than assuming the need to develop a new or realized model.

II. Matrix Exponential Method

Let us consider the following linear, time-invariant state space model.

$$\dot{x} = Ax \tag{1a}$$
$$y = Cx \tag{1b}$$

where

x - $2n$x1	state vector
A - $2n$x$2n$	system matrix
B - $2n$xm	input matrix
C - px$2n$	output matrix

where, $x(0)$ is an $2n$x1 vector of initial states. Let the system matrix A, be a function of system parameters, P_i's, as follows,

$$A = A(P) \tag{2}$$

where, $P^T = [P_1, P_2,...]$.

Now let us assume the measurements, Y_{meas}, are equal to the value of those predicted by the model Y, if we could adjust the parameters of the model by ΔP , e.g.,

$$Y_{meas} = Y(P + \Delta P) \tag{3}$$

Taking a Taylor series expansion of Eq. (3) we can say that,

$$Y_{meas} = Y(P) + \frac{\partial Y}{\partial P} \Delta P + ... \text{ higher order terms} \tag{4}$$

Note that $Y(P)$ is the output vector of the model. We now drop the higher order terms and solve for ΔP,

$$\Delta P = \left[\frac{\partial Y}{\partial P}\right]^{-1} (Y_{meas} - Y) \tag{5}$$

The model's output sensitivity with respect to a parameter, $\partial Y/\partial P_i$, is determined as follows. Take the partial derivative of Eq.(1b) with respect to the parameter, P_i,

$$\frac{\partial Y}{\partial P_i} = \frac{\partial C}{\partial P_i} x + C \frac{\partial x}{\partial P_i} \tag{6}$$

Since $\dfrac{\partial C}{\partial P_i} = 0$,

$$\frac{\partial Y}{\partial P_i} = C \frac{\partial x}{\partial P_i} \tag{7}$$

To find $\dfrac{\partial x}{\partial P_i}$, we take the derivative of Eq. (1a) with respect to the parameter in question, P_i, i.e.,

$$\frac{\partial \dot{x}}{\partial P_i} = \frac{\partial A}{\partial P_i} x + A \frac{\partial x}{\partial P_i} \tag{8}$$

We now define a new state space, $Z^T = [x^T : \partial x/\partial P_i{}^T]$, so that, and solve Eqs. (8) and (1a) simultaneously, i.e.,

$$\dot{Z} = A' Z \tag{9}$$

where

$$A' = \begin{bmatrix} A & . & 0 \\ \cdots & & . \\ \dfrac{dA}{dP_i} & . & A \end{bmatrix}$$

and

$$Z(0) = \begin{bmatrix} x(0) \\ \cdots \\ 0 \end{bmatrix}$$

Equation (9) is solved by finding a matrix exponential of the matrix A'. Here it has been assumed that the initial conditions of the physical system, hence, those of the model $x(0)$, do not depend upon the parameter, P_i, i.e.,

$$\frac{\partial x(0)}{\partial P_i} = 0 \tag{10}$$

The state vector $Z(t)$ contains the response of our model, $x(t)$, and the sensitivity of the state vector $\dfrac{\partial x}{\partial P_i}(t)$.

Computational Implementation
A more general form of Eq. (5) can be written as follows. If the number of parameters that are being adjusted is j, and k measurements of the time histories are measured, Eq. (6) becomes,

$$
\begin{bmatrix}
Y_{meas}(t_0) & - & Y(t_0) \\
Y_{meas}(t_1) & - & Y(t_1) \\
& \vdots & \\
& \vdots & \\
Y_{meas}(t_{k-1}) & - & Y(t_{k-1})
\end{bmatrix}
=
\begin{bmatrix}
\dfrac{\partial Y(t_0)}{\partial P_1} & \cdots & \dfrac{\partial Y(t_0)}{\partial P_j} \\
\cdot & \cdot & \cdot \\
\cdot & \cdot & \cdot \\
\cdot & \cdot & \cdot \\
\dfrac{\partial Y(t_0)}{\partial P_1}(t_{k-1}) & \cdots & \dfrac{\partial Y}{\partial P_j}(t_{k-1})
\end{bmatrix}
\begin{bmatrix}
\Delta P_1 \\
\vdots \\
\Delta P_j
\end{bmatrix}
\tag{11}
$$

or, in matrix form,

$$
E = S \Delta P \tag{12}
$$

where E - $k \cdot m$ x 1, vector of model error

S - $k \cdot m$ x j, matrix of output sensitivities

ΔP - j x 1, vector of parameter adjustments

Equation (12) is an over-determined problem which can be solved using the least squares approach[4], i.e.,

$$
\Delta P = (S^T S)^{-1} S^T E \tag{13}
$$

In large order problems where the inverse of $S^T S$ may not exist, and it may be necessary to apply a rank decomposition technique, such as, singular value decomposition.

Algorithm
The only rational reason for dropping the higher order terms from Eq. (4) was convenience. Therefore, there is no reason to believe a first order expansion of the measurements is accurate.

Hence, in order to find the total change in parameters, ΔP_i's we must apply Eq. (5) in a recursive manner. First an initial value is chosen for all P_i's (this may be $P = 0$), and then following procedure is applied.

(1) Find the model's output time histories $Y(t_0)...Y(t_{k-1})$ and subtract this form the measurements, $[Y_{meas}(t_{l-1}) - Y(t_{l-1})]$ where $l = 1,...,k$.

(2) Find the output sensitivities, $\dfrac{\partial Y}{\partial P_i}$ $i = 1,...,j$. (Recall that sensitivities and predicted outputs are solved simultaneously.)

(3) Find ΔP

(4) Add ΔP to P, update the model and repeat (1)-(3) until $|\Delta P_i| \ll |P_i|$ for $i = 1,...,j$. Note that only one set of measurements are needed.

III.   Modeling
The following formulation is similar to the modeling approach formulation found in Ref.6. The apparatus used in the slewing control experiment can be described as a flexible beam clamped to a rigid hub(see figure 1), where, $Y - X$ is in the horizontal plane, τ is a torque applied to the hub, and $y(x,t)$ is the displacement of the beam with respect to x. The hub parameters are the radius, a, and the hub inertia, I_H. The beam has the following properties, EI, the flexural rigidity , ρ, the mass density per unit length, and L , the beam length.

The Lagrangian, L_g, is the total kinetic energy of the system minus the total potential, so that,

$$L_g = \frac{1}{2} \int_0^L (\rho(a+x)\dot{\theta} + \dot{y})^2 dx + I_H \dot{\theta}^2 - \frac{1}{2} \int_0^L EI \left(\frac{\partial^2 y}{\partial x^2}\right)^2 dx \qquad (14)$$

We assume a separation of variables solution for the motion of the beam, i.e.,

$$y(x,t) = \sum_{i=1}^n q_i(t)\, \phi_i(x) \qquad (15)$$

where, n is the finite number of of the beam modes included in the model. The functions, $\phi_i(x)$, are the beam's eigenfunctions, and the equations of motion are derived from Hamilton's principle.

$$\delta \int_{t_f}^{t_0} [\, L_g + W_{nc}\,]dt = 0 \qquad (16)$$

where, $W_{nc} = \tau\theta$, is the work performed by non-conservative forces, i.e., the applied torque. The eigenfunctions of the beam are orthogonal and normalized with respect to mass density.[5] Using a three mode expansion for the motion of the beam, we arrive at the open loop equations of motion.

$$\tilde{M}\ddot{q} + \tilde{K}q = B\tau \qquad (17)$$

where, $q^T = [\theta, q_1, q_2, q_3]$, $B^T=[1, 0, 0, 0]$,

$$\tilde{M} = \begin{bmatrix} \int_0^L \rho(a+x)^2 dx + I_H & I_1 & I_2 & I_3 \\ I_1 & 1 & 0 & 0 \\ I_2 & 0 & 1 & 0 \\ I_3 & 0 & 0 & 1 \end{bmatrix}$$

$$\tilde{K} = \begin{bmatrix} 0 & 0 & 0 & 0 \\ 0 & \omega^2_1 & 0 & 0 \\ 0 & 0 & \omega^2_2 & 0 \\ 0 & 0 & 0 & \omega^2_3 \end{bmatrix}$$

and

$$I_i = \int_0^L \rho(a+x)\phi_i(x)dx.$$

The terms q_i are the modal coordinates of the beam.

Actuator Dynamics
The torque applied to the hub is generated by an armature controlled electric motor whose dynamics are characterized by the circuit in figure 2. By applying Kirchoff's law to this circuit, and summing the moments about the motor's armature, the following expression for the torque is derived as a function of armature voltage.

$$\tau = \frac{K_t}{R_a} e_a - I_M \ddot{\theta} - \left(C_v + \frac{K_b K_t}{R_a}\right)\dot{\theta} \qquad (18)$$

Since the motor inductance is small in our experiment, its contribution to the dynamics is neglected in Eq. (18).

Closed Loop Response
A simple closed loop response is given by setting the armature voltage proportional to the position,

$$e_a = K_p(\theta_{ref.} - \theta) \tag{19}$$

where, K_p is the position feedback gain.

Combining Eqs. (18) and (19) with the beam dynamics of Eq. (17), we arrive at Eq. (20) which describes the response of the closed loop system with the simple position control law.

$$M\ddot{q} + D\dot{q} + Kq = B\theta_{ref} \tag{20}$$

where

$$M = \tilde{M} + \begin{bmatrix} I_m & 0_{1 \times 3} \\ 0_{3 \times 1} & 0_{3 \times 3} \end{bmatrix} \tag{21}$$

$$D = \begin{bmatrix} (C_v + K_b K_t/R_a) & 0_{1 \times 3} \\ 0_{3 \times 1} & \text{DIAG}(2\zeta_1\omega_1, 2\zeta_2\omega_2, 2\zeta_3\omega_3) \end{bmatrix}$$

$$K = \begin{bmatrix} K_p K_t/R_a & 0_{1 \times 3} \\ K_p K_t/R_a \begin{Bmatrix} \Gamma_1 \\ : \\ \Gamma_n \end{Bmatrix} & \text{DIAG}(\omega_1^2, \omega_2^2, \omega_3^2) \end{bmatrix}$$

and

$$B^T = [\ 1.0, \ K_p K_t/R_a \ \Gamma_1, \ ..., K_p K_t/R_a \ \Gamma_n]$$

Note that the modal damping terms, $2\zeta_i\omega_i$, were added to the damping matrix, D. The assumed modes of vibration for the beam were found using Euler-Bernoulli beam analysis where the boundary conditions were assumed to be spring-hinged at the slewing axis and free at the other end.[9] The value of the spring constant is determined by the servo-stiffness term, $K_p K_t/R_a$. The modal participation factors were added to the stiffness and control matrices, K and B. The modal participation factors account for the direct transmission of the control's restoring torque to the modal deflections of the flexible structure.

IV. Set Up and Experimental Response
The experimental apparatus, depicted in figure 1, consists of a steel beam clamped to a rotating axis. The hub is the rigid mechanical interface between the beam and the slewing axis. The beam is 3" wide and 1/32" thick. An Electrocraft permanent magnet DC electric motor (Model #586) is attached concentrically to the axis of rotation. Angular sensing is performed using a potentiometer, and a tachometer provides an angular velocity sensor. A strain gauge, located at the root of the beam, is used for additional sensing. The physical characteristics of the motor/beam system are as follows.

$EI/\rho = .857$ Nm^3/kg	$K_b = 5.539 \times 10^{-2}$ volts/rad/sec
$I_m = 6.02 \times 10^{-2}$ kg m^2	$K_t = 5.508 \times 10^{-2}$ Nm/A
$L = 1.19$ m	$L_a = 2.3 \times 10^{-3}$ H
$a = .06$ m	$R_a = 2.0$ ohms

$$I_H = 3.49 \times 10^{-3} \text{ kgm}^2$$

The position control was implemented using an EAI 2000 analog computer, where the feedback constant was set to 8 volts/rad. The viscous damping parameter, C_v, is unknown, hence, is one of the parameters in the identification procedure.

The beam was set to an initial position in the slewing plane. The feedback circuit was then closed and the beam returned to the zero voltage reference point of the potentiometer. The potentiometer, tachometer, and strain gauge signals were recorded during the response (figure 3). The responses were sampled at a frequency of 128 Hz, although only a 12.8 Hz sampling frequency was used in the identification procedure to reduce the number of data points, hence, the computational effort. The flatness in the peaks of the position response were due to the discrete number of windings in the potentiometer.

V. Results of the Identification Procedure

The position response of the system was dominated by the rigid body motion of the structure, θ. The effects of the structural modes on the measured position response of the beam were secondary. The only contribution to the position measurement came from the 1st flexible mode of the structure. The measured position response was used to apply MEM to the model.

The initial unknown parameters of the model were arbitrarily set to $C_v = .0528$ and the modal damping term was set $2\zeta_1\omega_1 = 0.5$. The higher mode damping terms were set to $2\zeta_2\omega_2 = 2\zeta_3\omega_3 = 1$. Since the modes of the beam did not participate strongly in the position response, the modal damping was not included in the identification procedure. The focus here was to find the correct viscous damping constant which would yield a more accurate model. Figures 4a and 4b contain plots of the measurements, the initial model and the improved model for the single parameter tuning of C_v, and the multiple parameter tuning of C_v and K_p, respectively. Figures 5a and 5b show the convergence of the algorithm. The error is defined as,

$$\|Y_{error}\| = (Y_{meas} - Y_{model})^T (Y_{meas} - Y_{model}) \tag{22}$$

where, Y_{error}, Y_{meas} and Y_{model} are vectors in time. Table 1 contains the changes in parameters for our model, and table 2 contains the natural frequencies and damping ratios for the measurements and the model responses. Measurement frequencies and damping ratios were determined by a version of ERA[7] found in Ref. 8.

Run 1: Single Parameter Adjustment
The simple case was considered where only one parameter, C_v, is adjusted. Figure 5a shows the model error, $\|Y_{error}\|$, was reduced from 40.21 to 8.78 and shows the algorithm converged smoothly in a few iterations. In this case the response of the final model simply contains too much damping (see Fig. 4a), i.e., the 1st modal damping of the closed loop response is $\zeta_1 = 24.4\%$.

Run 2: Multiple Parameter Adjustment
Due to current limits in the amplifier circuit, simulations indicated that some amplifier saturation occurred. To correct for this, the model's position feedback constant was also adjusted. The final model of Run 1 was used as the initial model for this run. The model error was further reduced from 8.78 to 3.65. The first natural frequency error was reduced from 6.7% in our initial model to 3.1% in our final model. However, the model error, $\|Y_{error}\|$, did not show a smooth convergence.

VI. Discussion and Conclusions

An important point of this analysis is that the damping term C_v, and the final positions feedback, K_p, adjusted our linear model to account for what is often nonlinear effects in the actual system. For instance, analysis in the effects of air damping on slewing experiments show that air drag effects are nonlinear functions.[10] Our resulting improved model is a linear approximation to the linear and nonlinear parameters of the physical system, while not perfect, such linear models are of much interest for design purposes for the control engineer.

Uniqueness is another important topic in modeling improvement. Although, the least squares solution of Eq.(12) is a unique solution[4], the recursive procedure does not guarantee the final solution is a global minimum of the modeling error. The algorithm proposed is similar to the classic Newton-Raphson method, and as in the Newton-Raphson method, very ignorant initial guesses can lead to numerical instabilities. Moreover, numerical minimums may not be physically significant, i.e., in *Run 1* the numerical minimum simply contained too much damping. This is because the degree to which the modeling error is minimized depends on a judicious choice of parameters which are tuned.

MEM fine tunes a current model such that there is better agreement between the predicted response of the response of the physical system. The algorithm requires only one set of measurements, and is a time domain technique which requires only modest computational effort. The MEM method has been applied to a slewing control experiment. This method reduced the disagreement between the model and the measurements.

VII. Acknowledgment

VIII. References

1) Tsen, F.M.," System Identification by a Matrix Exponential Method," M.S. Thesis, State University of New York at Buffalo, 1986.

2) Tsen, F.M., Mook, D.J.,"Linear System Identification Using Matrix Exponential Sensitivities," Proceedings of 6th VPISU/AAA Symposium on Dynamics and Control of Structures, Blacksburg, Va., 1986.

3) Rajaram, S., Junkins, J.L.,"Identification of Vibrating Flexible Structures", *Journal of Guidance , Control and Dynamics*, vol. 8, no. 4, July-Aug., 1985.

4) Golub, G.H., Van Loan, C.F., *Matrix Computations*, John Hopkins Univ. Press, Baltimore, Maryland, 1983.

5) Inman, D.J., *Vibrations with Control, Measurement, and Stability*, Prentice Hall, Englewood Cliffs, New Jersey, 1989.

6) Juang, J.N., Horta, L.G., Robertshaw, H.H., " A Slewing Control Experiment for Flexible Structures," *Journal of Guidance, Control and Dynamics*, vol. 9, no. 5, Sept-Oct., 1986.

7) Juang, J.N., Pappa, R.S., " An Eigensystem Realization Algorithm for Modal Parameter Identification and Model Reduction," *Journal of Guidance, Control , and Dynamics*, vol. 8, Sept-Oct., 1985.

8) Garcia, E., "System Identification in the Microcomputer Environment," M.S. Thesis, State University of New York at Buffalo, 1987.

9) Chun,K.R., "Free Vibration of a Beam with One End Spring-Hinged and the Other Free," ASME Journal of Applied Mechanics, vol. 39, pp.1154-1155, 1972.

10) Juang, J.N., Horta, L.G., "Effects of Atmosphere on the Slewing Control of a Flexible Structure," *Journal of Guidance, Control, and Dynamics,* vol. 10, no. 4, July-Aug.,1987.

Table 1 Parameter Values

		Initial	Final	ΔP_i's
Run 1:				
	C_v	.0528	.2048	.1520
	$\|Y_{error}\|$	40.2109	8.7819	
Run 2:				
	C_v	.2048	.1299	-.0741
	K_p	8.0	6.5753	-1.4247
	$\|Y_{error}\|$	8.7819	3.6512	

Table 2 Modal Parameters Closed Loop Response

	Mode 1		Mode 2	
	ω_1	ζ_1	ω_2	ζ_2
Measurements.	.1421	9.92%	1.5648	3.10%
Run 1:				
Initial	.1520	6.32%	1.72%	2.31%
Final	.1519	24.48%	1.724%	2.46%
Run 2:				
Final	.1377	17.73%	1.7249	2.42%
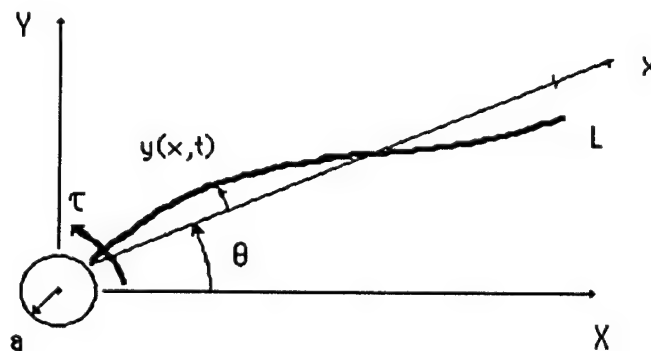
figure 1. Flexible Beam Attached to Rigid a Hub.
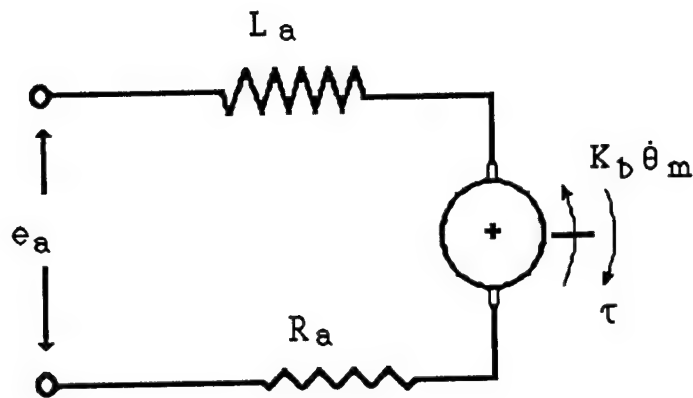
figure 2. Motor Armature Circuit.
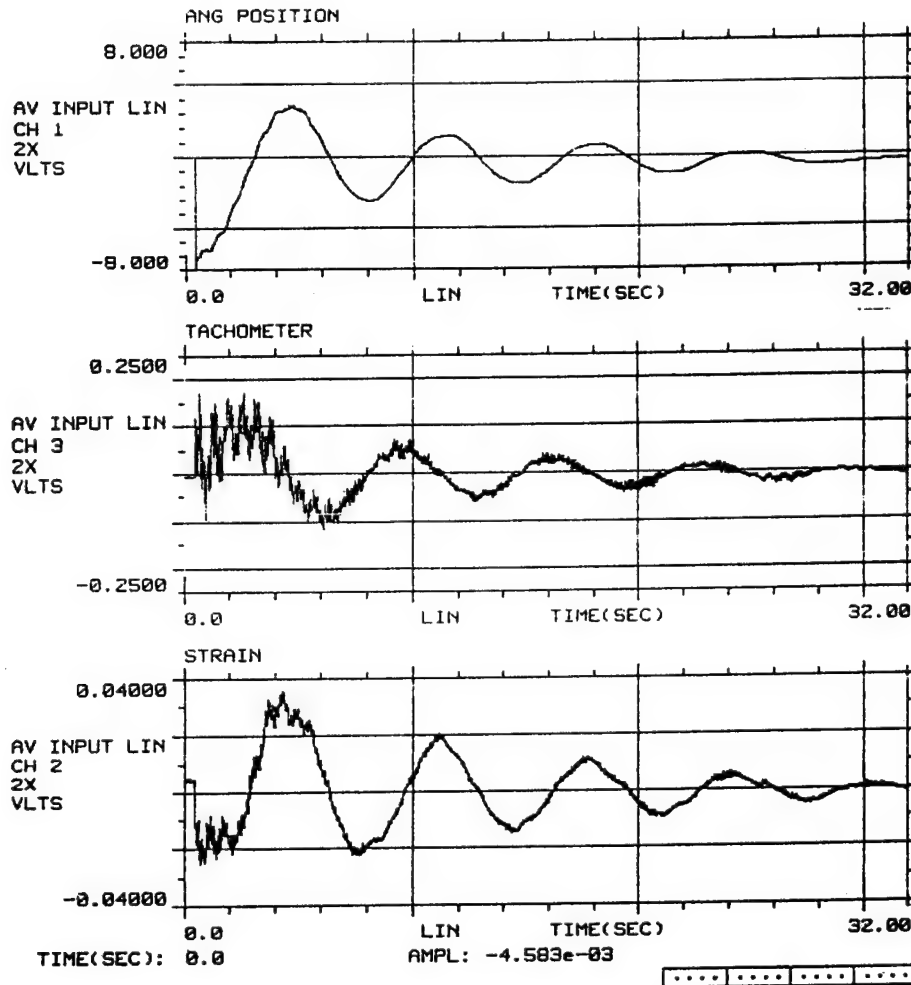
Figure 3. Measured Time Histories- Free Decay.
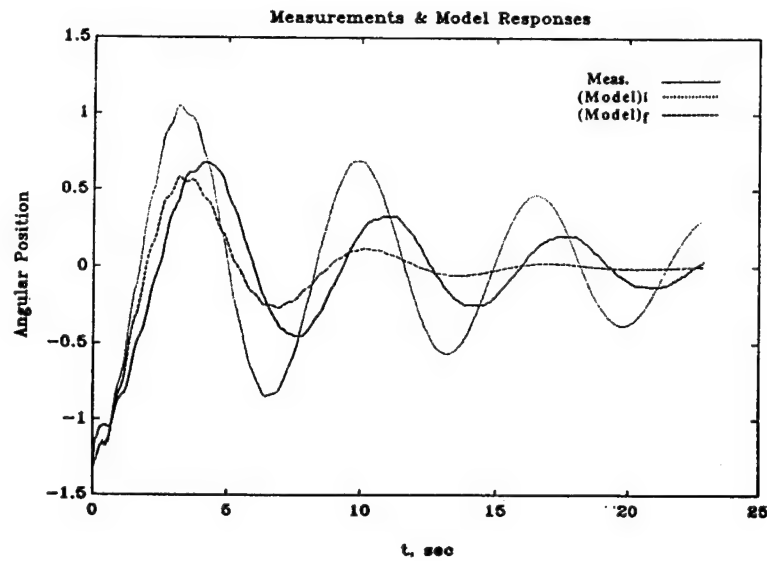
Figure 4a. Measurements and Initial and Final Models-*Run 1*.
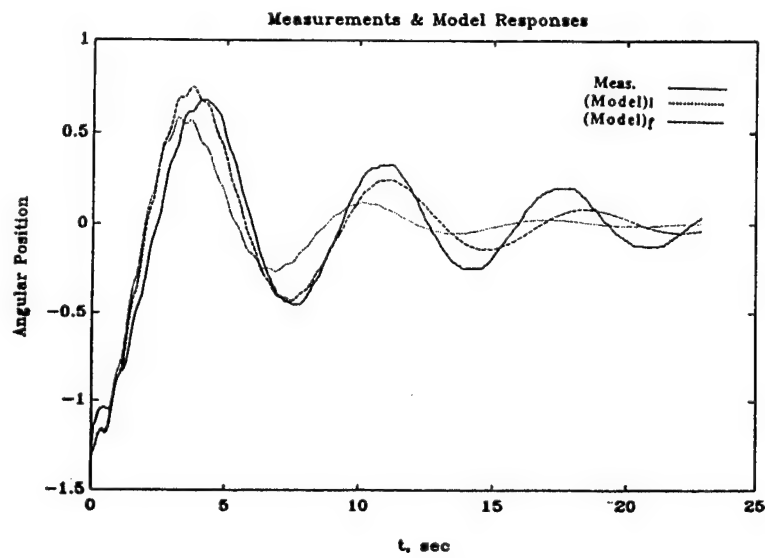
Figure 4b. Measurements and Initial and Final Models-*Run 2*.
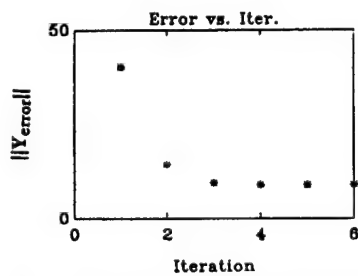
Figure 5a. Algorithm Convergence-*Run 1*.
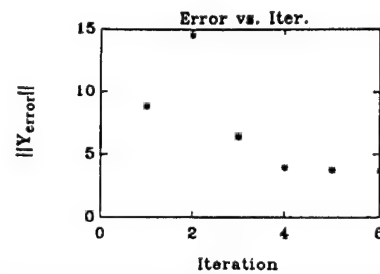
Figure 5b. Algorithm Convergence-*Run 2*.

An Alternative To FFT For Precise Damping Estimates

Sudhakar M. Pandit
Mechanical Engineering-Engineering Mechanics Department
Michigan Technological University
Houghton, MI   49931

ABSTRACT

The prevalent methods of estimating structural damping are based on the FFT of the test data. The paper discusses the distortion introduced by FFT to show that any post-processing of the FFT will provide a poor estimate of damping, typically overestimating it; this will be the case even with curve fitting in frequency domain, or in time domain after applying inverse FFT. The paper then presents an alternative time domain methodology called Data Dependent Systems (DDS) for precise damping estimation. The DDS methodology uses difference equation models directly fitted to the time domain data for estimating damping ratios, natural frequencies, and mode shapes.   After explaining the rationale of why the DDS damping estimates are more precise compared to those from FFT, the paper gives examples to highlight the precision.   These examples demonstrate that the DDS is capable of precise system identification even in the presence of high damping, high modal density and considerable noise.   In particular, it is shown that the frequency and the damping ratio are correctly identified even when the damping ratio is so high that the corresponding peak disappears from the authospectrum and hence it is impossible to identify it from FFT.

INTRODUCTION

Determination of structural damping is a difficult problem that can be solved only using test data in most cases. Although finite element modeling can be used to determine natural frequencies, modal testing is usually needed to provide the damping estimates necessary in predicting the realistic response from the finite element codes.

Much of the current modal testing hardware and modal analysis software is based on Fast Fourier Transform (FFT) of the test data to take advantage of the computational efficiency of FFT. However, the FFT of test data introduces distortions due to problems such as leakage and resolution, and also errors such as bias and variance (random error). Smoothing of raw FFT by averaging or windowing is necessary to reduce the effect of such errors. Such distortion and smoothing both affect the damping estimates. Therefore, damping estimates obtained by post-processing FFT of test data are usually unreliable; typically FFT overestimates damping.

This paper briefly outlines an alternative time domain methodology called Data Dependent Systems (DDS) for precise damping estimation and reviews some of the results illustrating the precision from references[1-8], which may be referred for more details. Difficulties in damping estimation from FFT of test data are discussed at the beginning. The rationale of more precise estimation by DDS is then explained. Examples from the literature demonstrating the precision of damping estimation by DDS are given at the end.

Why Does FFT Overestimate Damping?

Usually FFT and its post-processing tends to flatten a sharp peak and thus leads to overestimation of damping. The primary causes of such flattening of the peaks are discussed below briefly, more details may be found in texts such as[9-10].

1. **Frequency Resolution, Leakage and Aliasing:** When the record length say T of the data is not large enough, since the FFT is calculated at multiples of frequency $\frac{1}{T}$, the frequency resolution may not be adequate to capture sharp peaks. Even when the record length is increased, the leakage caused by the absence of integral number of cycles in the record length spreads over neighboring frequencies and flattens the peaks as illustrated in Figure 1. This flattening of peaks persists even when damping is high, as illustrated in Figure 2. Post-processing of FFT by averaging and windowing to reduce leakage and use of antialiasing filtering also adds damping. Figure 1 illustrates the peak flattening caused by truncation-another windowing effect.

2. **Bias and Variance (Random Errors):** The finite amount of data used in FFT may be considered as the original "infinite" data truncated by a rectangular "box-car" window, which introduces bias in the estimate of the peak. Since this bias is usually negative, it has the effect of increasing the damping. Moreover, when the test data is noisy, the FFT introduces variance (random error) and is consequently erratic and choppy, containing many spurious peaks in addition to the genuine ones. It is therefore usually necessary to smooth

the FFT by averaging, either simple or weighted, which applies another window that also increases damping. To make matters worse, one cannot reduce bias and variance simultaneously, a window that reduces bias inevitably increases variance and vice versa.

PRECISE DAMPING BY DDS

The DDS methodology [1-7] estimates damping by fitting difference equation models of successively higher order until the reduction in the residual sum of squares is statistically insignificant or the variance of the residuals drops below a known noise floor. The eigenvalues or characteristic roots of these models then yield the estimates of natural frequencies and damping ratios. No prior assumptions or conjectures about the model are needed, they can be obtained directly from the data by available computer routines[4]. The difference equation is in the form of an Autoregressive Moving Average model, ARMA (n,n-1):

$$X_t = \phi_1 X_{t-1} + \phi_2 X_{t-2} + \dots + a_t - \theta_1 a_{t-1} - \dots - \theta_{n-1} a_{t-n+1}$$

where X_t is a single scalar or multiple vector series of data, ϕ_i and θ_i are scalar or matrix parameters and a_t represents scalar or vector white noise. These a_t's model and remove the noise in the data to provide modal parameter estimates from one sample without any need for averaging.

The natural frequency and damping ratio corresponding to each mode are obtained from the characteristic roots or eigenvalues λ_i defined in the scalar case by

$$(1 - \phi_1 B - \phi_2 B^2 \dots - \phi_n B^n) = (1-\lambda_1 B)(1-\lambda_2 B) \dots (1-\lambda_n B).$$

If λ_i and λ_i^* are a complex conjugate pair of roots, then the corresponding damping and natural frequency terms are obtained by

$$2\zeta\omega_n = \ln (\lambda_i \lambda_i^*)/\Delta$$

$$\omega_n = \tan^{-1} \left[\frac{Im\lambda_i}{Re\lambda_i}\right]/\Delta$$

where Δ is the sampling interval and Im and Re represent imaginary and real parts respectively. The mathematical background, procedure and expressions for obtaining other parameters such as mode shapes and mass, damping and stiffness matrices from the response data may be found in references[3-7].

The number of parameters in the model fitted by DDS is limited by the actual effective degrees of freedom reflected in the response data. Therefore, as the number of data points is increased, the additional information improves the accuracy of the limited number of parameters such as

mode shapes and damping ratios. This is in contrast to the FFT, where such additional information from the increased number of data points is spread over the increased number of frequencies, and the accuracy of estimates at any given frequency does not improve; subsequent processing by averaging, smoothing or windowing adds its own distortion as explained earlier. This is the basic reasons why the DDS methodology provides far more precise damping estimates than the FFT.

ILLUSTRATIVE EXAMPLES

The relative precision of DDS compared to FFT is already clear graphically from Figures 1-2. These figures show that the DDS estimates of damping almost exactly match with the actual, whereas the FFT always overestimates it. This is true at low damping, Figure 1, as well as high damping, Figure 2. We will now give examples with numerical estimates to demonstrate the precision.

Table 1 gives results from reference[3] on a simulated 3-degrees-of-freedom system using 500 data points and scalar models. Note that the results are as precise with noise as without it; the only difference is that the model order needs to be higher for noisy data to model the noise modes. Results in Table 2 from the same reference[3] then show that closely spaced mode shapes can also be resolved if high enough model order is used. Similar results on a 2-degree-of-freedom system in Table 3, taken from reference[3], show that this precision extends to mass, damping and stiffness matrices [m], [C] and [K].

Table 1: Comparison of Estimates With and Without 17% Noise

	Theoretical	Noise-Free ARMA(12,11)	Noisy ARMA(26,25)
Natural Frequency (Rad/Sec)	0.58569 1.2319 1.6003	0.58567 1.2323 1.6002	0.58503 1.2312 1.5999
Damping Ratio ζ	0.03122 0.16404 0.10206	0.03122 0.16412 0.10200	0.03118 0.16412 0.10202
Mode Shapes (Relative Amplitudes)	2.4829 3.7044 1.0420 2.0963 1.0000 0.7122	2.4788 3.7023 1.0493 2.0959 0.9988 0.7149	2.4912 3.6976 1.0493 2.0651 1.0009 0.7111

Table 2: Comparison With Closely Spaced Modes

	Theoretical	ARMA(28,27)
Natural Frequency (Rad/Sec)	0.96697 1.8881 2.0000	0.96698 1.88888 2.0009
Damping Ratio ζ	0.15512 0.07944 0.07500	0.15503 0.07965 0.07471
Mode Shapes (Relative Amplitudes)	1.0669 1.0000 -1.4366 1.0000 0.0 -1.0	1.0667 1.0009 -1.4359 1.0071 0 -1.0010

Table 3: Comparison of Parameter Matrices

	[m]	[C]	[K]

Theoretical:

$$\begin{bmatrix} 5 & 0 \\ 0 & 10 \end{bmatrix} \quad \begin{bmatrix} 1 & -0.5 \\ -0.5 & 1.5 \end{bmatrix} \quad \begin{bmatrix} 4 & -2 \\ -2 & 6 \end{bmatrix}$$

DDS Estimated:

$$\begin{bmatrix} 5.001 & 0 \\ 0 & 10.001 \end{bmatrix} \quad \begin{bmatrix} 1.000 & -0.5002 \\ -0.5002 & 1.500 \end{bmatrix} \quad \begin{bmatrix} 4.000 & -2.001 \\ -2.001 & 6.001 \end{bmatrix}$$

Tables 4 and 5 present results from reference[7] obtained using vector models for a 2-degree-of-freedom system with light and heavy damping respectively. Note that since the vector models use multiple series of data simultaneously, their estimates are even more precise than the scalar models with the same number of data points per series. The precision of damping ratio estimates is quite good in both low and high damping environment.

Table 4: Comparison of DDS and Theoretical Mode Shapes and Natural Frequencies for ACSL-Simulated 2 DOF System With Light Damping

PARAMETER	THEORETICAL		DDS	
IST MODE SHAPE	Mag. 1.0 3.14603	Phase(deg) 0.0 -2.57608	Mag. 1.0 3.14573	Phase(deg.) 0.0 -2.5750
2ND MODE SHAPE	1.0 0.159754	0.0 175.714	1.0 0.159753	0.0 175.7140
1ST NATURAL FREQUENCY (Hz)	68.3069		68.3067	
2ND NATURAL FREQUENCY (Hz)	114.298		114.298	
1ST DAMPING RATIO	0.0216419		0.0216420	
2ND DAMPING RATIO	0.0601704		0.0601704	

Table 5: Comparison of DDS and Theoretical Mode Shapes and Natural Frequencies for ACSL-Simulated 2 DOF System With Heavy Damping

PARAMETER	THEORETICAL		DDS	
IST MODE SHAPE	Mag. 1.0 2.50746	Phase(deg) 0.0 14.8578	Mag. 1.0 2.50745	Phase(deg.) 0.0 14.8570
2ND MODE SHAPE	1.0 0.245211	0.0 163.0810	1.0 0.245211	0.0 163.0807
1ST NATURAL FREQUENCY (Hz)	68.7122		68.7122	
2ND NATURAL FREQUENCY (Hz)	113.624		113.624	
1ST DAMPING RATIO	0.212392		0.212392	
2ND DAMPING RATIO	0.606938		0.606936	

Some results of DDS modeling of tool vibrations from reference[8] are reproduced in Table 6. The second mode of tool vibration that is sensitive to tool wear is small compared to other modes and hence difficult to use for tool wear using FFT. Its damping increases with tool wear and the peak corresponding to it altogether disappears from the FFT plot. However, as Table 6 indicates, the DDS model continues to track it even at nearly 30% damping.

Table 6: Tool Vibration Modes With Increasing Tool Wear

Wear (mm)	First Mode		Second Mode	
	Nat. Freq. (Hz)	Damp. Ratio	Nat. Freq. (Hz)	Damp. Ratio
0.000	4340	0.007	8616	0.028
0.175	4320	0.007	8596	0.030
0.225	4276	0.007	8578	0.036
0.288	4328	0.006	8700	0.051
0.338	4354	0.009	8996	0.163
0.400	4526	0.007	9308	0.279

Finally, a comparison of DDS and FFT modal analysis of disc-brake rotor vibrations is partially reproduced from reference[6] in Figure 3. Overestimation of damping by FFT is evident for every model. This study further shows the capability of DDS in resolving repeated roots, characteristic of symmetric structures like rotors, by closely spaced modes that were illustrated by simulation in Table 2.

REFERENCES

[1] Pandit, S.M., 1977, Shock & Vibration Bulletin, **47**, 161-174. Analysis of vibration records by data dependent systems.

[2] Pandit, S.M., 1977, Trans. ASME Journal of Dynamic Systems, Meausrement and Control, **99G,** 221-226. Stochastic linearization by data dependent systems.

[3] Pandit, S.M., Mehta, N.P., 1984, Proceedings of the 2nd International Modal Analysis Conference, 35-43. Data dependent systems approach to modal parameter identification.

[4]   Pandit, S.M., Wu, S.M., 1983, Time Series & System Analysis With Applications, New York: John Wiley.

[5]   Pandit, S.M., Mehta, N.P., 1985, Trans. ASME, Jour. of Dyn. Systems, Measurement and Control, 107, 132-138.   Data dependent systems approach to modal analysis via state space.

[6]   Pandit, S.M., and Jacobson, E.N., 1988, Journal of Sound and Vibration, 122(2).   Data Dependent Systems Approach to Modal Analysis, Part II: Applications to Structural Modifications of a Disc-Brake Rotor.

[7]   Pandit, S.M., Helsel, R.J., and Evensen, H.A., 1986, Proceedings of the 4th Internaitonal Modal Analysis Conference, 414-421, Modal Estimation of Lumped Parameter Systems Using Vector Data Dependent System Models.

[8]   Pandit, S.M., Suzuki, H. and Kahng, C.H., 1980, ASME Journal of Mechanical Design, 102, 233-241, Application of Data Dependent Systems to Diagnostic Vibration Analysis.

[9]   Jenkins, G.M., and Watts, D.G., 1968, Spectral Analysis and Its Application, Holden-Day, San Francisco.

[10] Priestley, M.B., 1981, Spectral Analysis and Time Series, Academic Press, New York.

Figure 1: The Frequency Response

f(t)=10exp(-.01t)sin(2*pi*10t)
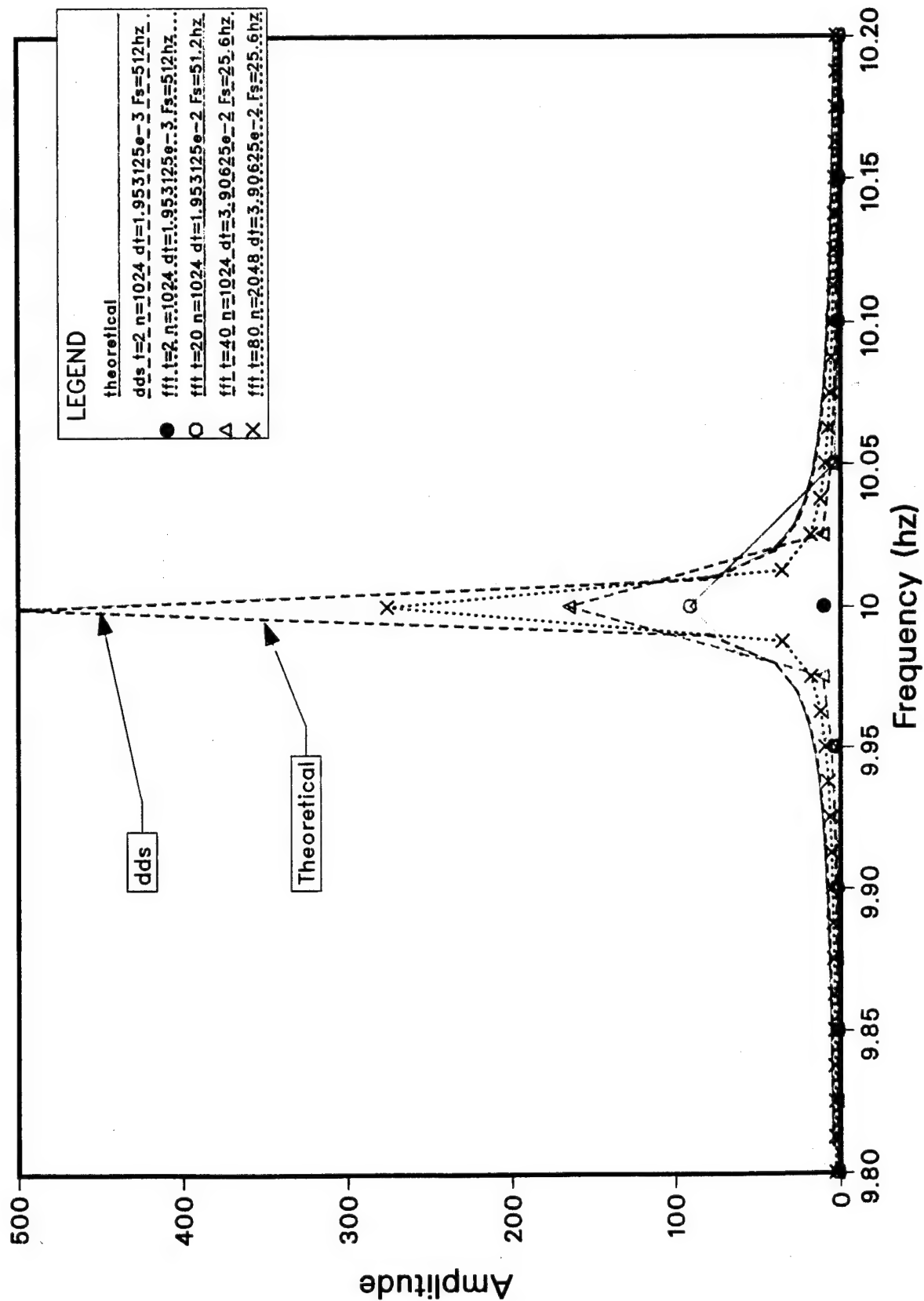
Figure 2: The Frequency Response
of f(t)=10*exp(-10t)*sin(2*pi*5t)

LEGEND
theoretical
dds_t=20_n=256_dt=7.8125e-2
fft.t=20.n=256.dt=7.8125e-2
fft.t=20_n=512_dt=3.90625e-2
fft.t=20_n=1024_dt=1.953125e-2
fft.t=10_n=1024.dt=.9765625e-2

fft Fs=51.2hz
dds Fs=12.8hz
fft Fs=102.4hz
fft Fs=25.6hz
Theoretical
fft Fs=12.8hz

Amplitude

Frequency (hz)
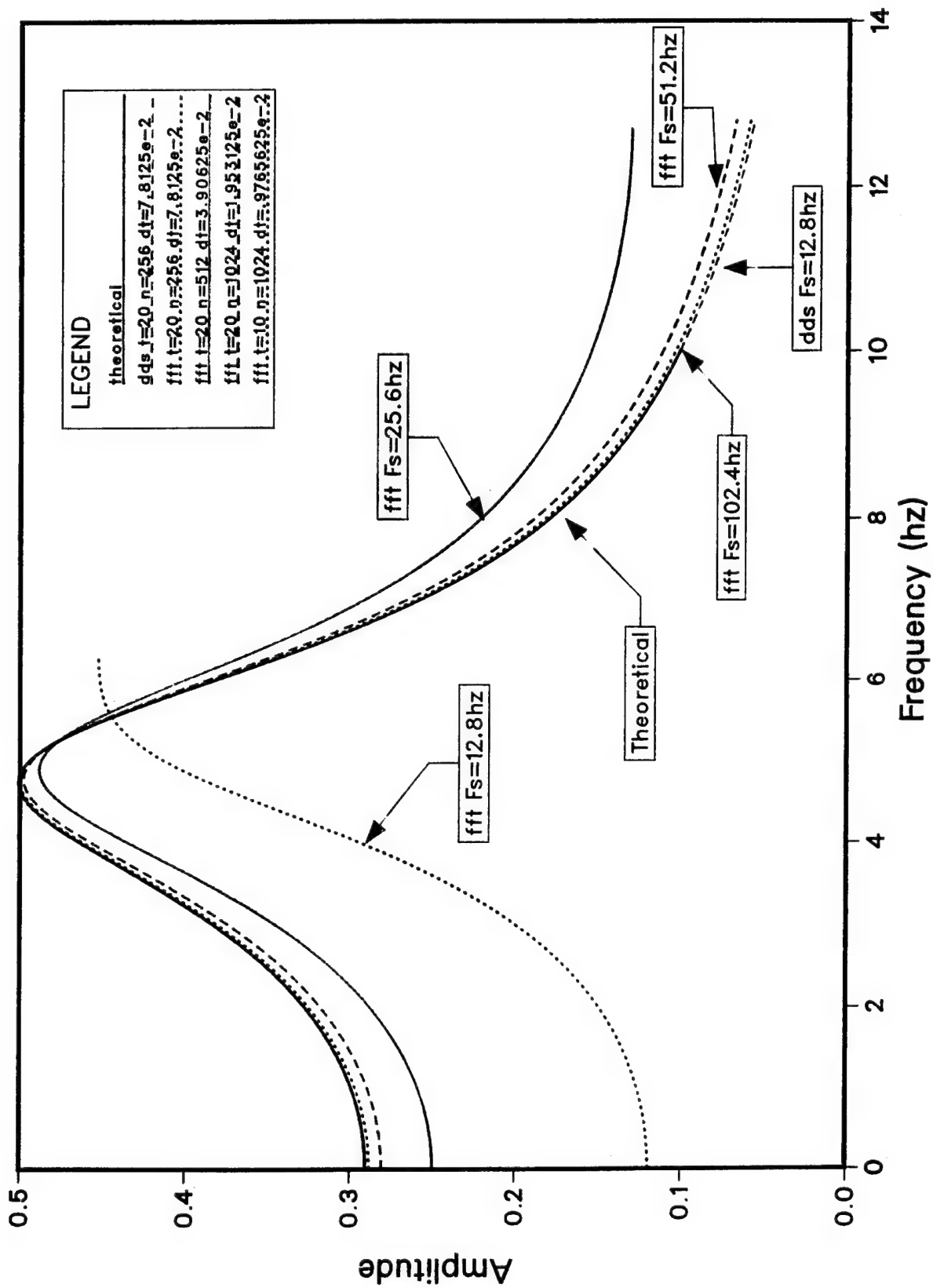
Figure 3: Comparison of DDS and FFT Modal
Analysis of Disc Brake Rotor
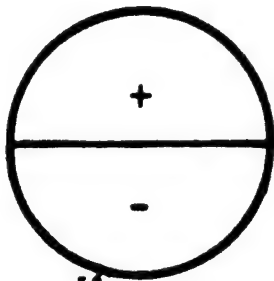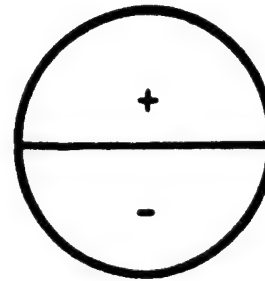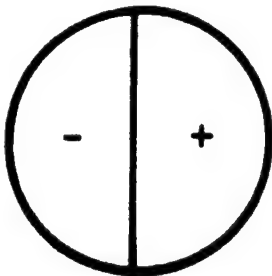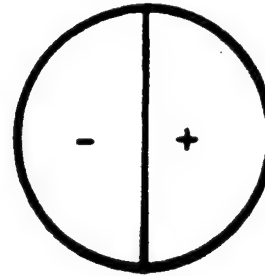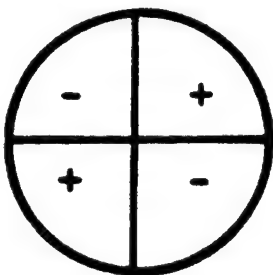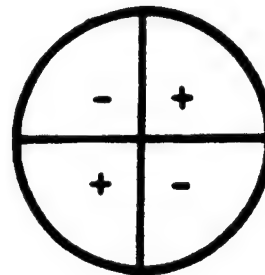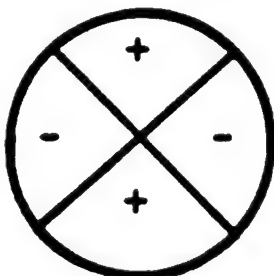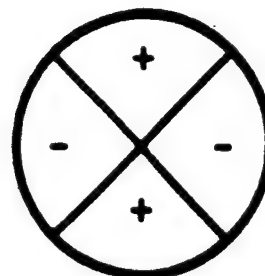
COUPLED MODES RESOLUTION
BY AN EXPONENTIAL WINDOW

A.AGNENI, L.BALIS-CREMA, A.CASTELLANI

Università di Roma "La Sapienza"

Dipartimento Aerospaziale

Via Eudossiana, 16 - 00184 ROMA (Italy)

Ph.no. 463211

ABSTRACT

This paper deals with the identification of coupled modes; the viscous damping ratio can be estimated with good precision by the complex signals generated via the Hilbert transform.

The proposed technique consists in windowing the time domain data with an increasing exponential window in order to decouple the modes by decreasing their half power bandwidths.

Natural frequencies and damping ratios have been estimated in the time domain because of the possible lack of frequency resolution or truncation.

In noise free data the method works quite well, whereas some troubles arise when noisy data is considered; for low noise levels, acceptable estimations can be obtained using an exponential window truncated before the time when the noise level becomes comparable or greater than the signal.

The limits and validity of the proposed approach have been explored considering different amplitudes and different damping ratios of two coupled modes.

1. INTRODUCTION

The identification and resolution of coupled modes is an important topic in the general field of modal analysis and it is a basic point in the aerospace structural design.

The viscous damping ratio estimation, for one or several modes, could be carried out with good precision from the complex signals generated by the Hilbert transform. The Hilbert transform technique permits, starting from the impulse response of a system, to get a complex signal, the real part of which is the original function and the imaginary one is its Hilbert transform.

Filtering one mode at a time, the modulus of the complex signal represents the envelope that exponentially decays, while its argument is the instantaneous phase. The slope of the envelope, in the semi-log plane, is the decay rate, whereas the damped angular frequency is derived from the slope of the instantaneous phase.

It is straightforward to get the natural angular frequency and the viscous damping ratio from the above mentioned estimated parameters.

The method, as said before, only works on a single degree of freedom system, and therefore, when two modes (or more) are excited as considered in this paper, it is necessary to filter the one of interest. This signal processing leads to a distorted envelope because of both the filtering itself [1] and the tail of the rejected mode.

Sometimes, for very tightly coupled modes, it is quite impossible to filter the mode of interest; actually two coupled modes may also appear as a single mode.

In these cases the data in the time domain can be multiplied by an increasing exponential window; the decreasing of the bandwidth of the two coupled modes allows one to filter each mode and then to evaluate with acceptable errors the natural angular frequency and the viscous damping ratio. Nevertheless this technique, as pointed out by Dossing [2], yields unacceptable errors if the parameters estimation is carried out in the frequency domain with the half power method. In fact the new signal could result highly truncated at the end of the observation window and then the half power method leads to an overestimation of the damping ratio [3,4]; on the other hand, the half power bandwidth could become so narrow that it results filled by an insufficient number of spectral lines. In addition the random noise, always present in the experimental time data, is amplified by the exponential window, that, for this reason, must be limited at a time when the impulse response level is still higher than the noise [5].

The parameters evaluation, using the Hilbert transform technique, is carried out from the instantaneous envelope and phase by linear least square regressions, which average out the residual random noise.

2. THEORETICAL BASIS

The impulse response of a system, with N modes excited, can be written as follows:

$$h(t) = \left[\sum_{k=1}^{N} |r_k| \exp(-\sigma_k t) \, \sin(\omega_{dk} + \alpha_k) \right] u(t) \tag{1}$$

where $|r_k|$ is the residue magnitude of the k-th mode, α_k its phase, σ_k the decay rate and ω_{dk} the damped angular frequency (u(t) states the causality of the function).

Hereafter only two real modes will be considered, then h(t) reduces to:

$$h(t) = [|r_1| \exp(-\sigma_1 t) \sin(\omega_{d1} t) + |r_2| \exp(-\sigma_2 t) \sin(\omega_{d2} t)] u(t) \qquad (2)$$

If the modes are close together, calling:

$$\Delta\omega_d = (\omega_{d2} - \omega_{d1}) \qquad (3)$$

with $\omega_{d2} > \omega_{d1}$, the damped angular frequencies are:

$$\left\{ \begin{array}{l} \omega_{d1} = \bar{\omega}_d - \dfrac{\Delta\omega_d}{2} \\[4mm] \omega_{d2} = \bar{\omega}_d + \dfrac{\Delta\omega_d}{2} \end{array} \right. \qquad (4)$$

where $\bar{\omega}_d$ is their average value:

$$\bar{\omega}_d = (\omega_{d1} + \omega_{d2})/2 \qquad (5)$$

The impulse response (2) can be also expressed with the product:

$$h(t) = \{M(t) \sin[\bar{\omega}_d t + \varphi(t)]\} u(t) \qquad (6)$$

wherein the modulation function is equal to:

$$M(t) = \{|r_1|^2 \exp(-2\sigma_1 t) + |r_2|^2 \exp(-2\sigma_2 t) + 2|r_1||r_2| \exp[-(\sigma_1 + \sigma_2)t] \cos(\Delta\omega_d t)\}^{1/2} \qquad (7)$$

and the phase is:

$$\varphi(t) = \text{arctg} \left\{ \frac{|r_2| \exp(-\sigma_2 t) - |r_1| \exp(-\sigma_1 t)}{|r_2| \exp(-\sigma_2 t) + |r_1| \exp(-\sigma_1 t)} \; \text{tg}\left(\frac{\Delta\omega_d}{2} t\right) \right\} \qquad (8)$$

Let us consider the Bedrosian theorem [6,7] valid, at least in limit sense [8], thus the Hilbert transform of the impulse response is given by the following relationships:

$$\overset{\vee}{h}(t) \cong -\{|r_1| \exp(-\sigma_1 t) \cos(\omega_{d1} t) + |r_2| \exp(-\sigma_2 t) \cos(\omega_{d2} t)\} \qquad (9)$$

or

$$\overset{\vee}{h}(t) \cong -M(t) \cos\left[\bar{\omega}_d t + \varphi(t)\right] \qquad (10)$$

The complex signal z(t) formed by the original impulse response and its Hilbert transform:

$$z(t) = h(t) + j\overset{\vee}{h}(t) \qquad (11)$$

permits to obtain the average value of the damped angular frequency from the slope of the total phase:

$$\arctg\left[\frac{\overset{v}{h}(t)}{h(t)}\right] = \bar{\omega}_d t + \varphi(t) - \frac{\pi}{2} \tag{12}$$

in fact, the values assumed by $\varphi(t)$ are in general much smaller than those ones of the linear term; while from the envelope:

$$|z(t)| = \{h^2(t) + \overset{v}{h}^2(t)\}^{1/2} \tag{13}$$

it is possible to get a global decay rate and after dividing by $\bar{\omega}_d$, a damping ratio ζ_c from which the window parameter can be derived:

$$\sigma_w \cong \frac{1}{2}\zeta_c\bar{\omega}_d \tag{14}$$

When the increasing exponential window:

$$w(t) = \left[\exp(\sigma_w t)\right] u(t) \tag{15}$$

is multiplied by the impulse response:

$$h_w(t) = h(t)\,w(t) \tag{16}$$

the half power bandwidths of the two coupled modes reduce to $[2(\sigma_1 - \sigma_w)]$ and $[2(\sigma_2 - \sigma_w)]$ respectively. After this reduction it is possible to evaluate the damping ratios either by the half power method or by the Hilbert transform approach (Figure 1).
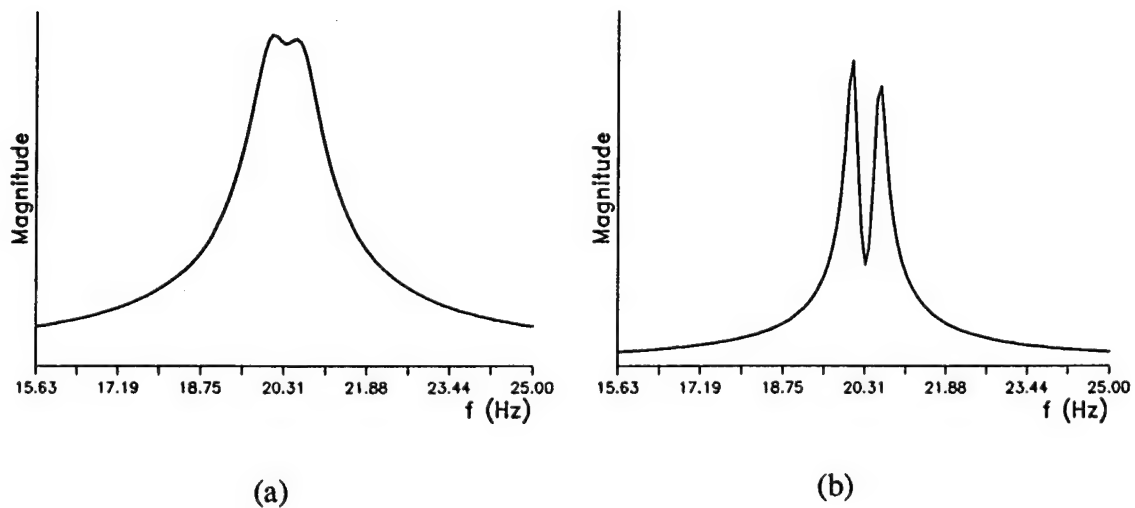
Fig.1 - Magnitudes of Frequency Response Functions derived from unwindowed (a) and windowed time histories (b).

Some troubles can arise with the first method, in fact the bandwidth of the mode of interest could be so narrow that an insufficient number of spectral lines is contained within it, besides for small decay rates the windowed impulse response can be truncated at the end of the observation time and that leads to overestimated damping ratios [3,4].

On the contrary, evaluations, carried out in the time domain through the complex signals obtained by the Hilbert transform, seem not to feel the effects of either the truncation[4] or the poor frequency resolution [5].

Actually this method must be applied to a mode at a time and thus the mode of interest has to be filtered in order to obtain its decay rate from the slope of the envelope (in the semi-log plane) and its damped angular frequency from the slope of the total phase [4,8].

The scheme of the technique used in the numerical tests and based on the Hilbert transform is presented in Figure 2.

Some noise is always present in an impulse response derived from experimental tests, therefore when the exponential window is applied, whereas $h_w(t)$ decreases, the additive noise, supposed as incorrelated with the impulse response and with zero mean value, results amplified [2]:

$$h_w^n(t) = h_w(t) + n(t)\ w(t) \tag{17}$$

For this reason the time duration of the increasing exponential window must be limited at the time t_0, when the level of the impulse response is higher than the noise [5]:

$$h_w^n(t;t_0) = h_w^n(t)\ \text{rect}\ [(t-t_0/2)/t_0] \tag{18}$$

Attention must be paid to the length of the observation time, in fact if t_0 is too short the main lobe of the Dirichlet kernel becomes so wide that the coalescence of the two peaks occurs in the frequency domain [9] and neither filtering nor parameters evaluation can be carried out.

The possibility to separate two coupled modes was investigated by Pendered [10], who calculated the critical value of the dimensionless quantity:

$$\tau = \frac{\varepsilon}{2\zeta_1} \qquad \text{or} \qquad \tau = \frac{\varepsilon}{2\zeta_2} \tag{19}$$

where:

$$\varepsilon = 1 - \left(\frac{\omega_{n2}}{\omega_{n1}}\right)^2 \tag{20}$$

and $\omega_{n2} > \omega_{n1}$. For $\tau < \tau_{cr}$ it is not possible to separate the modes and only one natural frequency can be found. If equal damping ratios are considered, the common critical value can be achieved from the following relationship:

$$\zeta_{cr} = \frac{\Delta\omega_n}{\tau_{cr}\omega_{n2}\left[1+\frac{\Delta\omega_n}{2\bar{\omega}_n}\right]} \cong \frac{\Delta\omega_n}{\tau_{cr}\omega_{n2}} \tag{21}$$

where $\Delta\omega_n$ is the difference between the two natural frequencies, while $\bar{\omega}_n$ is their mean value (ω_{n2} appears because the mode with the widest half power bandwidth has been considered).
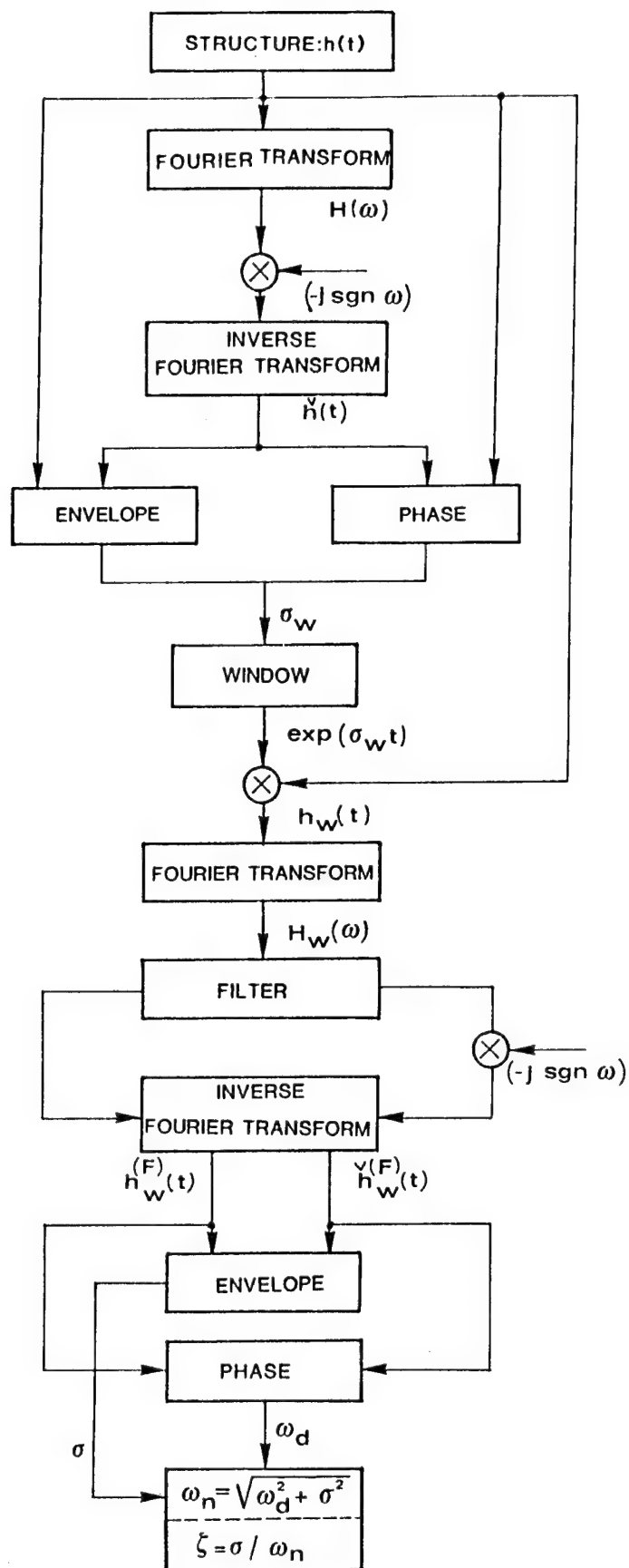
Fig.2 - Procedure for the window parameter estimation, for the natural frequency and damping ratio evalution of two coupled modes.

As shown by Pendered, τ_{cr} depends on the method used to analyse the frequency response function, in particular the maximum frequency spacing technique, introduced by Kennedy and Pancu [11], is the most sensible, i.e. it has the lowest τ_{cr} and then it permits to single out the presence of two modes when the other methods fail.

3. NUMERICAL TESTS AND COMPARISONS

Numerical simulations have been carried out using the Hilbert approach, that seems to give more reliable results [4,8].

As it is necessary to filter the spectrum of the impulse response, the discrete Fourier transform has been used in order to get the discrete Hilbert transform; for this purpose a null buffer, the length of which was equal to the data block, has been added at the end of the time samples so that the circularity of convolution is avoided.

In Table 1 estimations derived from two coupled modes, with one of the residue decreasing are shown.

$|r_1|$	$\hat{f}_1$	$|\varepsilon_{f1}|$ (%)	$\hat{\zeta}_1$	$|\varepsilon_{\zeta 1}|$ (%)	$\hat{f}_2$	$|\varepsilon_{f2}|$ (%)	$\hat{\zeta}_2$	$|\varepsilon_{\zeta 2}|$ (%)
10	20.001599	0.0109	0.004603	7.9317	20.497197	0.0137	0.004912	1.7617
7	19.993841	0.0308	0.004475	10.4954	20.494073	0.0289	0.005021	0.4220
5	19.998928	0.0054	0.004724	5.5280	20.503985	0.0194	0.004763	4.7323
3	19.977730	0.1113	0.004402	11.9654	20.500705	0.0034	0.004674	6.5168
1	20.019244	0.0962	0.005918	18.3534	20.492994	0.0342	0.004669	6.6256

$|r_2| = 10$; $f_1 = 20$ (Hz); $f_2 = 20.5$ (Hz); $\zeta_1 = \zeta_2 = 0.005$

Table 1 - Coupled modes with the same damping ratio ($\zeta_1 = \zeta_2 = 0.005$) and one variable residue

The errors in the damping ratio evaluation increase as the ratio $|r_1|/|r_2|$ decreases, in fact the two half power bandwidths remain constant and then the interaction between the greater mode and the smaller one becomes more significant.

The same cases are presented in Table 2, where natural frequencies and damping ratios are evaluated applying the method of the increasing exponential window; the errors are always negligible and however much lesser than those ones obtained from a direct estimation.

$|r_2| = 10;$ $f_1 = 20$ (Hz); $f_2 = 20.5$ (Hz); $\zeta_1 = \zeta_2 = 0.005$								
$|r_1|$	$\hat{f}_1$	$|\varepsilon_{f1}|$ (%)	$\hat{\zeta}_1$	$|\varepsilon_{\zeta 1}|$ (%)	$\hat{f}_2$	$|\varepsilon_{f2}|$ (%)	$\hat{\zeta}_2$	$|\varepsilon_{\zeta 2}|$ (%)
10	19.997749	0.0113	0.005023	0.4685	20.502273	0.0111	0.004990	0.1957
7	19.997583	0.0121	0.005025	0.5077	20.501585	0.0077	0.005017	0.3300
5	19.996528	0.0174	0.004981	0.3769	20.501337	0.0065	0.005003	0.0526
3	19.995084	0.0246	0.005118	2.3586	20.500651	0.0032	0.005014	0.2765
1	19.986315	0.0684	0.005003	0.0589	20.500233	0.0011	0.004993	0.1469

Table 2 - Coupled modes with variable amplitudes (increasing exponential window)

In Tables 3 and 4 similar numerical simulations are shown; due to the higher damping ratios, worse evaluations than those in Table 1 have been obtained, nevertheless also in this case the use of the proposed technique permits to obtain good results.

$|r_2| = 10$; $f_1 = 20$ (Hz); $f_2 = 20.5$ (Hz); $\zeta_1 = \zeta_2 = 0.01$								
$|r_1|$	$\hat{f}_1$	$|\varepsilon_{f1}|$ (%)	$\hat{\zeta}_1$	$|\varepsilon_{\zeta 1}|$ (%)	$\hat{f}_2$	$|\varepsilon_{f2}|$ (%)	$\hat{\zeta}_2$	$|\varepsilon_{\zeta 2}|$ (%)
10	19.973086	0.1346	0.008041	19.5950	20.536197	0.1766	0.007115	28.8508
7	20.016101	0.0805	0.007161	28.3903	20.455063	0.2192	0.008976	10.2372
5	20.041772	0.2089	0.009051	9.4935	20.477664	0.1090	0.007062	29.3810
3	19.987569	0.0622	0.006886	31.1412	20.544468	0.2169	0.007089	29.1125

Table 3 - Coupled modes with one variable amplitude and higher damping ratios

$|r_1|$	$\hat{f}_1$	$|\varepsilon_{f1}|$ (%)	$\hat{\zeta}_1$	$|\varepsilon_{\zeta1}|$ (%)	$\hat{f}_2$	$|\varepsilon_{f2}|$ (%)	$\hat{\zeta}_2$	$|\varepsilon_{\zeta2}|$ (%)
10	19.998091	0.0096	0.010012	0.1223	20.501640	0.0080	0.010009	0.0892
7	19.997747	0.0113	0.009988	0.1167	20.500241	0.0012	0.010017	0.1704
5	19.997330	0.0133	0.010055	0.5468	20.500887	0.0043	0.009986	0.1391
3	19.998745	0.0063	0.010091	0.9120	20.500416	0.0020	0.010003	0.0341

Table with header: $|r_2| = 10$; $f_1 = 20$ (Hz); $f_2 = 20.5$ (Hz); $\zeta_1 = \zeta_2 = 0.01$

Table 4 - Increasing exponential windows applied to coupled modes with one variable amplitude

When modes with variable coupling due to different damping ratios are considered (Table 5), better evaluations have been achieved, expecially for the mode with the smaller damping ratio, because it gets predominant while its half power bandwidth narrows. For these reasons the tail of the rejected mode, present in the bandpass filter used before the processing that permits to get the envelope and phase, is smaller and smaller and therefore an acceptable estimation of ζ_2 and at the same time an improvement of ζ_1 have been obtained for the last case.

ζ_2	$\hat{f}_1$	$|\varepsilon_{f1}|$ (%)	$\hat{\zeta}_1$	$|\varepsilon_{\zeta1}|$ (%)	$\hat{f}_2$	$|\varepsilon_{f2}|$ (%)	$\hat{\zeta}_2$	$|\varepsilon_{\zeta2}|$ (%)
0.01	19.973075	0.1346	0.007971	20.2923	20.538392	0.1873	0.007670	23.2974
0.007	19.950628	0.2469	0.007976	20.2324	20.531764	0.1588	0.005662	19.1099
0.003	19.962001	0.1900	0.008379	16.2111	20.501625	0.0079	0.029280	2.3914

Table with header: $|r_1| = |r_2| = 10$; $f_1 = 20$ (Hz); $f_2 = 20.5$ (Hz); $\zeta_1 = 0.01$

Table 5 - Coupled modes with variable coupling

The use of an exponential window leads to very good results (Table 6) if the damping ratios of the two modes are similar, whereas if the damping ratios are different enough as in the case $\zeta_1 = 0.01$ and $\zeta_2 = 0.003$ it is convenient to apply a first window, the parameter of which is determined from the initial part of the envelope where the most

damped mode is still present, in order to estimate ζ_1 and a second window, derived from the second part of the envelope, for ζ_2. Actually for the second mode it could be possible to evalutate the damping ratio directly, without any window, from the envelope of the two coupled modes when the first of them is damped out.

$|r_1| = |r_2| = 10$;$f_1 = 20$ (Hz); $f_2 = 20.5$ (Hz); $\zeta_1 = 0.01$								
ζ_2	$\hat{f}_1$	$|\varepsilon_{f1}|$ (%)	$\hat{\zeta}_1$	$|\varepsilon_{\zeta1}|$ (%)	$\hat{f}_2$	$|\varepsilon_{f2}|$ (%)	$\hat{\zeta}_2$	$|\varepsilon_{\zeta2}|$ (%)
0.01	19.998411	0.0079	0.009992	0.0815	20.501839	0.0090	0.009954	0.4574
0.007	19.999648	0.0018	0.010003	0.0318	20.502988	0.0146	0.007006	0.0852
0.003	20.022103	0.1105	0.011088	10.8792	20.501602	0.0078	0.003004	0.1457

Table 6 - Estimation obtained with the proposed technique for the examples of Table 5

In Table 7 both the damping ratios are variable and the estimations have been only carried out by the exponential window approach. The results are always acceptable also in that case ($\zeta_1 = \zeta_2 = 0.03$) wherein it is not possible to discern the presence of two modes from the frequency response function.

This damping ratio is critical, for the theoretical study carried out by Pendered, for all the methods used in the frequency domain, except for the Kennedy-Pancu technique that permits, only with an accurate study of the frequency spacing, to single out that two close natural frequencies are present.

Actually the presence of two modes could be revealed from the envelopes [12], in fact if only one mode is present in the frequency response function its envelope in the semi-log plane is represented by a straight line, on the contrary for two modes the slope is not constant due to the modulation, see relationship (7), Figure 3.

(a)   (b)
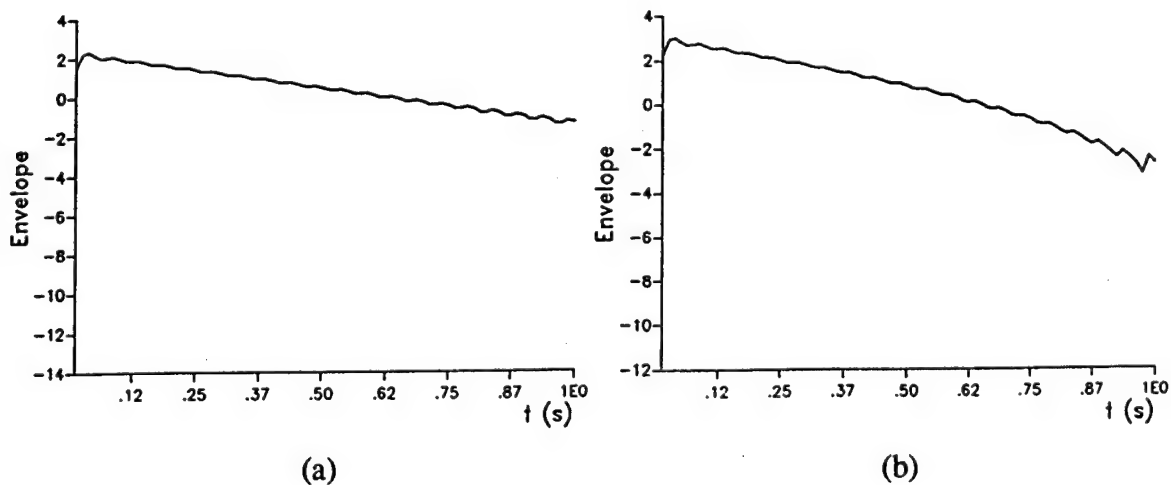
Fig. 3 - Envelopes of a single mode (a) and of two tightly coupled modes (b)

$\zeta_1=\zeta_2$	$\hat{f}_1$	$\lvert\varepsilon_{f1}\rvert$ (%)	$\hat{\zeta}_1$	$\lvert\varepsilon_{\zeta 1}\rvert$ (%)	$\hat{f}_2$	$\lvert\varepsilon_{f2}\rvert$ (%)	$\hat{\zeta}_2$	$\lvert\varepsilon_{\zeta 2}\rvert$ (%)
0.015	19.999378	0.0031	0.014857	0.9565	20.499313	0.0034	0.015079	0.5293
0.02	20.004927	0.0246	0.020207	1.0343	20.499645	0.0017	0.020230	1.1476
0.025	20.016885	0.0844	0.023802	4.7916	20.468004	0.1561	0.024475	2.0996
0.03	19.977632	0.1118	0.026540	11.5340	20.507453	0.0364	0.026589	11.3712

Table 7 - Two modes with different damping ratios

The window parameter, evaluated with the abovementioned technique, resulted too small and therefore the modes remained rather coupled and errors greater than 10% , in the last case, are due to the high influence of the tails within the filter. An interactive procedure permits to get much better results, in fact using $\sigma_w = 3.2$ (rad/s) the following results have been obtained: $\hat{\zeta}_1 = 0.03008$ and $\hat{\zeta}_2 = 0.02966$.

An evalutation from modes with low frequencies and damping ratios is presented in Table 8. It is interesting to note that, even if the theoretical critical value of the damping ratio is far from the ones considered, the half power bandwidths of the two modes equals $(2\sigma) \cong 0.0025$ (rad/s), whereas the angular frequency spacing is $\delta\omega = 0.0049$ (rad/s) and therefore it is impossible to use the half power method.

$\lvert r_1\rvert = \lvert r_2\rvert = 10$; $f_1 = 0.2$ (Hz); $f_2 = 0.201$ (Hz); $\zeta_1 = \zeta_2 = 0.001$				
	$\hat{\zeta}_1$	$\lvert\varepsilon_{\zeta 1}\rvert$ (%)	$\hat{\zeta}_2$	$\lvert\varepsilon_{\zeta 2}\rvert$ (%)
raw data	0.000849	15.1337	0.000873	12.6637
windowed data	0.000991	0.8626	0.001043	4.2762

Table 8 - Coupled modes with low frequencies and damping ratios

In order to simulate the noise present in an actual acquisition, a random noise with zero mean value and standard deviation given in per cent of the residue

magnitude has been added to the impulse response. If an increasing exponential window is applied, the impulse responses still result exponentially damped, whereas the noise is amplified and therefore if the modes are damped out before the end of the observation time and all the data block is employed a useless frequency response function is obtained. For this reason the time window must be limited at an instant when the noise level is lower than the function. In Table 9 examples with different σ_N of the added noise are presented, errors less than 10% have been obtained also in the worst condition. Actually the considered noise is relatively low, therefore in a high noise environment it is necessary to process the impulse response in order to decrease the noise level.

$\|r_1\| = \|r_2\| = 10 ;$		$f_1 = 20$ (Hz);		$f_2 = 20.5$ (Hz);		$\zeta_1 = \zeta_2 = 0.01$		
σ_N (%of$\|r\|$)	$\hat{f}_1$	$\|\varepsilon_{f1}\|$ (%)	$\hat{\zeta}_1$	$\|\varepsilon_{\zeta1}\|$ (%)	$\hat{f}_2$	$\|\varepsilon_{f2}\|$ (%)	$\hat{\zeta}_2$	$\|\varepsilon_{\zeta2}\|$ (%)
0.03	19.981120	0.0944	0.009719	2.8063	20.535809	0.1747	0.009445	5.5506
0.07	19.957235	0.2138	0.009537	4.6306	20.547187	0.2302	0.009425	5.7464
0.10	19.945065	0.2747	0.009410	5.8980	20.552418	0.2557	0.009341	6.5945

Table 9 - Estimations from noisy impulse responses

4. CONCLUDING REMARKS

A precise evaluation of natural frequencies and damping ratios of tightly coupled modes can be obtained by windowing the impulse response with an increasing exponential function.

The numerical tests have been carried out using the complex signals generated via the Hilbert trasform because estimations in the frequency domain could have been affected by poor frequency resolution and truncation effects.

The method suggested in this paper has leaded, in all the considered cases, to good results and for many examples the errors in the damping ratio estimations have been reduced to immaterial values.

Troubles can arise when very different damping ratios are considered, in fact in this case it is convenient to use a first window, in order to obtain an acceptable damping ratio estimation for the most damped mode and a second one for the other mode.

Also in presence of an additive random noise the method gave acceptable results; due to the amplification of the noise by the increasing exponential window, it is necessary to limit its duration up to the time when the noise level is less than the signal. This implies a preprocessing of the time data in order to increase the signal to noise ratio when high noise measurements are encountered.

5. REFERENCES

[1]   J.Soovere, M.L.Drake: "Aerospace Structure Technology. Damping design guide. Vol.I - Technology Review"
AFWL - TR - 84- 3089, 1085, pp.6-8/6-10

[2]   O.Dossing: "A method of determining the modal frequencies of structures with coupled modes"
Bruel &Kjaer Technical Review, 1986 no.3,pp.3-22

[3]   R.G.White: "Use of transient excitation in the dynamic analysis of structures"
Journal of the Royal Aeronautical Society, 73, 1969, pp.1047-1050

[4]   A.Agneni, L.Balis-Crema: "Damping measurements from truncated signals via Hilbert transform"
Mechanical System and Signal Processing, Vol.3,no.1, January 1989

[5]   A.Agneni: "Investigation into the use of an exponential window in the damping ratio estimation"
(to be published)

[6]   E.Bedrosian: "The analytic signal representation of modulated waveforms"
Proc. IRE, 50, 1962, pp.2071-2076

[7]   E.Bedrosian: "A product theorem for Hilbert transform"
Proc. IEEE, 51, 1963, pp.868-869

[8]   A.Agneni, L.Balis-Crema: "Analytic signals in the damping coefficient estimation"
ESA/CNES/DFVLR International Conference on "Spacecraft structures and mechanical testing", Nordwijk, The Netherlands, 19-21 Oct. 1988
ESA SP - 289

[9]   M.Kunt: "Traitement numérique des signaux"
Dunod, Lousanne 1981, pp.121-123

[10]   J.W.Pendered:"Theoretical investigation into the effects of close natural frequencies in resonance testing"
Journal Mechanical Engineering Science, Vol.7 no.4, 1965, pp.372-379

[11]   C.C.Kennedy, C.D.P. Pancu: "Use of vectors in vibrating measurements and analysis"
Journal of the Aeronautical Sciences, Vol.14 no.11, Nov.1947, pp.603-625

[12]   G.Collot: "A new method for loss factor measurements, using the Hilbert transform, implementation in a software to automatize the Oberst method"
Proc.of the 7th.IMAC Conference, London, April 6-9, 1987, pp.389-393

6. AKNOWLEDGEMENTS

PASSIVE DAMPING DESIGN METHODS USING NASTRAN

Michael J. Matla

Eastman Kodak Company
Federal Systems Division
Rochester, New York 14653-9527
(716) 726-0577

Abstract:

Improved finite element methods for the design and analysis of passive damping treatments in complex structures have been developed. These methods account for the non-linear properties of the viscoelastic materials commonly used in damping treatments and were implemented in the design of a constrained layer damping treatment for a large ring-and-truss structure. Modal damping for this structure was analytically predicted and then experimentally measured to verify the accuracy of these methods.

Specifically, a simplified method for modeling constrained layer damping treatments in finite element analysis was developed. This reduces the number of degrees-of-freedom required permitting faster and less costly analysis while accurately modeling the dynamic effects of the treatment.

A Damping design program was also developed which calculates modal damping for any number of modes simultaneously. The program accounts for the non-linear properties of viscoelastic materials and allows quick evaluations of designs. It is based on the modal strain energy method and utilizes Nastran strain energy calculations from complete dynamic math models.

Lastly, an enhanced Nastran-based modal frequency response analysis method for damped structures was developed. The analysis generates response curves using a non-orthogonal eigenstructure created by the above-mentioned design program to account for the non-linear properties of the viscoelastic materials used. This model is more representative of the damped structure than that of a conventional, constant stiffness model.

Table of Contents

Introduction

Large complex structures are typically designed and analyzed using finite element analysis (FEA). Visco-elastic materials (VEM) are being used to passively damp their vibration for improved performance, and to increase stability in active control systems. Analysis of a damping treatment design must involve the structure so it is only logical that it too be done in FEA. The modal strain energy method (MSE method) is a manner of calculating damping values which works well with FEA. It was therefore employed in the damping design program discussed in this paper. Implementation of FEA to damping design presents one problem. Conventional FEA solutions assume linear materials and utilize a constant stiffness matrix. This is inaccurate when non-linear VEM constitute part of the model. To overcome this, the damping design program employs the use of a family of FEA models which differ only in their VEM modulus values. The values cover the analysis frequency range. The program then interpolates the modal properties of not only modal damping and eigenvalues, but also the eigenvectors from among the discrete states presented by this family of finite element models.

With the total eigenstructure now defined, it is possible to create an enhanced frequency response (FR) analysis solution to utilize this eigenstructure, which better represents the true dynamics of the structure with VEM damping.

A simplified method to model constrained layer (CL) damping in FEA was also developed which reduces the number of degrees-of-freedom (DoF), and hence time and cost, for coverage on beam members.

All these methods were developed for use with MSC/Nastran.

1.0 Simplified Finite Element Modeling of Constrained Layer Damping

The MSE method requires accurate modeling of the damping materials in the structure to be analyzed. Previous to this study, CL damping treatments were modeled in FEA using solid elements for the damping material, and plate elements for the CL. This required at least two grid points across the width. Since the damping material thicknesses are typically quite small compared to other structural dimensions, aspect ratio concerns dictated the need for many elements along the length to model the treatment. If the structure was curved, even more elements were required. This can lead to very large models which are time consuming and expensive. The objective was to develop a simpler method of modeling the treatment in FEA by requiring fewer DoF.

The method developed proved to greatly reduce analysis time while sacrificing little in the way of accuracy. It utilizes spring elements and concentrated masses to model the damping material's stiffness and mass. Grid points from the structure are rigidly attached to one set of coincident-pair grid points placed at the damping material's center of thickness. Three concentrated springs connect the coincident-pair grid points' three translational DoF. Spring rates are based on area percentages of the damping material in the vicinity of each. The CL is modeled by bar elements whose end DoFs are offset to the other grid point of the spring pair. By modeling the damping material this way, only one DoF through the treatment width is necessary versus two for the solid element method. Figure 1 illustrates this method of modeling.

Results from a Nastran model of a cantilevered beam with a constrained layer damping treatment showed that modeling the damping material with springs results in frequencies for the bending modes within 2% of those calculated using solid elements (see table 1). Strain energy calculations for the first three bending modes were within 2%. Error in strain energy for higher modes increased rapidly, due to coarseness of the model for these higher modes. Computer run time, and therefore costs, were 55 percent lower for the spring modeling versus the solid modeling due to the fact that only one grid point through the treatment width is necessary for the springs. Table 1 compares frequency and strain energy calculations using solid elements and the spring elements in Nastran.
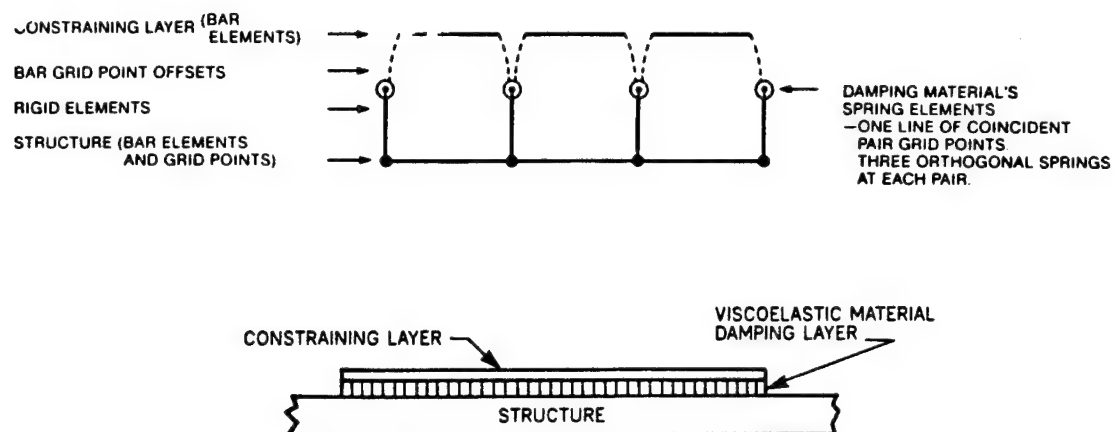
FIGURE 1: Modeling of Constrained Layer Damping Using Spring Elements.

TABLE 1
Accuracy of Simplified Modeling Method
Cantilevered Beam with Constrained Layer Damping

		Solid Elements		Springs	
Run Time (sec)		308		132	
Bending Mode					
1	Hz.	16.6		16.4	
	%SE		17.8		17.8
2		107.6		106.6	
			23.1		23.1
3		269		266	
			14.9		15.2
4		503		496	
			8.4		9.2
5		814		799	
			5.1		6.1

2.0 Damping Design Program

A damping design program has been written which calculates both modal damping values, and a corrected eigenstructure for use in dynamic analysis of structures damped by VEM. The term eigenstructure refers to both the eigenvalues and eigenvectors of a structure's math model.

The program is based on the MSE method * , whose basic principle is:

$$\eta^{(r)} = \sum_{j=1}^{M} \eta_j \frac{SE_j^{(r)}}{SE_{Total}^{(r)}}$$

where

$\eta^{(r)}$ = damping loss factor for mode (r).

η_j = material loss factor for material region, j .

$SE_j^{(r)}$ = strain energy in material region, j, for mode (r).

$SE_{Total}^{(r)}$ = total strain energy for mode (r).

The design program consists of four segments, which are run in series to complete an entire design and analysis.

The program uses Nastran real eigenvalue finite element solutions to calculate the structure eigenvalues, eigenvectors, and strain energy in each material for each mode of interest. Since the moduli and loss factors for VEMs are strong functions of frequency, a single analysis would not result in accurate frequencies and mode shapes over a wide frequency range. This is overcome by performing a series of real eigenvalue analyses on the same structure, which differ only in the value of the VEM's modulus. The modulus values correspond to frequencies which are logarithmically spread over the analysis bandwidth.

---

* Johnson, Conor D. and David A. Kienholz. Finite Element Prediction of Damping in Structures with Constrained Viscoelastic Layers. AIAA Journal, Vol. 20, No. 9, Sept. 1982, pp. 1284-1290.

The F06 output file from each Nastran run is read into the first segment, named GET_SD for " get strain data" , where mode frequencies, and percentage of mode strain energy for all user defined material groups, are extracted for each user identified mode of interest. The loss factor for all material groups other than the VEM group are also entered. This segment is done for each Nastran run, creating a separate output file for each. Although the damping design program can only work on one VEM type at a time, the identification and use of multiple material groups allows for the computation of damping contribution from frequency independent mechanisms, such as frictional and structural damping.

The second segment, named SORT_SD for " sort strain data", reads in all the output files from GET_SD and organizes the data into two matrices: 1) modal frequency versus VEM modulus for each mode, and 2) percentage of modal strain energy in each material region versus VEM modulus for each mode. This data contains two very important functions of the structure: 1) modal frequency versus VEM modulus, for each mode, and 2) percentage strain energy in the VEM versus it's modulus, for each mode. Third order and fourth order polynomials are fitted to this data, respectively, to simplify it's handling and further calculation operations. The equations are included in SORT_SD's output file along with plots of these two functions. Figures 2 and 3 are examples of these plots.

The third segment, named MSEM, is where the calculation of modal damping and the interpolation of eigenvalues occur. Two functions of the VEM under consideration are supplied to MSEM, namely: 1) VEM modulus versus frequency, and 2) VEM loss factor versus frequency. Third order polynomial functions are fitted to this data, and plots are created so that the user can verify the accuracy of the curve fitting (see Figures 4 and 5 for examples). The program then calculates modal damping by first finding the intersection points of the VEM's modulus versus frequency function   (Figure 4) with that of the structures (Figure 2), for each mode. Figure 6 illustrates this operation. This gives the frequency at which each mode of the structure with this VEM damping treatment will vibrate, and the modulus that the VEM will have for each mode. With the modal frequencies now determined, the loss factor of the VEM can be found for each mode from the polynomial for VEM loss factor versus frequency (Figure 5). Likewise, with the VEM modulus known for each mode, the percentage strain energy in the VEM can be found from the structure functions of strain energy versus modulus of the VEM material (Figure 3). The
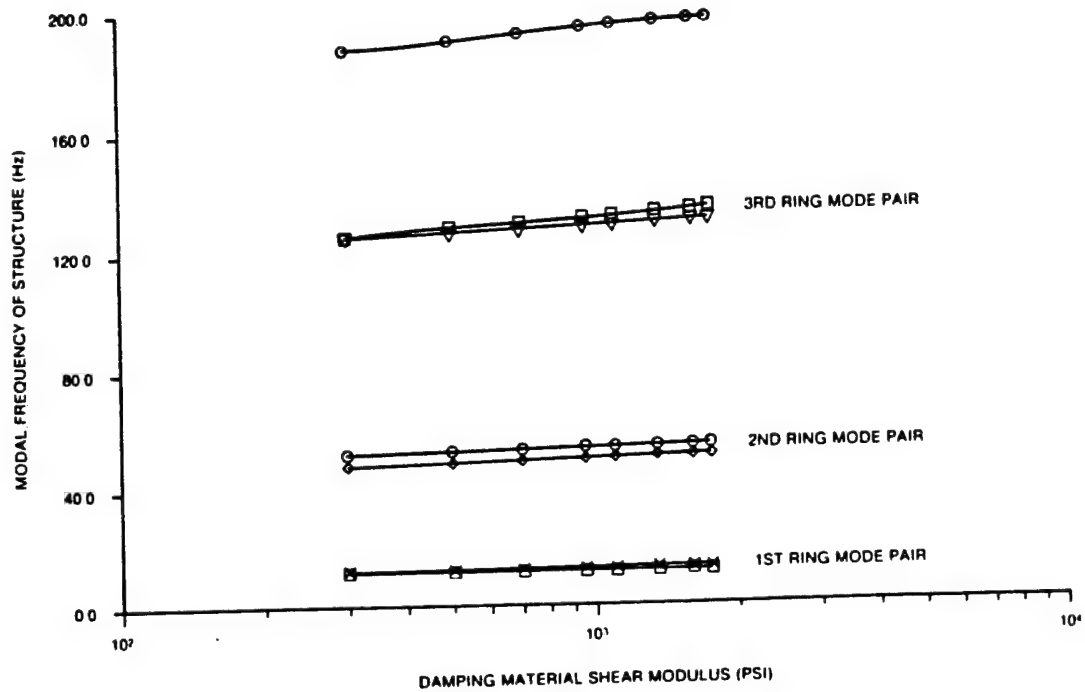
FIGURE 2:   Modal Frequency of Structure versus Damping Shear Modulus,
             SORT-SD Program; Model: Ring/Truss Structure.
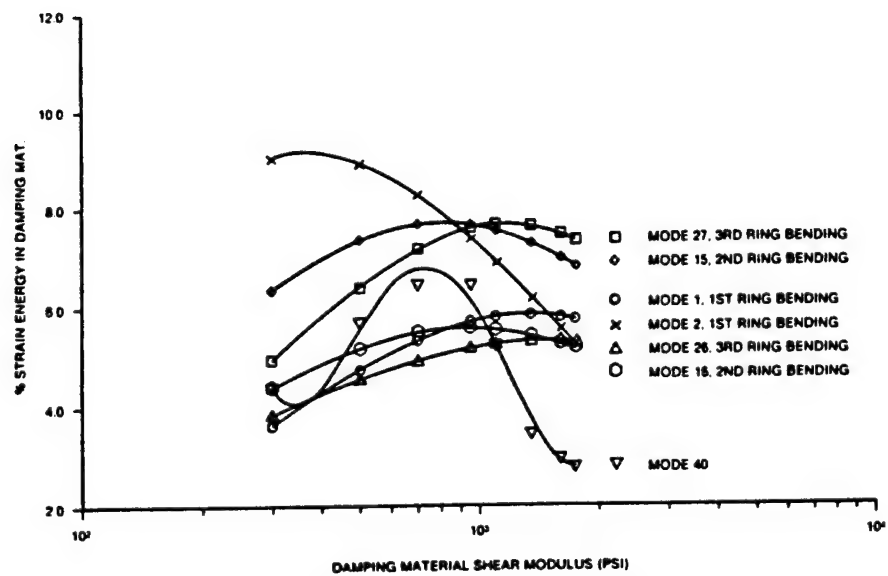
FIGURE 3:   Percentage Strain Energy in Damping Material verus Damping
             Shear Modulus, SORT-SD Program; Model: Ring/Truss Structure.

CCA-8
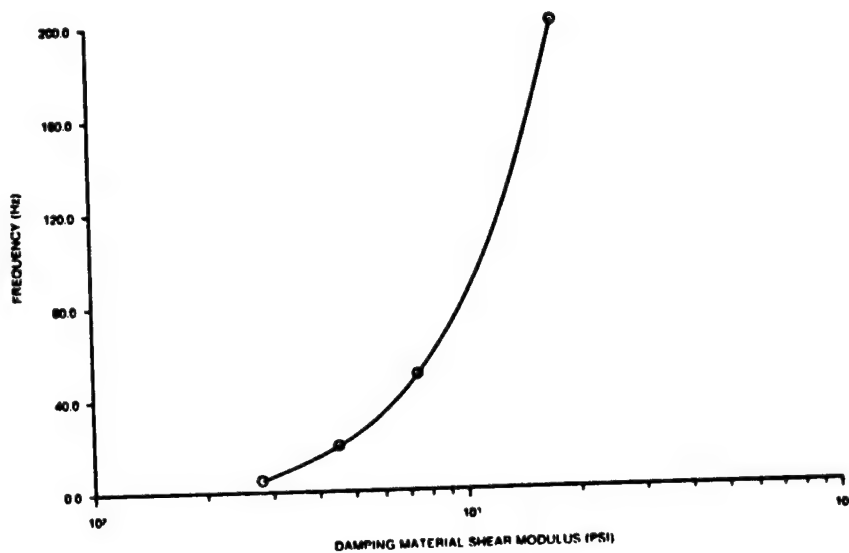
FIGURE 4: Damping Material Shear Modulus as a Function of Frequency, MSEM Program. Damping Material: 3M–4945.
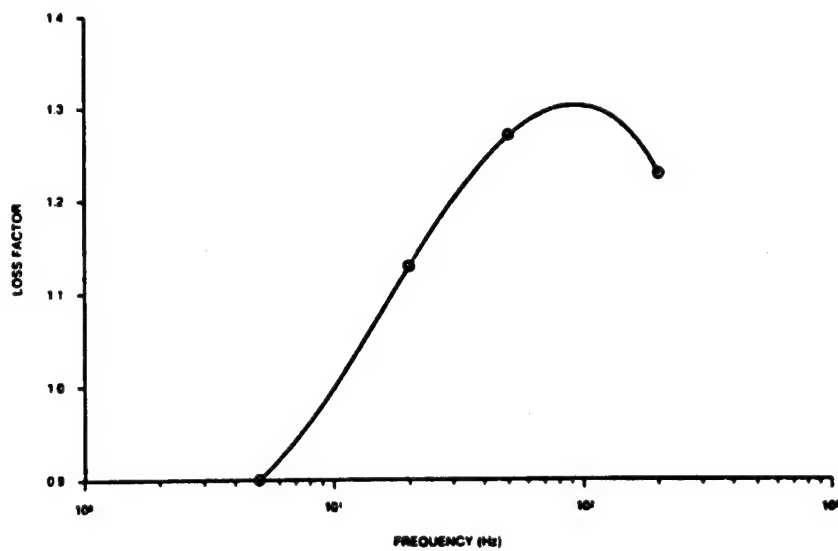
FIGURE 5: Damping Material Loss Factor versus Frequency, MSEM Program Damping Material: 3M–4945.
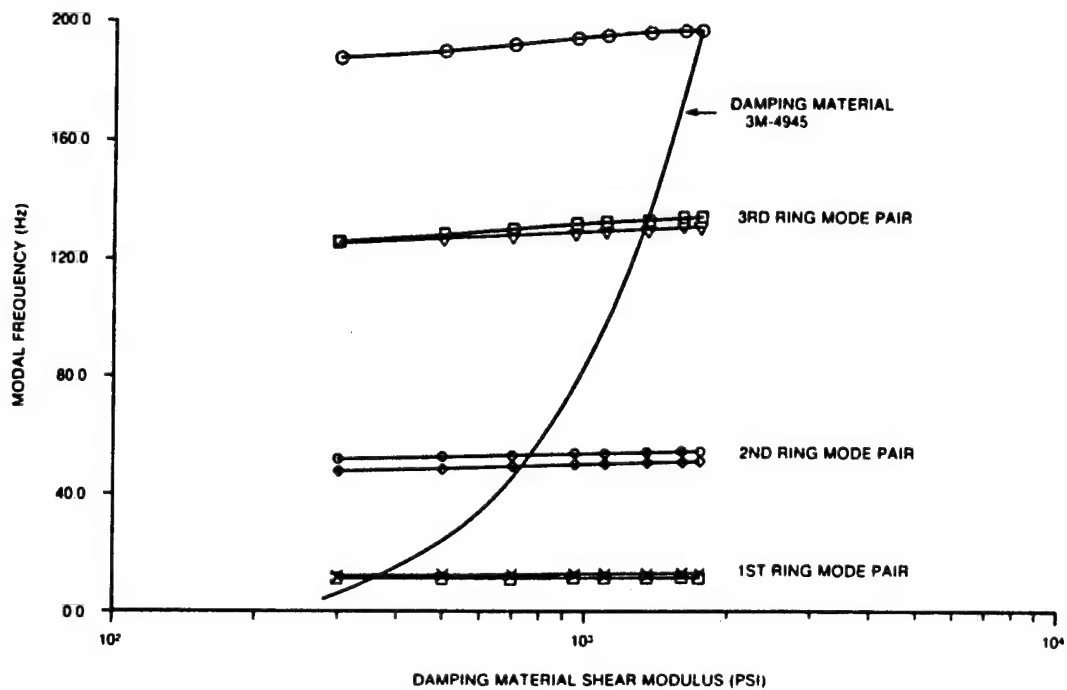
FIGURE 6: Modal Frequency versus Damping Shear Modulus, Damping Design Program. Model: Ring/Truss Structure; Damping Material: 3M-4945.

percentage strain energy in each of the other material groups is found by linearly interpolating the data from SORT_SD with the known VEM modulus for each mode. With loss factors and percentage strain energy now calculated for each material group, for each mode, the modal damping values are calculated using the MSE method equation. The eigenvalues are determined from their simple relationship with modal frequency.

The fourth and final segment of the design program, named "INTERP_EIGEN", calulates the eigenvectors which correspond to the eigenvalues found earlier. This is accomplished by retrieving output information from the third and first segments, MSEM and GET_SD, respectively. The VEM modulus for each mode is used to select the two Nastran F06 files containing the eigenvectors between which the interpolation will occur for a given mode. The interpolation point is determined by the relationship of the calculated eigenvalue to the eigenvalues corresponding to the two retrieved eigenvectors. The validity of determinig eigenvectors by interpolation is discussed in the following section on enhanced FR analysis.

This completes the damping design program. In summary, it enables the calculation of modal damping values, eigenvalues, and eigenvectors for a structure with damping treatment. This eigenstructure better describes the true resonant frequencies and mode shapes of the actual structure compared to standard FEA modeling means.

3.0 Enhanced Frequency Response Analysis Method

The damping design program calculates modal damping values for use in dynamic modal analyses, such as frequency response (FR). However, Nastran assumes a constant stiffness matrix which is not true for structures with VEMs. For an approximate FR analysis, a modulus of the VEM can be used which corresponds to a frequency in the middle of the analysis range. Resonant frequencies and amplitudes will be accurate in the vicinity of this assumed frequency, but will be less accurate for higher and lower resonances.

An improvement in the modal FR can be made if, instead of using the orthogonal eigenstructure of the middle-frequency structure, it is replaced by an eigenstructure consisting of the interpolated modes found in the damping design program. This results in an eigenstructure which is no longer orthogonal, but orthogonal eigenstructures are only true for structures with linear material properties. This non-orthogonal eigenstructure of interpolated eigenvalues and eigenvectors better desribes the true resonant frequencies and mode shapes of the actual structure with VEM damping by accounting for the frequency dependency of VEM properties.

The approach is based on the ability to accurately interpolate modal parameters. This was demonstrated in an excercise where interpolated parameters errored less than 0.2 percent from actual values. Table 2 shows one set of interpolated parameters from a structure whose damping material modulus was varied over a significant range.

TABLE 2
Interpolation of Modal Parameters

	Nastran Solution	Interpolated Values	% Error
Damping Material Shear Modulus	350 psi	350 psi	
Generalized Mass	1.450 E-3	1.4528 E-3	0.15
Generalized Stiffness	16.84	16.81	0.17
Eigenvector Component	2.203	2.206	0.12
Eigenvalue	17.14 Hz.	17.12 Hz.	0.16

An enhanced FR solution method was created which makes use of this non-orthogonal, interpolated eigenstructure. The method uses a standard finite element method FR solution sequence, with commands added to enable the substitution of the interpolated eigenstructure from the damping design program. The tedious writing of these commands has been automated by another program.

The other quantities required to perform a standard modal frequency response analysis are:

Generalized stiffness matrix

Generalized mass matrix

Generalized force vector

Modal damping matrix

The generalized stiffness matrix is a diagonal matrix with components equal to the corresponding eigenvalue, squared. In the enhanced FR analysis the eignvalues are replaced as mentioned early and therefore cause the proper adjustment to the stiffness matrix. If the eigensolution normalizes the eigenvector to unit modal mass, the generalized mass matrix is equal to the identity matrix and hence remains unchanged for the enhanced method. The modal forces for the enhanced method are calculated in the same manner as those in a standard FR solution. The modal damping values are calculated by the damping design programs as mentioned earlier, and are included in the solution sequence.

4.0 Application of Methods

The methods described above were implemented in the design and analysis of a CL damping treatment for a structure of moderate complexity to demonstrate the ability and accuracy of these methods.

The structure choosen was a ring-and-truss shown in figure 7. It consists of an aluminum ring 100" in diameter with a box cross section, and a fixture kinematically supported above the ring by six composite tubes approximately 70" in length. For test purposes, the structure was secured to a large, isolated granite surface plate by means of 12 rod flexures and 3 plate flexures.

4.1 Damping Treatment Design

The objective of this task was to design and test a CL damping treatment for the ring/truss structure using the simplified modeling method and the damping design program. The goal was to significantly damp the first three ring modes of the structure with an inexpensive, easily constructed and applied damping treatment.

3M Company's acrylic core foam tape, Y-4945, was chosen for the design for two reasons: 1) ease of application due to high compliance, 2) excellent loss factor at room temperature and 1-200 Hz. frequency range (the analysis bandwidth).

The first segment of the design program, GET_SD, was used to design the damping treatment. Five conclusions were drawn from this work:

- Increasing extensional stiffness of the constraining layer increases the strain energy in the damping material.

- Increasing bending stiffness of the CL increases the strain energy in the damping material.

- All the strain energy in the damping material is due to shear strain. Tension and compression contribute an insignificant amount.
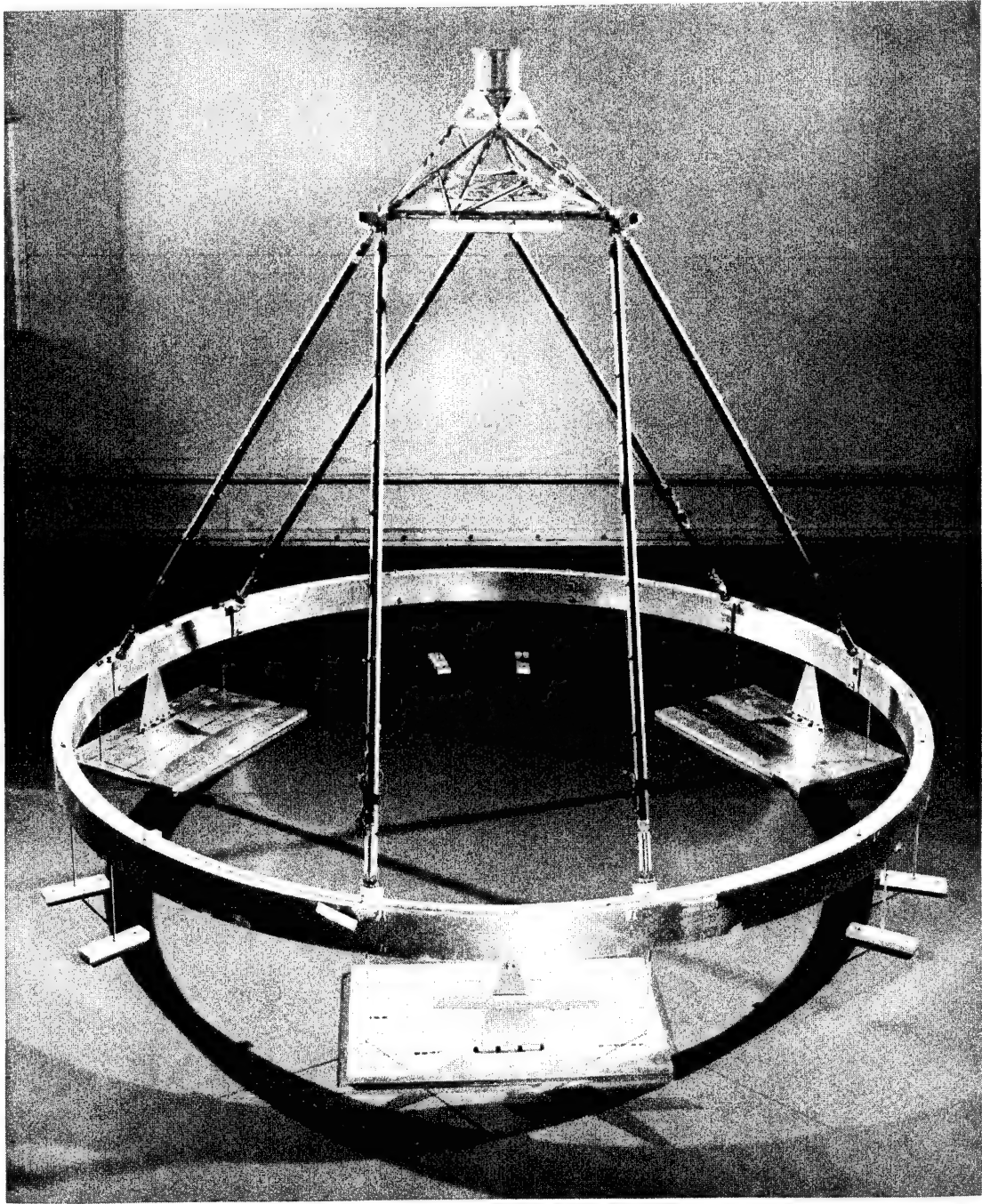
FIGURE 7:   Ring/Truss Test Structure

-An optimum shear stiffness of the damping material exists for a given structure and CL.

- The effect of segmenting the constraining layer is mode specific. For treatments covering the entire circumference, segmenting it in four equal sections, causes a decrease in strain energy > 10 %.

The design chosen consisted of the 3M tape two inches wide, doubled to a thickness of 0.090 inches, and constrained by a steel band three inches wide, 0.125 inches thick and covering the entire circumference with four equal segments rolled to the outer curvature of the structure's ring.

The CL was made of steel because it is inexpensive and has a high modulus. Extensional and bending stiffnesses were limited to that afforded by the 3.0 inch by 0.125 inch dimensions because of handling, application, and removal limits. Doubling the 3M tape thickness to 0.090 inches gave the design the optimal damping material shear stiffness to damp the first three rings modes.

Modal damping values were calculated for this design and are shown in Table 3. Significant levels of structural damping were achieved by this design (damping loss factor > .10). Figures 2 - 6 were produced by the damping design program. Figure 2 shows how modal frequencies for the structure and this damping design change with modulus of the VEM. It is important to note that these numbers are based only on the asumed dimensions of the damping material and the range of modulus values used. The numbers are not based on a particular damping material. Figure 3 shows how strain energy in the VEM changes with VEM modulus for each mode. Note the strong maximums for many modes. Figures 4 and 5 show the material properties of the VEM used in this design.

4.2 Damping Test Measurement

The objective was to measure the actual damping levels of the first three ring modes of the structure to verify the passive damping values predicted by the damping design program with the simplified modeling method. This was accomplished by a modal survey test.

Test data was first acquired for the structure without the CL damping treatment to check the accuracy of the math model, and to measure damping values before addition of the treatment. Results show that the math model

calculated ring bending mode frequencies to within 1 - 5 % of the test measurements (see Table 3). This is very good considering the ring is an assembly of plate sections welded to form a box cross-section. Structural damping values are also shown for the ring/truss before the damping treatment was added.

Modal properties of the ring/truss with the CL damping are also shown in Table 3. Comparing analytical to test values, the modal frequencies again agree to within 2 - 4.5 % even though the frequencies changed significantly after the damping treatment was added (compare test values before and after the damping treatment was added). This confirms the simplified modeling method's and the damping design program's ability to accurately represent the mass and stiffness of the CL treatment.

Significant structural damping values were measured, ranging from 2.8 - 6.8 %. This compares with values for the bare ring/truss ranging from 0.2 - 1.4 %. Figure 8 illustrates the increased damping for these modes. Comparing test damping values to analytical for the structure with the CL treatment, shows test values ranging from 42 - 89% of those predicted. Although it was hoped that these values would have agreed better, these first-attempt results are not discouraging. The design program and simplified modeling method enabled the conscientious design of a CL damping treatment which significantly increased modal damping by as much as 18 times. The agreement between test and analytical values is significant when the following sources of error are considered:

- The MSE method calculates approximate damping values for a nonlinear structure using linear analyses.

- Error in Nastran's calculation of modal strain energy is difficult to quantify by experimental testing.

- VEM properties are complex and less consistent than that of elastic materials, making their measurement more difficult.

- The extraction of damping values from test data of highly damped, closely spaced resonances is difficult and prone to errors. Modal analysis software is least accurate in it's determination of damping. It is most accurate and more commonly used to determine resonant frequencies and mode shapes.

TABLE 3
Ring-Truss Structure Modal Properties.
Analytical versus Test Values.

Structure <u>without</u> constrained layer damping:

Ring Bending Mode Pair	Frequency (Hz)		Structural Damping
	NASTRAN	Test	Test
1st	11.474	11.304	.0021
	11.478	11.372	.0037
2rd	49.1	51.40	.0038
	53.5	56.20	.0086
3rd	141.5	137.6	.0120
	142.1	138.1	.0116

Structure <u>with</u> constrained layer damping:

Ring Bending Mode Pair	Frequency (Hz)		Structural Damping	
	NASTRAN	Test	MSE	Test
1st	11.11	10.88	.036	.032
	11.77	11.50	.095	.068
2nd	48.1	49.5	.106	.056
	51.1	53.40	.067	.028
3rd	128.8	125.5	.078	.037
	131.2	127.3	.107	.065
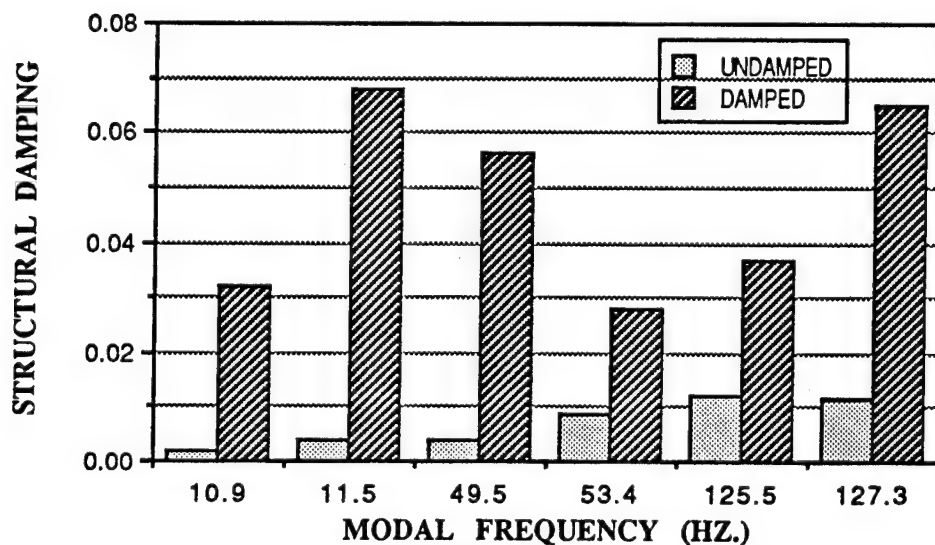
FIGURE 8:   Ring/Truss Passive Test Results

- The results reported are for one treatment designed and one modal test at one shaker location. Given sufficient time, multiple designs should be tested numerous ways to better account for the origin and extent of errors.

Effort will continue to increase the match-up of analytical damping predictions to test measurements. Possible errors will be pursued in both the analytical calculation, and the measurement techniques.

4.3) Enhanced Frequency Response of Test Structure

An enhanced FR analysis was performed on the ring/truss test structure with it's constrained layer damping treatment as described earlier in section 4.1 .

Figure 9 is a plot of the enhanced FR analysis for a point on the ring of the damped ring/truss structure. Acceleration is plotted verses frequency (Hz.). The first three ring bending modes (six modes total since each bending shape has a twin) are marked. The damping treatment damped only the ring modes appreciably and hence eigenvalues and eigenvectors for only these modes were calculated by the damping design program. All other modes are as normally calculated for the structure with a damping material shear modulus corresponding to a frequency in the middle of the analysis bandwidth.

A standard Nastran FR analysis for the damped structure (using damping material shear modulus corresponding to a frequency in the middle of the analysis bandwidth) was also performed. Table 4 shows differences of up to 5% in eigenvalue, and 12% in response amplitude at resonance. These are small, but may be greater for different treatments and other structures.
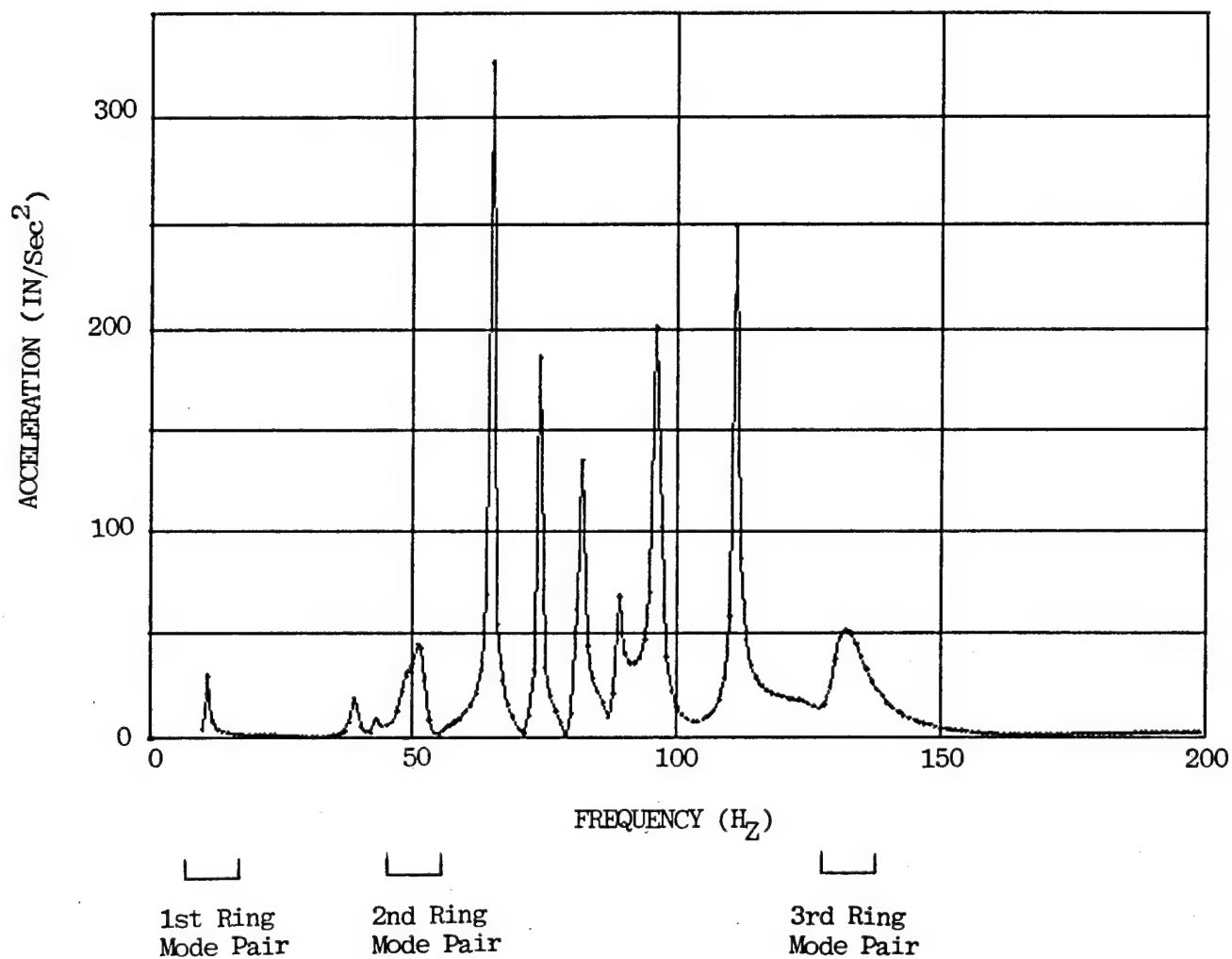
FIGURE 9: Enhanced Frequency Response of a Point on the Ring/Truss Structure.

TABLE 4
Comparison of Resonant Frequency and Amplitude
between Enhanced and Standard FR
for the Ring/Truss Structure

Ring Bending Mode Pair	Resonant Frequency			Peak Amplitude		
	Enhanced	Standard	%Diff.	Enhanced	Standard	% Diff.
1	11.18	11.60	4%	29.7	29.2	2%
	11.94	12.57	5%	7.5	6.2	21%
2	48.7	49.6	2%	29.2	28.4	3%
	51.5	52.0	1%	43.0	42.4	1.5%
3	129.9	129.3	.5%	36.2	40.4	12%
	132.8	131.8	.75%	50.0	52.6	5%

Summary

Improved finite element methods for the design and analysis of passive damping treatments in complex structures have been developed. These methods account for the non-linear properties of the viscoelastic materials commonly used in damping treatments and were implemented in the design of a constrained layer damping treatment for a large ring-and-truss structure. Modal damping for this structure was analytically predicted and then experimentally measured to verify the accuracy of these methods.

Bibliography

1) Frater, N. K. . Implementation of Modal Strain Energy Method Using
     MSC/Nastran and Post-processing Utility Programs. Damping 1986
     Proceedings, AFWAL-TR-86-3059, Vol. 1, May 1986.

2) Johnson, C. D., and D. A. Kienholz. Finite Element Prediction of Damping in
     Structures with Constrained Viscoelastic Layers. AIAA Journal, Vol.
     20, No. 9, Sept1982.

3) Johnson, C. D., D. A. kienholz, E. M. Austin, and M. E. Schneider. Design and
     Analysis of Damped Structures Using Finite Element Techniques.
     ASME Journal, 85-DET-131.

4) Nashif, A. D., D. I. G. Jones, and J. P. Henderson. Vibration Damping. John
     Wiley and Sons, New York, 1985.

APPLICATION OF THE RITZ PROCEDURE
TO DAMPING PREDICTION
USING A MODAL STRAIN ENERGY APPROACH

By

Jatin C. Parekh and
Steven G. Harris

Anamet Laboratories, Inc.
3400 Investment Blvd.
Hayward, CA 94545

ABSTRACT

An automated procedure is defined to derive modal damping values in
constrained-layer damping problems. The procedure uses the NASTRAN finite
element program with DMAP modifications to derive modal loss factors using a
Modal Strain Energy (MSE) approach. The frequency-dependent properties of the
constrained viscoelastic layer are taken into account in an iterative
solution. The Ritz procedure, a specialized Lanczos method for eigenvalue
extraction, is used in the procedure together with standard NASTRAN super-
element techniques to increase eigenvalue solution efficiency. Sample
problems are discussed to illustrate the accuracy and efficiency of the
method.

INTRODUCTION

Vibration reduction in structures has been a subject of investigation for many years. One of the most weight-effective means of reducing vibration is to incorporate a viscoelastic material in the form of a constrained layer in a built-up structure. In this method, an elastomer is sandwiched between two metallic sheets and is bonded to both. Flexural vibration causes shearing strain in the core, which dissipates energy and thereby reduces vibration.

An additional advantage of constrained-layer damping is that analytical methods and modeling techniques exist to predict structural behavior of the damped system. Using these analytical techniques, studies can be performed to gauge the adequacy of different damping treatments in eliminating unwanted responses.

It is generally felt that the Modal Strain Energy (MSE) approach using commercially available finite element programs is the most computationally efficient for use in analyzing constrained-layer damping problems. One of the major problems confronting MSE, however, is the frequency-dependent material properties of the viscoelastic layer. An automated procedure to derive modal loss factors using the undamped mode shapes and the material loss factors of the frequency-dependent material is presented in this paper. The same concept can then be extended to solve the forced-response problem by evaluating modal stiffness and modal mass matrices from the resulting mode shapes and frequency-dependent system stiffness.

The Ritz procedure, first described by Wilson, et al. [1], has also been taken advantage of in this application to constrained layer damping problems. The Ritz procedure provides a means to reduce the number of eigenvectors used in a forced response analysis without reducing solution accuracy. It can also provide significant savings over other eigenvalue solution techniques.

OVERVIEW OF MODAL STRAIN ENERGY METHOD

In this approach, first suggested by Johnson, et al. [2], it is assumed that a standard mode superposition approach can be used to uncouple the equations of motion:

$$M\ddot{x} + C\dot{x} + Kx = p(t) \qquad (1)$$

where

M,C,K = physical coordinate mass, damping and stiffness matrices (all real and constant)

$\ddot{x}, \dot{x}, x$ = vectors of nodal displacements velocities, and accelerations

p = vector of applied nodal loads

The damped structure can be represented in terms of the real normal modes of the associated undamped system if appropriate damping terms are inserted into the uncoupled modal equations of motion:

$$\ddot{\alpha}_r + \eta^{(r)} \omega_r \alpha_r + \omega_r^2 \alpha_r = p_r(t) \tag{2}$$

$$x = \Sigma \phi^{(r)} \alpha_r(t) \qquad r = 1,2,3... \tag{3}$$

where

α_r = rth modal coordinate

ω_r = natural radian frequency of the rth mode

$\phi^{(r)}$ = rth mode shape vector of the associated undamped system

$\eta^{(r)}$ = loss factor of the rth mode

p_r = modal force vector for rth mode

It is implied that the damping matrix, C, of Eq. (1), need not be explicitly calculated, but that it can be diagonalized by the same real modal matrix that diagonalizes **K** and **M.**

Modal loss factors are calculated using the undamped mode shapes and the material loss factor for each material [3]. For a structure damped with a viscoelastic layer, the material loss factor of the metal sheet is very small compared with that of the viscoelastic layer. Hence, the modal loss factor is found from:

$$\eta^{(r)} = \eta_\upsilon \, [V_\upsilon^{(r)} \, / \, V^{(r)}] \tag{4}$$

where η_υ is the material loss factor of the viscoelastic core evaluated at the rth calculated resonant frequency and $V_\upsilon^{(r)} \, / \, V^{(r)}$ is the fraction of elastic strain energy attributable to the sandwich core when the structure deforms in the rth mode shape.

Eq. (4) implies that damping of a structure can be described by associating a single number, the modal loss factor, with each undamped natural mode shape and frequency. The composite loss factor for each mode is taken to be proportional to the material loss factor for the viscoelastic portion of the structure. This approximation has been shown to be accurate for practical applications.

A basic difficulty with the modal strain energy method is that the modal properties are obtained from system matrices that are assumed to be constant. Viscoelastic materials, however, have storage moduli that vary significantly with frequency. To resolve this contradiction, a simple correction is made to the modal loss factor described in Eq. (4). The corrected value of modal loss factor is given as:

$$\eta^{(r)'} = \eta^{(r)} \sqrt{G_2(f_r)/G_{2,ref}} \qquad (5)$$

where

$\eta^{(r)'}$ = adjusted modal damping ratio for the rth mode

$\eta^{(r)}$ = modal damping ratio for the rth mode obtained by iteration

$G_{2,ref}$ = core shear modulus used in final normal modes calculation to obtain modal frequencies, shapes, and masses

$G_2(f_r)$ = core shear modulus at $f = f_r$, where f_r is the rth mode frequency calculated with $G_2 = G_{2,ref}$

To design a damping treatment, one begins by making several normal mode runs for a range of different core shear moduli. A set of natural frequencies and damping ratios is obtained for each value of the core shear modulus. Curves are drawn for each mode, and the intersections with the material property curve are found as shown in Figure 1, taken from [2]. Each inter-section represents the shear modulus value which is appropriate for calcu-lating the damping ratio of the associated mode. An intermediate value of the core shear modulus within the frequency range of interest is then selected as a source for the final values of modal stiffness, mass and mode shape which are used in subsequent forced response calculations. Additionally, modal damping ratios obtained by the iterative scheme are corrected according to Eq. (5).

OVERVIEW OF THE RITZ PROCEDURE

The Ritz procedure, first described by Wilson, et al. [1], provides an efficient way of solving large eigenvalue problems. The procedure has been implemented in both COSMIC and MSC/NASTRAN [4,5]. The algorithm is illustrated in Figure 2.

To start the procedure, a Krylov sequence is used to compute a set of mass-orthogonal starting vectors. A static load is used to derive the initial vector of the set. Note that cases involving singular stiffness matrices are also easily handled. Given this set of starting vectors, an eigenvalue problem of order L is solved (where L is the size of the starting vector set, or number of desired eigenvalues) to derive both the structure eigenvalues and the generalized eigenvectors, Z. These eigenvectors are then applied as a transformation matrix to the starting vector set to produce the final set of
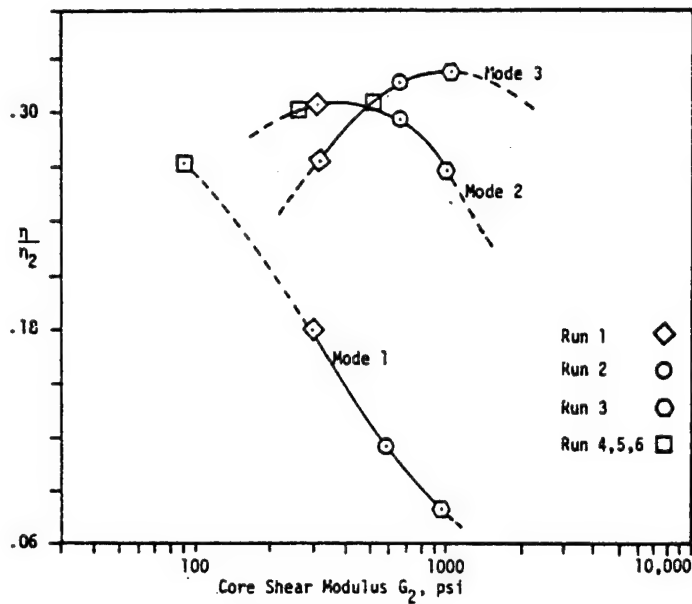
(a) Composite loss factor
vs. core shear modulus
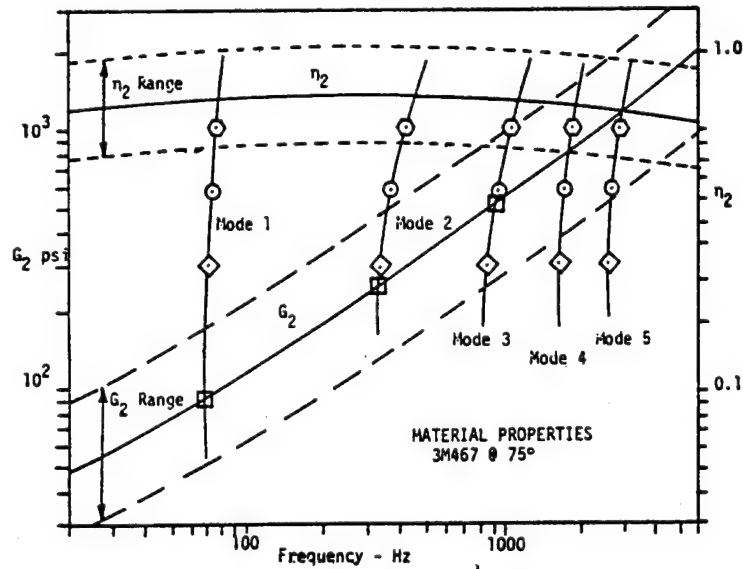
(b) Material properties

Figure 1 Design method for sandwich beam with viscoelastic
core (frequency-dependent material properties).

- Given mass matrix $\mathbf{M}$, stiffness matrix $\mathbf{K}$ and load vector $\vec{p}$

- Triangularize $\mathbf{K}$ such that

  $\mathbf{K} = \mathbf{L}^T\mathbf{DL}$

- Solve for starting vector $\vec{x}_1^*$

  $\mathbf{K}\vec{x}_1^* = \vec{p}$

  $\vec{x}_i^T\mathbf{M}\vec{x}_i = 1$

- Solve for additional vectors $i = 2, \ldots, L$, orthonormalizing with respect to $\mathbf{M}$

  $\mathbf{K}\vec{x}_i^* = \mathbf{M}\vec{x}_{i-1}$

  $c_j = \vec{x}_j^T\mathbf{M}\vec{x}_{i-1}^*$, for $j = 1, \ldots, i-1$

  $$\vec{x}_i^{**} = \vec{x}_i^* - \sum_{j=1}^{i-1} c_j\vec{x}_j$$

  $\vec{x}_i^T\mathbf{M}\vec{x}_i = 1$

- Form $\mathbf{M}^*$ and $\mathbf{K}^*$

  $\mathbf{X} = [\vec{x}_1, \cdots, \vec{x}_L]$

  $\mathbf{M}^* = \mathbf{X}^T\mathbf{MX}$

  $\mathbf{K}^* = \mathbf{X}^T\mathbf{KX}$

- Solve the L by L eigenvalue problem

  $[\mathbf{K}^* - \omega_i^2\mathbf{M}^*]\vec{z}_i = 0$

  $\mathbf{Z} = [\vec{z}_1, \cdots, \vec{z}_L]$

- Compute final Ritz vectors by orthogonalizing $\mathbf{X}$ with respect to $\mathbf{K}$

  $^0\mathbf{X} = \mathbf{XZ}$

Figure 2   The Ritz Procedure

Ritz vectors which are both mass and stiffness orthogonal. The resulting Ritz vectors and eigenvalues contain no components which are orthogonal to the applied static displacement used as the initial starting vector. This is an important property of the Ritz procedure -- unwanted eigenvectors which would be recovered in a standard normal modes analysis, but which would show no participation in subsequent forced-response analysis, are eliminated in the Ritz procedure.

Studies using the Ritz procedure [4,6] have indicated that for normal modes analysis, it provides a reduction by a factor of three to ten in the eigenvalue extraction procedure when compared to the FEER method used in COSMIC/NASTRAN for the same number of modes. In addition, because the static load vector can eliminate recovery of unwanted modes in the eigenvalue solution, fewer Ritz modes can be used to obtain the same level of accuracy for subsequent forced-response analysis. Use of the static load vector also eliminates any need for a static correction factor in forced-response analysis.

Following Wilson's original publication of the Ritz procedure, it has been demonstrated that the procedure is identical to the Lanczos method with full reorthogonalization. In fact, the Lanczos method has recently been implemented in MSC/NASTRAN [7], and its efficiency is comparable to the Ritz procedure for general eigenvalue extraction problems. Still, the Ritz procedure offers some advantages for applications in which the dynamic loading imposed in subsequent forced-response analysis is spatially invariant and well defined. Such may be the case for evaluation of constrained-layer damping concepts. In these cases, the numerical efficiency of the Lanczos procedure is obtained in solving the eigenvalue problem, while at the same time, the number of modes recovered is limited only to those that participate in the forced-response problem by dictating the starting vector used in the sequence.

The NASTRAN implementation of the Lanczos method will be used in this paper as an efficient means to derive true natural mode shapes and frequencies. The Ritz procedure is used to derive Ritz modes and frequencies which may or may not correlate directly with the true natural modes. Both procedures simply provide a set of normal modes and frequencies which can be used for efficient forced-response analysis, as well as to predict values of modal damping for constrained-layer problems.

AUTOMATIC EXTRACTION OF MODAL LOSS FACTORS FOR CONSTRAINED-LAYER DAMPING PROBLEMS

An automated iterative procedure has been developed to derive modal loss factors for constrained-layer damping problems. The key issue in deriving the mode shapes and normal modes of the facesheet and constrained-layer assemblage is the ability to update the stiffness matrix of the viscoelastic layer at the beginning of each iteration.

The structure stiffness matrix of the assemblage is partitioned, as in a standard NASTRAN superelement approach, into a frequency-independent part (i.e., facesheets) and frequency-dependent part (i.e., viscoelastic constrained layer). Initially, with a starting value of G, the shear modulus of the viscoelastic layer, the stiffness matrix is formed and assembled with the rest of the structure. The natural frequencies and mode shapes of the assembly are

then found using the Ritz procedure implemented in NASTRAN. A new estimate of shear modulus of the viscoelastic layer for the next iteration is found from the frequency vs. G table for the first natural frequency. With this new value of G, the stiffness matrix of the constrained layer is updated and assembled with that of the frequency-independent part, and the eigenvalue extraction proceeds again. The iterative operation for this mode is continued until the current estimate of the natural frequency is acceptably close to the previous estimate. This process is repeated for all modes requested by the user. The converged values for frequencies, eigenvectors, and corresponding shear moduli of the core are saved for each mode to determine the modal loss factors according to Eq. (4). Additionally, these values can be utilized for subsequent forced-response analysis of the candidate structure. Figure 3 shows the flow chart of the procedure described here.

A basic assumption in this method is that the mode shapes of the assemblage do not vary significantly with the change in core shear modulus. Each mode shape is derived using a different value for the shear modulus of the constrained layer. If there is no significant change in mode shape with shear modulus, then the diagonal terms of the generalized stiffness matrix, $\underline{K}_o$, will remain large in comparison to the off-diagonal terms:

$$\underline{K}_o = \Phi^T K_o \Phi \tag{6}$$

where

$$\Phi = [\phi_1, \phi_2 \ \cdots \ ]$$

ϕ_i = mode shape i, derived using stiffness matrix K_i

K_o = stiffness matrix assembled using intermediate value of core shear modulus

For truly normal modes, of course, $\underline{K}_o$ contains only diagonal terms. This assumption is implicit in any MSE approach, since the modal damping values which are derived are generally used in subsequent linear forced-response analysis.

FINITE ELEMENT MODELING METHOD

The method used for finite element modeling of a viscoelastic constrained layer is described in [2]. Briefly, the viscoelastic core is modeled with three-dimensional isoparametric solid elements called HEXA elements in NASTRAN. Each element has three translational degrees of freedom defined at each node. The face sheets are modeled with quadrilateral shell elements, QUAD4's, which have three translations and two rotational degrees of freedom at each corner node. Since the plate nodes are offset to one surface of the plate and coincident with the corner nodes of the adjoining solid elements, there exists a coupling between stretching and bending deformations of the plate elements. This membrane-bending coupling is defined via the property card of QUAD4's. After the model is assembled, a standard superelement normal mode extraction with the user-specified DMAP is performed. Specifically, the
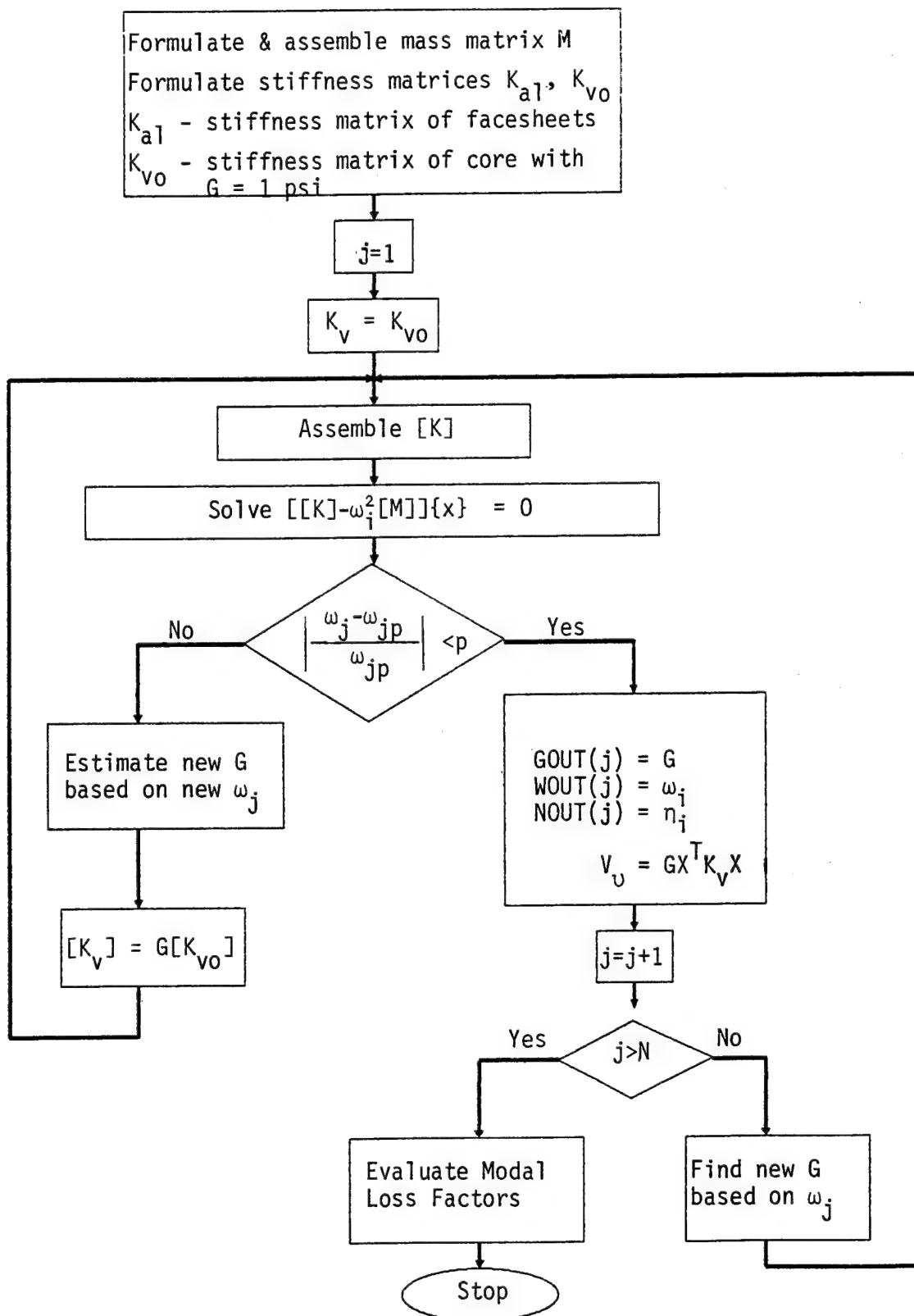
Figure 3   Flow chart for automatic extraction of modal loss factor.

facesheet elements are placed in an upstream superelement, whereas the solid elements making up the core are placed in the residual structure. This allows partitioning of the stiffness matrix into frequency-dependent and frequency-independent parts. The user is required to input a table defining the shear modulus, G, and the material loss factor, η, of the core as functions of frequency. Additionally, it is most convenient to set the initial value of G of the core to 1.0.

Calculation of elastic strain energy is performed using a standard option in MSC/NASTRAN. The fraction of total strain energy within a group of elements corresponding to the viscoelastic core for each normal mode will be output. Multiplying this value for each mode by the viscoelastic material loss factor yields the modal loss factor for that mode. The modal loss factors are output as a matrix print option in NASTRAN.

EXAMPLE PROBLEM

A cantilever beam similar to the one in [2] is analyzed using four different approaches to show the validation and advantages of the proposed solution method. The 7 inch long cantilever beam has identical aluminum face sheets 0.060 inch thick and a viscoelastic core 0.005 inch thick, as shown in Figure 4. The finite element model consists of 20 elements in the lengthwise direction and one element widthwise. All nodes are at element corners. Poisson's ratio of the core elements is taken to be 0.49. The viscoelastic material loss factor is assumed to be a constant (1.35) with respect to frequency. The tip of the cantilever beam is subjected to a random loading function as shown in Figure 5. The objective is to determine response functions which are accurate, in a cost-effective manner.

To establish a reference set of response functions, the sandwich beam is first analyzed using the direct frequency response (DFR) method. The viscoelastic core shear modulus is defined as a function of frequency as shown in Figure 6(a). The use of frequency-dependent material properties for direct frequency response analysis is described in [7]. Results from the other three approaches are compared with results from this method for validation.

The second approach is similar to the one used in [2]. Initially, a set of the lowest five modes and damping ratios is obtained for a range of different core shear moduli. For example, four shear moduli are examined in the present case, using the Lanczos method. The normalized structural damping factor and the first five natural frequencies are plotted versus G for each mode, as shown in Figure 6b. The intersection of the curve for each mode with the material property curve represents the G value which is appropriate for calculating modal damping of the associated mode. Subsequently, an intermediate value of G of 300 psi was used in the forced-response calculations to evaluate the responses. The damping ratios used for this analysis were adjusted with a correction factor obtained using Equation (5). The natural frequencies, corresponding shear moduli, and damping factors (after adjustment) used in the forced-response analysis are listed in Table 1.

In the third approach, the natural frequencies and unadjusted damping ratios for the first five modes are automatically obtained with an iterative procedure discribed earlier using the Lanczos method for the eigenvalue

T = 75°F

F(f)

F(f)

7 in.

.5 in.

FACE SHEET THICKNESS = 0.060 in.
CORE THICKNESS   = 0.005 in.

Upper and lower face sheets are aluminum.
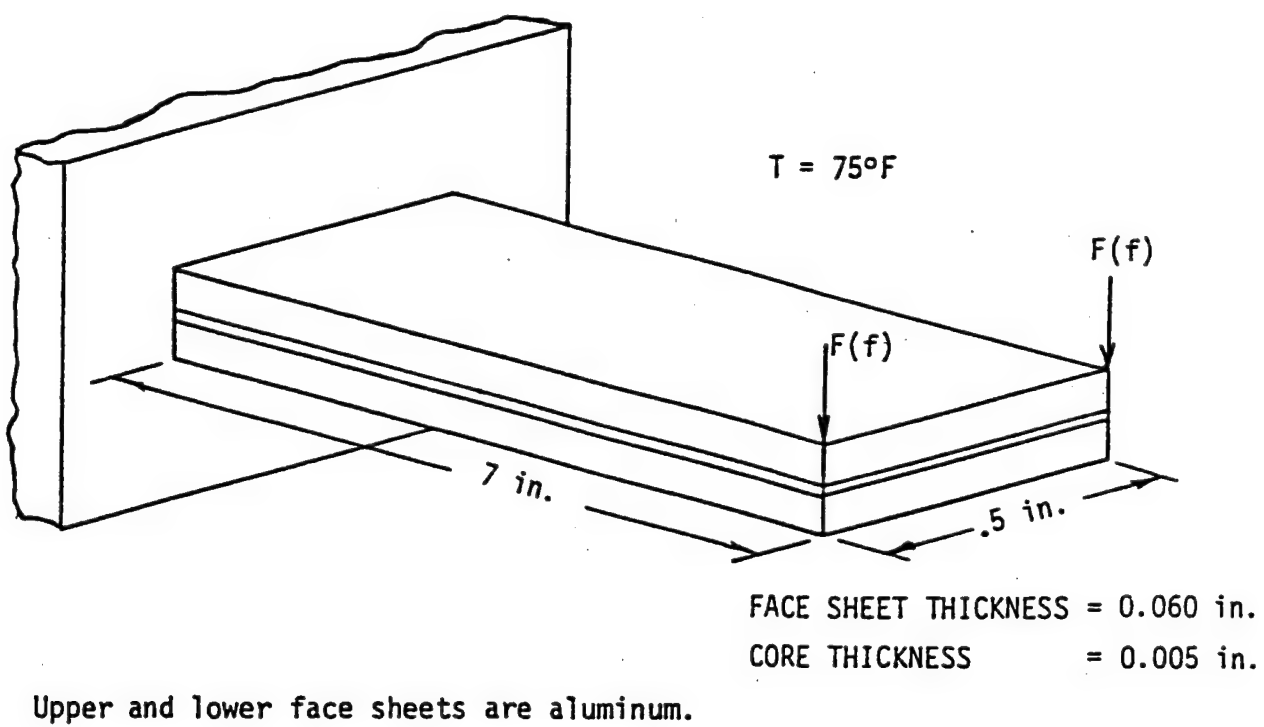
Figure 4   Cantilever Sandwich Beam Subjected to Random Loading.
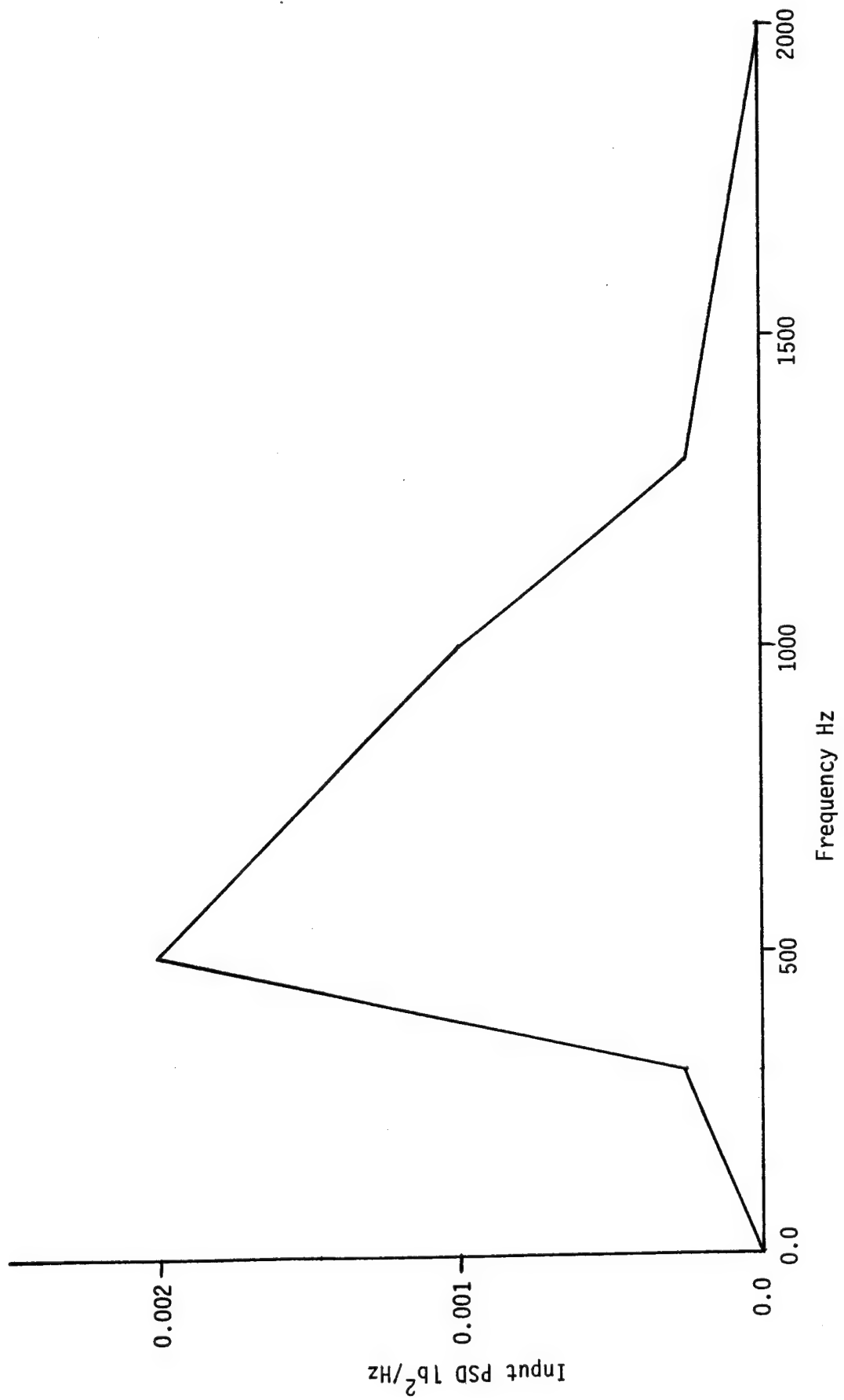
Figure 5   Random Loading Function.
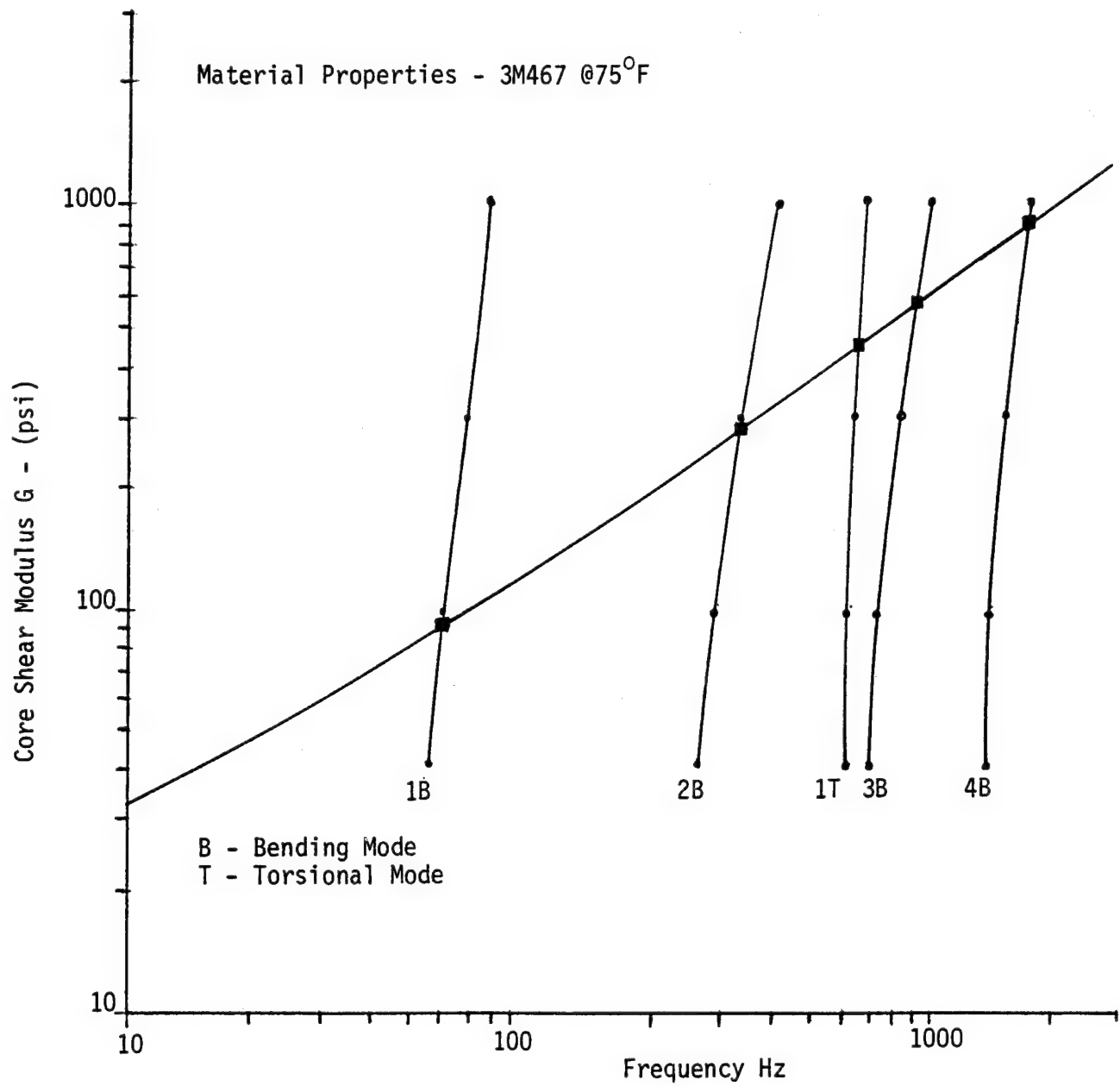
Figure 6(a) Material Properties vs. Frequency.
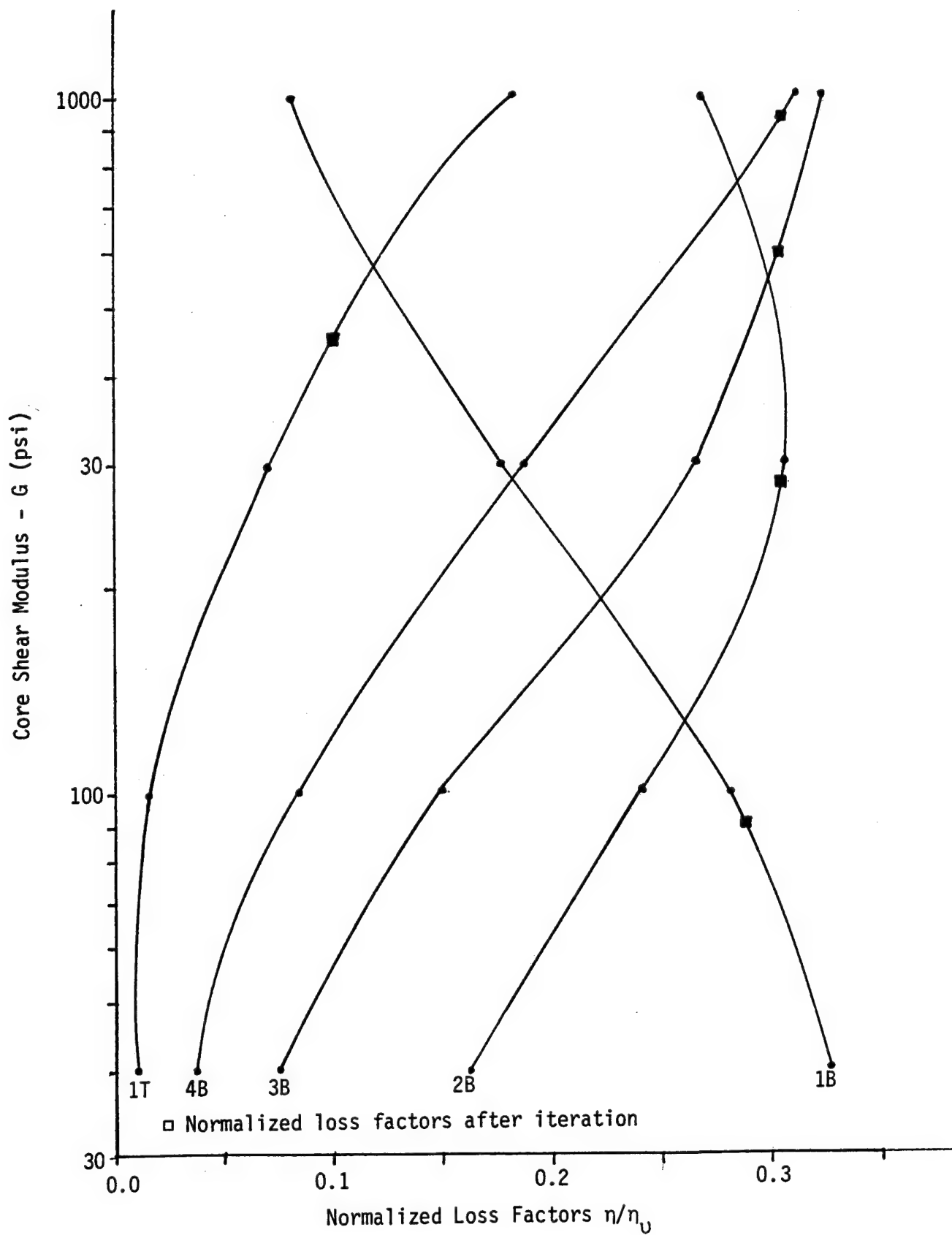
Figure 6(b)   Composite Loss Factors vs. Core Shear Modulus
Method to Obtain Damping Factors for
Frequency-Dependent Material Properties

CCB-14

TABLE 1

MODAL DAMPING RATIOS USING
NORMALIZED LOSS FACTORS
OBTAINED FROM A SET OF NORMAL MODE RUNS
WITH LANCZOS METHOD

Mode No.	Type	Frequency (Hz)	Core Shear Modulus psi	Normalized Loss Factor η/η_v	Modal* Damping Ratio
1	1B	64	90	0.290	0.214
2	2B	350	280	0.305	0.398
3	1T	650	450	0.095	0.157
4	3B	925	575	0.30	0.561
5	4B	1,720	920	0.30	0.709

* Used $G_{2,ref}$ = 300 psi; refer to Eq. (5).

extraction. The output eigenvalues, shear moduli, and damping ratios are as shown in Table 2. Since the output values of Table 1 and Table 2 are virtually identical, output from forced-response calculations will also be similar to the one obtained from the first approach.

The fourth approach is similar to the third approach, except that the Ritz procedure is used for eigenvalue extraction. The output from the eigen-value extraction run is listed in Table 3. Note that the first torsion mode at 650 Hz. is not extracted. Evidently, this is because the starting load vector used for eigenvalue extraction does not contain any components of the torsional mode. The forced-response analysis is then performed using modal loss factors derived from the Ritz procedure eignenvalue extraction, which are markedly different for higher modes compared to those obtained using the Lanczos method.

The response at the tip of the beam obtained by forced-response analyses using the first, second, and fourth approaches is presented in Figures 7 through 9. Note that the response from all three approaches is similar up to 500 Hz., at which the peak of the forcing function occurs. Moreover, the responses obtained from the Ritz procedure compare quite well with those from the Lanczos method throughout the frequency spectrum.

The differences in response at higher frequencies for the Ritz and Lanczos method compared to the DFR method can be be attributed to two factors. First, at higher frequencies, the error due to the correction factor (Eq. (5)) increases as the difference between the true shear modulus and the reference modulus increases. Secondly, at higher frequencies, modes six and higher contribute more significantly to the response. However, the contribution from higher modes is ignored in the Lanczos mode superposition analysis with just five modes, and only approximated in the Ritz modes.

For a further comparision between used Ritz modes and Lanczos natural modes, a set of mode superposition analyses (third and fourth approaches) were performed using only the first three modes. The output from an eigenvalue extraction run using the Ritz method is shown in Table 4. The eigenvalues and modal loss factors from the Lanczos method, which remain the same since it provides true natural modes, are in Table 2. The response from the forced-response analyses is plotted with that from the original DFR analysis in Figures 10 through 12. Note that the response from both methods, Ritz and Lanczos, compare well with that from DFR up to 500 Hz. At higher frequencies, however, the responses from the Lanczos method diverge considerably from DFR, whereas the responses from the Ritz method continue to correlate well with responses from the DFR method up to 1300 Hz.

This close correlation between the Ritz procedure results and the DFR is due to the use of a static load vector to derive the initial Ritz vector in the algorithm. The third Ritz mode (which is not the same as the third natural mode) contains components of all of the higher modes that are not orthogonal to the initial Ritz vector. Thus, the contribution to response from higher modes is approximated when the Ritz procedure is used, in the same manner as a static correction factor.
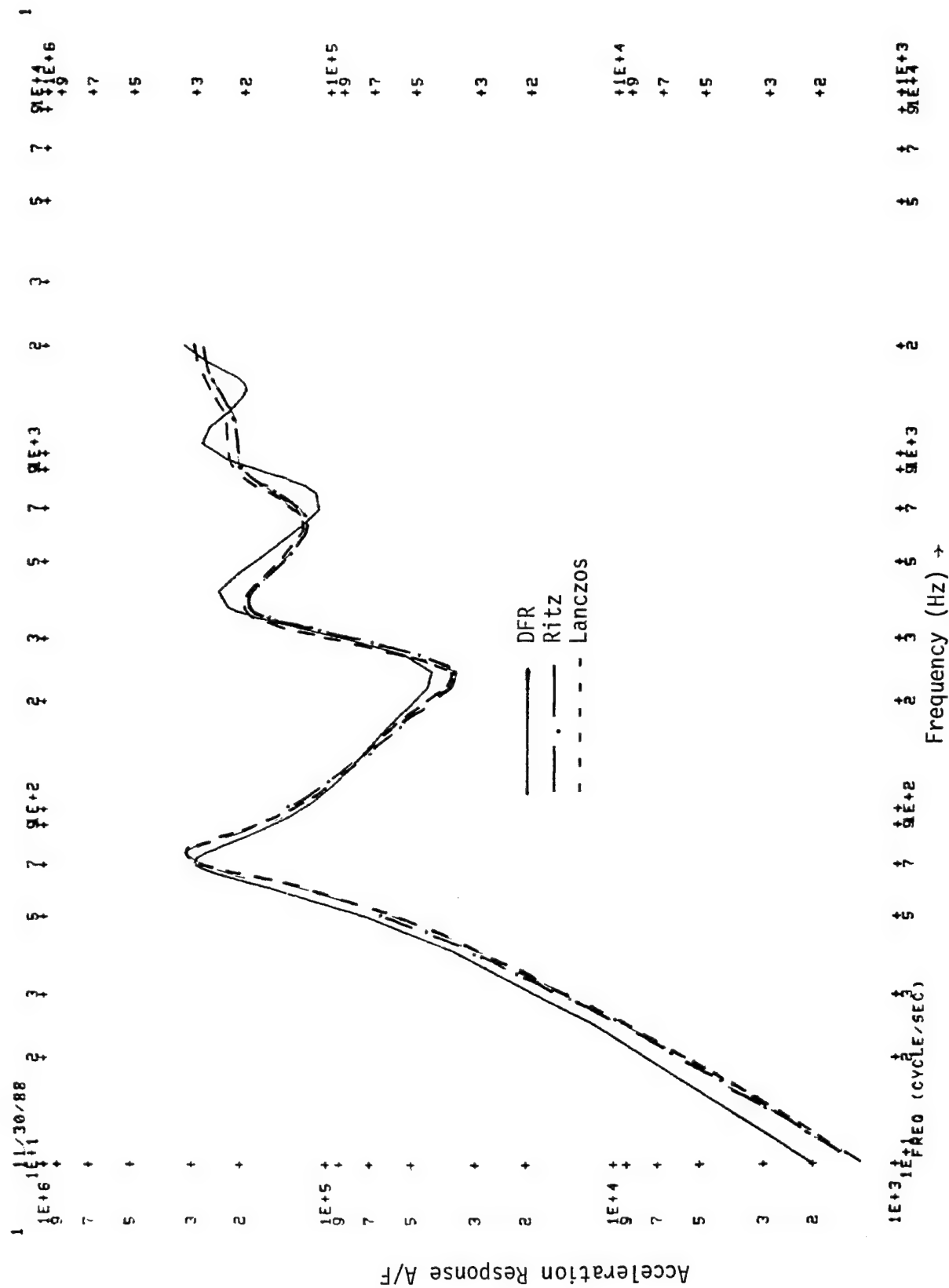
Figure 7 Comparison of Acceleration Frequency Responses at the Tip of the Beam Obtained From Direct Frequency Response Method & Modal Strain Energy Method using Lanczos & Ritz Procedure (with 5 Modes).
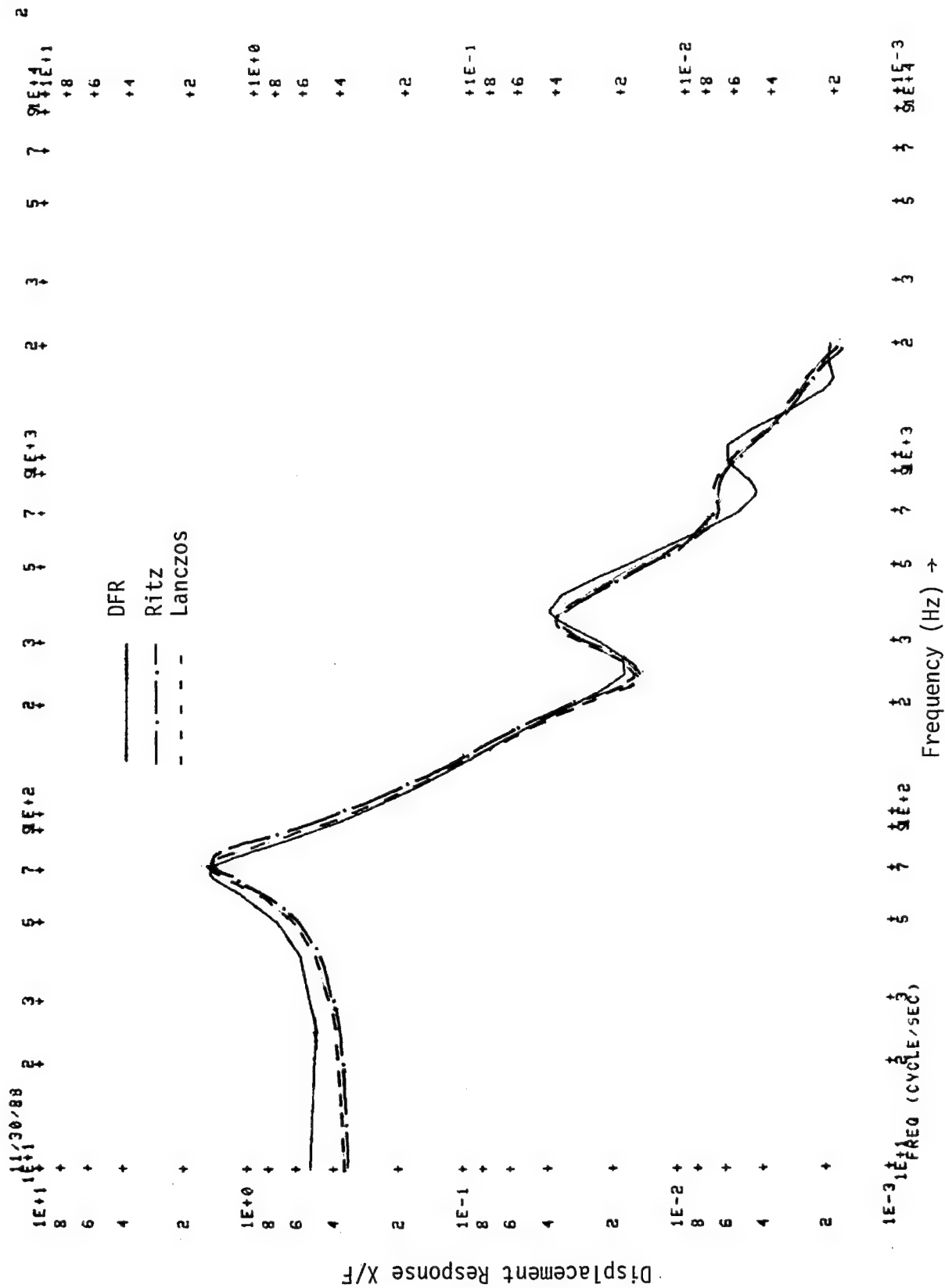
Figure 8 Comparison of Displacement Frequency Responses at the Tip of the Beam Obtained
from Direct Frequency Response Method & Modal Strain Energy Method using Lanczos
and Ritz Procedure (with 5 Modes).
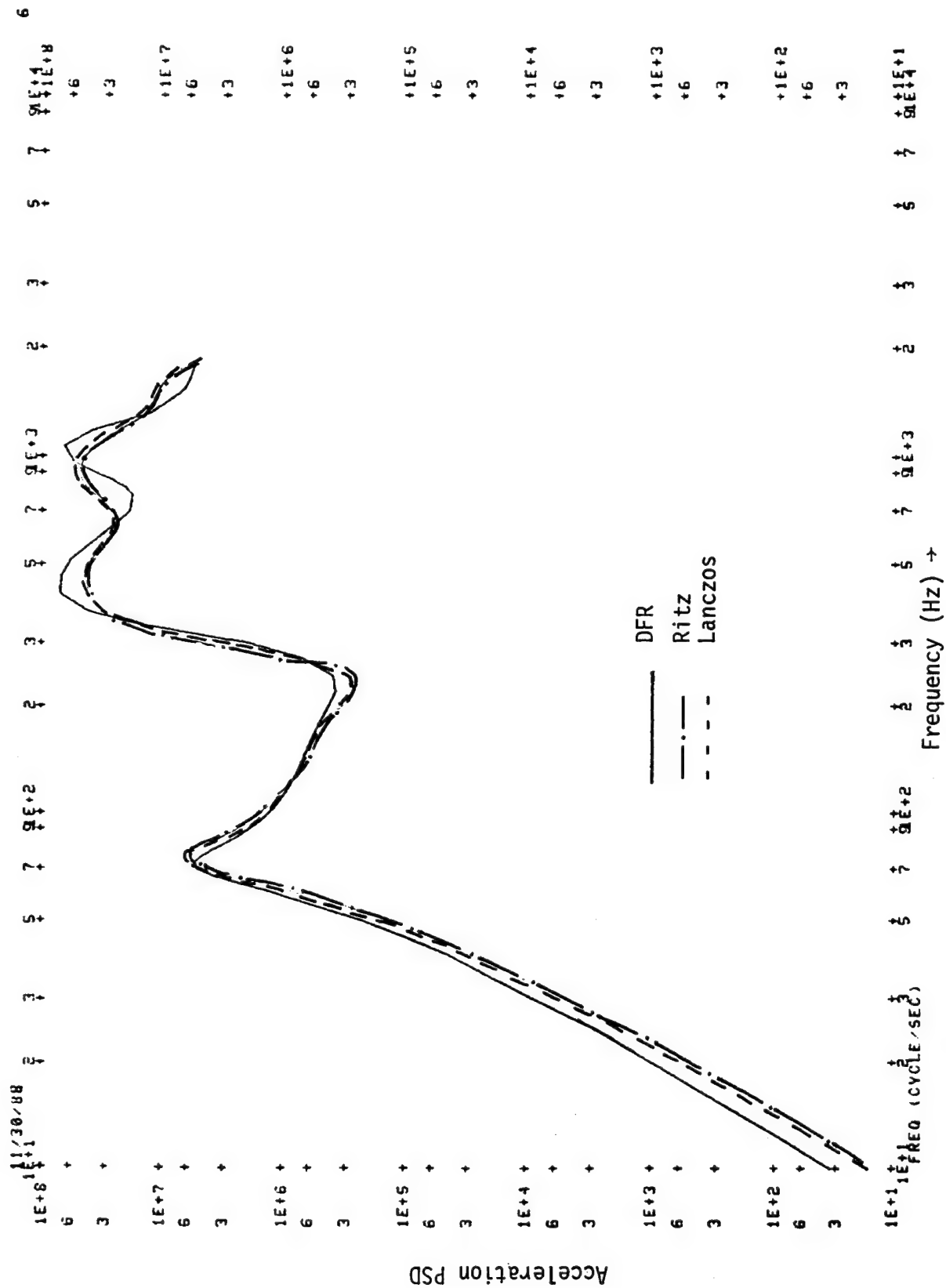
Figure 9 Comparison of Acceleration PSD Frequency Responses at the Tip of the Beam Obtained from Direct Frequency Response Method & Modal Strain Energy Method using Lanczos and Ritz Procedure (with 5 Modes).
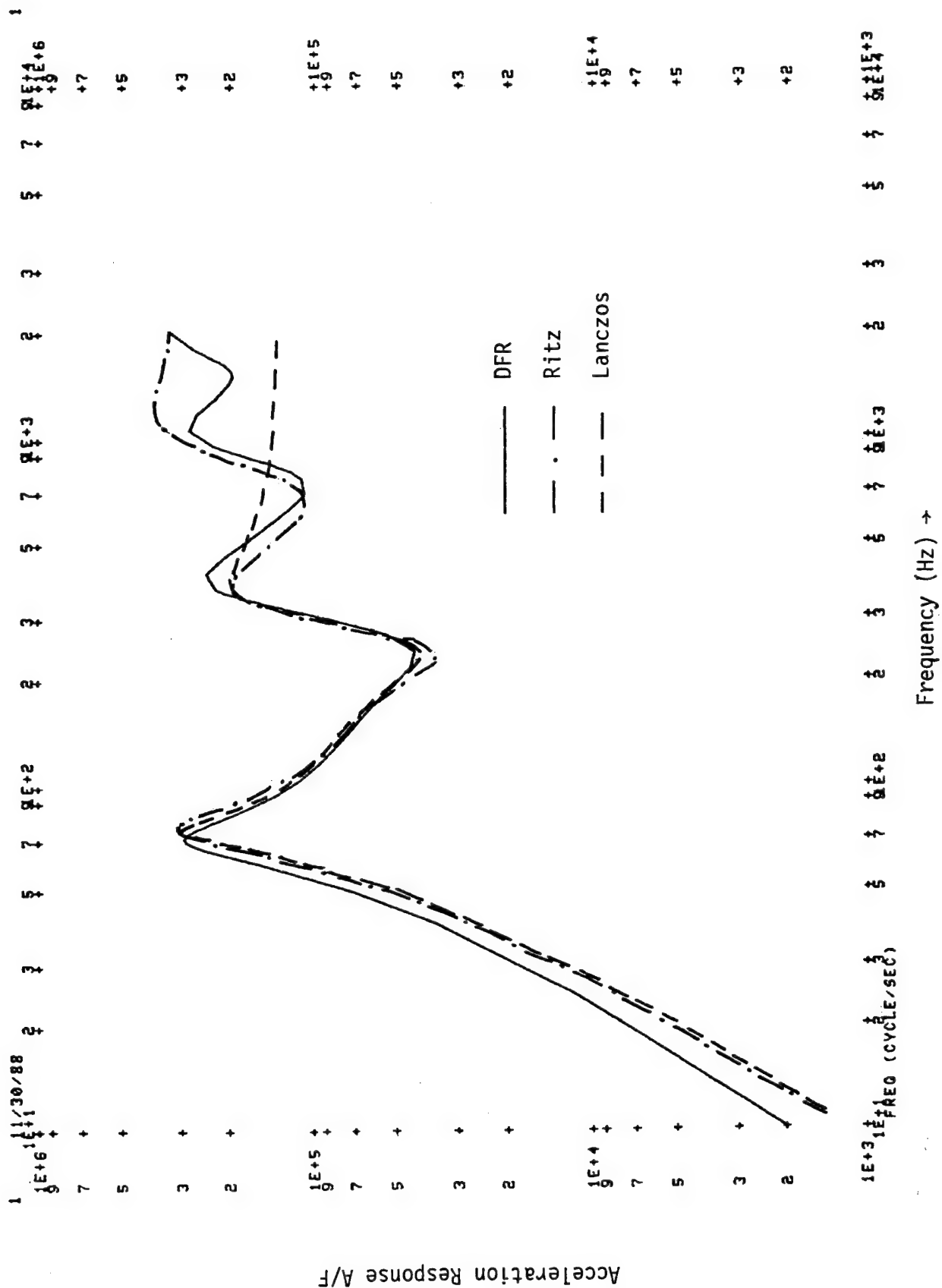
Figure 10 Comparison of Acceleration Frequency Response at the Tip of the Beam Obtained from DFR Method and MSE Method Using Lanczos and Ritz Procedure with 3 Modes
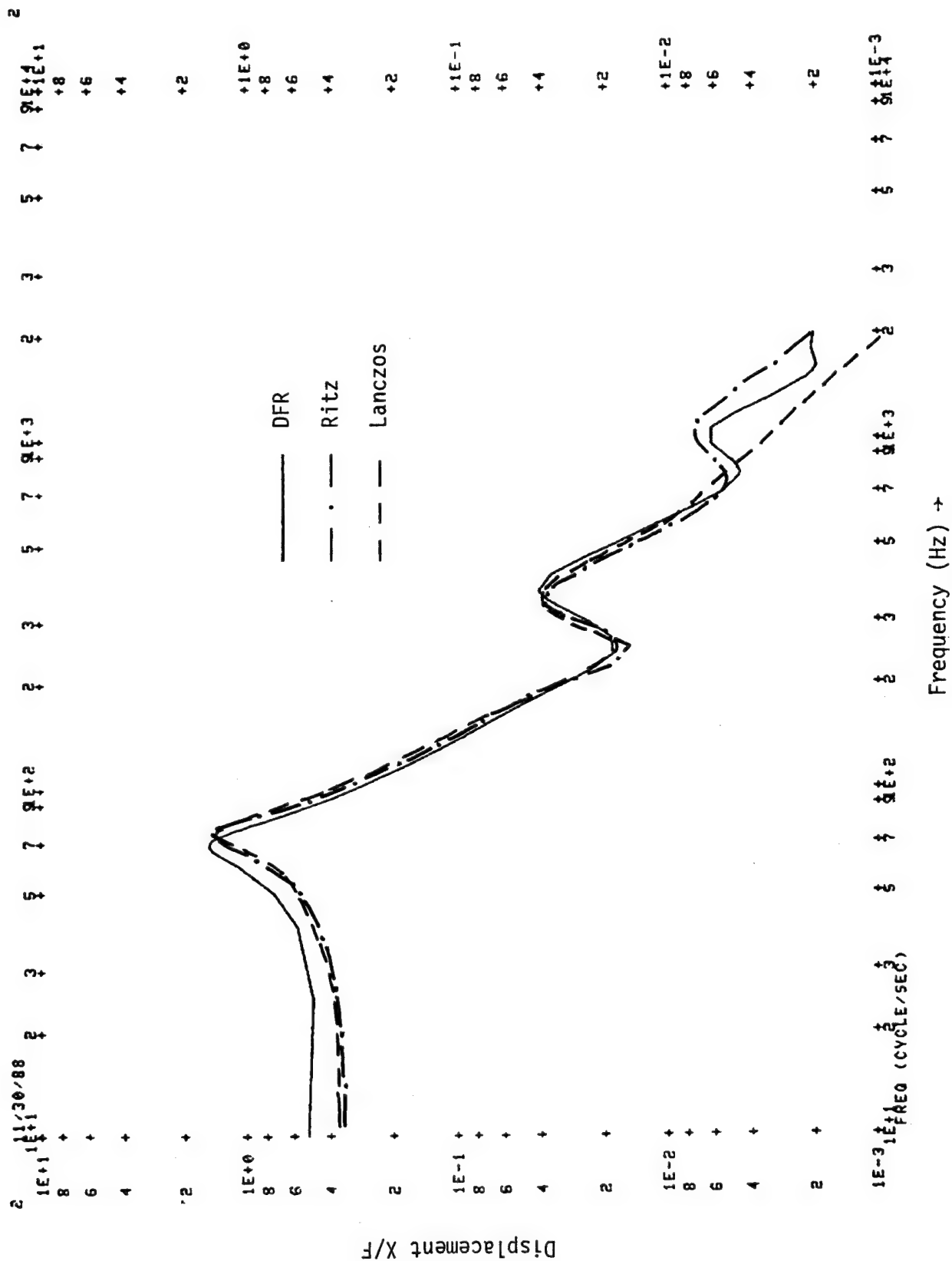
Figure 11 Comparison of Displacement Frequency Response at the Tip of the Beam Obtained from DFR Method and MSE Method Using Lanczos and Ritz Procedure with 3 Modes
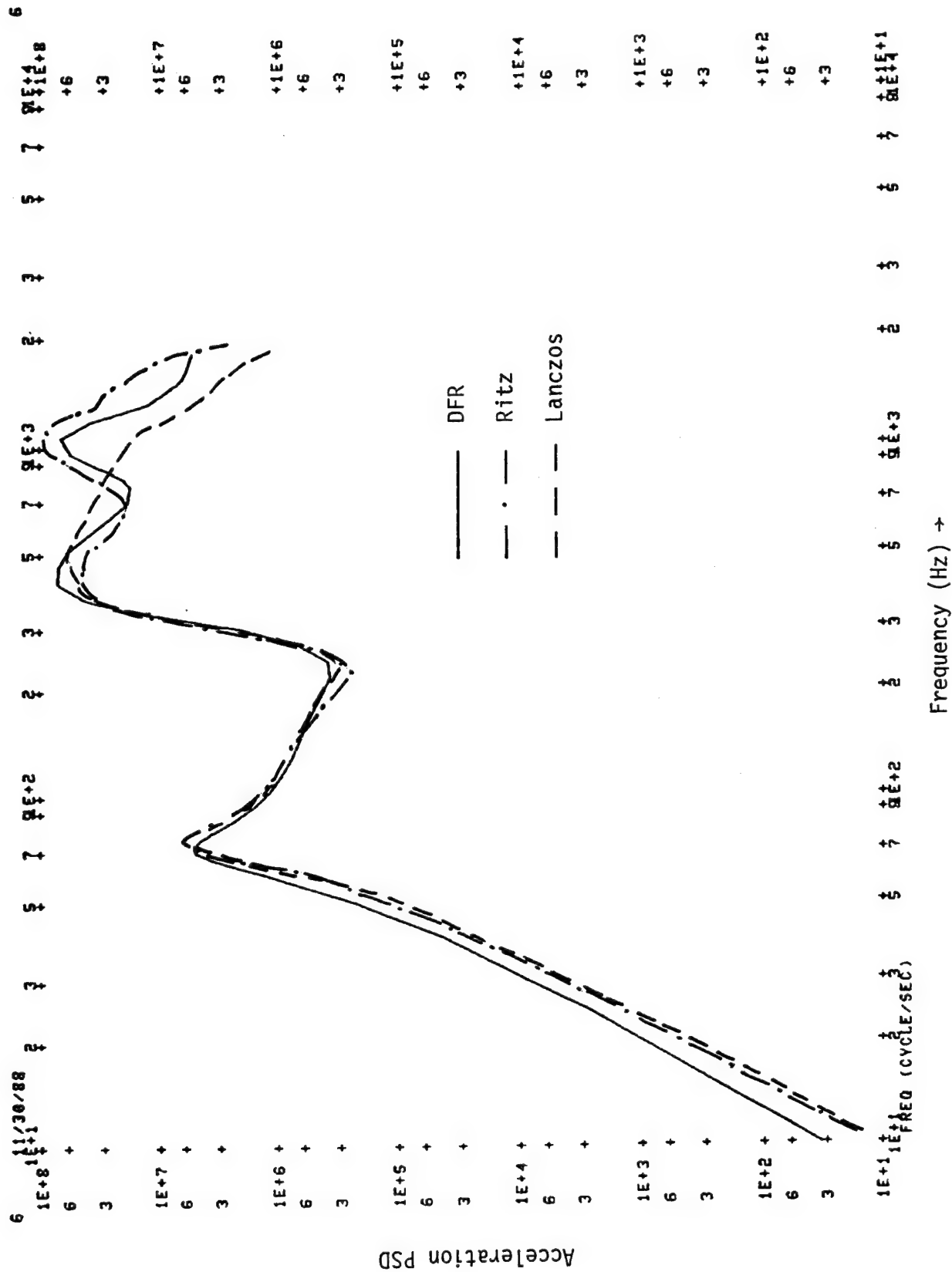
Figure 12 Comparison of Acceleration PSD Frequency Response at the Tip of the Beam Obtained from DFR Method and MSE Method Using Lanczos and Ritz Procedure with 3 Modes

TABLE 2

MODAL DAMPING RATIOS USING OUTPUT FROM THE AUTOMATIC PROCEDURE WITH LANCZOS METHOD

Mode No.	Type	Frequency (Hz)	Core Shear Modulus psi	Normalized Loss Factor η/η_v	Modal* Damping Ratio
1	1B	63.3	88.5	0.291	0.213
2	2B	343.8	282.3	0.302	0.395
3	1T	654.6	441.7	0.0995	0.163
4	3B	920	560.2	0.311	0.574
5	4B	1,748	930.9	0.305	0.726

* Used $G_{2,ref}$ = 300 psi; refer to Eq. (5).

TABLE 3

MODAL DAMPING RATIOS (FIVE MODES ONLY)
USING OUTPUT FROM THE AUTOMATIC PROCEDURE
WITH RITZ METHOD

Mode No.	Type	Frequency (Hz)	Core Shear Modulus psi	Normalized Loss Factor η/η_v	Modal* Damping Ratio
1	1B	63.1	86.9	0.291	0.211
2	2B	343.1	278.6	0.302	0.393
3	3B	918.8	556.8	0.311	0.572
4	4B	1,733.8	927.4	0.303	0.719
5	-	3,763.5	1,584.5	0.287	0.890

* Used $G_{2,ref}$ = 300 psi; refer to Eq. (5).

TABLE 4

MODAL DAMPING RATIOS (THREE MODES ONLY)
USING OUTPUT FROM THE AUTOMATIC PROCEDURE
WITH RITZ METHOD

Mode No.	Type	Frequency (Hz)	Core Shear Modulus psi	Normalized Loss Factor η/η_v	Modal* Damping Ratio
1	1B	63.1	86.9	0.29	0.211
2	2B	343.4	278.8	0.303	0.391
3	3B	1,182	682.2	0.33	0.672

* Used $G_{2,ref}$ = 300 psi; refer to Eq. (5).

TABLE 5

COMPARISON OF CPU SECONDS FOR VARIOUS METHODS

	Direct Frequency Response (DFR) Method	Modal Strain Energy Method				
		Manual	Automatic			
			Lanczos		Ritz	
		Lanczos	5 Modes	3 Modes	5 Modes	3 Modes
Eigenvalue Extraction	–	2,200	5,062	3,306	3,533	2,242
Modal Superposition	–	1,199	1,199	1,054	1,070	928
TOTAL	3,838	3,399	6,261	4,360	4,603	3,170

Table 5 shows the CPU seconds used for the analysis of the 360 DOF model which was used with the various approaches described above. The Ritz procedure requires 27% less CPU time compared to the Lanczos method. The manual method with five modes requires less CPU than either the Ritz or the Lanczos method, but the time required to submit and examine five computer runs, and then to plot contours to obtain the modal loss factors can be substantial. In addition, the manual method is more vulnerable to the possibility of human error.

CONCLUSIONS

The modal strain energy method has numerous attractive features as a means to estimate damping in structures with constrained viscoelastic layers. The procedure presented in this report automates the extraction of modal loss factors. Instead of making several normal modes extraction runs, the user needs to execute the finite element model only once, thus saving costly engineering time. Additionally, the automatic extraction of the loss factors minimizes the introduction of human error inherent in the manual method. Finally, a substantial savings in CPU time accrues due to the Ritz method, making the automatic extraction of loss factors and subsequent forced-response analysis using the Ritz procedure an attractive alternative for designs using constrained-layer damping.

AKNOWLEDGEMENTS

REFERENCES

1. Wilson, E., and Yuan, S., "Dynamic Analysis by Direct Superposition of Ritz Vectors," Earthquake Engineering and Structural Dyanmics, Vol. 10, 1982.

2. Johnson, C., Kienholz, D., and Rogers, L., "Finite Element Prediction of Damping in Beams with Constrained Viscoelastic Layers," Shock and Vibration Bulletin, No. 51, Part 1, Philadephia, PA, May 1981.

3. Unger, E.E. and Kerwin, E.M. Jr., "Loss Factors of Viscoelastic Systems in Terms of Energy Concepts," Journal of the Acoustical Society of America, Vol. 34, Jul 1962, pp. 954-957.

4. Arnold, R., Citerley, R., Chargin, M., and Galant, D., "Application of Ritz Vectors for Dynamic Analysis of Large Structures," Computers and Structures, Vol. 21, No. 3, 1985.

5. "Ritz Procedure for COSMIC/NASTRAN," ASIAC Report 685.1C, Aerospace Structures Information and Analysis Center, Wright-Patterson AFB, OH, June 1985.

6. Harris, S., "Computer Programs for Generation of NASTRAN and VIBRA-6 Aircraft Models," AFWL-TR-87-21, Air Force Weapons Laboratory, April 1988.

7. MSC/NASTRAN Application Manual, Vol I, Sec. 2.11, MacNeal-Schwendler Corp., Los Angeles, CA, J. A. Joseph, Ed., July, 1988.

FORMULATION AND INVERSION OF TRANSFER FUNCTIONS
OF COMBINED ELASTIC/VISCOELASTIC STRUCTURES

S. B. Skaar, Associate Professor
Engineering Science and Mechanics
Iowa State University

G. A. Nariboli, Professor
Engineering Science and Mechanics
Iowa State University

L. Tang, Graduate Student
Engineering Science and Mechanics
Iowa State University

Abstract

The paper develops and illustrates a new method for constructing system transfer functions for structures which may be regarded as assemblies of constituent members connected at joints. Several transfer functions for each individual member which describe required displacement-output to force-input relationships must be available. The individual members may be rigid, elastic, or viscoelastic, and the composite structure may be any combination of the three.

The method is illustrated with a triangular structure. First, an elastic version of the closed-form frequency response is verified using a comparison with a consistent, finite-element approximation for the same structure. Next, one of the elastic members is replaced with a highly damped viscoelastic member modeled with a fractional derivative constitutive law. Again, the frequency response is illustrated graphically. The damped and undamped responses are compared.

Finally, a method is developed in which the elastic/viscoelastic structure's impulse response can be determined by inverting the mixed transfer function. This ability to invert is of particular interest since the "composite" transfer function includes appearances of the Laplace variable s raised to fractional powers.

Introduction

Nonrigid satellite control has been, and continues to be, a subject of considerable interest. To date, much of the effort has been devoted to the study of elastic models for which governing finite-order differential equations of motion are determined from finite element analyses. Where linear damping is assumed to be present in the models, methods of approximation which rely on the availability of frequency-dependent loss factors are used to determine damping coefs. which are associated with each modal frequency and corresponding mode shape. Thus, the decoupled elastic (modal) equations of motion are replaced with corresponding damped equations of motion.

Other methods, too, have been developed[1] to approximate equations of motion for damped systems, but the difficulty remains that these approaches are limited to "small" damping, and that they may not easily incorporate experimental information available for individual members for which, due to internal complexity, the damping mechanism may not lend itself to accurate analysis.

It is likely that many applications of system response descriptions will not require complete equations of motion for the system, but that transfer functions which describe (absolute or relative) displacement outputs, or stress outputs, at points of interest to generalized force inputs at points of actuation or disturbance may be sufficient. Such transfer functions are useful for determining frequency response as well as the closed-loop behavior of feedback control systems. If the structure's transfer functions can be inverted, then transient responses also become available.

It has been shown[2] that transfer functions of structures composed of members for which individual-member transfer functions are available may be determined algebraically and exactly from the structure's geometry. Most often, these methods (which include the "transport matrix method"[3] and the "dynamic stiffness matrix method"[4]) are applied to cases where "exact," or transcendental, infinite dimensional transfer functions are used--producing, with a finite amount of computation, transfer function responses of infinite order. Nevertheless, the amount of computation that is necessary to solve such systems tends to grow with the cube of the number of joints which connect these members, making the approach impractical.

It is the purpose of the present paper to suggest--and to illustrate--how the computational burden that is associated with these calculations may be reduced substantially by taking advantage of geometric patterns and properties which are likely to inhere in actual structures. It is furthermore intended to indicate the ease with which one or several elastic members may be replaced by viscoelastic members (or vice versa) once the algebra that is associated with a given structural geometry has been established. This is a useful design capability, particularly since it becomes very convenient to consider the effect of a large variety of component options on both displacement and stress responses at points of interest within the overall structure. Another point of the paper is that the presence of substantial damping in component members of an otherwise elastic structure can alter radically the character of a structure's frequency response near certain frequencies which, for the corresponding elastic structure, represent resonant frequencies. At the same time, other resonant peaks remain largely

unchanged. Such occurrences could not have been forecast using modal strain
energy methods.

It has been shown[5,6] that viscoelastic material damping is often well
and concisely represented using fractional time derivatives operating on
stress and strain, and that therefore transfer functions for members which
include these kinds of materials might best be expressed[7] in terms of frac-
tional powers of the Laplace variable s.

There exists for various kinds of distributed-element models, such as
the member illustrated in Figure 1, a number of distinct displacement/output
to force/input relationships. These may be expressed using a "transfer
matrix," elements of which can be selected to give the desired relationship
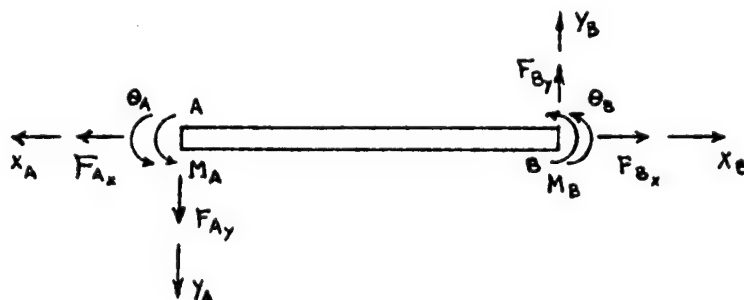
Figure 1.

among these input and output quantities of interest in the Laplace domain.
For a member such as that shown in Figure 1, the transfer matrix might
appear as follows:

$$
\begin{Bmatrix} \bar{x}_A \\ \bar{y}_A \\ \bar{\theta}_A \\ \bar{x}_B \\ \bar{y}_B \\ \bar{\theta}_B \end{Bmatrix} = \begin{bmatrix} G_1 & 0 & 0 & G_2 & 0 & 0 \\ 0 & G_4 & G_9 & 0 & G_3 & G_{10} \\ 0 & G_9 & G_6 & 0 & G_{10} & G_8 \\ G_2 & 0 & 0 & G_1 & 0 & 0 \\ 0 & G_3 & G_{10} & 0 & G_4 & G_9 \\ 0 & G_{10} & G_8 & 0 & G_9 & G_6 \end{bmatrix} \begin{Bmatrix} \bar{F}_{Ax} \\ \bar{F}_{Ay} \\ \bar{M}_A \\ \bar{F}_{Bx} \\ \bar{F}_{By} \\ \bar{M}_B \end{Bmatrix} \qquad (1)
$$

where the bar over each variable name denotes the Laplace transformation of
that time-varying quantity. The exact form of G_i will depend on the partic-
ular kind of model used for the member (e.g. Rayleigh beams, Timoshenko
beams, transversely rigid member, etc.). Various authors[8,9,10] have written
out forms for these sorts of transfer functions.

As an example (which will be referred to later herein), consider a
uniform member which deforms elastically in the axial direction, but which
is transversely rigid. A few of the examples of the transfer functions in
the matrix of Eq. (1) have the following forms:

$$G_1 = \overline{x}_B/\overline{F}_{Bx} = \overline{x}_A/\overline{F}_{Ax} = \frac{1}{s^2} \left[\frac{\sqrt{\rho A}}{s/\sqrt{E}} \tanh\,(aLs/\sqrt{E}) \right]^{-1} \tag{2}$$

$$G_2 = \overline{x}_A/\overline{F}_{Bx} = \overline{x}_B/\overline{F}_{Ax}$$

$$= -G_1[\cosh(aLs/\sqrt{E}) - \tanh(aLs/\sqrt{E})\sinh(aLs/\sqrt{E})] \tag{3}$$

$$G_3 = \overline{y}_B/\overline{F}_{Ay} = \frac{1}{2s^2} [L/(2I) - 2/M] \tag{4}$$

$$G_4 = \overline{y}_B/\overline{F}_{By} = \frac{1}{2s^2} [L/(2I) + 2/M] \tag{5}$$

where L is the length of the member, M is its mass, I is the mass moment of inertia about the mass center (axis normal to the page), E is Young's modulus, and a is given by

$$a = \sqrt{\rho/A} \tag{6}$$

where ρ is the mass per unit length, and A the cross-sectional area.

The transfer functions which describe a corresponding viscoelastic member (axially) will depend upon the particular constitutive law that is used to model the viscoelastic material behavior. In general, for axial stress and strain, and linear viscoelastic behavior, such a model may be expressed according to

$$P_\sigma[\sigma] = P_\varepsilon[E] \tag{7}$$

where P_σ and P_ε are linear operators, and σ and ε are the normal, axial stress and strain, respectively. For one particular constitutive form which has worked well in characterizing a number of viscoelastic materials:

$$P_\sigma = 1 + a \frac{\partial^\nu}{\partial t^\nu} \tag{8}$$

$$P_\varepsilon = E_1 + E_2 \frac{\partial^\nu}{\partial t^\nu} \tag{9}$$

This four-parameter model (ν is the fractional order of the derivative) is one of several[5,6] that have been suggested that involve a fractional-order derivative.

The correspondence principle[11] is used to convert transfer functions which are derived using the assumption of an elastic material (e.g. Eqs. (2,3)) to their viscoelastic counterparts. It is noted that in the expressions for G_1 and G_2 of Eqs. (2,3), the Laplace variable s appears in two contexts. One is where it multiplies $\sqrt{E}$, and the other is its (quadratic)

appearance in the denominator outside the bracketed term. The latter appearance represents rigid-body motion, and is unaffected by the transition to a viscoelastic material. The change that is made, however, involves converting each appearance of $(\nu/\sqrt{E}\,s)$ to the function $h(s)$ given by

$$h(s) = s\sqrt{\overline{P}_\sigma(s)/\overline{P}_\epsilon(s)} \tag{10}$$

or, using the constitutive equation example of Eqs. (8,9)

$$h(s) = s\sqrt{\frac{1 + as^\nu}{E_1 + E_2 s^\nu}} \tag{11}$$

and Eqs. (2) and (3) become

$$G_1 = \frac{1}{s^2}\left[\frac{\sqrt{\rho A}}{h}\tanh(ahL)\right]^{-1} \tag{12}$$

$$G_2 = -G_1[\cosh(ahL) - \tanh(ahL)\sinh(ahL)] \tag{13}$$

As a practical matter, the simple use of the correspondence principle may be inadequate to characterize many highly damped members. Highly damped members may be composites in which the actual damping mechanisms are very complex, involving not simply the constituent materials but also several complex interactions between materials. Such members may demonstrate considerably different properties from specimen to specimen, as small differences in manufacturing produce large differences in response.

To handle such a situation, it is useful to be able to incorporate transfer function descriptions for actual damped members which have been characterized experimentally in the laboratory. Such "fits" of experimental data for as-built members can be made using fractional order derivatives in a concise, infinite-dimensional form (which contains transcendental functions), and may even involve an estimation of the order ν of the derivative itself.[12] The methods of analysis which are discussed in the next section will work equally well regardless of whether individual-member transfer functions are determined experimentally or analytically.

Combining Transfer Functions

General methods which have been developed to combine individual-member transfer functions include the dynamic stiffness matrix method.[13] This approach is illustrated using a particular structure, illustrated in Figure 2. We consider the case where each of the five members is pinned at both ends (resulting in zero bending moment at these endpoints), and where the axial and transverse behavior of each end responds to forces as described in Eqs. (1-5). The problem in this illustration will be to determine the transfer function which describes the displacement response to the right, $\overline{X}(s)$, of the leftmost joint of the structure to an external force which acts upon the same point, and to the right.
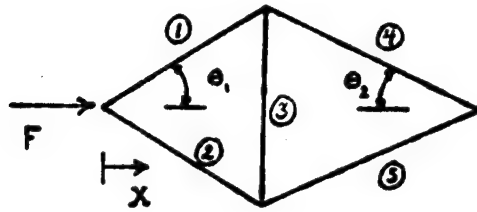
Figure 2

Initially, the 20 axial and transverse displacements associated with each member and the 20 axial and transverse forces are defined using the vectors $\underline{q}^* = [q_1^*, q_2^*, \cdots, q_{20}^*]^T$ for the displacements, and $\underline{f}^* = [f_1^*, f_2^*, \cdots, f_{20}^*]^T$ for the forces, as indicated in Figure 3a.
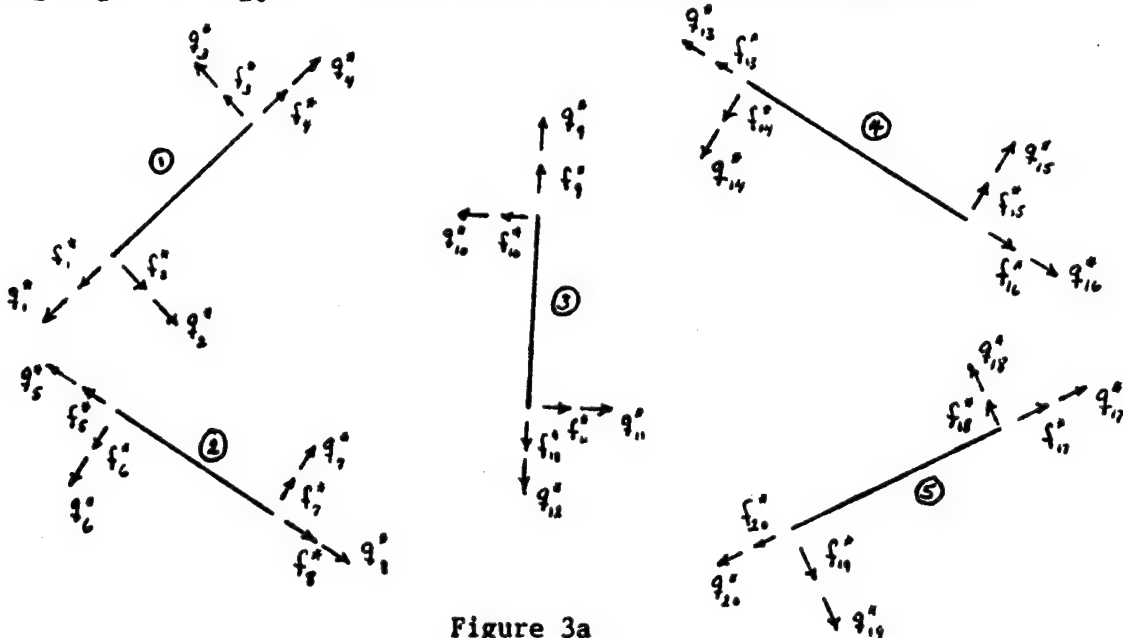
Figure 3a
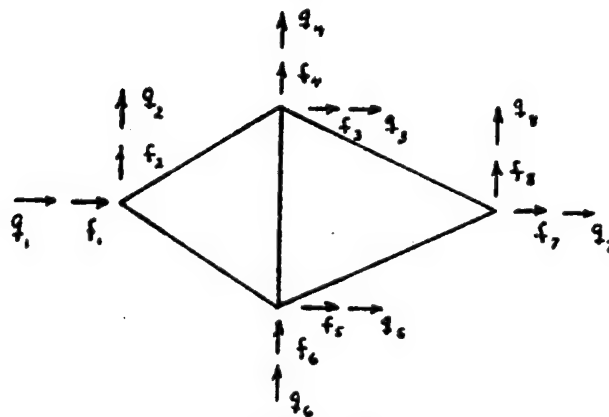
Figure 3b

The dynamic stiffness matrix for member 1 is then expressed using the transfer functions G_1^1, G_2^1, G_3^1, G_4^1 as given in Eqs. (2-5), where a subscript 1 has been added to denote that the elastic, mass, and geometric properties associated with member 1 apply. In the Laplace domain the "stiffness" relationship can be shown to be given by

$$
\begin{Bmatrix} f_1^* \\ f_2^* \\ f_3^* \\ f_4^* \end{Bmatrix} =
\begin{bmatrix}
G_1^1/[(G_1^1)^2 - (G_2^1)^2] & 0 & 0 & -G_2^1/[(G_1^1)^2 - (G_2^1)^2] \\
0 & G_4^1/[(G_4^1)^2 - (G_3^1)^2] & -G_3^1/[(G_4^1)^2 - (G_3^1)^2] & 0 \\
0 & -G_3^1/[(G_4^1)^2 - (G_3^1)^2] & G_4^1/[(G_4^1)^2 - (G_3^1)^2] & 0 \\
-G_2^1/[(G_1^1)^2 - (G_2^1)^2] & 0 & 0 & G_1^1/[(G_1^1)^2 - (G_2^1)^2]
\end{bmatrix}
\begin{Bmatrix} q_1^* \\ q_2^* \\ q_3^* \\ q_4^* \end{Bmatrix}
$$

(14)

where the matrix of Eq. (14) is given the name K_1^*. A similar matrix K_j^* can be developed for the jth of the five members by replacing each G_i^1, $i = 1,2,3,4$, in the matrix of Eq. (14) with G_i^j. Thus, a matrix $[K^*]$ can be formed which gives the stiffness relationship

$$\underline{f}^* = [K^*]\underline{q}^* \tag{15}$$

where K^* has the block diagonal form

$$
[K^*] =
\begin{bmatrix}
K_1^* & & \\
 & \ddots & \\
 & & K_5^*
\end{bmatrix}
\tag{16}
$$

Figure 3b indicates the definition of the coordinates $q = [q_1, q_2 \cdots q_8]^T$, which represent the actual, allowable displacements of the points of connection. From geometric considerations alone, a (20x8) connectivity matrix $[C]$ can be found which relates the unconstrained displacements $\underline{q}^*$ to the nodal displacements $\underline{q}$ according to

$$\underline{q}^* = [C]\underline{q} \tag{17}$$

where in the case of the structure of Figures 2 and 3, $[C]$ has the form

$$[C] = \begin{bmatrix}
-\cos\theta_1 & -\sin\theta_1 & & & & & & \\
-\sin\theta_1 & \cos\theta_1 & & & & & & \\
& & -\sin\theta_1 & -\sin\theta_1 & & & & \\
& & -\cos\theta_1 & \cos\theta_1 & & & & \\
-\cos\theta_1 & \sin\theta_1 & & & & & & \\
-\sin\theta_1 & -\cos\theta_1 & & & & & & \\
& & & & & \sin\theta_1 & \cos\theta_1 & \\
& & & & & \cos\theta_1 & -\sin\theta_1 & \\
& & & 1 & & & & \\
& & -1 & & & & & \\
& & & & 1 & & & \\
& & & & & -1 & & \\
& & -\cos\theta_2 & -\cos\theta_2 & & & & \\
& & \sin\theta_2 & \sin\theta_2 & & & & \\
& & & & & -\sin\theta_2 & -\cos\theta_2 & \\
& & & & & \cos\theta_2 & -\sin\theta_2 & \\
& & & & & \cos\theta_2 & \sin\theta_2 & \\
& & & & & -\sin\theta_2 & \cos\theta_2 & \\
& & \sin\theta_2 & -\cos\theta_2 & & & & \\
& & -\cos\theta_2 & -\sin\theta_2 & & & &
\end{bmatrix}$$

$$(18)$$

If the vector of external force components $\underline{f} = [f_1, f_2, \ldots f_8]^T$ which corresponds with the elements of $\underline{q}$ is defined as indicated on Figure 3b, then it can be shown that $\underline{f}$ is related to $\underline{f}^*$ according to

$$\underline{f} = [C]^T \underline{f}^* \tag{19}$$

Combining Eqs. (15,17,19) produces

$$\underline{f} = [K]\underline{q} \tag{20}$$

where

$$[K] = [C]^T [K^*] [C] \tag{21}$$

The transfer function of interest is

$$\overline{X}/\overline{F} = q_1/f_1 \tag{22}$$

which is the 1,1 element of $[K]^{-1}$.

At this juncture three points should be made.

First, the method outlined above is general in the sense that it is not restricted to members which are pinned (provided transfer functions giving responses to applied end-moments are available for each member). Furthermore, the method can be applied with little additional effort to three-dimensional structures.

The second point is that the numerical burden that will be associated with evaluating the function $\overline{X}/\overline{F} = H(s)$ at a given value of s will, in general, grow with the cube of the number of nodal points (n^3) present on the structure.

And thirdly, the method outlined above does not exploit certain very elemental geometric properties likely to be found in most actual structures. Neither does it provide for a means to exploit repeated geometric patterns as they may appear in actual structures. Based on the experience which we have gained with the exercise that follows, we believe that there may be some significant reduction to (at most) a computational burden which grows with n^1, where n is the number of nodal points, if such things are considered carefully.

Consider the simpler triangular structure of Figure 4, which represents the left portion of the more elaborate structure of Figure 2. An analysis similar to that which is described above can be performed on this new structure to produce an elastic frequency response. The algebra associated with performing the inversion of K can, however, be reduced by using geometric properties which are possessed by any triangle.
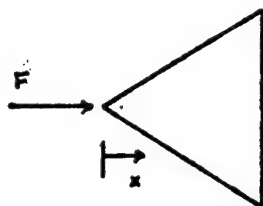
Figure 4
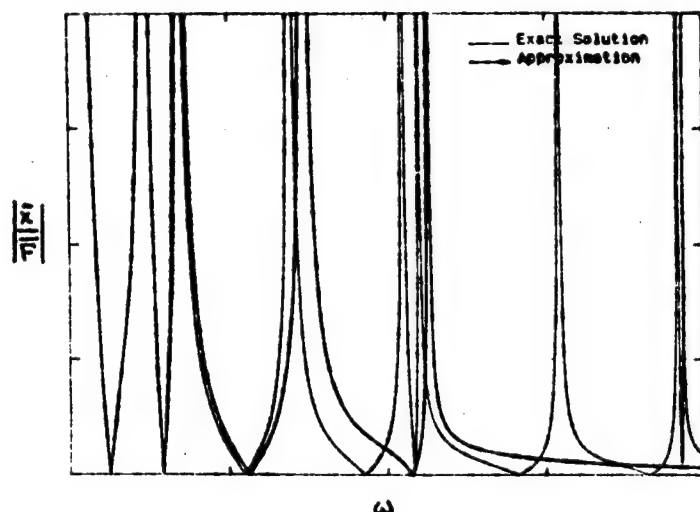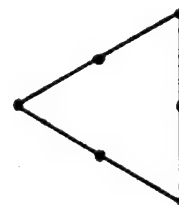
Figure 5

Figure 5 gives the (amplitude) frequency response for the triangular structure of Figure 4. The elastic properties that are associated with the axial deformation of each member, along with geometric and inertial properties, are indicated on the figure. Superimposed onto the "exact" frequency response solution is a finite-element approximation (Ritz approach, 6 nodal points)[14] for the same structure. As expected for any consistent approximation, the frequencies at which (infinite, resonant) peaks for the approximation occur move progressively further to the right of their counterparts in the exact solution, until peaks for the approximation run out altogether. This, combined with the marked similarity of the two solutions at the lower frequencies, gives confidence in the accuracy of the two solutions.

Figure 6 repeats the exact frequency response of Figure 5. This time, however, a different exact solution is superimposed. Using the viscoelastic material properties which are indicated to the right of Figure 6, the elastic model that was used for the material description of the vertical member was replaced by the viscoelastic model. The two diagonal members were left unchanged. All of the computational economies which were established for the elastic triangle remain intact for the mixed case.
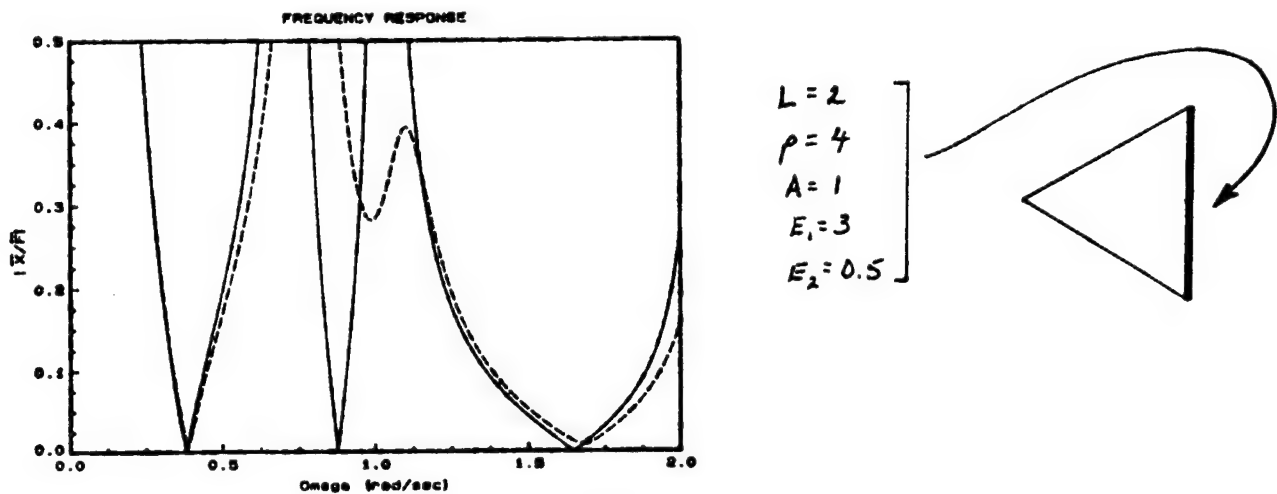
Figure 6

In addition to the transfer function of interest, $\overline{X}/\overline{F}$, the inversion of K provided a full complement of displacement/output to force/input transfer functions for the single triangle. As such, this triangle can be thought of as one member of a second triangle which in reality is the structure of
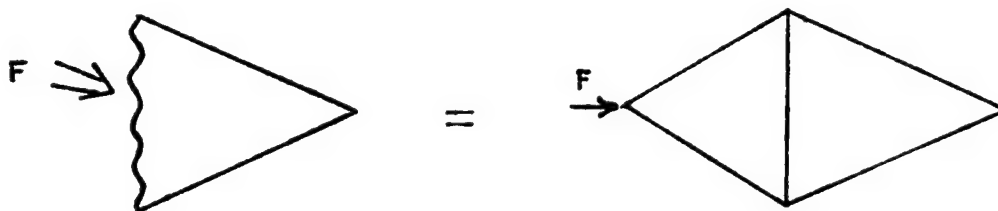
Figure 7

interest of Figure 2. This is suggested in Figure 7. It must be noted that
the analysis of this second "triangular structure" will differ somewhat from
the first triangle. In particular, the more complex new member carries with
it input/output relationships which were zero for the axially symmetric mem-
bers of the first analysis. These include the axial displacement response
to transverse force inputs, and vice versa. In addition, the response of
nodal points at which the "new member" is connected are sensitive to actu-
ation at a location in the member which, in the context of the second tri-
angle, is not a joint. Although these added transfer functions do increase
the computational burden that is associated with evaluating K^{-1} for the new
triangle, the number of computations (after a prior evaluation of K^{-1} for
the first triangle) is not significantly higher.

Figure 8 illustrates the same comparison between exact and (9 nodal
point) finite-element approximation for the elastic double-triangle struc-
ture that Figure 6 illustrated for the single triangle. Again, the rela-
tionship between the "exact" and approximate solutions tends to give
credence to the accuracy of both. The exact solution shown in Figure 8 was
generated by regarding the triangular structure of Figure 5 as one of the
members of a second triangle, as discussed above.
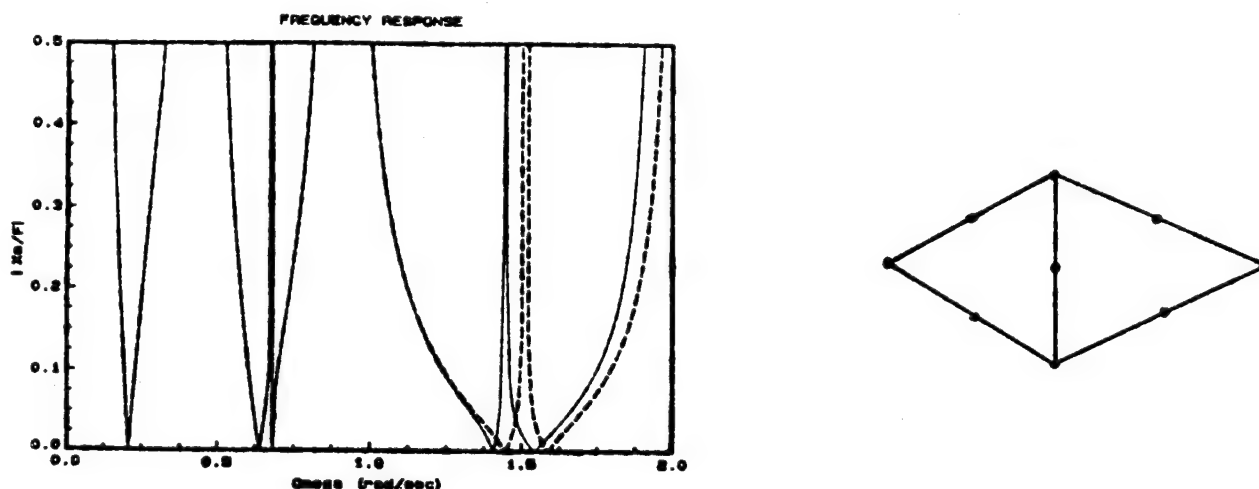
Figure 8

Again, once the algebraic formulation has been established, there is no
difficulty substituting viscoelastic members at will for elastic members.
Figure 9 illustrates a superposition of ("exact") elastic versus ("exact")
composite structures for which viscoelastic members have been used in place
of the two rightmost members in the mixed structure. It is interesting to
observe how the elastic frequency response has been altered in the presence
of the viscoelastic members. The resonant peak that appears near $\omega = 1.5$ in
the purely elastic structures is evidently eliminated completely with the
insertion of the two viscoelastic members. Other peaks, meanwhile, appear
on the plots of Figure 9, to be largely unaffected by the introduction of
the viscoelastic members. The result would be not be predicted by existing
methods of approximation for damped structures.
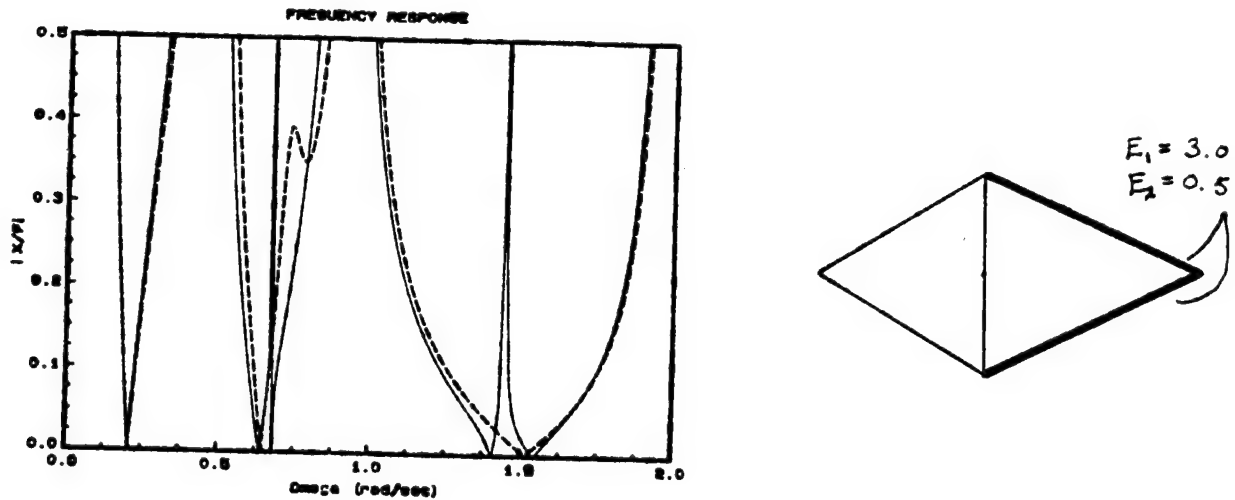
Figure 9

It is noted that this method can be applied successively and recursively to structures as indicated in Figure 10a, which would have the effect of reducing the computational burden to something of order n rather than n^3.

(a)

(b)
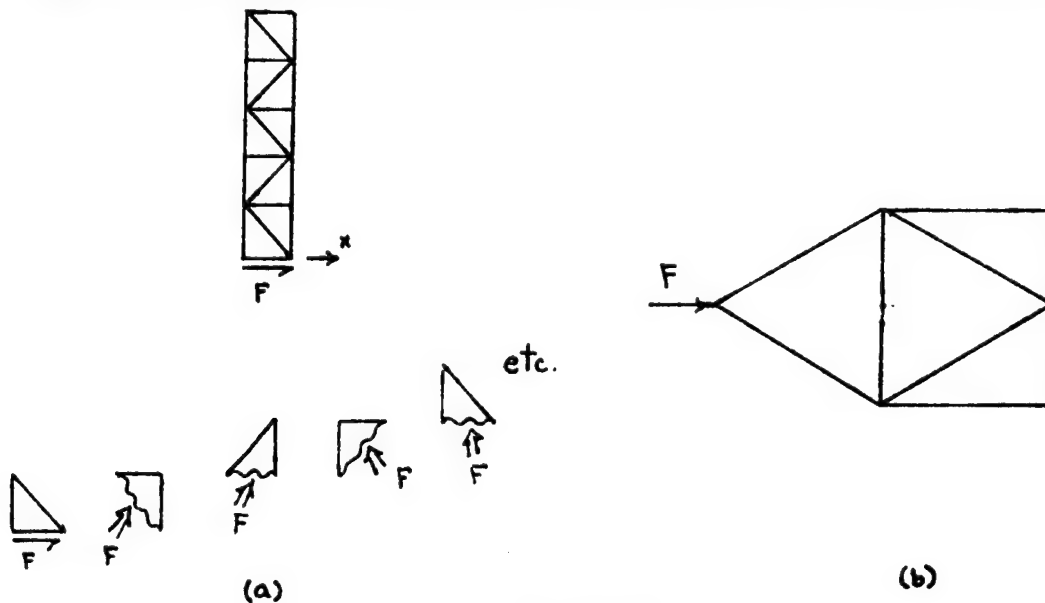
Figure 10

Preferably, however, for actual, complex structures, a means of subdividing the structure judiciously such that repetitions of substructures are fully exploited would be identified. Consider, for example, the structure of Figure 10b. The two small triangles (top and bottom) are mirror images, but otherwise identical and the set of required transfer functions for both may be found using a single treatment. The leftmost triangle, meanwhile, is an equilateral triangle which can be examined next. Finally, the general form from this result can be reused to complete the analysis by treating the whole structure as a second equilateral triangle, with the leftmost member

consisting of the earlier equilaterial triangle, while the upper and lower members are described by results from the small triangle which was analyzed initially. Rather than doing the required algebra (K^{-1}) on four triangles (which would be the case if the successive method were used blindly), only three are required.

Inverting Mixed Transfer Functions

Transcendental transfer functions of combination elastic/viscoelastic systems of the kind used for illustration in the previous section can be shown to be expandable to the form

$$H(s,h(s)) = \frac{\prod_i (s^2 + z_i^2) \prod_j (h^2(s) + z_j^{*2})}{\prod_k (s^2 + p_k^2) \prod_l (h^2(s) + p_l^{*2})}$$

$$= \sum_k \frac{r_k}{s^2 + p_k^2} + \sum_l \frac{r_l^*}{h^2(s) + p_l^{*2}} \tag{23}$$

where the two kinds of poles p_k^2 and p_l^{*2} are found using standard (real) root finders[15] together with the definition of h(s), (e.g. Eqs. 10,11). Residues r_k and r_l^* are then found according to[16]

$$r_k = \lim_{s^2 \to -p_k^2} \left[\left(s^2 + p_k^2 \right) H\left(s, h(s)\right) \right] \tag{24}$$

$$r_1 = \lim_{h^2 \to -p_1^2} \left[\left(h^2(s) + p_1^{*2} \right) H\left(s(h), h\right) \right] \tag{25}$$

With the transfer function of interest, H(s,h(s)), in the desired form of Eq. (23) (retaining an "adequate" number of terms), it remains to invert terms of two types. The first of the two is easily expressed as[16]

$$\mathcal{L}^{-1} \left\{ \frac{r_k}{s^2 + p_k^2} \right\} = \frac{r_k}{p_k} \sin(p_k t) \tag{26}$$

Terms of the second type have the form

$$\frac{r_1^*}{h^2(s) + p_1^{*2}} = g_1(\sqrt{s}) \tag{27}$$

where it is understood that the order of the fractional derivative of Eqs. (8,9) is $\nu = \frac{1}{2}$.

In order to invert such expressions, one uses the formula[16]

$$\mathcal{L}^{-1}\left\{g_1(\sqrt{s})\right\} = \int_0^\infty k(t,u)\, f_1(u)\, du \qquad (28)$$

where

$$\mathcal{L}\{f_1(t)\} = g_1(s) \qquad (29)$$

and

$$k(t,u) = \frac{1}{2t\,\sqrt{\pi t}}\, u\, \exp\left(-\frac{u^2}{4t}\right) \qquad (30)$$

Using Eq. (11) in Eq. (27), we are thus lead to invert

$$\frac{(E_1 + E_2 s)\, r_1^\star}{s^4(1 + as) + p_1^{\star 2}(E_1 + E_2 s)} \qquad (31)$$

If the roots of the fifth degree polynomial in the denominator of (31) are "s_i" ($i = 1,2,3,4,5$), then it is straightforward to write it as partial fractions, with each term having the form of a constant multiplying

$$\frac{1}{-s + s_i} \qquad (32)$$

the inverse of which is given by

$$\mathcal{L}^{-1}\left\{\frac{1}{-s + s_i}\right\} = -\exp(s_i t) \qquad (33)$$

Use of the formula (28) then gives an integral representation of the solution.

It may be noted that s_i are in general complex, and one may require numerical work to get the complete structure of the solution.

It may also be noted that, if, instead of the square root, one has any rational fraction, it is still possible to develop integral formulas of the type of (28).

Summary and Conclusions

Transcendental (infinite dimensional) expressions for transfer functions of individual members which may comprise a structure can often be formulated with a concise algebraic expression either analytically or experimentally, using a suitable form determined on the basis of a plausible constitutive equation as well as geometric considerations. Once established, these individual-member transfer functions can be combined algebraically to form transfer functions of the larger structure. By taking advantage of geometric properties that are likely to arise in such structures, the computational burden that is associated with evaluating the transfer function associated with the input and output points of interest for any desired value of s can be reduced significantly from that which is incurred from direct application of methods such as the dynamic stiffness matrix method.

Using a sample structural configuration, the method was shown to compare well in terms of frequency response in the elastic case with results from a finite-element analysis. Replacement of certain elastic members with viscoelastic members substantially changed the character of the frequency-response profile near certain (formerly) resonant frequencies. Such alterations would not likely result with the use of methods of approximation that are often employed to model the effects of viscoelastic damping, based on a modification of results from the elastic eigenvalue problem.

Finally, an approach was outlined to indicate how time-domain impulse responses can be determined on the basis of transfer functions which may include both elastic and viscoelastic members where constitutive equations which describe the latter include fractional-order derivatives.

Acknowledgments

References

1. Segalman, D. J., "Calculation of Damping Matrices for Linearly Viscoelastic Structures," ASME Journal of Applied Mechanics, 54:585-588, September 1987.

2. Clough, R. W., and Penzien, J., Dynamics of Structures, McGraw-Hill, New York, 1975.

3. Tuma, J. J., and Cheng, F. Y., Schaum's Outline of Theory and Problems of Dynamic Structural Analysis, McGraw-Hill, 1983.

4. Ariaratnam, S. T., "Vibration in Plane Frame Works," Applied Scientific Research, 13:249-259, 1964.

5. Bagley, R. L., and Torvik, P. J., "Fractional Calculus in the Transient Analysis of Viscoelastically Damped Structures," AIAA Journal, 23(6):918-925, June 1985.

6. Rogers, L., "Damping: On Modeling Viscoelastic Behavior," <u>Shock and Vibration Bulletin</u>, <u>51</u>:55-59, 1981.

7. Skaar, S. B., Michel, A. N., and Miller, R. K., "Stability of Viscoelastic Control Systems," IEEE <u>Transactions on Automatic Control</u>, <u>33</u>(4):348-357, April 1988.

8. Pestel, E. C., and Leckie, F. A., <u>Matrix Methods in Elastodynamics</u>, McGraw-Hill, New York, 1963.

9. Clark, S. K., <u>Dynamics of Continuous Elements</u>, Prentice-Hall, Englewood Cliffs, New Jersey, 1972.

10. Skaar, S. B., Tang, L., and Yalda-Mooshabad, I., "On-Off Attitude Control of Flexible Satellites," AIAA <u>Journal of Guidance, Control, and Dynamics</u>, <u>9</u>(4):507-510, 1986.

11. Christensen, R. M., <u>Theory of Viscoelasticity, An Introduction</u>, Academic Press, New York, 1971.

12. Rogers, J. D., and Skaar, S. B., "Parameter Estimation for a Viscoelastic Constitutive Model," <u>Proceedings</u>, 1989 Spring Conference on Experimental Mechanics, Cambridge, Massachusetts, May 28-June 1, 1989.

13. Piché, R., "Analysis of Structural Control Problems Using Frequency-Domain Continuum Models," PhD Thesis, Civil Engineering, University of Waterloo, 1986.

14. Meirovich, L., <u>Computational Methods in Structural Dynamics</u>, Sijthoff and Noordhoff, The Netherlands, 1980.

15. Wittrick, W. H., and Williams, F. W., "A General Algorithm for Computing Natural Frequencies of Elastic Structures," <u>Quarterly Journal of Mechanics and Applied Mathematics</u>, <u>XXIV</u>(3):263-284, 1971.

16. Wylie, C. Ray, <u>Advanced Engineering Mathematics</u>, McGraw-Hill, New York, 1960.

THE FRACTIONAL ORDER ESTIMATOR

R. Bagley
Gregory Warholla
David Yang**

* faculty
** student

The Fractional Order State Equations
for the Control of Viscoelastically Damped Structures

R. L. Bagley[*] and R. A. Calico[**]
Department of Aeronautics and Astronautics
Air Force Institute of Technology
Wright-Patterson AFB, Ohio 45433

Abstract

The fractional order state equations are developed to predict the effects of feedback intended to reduce motion in damped structures. The mechanical properties of damping materials are modeled using fractional order time derivatives of stress and strain. These models accurately describe the broad-band effects of material damping in the structure's equations of motion. The resulting structural equations of motion are used to derive the fractional order state equations. Substantial differences between the structural and state equations are seen to exist. The mathematical form of the state equations suggests the feedback of fractional order time derivatives of structural displacements to improve control system performance. Several other advantages of the fractional order state formulation are discussed.

Nomenclature

$\underline{\underline{A}}$: state Matrix

$-a^{\beta}$, : system eigenvalue

$-\underline{\underline{a}}^{\beta}$: diagonal matrix of eigenvalues

$\underline{\underline{B}}$: state control matrix

b : viscoelastic model parameter

D^{β} : the beta order fractional derivative

---

* Associate Professor, Associate Member ASME

** Professor, Associate Fellow AIAA

$\hat{D}^{\beta}$: modified beta order fractional derivative

$E_o; E_1$: viscoelastic model parameters

$E_{\beta}(x)$: the beta order Mittag-Leffler function

$\tilde{F}(t)$: applied loads prior to initial time, $t = 0$

$\tilde{\tilde{F}}(t)$: applied loads after initial time, $t = 0$

$\tilde{f}(t)$: modal loads prior to initial time, $t = 0$

$\tilde{\tilde{f}}(t)$: modal loads after initial time, $t = 0$

$f^*(t)$: stress operator acting on loads

$\tilde{G}(t)$: structural pseudo loads

$g(t)$: modal load

$\tilde{g}(t)$: modal psendo load

$-\underline{\underline{G}}$: feedback gain matrix

$I^{1-\alpha}$: the one minus α order fractional integral

$\underline{\underline{k}}_o$: structural stiffness matrix

$\underline{\underline{k}}_1$: structural visco-stiffness matrices

N : number of physical degrees of freedom

$\underline{\underline{M}}$: structural mass matrix

$\tilde{t}$: time starting at the onset of motion

t : time starting at the initial time

t_o : time interval between $\tilde{t} = 0$ and $t = 0$

$\underline{w}(t)$: structural displacements

x_i : spatial coordinates

$\underline{x}_r$: the reduced state vector

$\underline{x}(t)$: state vector

$\underline{x}_o$: intial state vector

$y(t)$: modal response

$\tilde{y}(t)$: modal response for loading prior to $t = 0$

$\tilde{\tilde{y}}(t)$: modal response for loading after $t = 0$

$\underline{z}$: impulsive load coefficients vector

β : basis fraction $(1/n)$ for the system

Γ : the gamma function

$\epsilon(t)$: strain history

ϕ : system orthonormal transformation

$\sigma(t)$: stress history

$(E_o + E_1 D^\alpha)$: Strain operator

$(1 + bD^\alpha)$: stress operator

Introduction

In the modeling of the linear elastic behavior of large space structures, damping has typically either been ignored or modeled as being linearly dependent on velocity. This damping model is adequate for very lightly damped structures and also allows a linear state space model to be defined for the structure's motion. This formulation is well suited to the design of active control systems using state space techniques.

However, for heavily damped structures ignoring the damping is imprudent and modeling it as being linearly dependent on velocity is inadequate. Velocity dependent damping models, while mathematically straightforward, fail to describe the broad band mechanical behavior of damping materials. Historically, the need for more refined models has pushed the development of viscoelasticity as a discipline within engineering mechanics. Applicable viscoelastic models relate time dependent stress and strain fields with series of ordinary time derivatives. These models yield acceptable broad band Bode plots of material properties, but they have drawbacks. Typically these models contain many terms, making them mathematically cumbersome and increasing the order of the differential equations describing the system.

As an alternative we will present accurate broad band viscoelastic damping models having only four parameters[2] and posed in terms of non-integer order time derivatives. The real strength of this approach is that these non-integer or fractional order derivatives describe inertial effects, damping effects, elastic effects and control effects with equal precision. Substantial accompanying benefits are that the order of differentiation in the system equations does not exceed three and that a potentially infinite number of additional feedback states arise to improve system performance.

To reap the benefits of this approach; however, one must become comfortable with the concept of fractional order

differentiation. While the convolution operator that produces these time derivatives at first appears alien, frational differentiation in the Laplace transform domian is exceedingly simple. Multiplying a transform by s^{α}, in effect, produces the transform of the α order derivative.

The development and applications of fractional order derivatives in viscoelasticity and structural dynamics are well documented.[1-9,12-14,16,18] The models are consistent with themodynamic constraints[6] and have their foundation in classical molecular theories predicting the macro mechanical properties of viscoelastic materials.[4]

The resulting structural equations of motion serve as the foundation for the state equations, but they are substantially different. The hereditary nature of the structural equations suppresses the existence of homogeneous solutions found in the state equations. In addition, the two sets of equations employ different operators that lead to different requirements for initial conditions. It should come as no suprise that the generalized or fractional order state equations comprise a generalization of the initial value problem. The generalization begins with the structural equations of motion.

The Structural Equations of Motion

The structural equations of motion differ from classical formulations in that fractional order derivatives are used to model the viscoelastic damping phenomenon. The extended Riemann Liouville fractional derivative is a linear operator

$$D^{\alpha}_{(t)}[w(t)] \equiv \frac{d}{dt}\int_0^t \frac{w(t)}{\Gamma(1-\alpha)(t-\tau)^{\alpha}}\, d\tau \qquad 0 \le \alpha \le 1 \qquad (1)$$

and serves as the basis of the generalized model of the viscoelastic phenomenon. The most general form of the models is

$$\sigma(t,x_i) + \sum_{p=1}^{N} b_p D^{\alpha_p}_{(t)}[\sigma(t,x_i)] = E_o \epsilon(t,x_i) + \sum_{p=1}^{N} E_p D^{\alpha_p}_{(t)}[\epsilon(t,x_i)] \qquad (2)$$

where the derivatives acting on the stress and strain fields are of real, rational fractional order. Note that this model becomes the classical viscoelastic model[10] when the orders of differentiation are taken to be integers.

The Fourier transform of the fractional derivative of a function has a special property when the function is zero for negative time.

$$F\left[D^{\alpha}_{(t)}[x(t)]\right] = (i\omega)^{\alpha} F[x(t)] \tag{3}$$

where

$$F[x(t)] = \int_{-\infty}^{\infty} x(t)e^{-i\omega t} dt \tag{4}$$

This property, eqn 3, is that the transform of the α order derivatives is the transform parameter, $i\omega$, raised to the α power times the transform of the function. Note the similarity of this transform with the Fourier transform of an ordinary derivative.

The attractive feature of the fractional derivative operator is the ability to vary the degree of its frequency dependence through the choice of α. As a direct result, fractional derivative models are capable of modeling linear, frequency-dependent phenomena not easily captured by the transforms of ordinary derivatives. This leads to models accurate over several decades of frequency needing very few, typically four, parameters[6].

In the time domain the four parameter model for uniaxial deformation takes the form

$$(1 + bD^{\alpha})\sigma(t) = (E_o + E_1 D^{\alpha})\epsilon(t) \tag{5}$$

where b, E_o, E_1 and α are the parameters. This model has been used to construct the general three-dimensional constitutive equations for linear, homogeneous, isotropic viscoelastic materials[1]. When these general constitutive equations are employed, it can be shown that the general form of the finite element equations of motion take the form[3]

$$b\underline{\underline{M}}D^{2+\alpha}\underline{w}(t) + \underline{\underline{M}}D^2\underline{w}(t) + \underline{\underline{k}}_1 D^{\alpha}\underline{w}(t) + \underline{\underline{k}}_o\underline{w}(t) = bD^{\alpha}\underline{F}(t) + \underline{F}(t). \tag{6}$$

where $\underline{\underline{M}}$ is the mass matrix, $\underline{\underline{k}}_o$ is the stiffness matrix, $\underline{\underline{k}}_1$ is the visco-stiffness matrix, $\underline{F}(t)$ are the applied forces and $\underline{w}(t)$ are the structure's deflections. Note that the equations of motion are posed in terms of three real, square symmetric matrices. In general the visco-stiffness matrix $\underline{\underline{k}}_1$ will not be a linear combination of $\underline{\underline{M}}$ and $\underline{\underline{k}}_o$ and usually the equations of motion cannot be decoupled in their present form.

To overcome this obstacle to spectral analysis and begin the

derivation of the state equations, we will pose the structural equations of motion in terms of two real, square symmetric matrices, for which an orthonormal transformation exists. To begin this process one takes advantage of the composition property of the fractional order derivative,

$$D^{\alpha}\left[D^{\gamma}\left[w(t)\right]\right] = D^{\alpha+\gamma}\left[w(t)\right],\tag{7}$$

and poses the structural equations of motion as

$$\left(b\underline{\underline{M}}(D^{\beta})^{m} + \underline{\underline{M}}(D^{\beta})^{r} + \underline{\underline{k}}_{1}(D^{\beta})^{q} + \underline{\underline{k}}_{o}\right)\underline{w}(t) = \left(1 + b(D^{\beta})^{q}\right)\underline{F}(t)\tag{8}$$

Here m, r and q are integers and $(D^{\beta})^{m}$ is the β order derivative taken m times.

$\beta m = 2 + \alpha$

$\beta r = 2$

$\beta q = \alpha$

$\beta = 1/n$

β is chosen to be the largest fraction of the form 1/n, where n is an integer, common to all the rational orders of differentiation in the structural equations of motion,. As we will see later, this form for β is necessary to insure that initial velocities appear in the fractional order state equations. The most general form of these equations of motion is

$$\sum_{p=0}^{m} \underline{\underline{c}}_{p}(D^{\beta})^{p}\underline{w}(t) = (1 + b(D^{\beta})^{q})\underline{F}(t) = \underline{f}^{*}(t).\tag{9}$$

Here the $\underline{\underline{c}}_{p}$ are real and constant, although many may be zero, and $\underline{f}^{*}(t)$ is the result of the viscoelastic stress operator acting on the applied forces, $\underline{F}(t)$, as shown in eqn 8.

Eqn 9 describes the structures with N degrees of freedom producing N equations of order βm that can be alternatively posed as m·N equations of order β. In matrix form the m·N equations of β order are

$$
D^\beta \begin{bmatrix} \underline{\underline{0}} & & & \\ \vdots & & H & \\ \underline{\underline{0}} & & & \\ \underline{\underline{0}} & & & \\ \hline \underline{\underline{c}}_m & \cdots & \underline{\underline{c}}_3 \underline{\underline{c}}_2 \underline{\underline{c}}_1 \end{bmatrix} \begin{Bmatrix} (D^\beta)^{m-1}\underline{w}(t) \\ \vdots \\ (D^\beta)^2\underline{w}(t) \\ (D^\beta)^1\underline{w}(t) \\ \underline{w}(t) \end{Bmatrix}
$$

$$\tag{10}$$

$$
+ \begin{bmatrix} & & & \underline{\underline{0}} \\ & -H & & \vdots \\ & & & \underline{\underline{0}} \\ & & & \underline{\underline{0}} \\ \hline \underline{\underline{0}} & \cdots & \underline{\underline{0}}\;\underline{\underline{0}} & \underline{\underline{c}}_0 \end{bmatrix} \begin{Bmatrix} (D^\beta)^{m-1}\underline{w}(t) \\ \vdots \\ (D^\beta)^2\underline{w}(t) \\ (D^\beta)^1\underline{w}(t) \\ \underline{w}(t) \end{Bmatrix} = \begin{Bmatrix} \underline{0} \\ \vdots \\ \underline{0} \\ \underline{0} \\ \underline{f}^*(t) \end{Bmatrix}
$$

where the lowest set of partitioned equations is seen to be eqn 9. The matrix [H] is chosen such that both square matrices of order m·N become symmetric and the top (m-1)·N equations are satisfied identically. This is accomplished by constructing H such that all matrices, $\underline{\underline{c}}_p$ lying on any given diagonal running from lower left to upper right in the first matrix of eqn 10 are equal. We will refer to this form of the equations of motion as the expanded equations of motion.

For example, if α is one half in eqn 6, then β is one half making m=5 in eqn 8 and the expanded equations of motion become

$$
D^{1/2} \begin{bmatrix} \underline{\underline{0}} & \underline{\underline{0}} & \underline{\underline{0}} & \underline{\underline{0}} & b\underline{\underline{M}} \\ \underline{\underline{0}} & \underline{\underline{0}} & \underline{\underline{0}} & b\underline{\underline{M}} & \underline{\underline{M}} \\ \underline{\underline{0}} & \underline{\underline{0}} & b\underline{\underline{M}} & \underline{\underline{M}} & \underline{\underline{0}} \\ \underline{\underline{0}} & b\underline{\underline{M}} & \underline{\underline{M}} & \underline{\underline{0}} & \underline{\underline{0}} \\ b\underline{\underline{M}} & \underline{\underline{M}} & \underline{\underline{0}} & \underline{\underline{0}} & \underline{\underline{k}}_1 \end{bmatrix} \begin{Bmatrix} (D^{1/2})^4\underline{w}(t) \\ (D^{1/2})^3\underline{w}(t) \\ (D^{1/2})^2\underline{w}(t) \\ (D^{1/2})^1\underline{w}(t) \\ \underline{w}(t) \end{Bmatrix}
$$

$$\tag{11}$$

$$
+ \begin{bmatrix} \underline{\underline{0}} & \underline{\underline{0}} & \underline{\underline{0}} & -b\underline{\underline{M}} & \underline{\underline{0}} \\ \underline{\underline{0}} & \underline{\underline{0}} & -b\underline{\underline{M}} & -\underline{\underline{M}} & \underline{\underline{0}} \\ \underline{\underline{0}} & -b\underline{\underline{M}} & -\underline{\underline{M}} & \underline{\underline{0}} & \underline{\underline{0}} \\ -b\underline{\underline{M}} & -\underline{\underline{M}} & \underline{\underline{0}} & \underline{\underline{0}} & \underline{\underline{0}} \\ \underline{\underline{0}} & \underline{\underline{0}} & \underline{\underline{0}} & \underline{\underline{0}} & \underline{\underline{k}}_0 \end{bmatrix} \begin{Bmatrix} (D^{1/2})^4\underline{w}(t) \\ (D^{1/2})^3\underline{w}(t) \\ (D^{1/2})^2\underline{w}(t) \\ (D^{1/2})^1\underline{w}(t) \\ \underline{w}(t) \end{Bmatrix} = \begin{Bmatrix} 0 \\ 0 \\ 0 \\ 0 \\ (1+bD^{1/2})\underline{F}(t) \end{Bmatrix}
$$

Both the general form (eqn 10) and the example in eqn 11 are now posed in terms of two real, square, symmetric matrices for which an orthonormal transformation exists,

$$
\left\{
\begin{array}{c}
(D^{\beta})^{m-1}\underline{w}(t) \\
\vdots \\
(D^{\beta})^{2}\underline{w}(t) \\
(D^{\beta})^{1}\underline{w}(t) \\
\underline{w}(\bar{t})
\end{array}
\right\}
=
\left[
\quad \Phi \quad
\right]
\left\{
\begin{array}{c}
y_{m \cdot N}(t) \\
\vdots \\
y_{3}(t) \\
y_{2}(t) \\
y_{1}(t)
\end{array}
\right\}
\tag{12}
$$

which leads to a system of $m \cdot N$ uncoupled differential equations of order β.

$$
D^{\beta}\left[\diagdown I \diagdown\right]\left\{y(t)\right\} + \left[\diagdown a^{\beta} \diagdown\right]\left\{y(t)\right\} = \left[\phi\right]^{T}\left\{f^{*}(t)\right\} = \left\{f(t)\right\} . \tag{13}
$$

Constructing the Modal State Equations

The decoupled structural equations of motion or basis equations (eqn 13) individually take the form

$$
(D^{\beta} + a^{\beta})y(t) = f(t) \qquad\qquad \beta = 1/n \tag{14}
$$

where the subscripts have been dropped to simplify notation. Green's function solutions for these equations are relatively straightforward and the resulting expressions for the forced response of the structure can be shown to be real, continuous and causal (1:73). These solutions to eqn 14 may be viewed as particular solutions of the structural equations of motion.

It is important to note that the only homogeneous solution to eqn 14 is the trivial solution. This is consistent with a strict interpretation of eqn 2, the generalized visocoelastic constitutive model. Inherent in the model is the implication that at time zero the viscoelastic material should be in its virgin, undeformed state and the structure is commencing motion from a quiescent state. Attempting to impose non-trivial initial conditions implies the existence of previous motion that is inconsistent with the hereditary viscoelastic model and hence, homogeneous solutions are not needed.

To construct the modal state equations, one needs to shift the time scale such that the initial time occurs at some time, t_o, after the onset of structural motion. This shifted time scale is shown in figure 1. Posing the basis equations, eqn 14, in terms of this shifted time scale yields[19:48].

$$
\frac{1}{\Gamma(1-\beta)} \; \frac{d}{d\tilde{t}} \int_{o}^{\tilde{t}} \frac{y(\tau - t_o)}{(\tilde{t}-\tau)^{\beta}} \, d\tau + a^{\beta}y(\tilde{t}-t_o) = f(\tilde{t}-t_o) \tag{15}
$$

The applied loads prior to t_o $(0 \leq \tilde{t} \leq t_o)$ are $\tilde{f}(\tilde{t}-t_o)$ and the corresponding response is $\tilde{y}(\tilde{t}-t_o)$. The equation predicting this response is

$$D^\beta \tilde{y}(\tilde{t}-t_o) + a^\beta \tilde{y}(\tilde{t}-t_o) = \tilde{f}(\tilde{t}-t_o) \tag{16}$$

The loads for the episode of interest $(\tilde{t} \geq t_o)$ are $\tilde{\tilde{f}}(\tilde{t}-t_o)$ and the equation for the corresponding response $\tilde{\tilde{y}}(\tilde{t}-t_o)$ is

$$D^\beta \tilde{\tilde{y}}(\tilde{t}-t_o) + a^\beta \tilde{\tilde{y}}(\tilde{t}-t_o) = \tilde{\tilde{f}}(\tilde{t}-t_o) \tag{17}$$

The total response for $t \geq t_o$ is $\tilde{\tilde{y}} + \tilde{y}$ and the general expression for the response is

$$\frac{1}{\Gamma(1-\beta)} \int_0^t \frac{\dot{\tilde{\tilde{y}}}(r-u) + \dot{\tilde{y}}(r-u)}{u^\beta} \, du + a^\beta \left(\tilde{\tilde{y}}(r) + \tilde{y}(r) \right)$$
$$\tag{18}$$
$$= \tilde{\tilde{f}}(r) + \tilde{g}(r)$$

where $r = \tilde{t}-t_o$, $u = \tilde{t}-\tau$. Here $g(r)$ is a pseudo forcing function that produces the residual response of the structure due to the prior application of $\tilde{f}(t-t_o)$.

$$\tilde{g}(r) = -\frac{1}{\Gamma(1-\beta)} \left\{ \int_r^{r+t_o} \frac{\dot{\tilde{y}}(r-u)}{u^\beta} \, du + \frac{\tilde{y}(-t_o)}{(r+t_o)^\beta} \right\} \tag{19}$$

Expressing eqn 18 in terms of the time t scale in Figure 1, where zero time is now t_o after the onset of structural motion, yields

$$\frac{1}{\Gamma(1-\beta)} \int_0^t \frac{\dot{y}(t-\tau)}{\tau^\beta} \, d\tau + a^\beta y(t) = \tilde{\tilde{f}}(t) + \tilde{g}(t) = g(t). \tag{20}$$

Note that here the order of differentiation and integration in the fractional derivative operator is the opposite of eqn 1. This reversal of operations occurred when Leibnitz's rule was used

to differentiate in eqn 15, producing eqns 18 and 19. This change will prove crucial to solving the initial value problem, because in contrast with eqn 14, eqn 20 possesses both a particular solution, uniquely dependent on the forcing function, and a homogeneous solution, uniquely dependent on the initial value, $y(0)$.

Before presenting these solutions it is important to address the relationship between the operator appearing in eqn 20 and the original definition shown in eqn 1. Using Leibnitz's rule to differentiate the integral in eqn 1 yields

$$\frac{1}{\Gamma(1-\alpha)} \frac{d}{dt} \int_0^t \frac{w(t-\tau)}{\tau^\alpha} d\tau = \frac{1}{\Gamma(1-\alpha)} \left\{ \frac{w(0)}{t^\alpha} + \int_0^t \frac{\dot{w}(t-\tau)}{\tau^\alpha} d\tau \right\} \quad (21)$$

or in operator form

$$D^\alpha\left[w(t)\right] = \frac{w(0)t^{-\alpha}}{\Gamma(1-\alpha)} + \hat{D}^\alpha\left[w(t)\right] = \frac{w(0)t^{-\alpha}}{\Gamma(1-\alpha)} + I^{1-\alpha}\left[\dot{w}(t)\right] \quad (22)$$

$$\hat{D}^\alpha\left[w(t)\right] = I^{1-\alpha}\left[\dot{w}(t)\right]$$

where D^α is the definition and $\hat{D}^\alpha$ is the modified derivative operator appearing in eqn 21. In fact D^α is the Riemann-Liouville indefinite, fractional order $(1-\alpha)$ integral of the first derivative of the function or effectively an order $-\alpha$ integral of a function.[15,17] The key observation here is that the indefinite fractional order integral operator in effect produces a constant of integration in each modal response. These constants will be used to statisfy the initial conditions in the fractional order state equations.

Posing equation 20 in terms of the modified fractional derivative operator, $\hat{D}^\beta$,

$$(\hat{D}^\beta + a^\beta) y(t) = \tilde{\tilde{f}}(t) + \tilde{g}(t) = g(t) \quad (23)$$

produces the modal state equations. Note the similar appearance of eqns 14 and 23. Recall that eqn 14 is based on the $\bar{t}$ time scale and has a trivial homogeneous solution. On the other hand, eqn 25 is based on the t time scale, posses a non-trivial homogeneous solution and accounts for the effects of previous motion through the initial value, $y(0)$, and pseudo forcing function, $\tilde{g}(t)$.

Constructing the Fractional Order State Equations

The overall goal is to determine the nature of the fractional order state equations from the modal state equations. The immediate goal is to use the modal state equations, eqn 23 to predict structural response, where the relaxation effects induced by previous motion are accounted for by the pseudo forcing functions, $\tilde{g}(t)$. The transient structural response will be a superposition of the homogeneous solutions of the modal state equations and will be shown to satisfy the initial conditions. The forced structural response will be constructed from the particular solutions to the modal state equations derived using Green's functions. Superimposing the transient and forced response produces the total structural response.

The transient structural response is constructed by first determining the general form of the homogeneous solution for the modal state equations, eqn 23. These solutions take the form

$$y_h(t) = y_h(0) \sum_{p=0}^{\infty} \frac{(-(at)^{\beta})^p}{\Gamma(1+p\beta)} \tag{24}$$

which is a special case of the beta order Mittag-Leffler function defined as (14:102)

$$E_\beta(x) \equiv \sum_{p=0}^{\infty} \frac{(x)^p}{\Gamma(1+p\beta)} . \tag{25}$$

In Mittag-Leffler notation the homogeneous solution is

$$y_h(t) = y_h(0) \ E_\beta\left(-(at)^{\beta}\right), \tag{26}$$

where this special Mittag-Leffler function has the property

$$\hat{D}^{\beta} E_\beta\left(-(at)^{\beta}\right) = -a^{\beta} E_\beta\left(-(at)^{\beta}\right). \tag{27}$$

The property should come as no surprise because the Mittag-Leffler function has long been viewed as a generalized exponential function[11]. In related work[12-14] Koeller has shown that the quasi-static fractional calculus viscoelastic formulation leads to Mittag-Leffler functions.

Including the particular solution, the total solution to each of the modified basis equation is

$$y(t) = y_h(0) \ E_\beta\left(-(at)^{\beta}\right) + \int_0^t D^{1-\beta}\left[E_\beta\left(-(a\tau)^{\beta}\right)\right]g(t-\tau)d\tau \tag{28}$$

which can be determined using Laplace transforms or other traditional solution techniques for integral-differential equations. The kernel in the convolution integral of eqn 28 is the unit impulse solution (Green's function) for the modified basis equations, and is singular. Note that $E_\beta(0)$ is not zero and

that the singular behavior of the kernel can be determined through a straightforward application of eqn 1.

It is the singular nature of fractional order derivatives of $E_\beta(-(at)^\beta)$ that is useful in resolving an apparent paradox in the

overall initial value problem. Recall that there are m·N (eqn 23) modal state equations needed to characterize the structure, where the solution for each equation has a homogeneous solution containing a different initial value. This paradox becomes apparent when eqn 12 is used to solve for the m·N initial values of the homogeneous basis functions in terms of the structure's initial displacements $w_h(t)$ and their derivatives evaluated at

time zero.

$$
\left\{
\begin{array}{c}
(D^\beta)^{m-1} w_h(t) \\
\vdots \\
(D^\beta)^2 w_h(t) \\
(D^\beta)^1 w_h(t) \\
w_h(t)
\end{array}
\right\}_{t=0}
=
\left[\; \overline{\Phi} \; \right]
\left\{
\begin{array}{c}
y_{m \cdot N}(t) \\
\vdots \\
y_3(t) \\
y_2(t) \\
y_1(t)
\end{array}
\right\}_{t=0}
\qquad (29)
$$

The paradox is that at this point only $w_h(0)$ and $D^1 w_h(0)$ can be

specified, while the remaining elements in the state vector on the left of eqn 29 are undetermined. Note that the order of the differential equations of motion (eqn 6) is order $2 + \alpha$ or equivalently βm and that the state vector in eqn 31 calls for the initial values of derivatives up through $2 + \alpha - \beta$ or equivalently $\beta(m-1)$. In other words, when posing N, βm order differential equations as a system of m·N differential equations of order β, the corresponding initial value problem calls for all the initial values of the $p\beta$ order derivatives of the displacement vector, $w_h(t)$: $p = 0,1,2,\cdots,$ m-1. These requirements appear to be

analogous to the traditional initial value problem, but also leave one with the requirement for yet more initial conditions.

It is proven in reference[19:54] that all of the non-integer derivatives of $w_h(t)$ of order less than two appearing in the state

vector have zero initial value. The initial values for acceleration and the accompanying higher order derivations appearing in the state vector can be determined by returning to the original equation of motion, eqn 6, and using successive applications, of eqn 22 to determine the singular terms in the equation of motion. The resulting equation of motion for the response to turning off the previous forcing function is
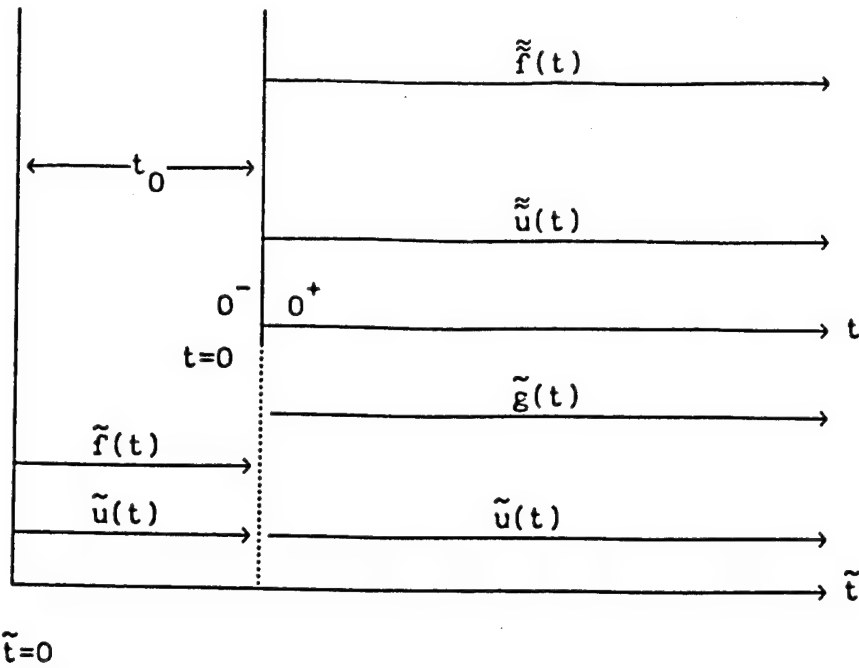
Figure 1 - Time Scales for the Loads and Responses of the Initial Value Problem.
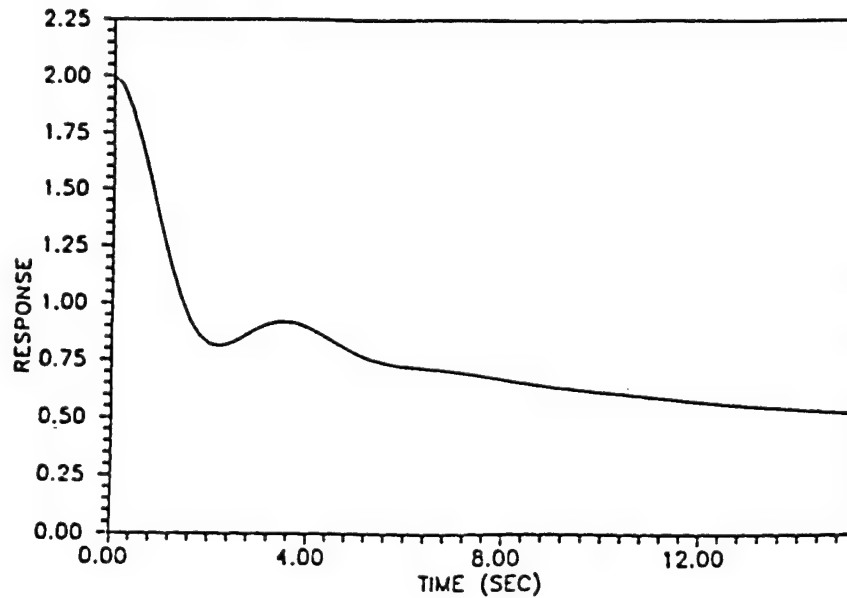
Figure 2 - The Response of the Damped Oscillator

$$-b\underline{\underline{M}}\,\frac{\ddot{\tilde{\underline{w}}}(0^-)t^{-\alpha}}{\Gamma(1-\alpha)} \;-\; b\underline{\underline{M}}\sum_{\ell=1}^{m-2n-1}\frac{t^{-\ell\beta}}{\Gamma(1-\ell\beta)}\hat{D}^{(m-2n-\ell)\beta}\,\tilde{\underline{w}}(0^-)$$

$$+(1+b\hat{D}^{\alpha})\,\underline{\underline{M}}\,\ddot{\tilde{\underline{w}}}(t)\;-\;\underline{\underline{k}}_1\frac{\ddot{\tilde{\underline{w}}}(0^-)t^{-\alpha}}{\Gamma(1-\alpha)}\;+(\underline{\underline{k}}_o+\underline{\underline{k}}_1\hat{D}^{\alpha})\tilde{\underline{w}}(t) \qquad\qquad (30)$$

$$=-\,b\,\frac{\tilde{\underline{F}}(0^-)t^{-\alpha}}{\Gamma(1-\alpha)}\;+\;\tilde{\underline{G}}(t)$$

The fractional derivatives in this equation of motion are evaluated for $t = 0^-$ or equivalently $\tilde{t} = t_o^-$. $\tilde{\underline{G}}(t)$ are the pseudo forces needed to produce the residual motion associated with the previous loading history, already accounted for in the modified basis equations. The singular forcing function is the result of the α order derivative of the step function turning of $\tilde{F}(t)$. The remaining singular behavior is the result of repeatedly applying eqn 22 to separate out the singular behavior of the fractional derivatives of acceleration.

The corresponding equation of motion for the response to the new loads is

$$b\underline{\underline{M}}\,\frac{\ddot{\approx}{\underline{w}}(0^+)t^{-\alpha}}{\Gamma(1-\alpha)}\;+\;b\underline{\underline{M}}\sum_{\ell=1}^{m-2n-1}\frac{t^{-\ell\beta}}{\Gamma(1-\ell\beta)}\hat{D}^{(m-2n-\ell)\beta}\,\ddot{\approx}{\underline{w}}(0^+)$$

$$\qquad\qquad (31)$$

$$+ (1+b\hat{D}^{\alpha})\underline{\underline{M}}\,\ddot{\approx}{\underline{w}}(t)\;+\;\underline{\underline{k}}_1\frac{\ddot{\approx}{\underline{w}}(0^+)t^{-\alpha}}{\Gamma(1-\alpha)}\;+\;(\underline{\underline{k}}_o+\underline{\underline{k}}_1\hat{D}^{\alpha})\approx{\underline{w}}(t)$$

$$=\frac{b\ddot{\approx}{\underline{F}}(0^+)t^{-\alpha}}{\Gamma(1-\alpha)}\;+\;(1+bD^{\alpha})\approx{\underline{F}}(t)$$

where the singular forcing function results from again using eqn 22 to express the effects of the step function turning on $\tilde{F}(t)$.

The remaining singular behavior is also the result of using eqn 22 to separate out the singular behavior of the fractional derivatives of acceleration. Again the tilde and double tilde notation identify motion due to previous forces, $\tilde{F}(t)$, and present forces, $\approx{F}(t)$, respectfully, as in eqns 16 and 17.

Equating the coefficients of the strongest singularities (order α) in eqn 30 and then in eqn 31 yields two equations needed to establish the initial conditions acceleration.

$$-b\underline{\underline{M}}\,\ddot{\tilde{\underline{w}}}(0^-) - \underline{\underline{k}}_1\tilde{\underline{w}}(0^-) = -b\tilde{\underline{F}}(0^-) \tag{32}$$

$$b\underline{\underline{M}}\,\ddot{\tilde{\tilde{\underline{w}}}}(0^+) + \underline{\underline{k}}_1\tilde{\tilde{\underline{w}}}(0^+) = b\tilde{\tilde{\underline{F}}}(0^+) \tag{33}$$

Adding these two equations produces the relationship needed to establish changes in the initial conditions due to stopping and starting of the load histories.

$$\underline{\underline{M}}\left(\ddot{\tilde{\tilde{\underline{w}}}}(0^+) - \ddot{\tilde{\underline{w}}}(0^-)\right) + b^{-1}\underline{\underline{k}}_1\left(\tilde{\tilde{\underline{w}}}(0^+) - \tilde{\underline{w}}(0^-)\right) = \tilde{\tilde{\underline{F}}}(0^+) - \tilde{\underline{F}}(0^-) \tag{34}$$

Since this relationship is based on step loading, which is incapable of instantaneously changing the displacement or velocity time history between time 0^- and 0^+, one can conclude that

$$\tilde{\tilde{\underline{w}}}(0^+) = \tilde{\underline{w}}(0^-) \tag{35}$$

$$\dot{\tilde{\tilde{\underline{w}}}}(0^+) = \dot{\tilde{\underline{w}}}(0^-) \tag{36}$$

and eqn 36 can now be re-expressed as

$$\ddot{\tilde{\tilde{\underline{w}}}}(0^+) - \ddot{\tilde{\underline{w}}}(0^-) = \underline{\underline{M}}^{-1}\left(\tilde{\tilde{\underline{F}}}(0^+) - \tilde{\underline{F}}(0^-)\right) \tag{37}$$

Thus we see that the change in the initial accelerations is proportional to any instantaneous changes (steps) in the magnitudes of the applied loads at $t = 0$. It is reassuring to note that eqn 37 is strongly reminiscent of Newton's second Law. To determine the initial accelerations at time 0^+ one needs to determine the accelerations at time 0^- and then add to them the additional component of acceleration from the change in load histories. Should there be a continuous transition from one load history to the other, then

$$\ddot{\tilde{\tilde{\underline{w}}}}(0^+) = \ddot{\tilde{\tilde{\underline{w}}}}(0^-) \tag{38}$$

and the accelerations at time 0^- are the accelerations used in the initial value problem. Satisfying the initial conditions on acceleration in this manner effectively removes the α order singular terms on both sides of eqns 30 and 31.

The remaining singular terms in these equations do not have corresponding terms on the respective force sides of the

equations. To preserve the equality one must conclude that the coefficients of these singular terms are zero. Note that setting these coefficients to zero in effect generates the remaining initial conditions needed in eqn 29. From eqn 30

$$\hat{D}^{(m-2n-\ell)\beta}\left[\underaccent{\tilde}{\ddot{w}}(0^-)\right] = \underline{0} \qquad\qquad \ell = 1,2,3,\cdots,m-2n-1 \qquad (39)$$

and from eqn 31

$$\hat{D}^{(m-2n-\ell)}\left[\underaccent{\approx}{\ddot{w}}(0^+)\right] = \underline{0} \qquad\qquad \ell = 1,2,3,\cdots,m-2n-1. \qquad (40)$$

Proof is given in reference[19:54]. Hence, one can see that the initial values of the fractional derivatives of displacement greater than second order and less than order βm must be zero to preserve the equation of motion. Adding the two equations of motion and recalling that

$$\underaccent{\approx}{w}(t) + \underaccent{\tilde}{w}(t) = \underline{w}(t) \qquad\qquad t \geq 0 \qquad (41)$$

yields

$$\underline{\underline{M}}(1 + b\hat{D}^\alpha)\ddot{\underline{w}}(t) + (\underline{\underline{k}}_o+\underline{\underline{k}}_1\hat{D}^\alpha)\underline{w}(t) = (1+b\hat{D}^\alpha)\,\underaccent{\approx}{\underline{F}}(t) + \underaccent{\tilde}{\underline{G}}(t) \qquad (42)$$

which is identical to eqn 8 except for one very important detail. The fractional derivative operator has changed from the original definition, eqn 1, to the modified definition eqn 22. Recall that the modified basis functions use this modified definition as well.

In fact, the entire initial value problem (constituted by eqns 42, 10, 23, and 29) and its solutions (eqn 28) can be cast in terms of the modified definition of fractional differentiation. The composition property for the modified operator

$$\hat{D}^\alpha[\hat{D}^\gamma[w(t)]] = \hat{D}^{\alpha+\gamma}[w(t)], \qquad (43)$$

holds when the initial values of the fractional derivatives are zero as stipulated in the initial value problem. One can now straightforwardly demonstrate that eqn 42 leads to a corresponding form of eqn 10 where the D^β operator is replaced by D^β. The D^β operators in eqn 29 can now be replaced by D^β as well. Noting that the particular solution in eqn 28 is independent of the initial value and may be viewed as an excitation from a quiescent state, one can show that the solution of the modal state equation takes the form

$$y_j(t) = y_j(0) \, E_\beta\left[-(a_j t)^\beta\right]$$

$$+ \int_0^t (-a_j^\beta)^{m-1} \, \hat{D}^{-1-\alpha}\left[E_\beta\left[-(a_j t)^\beta\right]\right] g_j(t-\tau) \, d\tau \tag{44}$$

Proof is given in reference[19:62] and note that the kernel is now non-singular. One can now conclude that eqn 44 is the solution of a well-posed problem. The uniqueness of the solution follows immediately from Laplace transforms. Multiplying the initial value and the modal forcing function, $g_j(t)$, by $(1+\epsilon)$ and taking ϵ small demonstrates continuous dependence on the data, so long as the convolution integral is bounded.

To test the robustness of the modal state equations, one needs to ascertain its ability to generate the structural response to impulsive loading. The method entails solving the initial value problem for a step response (using initial accelerations, eqn 37) from a quiescent state and noting that the impulse response is the first derivative of the step response. The structural response for a unit impulse load at the zth degree of freedom of the structure is

$$w_{\delta z}(t) = b \sum_{j=1}^{m \cdot N} \underline{\phi}_{1j} (-a_j^\beta)^{2n+2q-1} \hat{D}^{-1-\alpha}\left[E_\beta\left[-(a_j t)^\beta\right]\right] \underline{\phi}_{1j}^T \underline{z}$$

$$+ b \sum_{j=1}^{m \cdot N} \underline{\phi}_{1j} (-a_j)^{2n+q-1} \underline{\phi}_{1j}^T \underline{z} \cdot t \tag{45}$$

where $\underline{z}$ is a N order column vector of zeroes except the zth element, which is one. Here $\underline{\phi}_{1j}$ are the structure's mode shapes which constitute the lowest N terms of the jth eigenvector of the expanded equations of motion, eqn 10. Again the solution is seen to be continuous and is expressed in terms of the modified operator and the Mittag-Leffler function. Derivation of this expression is given elsewhere[19:67].

At this point one might be tempted to assert that the original definition of fractional order differentiation, eqn 1, is somehow inappropriate for the initial value problem. Not true. Recall that the initial value problem has insufficient numbers of physically motivated initial values to determine uniquely the overall homogeneous solution as a superposition of solutions to the modified basis equations. The additional auxiliary initial conditions, developed by suppressing singular behavior at time zero, provided precisely the number of needed initial conditions for a unique solution. Recall that the original definition, eqn 1, produced this singular behavior without which the initial value problem would flounder for lack of initial information[19].

Moreover, having derived the structural equations of motion in terms the modified fractional derivative operator, eqn 42, and having established the robustness of the formulation through the existence of its impulse response, one can now proceed to construct the structure's fractional order state equations. Casting equation 42 in terms of two real, square and symmetric matrices, as shown in eqn 10, produces the fractional order state equations.

$$
\hat{D}^\beta
\begin{bmatrix}
\underline{\underline{0}} & & \\
\vdots & & H \\
\underline{\underline{0}} & & \\
\underline{\underline{0}} & & \\
\underline{c}_m & \cdots \underline{c}_3 \underline{c}_2 \underline{c}_1
\end{bmatrix}
\left\{
\begin{array}{c}
(\hat{D}^\beta)^{m-1}\underline{w}(t) \\
\vdots \\
\vdots \\
(\hat{D}^\beta)^2 \underline{w}(t) \\
(\hat{D}^\beta)^1 \underline{w}(t) \\
\underline{w}(\overline{t})
\end{array}
\right\}
\tag{46}
$$

$$
+
\begin{bmatrix}
 & & \underline{\underline{0}} \\
 & -H & \vdots \\
 & & \underline{\underline{0}} \\
 & & \underline{\underline{0}} \\
\underline{\underline{0}} \cdots \underline{\underline{0}} \underline{\underline{0}} & \underline{c}_0
\end{bmatrix}
\left\{
\begin{array}{c}
(\hat{D}^\beta)^{m-1}\underline{w}(t) \\
\vdots \\
(\hat{D}^\beta)^2 \underline{w}(t) \\
(\hat{D}^\beta)^1 \underline{w}(t) \\
\underline{w}(\overline{t})
\end{array}
\right\}
=
\left\{
\begin{array}{c}
0 \\
\vdots \\
0 \\
0 \\
\underset{\approx}{*}\underline{f}^*(t)+\underline{\tilde{G}}(t)
\end{array}
\right\}
$$

with straightforward matrix manipulation these state equations take the form

$$\hat{D}^\beta \underline{x}(t) = \underline{\underline{A}}\ \underline{x}(t) + \underline{\underline{B}}\ \underline{u}(t) + \underline{\underline{B}}\ \underline{\tilde{G}}(t)$$

Note that applying the orthogonal transformation given in eqn 12 to the state equations yields the modal state equations, eqn 23. In effect one has come full circle and derived equations of motion capable of describing the hereditary viscoelastic damping effects as well as characterize the system in terms of its initial states.

It is reassuring that the fractional order state equations predict a response that is, strictly speaking, a function of all its previous states, as it should be for a system that exhibits hereditary behavior. The pseudo forces $\tilde{G}(t)$ describe the effects of previous internal viscoelastic deformation, and the initial states (taken at some time t_o after the onset of motion) describe the effects of immediately previous motion. To predict accurate short term system response, records of previous motion must be kept to construct the pseudo forces. This is necessary for heavily damped structures. In lightly damped structures the hereditary effects are much smaller and the pseudo forces may be ignored.

With or without the pseudo forces included the fractional order state equations one can predict open or closed loop system response. The closed loop feedback relationship between the state vector and the applied forces is

$$\widetilde{\underline{\ddot{F}}}(t) = -\underline{\overset{*}{\underline{G}}} \, \underline{x}_r$$

$$\widetilde{\underline{f}}^*(t) = -(1+b\hat{D}^\alpha)\underline{\overset{*}{\underline{G}}} \, \underline{x}_r = -\underline{\underline{G}} \, \underline{x} \tag{47}$$

Here $\underline{x}_r$ is the reduced state vector containing the displacements $\underline{w}(t)$ and all derivatives (including fractional order) of $\underline{w}(t)$ up to, but not including, the second derivative. When the stress operator takes the α order derivative of $\underline{x}_r$, this generates the higher order derivatives of $\underline{w}(t)$ in the full state vector. Here the $-\underline{\overset{*}{\underline{G}}}$ is the matrix of actual gain coefficients, $-\underline{\underline{G}}$ is the matrix of effective gain coefficients and $\underline{x}$ is the full state vector appearing in eqn 46.

Note that when b is zero in the stress operator the reduced state vector is the full state vector and no distinction is necessary between actual gains and effective gains. Substituting eqn 47 into eqn 46 produces the equations for the closed loop response.

$$\hat{D}^\beta \underline{x} = (\underline{\underline{A}} - \underline{\underline{B}} \, \underline{\underline{G}}) \, \underline{x} \tag{48}$$

This equation includes the feedback of fractional order derivatives of the structure's response. Recall that the fractional derivatives actually being fed back are those of order less than two, namely those in the reduced state vector $\underline{x}_r$. The fact that the full state vector appears in eqn 48 is a consequence of the mathematics in eqn 47. However, eqn 48 is in fact the closed loop state equations. There is no a priori reason to exclude the fractional derivatives from feedback.

In fact Oldham[20] has developed RLC circuits that generate the fractional order derivatives and integrals of input signals over limited frequency ranges. It is possible to take signals proportional to structural deflections and accelerations and produce signals proportional to their fractional derivatives and feed them back.

The Fractional Order Matrix Exponential Function

Although the modal equations are an effective tool in deriving the fractional order state equations, solution formats for these state equations are not limited to modal analysis. When modal analysis is unwarranted, the fractional order analogue of the matrix exponential function can serve as an alternate

solution format.

  The development begins with the open loop state equations without the pseudo force.

$$\hat{D}^{\beta}\underline{x} = \underline{\underline{A}}\,\underline{x} \tag{49}$$

One can use the following approach to determine the closed loop response by substituting $\underline{\underline{A}} - \underline{\underline{B}}\underline{\underline{G}}$, into eqn 48 for $\underline{\underline{A}}$ here and replacing the orthogonal transformation that follows with a similarity transformation for the asymmetric matrix $\underline{\underline{A}} - \underline{\underline{B}}\,\underline{\underline{G}}$. For simplicity of notation the open loop case is considered.

  One assumes a time series solution of the form.

$$\underline{x}(t) = \underline{x}_0 + \underline{x}_1\,t^{\beta} + \underline{x}_2\,t^{2\beta} + \cdots + \underline{x}_p\,t^{p\beta} + \cdots \tag{50}$$

Substituting this solution into eqn 49, evaluating the fractional derivatives term by term using the modified operator defined in eqn 22 and equating terms of like power in time yields the following solution.

$$\underline{x}(t) = \left[\underline{\underline{I}} + \frac{\underline{\underline{A}}\,t^{\beta}}{\Gamma(1+\beta)} + \frac{\underline{\underline{A}}^2\,t^{2\beta}}{\Gamma(1+2\beta)} + \cdots + \frac{\underline{\underline{A}}^P t^{P\beta}}{\Gamma(1+P\beta)} + \cdots \right]\underline{x}_0 \tag{51}$$

or

$$\underline{x}(t) = E_{\beta}(\underline{\underline{A}}\,t^{\beta})\,\underline{x}_0 \tag{52}$$

Here $E_{\beta}(\underline{\underline{A}}t^{\beta})$ is the fractional order matrix exponential function. It may be viewed as the generalized matrix form of the scalar Mittag-Leffler function given in eqn 24. Similar to its scalar counterpart, the fractional order matrix exponential function has the property

$$\hat{D}^{\beta}\left[E_{\beta}(\underline{\underline{A}}\,t^{\beta})\right] = \underline{\underline{A}}\,E_{\beta}(\underline{\underline{A}}\,t^{\beta}). \tag{53}$$

  One can relate this form of the solution back to the modal solutions, eqn 22, by using the orthogonal transformation given in eqn 12

$$\underline{x} = \underline{\underline{\phi}}\,\underline{y} \tag{54}$$

to decouple the homogeneous form of eqn 46. The result is the homogeneous modal state equations.

$$\hat{D}^{\beta} \underline{y} = -\underline{\underline{a}}^{\beta} \underline{y} \tag{55}$$

where $-\underline{\underline{a}}^{\beta}$ is a diagonal matrix containing the system's eigenvalues. Solutions of this equation take the form

$$y_j(t) = E_{\beta}(-(at)^{\beta})y_j(0) \tag{56}$$

which are identical to those in eqn 26. However, using the orthogonal transformation to construct the structure's response from eqn 56 produces

$$\underline{x}(t) = \underline{\underline{\phi}} \, E_{\beta}(- \, \underline{\underline{a}}^{\beta} t^{\beta}) \, \underline{\underline{\phi}}^{T} \, \underline{x}_{o} \tag{57}$$

This result is equivalent to that shown in eqn 52.

Example Problems

To demonstrate the solution techniques developed for the fractional order state equations, one will first apply them to two simple cases. The first case is a homogeneous first order differential equation with constant coefficients. The second example is a second order differential equation for a single degree of freedom viscoelastically damped oscillator.

If one is to view the fractional order state formulation as a generalization of the initial value problem, its solution techniques should apply to ordinary differential equations with constant coefficients. The first order differential equation is

$$\hat{D}^{1}w + a^{2} w = 0 \qquad\qquad w(0) = w_{0}$$

which using the composition property can also be expressed as

$$\hat{D}^{2/2}w + a^{2} w = 0$$

Posed in fractional order state form this equation becomes

$$\hat{D}^{1/2}\begin{bmatrix} 0 & 1 \\ 1 & 0 \end{bmatrix} \left\{ \begin{array}{c} \hat{D}^{1/2}\,w \\ w \end{array} \right\} + \begin{bmatrix} -1 & 0 \\ 0 & a^{2} \end{bmatrix} \left\{ \begin{array}{c} \hat{D}^{1/2}\,w \\ w \end{array} \right\} = \left\{ \begin{array}{c} 0 \\ 0 \end{array} \right\}$$

The associated eigenvalue problem is

$$\lambda \begin{bmatrix} 0 & 1 \\ 1 & 0 \end{bmatrix} \left\{ \phi \right\} + \begin{bmatrix} -1 & 0 \\ 0 & a^{2} \end{bmatrix} \left\{ \phi \right\} = \left\{ \begin{array}{c} 0 \\ 0 \end{array} \right\}$$

which has eigenvalues

$$\lambda = \pm \, ia$$

and associated eigenvectors of the form

$$\{ \phi \} = \left\{ \begin{array}{c} \pm ia \\ 1 \end{array} \right\}$$

The solution takes the form

$$\left\{ \begin{array}{c} \hat{D}^{1/2} w(t) \\ w(t) \end{array} \right\} = \left[\begin{array}{cc} ia & -ia \\ 1 & 1 \end{array} \right] \left\{ \begin{array}{c} y_1(0) E_{1/2}(-(iat^{1/2})) \\ y_2(0) E_{1/2}(-(-iat^{1/2})) \end{array} \right\}$$

To determine the initial values $y_1(0)$ and $y_2(0)$, one evaluates this expression at $t = 0$

$$\left\{ \begin{array}{c} 0 \\ w_0 \end{array} \right\} = \left[\begin{array}{cc} ia & -ia \\ 1 & 1 \end{array} \right] \left\{ \begin{array}{c} y_1(0) \\ y_2(0) \end{array} \right\}$$

and solves for $y_1(0)$ and $y_2(0)$

$$\left\{ \begin{array}{c} y_1(0) \\ y_2(0) \end{array} \right\} = \frac{1}{2ia} \left[\begin{array}{cc} 1 & ia \\ -1 & ia \end{array} \right] \left\{ \begin{array}{c} 0 \\ w_0 \end{array} \right\} = \left\{ \begin{array}{c} w_0/2 \\ w_0/2 \end{array} \right\}$$

Substituting these values into the solution for $w(t)$ given above yields

$$w(t) = \frac{w_0}{2} E_{1/2}(-(iat^{1/2})) + \frac{w_0}{2} E_{1/2}(-(-iat^{1/2}))$$

Using the series representation of the Mittag-Leffler function given in eqn 25 and summing the two series, the terms having fractional order powers of time add out and one is left with

$$w(t) = w_0 \sum_{p=0}^{\infty} \frac{(-a^2 t)^p}{\Gamma(1+p)}$$

or

$$w(t) = w_0 e^{-a^2 t}$$

as expected.

In the second example the fractional order time behavior does not add out, but instead describes the decaying motion of a damped oscillator.

$$\hat{D}^2 w(t) + 2\hat{D}^{1/2} w(t) + w(t) = 0$$

For simplicity the coefficient of the 1/2 order derivative in the stress operator is taken to be zero. The remaining half order derivative describes the low frequency viscoelastic damping and the mass and stiffness coefficients are taken be to one. Again using the composition property the equation may be posed as

$$\hat{D}^{4/2}w(t) + 2\hat{D}^{1/2}w(t) + w(t) = 0$$

In expanded form the equations become

$$\hat{D}^{1/2}\begin{bmatrix} 0 & 0 & 0 & 1 \\ 0 & 0 & 1 & 0 \\ 0 & 1 & 0 & 0 \\ 1 & 0 & 0 & 2 \end{bmatrix}\begin{Bmatrix} \hat{D}^{3/2}w(t) \\ \hat{D}^{2/2}w(t) \\ \hat{D}^{1/2}w(t) \\ w(t) \end{Bmatrix} + \begin{bmatrix} 0 & 0 & -1 & 0 \\ 0 & -1 & 0 & 0 \\ -1 & 0 & 0 & 0 \\ 0 & 0 & 0 & 1 \end{bmatrix}\begin{Bmatrix} \hat{D}^{3/2}w(t) \\ \hat{D}^{2/2}w(t) \\ \hat{D}^{1/2}w(t) \\ w(t) \end{Bmatrix} = \begin{Bmatrix} 0 \\ 0 \\ 0 \\ 0 \end{Bmatrix}$$

The eigenvalues and eigenvectors for this system appear in Table 1. Applying the initial conditions

$$\lambda_1 = -0.5437 \qquad \lambda_2 = -1.0 \qquad \lambda_3 = 0.7718 + 1.1151i \qquad \lambda_4 = 0.7718 - 1.1151i$$

$$\phi_1 = \begin{Bmatrix} \lambda_1^3 \\ \lambda_1^2 \\ \lambda_1 \\ 1 \end{Bmatrix} \quad \phi_2 = \begin{Bmatrix} \lambda_2^3 \\ \lambda_2^2 \\ \lambda_2 \\ 1 \end{Bmatrix} \quad \phi_3 = \begin{Bmatrix} \lambda_3^3 \\ \lambda_3^2 \\ \lambda_3 \\ 1 \end{Bmatrix} \quad \phi_4 = \begin{Bmatrix} \lambda_4^3 \\ \lambda_4^2 \\ \lambda_4 \\ 1 \end{Bmatrix}$$

Table 1 - The Eigenvalues and Eigenvectors of the Fractional Order State Equation for the Damped Oscillator.

$$x(0) = 2.0 \quad \hat{D}^{1/2}w(0) = 0 \quad \hat{D}^{2/2}w(0) = 0 \quad \hat{D}^{3/2}w(0) = 0$$

and solving for the coefficients of the Mittag-Leffler functions as before yields the response of the heavily damped oscillator. A plot of the response is given in figure 2.

Conclusions

The fractional derivative model of viscoelastic damping appears to be a useful tool in constructing state equations that describe the motion of damped structures. The essential value of this viscoelastic model lies in its use of generalized derivative operators. When the model is incorporated into equations of motion, the accelerations describing inertial effects can be expressed in terms of the same operator that describes viscoelastic effects. Furthermore when the external loads are related to structural responses through constant gain feedback, the feedback forces can be described in terms of this operator as well. Given that these fractional order state equations contain fractional order time derivatives of structural motion in the state vector, this formulation suggests the feedback of rational order time derivatives of structural response.

These fractional order state equations appear to constitute a generalization of the classical initial value problem. Posing a system of integro-differential equations as higher order matrix equations with lower, fractional order differential operators produces additional homogeneous solutions with accompanying requirements for additional initial conditions. These additional or auxiliary initial conditions are developed by suppressing singular behavior in the equations of motion. Eliminating the singular behavior in the equations of motion also leads to the use of a modified fractional order derivative that accommodates initial conditions (initial states) in the state equations. Thus the state equations are seen to be related to the original structural equations of motion, but not identical as they would be in a classical formulation.

Moreover, this formulation apppears to be a strong candidate for the general description of linear systems exhibiting strong hereditary behavior with weak frequency dependence. The advantages for the controls engineer are numerous. First, one avoids the use of time dependent coefficients in the state equations. Also the fractional derivative models are compact, making least squares fits to data tractable and manipulation of the model practical. The resulting state equations have analytic solutions and the solution techniques are similar to classical approaches. Finally, the inclusion of the fractional order derivatives in the state vector provides additional forms of feedback to improve system performance. Given that a fractional derivative model accurately captures the hereditary effects, the fractional order state equations appear to be a useful tool in the design and analysis of a feedback control system.

References

1.   R. L. Bagley, Applications of Generalized Derivatives to Viscoelasticity, PhD Dissertation, Air Force Institute of Technology, also published by Air Force Materials Laboratory, AFML-TR-79-4103, 1979.

2.   R. L. Bagley and P.J. Torvik, "A Generalized Derivative Model for an Elastomer Damper," Shock and Vibration Bulletin, No 49, Part 2 (1979), pp 135-143.

3.   R. L. Bagley and P.J. Torvik, "Fractional Calculus - A Different Approach to the Analysis of Viscoelastically Damped Structures," AIAA Journal, Vol 21, No 5 (1983), pp 741-748.

4.   R.L. Bagley and P.J. Torvik, "A Theoretical Basis for the Application of Fractional Calculus to Viscoelasticity," Journal of Rheology, Vol 27, No 3 (1983), pp 201-210.

5.   R.L. Bagley and P.J. Torvik, "Fractional Calculus in the Transient Analysis of Viscoelastically Damped Structures," AIAA Journal, Vol 23, No 6 (1985), pp 918-925.

6.   R.L. Bagley and P.J. Torvik, "On the Fractional Calculus Model of Viscoelastic Behavior," Journal of Rheology, Vol 30, No 1 (1986) pp 133-155.

7.   M. Caputo, "Vibrations of an Infinite Plate with a Frequency Independent Q," Journal of the Acoustical Society of America, Vol 60 (1976) pp 634-637.

8.   M. Caputo, Elasticita e Dissipazione, Zanichelli, Bologna (1969).

9.   M. Caputo, "Linear Models of Dissipation Whose Q is Almost Frequency Independent," Ann. Geofisica, Vol 19, No 4 (1986), pp 383-393.

10. R.M. Christensen, Theory of Viscoelasticity: An Introduction, Academic Press, New York 1971.

11. H.T. Davis, The Theory of Linear Operators, The Principia Press (1936).

12. R.C. Koeller, "Application of Fractional Calculus to the Theory of Viscoelasticity," Journal of Applied Mechanics, Vol 51 (1984), pp 299-307.

13. R.C. Koeller, "Polynomial Operators, Stieltjes Convolution and Fractional Calculus in Hereditary Mechanics," Acta Mechanica, Vol 58 (1986 pp 251-264.

14. G. Mittag-Leffler, "Sur La Représentation Analytique D'une Branch Uniforme D'une Function Monagine," Acta Mathematica, Vol 29 (1905), pp 101.

15. K.B. Oldham and J. Spanier, The Fractional Calculus, Academic Press, Orlando, 1974.

16. Y.N. Rabotnov, "Elements of Hereditary Solid Mechanics," Mir Publishers, Moscow (1980) pp 44-47

17. B. Ross, "A Brief History and Exposition of the Fundamental Theory of Fractional Calculus," Fractional Calculus and Its Applications, Lecture Notes in Mathematics, Vol 457, Springer-Verlag, Berlin (1975) pp 1-36.

18. P.J. Torvik and R.L. Bagley, "On the Appearance of the Fractional Derivative in the Behavior of Real Materials," Journal of Applied Mechanics, Vol 51, pp 294-298.

19. R.L. Bagley, "The Initial Value Problem for Fractional Order Differential Equations with Constant Coefficients," Air Force Institute of Technology, AFIT-TR-EN-88-1, September 1988.

20. K.B. Oldham and C.G. Zoski, "Analogue Instrumentation for Processing Polorographic Data," Journal of Electroanalytical Chemistry, Vol 157, (1983) pp 27-51.

IMPROVED SOLUTION TECHNIQUES FOR THE EIGENSTRUCTURE OF FRACTIONAL ORDER SYSTEMS

Michele Gaudreault* and Ronald Bagley[†]
Air Force Institute of Technology
Wright-Patterson AFB, Ohio

March 29,1989

Abstract

The structural problem of a viscoelastically damped rod is considered. A four parameter fractional derivative viscoelastic model rather than the traditional viscous model is used to describe the stress-strain relationship. The introduction of fractional order derivatives leads to high order matrix equations, which are cumbersome and time consuming to solve. Thus, there exists a motivation to seek alternate solution techniques. An existing technique, modified matrix iteration, is presented, and a new one, employing spectrum shift concepts, is proposed. The spectrum shift technique is shown to be significantly more efficient.

---

*Ph. D. Student, Dept. of Aeronautics and Astronautics
[†]Associate Professor, Dept. of Aeronautics and Astronautics

Nomenclature

$[\ ]$	square matrix
$[\ ]^T$	transpose of matrix
$[\ ]^{-1}$	inverse of matrix
$\{\ \}$	column vector
A	cross-sectional area
b_m	parameters of viscoelastic model
$[D(\lambda)]$	dynamical matrix
$D^\alpha[\ ]$	generalized derivative of order α
E	Young's modulus
E_n	parameters of viscoelastic model
$F[\ ]$	Fourier transform operator
$\{F(s)\}$	Laplace transform of the vector of forcing functions
i	square root of negative one
$[K(s)]$	viscoelastic stiffness matrix
$[\widetilde{K}]$	pseudo stiffness matrix of expanded equations of motion
$L[\ ]$	Laplace transform operator
L	length of a rod element
$[M]$	mass matrix
$[\widetilde{M}]$	pseudo mass matrix of expanded equations of motion
s	Laplace parameter
$\{x(t)\}$	column vector of structural displacements
$\{X(s)\}$	Laplace transform of $\{x(t)\}$
α_n	parameters of viscoelastic model
β_m	parameters of viscoelastic model
$\epsilon(t)$	strain history
$\Gamma(\alpha)$	gamma function of α
λ	eigenvalue associated with expanded equations of motion
$\{\phi\}$	mode shape
μ	shift factor
$\sigma(t)$	stress history
ω	Fourier parameter and frequency

Introduction

The fractional derivative viscoelastic model has its earliest roots in Nutting's observations that fractional powers of time could model the stress relaxation phenomenon [5]. Gemant later noted that stiffness and damping properties of viscoelastic materials seemed proportional to fractional powers of frequency, implying that fractional order time differentials might be used to model the behavior [14]. Scott-Blair combined the ideas of Nutting and Gemant by proposing

the use of fractional order time derivatives [2]. Caputo applied the concept to the viscoelastic behavior of geological strata [4]. Then he and Minardi showed that constitutive relationships employing the fractional calculus described the mechanical properties of some metals and glasses [5]. Bagley proposed incorporating fractional derivatives into finite element models of viscoelastically damped structures. Since then, he and Torvik have jointly published several papers demonstrating the feasibility and benefits of using fractional calculus. Of particular note is "A Theoretical Basis for the Application of Fractional Calculus to Viscoelasticity" [5], which uses molecular theory to derive the existence of generalized derivatives. Their efforts have shown that fractional calculus is an attractive approach to modelling viscoelastically damped structures. The resulting model requires very few parameters and is often accurate over six decades of frequency [2].

Generalized calculus is not a new concept — mathematicians have dealt with it for some time [10, 115-118]. A generalized derivative is represented in this paper as

$$D^\alpha[x(t)].$$

The generalized derivative can be defined for complex α, but only real values will be considered here. Fractional derivatives are generalized derivatives with rational α. The term "fractional calculus" implies the use of fractional derivatives.

This paper reviews the properties of generalized derivatives and the expanded equations of motion for a fractional order system describing a viscoelastically damped rod. The technique proposed by Bagley to solve for the eigenstructure is presented. A more efficient method is presented later, along with some examples.

Generalized Derivatives Applied to Viscoelastic Materials

Before applying generalized derivatives to structural problems, it is necessary to understand the properties of generalized derivatives and their use in viscoelastic theory. As will be shown, generalized derivatives behave in much the same way as conventional derivatives. When used to model viscoelastic materials, generalized derivatives typically provide an excellent model over a broad range of frequencies [4]. To show how generalized derivatives can be used to model viscoelastic materials, it is appropriate to present first the properties of generalized derivatives, especially the Laplace and Fourier transforms. The generalized derivative is defined as [1, 2]

$$D^\alpha[x(t)] \equiv \frac{1}{\Gamma(1-\alpha)} \frac{d}{dt} \int_0^t \frac{x(\tau)}{(t-\tau)^\alpha}\, d\tau \quad \text{for } 0 \le \alpha < 1 \qquad (1)$$

Note that this definition is only valid for $\alpha < 1$. However, the definition requires only a slight modification for a generalized derivative of order greater than one.

Let m be a nonnegative integer, and α defined as before. Then [1, 11]

$$D^{m+\alpha}[x(t)] \equiv \frac{1}{\Gamma(1-\alpha)} \frac{d^{m+1}}{dt^{m+1}} \int_0^t \frac{x(\tau)}{(t-\tau)^\alpha} \, d\tau \tag{2}$$

Although imposing in the time domain, in the Laplace (or Fourier) domain, the generalized derivative manifests itself as a fractional power of s (or ω). To calculate the Laplace transform, let $\tau = t - \eta$. Then,

$$D^{\alpha}[x(t)] = \frac{1}{\Gamma(1-\alpha)} \frac{d}{dt} \int_0^t \frac{x(t-\eta)}{\eta^\alpha} \, d\eta \tag{3}$$

Applying Leibnitz's rule,

$$D^{\alpha}[x(t)] = \frac{1}{\Gamma(1-\alpha)} \int_0^t \frac{1}{\eta^\alpha} \frac{\partial}{\partial t} x(t-\eta) \, d\eta + \frac{x(0)}{\Gamma(1-\alpha)t^\alpha} \tag{4}$$

Noting that the integral is a time convolution, and that

$$L\left[\frac{t^{-\alpha}}{\Gamma(1-\alpha)}\right] = \frac{1}{s^{1-\alpha}} \tag{5}$$

the Laplace transform is

$$L[D^{\alpha}[x(t)]] = \frac{1}{s^{1-\alpha}} \left(sL[x(t)] - x(0)\right) + \frac{x(0)}{s^{1-\alpha}} \tag{6}$$

or, more simply,

$$L[D^{\alpha}[x(t)]] = s^{\alpha} L[x(t)] \tag{7}$$

where

$$L[x(t)] = \int_0^\infty x(t) \, e^{-st} \, dt \tag{8}$$

Notice that for initial conditions equal to zero, the Laplace transform of a generalized derivative of order α has the same property as the conventional derivative: the transform is s^{α} times the transform of the function. In fact, the generalized derivative satisfies many of the same properties as the conventional derivative, particularly linearity and the composition property [1, 8-10]

$$D^{\alpha}[y(t) + x(t)] = D^{\alpha}[y(t)] + D^{\alpha}[x(t)] \tag{9}$$

$$D^{\alpha}[D^{\beta}[x(t)]] = D^{\alpha+\beta}[x(t)] \tag{10}$$

The Fourier transform is defined as

$$F[x(t)] \equiv \int_{-\infty}^\infty x(t) \, e^{-i\omega t} \, dt \tag{11}$$

If $x(t) = 0$ for $t < 0$, then the Fourier transform can be written as

$$F[x(t)] = \int_0^\infty x(t)\, e^{-i\omega t}\, dt \tag{12}$$

It is easily seen that the Fourier transform of a generalized derivative is

$$F[D^\alpha[x(t)]] = (i\omega)^\alpha F[x(t)] \tag{13}$$

In the preceding discussion, the only restriction placed on α was that it be a nonnegative real number less than one. However, for engineering applications, an irrational number can be approximated by a rational number. So α will now be restricted to be rational as well. Using the term "fractional derivative" will indicate this additional restriction.

To illustrate the use of fractional derivatives in viscoelastic theory, consider the standard linear viscoelastic model relating stress and strain [2]

$$\sigma(t) + \sum_{m=1}^{M} b_m \frac{d^m \sigma(t)}{dt^m} = E_0 \epsilon(t) + \sum_{n=1}^{N} E_n \frac{d^n \epsilon(t)}{dt^n} \tag{14}$$

Recalling Scott-Blair's proposal, replace the conventional derivatives by derivatives of fractional order. The result is the general form of the fractional derivative viscoelastic model [2]

$$\sigma(t) + \sum_{m=1}^{M} b_m D^{\beta_m}[\sigma(t)] = E_0 \epsilon(t) + \sum_{n=1}^{N} E_n D^{\alpha_n}[\epsilon(t)] \tag{15}$$

A large number of materials can be modelled by replacing each sum in Equation 15 by a single term involving a fractional derivative

$$\sigma(t) + b\, D^\beta[\sigma(t)] = E_0 \epsilon(t) + E_1 D^\alpha[\epsilon(t)] \tag{16}$$

Invoking the Second Law of Thermodynamics requires that [3]

$$\begin{array}{ccc}
E_0 \geq 0 & E_1 \geq bE_0 \\
E_1 \geq 0 & \alpha = \beta \\
b > 0 &
\end{array} \tag{17}$$

These constraints ensure nonnegative energy dissipation and nonnegative work. The stress-strain relation in the Laplace domain is

$$\frac{\sigma(s)}{\epsilon(s)} = \frac{E_0 + E_1 s^\alpha}{1 + bs^\alpha} \tag{18}$$

This is known as the four parameter model, and has been shown to be very accurate over several decades of frequency [4, 14, 15].
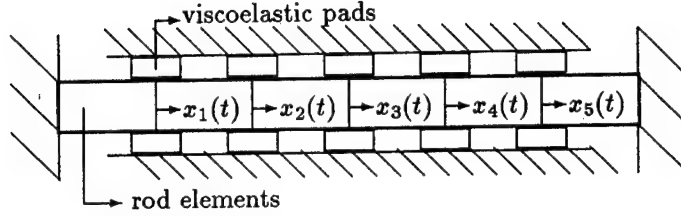
Figure 1: Finite Elements of Rod

Expanded Equations

Although the fractional derivative viscoelastic model may provide an excellent description of a material's properties, in order for it to be useful, its application to a structure must lead to a solvable problem. This section illustrates the existence of a solution by examining the finite element model of a viscoelastically damped rod. The equations of motion are developed using the elastic-viscoelastic correspondence principle, which states that a viscoelastic problem is equivalent to an elastic problem with the elastic moduli replaced by the appropriate viscoelastic moduli [7, 42]. This section develops the finite element model of a viscoelastically damped rod, constrained at each end. Figure 1 shows a five degree-of-freedom rod, constrained at each end, with viscoelastic damping pads at each node. Assume the rod is uniform and purely elastic. Using standard finite element techniques, the stiffness matrix for the elastic rod is of the form [8, 300]

$$[K_E] = \frac{EA}{L} \begin{bmatrix} 2 & -1 & 0 & 0 & 0 \\ -1 & 2 & -1 & 0 & 0 \\ 0 & -1 & 2 & -1 & 0 \\ 0 & 0 & -1 & 2 & -1 \\ 0 & 0 & 0 & -1 & 2 \end{bmatrix} \tag{19}$$

where E is the Young's modulus for the material in the rod, A is the cross-sectional area, and L is the length of one element. Assume the modulus of the viscoelastic material is

$$E(s) = \frac{\sigma(s)}{\epsilon(s)} = \frac{E_0 + E_1 s^\alpha}{1 + b s^\alpha} \tag{20}$$

as derived in the previous section. The damping pads provide an out of phase shear stress to the rod. The shear stress is partially elastic and partially viscous.

due to the real and imaginary parts of the modulus. As an example, let $\alpha = 1/2$, $b = 0$, and $s = i\omega$, where ω is an observed frequency of the system. Then

$$
\begin{aligned}
E(\omega) &= E_0 + E_1(i\omega)^{1/2} \\
&= E_0 + (\omega)^{1/2}E_1 e^{i\pi/4} \\
&= (E_0 + (\omega)^{1/2}E_1 \cos \tfrac{\pi}{4}) + i(\omega)^{1/2}E_1 \sin \tfrac{\pi}{4}.
\end{aligned}
\tag{21}
$$

The real part represents the elastic component of the shear stress, and the imaginary part represents the viscous component, which is ninety degrees out of phase.

The contribution to the structure's stiffness matrix due to the viscoelastic pads is

$$
G(s)[K_V] = \frac{G_0 + G_1 s^\alpha}{1 + bs^\alpha}
\begin{bmatrix}
A_1/t_1 & 0 & 0 & 0 & 0 \\
0 & A_2/t_2 & 0 & 0 & 0 \\
0 & 0 & A_3/t_3 & 0 & 0 \\
0 & 0 & 0 & A_4/t_4 & 0 \\
0 & 0 & 0 & 0 & A_5/t_5
\end{bmatrix}
\tag{22}
$$

where A_i is the area of the pad attached to the rod at i^{th} degree of freedom and t_i is the pad's thickness. The ratios A_i/t_i are the stiffness coefficients for the damping material at the corresponding degree of freedom. Then the stiffness matrix for the total structure is

$$
[K(s)] = [K_E] + \frac{G_0 + G_1 s^\alpha}{1 + bs^\alpha}[K_V]
\tag{23}
$$

The mass matrix for the rod is [8, 301-302]

$$
[M] = \frac{\rho A L}{6}
\begin{bmatrix}
4 & 1 & 0 & 0 & 0 \\
1 & 4 & 1 & 0 & 0 \\
0 & 1 & 4 & 1 & 0 \\
0 & 0 & 1 & 4 & 1 \\
0 & 0 & 0 & 1 & 4
\end{bmatrix}
\tag{24}
$$

where ρ is the density of the rod, and A and L are defined as above.

The equations of motion in the Laplace domain are

$$
\left[s^2[M] + [K(s)]\right]\{X(s)\} = \{F(s)\}
\tag{25}
$$

where $\{F(s)\}$ is the Laplace transform of the forcing function. Setting $\{F(s)\} = 0$ yields the homogeneous equation, from which the eigenstructure is found.

To clear the denominator in $[K(s)]$, multiply through by $(1+bs^\alpha)$. Defining

$$[A_0] = G_0[K_V] + [K_E] \tag{26}$$

$$[A_q] = G_1[K_V] + b[K_E] \tag{27}$$

and expressing α as a ratio in lowest terms, q/m, gives

$$\left(s^{(2m+q)/m} b[M] + s^{2m/m}[M] + s^{q/m}[A_q] + [A_0] \right) \{X(s)\}$$

$$= (1 + bs^{q/m})\{F(s)\} \tag{28}$$

In order to obtain an orthogonal transformation and decouple the equations of motion, cast the equations of motion in the following format

$$s^{1/m}[\widetilde{M}]\{\widetilde{X}(s)\} + [\widetilde{K}]\{\widetilde{X}(s)\} = \{\widetilde{F}(s)\} \tag{29}$$

$$[\widetilde{M}] = \begin{vmatrix} [0] & [0] & \cdots & [0] & b[M] \\ [0] & [0] & \cdots & b[M] & \vdots \\ \vdots & \vdots & \vdots & \vdots & [A_q] \\ [0] & b[M] & \cdots & [A_q] & \vdots \\ b[M] & \cdots & [A_q] & \cdots & [0] \end{vmatrix}$$

$$[\widetilde{K}] = \begin{vmatrix} [0] & [0] & \cdots & [0] & -b[M] & [0] \\ [0] & [0] & \cdots & -b[M] & \cdots & [0] \\ \vdots & \vdots & \vdots & \vdots & [-A_q] & \vdots \\ [0] & -b[M] & \cdots & [-A_q] & \cdots & [0] \\ -b[M] & \cdots & [-A_q] & \cdots & [0] & [0] \\ [0] & [0] & \cdots & [0] & [0] & [A_0] \end{vmatrix}$$

$$\{\widetilde{X}(s)\} = \left\{ \begin{array}{ll} s^{(2m-1)/m} & \{X(s)\} \\ s^{(2m-2)/m} & \{X(s)\} \\ \vdots & \\ s^{1/m} & \{X(s)\} \\ 1 & \{X(s)\} \end{array} \right\}$$

$$\{\widetilde{F}(s)\} = \left\{ \begin{array}{c} [0] \\ [0] \\ \vdots \\ [0] \\ (1 + bs^{q/m})\{F(s)\} \end{array} \right\}$$

With $\{F(s)\} = 0$, the problem is now in terms of real, square, symmetric matrices. Thus, the eigenvalues will be distinct and either real or occur in complex conjugate pairs. Also, the eigenvectors will be orthogonal to one another. It is a straightforward matter to decouple the expanded equations of motion using standard techniques [1, 67-68] Notice that for an n degree-of-freedom structure, the order of the expanded equations is $n(2m + q)$. From Equation 28, it can be seen that there are $(2m + q)$ branches to the problem, with n eigenvalues on each, resulting in $n(2m + q)$ eigenvalues. In a standard viscous formulation of the problem, only $2n$ eigenvalues would be found. The additional ones are due to the use of the fractional order derivatives. For a large structure, the higher order of the equations of motion represents a significant computational burden. Now that the existence of the solution has been proved, it will be beneficial to consider solution techniques that avoid solving the expanded equations of motion.

Modified Matrix Iteration Solution

The current method of determining the eigenstructure of the fractional order system developed in the previous section is to use a modified matrix iteration scheme on the homogeneous form of the original equation. Matrix iteration avoids computing and solving the characteristic polynomial of the matrix. Unlike using a Hessenberg matrix, which requires knowing the eigenvalue before the eigenvector can be calculated, matrix iteration determines both at the same time.

Matrix iteration is typically used to find the eigenstructure of undamped systems. With some modification, the concept can be applied to damped systems. Two different algorithms will be needed to find all $n(2m + q)$ modes. For convenience, the modes on a given branch will be numbered beginning with the one corresponding to the eigenvalue with the smallest magnitude. A mode corresponding to an eigenvalue with larger magnitude will be referred to as a higher mode. Lower modes are defined in the same way.

For an undamped system, the homogeneous form of the equations of motion in the Fourier domain is

$$-\omega^2 [M]\{\phi\} + [K]\{\phi\} = 0 \tag{30}$$

or

$$[K]^{-1}[M]\{\phi\} = \frac{1}{\omega^2}\{\phi\} \tag{31}$$

To demonstrate matrix iteration, select a trial vector, $\{\psi\}$, and express it as a linear combination of the eigenvectors of $[K]^{-1}[M]$:

$$\{\psi\} = \sum_{i=1}^{n} c_i \{\phi_i\} \tag{32}$$

This is possible since the eigenvectors of $[K]^{-1}[M]$ span n-space. The only restriction on the c_i's is that $c_1 \neq 0$. Premultiplying both sides of Equation 32 by $[K]^{-1}[M]$ produces

$$[K]^{-1}[M]\{\psi\} = \sum_{i=1}^{n} \frac{c_i}{\omega_i^2} \{\phi_i\} \tag{33}$$

Subsequent multiplications produce

$$\left([K]^{-1}[M]\right)^k \{\psi\} = \sum_{i=1}^{n} \frac{c_i}{\omega_i^{2k}} \{\phi_i\} \tag{34}$$

Since for large k,
$$\omega_1^{2k} \ll \omega_2^{2k} \ll \cdots \ll \omega_n^{2k} \tag{35}$$

it is clear that Equation 34 converges to the lowest mode [11, 124- 125]. If Equation 34 is normalized with respect to the same element between premultiplications by $[K]^{-1}[M]$, the the normalization factor reaches a constant value, equal to $1/\omega_1^2$ (since $c_1 \neq 0$), and the normalized vectors converge to the first mode. To find higher modes, subtract off lower modes using Turner's method [6, 168-269]. Letting

$$[D] = [K]^{-1}[M] - \sum_{i=1}^{j-1} \frac{1}{\omega_i^2} \{\phi_i\}\{\phi_i\}^T[M] \tag{36}$$

then

$$[D]\{\phi\} = \frac{1}{\omega^2}\{\phi\} \tag{37}$$

converges to the jth mode. Note that the lower modes must be normalized such that $\{\phi_i\}^T[M]\{\phi_i\} = 1$.

To apply this technique to a fractional order system, let $\lambda = s^{1/m}$. Then Equation 30 can be written as

$$\lambda^{2m}[M]\{\phi\} + [K(\lambda)]\{\phi\} = 0 \tag{38}$$

or

$$[K(\lambda)]^{-1}[M]\{\phi\} = \frac{-1}{\lambda^{2m}}\{\phi\} \tag{39}$$

where $[K(\lambda)]$ is equivalent to $[K(s)]$ in Equation 25. Each time the estimate of λ is updated, $[K(\lambda)]$ must be recomputed. Notice that for λ^{2m}, there are $2m$

possible values of λ. The different values arise because $z^{1/2m}$ is a multivalued function and has $2m$ branches. The value of λ on the kth branch is computed using DeMoivre's Theorem [13, 22]. Using the form $\lambda^{2m} = re^{i\theta}$,

$$\lambda = r^{1/2m} \left(\cos \frac{\theta + 2k\pi}{2m} + i \sin \frac{\theta + 2k\pi}{2m} \right) \tag{40}$$

The primary branch is assigned the number "0", so $k = 0, 1, 2, \ldots, 2m - 1$.

Since the stiffness matrix is a function of λ, to find the higher modes Equation 36 must be modified:

$$[D(\lambda)] = [K(\lambda)]^{-1}[M] - \sum_{i=1}^{j-1} \frac{1}{\Lambda_i^{2m}} \{\Phi_i\}\{\Phi_i\}^T[M] \tag{41}$$

The quantities Λ_i and $\{\Phi_i\}$ are called pseudoeigenvalues and pseudoeigenvectors. They are computed from the eigenvector problem:

$$[K(\lambda)]^{-1}[M]\{\Phi\} = \frac{-1}{\Lambda^{2m}}\{\Phi\} \tag{42}$$

It is important to realize that the pseudoeigenvalues and pseudoeigenvectors are not modes of the system. Their computation is merely an intermediate step in calculating the solutions of the equations of motion. In computing the jth mode of the system, only the first $j - 1$ pseudomodes of Equation 42 are needed. Then Equation 41 is used to converge on the jth mode of the system. Notice that for each new guess of λ, $j - 1$ pseudoeigenvalues and pseudoeigenvectors must be recalculated. This represents a significant computational burden. The next section proposes a technique to reduce the amount of computation required.

Note that this technique produces $2mn$ eigenvalues, but Equation 28 predicted $n(2m + q)$ eigenvalues. The remaining qn of the $n(2m + q)$ eigenvalues and eigenvectors are found using a scheme very similar to the one above [1, 80-83]. After clearing the denominator of Equation 38, it can be written as

$$\lambda^{2m}(1 + b\lambda^q)[M]\{\phi\} + (1 + b\lambda^q)[K_E]\{\phi\} + (E_0 + E_1\lambda^q)[K_V]\{\phi\} = 0 \tag{43}$$

Writing the equation in this form allows λ^q to appear explicitly in the equation, making it possible to find the remaining roots. Notice that these additional roots only exist for $b \neq 0$.

The solution method used to find the additional roots is somewhat subtle. By defining

$$Q = b\lambda^{2m+q} + \lambda^{2m} \tag{44}$$

$$[K'(\lambda)] = (1 + b\lambda^q)[K_E] + (E_0 + E_1\lambda^q)[K_V] \tag{45}$$

Equation 43 can be written in the more recognizable form

$$[K'(\lambda)]^{-1}[M]\{\phi\} = \frac{-1}{Q}\{\phi\} \tag{46}$$

Matrix iteration is applied to this equation, with the ith estimate of λ determined from

$$\lambda_i = \left[\left(\frac{Q - \lambda_{i-1}^{2m}}{b\lambda_{i-1}^{2m+q-1}} \right)^q \right]^{1/q} \tag{47}$$

The kth branch of the qth root of the quantity in brackets is used to determine the eigenvalue on that branch.

Turner's method is again employed to find the higher modes on each branch, as in Equation 41, with $Q(\lambda_i)$ replacing ω_i^2.

This section has shown that it is possible to find all $n(2m+q)$ eigenvalues and eigenvectors without solving the expanded equations of motion. However, the technique still requires a substantial amount of computation. In the next section, a technique is proposed which greatly reduces the computational burden.

Spectrum Shift Technique

While the modified matrix iteration technique is effective, it is not very efficient. In this section, spectrum shift methods will be combined with the matrix iteration technique, reducing the amount of computation required. The purpose of spectrum shift is to shift the eigenvalues of the system so that the desired eigenvalue becomes the fundamental one. Matrix iteration will then produce the desired eigenvalue. If spectrum shift methods could be used to compute the higher modes in the viscoelastic model, the pseudoeigenvalues and pseudoeigenvectors of the corresponding $[K(\lambda)]^{-1}[M]$ would not have to be computed. Determining the appropriate spectrum shifts is not easy, and requires certain precautions, which will be presented later.

The spectrum shift technique is usually used in elastic systems when a particular frequency and corresponding mode shape are of interest. To illustrate the theory behind the spectrum shift technique, consider again an undamped system

$$\left[[K] - \omega^2[M] \right] \{\phi\} = 0 \tag{48}$$

Picking the shift factor, μ, close to the desired ω_i^2 gives the shifted equations [8, 330]

$$\left[[K] - \mu[M] - (\omega^2 - \mu)[M] \right] \{\phi\} = 0 \tag{49}$$

Letting

$$[\widehat{K}] = [K] - \mu[M] \quad \text{and} \quad \widehat{\omega^2} = \omega^2 - \mu \tag{50}$$

Then

$$\left[[\widehat{K}] - \widehat{\omega^2}[M] \right] \{\phi\} = 0 \quad \text{or} \quad [\widehat{K}]^{-1}[M]\{\phi\} = \frac{1}{\widehat{\omega^2}}\{\phi\} \tag{51}$$

Applying matrix iteration to this equation produces the mode closest to μ.

Now consider the matrix $[K(\lambda_i)]^{-1}[M]$ of the viscoelastic model. Only the ith eigenvalue and eigenvector are desired. By letting $\lambda = s^{1/m} = (i\omega)^{1/m}$, Equations 50 and 51 can be written as

$$\widehat{\lambda^{2m}} = \lambda_i^{2m} + \mu$$
$$[\widehat{K}(\lambda_i)] = [K(\lambda_i)] - \mu[M] \qquad (52)$$
$$[\widehat{K}(\lambda_i)]^{-1}[M]\{\phi\} = \tfrac{-1}{\widehat{\lambda^{2m}}}\{\phi\}$$

As a first guess of the appropriate shift factor for the ith mode, the eigenvalue of $[K(\lambda_{i-1})]^{-1}[M]$ closest to λ_{i-1} is used. It is computed by using Turner's method. The dynamical matrix is

$$[D(\lambda_{i-1})] = [\widehat{K}(\lambda_{i-1})]^{-1}[M] - \tfrac{1}{\lambda_{i-1}^{2m}}\{\phi_{i-1}\}\{\phi_{i-1}\}^T[M]$$
$$[D(\lambda_{i-1})]\{\phi\} = \tfrac{1}{\widehat{\lambda^{2m}}}\{\phi\} \qquad (53)$$

If μ_{i-1} was the shift used to find λ_{i-1}, then by Equation 52, the new shift factor is

$$\mu_i = \mu_{i-1} - \widehat{\lambda^{2m}} \qquad (54)$$

Since the magnitude of the ith eigenvalue must be larger than the magnitude of λ_{i-1}, if

$$|\mu_i| < |\mu_{i-1}| \qquad (55)$$

then $\widehat{\lambda^{2m}}$ was in the wrong direction. The shift is recomputed as

$$\mu_i = \mu_{i-1} + \widehat{\lambda^{2m}} \qquad (56)$$

Notice that matrix iteration on

$$[\widehat{K}(\widehat{\lambda_i}, \mu_i)]^{-1}[M] = \frac{1}{\widehat{\lambda_i^{2m}}}\{\phi_i\} \qquad (57)$$

will converge to the $i - 1$ mode if the magnitude of μ_i is not large enough. If this occurs, μ_i is adjusted by adding the new $\widehat{\lambda^{2m}}$ (as in Equation 56).

For undamped systems, the jth eigenvalues on all $2m$ branches have the same magnitude and are evenly spaced on a circle about the origin. For lightly damped systems, the jth eigenvalues lie near the those for an undamped system. This is portrayed graphically for a single degree of freedom system with $\alpha = 1/2$ in Figure 2a. Since λ^{2m} is roughly the same magnitude for all the eigenvalues, the method can be modified slightly to use the λ_i^{2m} values on the principal branch to calculate shifts for the other branches. This modification is valid for systems with less than a 0.01 damping ratio.

To understand the location of the λ^2 values in the s-plane, it is necessary to realize that the Riemann surface for the function $w = z^{1/2}$ consists of two
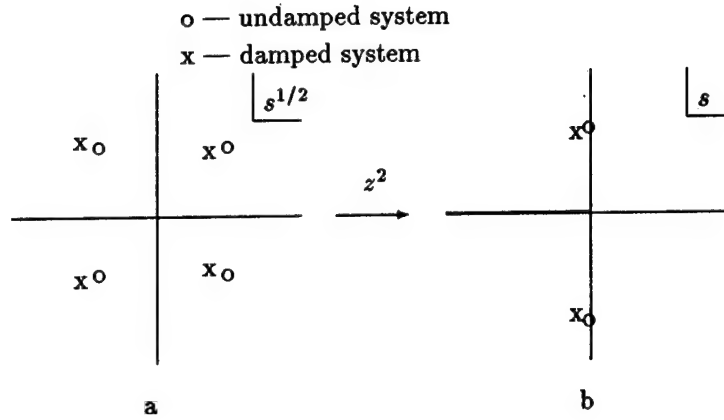
Figure 2: Locations of λ and λ^2 values

Riemann sheets, joined together at the branch cut. Taking the branch cut along the negative real axis, the sheets can be defined by

$$
\begin{array}{rcl}
S_0 & = & \{z| -\pi \leq \arg(z) < \pi\} \\
S_1 & = & \{z|\pi \leq \arg(z) < 3\pi\}
\end{array} \tag{58}
$$

So the eigenvalues in the first and fourth quadrants of the $s^{1/2}$-plane map into the second and third quadrants, respectively, of S_0. These are shown in Fiqure 2b. But the eigenvalues in the second and third quadrants of the $s^{1/2}$-plane map into the fourth and first quadrants, respectively, of S_1. To see this let $re^{i(3\pi/4+\delta)}$ represent the second quadrant eigenvalue, where δ is an small angle. Then

$$
\arg(\lambda^2) = \frac{3\pi}{2} + 2\delta \tag{59}
$$

Since this angle is greater than π, λ^2 is on S_1 at the angle given by Equation 59.

The third quadrant eigenvalue is a little more subtle. Its angle is $-(3\pi/4+\delta)$, so

$$
\arg(\lambda^2) = -\frac{3\pi}{2} - 2\delta \tag{60}
$$

But neither sheet contains values with this angle. When the value crossed the negative real axis in the negative direction, its angle experienced a 4π jump discontinuity from $-\pi$ to 3π. Therefore the angle is really

$$
\arg(\lambda^2) = -\frac{3\pi}{2} - 2\delta + 4\pi = \frac{5\pi}{2} - 2\delta \tag{61}
$$

DAC-14

Technique	$t = 0.1$m	$t = 0.05$m
Modified matrix iteration	0:52.11	1:14.51
Spectrum shift	0:21.78	0:32.43
Modified spectrum shift	0:12.06	0:15.15

Table 1: Computation Times (in CPU minutes)

This angle is in the first quadrant of S_1. Notice that for undamped systems, the λ^2 values in S_1 lie directly above those in S_0. To map back into the $s^{1/2}$-plane, the 4π must be subtracted off before taking the square root.

For a ten degree-of-freedom system, the spectrum shift technique more than halved the computation time required by the modified matrix iteration technique. Storing the principal branch's λ^{2m} values reduced the computation time by another 50%. (Exact computation times are given in Table 1.) Computed eigenvalues were accurate to at least five significant figures.

Example Problem

To demonstrate the efficiency of this technique, a ten degree-of-freedom model was considered. The rod was similar to the one in Figure 1, and its equations of motion had the same form. The rod was assumed to be pure aluminum, with Butyl B252 damping pads. The values of the parameters were [4](all values are in compatible mks SI units)

$$
\begin{aligned}
\rho &= 2.71 \cdot 10^3 & E &= 5.516 \cdot 10^{10} \\
A &= 0.0625 & G_0 &= 7.6 \cdot 10^5 \\
A_i &= 0.0625 & G_1 &= 2.95 \cdot 10^5 \\
L &= 0.909 & b &= 0.001 \\
t_i &= 0.1
\end{aligned}
$$

These parameters resulted in low damping, on the order of 10^{-2}, so it could be solved using the modified spectrum shift technique, as well as by using modified matrix iteration or spectrum shift. The computation times for two different pad thicknesses are given in Table 1. The solution took longer than for the thinner pad due to the increased damping.

The damping in the system was increased by decreasing the thickness of the viscoelastic pads to 0.01m. For this case, the equivalent damping ratio was 0.069, as computed from the fundamental mode. For the principal branch, the complex frequencies and mode shapes were found to be

$$\left\{ \begin{array}{rcr} -107 & + & 1545i \\ -77 & + & 2962i \\ -66 & + & 4459i \\ -61 & + & 6051i \\ -60 & + & 7762i \\ -61 & + & 9606i \\ -64 & + & 11566i \\ -69 & + & 13567i \\ -74 & + & 15415i \\ -79 & + & 16779i \end{array} \right\}$$

and

$$\begin{bmatrix} 1.0 & 1.0 & 1.0 & 1.0 & 1.0 & 1.0 & 1.0 & 1.0 & 1.0 & 1.0 \\ 1.9 & 1.7 & 1.3 & 0.8 & 0.3 & -0.3 & -0.8 & -1.3 & -1.7 & -1.9 \\ 2.7 & 1.8 & 0.7 & -0.3 & -0.9 & -0.9 & -0.3 & 0.7 & 1.8 & 2.7 \\ 3.2 & 1.4 & -0.4 & -1.1 & -0.5 & 0.6 & 1.1 & 0.4 & -1.4 & -3.2 \\ 3.5 & 0.5 & -1.2 & -0.6 & 0.8 & 0.8 & -0.6 & -1.2 & 0.5 & 3.5 \\ 3.5 & -0.5 & -1.2 & 0.6 & 0.8 & -0.8 & -0.6 & 1.2 & 0.5 & -3.5 \\ 3.2 & -1.4 & -0.4 & 1.1 & -0.5 & -0.6 & 1.1 & -0.4 & -1.4 & 3.2 \\ 2.7 & -1.8 & 0.7 & 0.3 & -0.9 & 0.9 & -0.3 & -0.7 & 1.8 & -2.7 \\ 1.9 & -1.7 & 1.3 & -0.8 & 0.3 & 0.3 & -0.8 & 1.3 & -1.7 & 1.9 \\ 1.0 & -1.0 & 1.0 & -1.0 & 1.0 & -1.0 & 1.0 & -1.0 & 1.0 & -1.0 \end{bmatrix}$$

The first three mode shapes are plotted in Figures 3 to 5. The magnitude of the complex frequencies for the first five modes is less than 10% higher than those for an undamped continuum model, but the higher frequencies differ by up to 20%.

The spectrum shift method complements the finite element model. With spectrum shift, finite element problems with viscoelastic damping can be solved much faster than with modified matrix iteration. For a ten degree-of-freedom model, the savings was more than 50% of the CPU time.

Conclusions and Recommendations

The spectrum shift technique is more efficient than the matrix iteration technique. The computational burden does not increase as drastically with increasing degrees of freedom. For lightly damped systems, the modified spectrum shift technique represents even greater computational savings.

The existing program (presented in [9]) can be made more efficient by realizing that in real systems eigenvalues and eigenvectors appear in complex pairs, and by taking advantage of the symmetry of the stiffness and mass matrices. Also, for larger systems, it would be beneficial to examine matrix inversion techniques that are designed to handle large matrices.
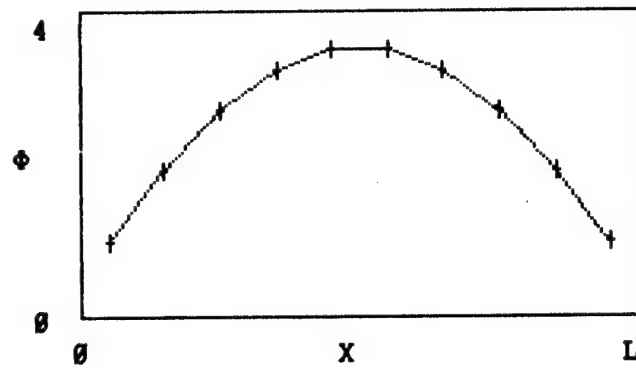
Figure 3: First Mode Shape for Damped Rod
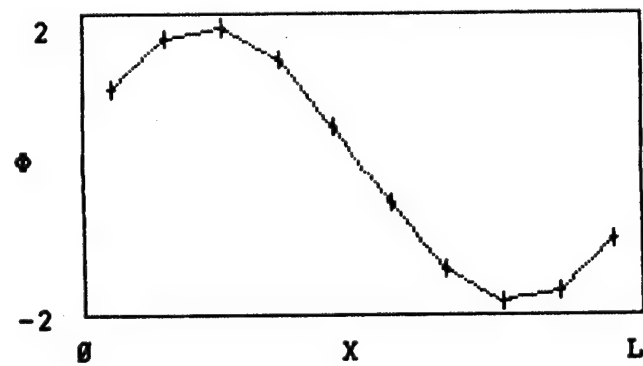
Figure 4: Second Mode Shape for Damped Rod
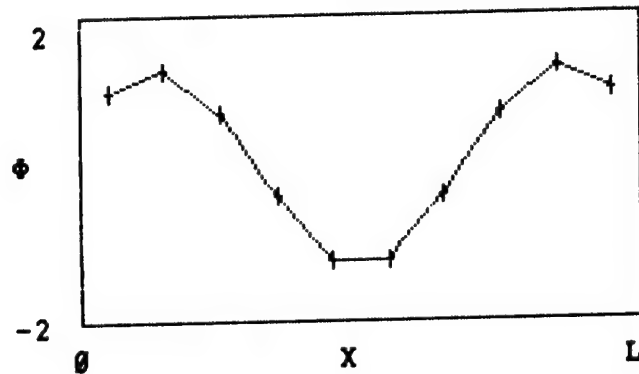
Figure 5: Third Mode Shape for Damped Rod

References

[1] Bagley, R. L., *Applications of Generalized Derivatives to Viscoelasticity*, Ph. D. Dissertation, Air Force Institute of Technology; also published as Air Force Materials Laboratory TR-79-4103, Nov. 1979 (AD- A071726).

[2] Bagley, R. L. and Torvik, P. J., "Fractional Calculus—A Different Approach to the Analysis of Viscoelastically Damped Structures," *AIAA Journal,* Vol. 21, May 1983, pp. 741-748.

[3] Bagley, R. L. and Torvik, P. J., "On the Fractional Calculus Model of Viscoelastic Behavior," *Journal of Rheology,* Vol. 30, No. 1, 1986, pp. 133-155.

[4] Bagley, R. L. and Torvik, P. J., "Fractional Calculus in the Transient Analysis of Viscoelastically Damped Structures," *AIAA Journal,* Vol. 23, June 1985, pp. 918-925.

[5] Bagley, R. L. and Torvik, P. J., "A Theoretical Basis for the Application of Fractional Calculus to Viscoelasticity," *Journal of Rheology,* Vol. 27, No. 3, 1982, pp. 201-210.

[6] Bisplinghoff, R. L., Ashley, H., and Halfman, R. L., *Aeroelasticity*, Addison-Wesley Publishing Company, Inc., Reading, Massachusetts, 1955.

[7] Christensen, R. M., *Theory of Viscoelasticity: An Introduction*, Academic Press, New York, 1971, p. 42.

[8] Craig, R. R., Jr., *Structural Dynamics: An Introduction to Computer Methods,* John Wiley & Sons, New York, 1981.

[9] Devereaux, M. L., *Improved Solution Techniques for the Eigenstructure of Fractional Order Systems*, Masters Thesis, Air Force Institute of Technology, 1988.

[10] Gel'fand, I. M., and Shilov, G. E. *Generalized Functions, Vol I*, Academic Press, New York, 1964.

[11] Hurty, W. C. and Rubinstein, M. F., *Dynamics of Structures*, Prentice-Hall, Inc. , Englewood Cliffs, New Jersey, 1964.

[12] Jenkins, W. M., *Matrix and Digital Computer Methods in Structural Analysis*, McGraw-Hill, London, 1969, pp. 170-171.

[13] Spiegel, M. R., *Mathematical Handbook of Formulas and Tables*, McGraw-Hill Book Company, New York, 1968.

[14] Torvik, P. J. and Bagley, R. L.,"On the Appearance of the Fractional Derivative in the Behavior of Real Materials," *Journal of Applied Mechanics,* Vol. 51, No. 2, 1984.

[15] Torvik, P. J. and Bagley, R. L.,"Fractional Derivatives in the Description of Damping Materials and Phenomena," *The Role of Damping in Vibration and Noise Control,* DE-Vol. 5, The American Society of Mechanical Engineers.

STUDY OF THE RHEOLOGY OF AN ELASTIC MEDIUM THROUGH THE SPLITTING OF ITS EIGENFREQUENCIES.

Michele Caputo

Dipartimento di Fisica, Università "La Sapienza", Roma, Italy.

Abstract.

It is seen how the rheology causes the splitting of the eigenfrequencies of a harmonic elastic oscillator into a number of lines spread over a frequency band depending on the rheology of the medium. The observation of these lines may allow to infer properties of the rheology.

In most cases the splitting of the eigenvalues of a system of partial differential equations is due to the removal of some geometric symmetry in the model considered.

In the model of this note the splitting is due to the the removal of the symmetry of the time coordinate since the presence of the dissipation makes the phenomenon irreversible.

Introduction.

Among the phenomena occurring in Physics the dissipation of energy is of great interest in many branches of applied research ranging from general mechanics to aseismic constructions.

The effect .for a simple oscillator, is generally measured with the quality factor Q defined as the ratio

$$Q^{-1} = \Delta E/2\pi E \qquad (1)$$

where E is the peak energy and ΔE is the decrease in energy between two succesive peaks or the percenttual loss of energy per unit cycle.

From the experimental point of view the phenomenon results in a broadening of the spectral lines of the spectrum.

But the phenomenon may be see also from another point of view relating it to the eigenvalues of the oscillator.

We shall see here that in the case of an anelastic medium in which the stress-strain relations contain a memory mechanism represented by a convolution as follows

$$h * \tau^{(m+1)} + \mu\tau = \mu h * \varepsilon^{(m+1)} \qquad (2)$$

where τ is stress, ε is strain, μ is the elastic parameter, and h(t) represents the memory mechanism acting through the

convolution indicated by * .For a wide class of elastic materials h(t) may be assumed (Caputo 1967)

$$h(t) = \eta \, t^{-z}/\Gamma(1-z) \;,\; H(p) = LT\left[h(t)\right] = \eta \, p^{z-1} \qquad (3)$$

In that case the relation (2) becomes a generalization of that of Maxwell in which the derivative of first order with respect to time is substituted by that of real order m + z.

It was also shown that the stress strain relation (2) with h(t) as in (3) may represent also the phoenomenon of fatigue (Caputo 1979) by considering the hysteresis loop of the medium subject to a cyclic deformation; it allows to compute the number of cycles which would give the fatigue as function of the frequency and of the amplitude of the cyclic strain applied.

The solution for the harmonic oscillator.

We shall see here that the stress-strain relation (2) with h(t) as in (3), causes a splitting of each of the spectral lines of the oscillator in a set of lines depending on the value of z and limited in a and whose width depends on η, m, z and on the frequency.

In fact, indicating by u(x,t) the displacement of a point of the medium and assuming that this, for t = 0, is at rest, by taking the Laplace Transform (LT) of (2)

and (3) and substituting in the equilibrium condition we find

$$\eta p^{m+z} T(p,x) + \mu T(p,x) = \eta \mu E(p,x) p^{m+z}$$

(4)

$$\rho p^2 U = \frac{\mu \eta p^{m+z}}{\mu + \eta p^{m+z}} \frac{\partial^2 U}{\partial x^2}$$

where capital letters indicate the LT of the functions indicated by the corresponding lower case letter and p is the LT variable; ρ is the density.

To obtain (4) we used the theorem of Appendix A of Caputo (1969) which extends to the derivatives of real order the well known theorem of the LT of derivatives of integer order.

Equation (4) gives

$$U = A(p) e^{wx} + B(p) e^{-wx}$$

(5)

$$w^2 = \rho p^2 (\mu + \eta p^{z+m}) / \mu \eta p^{z+m}$$

As boundary conditions we may choose those when the displacement is nil for any t at $x = 0$ and $x = S$, which imply that

$$A + B = 0$$

(6)

$$e^{ws} - e^{-ws} = 0$$

DAD-4

Substituting $p = i\omega$ in (6), with ω angular frequency, we have

$$\sin\left[(a+ib)^{1/2} s \cdot \omega \sqrt{\rho/\mu}\,\right] = 0$$

$$a(\omega) = 1 + \frac{\mu}{\eta}\, \omega^{-z-m} \cos\left[\left(\frac{\pi}{2} + 2K\pi\right)(m+z)\right]$$

$$\hspace{11cm} (7)$$

$$b(\omega) = -\frac{\mu}{\eta}\, \omega^{-z-m} \cos\left[\left(\frac{\pi}{2} + 2K\pi\right)(m+z)\right]$$

The eigenvalues are obtained solving the equation

$$\rho(a+ib) s^2 \omega^2 = \mu n^2 \pi^2 \qquad\qquad (8)$$

It is seen that for every n there is more than one eigenvalue due to the presence of k. They are

$$\omega_{on}\Big/ Re\left[a(\omega_{on}) + ib(\omega_{on})\right]$$

$$\hspace{11cm} (9)$$

$$\omega_{on} = \frac{n\pi}{s}\sqrt{\mu/\rho}$$

For many elastic media we may reasonably assume that
$$\eta\omega^{m+z}/\mu \qquad \gg 1,\ \text{then}$$

$$\omega = \omega_{on}\left(1 - \frac{\mu\,\omega_{on}^{-z-m}}{2\eta}\cos\left[\left(\frac{\pi}{2} + 2K\pi\right)(z+m)\right]\right) \qquad (10)$$

It is thus clear that depending on the value of z one may have a finite or an infinite number of eigenvalues for each n.

The Q^{-1} of the spectral lines is one half the ratio of the immaginary to the real part of ω

$$Q^{-1} = \frac{\mu}{2\eta} \, \omega_{on}^{-z-m} \sin\left[\left(\frac{\pi}{2} + 2K\pi\right)(z+m)\right] \tag{11}$$

The solution, for each value of n, are limited in the band

$$\omega_{on}\left(1 - \omega_{on}^{-z-m} \mu/2\eta\right), \quad \omega_{on}\left(1 + \omega_{o}^{-z-m} \mu/2\eta\right) \tag{12}$$

The term $m(1/2 + 2k)\pi$ does not affect the number of eigenvalues, also, since n does not enter the corrective factor of (10), it is clear that each eigenvalue, corresponding to a value of n of the perfectly elastic case, is split in the same number of eigenvalues , for all z, which depends only on z.

The effect of m depends only on its parity and is limited to a shift of the solutions, in fact is m is even and multiple of four then the argument of the cosine is shifted by a multiple of 2π, if m is even and not multiple of four then the argument of the cosine is shifted by π , if m is even but not multiple of four then the

argument of the cosine is shifted by $\pi/2$.

If z is not rational then there is an infinite number of eigenvalues limited in the band defined by (12). If z is rational the number of eigenvalues is limited.

In the following we shall consider few cases in which z is rational which will illustrate how the solutions are spread in the range (12) and discuss the corresponding values of Q .

The number of eigenvalues generated in the splitting.

It is no limitation to the discussion to assume that m is a multiple of four, that $z = q/(4l + 1)$ with q and l integer and also that q, $4l + 1$ are relatively prime.

When $q = 4r + 1$, with r integer the values of $\cos(1/2 + 2k)$ z , as function of k in the range $-2l,2l$, are repeated periodically when $|k| > 2l$; the resulting eigenvalues (10) are therefore $4l + 1$ and correspond to an equal number of spectral lines.

When $q = 2r + 1$, with r odd, one may see that the spectral lines are again $2l + 1$. When q is even, due to the simmetry of the cosine and to the simmetry of its argument with respect to $k = \pm 1, \pm 3, \pm 5,\ldots$ the values of $\cos(1/2 + 2k)$ z, as function of k, in the range $-l,l$ are repeated when $|k| > l$; the resulting eigenvalues (10) are therefore $2l + 1$ and correspond to an equal number of spectral lines.

The values of Q corresponding to each of the spectral lines is given by (11); depending on the argument of the sine we may therefore have modes without dissipation, they correspond to frequencies on the extremes of the band defined by (12).

The spectral lines with the largest Q^{-1} are those for which the argument of the sine is $(2u + 1)\pi/2$ with u even; they correspond to the eigenfrequencies of the purely elastic case.

The eigenvalues which correspond to the argument of sine with u odd would have a negative Q and are therefore disregarded for their physical insignificance.

The discussion of the cases when $z = q/(2l + 1)$, with l odd, or $z = q/2l$ is similar to that made for the case when $z = q/(4l + 1)$.

Conclusions

It is seen how the rheology causes a splitting of the spectral lines of an oscillator.

In general the rheology of elastic media is studied observing phenomena with very low forced frequency therefore requiring that the observations are taken for very long

time, which is generally difficult to obtain. The observation of the splitting of the spectral lines may allow to infer properties of the rheology with observations taken for a time interval one order of magnitude longer than the length of the period of the fundamental mode.

References.

M.Caputo,Geophys. J. R. Astron. Soc. 13,529-539,1967.

M. Caputo, Elasticità e dissipazione (Zanichelli, Bologna), Chap. 2, pp.39-71; Chap. 3, pp. 73-114.

M.Caputo, J. Acoust. Soc. Am. 66, 176-179, 1979.

Table caption

Values of the cosine of formula (10) giving the eigenvalues for $z = q/(21 + 1)$, $m = 0$ with $1 = 3$ and $q = 1, 2, 3, 4, 5, 6$. When q is even there are 4 different eigenvalues when q is odd there are 7 different eigenvalues.

Table

Values of q							
2 6	1 3 5	4	1 3 5	2 6	1 3 5	4	1 3 5

Eigenvalues							
-1.00	-0.97	-0.90	-0.78	-0.62	-0.43	-0.22	0

Values of q						
2 6	1 3 5	4	1 3 5	2 6	1 3 5	4

Eigenvalues						
0.22	0.43	0.62	0.78	0.90	0.97	1.0

A Viscous Isolator for Shuttle
Hubble Space Telescope Resupply
by
Porter Davis,
Frank Schmitt, and Charles See

Honeywell Inc.
Satellite Systems Divsion
19019 N. 59th Avenue
Glendale, Arizona 85308
(602) 561-3000

ABSTRACT

Two isolator designs are being developed using the Hubble Space Telescope (HST) Reaction Wheel Assembly (RWA) isolator heritage. The first application provides a six-degree-of-freedom passive isolation system for space shuttle payloads. The HST solar arrays and science instrument packages cannot survive launch and reentry when directly exposed to shuttle vibration. The isolation mount for these payloads consists of a carrier assembly attached to the shuttle structure by an array of isolator struts. Various isolation characteristics, obtained by varying the strut's spring arrangement and damping coefficient, were evaluated. Twelve identical struts are arranged in tripods at each of the four corners of the carrier for redundancy and isoelasticity. The entire isolated mass has its resonance at 8 Hz with a damping ratio of 0.4; the effective loading is reduced by at least a factor of two. Prototype isolators have been built and characterization has been done. This provides the basis for the flight design currently underway.

The second application is to provide isolation between the Space Station and the Payload Pointing System. An array of struts, each containing damping and spring elements, was studied. The requirement for the first mode to be significantly lower than 0.05 Hz necessitates the use of novel approaches to design very soft springs.

INTRODUCTION

There is an increasing need for vibration isolation for spacecraft applications. Two specific applications of isolation technology are: 1) to reduce emitted vibrations from dynamic hardware, such as rotating machinery, and 2) to protect sensitive hardware from launch vibration and spacecraft disturbances. The Hubble Space Telescope (HST) Reaction Wheel Assembly (RWA) Isolator (Figure 1) is an example of the first application. It significantly reduces the vibrations emitted from the RWA, which would limit the telescopes imaging ability (Figure 2). Such isolation is also important to sensitive pointing systems and mircrogravity research and processing.

Two isolator designs are being developed using the HST-RWA isolator heritage for the second application, that of hardware isolation. The HST-Solar Array System Isolator (SASI) provides six-degree-of-freedom (DOF) passive isolation for space shuttle payloads. The Payload Pointing System (PPS) isolator provides isolation between the Space Station and the Payload Pointing System, which requires a first mode significantly lower than 0.05 Hz.
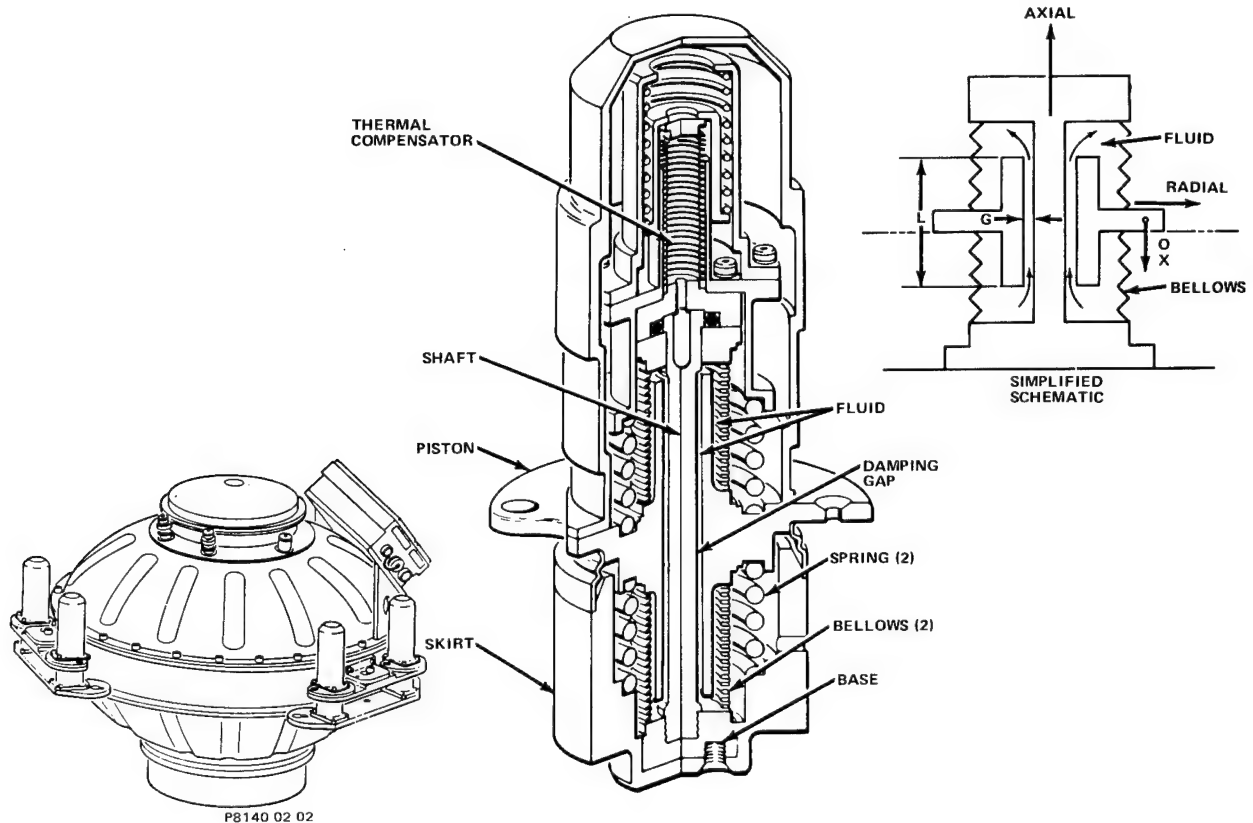
Figure 1. Hubble Space Telescope RWA Heritage
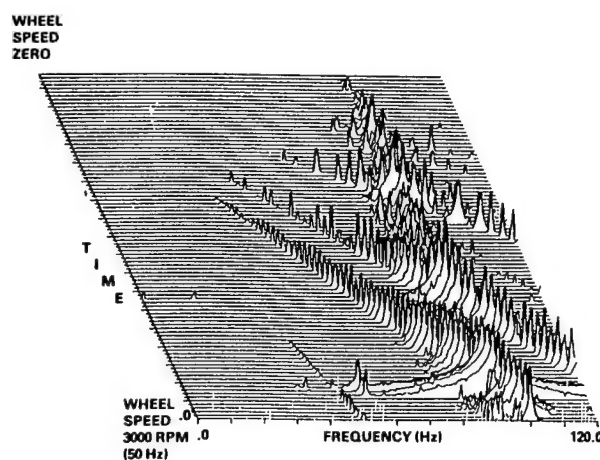
Hard-Mounted Reaction Wheel
Axial Force (3.39 lb Peak)
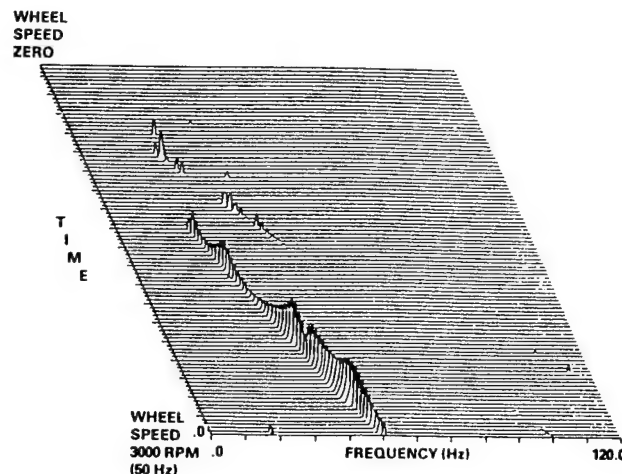
Isolated (Honeywell Viscous Isolator)
Reaction Wheel Axial Force (0.025 lb Peak)

Figure 2. RWA Disturbance Isolation

THE HST-SOLAR ARRAY SYSTEM ISOLATOR (SASI)

The significantly large mass of the HST satellite causes its first mode of vibration to be relatively low while mounted in the space shuttle cargo bay. Consequently, the vibration spectra seen by hardware attached to it, such as the solar arrays and axial scientific instruments, are attenuated for frequencies substantially above this mode. When considering resupply of these items to the HST vehicle, it is necessary to assure that launch vibrations experienced do not exceed the design capabilities. Consequently, it is necessary to isolate these items from the shuttle.

The Solar Array (SA) Carrier (Figure 3) provides the needed isolation for the SAs by using twelve spring-damper isolations elements configured in four tripods. The carrier attaches to the shuttle via a removable/jettisonable deck. The tripod arrangement, as presented in Figure 4, is configured to provide iso-elastic isolation and failsafe redundancy at each attachment point. The effect of this isolation system is presented in Figure 5. Unisolated, the response spectrum produces stresses in the solar arrays in excess of their design limits. This spectrum consists primarily of high-frequency components. Isolating the carrier with spring elements tuned to significantly lower frequency, in this case, 8 Hz, substantially reduces the higher frequency response. However, the spring elements introduce a response peak at the resonant frequency. Introducing damping limits the resonant peaking and produces a substantially reduced response spectrum. The result is induced stresses within the design limits of the solar arrays.
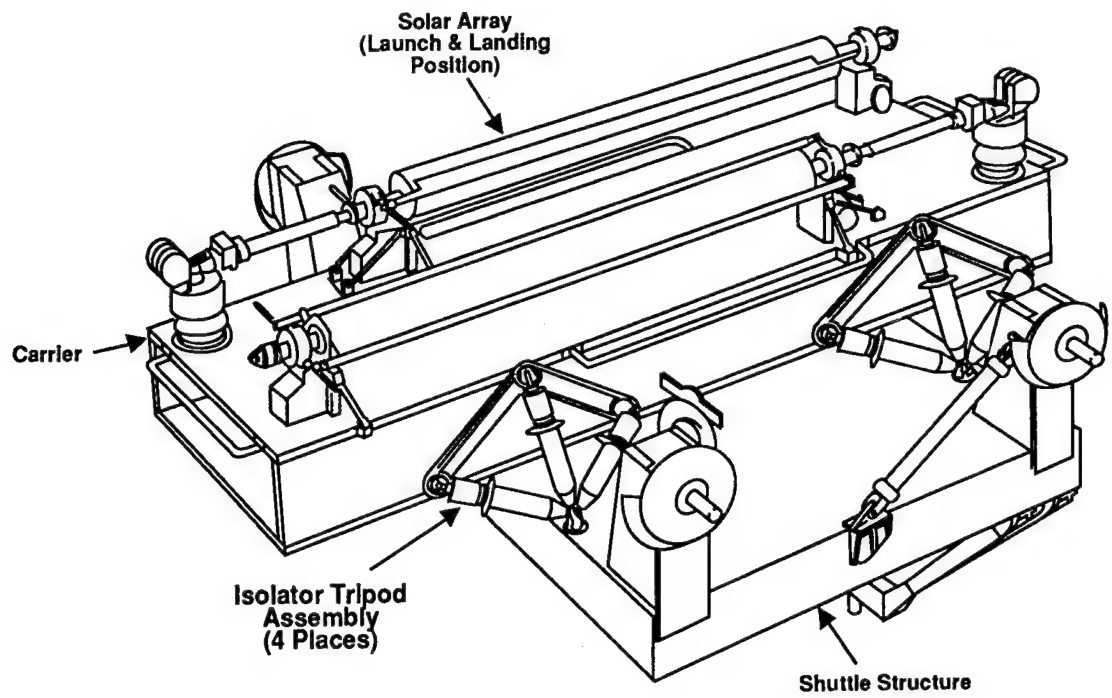
Figure 3. Isolated Solar Array Carrier
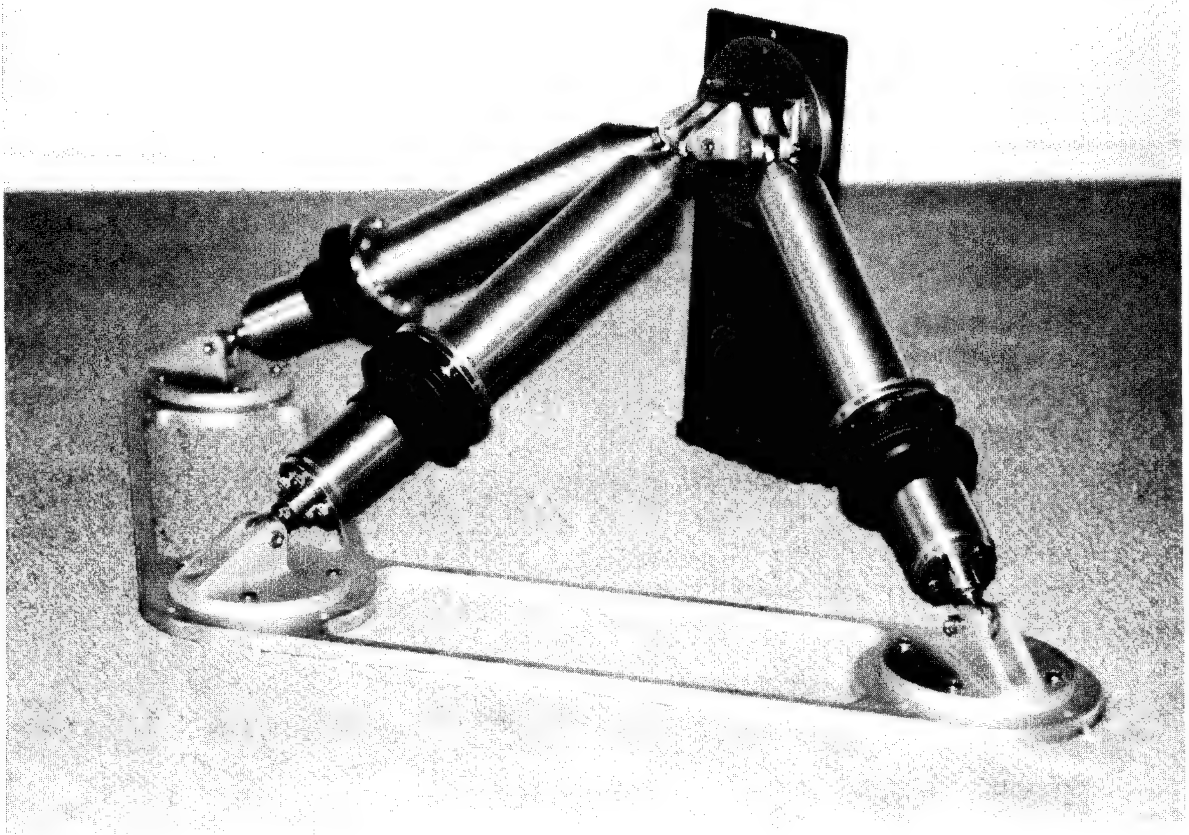
Figure 4. SASI Tripod Arrangement

Acceleration Response to Landing

Unisolated (a) — SA Net Z (G) vs Time (sec)

Isolated and Undamped (b) — Time (sec)

Isolated and Damped (c) — Time (sec)
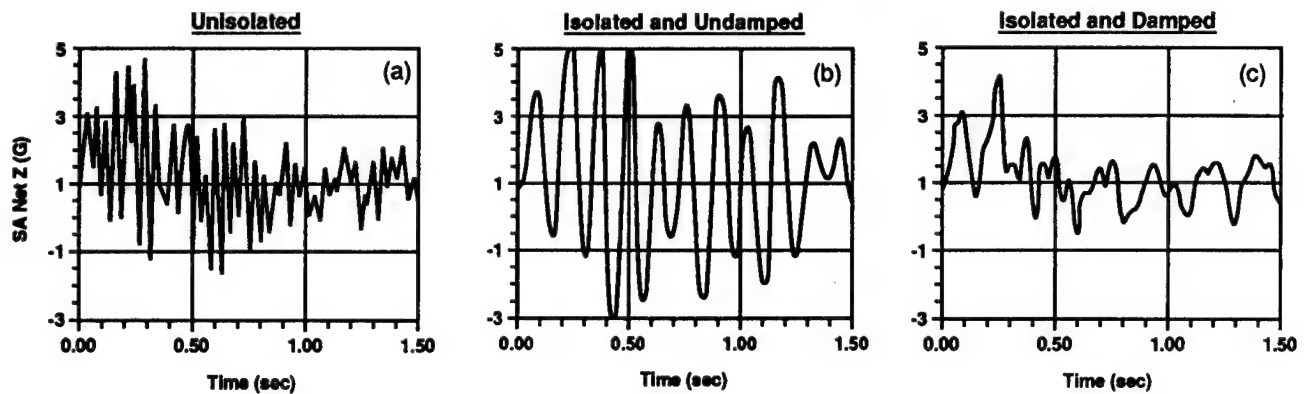
Acceleration Shock Spectrum (Q = 50)

(d) — SA Net Z (G) vs Freq (Hz)

(e) — Freq (Hz)

(f) — Freq (Hz)
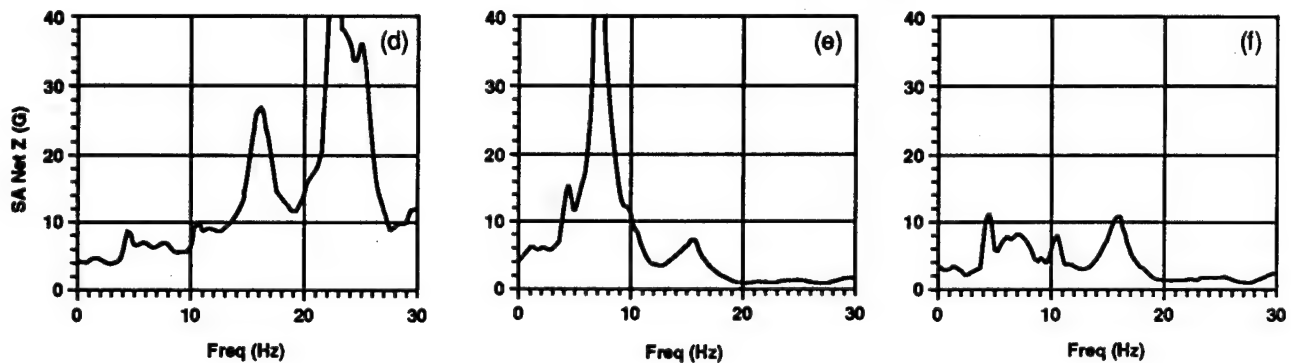
Courtesy of Bill Haile, Swales and Associates, Beltsville, MD

Figure 5. Representative Solar Array Response Changes

To verify manufacture isolator element performance against the characteristics of those in the analytical model, prototype isolator elements were designed, built, and tested to the specifications presented in Table 1. The prototype elements presented in Figures 6 and 7 provide passive damping via a viscous silicon fluid that is forced through an annular passage between two bellows-type pressure chambers. As the isolator is exercised, the volume of one of the chambers is increased at the same rate as the other is decreased, resulting in consistent damping. A compensation device provides for thermal expansion of the fluid and preloads the chambers to avoid cavitation. Helically wound coil springs are used to provide the correct stiffness for isolation.

Two types of dynamic tests were run on the prototype isolators: a transmissibility transfer function test and a velocity/pressure margin test. The transfer function test, as shown in Figure 8, consisted of connecting the isolator element between a suspended mass and an electromagnetic shaker. The mass was sized to provide an 8-Hz resonant frequency. The shaker was swept at a constant acceleration from approximately 4 to 200 Hz. Accelerometers on the shaker and mass were used to plot the transfer function, from which the Q and damping coefficients were calculated. The test was run for two different viscosity fluids: 250 centistoke and 500 centistoke. The results are presented in Figure 9.

Table 1. SASI Prototype Element Specification

Deflection	±0.5 in.
Velocity	11.5 in./s
Damping	2.6 lb-s/in.
Stiffness	400 lb/in.
Temperature	
Design	14°C to 36°C
Storage	-25°C to +40°C
Length	15 in.
Diameter	3 in.
Weight	≈ 3 lb
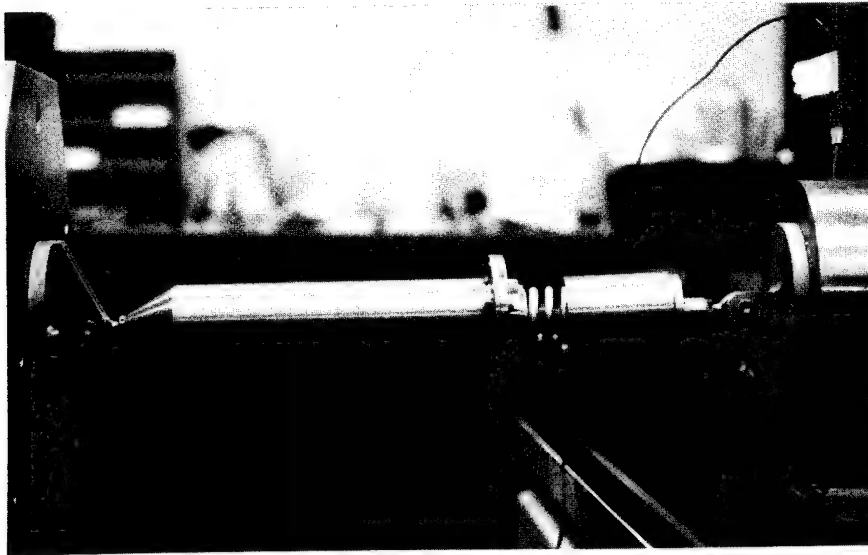
Figure 6. SASI Prototype
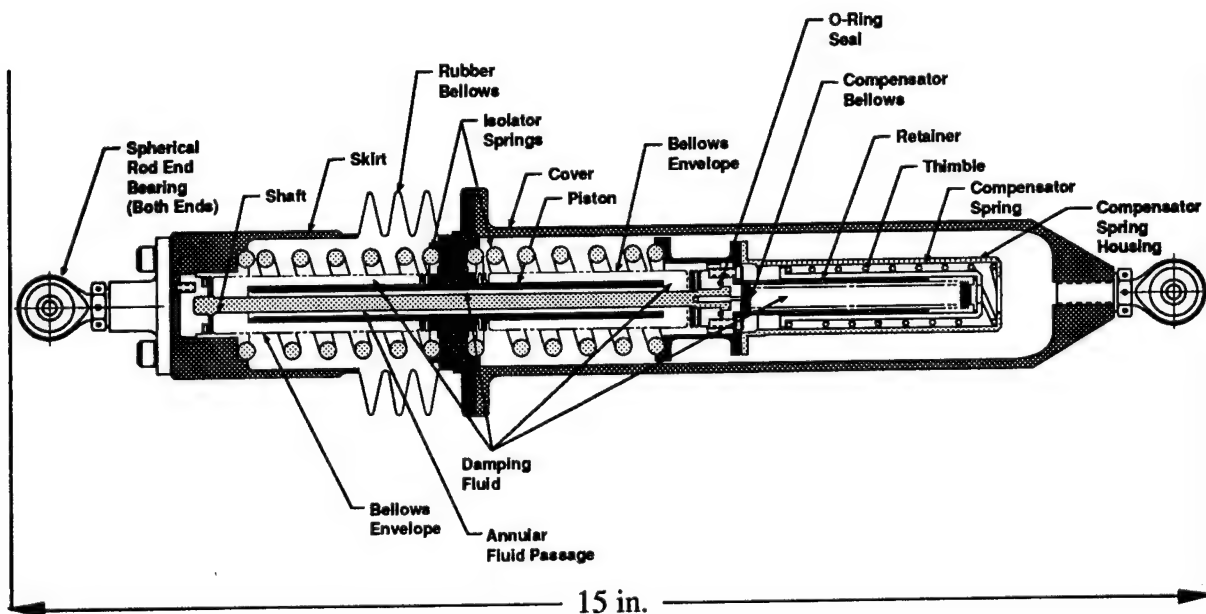
Figure 7. SASI Prototype Element
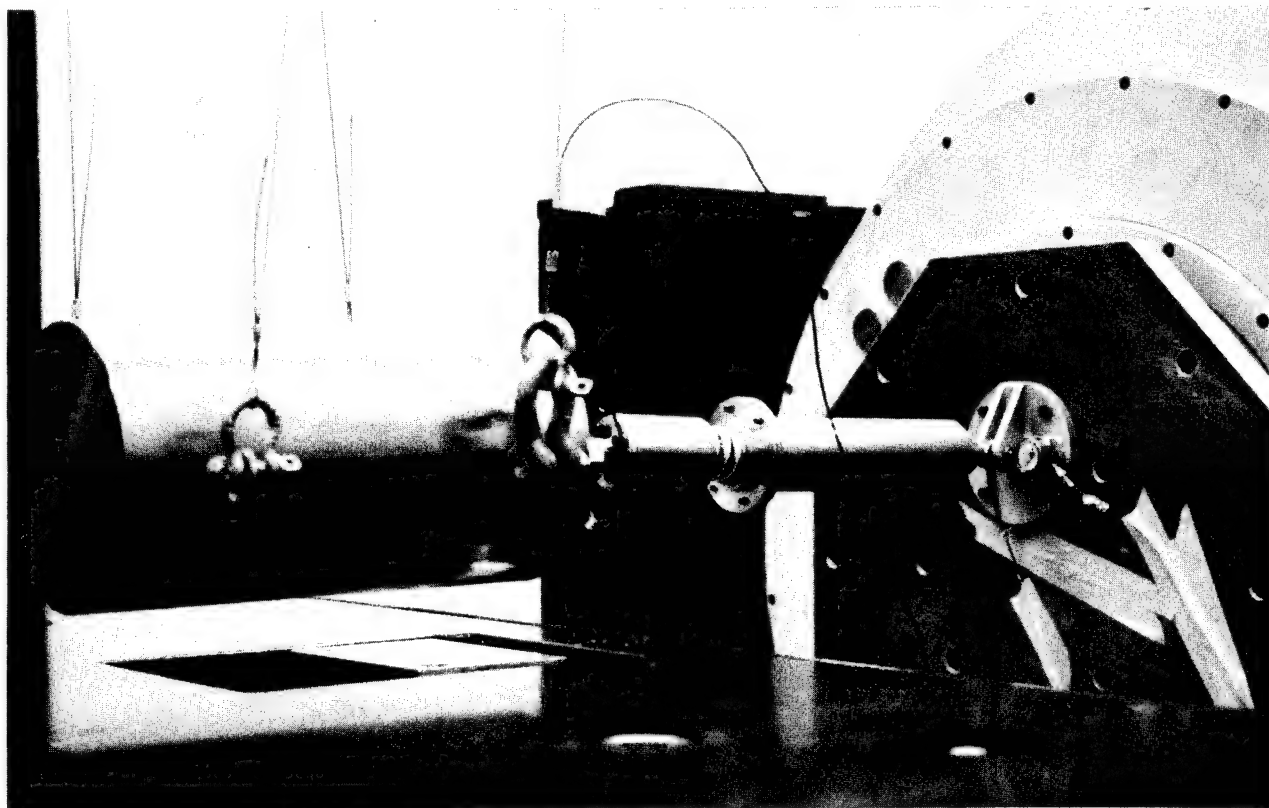
Figure 8. Transfer Function
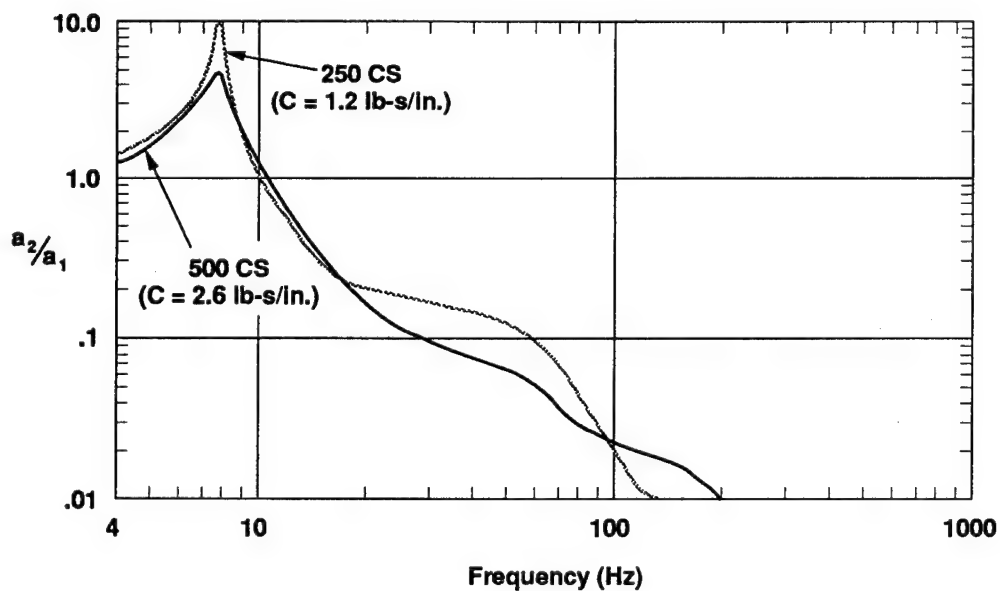
Figure 9. Transfer Function Test Results

Verification of the damper design was accomplished by rigidly fixing one end of the isolator to the shaker frame and driving the other end at a constant amplitude displacement, as shown in Figure 10. The frequency of excitation was swept to provide velocities from below nominal to those that produced chamber pressures equal to the bellows-proof pressure.
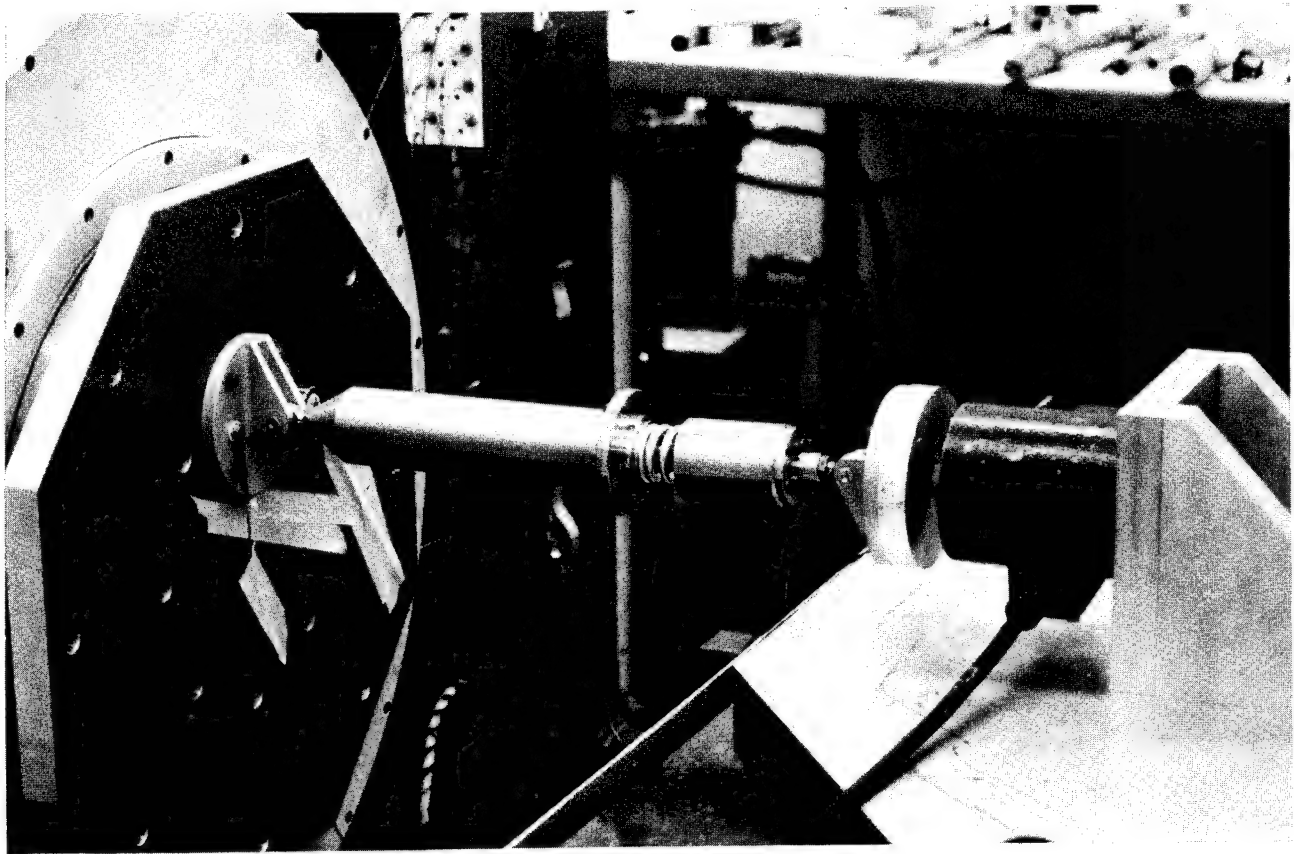
Figure 10. Velocity Test

The storage temperature range was demonstrated by thermal cycling the prototype and rerunning the transfer function test. The stiffness, stroke, and weight were measured during assembly. A summary of the prototype test results is presented in Table 2. Off-the-shelf springs were used to decrease procurement time; consequently, their stiffness did not match the design goal. Variation in spring length and stiffness resulted in asymmetric assembly, causing less usable stroke to be available than was originally desired. With these exceptions, the prototypes behaved very much as expected.

Table 2. Prototype Test Summary

	Design Goal	Test Results (500 cs)
Stiffness (lb/in.)	400	570
Damping (lb-s/in.)	2.6	2.6
Resonance (Hz)	8.0	7.8
Stroke (in.)	±0.5	±0.44
Weight (lb)	≈ 3.0	3.02
Velocity Capacity (in./s)	11.5	41.5
Storage Temperature (°C)	-25 to +40	-25 to +40

The actual isolation requirements for the solar array carrier necessitate isolator elements that are considerably larger than those used for prototype testing (Figure 11). The flight isolator design requirements are presented in Table 3. The higher peak velocity requirements necessitate extremely large bellows in order to keep the chamber pressure within the design limits. The increased stroke requirements also drive the bellows' size up, due to increased fatigue loading.
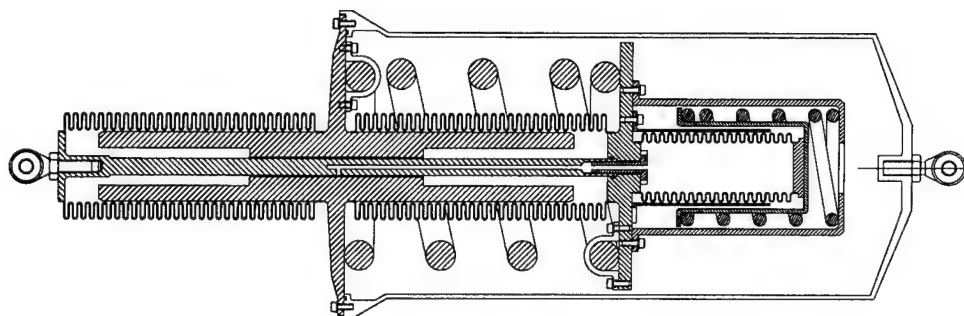
Figure 11. SASI Bellows-Type Isolator Element

Table 3. Isolator Element Flight Specification

Deflection	±0.91 in.
Velocity	±15 in./s
Damping	35 lb-s/in.
Stiffness	1875 lb/in.
Temperature	
Design	25 ± 5°C
Storage	-35°C to +49°C
Length	27 in. Brg $\mathcal{C}_L$ to Brg $\mathcal{C}_L$
Body Diameter	8 in. max
Fatigue Life	10,000 full stroke cycles
Weight	33 lb

To combat the increased size and weight, a higher pressure capacity damper (originally designed for isolation from Titan launch loads) was adapted to the isolator (Figure 12). It operates on the same principal of viscous flow through an annular gap to provide damping, but can withstand much higher internal pressures. Small displacement performance is sacrificed, however due to stiction in the O-ring seals. The parameters used in the design of the isolators presented in Figure 12 are listed in Table 4. A metal bellows could be added to provide a hermetic seal.
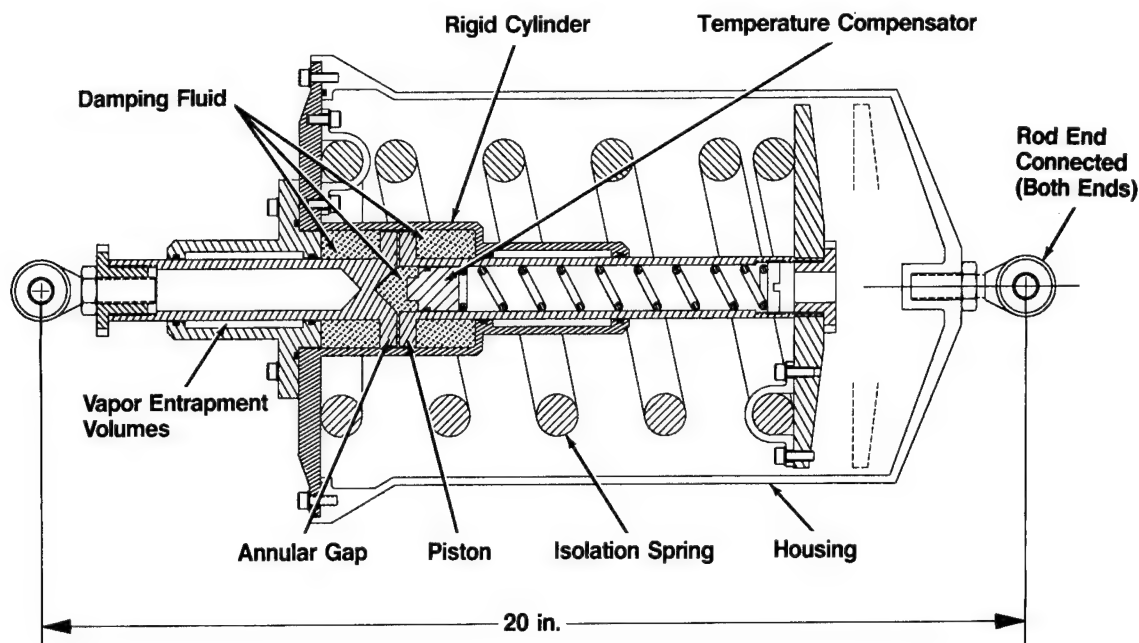
Figure 12. Rigid Volume Damper Isolators

Table 4. Rigid Volume Damper Isolator Specifications

Deflection	±0.91 in.
Velocity	±15 in./s
Damping	35 lb-s/in.
Stiffness	1875 lb/in.
Temperature	
Design	25 ± 5°C
Storage	-35°C to +49°C
Length	20 in. Brg ₵ to Brg ₵
Body Diameter	6.5 in. max
Fatigue Life	Extended
Weight	22 lb

The major features of each type of isolator considered for the SASI application are presented in Table 5. The bellows-type design is superior for on-orbit, small amplitude vibration isolation due to its excellent small displacement (microinch) performance and large dynamic range (five orders of magnitude). The rigid-volume, piston-type isolator has advantages for launch/landing load isolation. Its simplicity, ruggedness, and increased pressure margin make it more economical to manufacture.

Table 5. Isolator Features

<u>Bellows</u>	<u>Piston With Bellows</u>	<u>Piston Without Bellows</u>

• Heritage
  - Fluidic viscous damping
  - Hermetic seal
  - Wide dynamic range
  - Silicon fluid
  - Annular flow damper
  - Pressure preload and Temperature compensation
• Lightweight spring
	• Heritage
	  - Fluidic viscous damping
	  - Hermetic seal
	  - Silicon fluid
	  - Annular flow damper
	  - Pressure preload and temperature compensation
	• Lightweight spring
	• Improved fatigue margin
	• Reduced fluid leakage potential
	  - Reduced fluid volume
	  - Increased pressure margin
	  - Rugged pressure chamber
	• Reduced size and weight
	• Increased adaptability
		• Heritage
		  - Fluidic viscous damping
		  - Silicon fluid
		  - Annular flow damper
		  - Pressure preload and temperature compensation
		• Lightweight spring
		• Improved fatigue margin
		• Reduced fluid leakage potential
		  - Reduced fluid volume
		  - Increased pressure margin
		  - Rugged pressure chamber
		  - Redundant seal
		• Reduced size and weight
		• Increased adaptability
		• No offset loading
		• Rugged design
		• Improved manufacturability

THE PAYLOAD POINTING SYSTEM ISOLATOR

A study to determine the applicability of the HST viscous damped isolator to the Space Station Payload Pointing System was performed for the Jet Propulsion Laboratory. Such a passive isolation system would probably have cost, reliability, and possibly weight advantages over an active isolation system.

The baseline concept for the study is shown in Figure 13, with eight isolator struts comprising the passive isolation system. Several payloads are planned. However, the study was done using the requirements shown in Figures 14 and 15. These requirements are based on JPL's modelling of the system. The resonant frequency of <0.05 Hz is fundamental for this study. The stroke, damping, and stiffness values K_1 and K_2 are derived from the modelling.

The mass load (1375 pounds) is used as the effective load in the analysis of a single strut. Stiction effects in the end joints can be minimized by using flexure pivots in a two-degree-of-freedom (DOF) gimbal at one end and a three-DOF arrangement at the other.

The appropriate model for a mass-loaded strut is shown in Figure 15; Figure 7 represents the baseline design concept. The spring K_1 represents the stiffness of the bellows (or the parallel spring if it were used). The spring K_2 represents the spring effects in series with the damping element; that is, the compressibility of the fluid and the volume change of the bellows due to the pressure of the fluid. The stiffness ratio will be used in the evaluation of the transmissibility of the isolator strut.
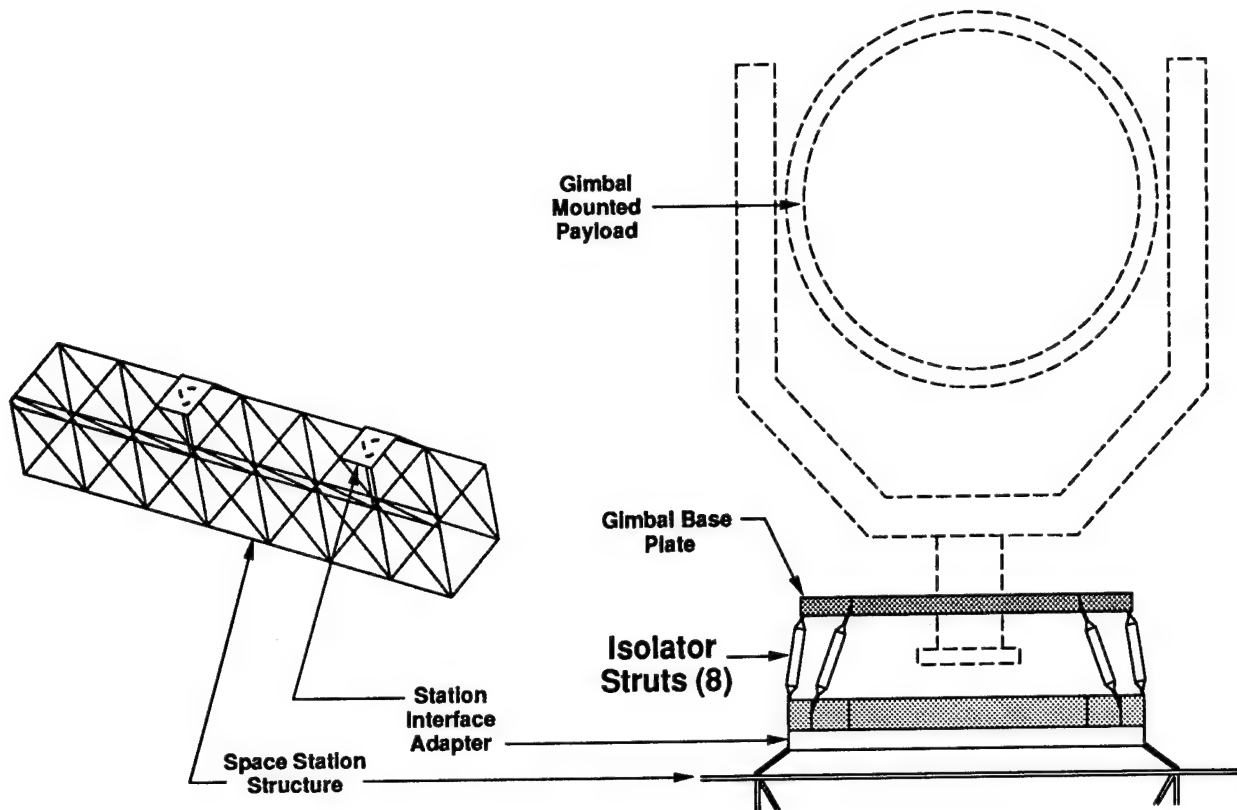
Figure 13. Passive Isolation of Space Station Attached Payload Pointing System
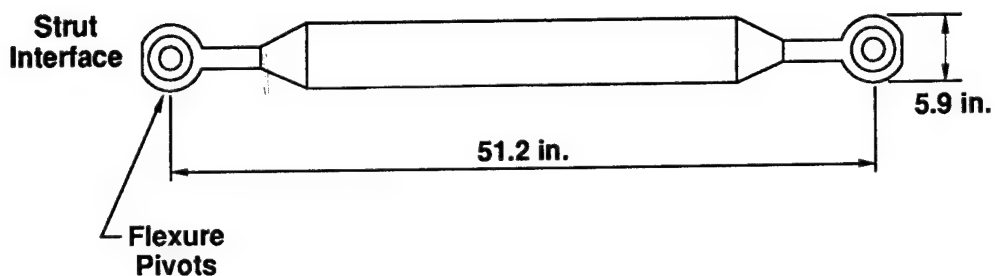
Resonant Frequency	<0.05 Hz
Stroke	±3.15 in.
Effective Mass Load	~1375 lb
Damping	3.4 lb/(in./s)
Stiction	Minimize
Life	>10 years
Linear Performance	µin. range

Figure 14. PPS Strut Specifications Derived from JPL Requirements
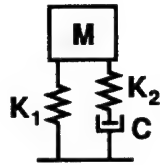
Design	K_1	K_2	C	K_2/K_1
1. SASI Scaled to PPS length	400 lb/in. spring 1.2 lb/in. bellows	3,800 lb/in.	0.26 lb/(in./s)	9.5 3,000
2. SASI Scaled and folded	0.45 lb/in.	1,350 lb/in.	3.4 lb/(in./s)	3,000
3. Design Potential (Double Length, Folded, with Air)	0.22 lb/in.	0.10 lb/in.	3.4 lb/(in./s)	0.5
Requirements	<0.23 lb/in.	<0.70	3.4 lb/(in./s)	—

Figure 15. Summary of Isolator Component Values

An evaluation of the general transfer function was performed to investigate the influence and importance of the various parameters. Figure 16 shows the model and the transfer function of a three-spring isolator and two simplifications of it.
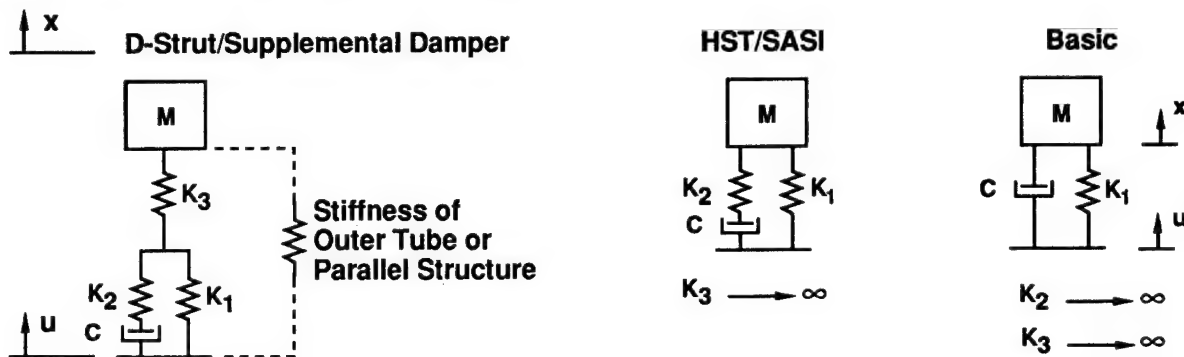
Transfer function

$$\frac{x}{u} = \frac{\dfrac{B}{Q}\left(1 + \dfrac{1}{N}\right) + 1}{\dfrac{B^3}{QN}\left(\dfrac{1+N}{P} + 1\right) + B^2\left(\dfrac{1}{P} + 1\right) + \dfrac{B}{Q}\left(\dfrac{1}{N} + 1\right) + 1}$$

$$B = \frac{S}{\sqrt{K_1/M}} \qquad Q = \frac{\sqrt{K_1 M}}{C} \qquad N = \frac{K_2}{K_1} \qquad P = \frac{K_3}{K_1}$$

Figure 16. Isolator Modules

DBA–13

The effects of varying the spring values are shown in Figure 17. The curve at the right shows the characteristic for both K_2 and K_3 relatively stiff with respect to K_1 (N&P large). Softening K_2 results in the curve that is second from the right; a high frequency isolation increase is seen but with an increased peak just above the break frequency of the basic isolator. Softening K_3, in addition, increases these two effects, as shown by the two left most curves. The middle curve shows the characteristic for a stiff K_2 and a softer K_3. It is shifted left from the baseline curve but shows a smaller peak, more damping, than the other curves. The shift is again due to the lower effective stiffness between the mass and the base. The stronger damping influence is due to the large K_2 imposing larger forces and velocities on the damping element. The roll-off is essentially second order for all curves.

The best combination of isolator elements required for a given application depends on the vibration input, the sensitivity of the isolated body to various frequencies, and the structural characteristics of the body and the base. Figure 5 illustrates this for single-spring isolator. The K_1 value is chosen to set the resonant frequency and then damping is added to reduce the resonant peaking, at some cost to high-frequency isolation. An acceptable balance for the SASI system is shown in Figures 5c and 5f.
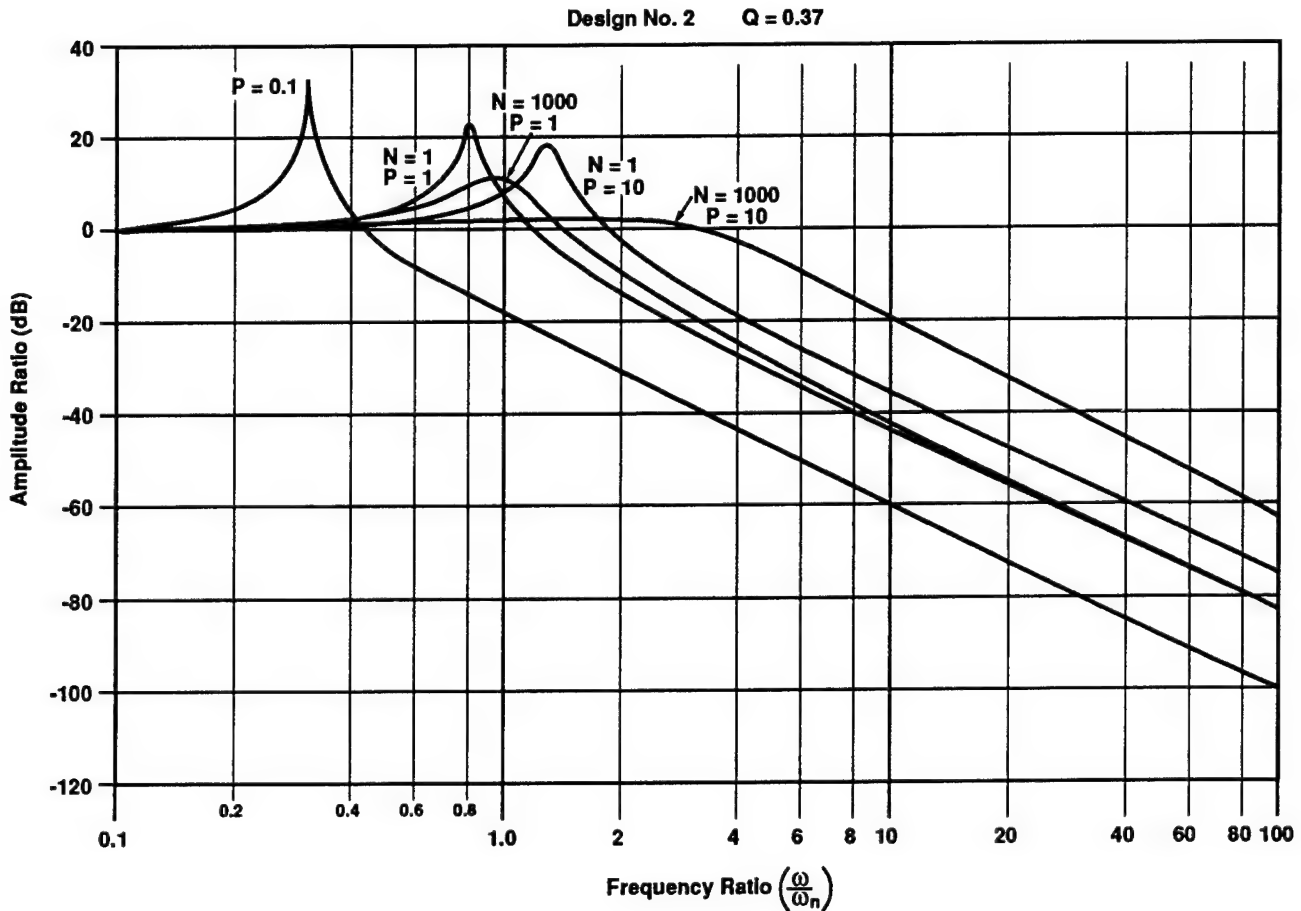
Figure 17. General Isolator Transfer Function

Figure 18 shows the transmissibility for the second design of Figure 15. This design represents the first attempt at meeting the requirements by scaling the SASI design. It is within the length requirement, but the effective bellows length is increased by "folding," that is, arranging the design so that the two active bellows and the compensator bellows are beside each other rather than end to end. The effective length is roughly tripled this way, reducing the bellows stiffness K_1 to one-third. The value for K_1 is still twice the required value; doubling the length would reduce the bellows stiffness, K_1, as needed. The value of K_2 is too large by nearly three orders of magnitude. A means must be used to reduce the effective compressibility of the fluid or effective expandibility of the bellows. Using air changes K_2 by the ratio of the compressibility of silicon damping fluid to that of air. At standard conditions, this ratio is 1/7500. Scaling K_2 by this ratio and doubling the length renders the third design in Figure 15.

Since the damping coefficient depends on the inverse of the radial gap cubed and directly on the viscosity, the damping coefficient can be maintained in spite of the 20:1 viscosity decrease by decreasing the fluid passage radial gap by a factor of about three.
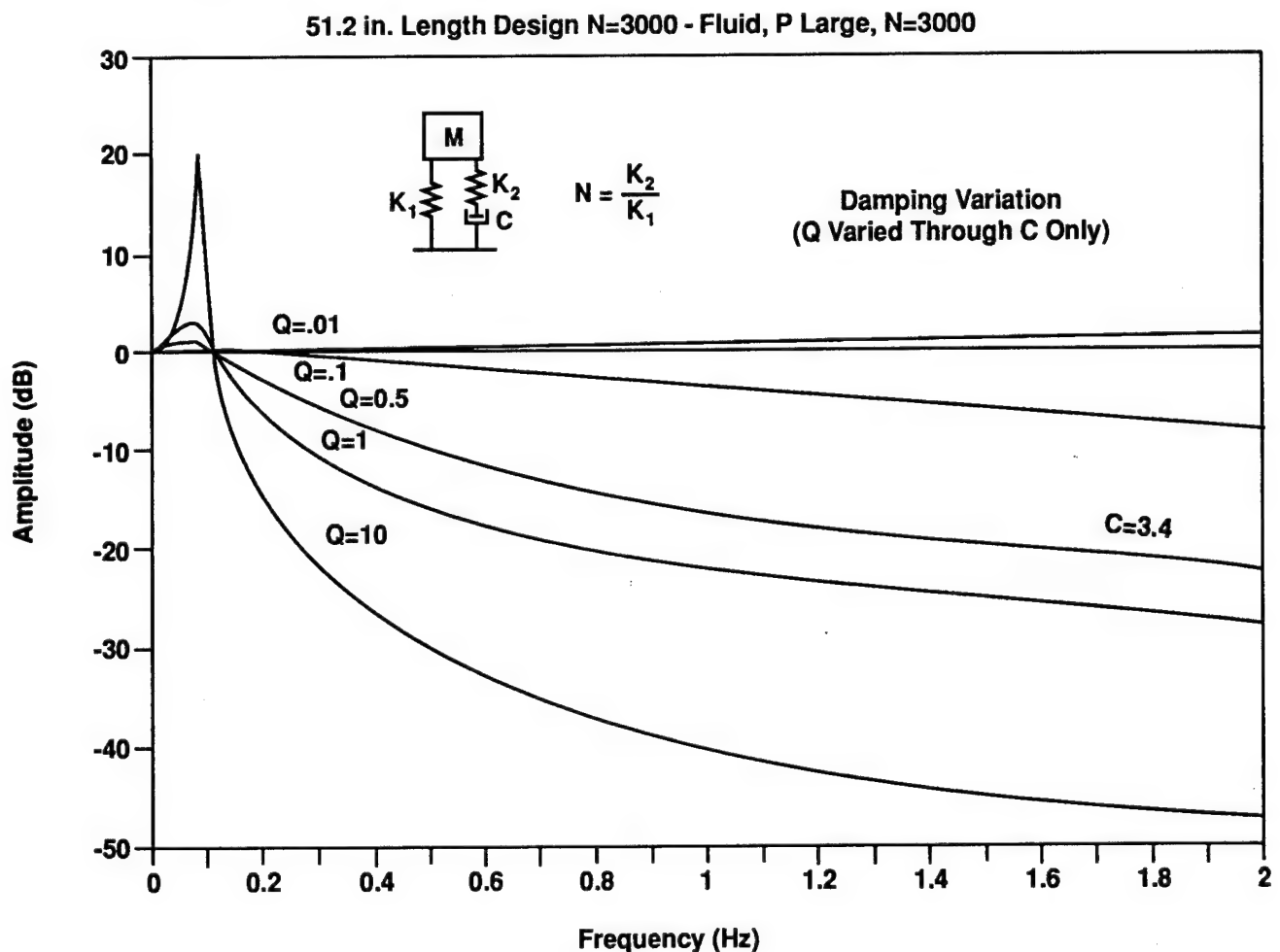
Figure 18. Isolator Transfer Function - Variable Damping

Figure 19 shows the effects on isolation of varying K_2. Note that for a very compressible damping fluid, such as air, high-frequency isolation is improved at the expense of resonant peaking.

Double Length Folded Design: Q = 0.26, C = 3.4
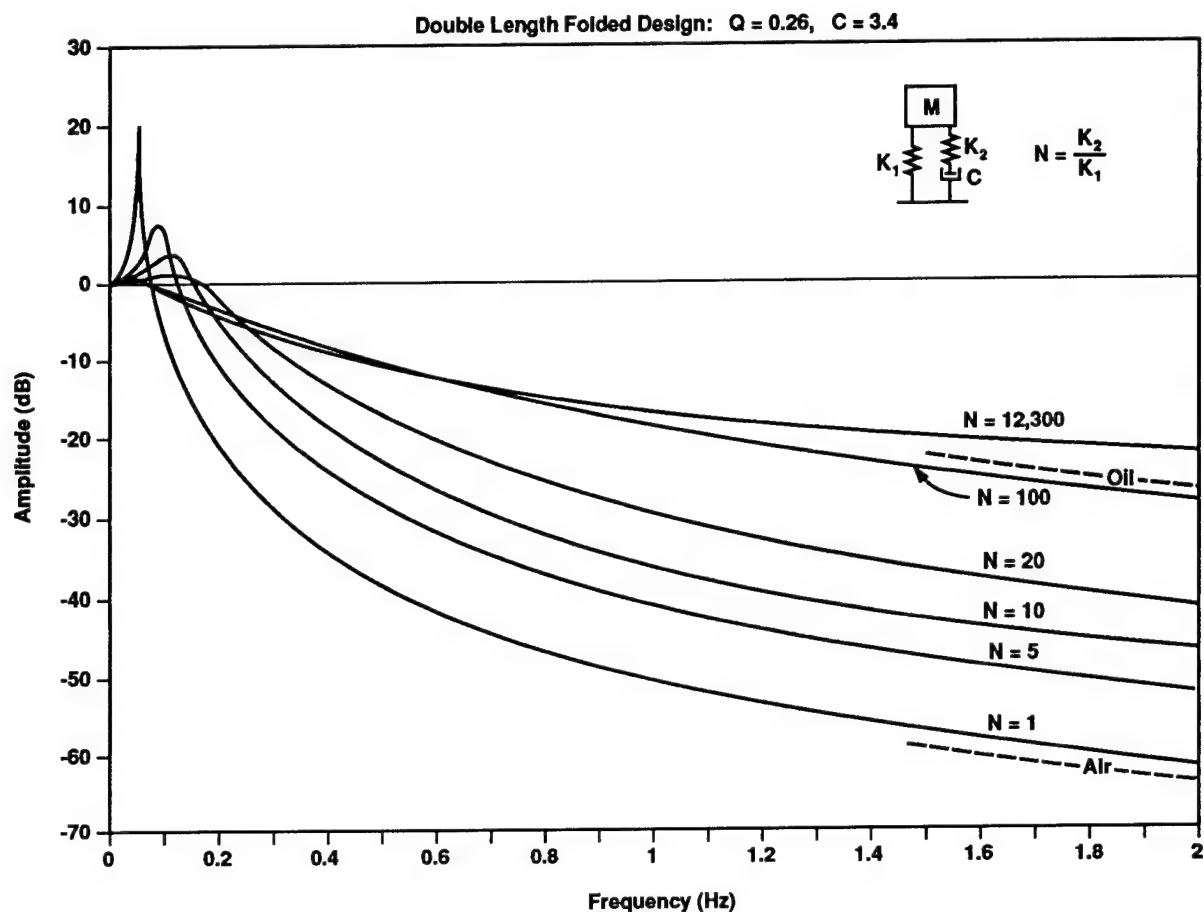
Figure 19. Isolator Transfer Function - Variable K_2

CONCLUSION

This study of an isolator for PPS has shown that the HST concept can be extended to a low stiffness, long stroke application with certain modifications. These include removing the coil spring and using lengthened bellows and a folded design to decrease K_1; air is used as the working fluid to decrease K2. In addition, K3 can be added to also vary the transfer function. In the final PPS isolator system layout and optimization, this versatility can be used to closely obtain the desired isolator strut properties. Some development steps will be necessary to arrive at a flight design. A means must be found to protect the long bellows against buckling (e.g. telescoping concentric tubes) without introducing excess stiction, and tests will be required to verify the damping equations for air.

For isolation of payloads from launch and landing loads, an adaptation of the HST viscous annular flow damping technology, using a high-pressure rigid chamber and piston, has shown to improve manufacturability and reduce weight.

ACKNOWLEDGEMENTS

The following people should be noted for their contributions:

Teresa Hollins; Honeywell Inc., Glendale, AZ
Tom Wilson, Dan Marks, and Dr. Bill Haile; Swales & Associates, Beltsville, MD
Frank Cepallina; Goddard Space Flight Center, Greenbelt, MD
Dr. Ed Wong; Jet Propulsion Laboratory, Pasadena, CA

REFERENCES

Papers:

- Hubble Space Telescope Reaction Wheel Assembly Vibration Isolation System, 1986 Las Vegas Vibration Workshop
- Viscous Damped Space Structure for Reduced Jitter, 1987 58th Shock and Vibration Symposium
- Very High Damping in Large Space Structures, 1987 ASME
- New Structure Design Criteria Offer Improved Pointing and Lower Weight, 1988 59th Shock and Vibration Symposium

Constrained Layer Damping For A
Space-Based Optical System

Naneen C. Bond
and
Robert M. Laurenson

McDonnell Douglas Missile System Company
Saint Louis, Missouri

Abstract

Pointing requirements for present space-based optical systems dictate state of the art precision structural designs. Future space-based optical systems will require even tighter pointing budgets. A vibration control technique, such as constrained layer damping, is an attractive approach for reducing vibration induced pointing error in these systems. This paper presents the results of a study to integrate constrained layer damping in the design of a graphite/epoxy truss structure. This precision structure is representative of those designed for space-based laser communication systems. Several constrained layer damping treatments were analytically and experimentally evaluated for a component of the structure. The component results were used to analytically predict system performance. Analysis of the system, with constrained layer damping integrated in the design, predicts an order of magnitude reduction in vibration induced pointing error. This reduction in pointing error results in decreased power requirements for the laser. Lower laser power leads to longer laser life and higher reliability. This results in a lower system weight and cost.

Introduction

A study was undertaken to evaluate the increased performance benefits of integrating constrained layer damping in the design of a representative structure of an optical system. The representative structure, shown in Figure 1, was designed for a space-based laser communication system. The design required very tight tolerances and a thermally stable structure to meet the on-orbit performance requirements. The result was a graphite/epoxy truss structure with very low intrinsic damping, on the order of 0.2 % of critical damping. Constrained layer damping was attractive for this structure to significantly increase the damping and reduce the jitter response. The objective of the damping design was to reduce the nominal line of sight error in the optical system by an order of magnitude.

Another consideration in the damping design was that the modal frequencies above 100 Hz were of interest. Below 100 Hz, an active control system was used for beam steering. For modes above 100 Hz, although magnitudes of displacement response were low, the vibration induced jitter contributed directly to the line of sight error of the system.

The components with high strain were identified from the nominal system structural response. Several constrained layer damping designs were identified which were consistent with the temperature and disturbance frequency bandwidth for the typical structure shown in Figure 1. These designs were analytically evaluated for a 'representative' graphite/epoxy truss component of the system.

The Modal Strain Energy technique[1,2] was used to calculate the structural system response with constrained layer damping. The constrained layer damping design led to predicted order of magnitude reduction in pointing error for a 1% system weight increase.

Testing was performed on a 'representative' component, a tubular graphite/epoxy truss member to validate the analytical system level predictions. Several constrained layer damping designs were experimentally evaluated to verify the range of damping values predicted in the analytical model.

Approach

Constrained layer damping has been shown to be more efficient than unconstrained layer damping for a given weight. To obtain constrained layer damping, a viscoelastic damping material is sandwiched between the structure and a constraining layer. A cross section of constrained layer damping is shown in Figure 2. The constraining layer forces the viscoelastic layer to deform in shear, which is the optimum manner to dissipate energy in a viscoelastic material. The performance of the constrained layer system depends on stiffness and geometry of the constraining layer and viscoelastic layer, the environmental conditions, and the location of the passive damping in the system.

The stiffness and geometry of the constraining layer and viscoelastic layer is characterized in the shear parameter[3] g_n:

$$g_n = G_2 \lambda_n / E_c h_c h_o$$

where: G_2 Shear modulus of viscoelastic material
         λ_n Semi-wavelength for n^{th} mode
         E_c Young's modulus for constraining layer
         h_c Constraining layer thickness
         h_o Damping layer thickness

For this application, a constraining layer stiffness equal to the stiffness of the structure produces the maximum shear strain in the viscoelastic layer.

Environmental conditions which determine the performance of the constrained layer damping system include operating temperature range, magnitude and frequency of dynamic excitation, and the response frequency range. Additionally, the viscoelastic material must be able to "survive" the non-operating temperature range. Outgassing of the viscoelastic material for space applications must be minimal since outgassing can result in material contaminating the optical system or degradation of the performance of the damping design. The environmental conditions, the response of the structure to these conditions, and the damping requirements are important elements in the damping design.

McDonnell Douglas

The performance of constrained layer damping system is influenced by its location in the structural system. Constrained layer damping is applied to areas of the structure which experience the highest strain levels during dynamic jitter response. The Modal Strain Energy approach[1,2] is a technique to analytically assess the effectiveness of passive damping in a structure.

The Modal Strain Energy method is based on the assumption that the damping in a a built up structure may be expressed as the sum of the damping dissipated by each of its structural components. The components with passive damping, having high damping with respect to the remainder of the components in the system, contribute to the equivalent modal damping. This equivalent modal damping is used when predicting the damped system structural response.

The shear parameter, the environmental conditions, and the location of constrained layer damping in the system are important elements that must be merged with system requirements such as performance and weight to develop an acceptable constrained layer damping design.

Analysis

Constrained layer damping was integrated in the design of a representative graphite/epoxy truss structure for a "typical" space-based optical system. The thermally stable graphite/epoxy structure, shown in Figure 1, was attached to the satellite at three points. An on-orbit disturbance was assumed to originate in the satellite due to events such as momentum wheel imbalances, slewing of solar arrays, thruster firing and drive the base of this representative structure. The goal of the constrained layer damping was to reduce the vibration induced jitter which contributes to the line of sight error in the optical system.

The following environmental conditions were assumed to develop the constrained layer damping design:

      Operating temperature range: 0°F to 86°F

      On-orbit dynamic disturbance: 100 to 150 Hz; 1 microradian at the base.

Using a finite element model of the truss structure, the on-orbit dynamic disturbance was input at the attach points. The line of sight error for the dynamic disturbance, as a function of frequency, is shown in Figure 3. The two modes, which contribute to the peak response shown in Figure 3, were selected for vibration control. The high strain areas for these modes were identified. About 25% of the strain area for the two modes resided in two pairs of truss members shown in Figure 4. These four truss member were selected as candidate for application of constrained layer damping.

A finite element model of a representative graphite/epoxy truss component was developed to evaluate different constrained layer damping designs. A 50 inch graphite/epoxy truss tube was modeled as shown in Figure 5. To simulate the dynamic behavior (modal frequencies) of the component in the structural system, the translation was restrained at one end and a mass moment of inertia was applied to the other end. The constrained layer damping design chosen consisted of four 0.25" width damping strips, covering the center two-thirds of the truss tube. The stiffness of the constraining layer and viscoelastic material were varied during the analysis (Figure 6). Strain energy increased with increasing stiffness of the constraining layer and viscoelastic material. DYAD 606, ISD 110 and SMRD 100F90 were candidate viscoelastic materials since they have been qualified and used in other space applications[4]. The SMRD 100F90 and a 0.20" graphite/epoxy constraining layer was one damping design that yielded a 2% equivalent modal damping for the two modes of interest. The resultant line of sight error, shown in Figure 7, met the objective of an order of magnitude reduction in dynamic jitter. This damping design resulted in a 1% increase in system weight.

Test Program

A test program was developed for a representative component of the system to validate range of damping values predicted analytically. The test configuration is shown in Figure 8. Six graphite/epoxy truss tubes, 54 inches in length, were fabricated as test articles. The lay up and fabrication procedure for the graphite/epoxy tubes were identical to the components in the structure of the optical system. Soft springs were attached to each end of the tubes to approximate free-free end conditions. Testing was conducted at Soundcoat, Inc.

Due to time constraints some compromises were made in selection of material for the constraining layer and the viscoelastic material. Steel was chosen for the constraining layer because of lower cost and ready availability. Three different steel constraining layer thicknesses were chosen, 1/16", 3/32" and 1/8" thick. SMRD 100F90 could not be obtained in the time available. The DYAD 606 and ISD 110 were readily available from the manufacturers. DYAD 601 was chosen for testing since its performance was better in the 0 to 86°F operating temperature range than the DYAD 606, which was analytically evaluated. The material compositions of DYAD 601 and 606 are very similar, therefore outgassing properties should be the same.

The graphite/epoxy tubes were excited by a force impulse from an instrumented hammer with a piezoelectric force transducer. Impact measurements were made at the center of the tube and 26 additional points spaced two inches apart. The accelerometer was mounted at an antinode for mode two of the beam, 12 inches from the end. The tubes were mass loaded at their ends and third points, in order to obtain the second mode frequency of 110 Hz. The intent was to approximate the second modal frequency and mode shape of the component in the complete structural system.

The test matrix is shown in Figure 9. The objectives of the test were threefold. First, to determine damping and modal characteristics for the first three mode, with mode two of particular interest. Second, determine damping measurement dependence on shear parameter, temperature and frequency. Third, to determine if the damping is the same for low and high excitation force levels.

Test Results - The six test configurations were tested with and without constrained layer damping treatments at room temperature. For two test specimens the temperature was varied from 30 to 80°F.

Second mode test results for the six test configurations, before applying the constrained layer damping treatment and with the constrained layer damping treatment, are presented in Figure 10. The results are compared to a value of 2% damping which is required to obtain an order of magnitude reduction in the vibration induced jitter. The intrinsic damping in the component without

constrained layer damping is partly due to the weights bolted to the end fittings and the weights attached at the third points.

A comparison of damping versus temperature for sample 2 and sample 4 is shown in Figure 11. The DYAD 601 loss factor for 100 Hz peaks between 50 and 60°F. The ISD 110 material loss factor peaks above 80°F. Material data for the DYAD 601 and ISD 110 confirm the loss factor peaks (at 100 Hz) are at 50°F and 110°F respectively. The DYAD 601 with a 3/32" steel constraining layer meets the 2% damping objective over the test temperature range (30 to 80°F). The material data for the DYAD indicates that below 30°F the damping value would fall below 2%. Another viscoelastic material is needed in the damping design to achieve the 2% damping over the entire operating temperature range.

The stiffness of the constraining layer versus damping relationship, shown in Figure 12, exhibits the same trend as the analytical data. Measured damping increased with stiffer constraining layer. The objective of 2% damping was met by all damping designs (at room temperature) except the DYAD 601 with 1/16" thick steel constraining layer.

Linearity of response with respect to input level was verified for the dynamic range of the test system. The measured damping response for low excitation force (response acceleration of .06 g) was the same as measured response at the high excitation force (response acceleration of 3 g).

Conclusions

It has been shown analytically that integrating a constrained layer damping treatment in the design of a space-based optical system can yield an order of magnitude reduction in the vibration induced line of sight error for the system. Testing of a graphite/epoxy truss component confirmed the range of damping used in the analytical model. Reducing line of sight error for space-based optical systems can have significant system benefits in terms of reduced laser power requirements, increased communication reliability, and longer laser life. Reduced pointing error can also result in performance improvements such as increased communication data rates, lighter weight designs, and better target discrimination.

References

1. Johnson, C.D., Kienholz, D.A., and Rogers, L.C., "Finite Element Prediction of Damping in Beams with Constrained Viscoelastic Layers," Shock and Vibration Bulletin, No. 51, May 1981, pp. 78-81.

2. Johnson, C.D., Kienholz, D.A., "Finite Element Prediction of Damping with Constrained Viscoelastic Layers," AIAA Journal, Vol. 20, No. 9, pp. 1284-1290, September 1982.

3. Nashif, A.D., Jones, D.I.G., Henderson, J.R., Vibration Damping, John Wiley and Sons, Inc., 1985.

4. Peebles, James H., Trudell, Richard W., Blevens, Creed E., Prucz, Jacky C., "Passively Damped Joints for Advanced Space Structures,"Final Report for Air Force Office of Scientific Research, Contract F49620-83-C-0117, 28 March 1986.

5. Koch, John E., "Report on Damping Measurements of Six Graphite Epoxy Tubes With and Without Viscoelastic Damping Systems," Soundcoat Report for Project No. S-1574, March 1988.
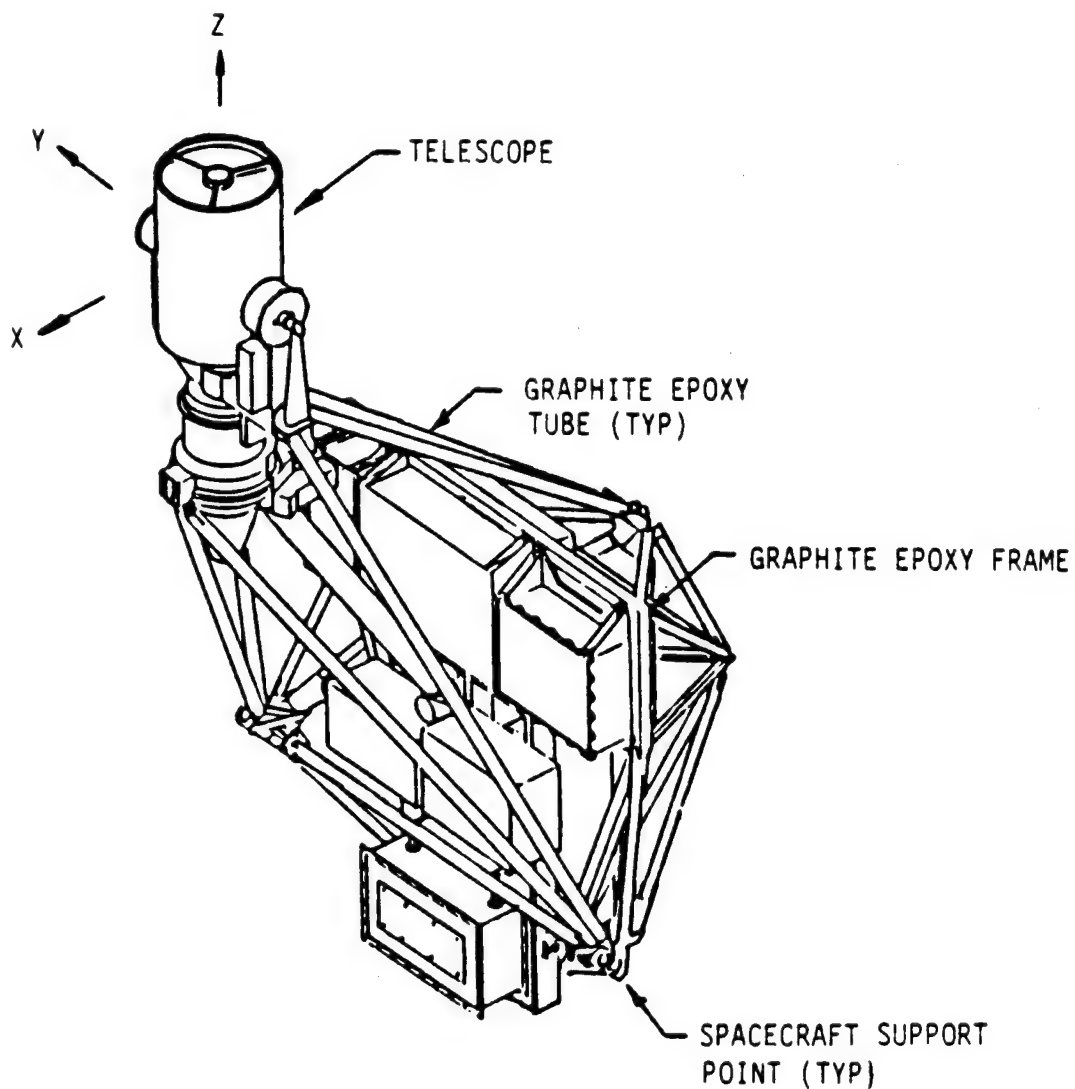
TYPICAL PRECISION STRUCTURE FOR SPACE-BASED OPTICAL SYSTEMS

Figure 1

CONSTRAINING
LAYER

VISCOELASTIC MATERIAL
(VEM)
DAMPING LAYER

EXTENSIONAL STIFFNESS
RESISTS ELONGATION AND
"CONSTRAINS" THE VEM

STRUCTURE

BENDING CAUSES
SURFACE ELONGATION
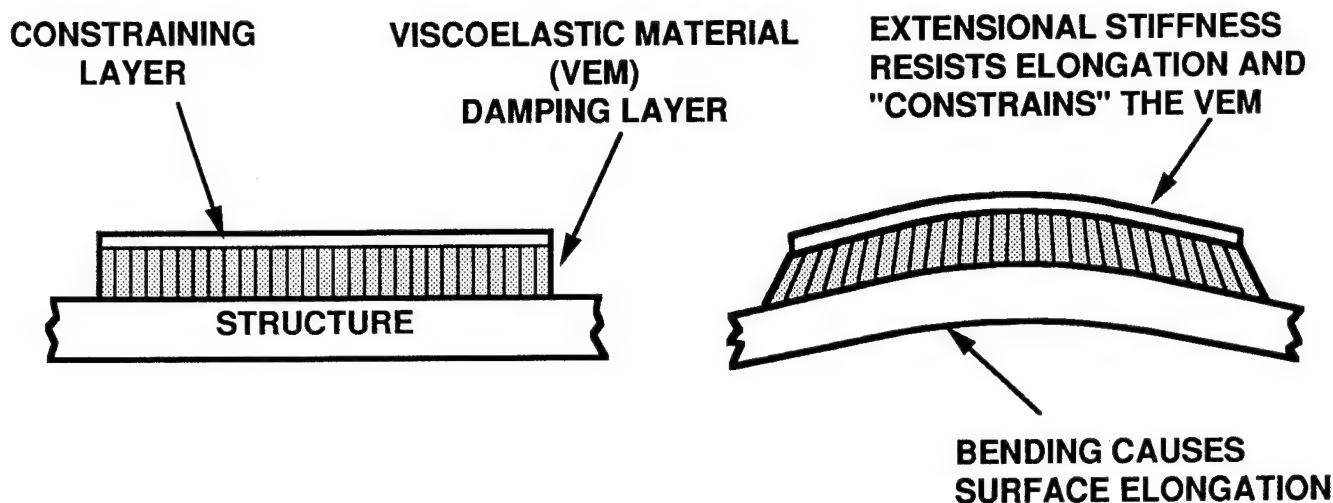
- **DIFFERENCE IN ELONGATION CAUSES VEM TO DEFORM IN SHEAR**

- **VIBRATION CYCLE DISSIPATES ENERGY UNDER STRESS-STRAIN HYSTERESIS LOOP OF VEM**

CONSTRAINED LAYER DAMPING

Figure 2

INTRINSIC DAMPING
(.2% MODAL
DAMPING)

107   115

RESPONSE - OUT/IN

FREQUENCY - Hz
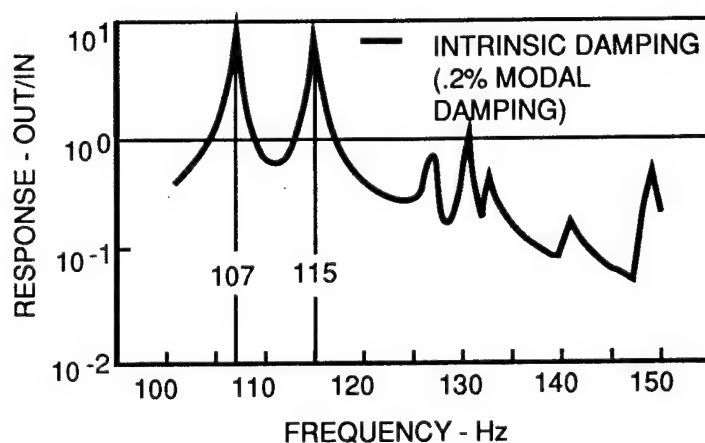
JITTER RESPONSE WITH INTRINSIC DAMPING (0.2 % C_C)

Figure 3

McDonnell Douglas
DBB-10

SPACECRAFT SUPPORT
POINT (TYP)

AREA OF
HIGH STRAIN

TELESCOPE

107 HZ MODE

23.6% STRAIN ENERGY
46.3 TUBE LENGTH
SECOND BEAM BENDING MODE

115 HZ MODE

23.2% STRAIN ENERGY
50.3 TUBE LENGTH
SECOND BEAM BENDING MODE
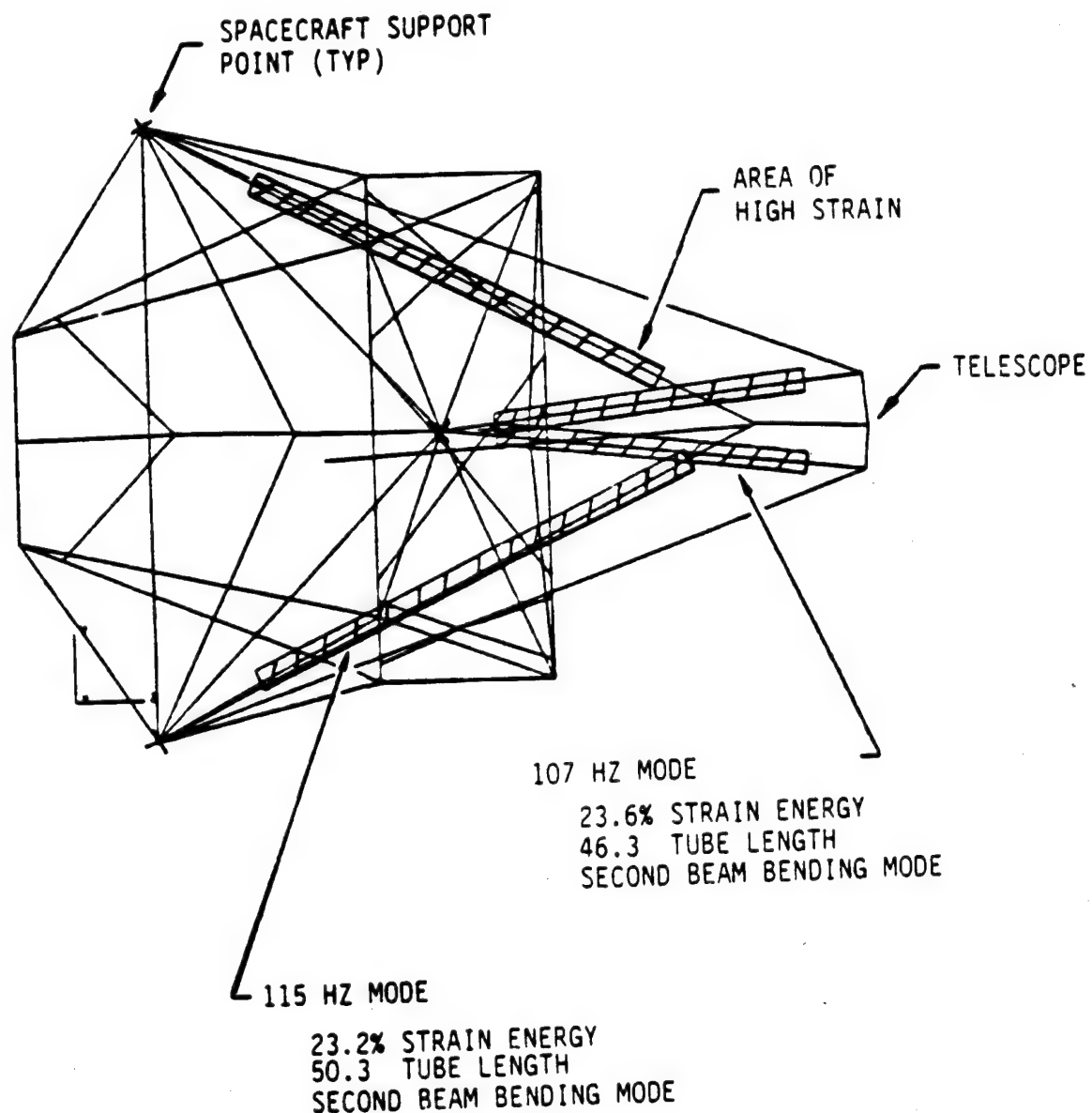
AREAS OF HIGH STRAIN ENERGY FOR 107 AND 115 HZ MODE

Figure 4

McDonnell Douglas

CONSTRAINED LAYER DAMPING

TRUSS TUBE
(PLATE ELEMENTS)

MODEL DATA
2104 GRID POINTS
11,684 DEGREES OF FREEDOM

CONSTRAINING LAYER
(PLATE ELEMENTS)

VISCOELASTIC MATERIAL
(SOLID ELEMENTS)

SECTION A-A
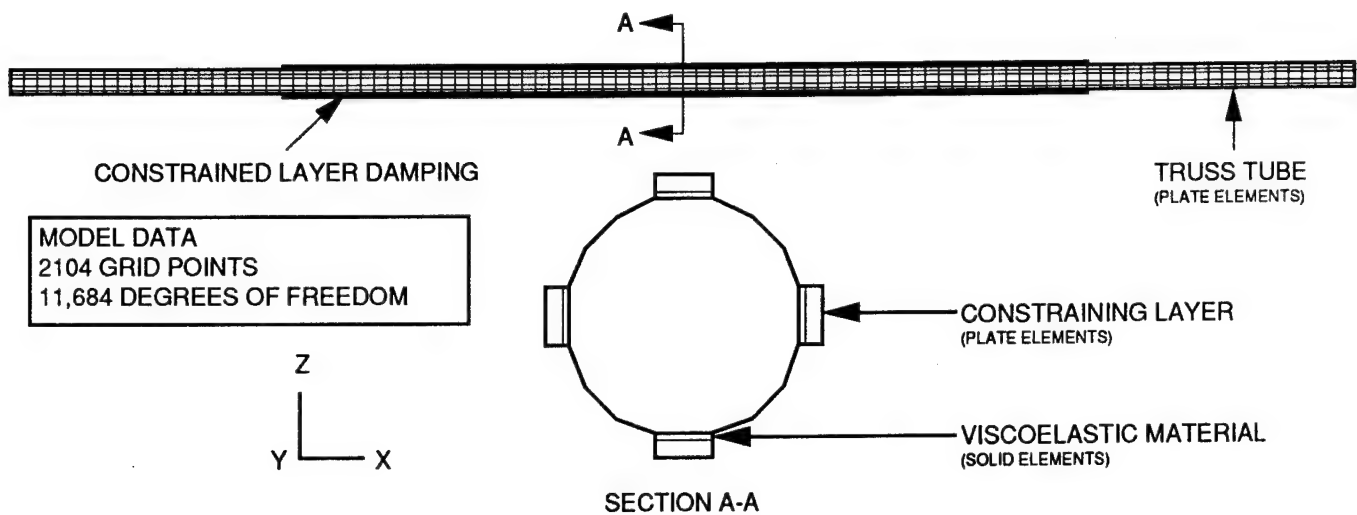
FINITE ELEMENT MODEL OF GR/EP TUBE WITH CONSTRAINED LAYER DAMPING

Figure 5

THICKNESS OF VISCOELASTIC LAYER - IN

VARYING VEM
NOTE: 0.2 IN. CONSTRAINING LAYER

VARYING CONSTRAINING LAYER
NOTE: 0.07 IN. VEM

THICKNESS OF CONSTRAINING LAYER* - IN

* NORMALIZED FOR STEEL - $t_s = t_m \cdot E_m / E_s$
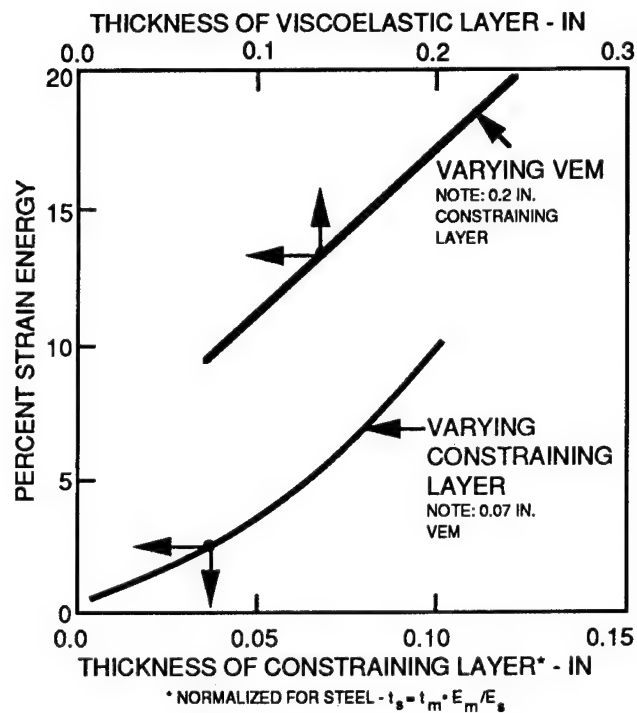
PARAMETRIC STUDY OF CONSTRAINED LAYER DAMPING DESIGNS

Figure 6

McDonnell Douglas
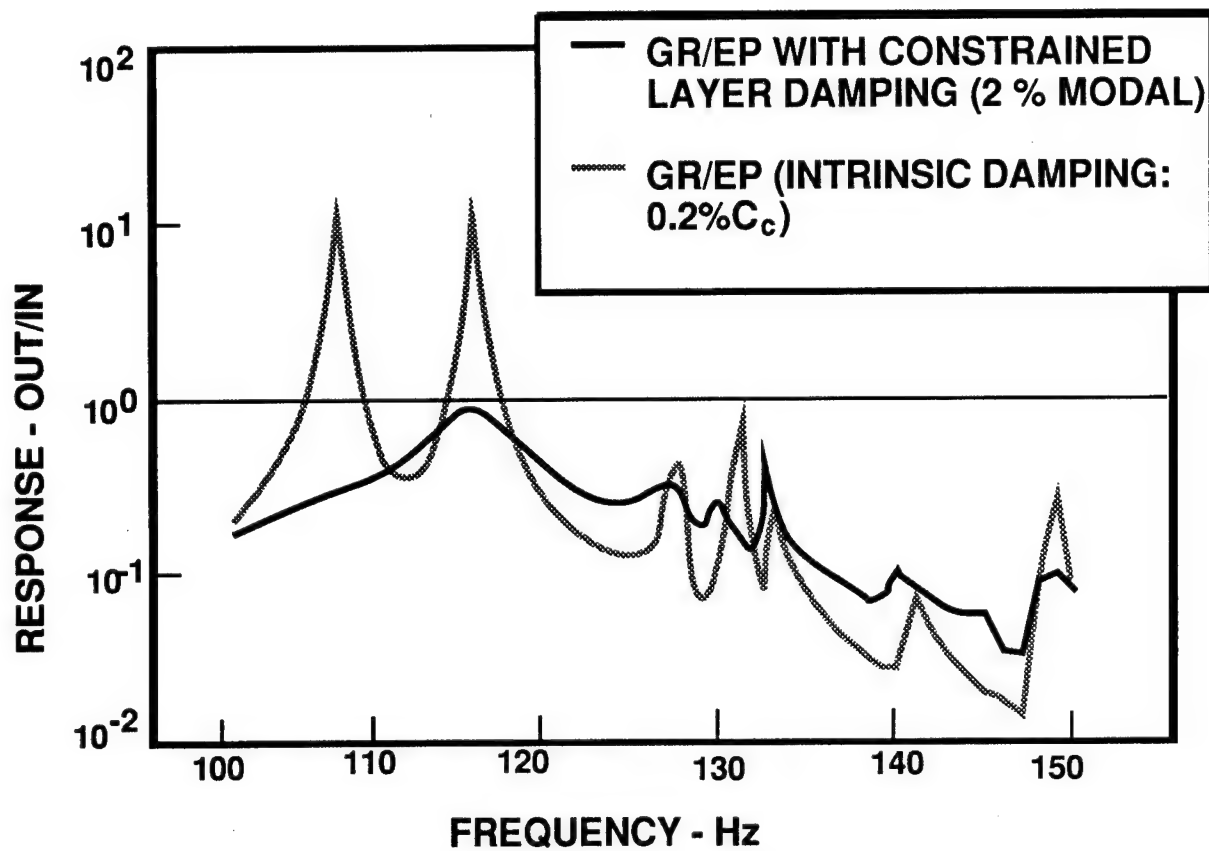
JITTER ATTENUATION WITH CONSTRAINED LAYER DAMPING

Figure 7

GOAL: MATCH FREQUENCY OF TRUSS TUBE IN SYSTEM

TEST CONFIGURATION
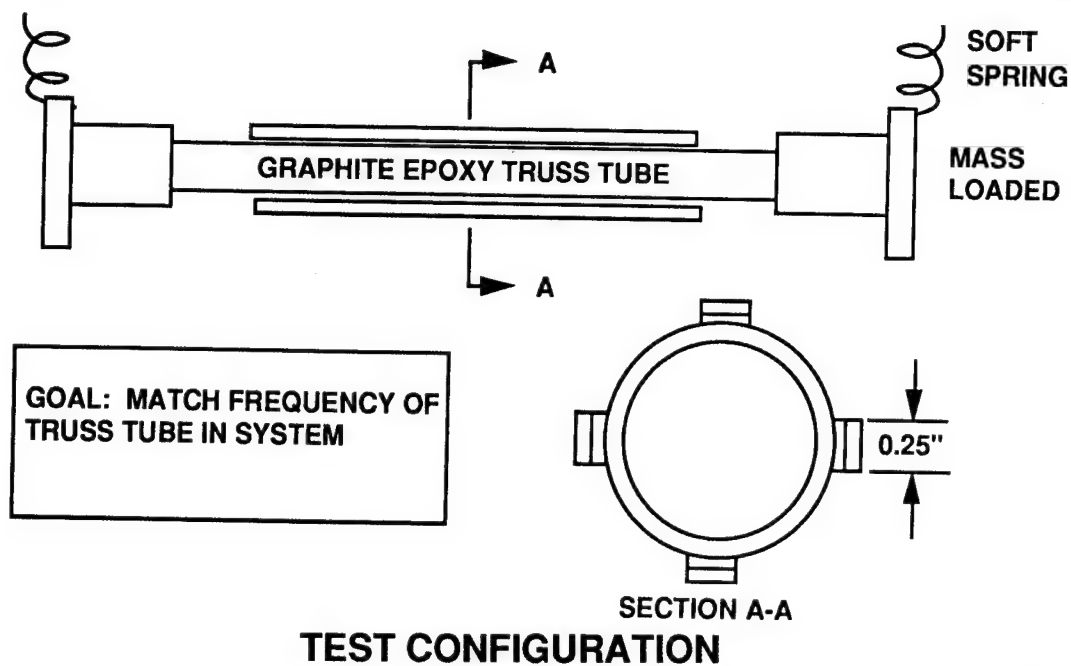
Figure 8

SAMPLE NUMBER	VISCOELASTIC DAMPING MATERIAL DESCRIPTION	CONSTRAINING LAYER DESCRIPTION
1	DYAD 601A - 80 MILS	STEEL - 1/16" THICKNESS
2	DYAD 601A - 80 MILS	STEEL - 3/32" THICKNESS
3	DYAD 601A - 80 MILS	STEEL - 1/8" THICKNESS
4	ISD 110 - 90 MILS	STEEL - 1/16" THICKNESS
5	ISD 110 - 90 MILS	STEEL - 3/32" THICKNESS
6	ISD 110 - 90 MILS	STEEL - 1/8" THICKNESS

PASSIVE DAMPING DESIGNS FOR COMPONENT TESTING

Figure 9

SAMPLE NUMBER	SAMPLE DESCRIPTION	INTRINSIC DAMPING %C_c	DAMPING W/ VEM %C_c
1	DYAD 601, 1/16" STEEL CONSTRAINING LAYER	0.7	1.4
2	DYAD 601, 3/32" STEEL CONSTRAINING LAYER	0.5	2.5
3	DYAD 601, 1/8" STEEL CONSTRAINING LAYER	0.5	2.5
4	ISD 110, 1/16" STEEL CONSTRAINING LAYER	0.5	3.2
5	ISD 110, 3/32" STEEL CONSTRAINING LAYER	0.5	3.9
6	ISD 110, 1/8" STEEL CONSTRAINING LAYER	0.6	4.3

MEASURED DAMPING VALUES WITH AND WITHOUT CONSTRAINED LAYER DAMPING

Figure 10
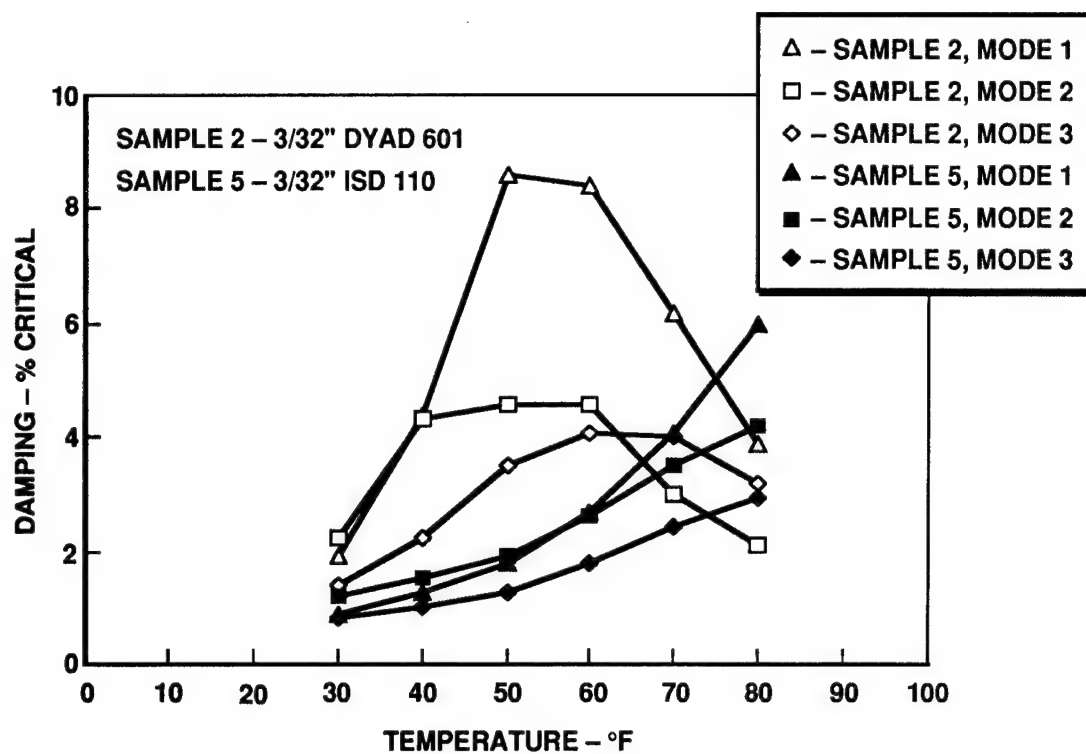
COMPARISON OF MEASURE DAMPING VALUES VERSUS TEMPERATURE

Figure 11
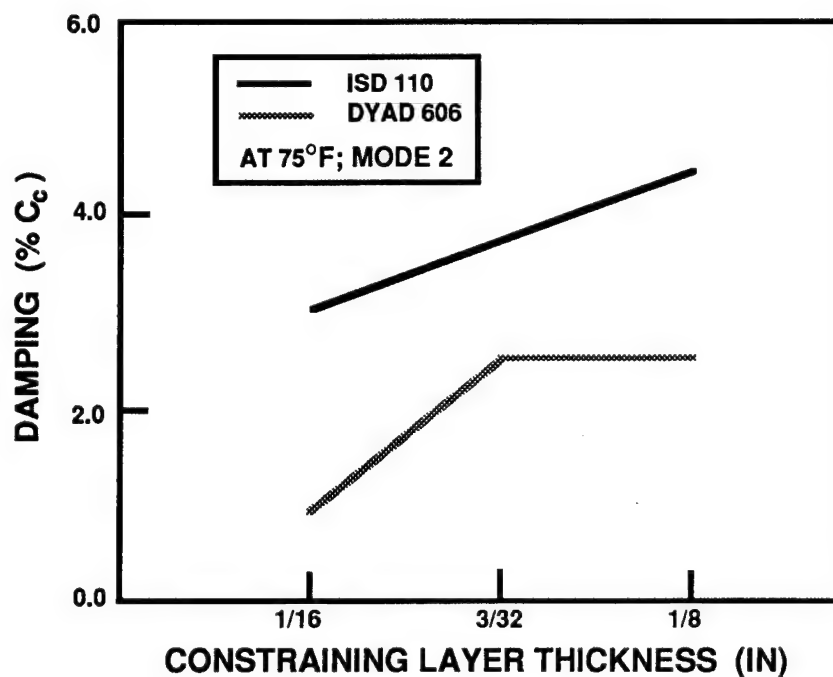
MEASURED DAMPING VALUES VERSUS STIFFNESS OF CONSTRAINING LAYER

Figure 12

HYDROSTATIC DAMPER FOR THE SPACE SHUTTLE MAIN ENGINE (SSME) HIGH PRESSURE OXIDIZER TURBOPUMP (HPOTP)

by David G. Goggin, Joseph K. Scharrer, and Robert F. Beatty

Rocketdyne Division
Rockwell International
6633 Canoga Avenue
Canoga Park, California 91303

ABSTRACT

Alternative methods were evaluated for increasing rotor damping on the SSME HPOTP to reduce bearing dynamic loads and extend their useful life. A unique application of a hydrostatic damper was developed by incorporating a hydrostatic element between stationary turbine bearing support components. Damper design is shown to be dependent on accurate rotordynamic response analysis. Optimization to achieve maximum damper performance under high loading conditions and limited supply flow is discussed. Damping levels approaching critical damping were achieved without major modifications. Bearing dynamic loads are reduced up to 70% and rotor mode logarithmic decrement was increased from 0.085 to as much as 1.0. Possible opportunities for further improvements in damper performance are also discussed.

INTRODUCTION

Hydrostatic bearings have been used as load support devices in many applications since they were invented in 1862 by L. Girard. However, only recently that they have been considered for use as an active damping device. Choy and Halloran[1] used a hydrostatic damper in conjunction with journal and tilting-pad bearings. Their theoretical and experimental results showed that the hydrostatic damper could ensure stable and low-vibration operation for a centrifugal compressor.

Goodwin and Roach[2] presented an experimental and theoretical investigation into the development of a hydrostatic bearing in series with a ball bearing where the dampers' dynamic characteristics could be tuned during rotor operation. Adams and Zahloul[3] presented an analytical study which showed the feasibility and potential benefits of using hydrostatic dampers as active control devices.

Ball bearings used in the SSME HPOTP have suffered wear attributed in part to large dynamic loads[4,5]. It was determined that a fluid film damper should be developed to reduce these loads. The damper would be required to use LOX with its low viscosity as the working fluid; consequently Reynolds' numbers would be high. The state-of-the-art in squeeze film damper technology was reviewed and found to be insufficient to support development of a high Reynolds' number damper. In contrast, hydrostatic bearing technology is well developed and a LOX hydrostatic bearing has been successfully tested by Pratt and Whitney[6].

A project was therefore initiated to develop a so called "hydrostatic damper" for the SSME HPOTP. Preliminary analysis indicated rotor damping could be significantly improved by using the radial clearance between the turbine bearing carrier and its backup support as a hydrostatic bearing. Although the bearing would need to support large static loads imparted by the rotor, risks would be minimized by placing the bearing between nonrotating components.

BACKGROUND

A cross section of the HPOTP is shown in Figure 1. Turbopump operating speeds extend from 19,700 RPM at Minimum Power Level (MPL) to 29,300 RPM at Full Power Level (FPL). Maximum design speed is 30,000 RPM.

The rotor is supported at both ends by duplex angular contact ball bearings. A 0.0005 in. radial clearance, or deadband, is retained between the ball bearing outer race OD and ID of their respective carriers to allow axial movement with the rotor. Additionally, the turbine bearing carrier, referred to as the "cartridge," is supported by a soft axial spring and has a 0.0010 in. radial clearance between it and its backup support for additional axial freedom (Figure 2).

Rotordynamic analysis is performed using rotor and housing finite element models verified through modal testing and integrated using using modal synthesis techniques[4,5,7,8]. Linear critical speeds and stability parameters are summarized in Table 1. Of importance is the 14.7% margin between the maximum design speed and second critical which is less than the 20% margin normally desired. Also of note is the moderate damping available to limit response of the first and second rotor modes.

Rotor unbalance response and the bearing loads experienced during operation are simulated using nonlinear analysis techniques[4,5]. Experience has shown that incorporating nonlinear characteristics such as floating ring seal stick-slip friction and ball bearing nonlinear stiffness and deadband in the analysis is essential for accurately reproducing HPOTP rotordynamic response.

Response predictions from the nonlinear model are correlated to bearing loads measured during engine tests by strain gages located on the pump end bearing carrier. A "test data match" is accomplished using a priori knowledge of sideloads, bearing deadbands, unbalance distributions, and rotor-housing boundary conditions. Bearing package design analysis is then based on the upper envelope of predicted bearing loads.

DESIGN REQUIREMENTS

Radial clearances in the turbine bearing package previously described are
necessary to allow axial movement with the rotor. During normal operation,
though, static rotor loads exceed dynamic loads such that the rotor operates
fully engaged against the bearing carrier and backup support. Rotor orbits do
not enter the deadband clearance, avoiding the detrimental effects of
"deadband interaction" on rotor response and stability[4].

Figure 3 shows a schematic of the bearing package nonlinear model and proposed
location for the hydrostatic damper. The damper is formed by developing a
hydrostatic film between the bearing carrier and backup support. The
corresponding analytical bearing model included ball bearing deadband,
nonlinear stiffness versus deflection, and cartridge-backup support radial
clearance. Ability to simulate contact between the bearing package and
hydrostatic damper components due to relative motion was retained.

The hydrostatic film is located in series with the bearings and backup support
that previously operated fully engaged, thereby reducing the effective rotor-
casing support stiffness. A design goal was to ensure the subsequent
reduction in margin between maximum operating speed and second critical is
offset by a proportionately larger increase in effective rotor damping. Also,
although the hydrostatic film is located between nonrotating components,
sufficient load capacity was required to avoid contact between damper
components.

Accurate nonlinear rotordynamic response analysis proved essential to the
damper design effort. By definition the effective increase in rotor damping
is dependent on the magnitude of the relative deflections across the damper
hydrostatic film. Maximum damping is achieved with relative deflections just
less than the available clearance. Accurate response analysis is necessary to
ensure the damper is optimized for maximum benefit without allowing contact
between component surfaces.

The nonlinear models described were used to determine loads and deflections
across each of the bearing/damper package components. Key results are shown

in Figure 4. The potential reduction in turbine bearing load is shown for a range of damper conditions, along with the minimum acceptable stiffness to avoid contact between damper surfaces.

Two phenomena are involved in producing the load reductions shown, one of which can only be predicted by a response analysis incorporating bearing/damper package nonlinear characteristics. For values of hydrostatic film stiffness near the minimum acceptable limit, maximum improvement in rotor damping is achieved minimizing the resulting dynamic bearing loads. At large values of stiffness, though, the hydrostatic film acts as a rigid support between the bearing carrier and backup structure, effectively eliminating the 0.0010 in. radial clearance between them. This clearance has a significant influence on the effective second critical speed and therefore on bearing loads at FPL as shown in Figure 5. Reductions in bearing load shown in Figure 4 for values of film stiffness greater than 6.0 E+06 lb/in are almost exclusively due to this reduction in effective bearing deadband.

Reductions in load due to increased rotor damping are preferable to load reductions via decreased bearing package deadband. The margin between the second critical speed and maximum operating speed, and correspondingly the dynamic bearing loads experienced at FPL, can be adversely affected by pump build tolerances and/or wear during operation. These factors might fully offset predicted reductions in response with a very stiff damper. In contrast, increased rotor damping would limit dynamic response regardless of these factors, producing uniform behavior for a wide range of pump conditions.

This is further illustrated by results from the linear eigenvalue analysis. Figures 6 shows the impact of damper characteristics on second rotor mode logarithmic decrement at FPL. As shown, the largest increase in effective rotor damping is achieved when damper stiffness is just sufficient to avoid bore contact.

Another key aspect of the damper was potential sensitivity to manufacturing tolerances. Preliminary damper designs optimized for nominal dimensions were found to exhibit unacceptable variations in stiffness for the expected range of manufacturing tolerances. Damper coefficients for a typical configuration

varied from 3.1 E+06 to 7.4 E+06 lb/in for a target radial clearance tolerance of 0.0010 - 0.0025 in. As shown in Figure 7, smaller radial clearances also result in larger values of damping as well as stiffness such that the nominal reduction in bearing load appears insensitive to damper operating clearance. As discussed, the predicted load reductions at high values of damper film stiffness would be less consistent than if the damper stiffness remained near the point of optimum damping regardless of manufacturing tolerances. A final design goal was therefore to optimize the damper design to produce nearly uniform film stiffness over the range of expected operating clearances.

DAMPER ANALYSIS

The hydrostatic bearing code used is based on the theory of Artiles, et. al.[9]. This code utilizes Reynolds' equations and accounts for turbulent flow, fluid inertia at the recess edge, and has been extended to account for a tapered bore. This code has been anchored to the available experimental results for hydrostatic bearings in oil[10,11,12,13], water[14,15], liquid hydrogen and liquid oxygen[6], liquid hydrogen[16], and liquid hydrogen and freon[17] and has been found to give reasonable results for leakage, torque, and direct stiffness. There are no reliable results in the literature for cross-coupled stiffness and direct damping.

Rotordynamic analysis determined the limiting design characteristic was damper stiffness. The parasitic nature of the damper supply flow also required that leakage be kept to a minimum. Consequently damper design revolved around optimizing the stiffness/leakage ratio. Parameters to be defined were the number of recesses, area ratio, dimensions of the recess, orifice diameter, recess depth, and radial clearance.

The number of recesses was constrained to a multiple of 3 by the configuration of the 18 bolt hole bearing package support flange which also serves as the damper supply annulus. Nine recesses were determined to provide the optimum balance between stiffness and manufacurability. Stress considerations would not allow the recesses to be located on the damper stator. A novel

configuration was therefore developed with the recesses located on the damper journal as shown in Figure 8.

Preliminary calculations showed a radial clearance of 0.0025 in. or less would be necessary to meet damper stiffness requirements. Figure 9 illustrates the stiffness/leakage ratio as a function of area ratio for the maximum radial clearance of 0.0025 inches. (Area ratio = Total Recess Area/Total Bearing Area.) The figure shows the 0.20 area ratio is optimum for this application. Figure 10 shows the stiffness/leakage ratio as a function of the axial length to circumferential width ratio for the 0.20 area ratio at the maximum radial clearance. The figure shows that a recess with a circumferential width twice the axial length is optimum for this application.

The orifice diameter was optimized according to the well known results in Figure 11. As shown, a pressure ratio of 0.5 yields the optimum combination of stiffness and damping. Testing proved necessary to accurately assess the orifice loss coefficient. Results of this testing are beyond the scope of this paper and will be published at a later date.

Preliminary analysis had shown that optimizing the orifice diameter for nominal damper clearances resulted in a wide variation in stiffnesses for the expected range of manufacturing tolerances. Analysis was performed to determine the effect of optimizing orifice diameter on the minimum, nominal, or maximum radial clearance case. An integrated flowpath/damper analysis was required since variations in damper radial clearance significantly alter the supply flowpath resistance. Figure 12 illustrates dimensionless damper stiffness as a function of radial clearance for the following four cases:

1) The orifices optimized for each clearance
2) The orifices optimized for the nominal clearance
3) The orifices optimized for the minimum clearance
4) The orifices optimized for the maximum clearance

As shown, the minimum variation in stiffness occurs when the orifice is optimized for the maximum radial clearance expected.

Depth of the hydrostatic damper recess was determined using the guidelines from Pratt and Whitney[6] for LOX. It is stated that the pressure variation within the recess should not exceed 10% of the pressure drop and that the ratio of the recess volume to the total volume of the bearing film be less than 2.0 for LOX.

Based on the analyses just described, the final damper configuration was defined as follows:

Number of recesses = 9
Recess dimensions = 0.457 X 0.914 in.
Recess depth: 0.009 < depth < 0.011 in.
Radial clearance: 0.001-0.0025 in.
Orifice diameter = 0.095-0.105 in.

RESULTS

The resulting improvement in rotordynamic characteristics are shown in Table 2 for the range of damper operating conditions. By designing the damper to provide uniform stiffness over the range of operating clearances, consistent performance is achieved. The only variation is in the degree of rotor damping, or in turn, the degree of dynamic bearing load reduction achieved.

The stiffness required to avoid contact results in only a slight loss in margin between maximum operating speed and the second critical. This is more than offset by improved second mode damping. A significant reduction in first critical speed is noted since the hydrostatic film is relatively soft at the lower speeds. The film stiffness increases approximately with the square of the operating speed, so the frequency of the first mode at FPL is not significantly lowered. (It is typically required that the first mode frequency remain greater than 50% of the operating speed). This, along with the increase in first mode damping, indicate there should be no problem with first mode stability. Linear stability analysis indicates both first and second mode stability threshold speeds exceed 50,000 RPM.

As expected from these results, there is a significant reduction in bearing loads at speeds near FPL. Figure 13 shows nominal turbine bearing dynamic loads for speeds ranging from 5,000 to 35,000 RPM. Figures 14 and 15 show reductions in pump and turbine end dynamic bearing loads at FPL. Dynamic loads are reduced from 50% - 65% depending on damper operating clearances.

Damper performance is currently limited to stiffness values greater than those shown in Figure 4 to prevent contact between damper components. If rotor loads are reduced as planned through other pump modifications, latitude would exist to improve damper performance. Engine tests with the damper will therefore be monitored closely to take advantage of potential performance improvements. Reductions in damper stiffness could be easily accomplished through minor adjustments in radial clearance or supply pressure.

Final damper design details are currently near completion. Fabrication and installation of a test damper in a development turbopump is expected during 1989. The turbopump, instrumented with accelerometers and strain gages on the pump end bearing carrier, will then be hot fire tested in simulated flight mission test profiles. Results will be compared against data from previous tests on this redesign pump as well as the data base from other configurations tested.

CONCLUSION

A novel hydrostatic damper configuration was developed for reducing ball bearing dynamic loads on the SSME HPOTP. The necessity for accurate rotordynamic response predictions in determining damper design requirements was illustrated. Damper design optimization was presented, including the benefits of optimizing the orifice diameter for the maximum expected radial clearance to produce uniform damper performance. Damping levels approaching critical damping were achieved without major modifications. Bearing dynamic loads are reduced up to 70% and rotor mode logarithmic decrement was increased from 0.085 to as much as 1.0. Possible opportunities for further improvements in damper performance are also discussed.

REFERENCES

1. Choy, K.C., and Halloran, J.D., "Application of Hydrostatic Squeeze-Film Dampers," ASLE Transactions, Vol. 25, No. 2, pp 245-251, 1982.

2. Goodwin, M. and Roach, M., "Vibration Control in Rotating Machinery Using Variable Dynamic Stiffness Squeeze Films," USGAD-A174433, March 1986.

3. Adams, M.L., and Zahloul, H., "Attenuation of Rotor Vibration Using Controlled-Pressure Hydrostatic Squeeze-Film Dampers," ASME 11th Biennial Conf. on Vibration and Noise, Boston, Mass., 27-30 Sept. 1987.

4. Childs, D.W., and Moyer, D.S., "Vibration Characteristics of the HPOTP (High-Pressure Oxygen Turbopump) of the SSME (Space Shuttle Main Engine)," ASME Paper #84-GT-31, 29th Intl. Gas Turbine Conf., Amsterdam, The Netherlands, 4-7 June 1984.

5. Beatty, R.F., and Hine, M.J., "Load Cell Verification of the Uprated High Pressure Oxygen Turbopump for the Space Shuttle Main Engine," 9th Aerospace Testing Seminar, El Segundo, CA, October 1985.

6. Pratt and Whitney, "Investigation of Hydrostatic Bearings for Use in High Pressure Cryogenic Turbopumps," AFRPL-TR-67-130, May 1967.

7. Glasgow, D.A., and Nelson, H.D., "Stability Analysis of Rotor-Bearing Systems Using Component Mode Synthesis," ASME Journal of Mechanical Design, Vol. 102, No. 2, pp 352-359, April 1980.

8. Nelson, H.D., et. al., "Nonlinear Analysis of Rotor-Bearing Systems Using Component Mode Synthesis," ASME Journal of Eng. for Power, Vol. 105, pp. 606-614, July 1983.

9. Artiles, A., Walowit, J. and Shapiro, W., "Analysis of Hybrid, Fluid Film Journal Bearings with Turbulence and Inertia Effects," Advances in Computer Aided Bearing Design, ASME, 1982, pp25-52.

10. Raimondi and Boyd, "An Analysis of Orifice and Capillary-Compensated Hydrostatic Journal Bearings," Lubr. Eng., 13, 1, Jan. 1957, pp28-37.

11. Ghosh, B., "Load and flow Characteristics of a Capillary Compensated Hydrostatic Journal Bearing," Wear, 23, pp. 377-386, 1973.

12. Ho, Y. and Chen, N., "dynamic Characteristics of a Hydrostatic Journal Bearing," Wear, 63, pp. 13-24, 1980.

13. Chaomleffel, J., "Influences des Forces D'inertie en Lubrification Hybride," Thése de Docteur Ingenieur, Université Claude Bernard, Lyon, 1983.

14. Aerojet, "Hydrostatic Bearing Feasibility Program," AFRPL-TR-65-120, December 1965.

15. Heller, S., "Static and Dynamic Performance of EXternally Pressureized Fluid Film Journal Bearings in the Turbulent Regime," ASME Journ. of Lubr. Tech., July 1974, pp. 381-389.

16. Spica, P., Hannum, N., and Meyer, S., "Evaluation of Hybrid Hydrostatic Bearing for Cryogenic Turbopump Application," NASA TM 87255, April 1986.

17. Butner, M. and Murphy, B., "SSME Long Life Bearings," NASA CR-179455, 1986.
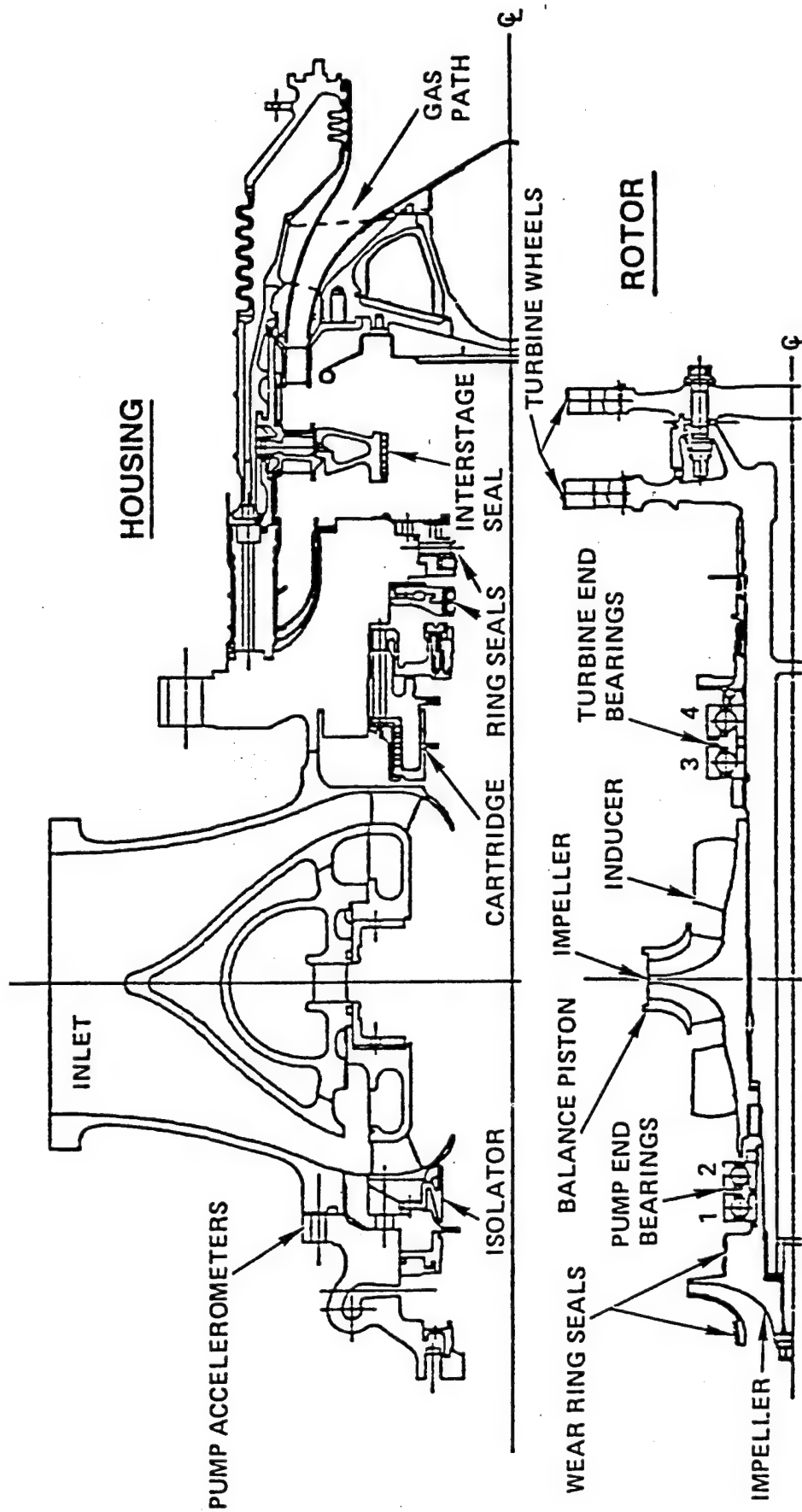
Figure 1. Half Cross Section of High Pressure Oxygen Turbopump

SSME HPOTP TURBINE BEARING PACKAGE

NORMAL OPERATION:
ROTOR FIXED LOADS > DYNAMIC LOADS
BEARING PACKAGE OPERATES FULLY
ENGAGED TO ONE SIDE OF DEADBAND
CLEARANCE

1.0 mil RADIAL
CLEARANCE BETWEEN
BEARING CARTRIDGE AND
BACKUP SUPPORT

0.5 mil RADIAL
DEADBAND
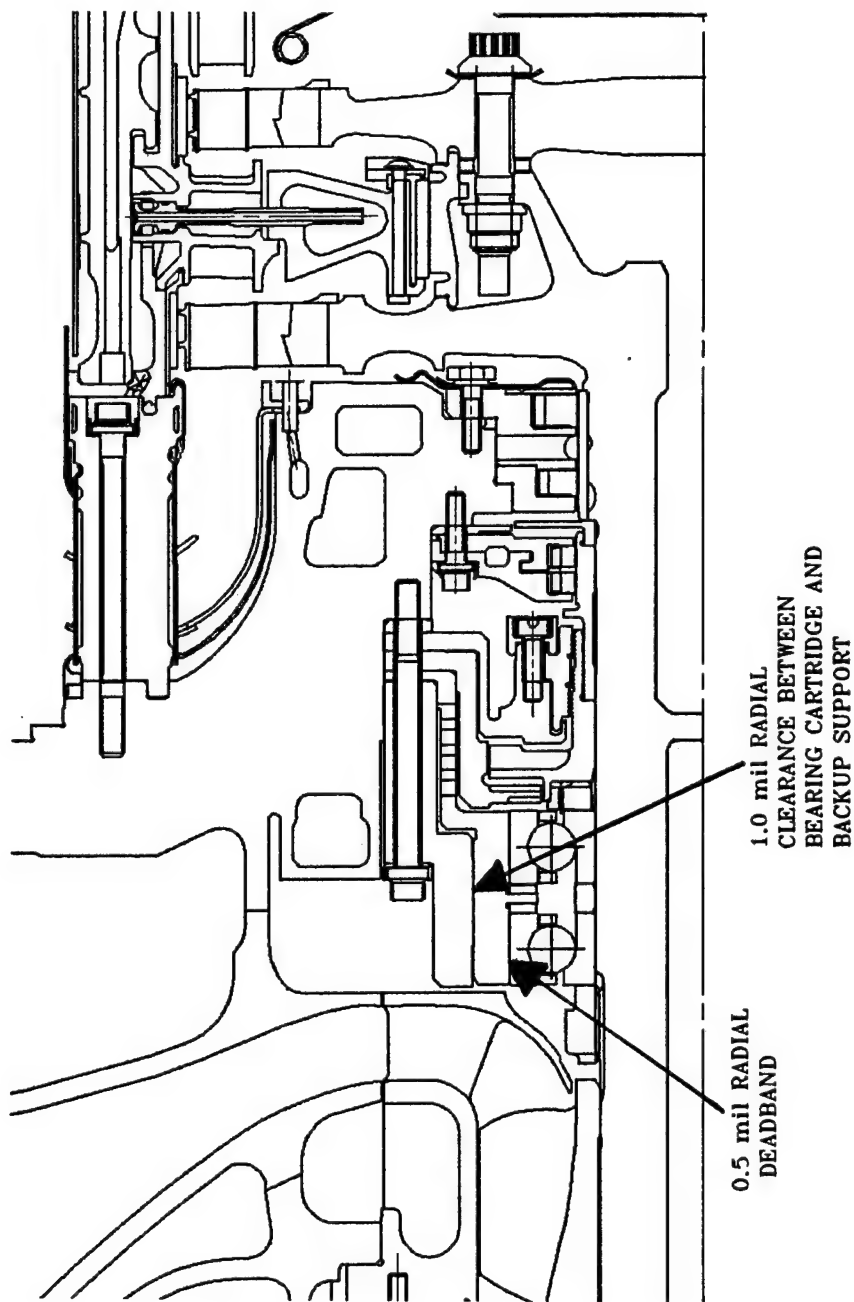
Figure 2.   SSME HPOTP Turbine Bearing Package

TABLE 1: NOMINAL BLOCK I HPOTP ROTORDYNAMIC CHARACTERISTICS

MODE	CRITICAL SPEED		SEPARATION MARGIN 2nd Critical to Operating Speed	LOG DEC @ FPL		STABILITY THRESHOLD SPEED		FIRST MODE FREQ. / OPERATING SPEED
	1st	2nd		1st	2nd	1st	2nd	
BLOCK I HPOTP	12,128	35,162	14.7 %	0.088	0.085	49,980	45,417	52.2 %
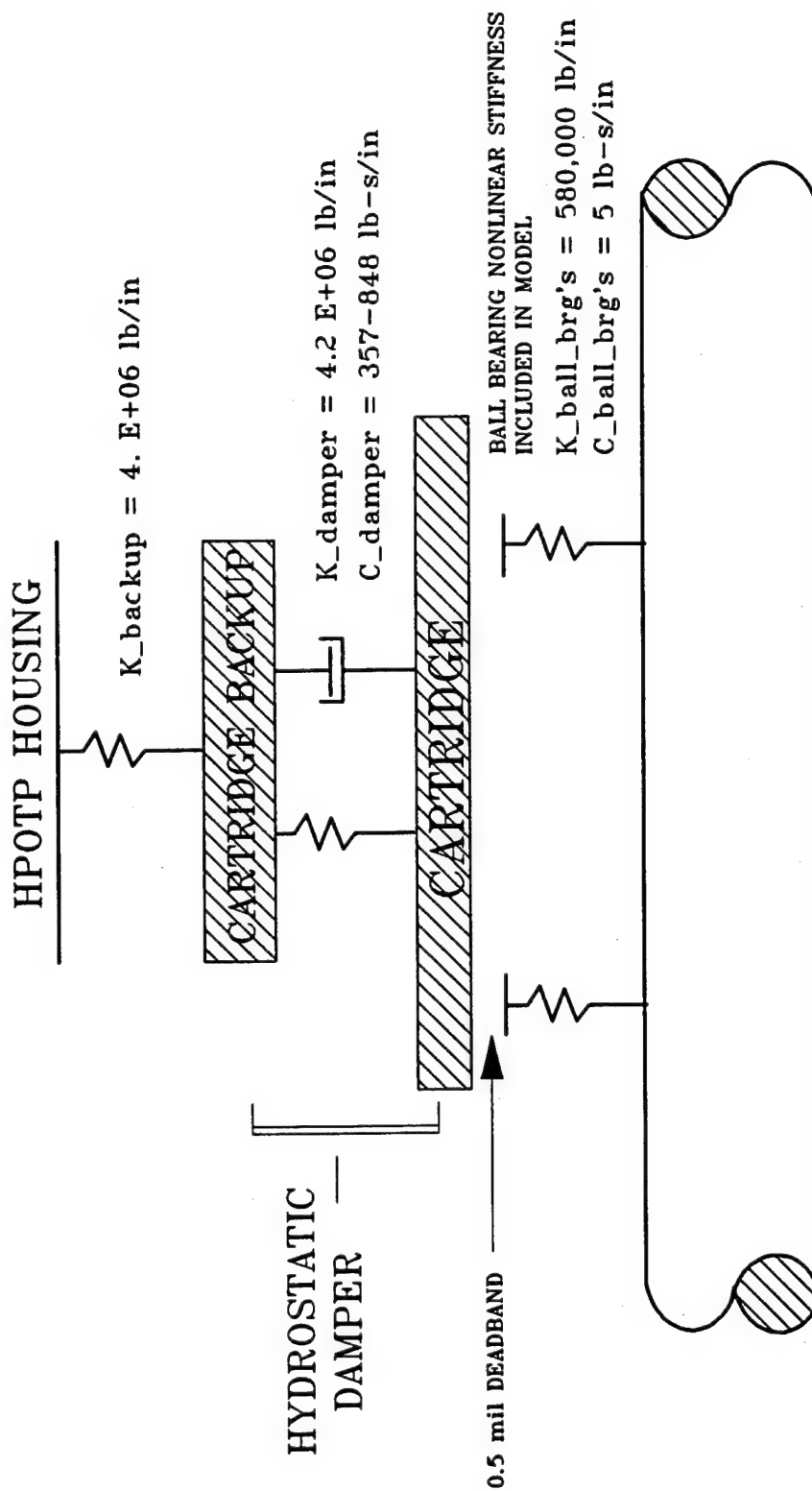
Figure 3. Turbine Bearing Package Nonlinear Model

HPOTP HOUSING

K_backup = 4. E+06 lb/in

CARTRIDGE BACKUP

K_damper = 4.2 E+06 lb/in
C_damper = 357–848 lb-s/in

CARTRIDGE

BALL BEARING NONLINEAR STIFFNESS
INCLUDED IN MODEL

K_ball_brg's = 580,000 lb/in
C_ball_brg's = 5 lb-s/in

HYDROSTATIC
DAMPER

0.5 mil DEADBAND
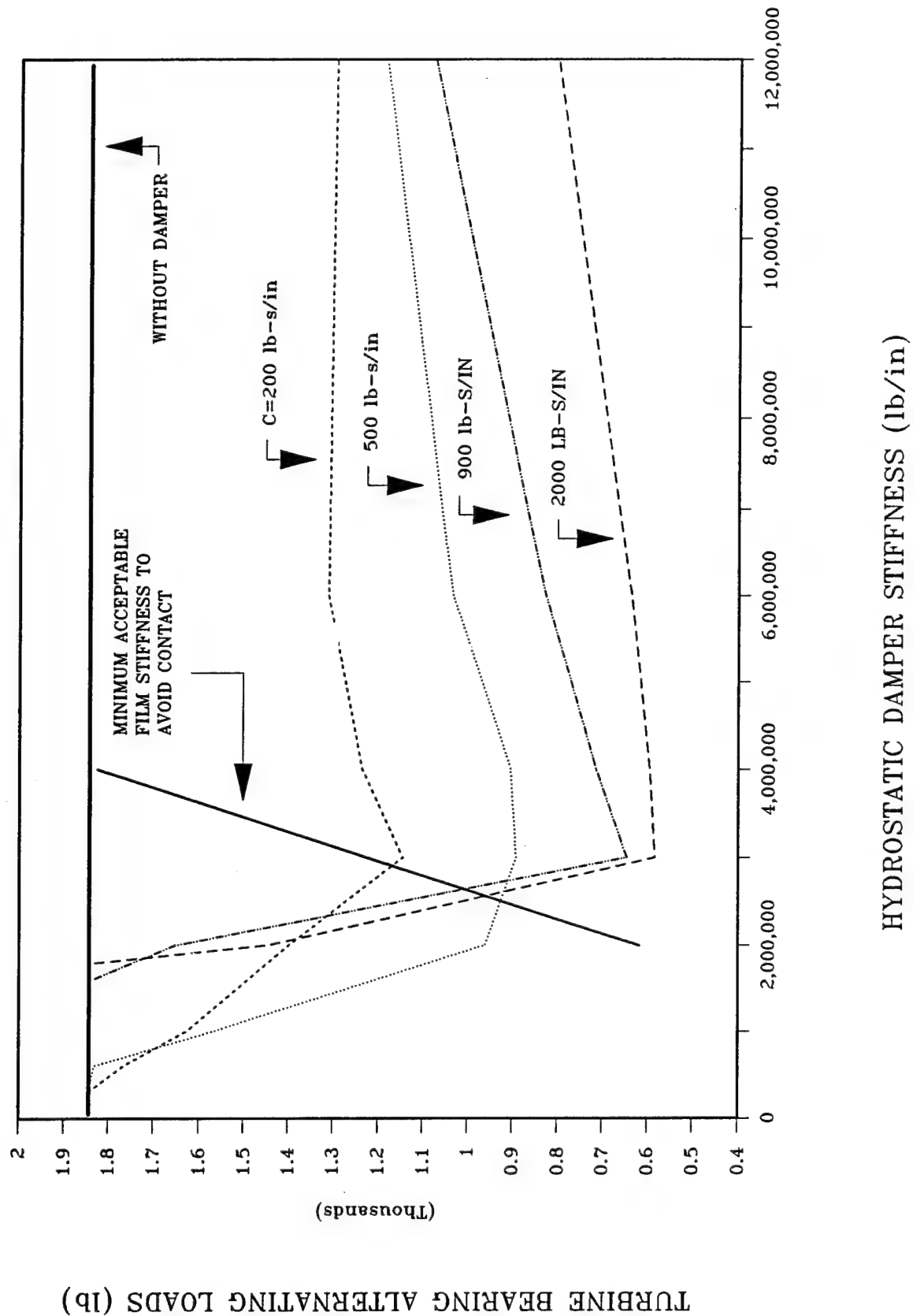
Figure 4. Turbine Bearing Dynamic Load vs. Hydrostatic Damper Characteristics

The figure plots TURBINE BEARING ALTERNATING LOADS (lb) (Thousands) on the vertical axis (0.4 to 2) versus HYDROSTATIC DAMPER STIFFNESS (lb/in) on the horizontal axis (0 to 12,000,000). Curves shown: WITHOUT DAMPER, C=200 lb-s/in, 500 lb-s/in, 900 lb-S/IN, 2000 LB-S/IN, and MINIMUM ACCEPTABLE FILM STIFFNESS TO AVOID CONTACT.
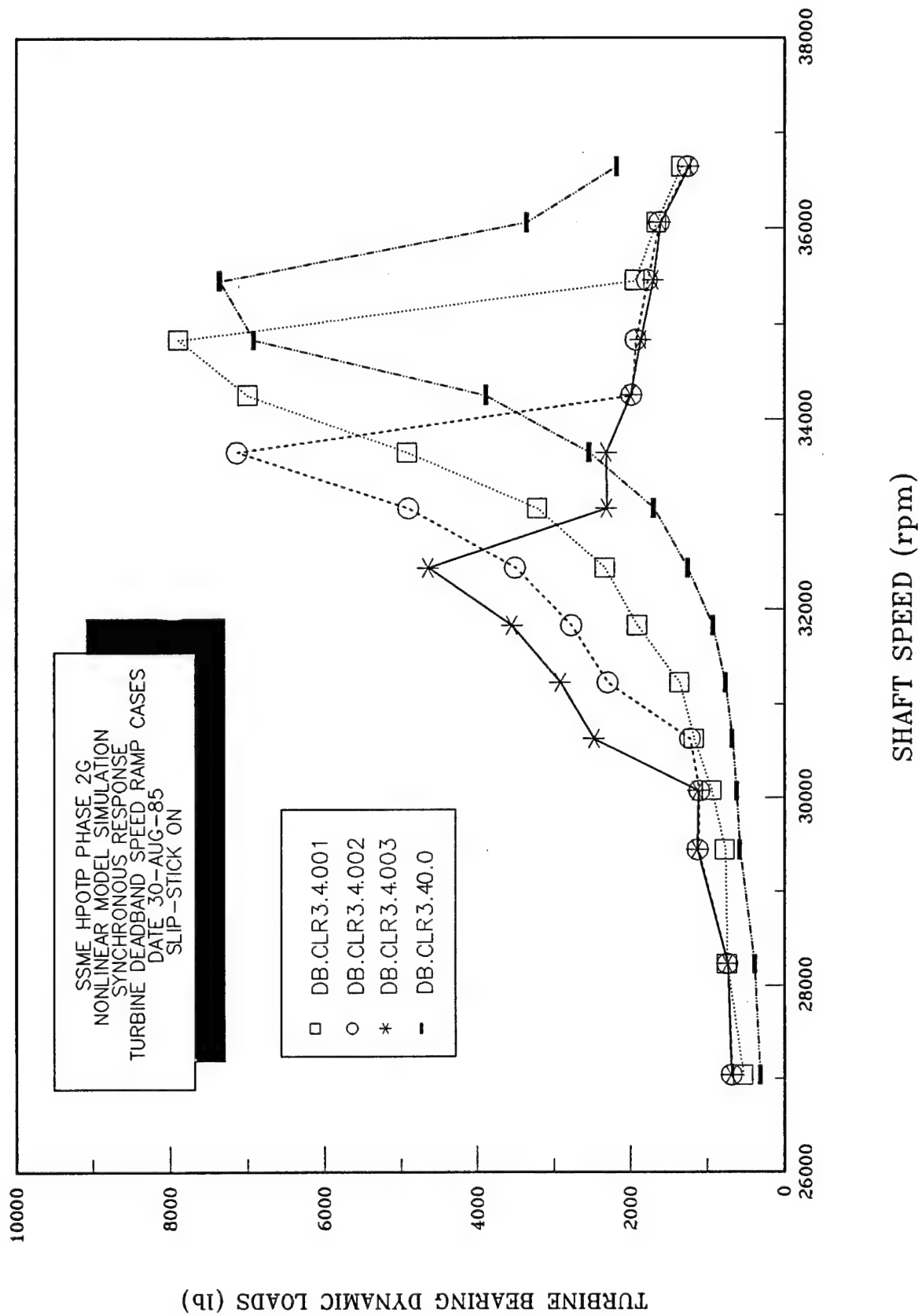
Figure 5. Effect of Cartridge - Backup Support Radial Clearance on Rotor Response
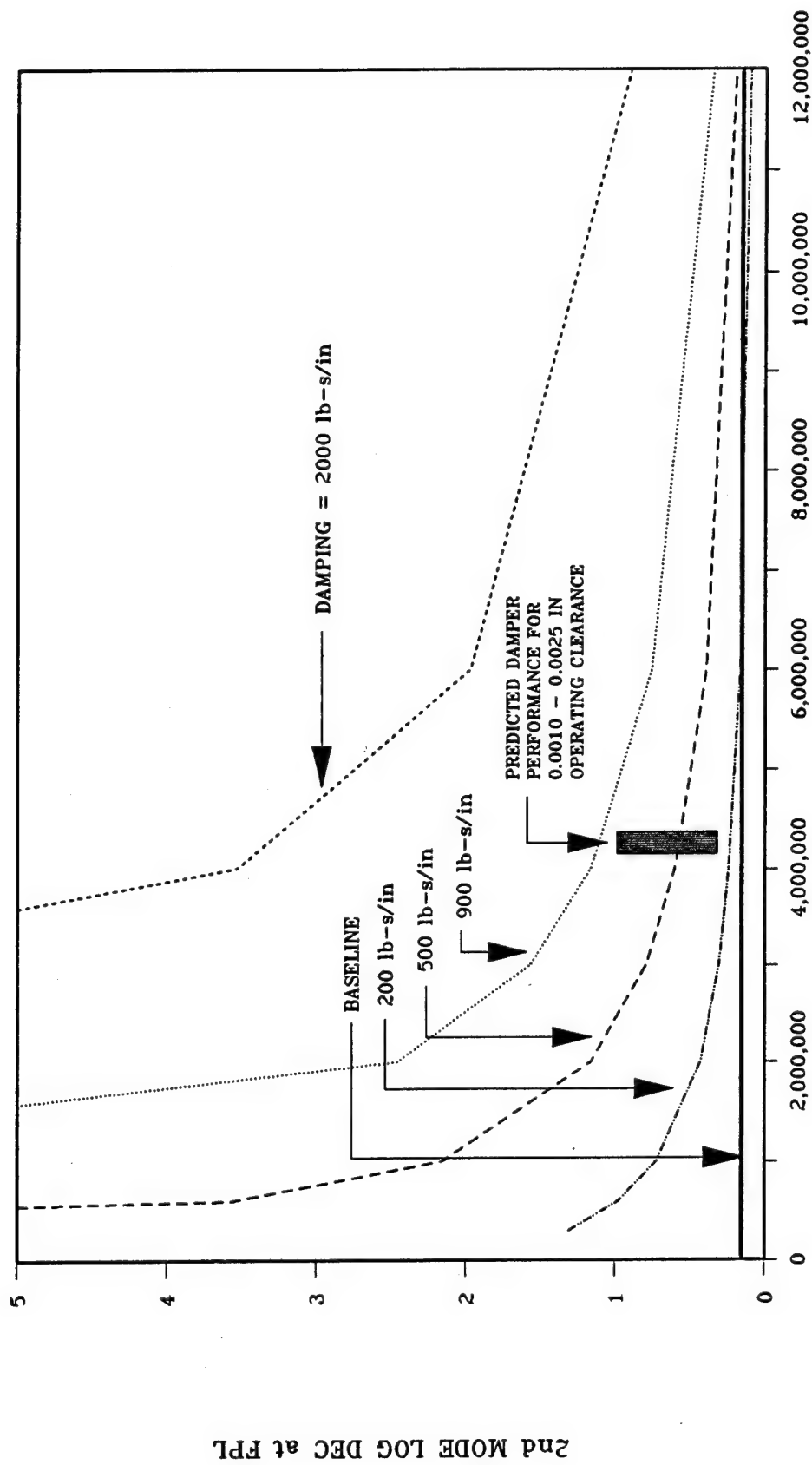
HYDROSTATIC DAMPER STIFFNESS (lb/in)

Figure 6. 2nd Rotor Mode Logarithmic Decrement at FPL
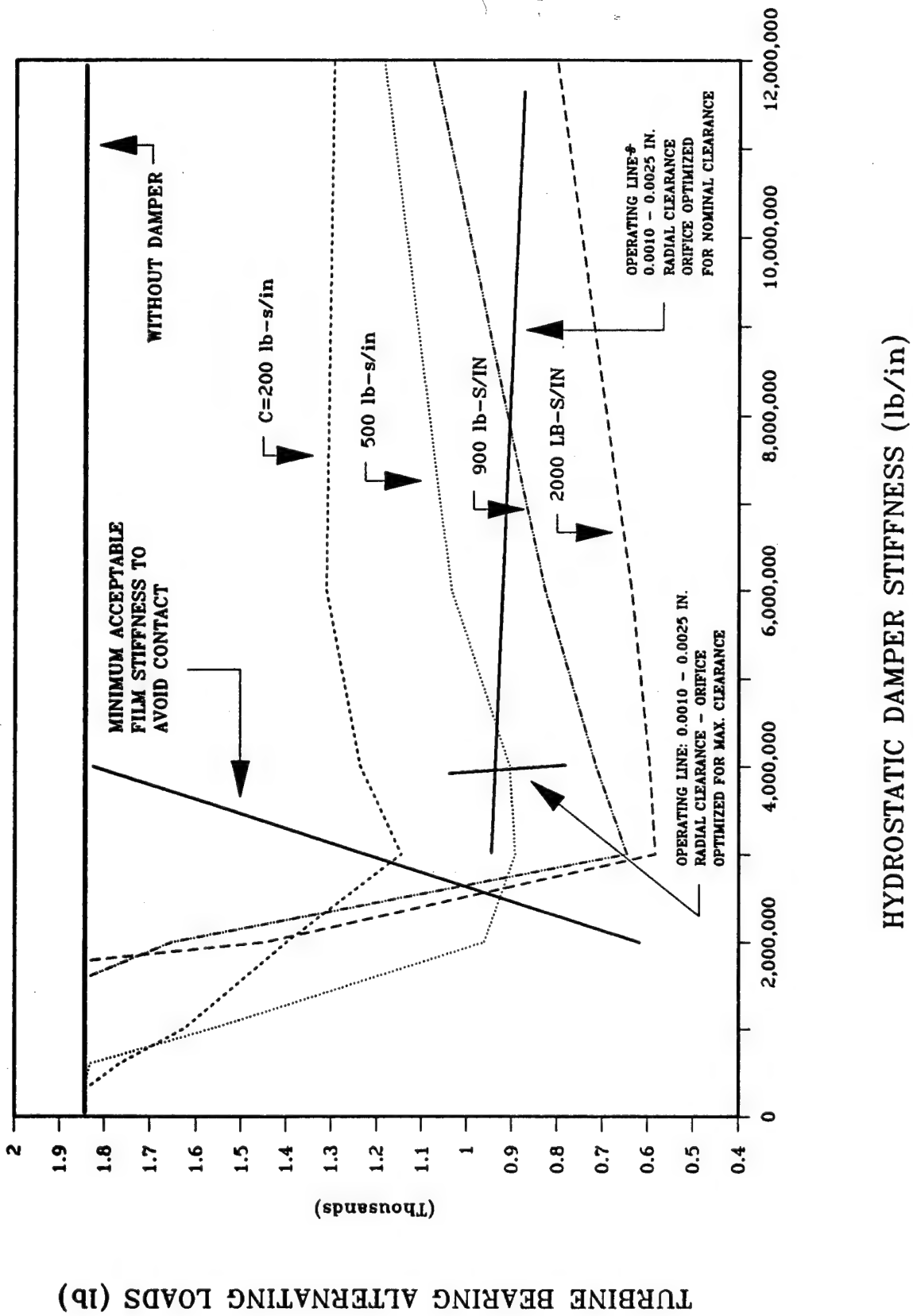
Figure 7. Typical Hydrostatic Damper Performance – Effect of Orifice Optimization

HYDROSTATIC
DAMPER
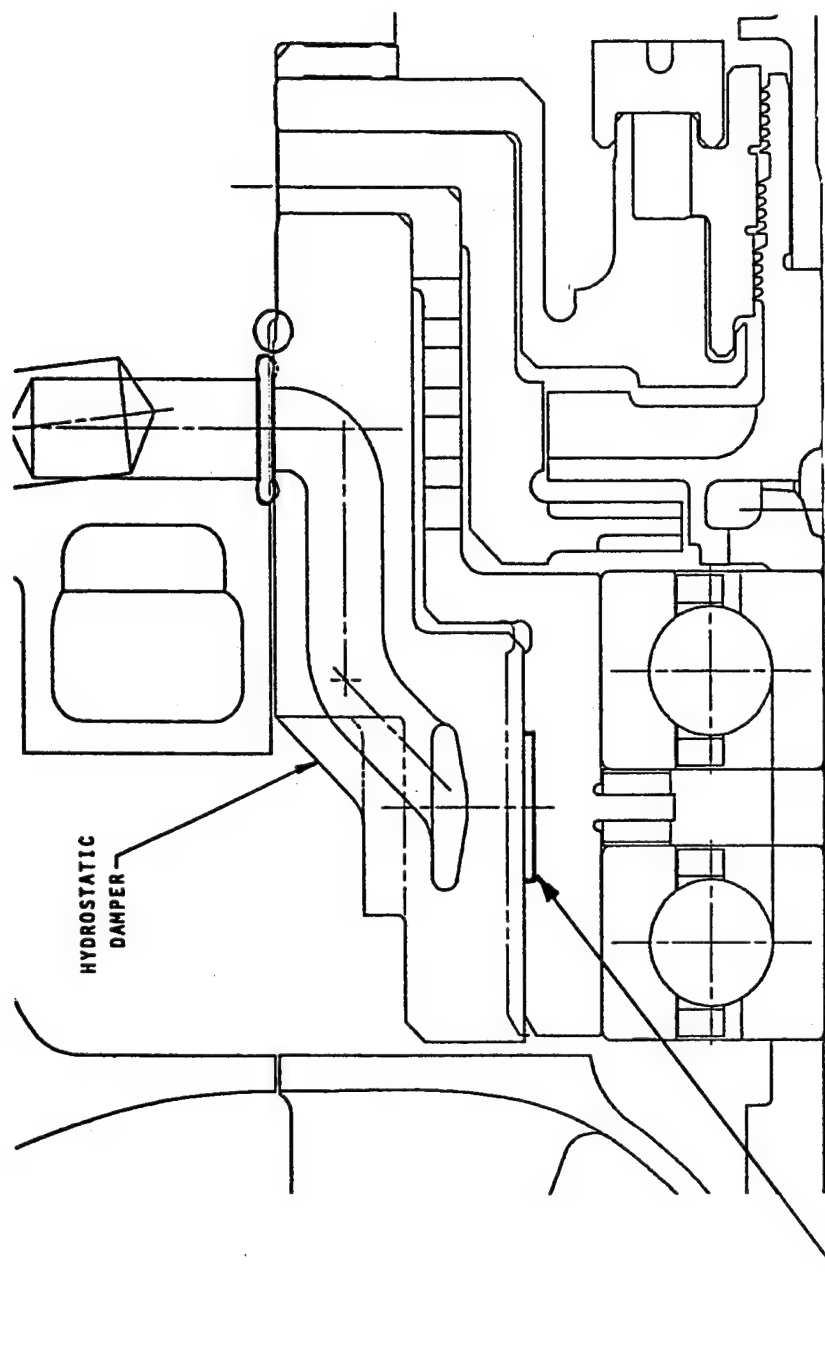
● RECESSES ARE ON CARTRIDGE

○ *NUMBER OF RECESSES = 9*

○ *RECESS DIMENSIONS = 0.457 x 0.914 in.*

○ *RECESS DEPTH = 0.009 - 0.011 in.*

○ *RADIAL CLEARANCE = 0.0010 - 0.0025 in.*

○ *DAMPER LENGTH = 1.25 in. DAMPER DIAMETER = 4.8 in.*

Figure 8. HPOTP Hydrostatic Damper

SSME HYDROSTATIC DAMPER
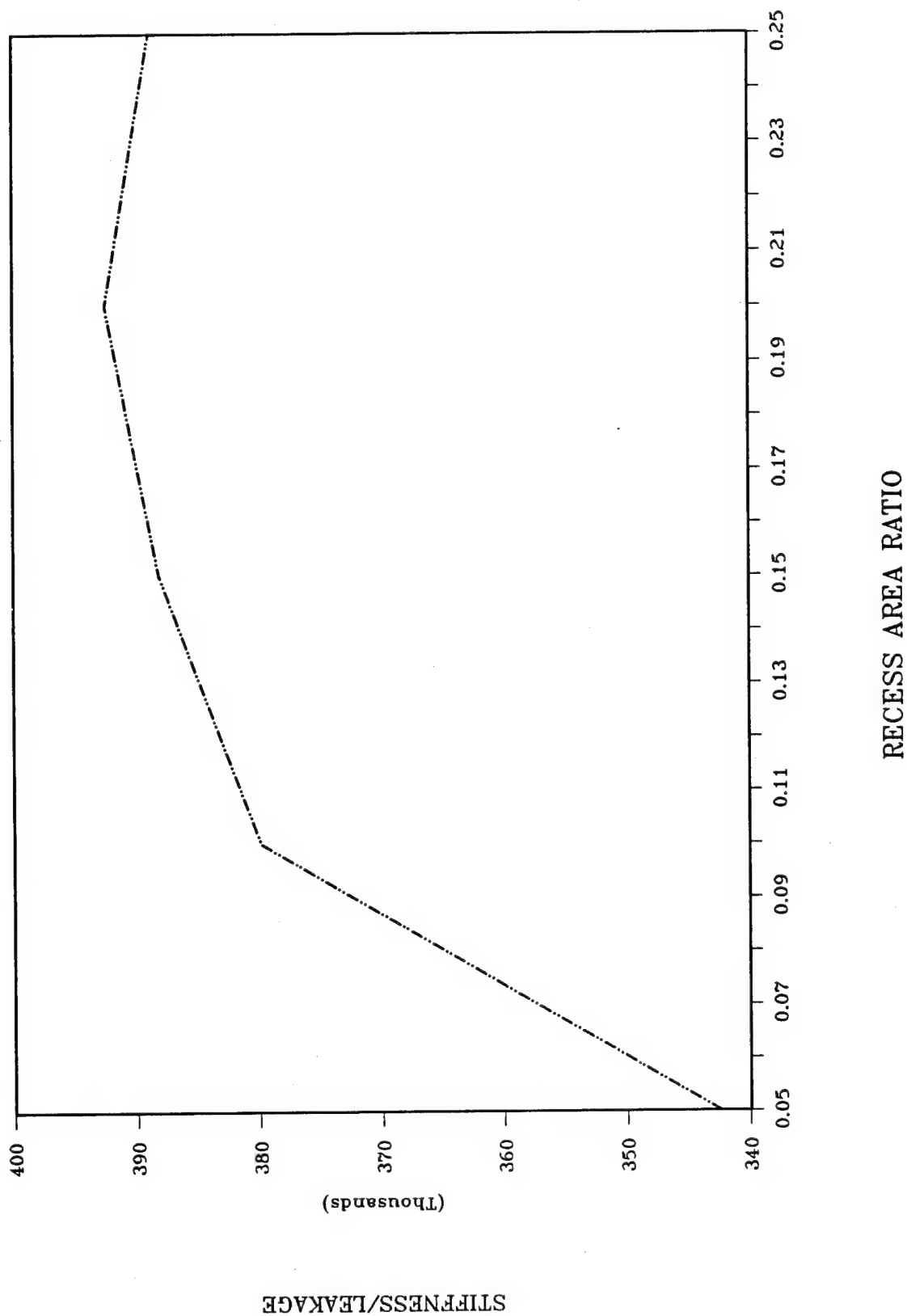
Figure 9. Hydrostatic Damper Stiffness/Leakage Ratio vs. Recess Area Ratio

DBC-21

SSME HYDROSTATIC DAMPER

RECESS AXIAL LENGTH-CIRC. WIDTH RATIO

STIFFNESS/LEAKAGE

(Thousands)
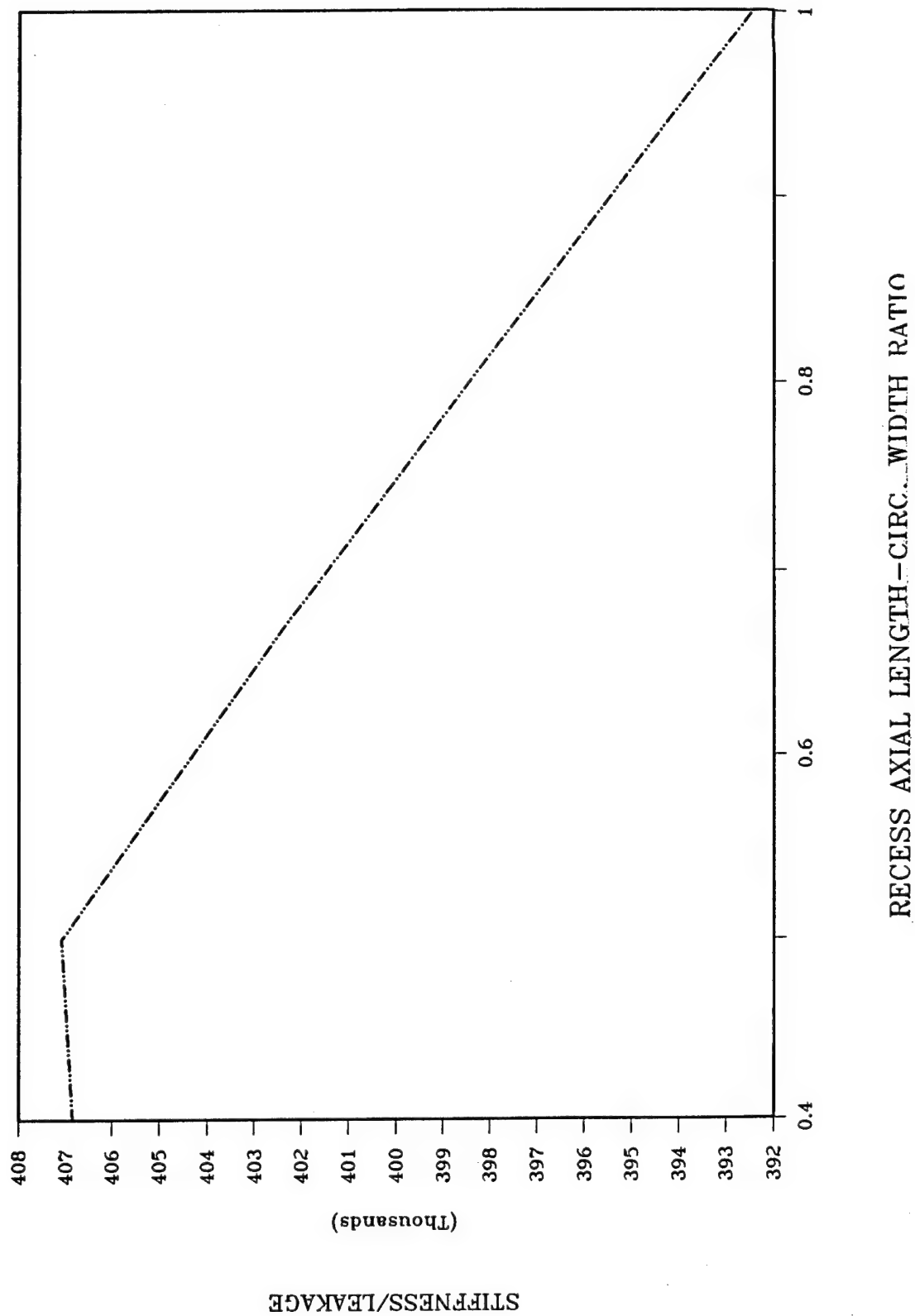
Figure 10. Stiffness/Leakage Ratio Recess vs. Recess Axial Length/Circumferential Width Ratio
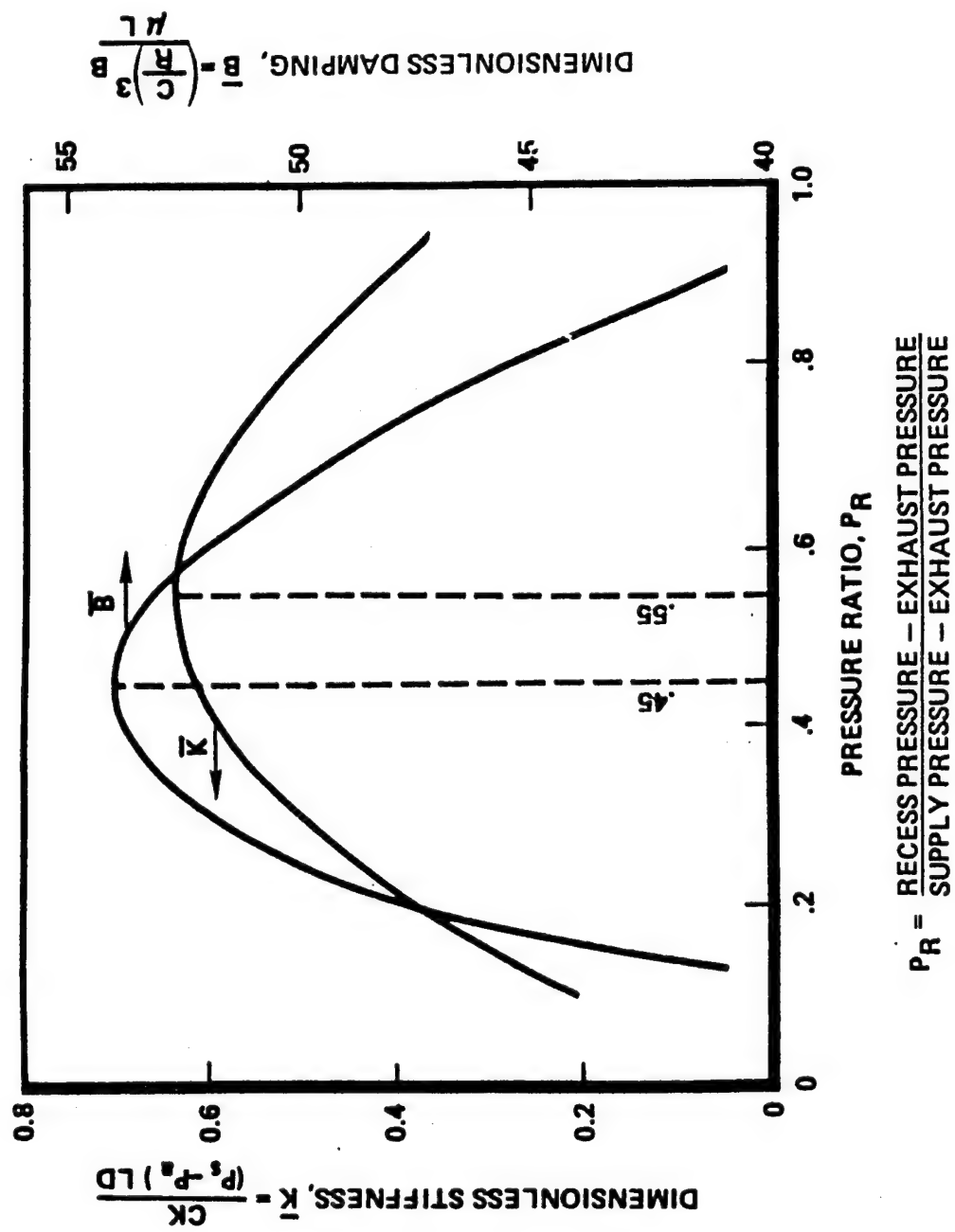
Figure 11. Orifice Diameter Optimization

SSME HYDROSTATIC DAMPER

RADIAL CLEARANCE (inches)

STIFFNESS/STIFFNESS(0.0025)
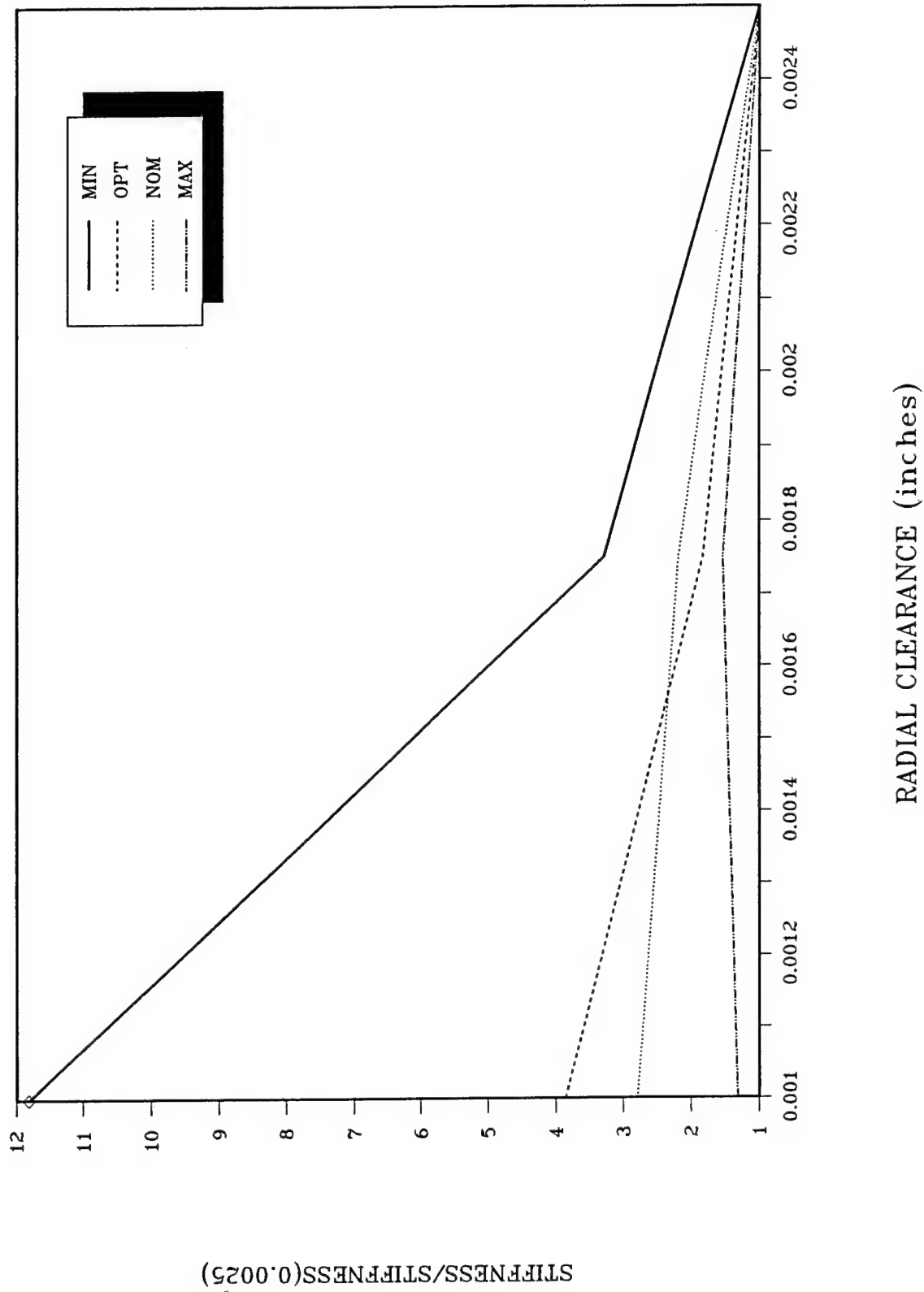
Figure 12.   Hydrostatic Damper Stiffness vs. Radial Clearance

TABLE 2: EFFECT OF HYDROSTATIC DAMPER ON

LINEAR CRITICAL SPEED

AND

STABILITY ANALYSIS

MODE	CRITICAL SPEED 1st 2nd	SEPARATION MARGIN 2nd Critical to Operating Speed	LOG DEC @ FPL 1st 2nd	STABILITY THRESHOLD SPEED 1st 2nd	FIRST MODE FREQ. / OPERATING SPEED
BLOCK I HPOTP	12,128 35,162	14.7 %	0.088 0.085	49,980 45,417	52.2 %
WITH HYDRO-STATIC DAMPER	8,900 34,950 -26% - 6%	14.1%	0.2 TO 0.4 TO 0.33 0.95	> 50 K >50 K	52.0%
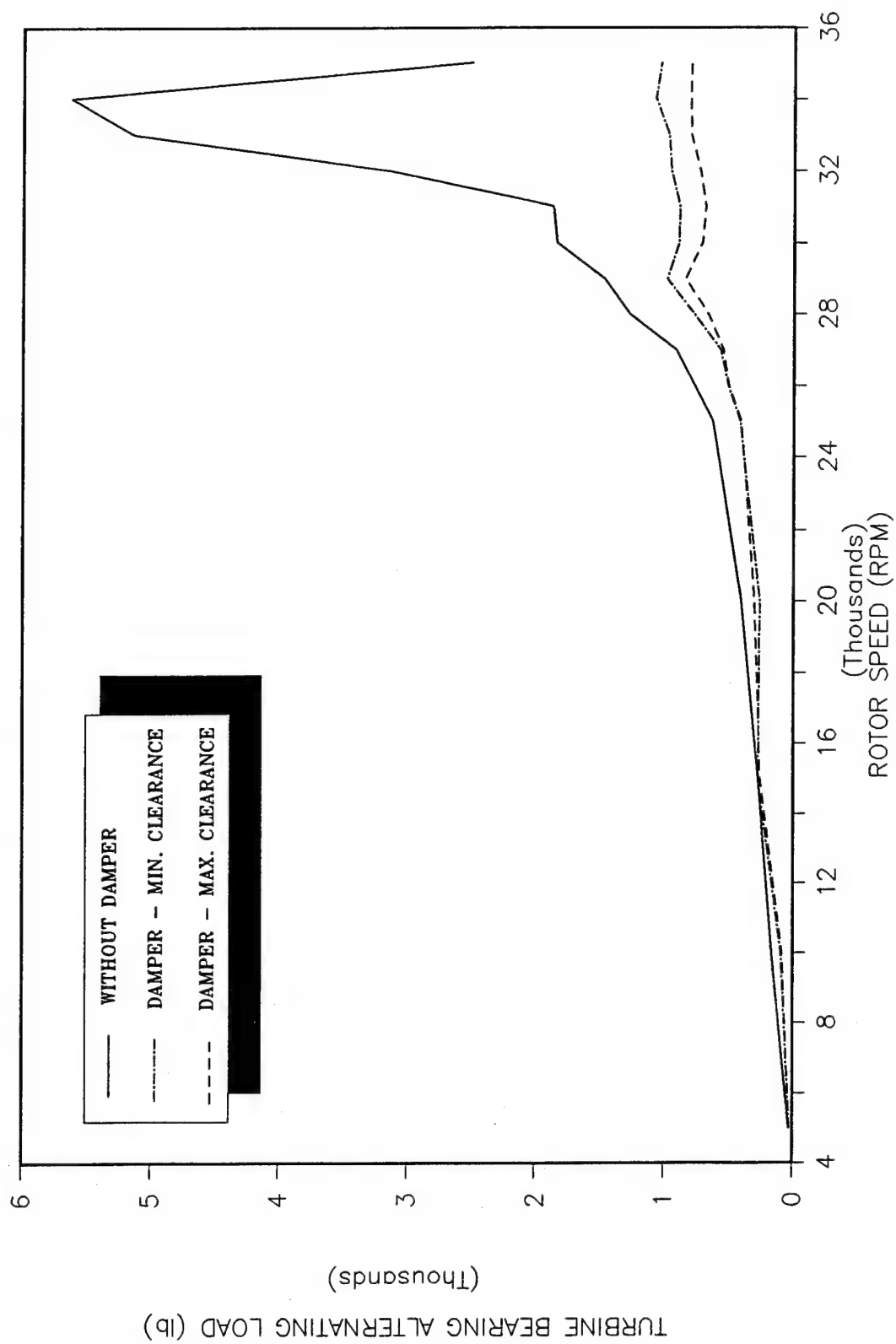
Figure 13. Effect of Hydrostatic Damper on HPOTP Response
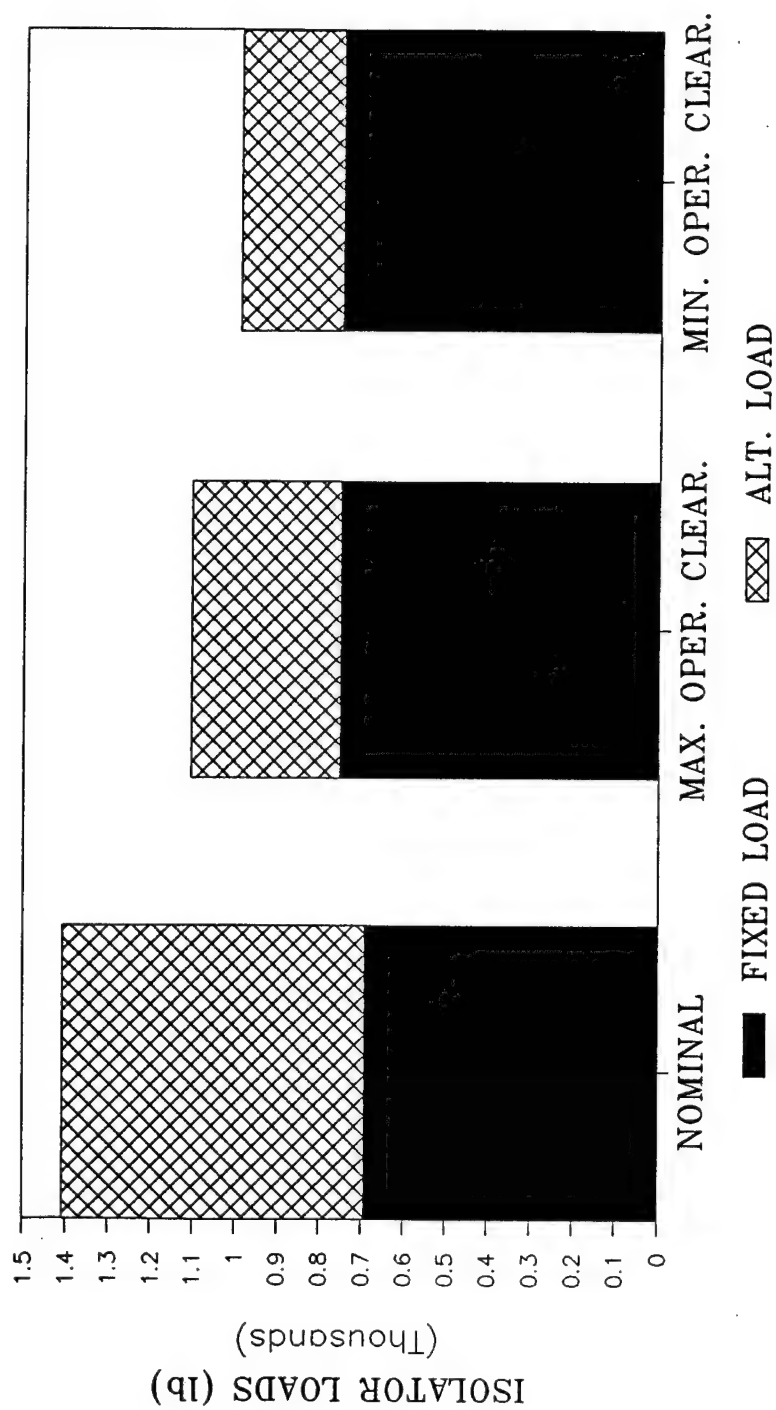
Figure 14. Effect of Hydrostatic Damper on Pump End Bearing Loads at FPL
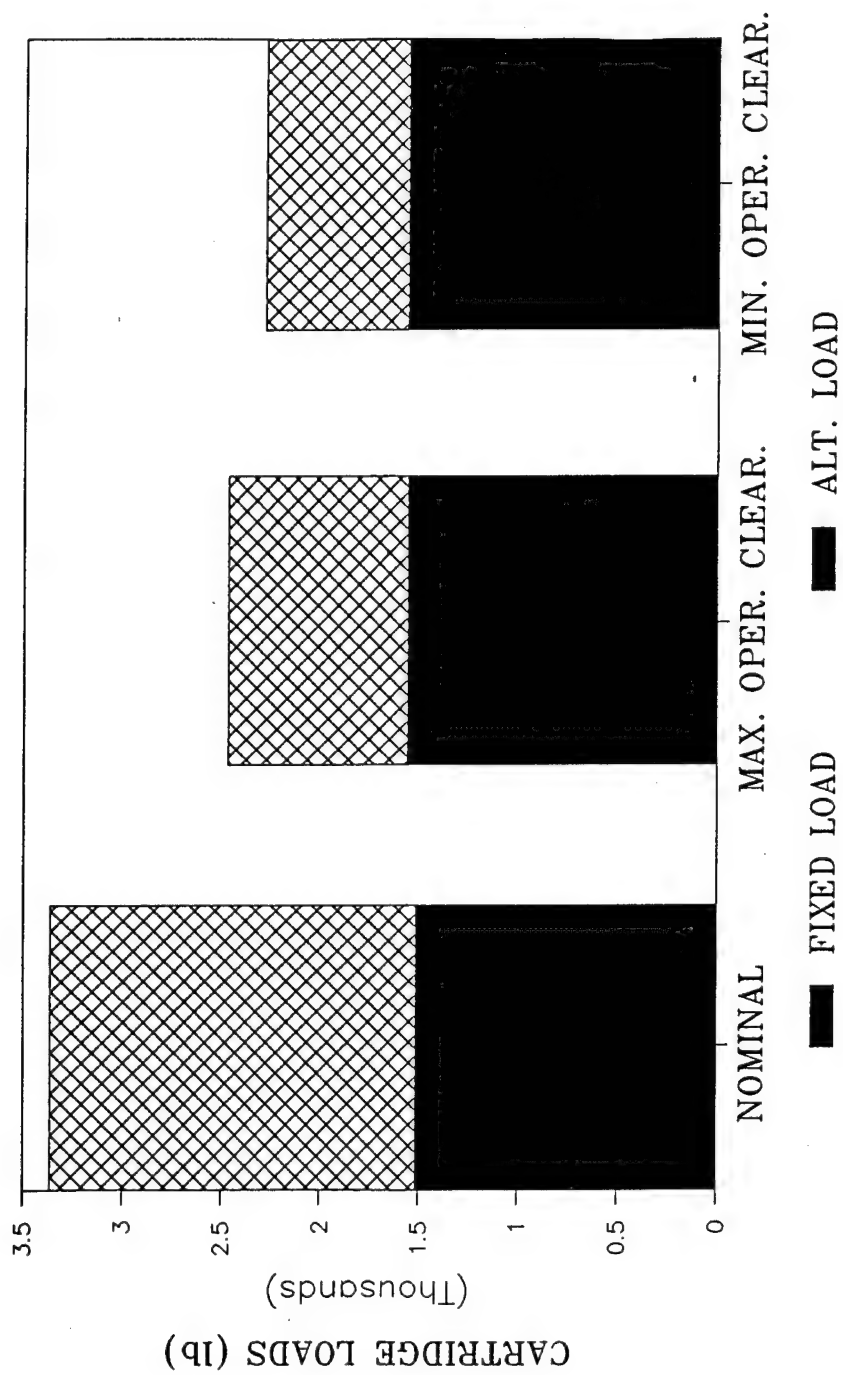
Figure 15. Effect of Hydrostatic Damper on Turbine Bearing Loads at FPL

OPTIMIZED DESIGNS OF
VISCOELASTIC DAMPING TREATMENTS

Warren C. Gibson, Ph.D.
Conor D. Johnson, Ph.D.

CSA Engineering, Inc.
Palo Alto, California

ABSTRACT

The modal strain energy method is a proven design tool for viscoelastic damping treatments. It provides a quantitative criterion for evaluation of candidate designs using finite element models coded for NASTRAN. This paper presents a method for optimizing damping treatments. As design variables, the method uses viscoelastic stiffness and layer thickness, and thicknesses of constraining layers or base layers. It seeks to maximize viscoelastic modal strain energy subject to constraints on weight or natural frequencies. Optimization of a damping treatment for a demonstration space structure is shown. Only four complete NASTRAN runs were required to produce a reduction in RMS response by a factor of more than seven, for a PSD base input. Current research aimed at increased efficiency is discussed.

1. Introduction

The modal strain energy method has proved valuable for design of viscoelastic damping treatments for a wide range of damping design problems.[1][2][3] Its effectiveness is such that analysis methods are now the strongest link in the design chain rather than the weakest. The success of the MSE method has spawned research and development in material characterization methods, testing methods, and in optimization.[4]

Simple structures such as cantilever beams can be designed manually for optimal damping performance. But with even moderate complexity, intuition and experience sometimes fail. Experienced structural engineers have often been chagrined when an automated optimization program generates a design that exceeds their manual efforts. Sometimes there are simply too many design variables or too many design goals to keep track of. Sometimes optimization programs produce solutions that seem counterintuitive (although in hindsight, designers generally come up with explanations).

Such is the case with design of viscoelastic damping treatments. Modal strain energy values are highly sensitive to variables like viscoelastic stiffness. When more than one mode is to be damped, there are usually tradeoffs: a design that is effective for one mode may be ineffective for another. When different treatments are proposed for different areas of a structure, where mode shapes are spatially complex, or where weight is critical, manual design efforts may be inadequate. This is the motivation for optimization. With some of the quantitative design decisions automated, the designer can spend more time investigating alternate configurations or performing tradeoff studies. The net result is better designs produced in less time.

This paper reports on a method that was developed for optimization of viscoelastic damping treatments. The method was implemented in a computer program called ODAMP, and is illustrated by a demonstration problem.

2. Review of Structural Optimization

2.1 Key Concepts in Optimization

Automated optimization is generally carried out by casting a constrained minimization problem in the form

$$\text{Minimize} \quad f(\mathbf{X})$$
$$\text{Subject to} \quad g_j(\mathbf{X}) \leq 0 \qquad j = 1, \ldots, m$$
$$\text{and} \quad \mathbf{X}_k^L \leq \mathbf{X}_k \leq \mathbf{X}_k^U \quad k = 1, \ldots, n$$

In general, the objective function $f(\mathbf{X})$ may be weight, cost, or some other measure of performance. (If $f(\mathbf{X})$ is to be maximized, one can simply minimize its negative, $-f(\mathbf{X})$). $\mathbf{X}$ is a vector of *design variables*, the parameters that the optimizer is allowed to vary. The inequality constraints $g_j(\mathbf{X})$ include any conditions that limit the acceptability of a proposed design. For example, if a natural frequency f is not to fall below f_{min}, then the corresponding constraint would be specified in normalized form as

$$g_j = 1 - \frac{f}{f_{min}} \leq 0 \qquad (1)$$

The limits $\mathbf{X}^U$ and $\mathbf{X}^L$ are called side constraints because they limit the region of search for the optimum. These could be included in the set of general inequality constraints, but are treated separately for efficiency, and because they must never be violated during the design process. For example, a member thickness less than zero would render the finite element analysis meaningless. Thus, it is important to provide an explicit limit on such design variables. However, other constraints such as frequency constraints can be and often are violated during all or part of the optimization process.

A textbook should be consulted for more information on optimization techniques.[5]

2.2 ADS Optimizer

ADS is a general-purpose optimization program which is used with ODAMP.[6] ODAMP sets up the design variable vector $\mathbf{X}$, objective function $f(\mathbf{X})$, and the constraints g_j, along with the sensitivities (partial derivatives) $\partial f/\partial \mathbf{X}_i$ and $\partial g_j/\partial \mathbf{X}_i$. This data is passed to ADS which then carries out one stage of approximate optimization as discussed under "Approximate Models."

ADS includes a wide variety of strategies and algorithms. The method used in ODAMP (subject to user override) is called "0,5,7," which is the method of feasible directions with bounded polynomial search.

2.3 Structural Optimization

In structural optimization, the design variables $\mathbf{X}$ are typically properties like thicknesses, bar areas, material properties, and shapes. All design variables must be related to the analysis model so that the optimizer can modify this model and get revised response predictions. The constraints $g_j(\mathbf{X})$ are typically responses like stresses, displacements, or natural frequencies. Minimum weight is often chosen as the objective function $f(\mathbf{X})$, but a particular response quantity can be chosen as an objective instead (e.g., maximize viscoelastic modal strain energy).

Sensitivity analysis is a key concept in structural optimization. This term denotes the calculation of partial derivatives or gradients of structural responses with respect to design variables. The optimizer needs this information in order to decide which way to move in "design space." In some optimization problems, calculation of $f(\mathbf{X})$ and $g_j(\mathbf{X})$ is simple, and in these cases the optimizer can calculate gradients by finite difference approximations. In structural optimization, $f(\mathbf{X})$ and $g_j(\mathbf{X})$ are very expensive to calculate (i.e., a complete finite element analysis is entailed). Therefore, it is necessary to calculate these gradients explicitly in the finite element code.

2.4 Approximate Models

A key concept used in ODAMP is an *approximate model*. This concept, developed by Schmit and Miura, makes it possible to achieve near-optimal designs with very few complete finite element analyses.[7] These analyses with their accompanying sensitivity calculations consume the vast majority of the computer time in an optimization cycle. Thus, when properly applied, approximation techniques can achieve a great improvement in efficiency when compared with direct coupling of an optimizer with a finite element code.

The basic idea is to use the sensitivity information to set up a Taylor series expansion of both the objective function and the constraint function, i.e., they are linearized. Provided these functions are reasonably well behaved, the linearized functions form a good approximation over a fairly wide range of design variable values. Thus, the optimizer can search for a local optimum within such a region. Since evaluation of the linearized functions is trivial, this local optimization process takes very little computer time. In fact, it is ironic that approximation techniques in many cases make questions of efficiency of the optimizer irrelevant. It does not matter if the optimizer makes a lot of iterations, if the iterations cost practically nothing.

Only after the approximate optimization is complete is the structure re-analyzed. The linearization process is then repeated and the new approximate optimization problem is solved. At each such stage, move limits are imposed to insure that the structure is not changed so drastically that the linearization is not valid. The process of constraint linearization and optimization is repeated until no further design improvements can be found.

Figure 1 shows the progress of an optimization problem using an approximate model in a hypothetical two-variable design space. The design begins at point 1, and is limited by the first box on the left. The move from point 1 to point 2 is accomplished by a series of calls to ADS, which returns proposed designs to be evaluated. The progress from point 1 to point 2 would not be a straight line, in

general. However, the intermediate points tried by ADS in getting from 1 to 2 are not shown because they are of no particular interest. At point 2, a NASTRAN analysis and a sensitivity calculation are performed. A new approximate model is set up, bounded by another set of move limits. Two more cycles of analysis and approximate model optimization are carried out, and the design terminates at point 4.
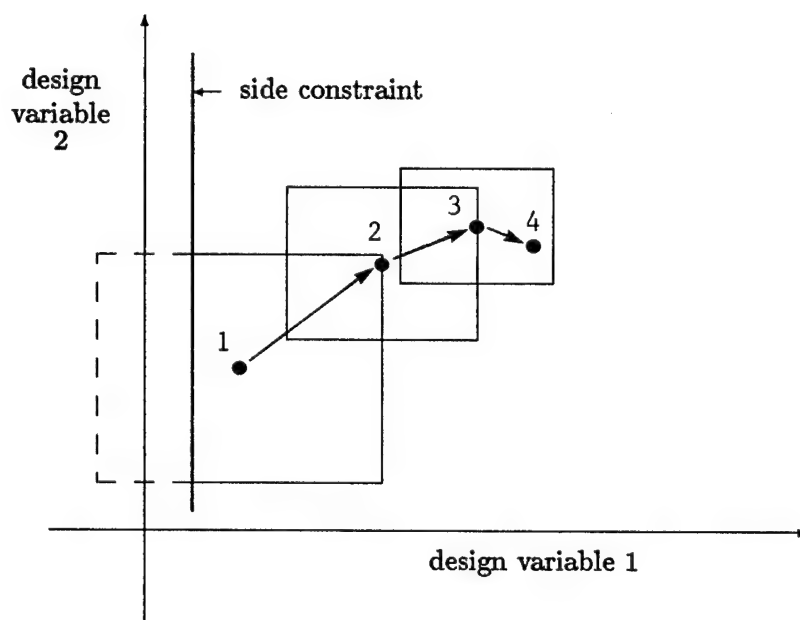
Figure 1. Move limits in approximate optimization

Note that the box surrounding point 1 would have extended into the negative region. In this case, the left move limit is pre-empted by a side constraint at a positive value for design variable 1. Also note that the first two moves were terminated on a move limit boundary, and that move limits were decreased as the design progressed.

3. Modeling Layered Damping Treatments

Layered damping treatments consist of a base layer, a layer of viscoelastic material, and an optional constraining layer. When integral damping treatments are designed, however, there may be no distinction between the constraining layer and the base layer, as both may be considered part of the basic structure.

These layups are typically modeled using QUAD4 or TRIA3 plate bending elements for the outer layers, and HEXA or PENTA solid elements for the viscoelastic layers. Solid elements are used even though the viscoelastic layer is typically much thinner than the metallic or composite layer, for two reasons: first, the material is nearly incompressible, and this is difficult to model with two-dimensional elements, and second, the only important actions in the viscoelastic are transverse shear deformation and sometimes in-plane extension, and these are best represented by solid elements.

Figure 2 shows a portion of a layered damping treatment model, with the node points located on the interfaces between the viscoelastic and the constraining or base layers. This means that the *offset* feature of the QUAD4 and TRIA3 elements must be used to indicate that the nodes are not at the plate elements' middle surfaces.
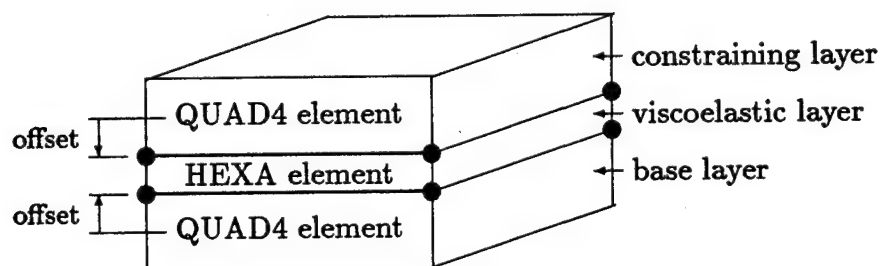
Figure 2. Modeling layered damping treatments

4. ODAMP Optimization Code

ODAMP (Optimization of DAMPing treatments) is a research code intended for development and demonstration of optimization methods for damping design.[8] It relies on MSC/NASTRAN for computation of modal strain energies and sensitivities. It also uses ADS (Automated Design Synthesis), a public-domain mathematical programming package, to perform constrained minimization.

The modal strain energy method relates the structural loss factor $\eta^{(j)}$ for mode j to the strain energy distribution and material loss factors:

$$\eta^{(j)} = \sum_{i=1}^{M} \frac{\eta_i S_i^{(j)}}{S^{(j)}} \tag{2}$$

where

$$
\begin{aligned}
\eta_i &= \text{material loss factor for viscoelastic material number } i \\
S_i^{(j)} &= \text{strain energy in material } i \text{ due to deformation} \\
&\quad \text{in natural vibration mode } j \\
S^{(j)} &= \text{total strain energy in natural vibration mode } j
\end{aligned}
$$

Stated differently, the effectiveness of a given damping treatment for a particular mode is best when its strain energy in the viscoelastic is maximized for that mode. Since eigenvectors are indeterminate with respect to scaling, the viscoelastic strain energy must be expressed as a fraction of the structure's total strain energy.

When MSC/NASTRAN is used, strain energies can be calculated in two ways. First, the GPFDR module may be used to compute strain energies broken down by element. This data can be written to a file for post-processing by CSA's MSET program.[9] With this method, users are free sum strain energies over groups of elements that may be selected arbitrarily after the NASTRAN run has finished.

The second method, used for optimization, is as follows: Divide the structural stiffness matrix $\mathbf{k}$ into separate matrices

$$\mathbf{k} = \mathbf{k}^{(m)} + \sum_{i=1}^{M} \mathbf{k}_i^{(v)} \tag{3}$$

where there are M distinct viscoelastics, $\mathbf{k}_i^{(v)}$ includes only the elements for viscoelastic i, and $\mathbf{k}^{(m)}$ is the stiffness of all the metallic (or other non-viscoelastic) elements. Then the strain energy ratio for viscoelastic i for a mode shape j is simply

$$S_i = \frac{\mathbf{\Phi}_j^T \mathbf{k}_i^{(v)} \mathbf{\Phi}_j}{\mathbf{\Phi}_j^T \mathbf{k} \mathbf{\Phi}_j} \tag{4}$$

This second method is more economical and easier to use for computing sensitivities (discussed below).

5.   Operation of ODAMP

ODAMP works in conjunction with MSC/NASTRAN, passing data to and from NASTRAN. The flow of control is shown in Figure 3. The process begins with a
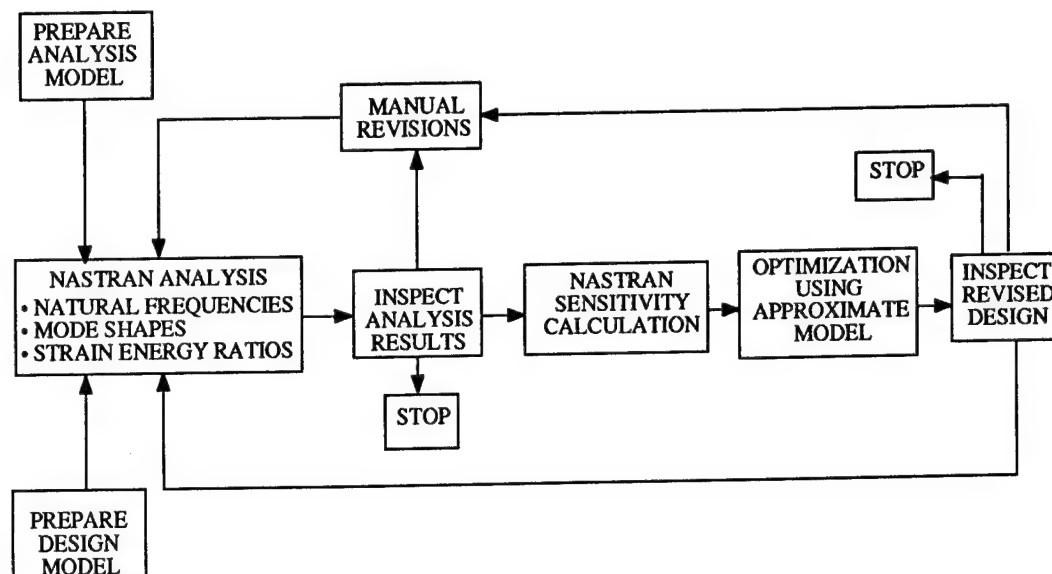
Figure 3. ODAMP flow of control

finite element model prepared in the usual manner. It is augmented by a *design model*, which is a description of the optimization problem in terms of design variables, constraints, and an objective. (An example of a design model is shown in Figure 7.) Natural frequencies, mode shapes, and modal strain energies are computed by NASTRAN. At that point, the user may inspect the results and make manual design revisions, or proceed with sensitivity calculations and a cycle of optimization. Each cycle of optimization involves an inner loop in which the response of the structure is represented by an approximate model as explained above. The revised design may be revised manually, or one can go directly back to NASTRAN for another analysis and another cycle of optimization. Several cycles can be scheduled for unattended computation.

The sensitivity calculations are particularly important. This operation is carried out by a program written in NASTRAN's DMAP language, for which details may be found in Appendix A.

6. Demonstration Problem: Equipment Tray

Figure 4 shows a sketch of a satellite equipment tray with stiffeners around the edges and at the centerlines. The tray provides support for a piece of sensitive electronic equipment. The tray is to be redesigned so as to reduce the response of the equipment to launch disturbances. Figure 5 shows the finite element model of the tray with displays of strain energies in its first three modes. Figure 6 shows the
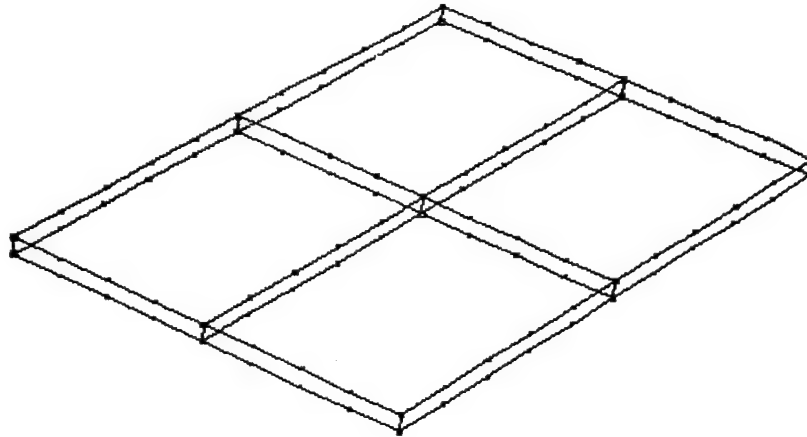
Figure 4. Equipment tray
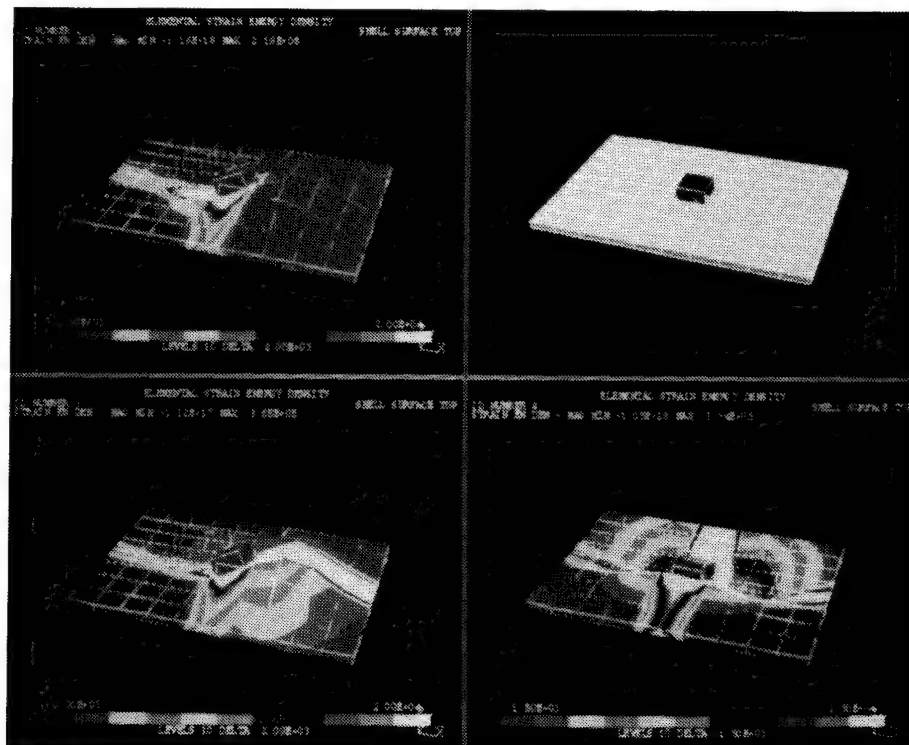
Figure 5. Equipment tray: strain energy display

excitation acceleration in the form of a power spectral density (solid line), together with the response of the payload with an undamped tray. A layer of viscoelastic material is to be applied to each section of the bottom of the tray, between the center stiffeners. The viscoelastic is to be covered by a metallic constraining layer which is not connected to the stiffeners. The goal is to reduce the response of the payload as much as possible without increasing the weight of the tray.

Acceleration response
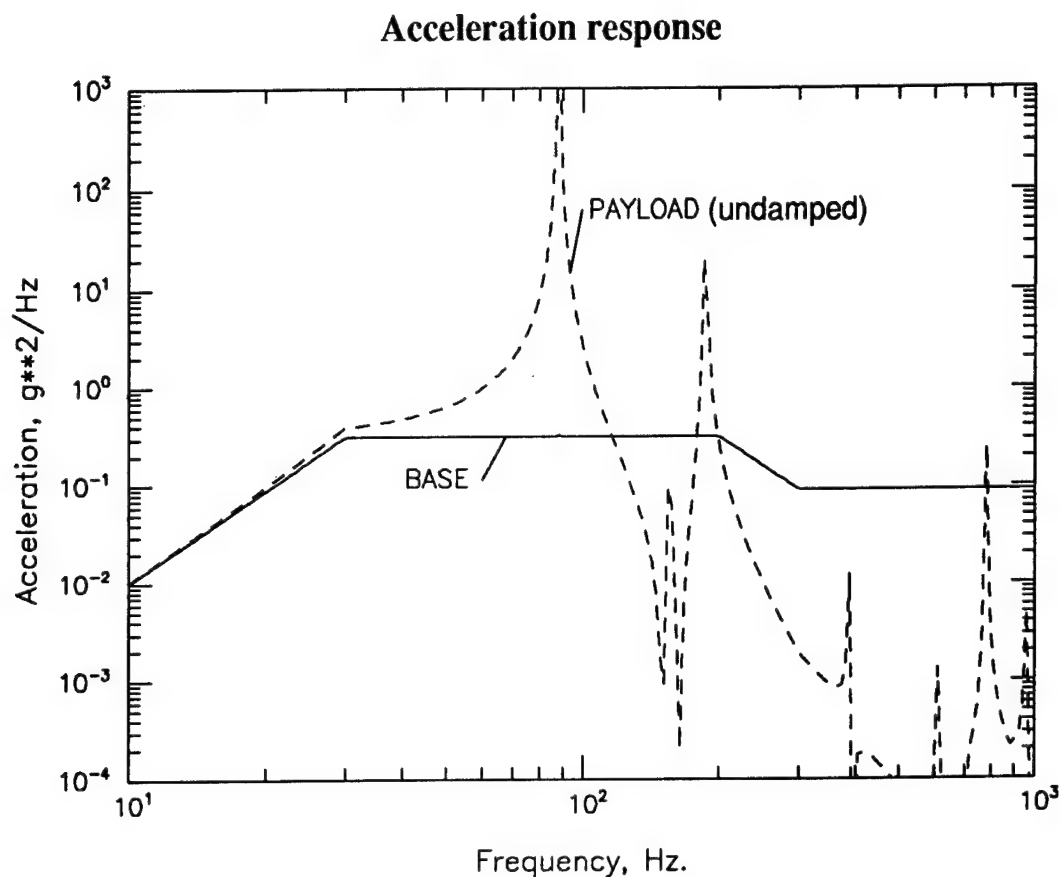
Figure 6. Undamped equipment tray: input and response

A design model (i.e., a definition of design variables, constraints, and an objective function) was prepared (Figure 7) for this problem. The optimizer is allowed to vary the thickness and shear modulus of the viscoelastic, the thickness of the base layer, and the thickness of the constraining layer.

```
$ Design model for equipment tray
$
CLT 1 CLT 4 .002 .100
$ Viscoelastic material thickness.  Refers to grid points 289-336
VEMT 2 VEMT .002 .050 -6
GLIST1 2 1.0 289 THRU 336
$ Viscoelastic material shear stiffness.
VEMG 3 VEMG 2 50.0 5000.0
$ Base layer thickness
CLT 2 BASE 1 .002 .500
$ Design objective: MSE for modes 2,3,4 (equally weighted)
DESOBJ SE MAX 2 1. 3 .5 4 .5
$ Constraint: weight not to exceed 22.7 lb.
CONSTR 11 WEIGHT 22.7
```

Figure 7. Equipment tray design model

An add-on treatment is initially selected. As shown in Figure 8, the response is reduced slightly, but the weight is increased substantially. Figure 9 shows the optimized damping tray obtained after just two cycles of optimization (i.e., two more complete NASTRAN analyses). The RMS response value (1.0 to 300 Hz) has been reduced by a factor of about seven while the weight has been reduced slightly below the weight of the undamped design. As the PSD response curve shows, the structure has been softened considerably, but the large increase in damping (over ten percent structural damping in the first three modes) has more than compensated for this softening in terms of response.

7. Current Research: Approximate Reanalysis

Computation of eigenvector sensitivities is rather time-consuming. Depending on the number of modes and the number of design variables involved, sensitivity analysis may take more computer time than the normal modes analysis itself. Approximate reanalysis promises to alleviate this problem by increasing the efficiency of the analysis itself in addition to the sensitivity computation.

Figure 10 illustrates how approximate reanalysis can contribute to the design process. For full optimization, it can be coupled with sensitivity analysis and an optimizer, as shown in the left branch of the chart. It could also be coupled with a curve-fitter for semi-automated optimization, or with manual redesign.
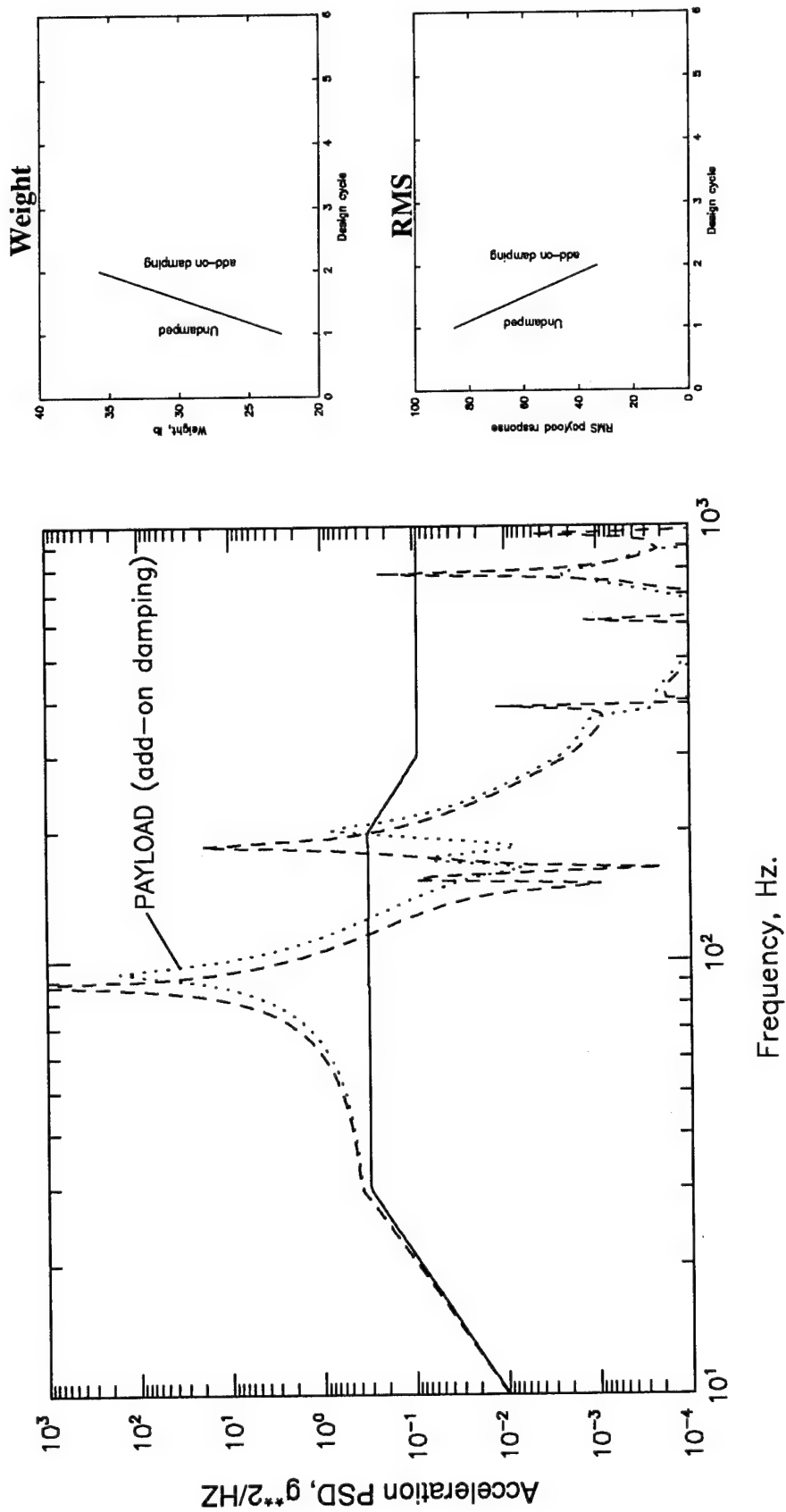
Figure 8. Manually selected add-on damping treatment
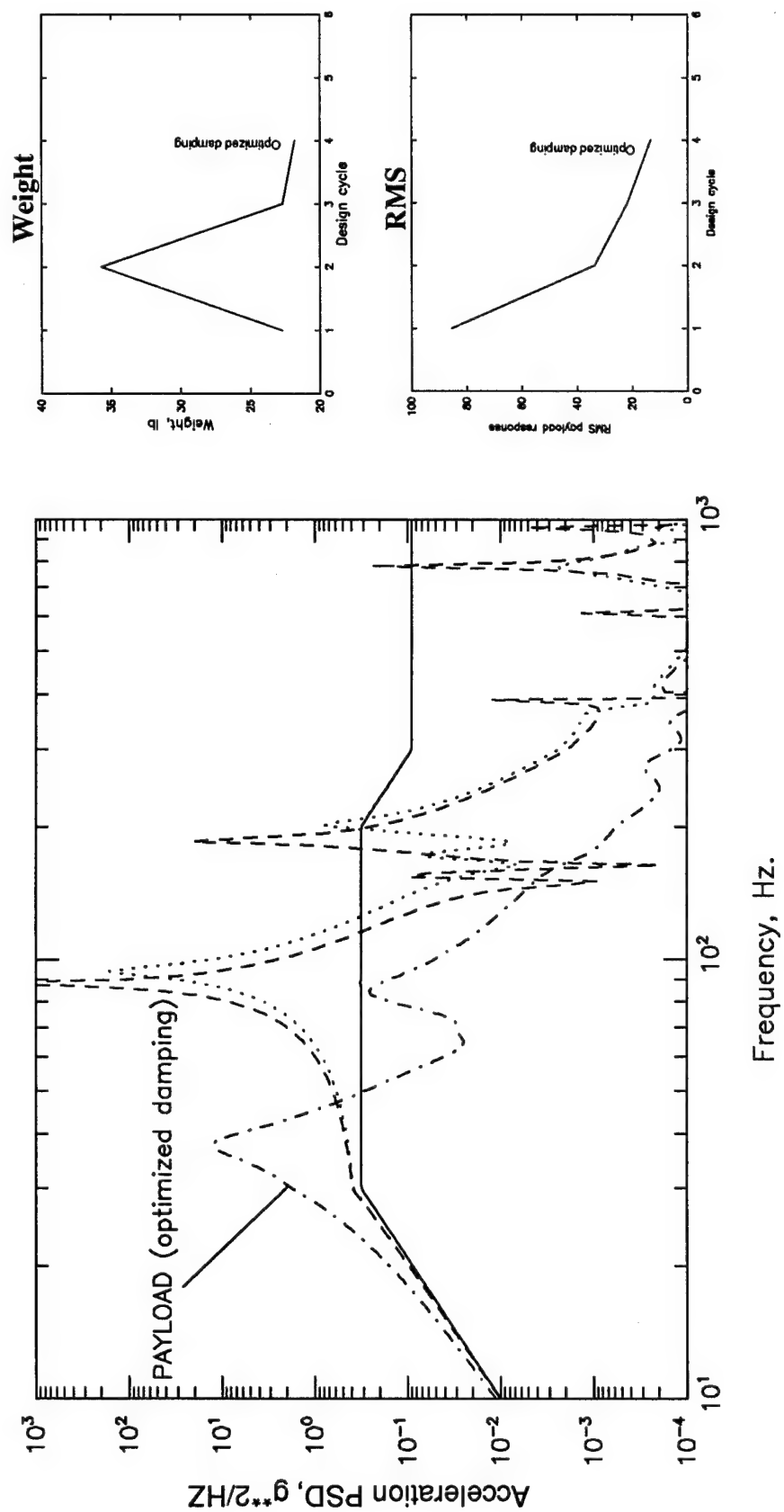
Figure 9. Optimized damping treatment
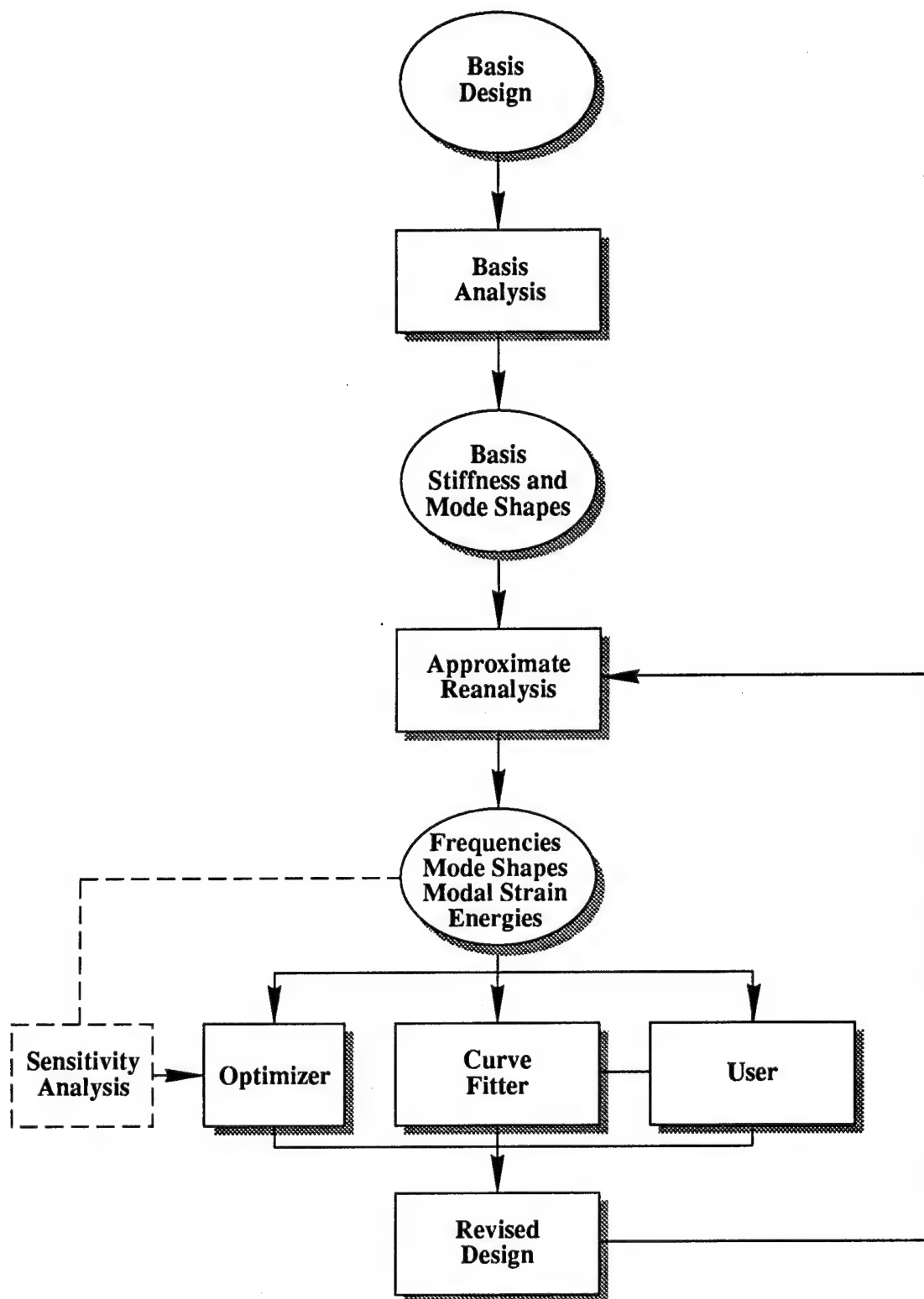
Figure 10. Approximate reanalysis for optimization

The basic premise of approximate reanalysis is that once a complete analysis has been performed for a particular design (the "basis" design), there is considerable information available from this analysis that can be "recycled" and used as the basis of a more economical redesign of a modified structure. At the outset, it was hoped that methods could be developed to provide both accurate reanalysis and accurate recomputation of sensitivities for "large" design variable changes (on the order of 100% or more). This goal has been met, as shown in the following section.

7.1   Basis Modes

The first approach that was pursued followed some work presented by Smith.[10] The idea is simply to use the modes of the basis design as a vector space for computation of revised eigenvalues and eigenvectors. Thus if one has a set of m basis modes collected in a matrix $\Phi^{(b)}$, the reanalysis problem, characterized by stiffness and mass matrices $\mathbf{K}$ and $\mathbf{M}$, may be transformed by

$$\mathbf{k} = \Phi^T \mathbf{K} \Phi \tag{5}$$

$$\mathbf{m} = \Phi^T \mathbf{M} \Phi \tag{6}$$

The reduced eigenvalue problem

$$(\mathbf{k} - \lambda \mathbf{m})\Psi = 0 \tag{7}$$

may be solved very economically, after which full sets of eigenvectors may be recovered as

$$\Phi = \Psi \Phi^{(b)} \tag{8}$$

This method is reminiscent of the modal superposition method of response calculation in that physical degrees of freedom are exchanged for a much smaller set of modal amplitudes.

Approximate sensitivity calculations could again be calculated economically by simply differentiating Eq. 8 to obtain

$$\frac{\partial \Phi}{\partial \mathbf{X}} = \frac{\partial \Psi}{\partial \mathbf{X}} \Phi^{(b)} + \Psi \frac{\partial \Phi^{(b)}}{\partial \mathbf{X}} \tag{9}$$

Computation of $\partial \Psi / \partial \mathbf{X}$ should be economical because of the small size of Ψ. Computation of the large set of sensitivities $\partial \Phi^{(b)} / \partial \mathbf{X}$, although time-consuming, would only have to be done once, or at least infrequently.

First experiments with this method were somewhat disappointing. While accurate frequencies could be obtained, the mode shapes, and particularly the modal strain energy values, were much less accurate. In one test problem it was necessary to compute as many as 75 modes of the basis structure in order to produce accurate modal strain energies for the first six modes of the revised structure.

Evidently the *change* in these mode shapes included significant contributions from many higher modes. This made the basis analysis rather costly and all but ruled out the possibility of computing sensitivities as in Eq. 9. That is, even if one culled out only those modes that made significant contributions to the approximate reanalysis, there would likely be so many that computation of their sensitivities ($\partial\Phi/\partial X$) would not be economical.

Upon rethinking this method, the authors noticed its resemblance to the well-known subspace iteration method of eigenanalysis (see Appendix B). After some experimentation, it was found that a single step of subspace iteration applied to the basis modes produced much better results. This consists of computing

$$\Psi = \mathbf{K}^{-1}\mathbf{M}\Phi^{(b)} \tag{10}$$

and then solving the reduced problem

$$\mathbf{k} = \Psi^T\mathbf{K}\Psi$$

$$\mathbf{m} = \Psi^T\mathbf{M}\Psi$$

$$(\mathbf{k} - \lambda\mathbf{m})\Phi = 0 \tag{11}$$

Early tests of this method show excellent agreement for the first fifteen modes of a test structure (natural frequencies, mode shapes, and modal strain energies) using only fifteen basis modes. Figure 11 shows timing figures for computation of the first fifteen modes of a structure having 2100 degrees of freedom. The solid line shows the time required for a complete NASTRAN analysis, and the dashed line shows the time required for approximate reanalysis. The dotted line shows the estimated additional savings using stiffness matrix extrapolation (explained below).

7.2 Extrapolation of Stiffness Matrices

The amount of time spent in computing and assembling element stiffness and mass matrices (as well as eliminating single- and multi-point constraints) is not trivial. If we focus attention on the particular kinds of elements and the particular design variables that are used in viscoelastic damping design, we can derive some simplifying assumptions that can be used to provide rapid regeneration of stiffness matrices for design changes.

Two kinds of elements are used in analysis of viscoelastic damping treatments: plate bending elements to represent the base layer and the optional constraining layer, and solid elements to represent the viscoelastic, as shown in Figure 2. The design variables, again, are viscoelastic thickness and shear modulus and constraining layer thickness.*

---

*The base layer thickness may also be included as a design variable, grouped with the constraining layer thickness design variables.
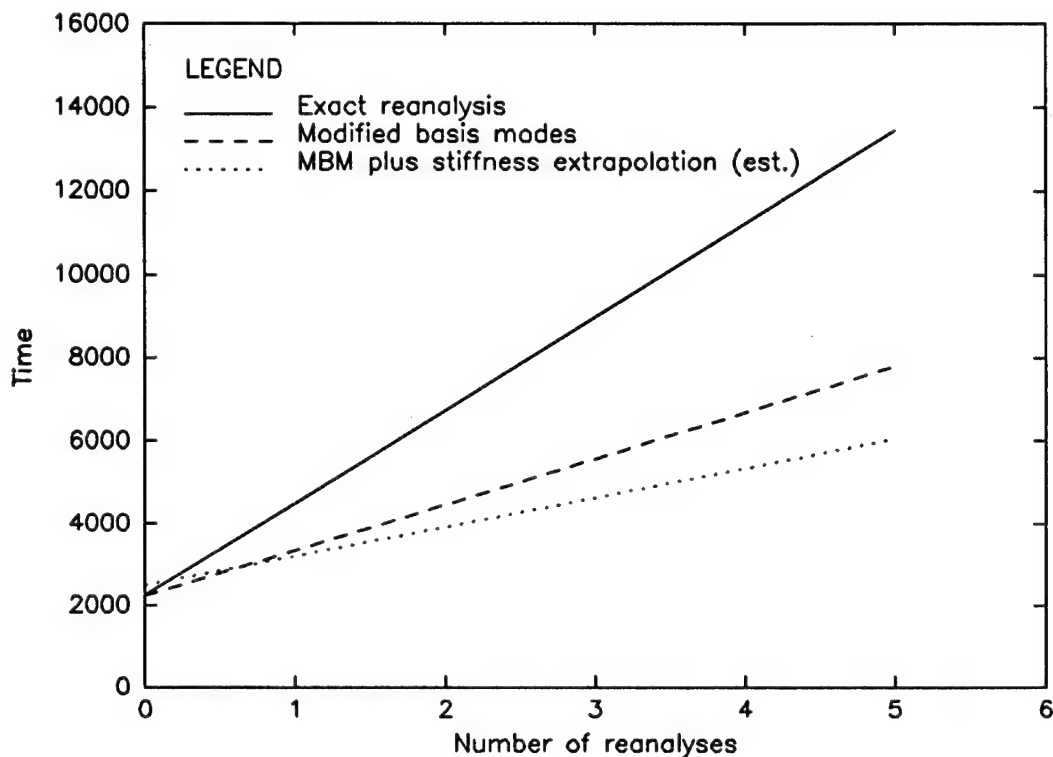
Figure 11. Time saved by approximate reanalysis

7.2.1 Plate Element Stiffness and Mass Matrix Variation

Plate bending element stiffnesses depend on the plate thickness t_c as follows:

- Membrane stiffness: proportional to t_c.

- Bending stiffness: proportional to t_c^3.

- Membrane-bending coupling stiffness (active in damping models due to placement of grid points at the plate elements' surfaces rather than at their center plane): proportional to t_c^2.

The plate stiffness is obviously insensitive to the viscoelastic shear modulus, and it is also insensitive to the viscoelastic thickness. Since this last assertion may contradict intuition, it needs some elucidation. Obviously a sandwich consisting of two plates separated by an intermediate material (viscoelastic, in this case) gets stiffer in bending roughly in proportion to the square of the distance separating the layers. Consider the assembled stiffness for such a layup as the sum of three parts: the upper layer, the middle layer, and the lower layer:

$$\mathbf{K} = \mathbf{K}_u + \mathbf{K}_m + \mathbf{K}_\ell \tag{12}$$

DBD-17

As t_v increases, $\mathbf{K}_u$ and $\mathbf{K}_\ell$ do not change. They consist of elements that merely undergo rigid-body motions and hence no change in stiffness.** The quadratic increase in stiffness comes from the fact that the grid points are farther apart. Thus a unit curvature of the sandwich means greater relative in-plane displacements of the two layers. The effect of these greater relative displacements multiplied by the modified total stiffness gives the overall quadratic variation with t_v.

The mass matrix for a constraining layer is clearly proportional to t_c.

While these arguments are well-grounded theoretically, we do not have access to the source code that generates stiffnesses for QUAD4 elements in MSC/NASTRAN. Hence it was deemed prudent to carry out some "experiments" that compared extrapolated stiffness and mass matrices with those generated by MSC/NASTRAN. These experiments yielded favorable results with and without offsets.

The details of the extrapolation are as follows. NASTRAN was used to generate an element stiffness matrix for four values of thickness: a reference value t_{c_0} and incremented values $t_{c_0}(1 + \delta)$ and $t_{c_0}(1 + 2\delta)$ where δ is an arbitrary increment, say 5%. Call the corresponding stiffnesses $\mathbf{K}_0$, $\mathbf{K}_1$, and $\mathbf{K}_2$. We then write the approximation formula as

$$\mathbf{K}(t_c) \approx \widehat{\mathbf{K}}_0(t_{c_0}) + \widehat{\mathbf{K}}_1(t_c - t_{c_0}) + \widehat{\mathbf{K}}_2(t_c - t_{c_0})^2 \tag{13}$$

It should be emphasized that each $\widehat{\mathbf{K}}$ is a complete matrix. This means that each term of the stiffness matrix can have a separate cubic variation. One would expect to see membrane terms having only $\widehat{\mathbf{K}}_1$ entries, bending terms having only $\widehat{\mathbf{K}}_2$ terms, etc. However, again due to the lack of access to the QUAD4 source code, not to mention reluctance to delve into it, an empirical approach has been taken.

Finally, after some algebra, we obtain expressions for the coefficient matrices $\widehat{\mathbf{K}}$ in terms of $\mathbf{K}$:

$$\widehat{\mathbf{K}}_0 = \mathbf{K}_0 \tag{14}$$

$$\widehat{\mathbf{K}}_1 = \frac{1}{2(t_c - t_{c_0})}\left[-3\mathbf{K}_0 + 4\mathbf{K}_1 - \mathbf{K}_2\right] \tag{15}$$

$$\widehat{\mathbf{K}}_2 = \frac{1}{2(t_c - t_{c_0})^2}\left[\mathbf{K}_0 - 2\mathbf{K}_1 + \mathbf{K}_2\right] \tag{16}$$

The case of a singly-curved damping layer has not been considered but should be straight-forward. NASTRAN has no curved shell elements and hence a curved shell has to be modeled as a facetted assemblage of flat plate elements. This is not particularly controversial among finite element analysts as long as the angle subtended by a single element is reasonable, say, 30 degrees or less. In this case two opposite sides of the element get longer in proportion to changes in the viscoelastic

---

**Assuming flat damping treatments. Curved treatments are considered later.

thickness. One would expect a cubic increase in *flexibility* in this case which might lead to the expanded approximation

$$\mathbf{K}(t_c) \approx \mathbf{K}_0(t_{c_0}) + \widehat{\mathbf{K}}_1(t_c - t_{c_0}) + \widehat{\mathbf{K}}_2(t_c - t_{c_0})^2$$
$$+\widehat{\mathbf{K}}_{-1}(t_v - t_{v_0})^{-1} + \widehat{\mathbf{K}}_{-2}(t_v - t_{v_0})^{-2} \tag{17}$$

The case of a doubly-curved viscoelastic layer is possible but is not considered here.

7.2.2   Solid Element Stiffness and Mass Matrix Variation

The viscoelastic solid element stiffnesses are clearly affected only by changes in the viscoelastic shear modulus and layer thickness, and not by the constraining layer thickness.

The shear modulus is dealt with most easily. The entire element stiffness matrix is proportional to G. This may be clearer if E and ν are used as independent elasticity constants. E is proportional to G and E appears as a scalar factor in front of the stiffness matrix.[11] However, this assertion was tested and confirmed with HEXA elements. Thus changes in shear modulus may be handled by simply scaling the viscoelastic stiffness matrix:

$$\mathbf{k}_v = \frac{G}{G_0}\mathbf{K}_{v_0} \tag{18}$$

We now turn to the variation in solid element stiffness as the length of one side (i.e., the layer thickness) varies. Refer to Figure 12 which shows a thin solid element with sides a and b and thickness t. For simple in-plane extension, one would expect stiffness terms like the AE/ℓ of a rod, i.e., Ebt/a or Eat/b. For in-plane shear, one would expect Gt/ab. For extension in the thin direction, Eab/t. From these observations we jump to the conclusion that each term in the stiffness matrix is either directly or inversely proportional to t. This assumption is only applied to the limited shape we are considering here, namely a completely rectangular element with one side much shorter than the others. This assumption was tested empirically for a small thickness change. From a printout, it was observed that all the terms seemed to be *nearly* proportional to t_v or $1/t_v$, with some staying constant. This was enough to proceed boldly with the assumption

$$\mathbf{K}_v \approx \mathbf{K}_c + \frac{t_{v_0}}{t_v}\mathbf{K}_{-1} + \frac{t_v}{t_{v_0}}\mathbf{K}_1 \tag{19}$$
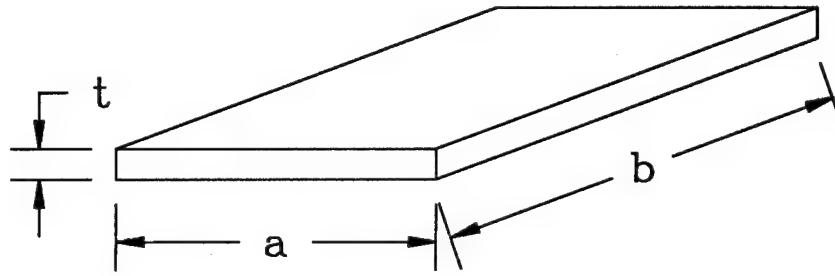
Figure 12. Solid element

The variation of the viscoelastic and constraining layer thicknesses with the various design variables is summarized in the following table:

Design	Stiffness		Mass	
variable	VEM	CL	VEM	CL
G	linear scalar	independent	independent	independent
t_v	linear, constant, inverse matrices	independent	linear scalar	independent
t_c	independent	constant, linear, quadratic, cubic matrices	independent	independent

Appendix A: Modal Strain Energy Sensitivity Calculations

The sensitivity analysis for modal strain energies, coded in NASTRAN's DMAP language, proceeds as follows:

For each design variable X_i:

1. Compute approximations to the stiffness and mass matrix sensitivities $\partial K/\partial X_i$ and $\partial M/\partial X_i$ by finite differences. This involves incrementing grid locations, a shear modulus, or a plate thickness, depending on whether design variable X_i represents a viscoelastic thickness, viscoelastic shear modulus, or constraining layer thickness.

2. For each mode j whose strain energy sensitivity is required, do the following:

(a) Compute the eigenvalue sensitivity using the formula

$$\frac{\partial \lambda_j}{\partial \mathbf{X}_i} = \mathbf{\Phi}_j^T \left(\frac{\partial \mathbf{K}}{\partial \mathbf{X}_i} - \lambda_j \frac{\partial \mathbf{M}}{\partial \mathbf{X}_i} \right) \mathbf{\Phi}_j$$

from which the frequency sensitivity is

$$\frac{\partial f_j}{\partial \mathbf{X}_i} = \frac{1}{8\pi^2 f_j} \frac{\partial \lambda_j}{\partial \mathbf{X}_i}$$

(b) Compute the eigenvector sensitivity using Nelson's method.[12] Solve

$$\frac{\partial \mathbf{\Phi}_j}{\partial \mathbf{X}_i} = (\mathbf{K} - \lambda_j \mathbf{M})^{-1} \left[\frac{\partial \lambda_j}{\partial \mathbf{X}_i} \mathbf{M} + \lambda_j \frac{\partial \mathbf{M}}{\partial \mathbf{X}_i} - \mathbf{K} \right] \mathbf{\Phi}_j$$

Since $(\mathbf{K} - \lambda_j \mathbf{M})$ is singular, its order is first reduced by one by invoking the normalization that was used for $\mathbf{\Phi}_j$.

(c) Compute modal strain energy ratio sensitivities. Let

$$S_j^{(v)} = \frac{1}{2} \mathbf{\Phi}_j^T \mathbf{K}^{(v)} \mathbf{\Phi}_j \quad \text{(viscoelastic strain energy)}$$

$$S_j = \frac{1}{2} \mathbf{\Phi}_j^T \mathbf{K} \mathbf{\Phi}_j \quad \text{(total strain energy)}$$

$$R_i = \frac{S_i^{(v)}}{S_i} \quad \text{(ratio)}$$

(d) Differentiate:

$$\frac{\partial S_j^{(v)}}{\partial \mathbf{X}} = \mathbf{\Phi}_j^T \mathbf{K}^{(v)} \mathbf{\Phi}_j + \frac{1}{2} \mathbf{\Phi}_j^T \frac{\partial \mathbf{K}^{(v)}}{\partial \mathbf{X}} \mathbf{\Phi}_j$$

$$\frac{\partial S_j}{\partial \mathbf{X}} = \mathbf{\Phi}_j^T \mathbf{K} \mathbf{\Phi}_j + \frac{1}{2} \mathbf{\Phi}_j^T \frac{\partial \mathbf{K}}{\partial \mathbf{X}} \mathbf{\Phi}_j$$

$$\frac{\partial R_j}{\partial \mathbf{X}} = \frac{1}{S_j} \left[\mathbf{\Phi}_j^T \mathbf{Q}_j + \frac{1}{2} \mathbf{\Phi}_j^T \hat{\mathbf{Q}}_j \right] \mathbf{\Phi}_j$$

where

$$\mathbf{Q}_j = \mathbf{K}^{(v)} - R_j \mathbf{K}$$

$$\hat{\mathbf{Q}}_j = \frac{\partial \mathbf{K}^{(v)}}{\partial \mathbf{X}_i} - R_j \frac{\partial \mathbf{K}}{\partial \mathbf{X}_i}$$

Derivations of the expressions used here may be found in reference 8.[8]

Appendix B: Subspace Iteration

Subspace iteration is a popular eigenvalue analysis method.[13] Briefly, this method consists of the following steps:

1. Select a set of starting vectors $\hat{\boldsymbol{\Phi}}^{(1)}$. Set the iteration count $k = 1$.

2. Compute $\boldsymbol{\Phi}^{(k+1)} = \mathbf{K}^{-1}\mathbf{M}\hat{\boldsymbol{\Phi}}^{(k)}$

3. Orthonormalize the new approximation $\boldsymbol{\Phi}^{(k+1)}$ by forming and solving the following small eigenproblem:

    (a) Let $\mathbf{k}^{(k+1)} = \boldsymbol{\Phi}^{(k+1)T}\mathbf{K}\boldsymbol{\Phi}^{(k+1)}$

    (b) Let $\mathbf{m}^{(k+1)} = \boldsymbol{\Phi}^{(k+1)T}\mathbf{M}\boldsymbol{\Phi}^{(k+1)}$

    (c) Solve $[\mathbf{k}^{(k+1)} - \lambda\mathbf{m}^{(k+1)}]\boldsymbol{\Psi} = 0$

4. For the next iteration, use $\hat{\boldsymbol{\Phi}}^{(k+1)} = \boldsymbol{\Phi}^{(k+1)}\boldsymbol{\Psi}$. It can be shown that because the vectors $\boldsymbol{\Psi}$ are orthonormal with respect to $\mathbf{m}^{(k+1)}$, $\hat{\boldsymbol{\Phi}}^{(k+1)}$ is orthonormal with respect to $\mathbf{M}$.

5. Increment k; go to step 2.

The efficiency of subspace iteration depends on selection of a suitable set of trial vectors. There is also a theoretical possibility of selecting trial vectors that are exactly orthogonal to one of the eigenvectors so that this eigenvector would be missed. In practice, numerical roundoff makes it very likely that some component of such an eigenvector will creep into the solution set so that the eigenvector will be computed.

References

1. Johnson, C. D., Kienholz, D.A., and Rogers, L. C, "Finite Element Prediction of Damping in Beams with Constrained Viscoelastic Layers," *Shock and Vibration Bulletin*, No. 51, May 1981.

2. Johnson, C. D. and Kienholz, D. A., "Finite Element Prediction of Damping in Structures with Constrained Viscoelastic Layers," *AIAA J.*, Vol. 20, No. 9, Sept. 1982.

3. Johnson, C. D., "Design and Analysis of Damped Structures using Finite Element Techniques," ASME Paper No. 85-DET-131, Conference on Mechanical Vibration and Noise, Cincinnati, OH, Sept. 1985.

4. Fowler, B. L., "Interactive Characterization and Database Storage of Complex Modulus Data," presented at DAMPING '89, West Palm Beach, FL, January 1989.

5. Vanderplaats, G. N., *Numerical Optimization Techniques for Engineering Design with Applications*, McGraw-Hill, 1984.

6. Vanderplaats, G. N., *ADS – A Fortran Program for Automated Design Synthesis*, Version 1.10, May 1985. Available from EDO, Inc., 1275 Camino Rio Verde, Santa Barbara CA 93111.

7. Schmit, L. A., and Miura, H., "Approximation Concepts for Efficient Structural Synthesis," *NASA CR2552*, March 1976.

8. Gibson, W. C., "ODAMP User's Manual," CSA Engineering Report No. 87-05-02, May 1987.

9. Fowler, B. L., and Gibson, W. C., "MSET (Modal Strain Energy Tabulator) User's Manual, CSA Engineering Report No. 88-04-02, April 1988.

10. Smith, C. M., "The Application of Reanalysis Techniques to Large Finite Element Models Through NASTRAN DMAP," 1988 MSC World User's Conference, Universal City, CA, March 1988.

11. Zienkiewicz, O. C., *The Finite Element Method in Engineering Science*, McGraw Hill, Chapter 6, 1971.

12. Nelson, R., "Simplified Calculation of Eigenvector Derivatives," *AIAA J.*, Vol. 14, No. 9, pp. 1201-1205, 1976.

13. Meirovitch, L., *Computational Methods in Structural Dynamics*, Sijthoff & Noordhoff, Section 10.5, 1980.

CONSIDERATIONS OF SYNTHESIZED SYSTEM DAMPING IN DYNAMIC ANALYSIS OF SPACE STRUCTURES

Wan T. Tsai *

ABSTRACT

In considerations of space structures, a great number of degree-of-freedoms (DOFs) are modelled and thousands of them are retained for dynamic analysis. Natural frequencies of the structure represented by the retained DOFs may be very close to each other and the system is easily over-excited by the applied forcing function when it contains frequencies in the vicinity of the natural frequencies. In order to bring the excessive excitement down to a somewhat more realistic response level, viscous damping is usually applied. Since the damping coefficient for a flight system can not be directly obtained from ground tests, no test derived system damping is available. Damping coefficient for substructure constrained at the interface DOFs to a rigid base is obtained instead. The coefficients obtained from this test are applied to appropriate DOFs of the discrete substructure and the coefficients related to the interface DOFs are assumed to be zero. The damping matrix so constructed, upon releasing the constrained DOFs of the discrete substructure, is then transformed into an equivalent matrix for flight system analysis. Known as triple-matrix-product (TMP), this method of constructing a damping matrix by neglecting the off-diagonal elements has been widely adopted in aerospace industries. This paper is first to assess the validity of the above stated damping matrix of a discrete structure and the TMP approach, and then to propose a new method in constructing the system damping matrix by using the damping coefficient obtained from ground test. Specifically, the proposed damping matrix is synthesized by a diagonal matrix in the free-free system coordinates. Its corresponding damping elements in the substructural coordinates are best fitted to the test derived damping by using Gaussian least square technique. Applicability of the result is illustrated and assesed.
----

* Member of Technical Staff, Payload Cargo Loads Analysis, Rockwell International, Downey, California. Members of ASME, ASCE.

CONSIDERATIONS OF SYNTHESIZED SYSTEM DAMPING
IN DYNAMIC ANALYSES OF SPACE STRUCTURES

Wan T. Tsai

Member of Technical Staff
Payload Cargo Loads Analysis, Rockwell International
Downey, California

INTRODUCTION

In dynamic analyses of a large structural system, geometric and
material characteristics are represented by a system of mass and
stiffness matrices. Together with a damping matrix, they
constitute a complete set of governing differential equations for
structural response analyses when applied forcing functions and
appropriate initial conditions are given. Both mass and stiffness
matrices are derived from analytical means. The damping matrix
which can not be determined by analysis is usually obtained in
conjunction with generalized modes of the structural system.
Specifically, the analytically derived mass and stiffness matrices
are used to establish a transformation matrix. Through this, the
mass matrix can be transformed into an identity matrix and the
stiffness matrix into a diagonal matrix in which the diagonal
elements are the square of circular frequencies. Thus, a damping
matrix, called system damping, is defined by multiplying a set of
coefficients to a diagonal matrix consisting of circular
frequencies. At this point, the set of equations in the
generalized coordinate system consists of many independent
differential equations. Each is a single degree-of-freedom (DOF).
This set of equations can be solved by using the TRD module of the
NASTRAN computer program [1]. Structural responses are then
obtained by inverse transformation of the generalized DOFs.

It is known that coefficients of system damping are different for
each mode. Their magnitudes can be derived from modal survey test
results of the complete structural system. Since a space structure
consists of a great number of DOFs and is actually operated in
space of near zero gravity environment, it is very difficult, if
not impossible, to establish system damping values through testing
of the complete structure on the ground before a flight. In order
to estimate the damping coefficients, an alternate method using
modal survey test of the substructures constrained at their
boundary DOFs is usually performed. The damping matrices obtained
from modal survey tests of all the substructures together with
assumed damping values in their boundary DOFs are then coupled into
a Craig-Bampton (C-B) form [2] in the same manner as that for
coupling the mass and stiffness matrices. However, a mathematical
difficulty arises now. This newly coupled damping matrix, the
discrete damping, can only be transformed into a fully populated
damping matrix in the generalized coordinates. Thus, all
generalized DOFs are still coupled to each other through the
transformed damping matrix. The advantage for reducing
computational time by using the TRD module is lost and the cost to

solve these equations for a large structural system can not be
saved. In order to take the advantage of using TRD module, an
approximation by removing the off-diagonal elements from the
transformed damping matrix has been commonly practiced. When this
is done, the damping matrix becomes a diagonal, known as the triple
matrix product (TMP) damping [3]. The set of generalized equations
now become independent. The TRD module can then be readily applied
to perform loads analyses with low computer cost.

The TMP damping technique has been proved to be a good
approximation. Usually, results within an acceptible range of
error can be obtained. Occasionally, unexplainable reponses occur.
In a study of loads analysis for space transportation system
payload, a larger response at a larger damping coefficient has been
seen for a particular DOF when the damping value is within a
particular range. The cause for this type of behavior is yet
unclear. It may be partially induced by the use of TMP damping,
since the practice of neglecting the off-diagonal elements is
arbitrary. A new approach is proposed to refine the damping matrix
used in system analyses. The proposed method applies Gaussian
least square technique to synthesize the system damping. The
condition is that the synthesized damping yields a smallest error
between the converted and the given discrete damping values.

As an introductory development, the paper starts with a brief
review of the TMP method. Derivations for the proposed approach
follows. The goals of this approach are: (1) the synthesized
system damping is a diagonal matrix; (2) the converted values of
the synthesized damping are best fitted to the discrete damping;
and (3) structural responses using the proposed method are at least
as good as the results of TMP method. An example of a uniform beam
is used to illustrate the characteristics of the proposed method.
Results are compared to those obtained from both direct integration
and TMP methods.

BRIEF REVIEW OF TRIPLE MATRIX PRODUCT DAMPING METHOD

To simplify matrix formulations for a structural system, let the
mass, damping, and stiffness matrices of substructures be expressed
in the C-B form. Explicitly, the boundary DOFs are kept in
physical coordinates. The interior DOFs are represented by modal
coordinates while the boundary DOFs are assumed to be completely
constrained for each substructure. Upon coupling several
substructures together to form a complete structural system, the
governing differential equations for the system is given by

$$M\ddot{y} + D\dot{y} + Ky = P \qquad\qquad (1)$$

where M, D, and K are respectively the mass, damping, and stiffness
matrice, y the displacement vector consisting of physical
components at boundary DOFs and modal components at interior DOFs,
$\dot{y}=dy/dt$, and P the forcing vector associated with the y component
coordinates. Explicitly expressed into the C-B form, M, D, and K
appeaar

$$M = \begin{bmatrix} M_{bb} & | & M_{bi} \\ \hline M_{ib} & | & M_{ii} \end{bmatrix}, \qquad K = \begin{bmatrix} K_{bb} & | & K_{bi} \\ \hline K_{ib} & | & K_{ii} \end{bmatrix} \qquad (2a,b)$$

$$D = \begin{bmatrix} D_{bb} & | & D_{bi} \\ \hline D_{ib} & | & D_{ii} \end{bmatrix} \qquad (2c)$$

In these matrices, the subscripts b and i are respectively associated with boundary and interior DOFs of substructures. The submatrices with subscripts ii are diagonal. D_{ii} is the diagonal discrete damping obtained from substructural modal test. D_{bi}, D_{ib}, and D_{bb} are usually left empty due to the lack of test data. This assumption is believed to be conservative. Occasionally, D_{bi} and D_{ib} are assumed to be empty and D_{bb} is given by a set of nonzero values associated with a subsystem damping when boundary DOFs alone are treated as an independent subsystem [4].

The exact method of transforming Eq.(1) into a generalized coordinate system is through the use of complex variable modes. This method of analysis has been shown in many publications, for instance [5]. However, a real variable transformation appears to be more popularly accepted even though it is an approximate approach. The procedure of the approximation is as follows. Let η be the generalized DOFs corresponding to y by

$$y = \phi\eta \qquad (3)$$

where ϕ is the transformation matrix satisfying

$$\phi'M\phi = I, \qquad \phi'K\phi = W \qquad (4a,b)$$

In Eqs.(4a,b), ϕ' is the transpose of ϕ, I an identity matrix, and W a diagonal matrix. The diagonal elements of W are the square of circular frequencies. Introduction of Eqs.(3,4) into Eq.(1) gives

$$\ddot{\eta} + C\dot{\eta} + W\eta = Q \qquad (5)$$

where $Q=\phi'P$ and

$$C = \phi'D\phi \qquad (4c)$$

C is a fully populated matrix. Since the off-diagonal elements are generally smaller than the diagonal elements, the response using the fully populated matrix, C, makes little difference from that using the diagonalized TMP damping, C_d=diag(C). Using this matrix, the generalized DOFs are approximately computed from Eq.(5) upon replacing C by C_d. Namely,

$$\ddot{\eta} + C_d\dot{\eta} + W\eta = Q \qquad (5*)$$

Effectively, the responses obtained from Eq.(5*) are actually not associated with the provided discrete damping matrix D, but with a fully populated equivalent damping matrix, D_d. Namely;

$$D_d = (\phi^{-1})'C_d(\phi^{-1}) \tag{6}$$

Using the responses determined from Eq.(5*), the physical responses of structures are then computed from Eq.(3).

SYNTHESIS OF SYSTEM DAMPING

Let B be the diagonal matrix to be synthesized in the generalized coordinates and F the converted matrix of B in the C-B coordinates. The correlation between B and F is

$$F = (\phi^{-1})'B(\phi^{-1}) \tag{7}$$

By letting b_k be the diagonal elements of B and f_{ij} be the elements of F, the element correlations in Eq.(7) can be written by

$$f_{ij} = \sum_{k=1}^{n} b_k \, g_{kij} \tag{8}$$

where g_{kij} is the coefficient associated with f_{ij} when the kth element alone in matrix B is a unity, all other elements are zero.

Now, let d_{ij} be the elements of discrete damping matrix D. The sum of the square of the differences between converted damping f_{ij} and provided discrete damping d_{ij} is

$$S = \sum_{j=1}^{n_b} \sum_{i=j}^{n_b} (f_{ij} - d_{ij})^2 + \sum_{j=n_b+1}^{n} (f_{jj} - d_{jj})^2 \tag{9}$$

where n_b is the number of boundary DOFs. Upon substituting Eq.(8) into Eq.(9), the sum becomes a function of the diagonal elements b_k. Thus, a set of Gaussian least square functions is formed when S is minimized by the condition

$$\frac{\partial S}{\partial b_m} = 0, \qquad m = 1,2,\ldots,n \tag{10}$$

Explicitly, Eqs.(8-10) give a system of linear algebraic equations for elements b_k in the form

$$\sum_{k=1}^{n} \left(\sum_{j=1}^{n_b} \sum_{i=j}^{n_b} g_{kij} g_{mij} + \sum_{j=n_b+1}^{n} g_{kjj} g_{mjj} \right) b_k$$

$$= \sum_{j=1}^{n_b} \sum_{i=j}^{n_b} d_{ij} g_{mij} + \sum_{j=n_b+1}^{n} d_{jj} g_{mjj} \quad , \; m=1,2,\ldots,n. \tag{11}$$

Using Eq.(11), the synthesized elements of system damping matrix B are obtained. The generalized DOFs can then be determined by using Eq.(5) upon replacing C by the synthesized damping matrix B. The structural responses can then be evaluated by using Eq.(3).

It is noted that the best fit shown in Eq.(9) includes only the specified discrete damping elements, those belonging to the boundary DOFs and the diagonal elements of internal DOFs. The rest of elements are not included in the fitting. In fact, it is uncertain if the off-diagonal discrete damping elements are really zero [6]. Therefore, it may be acceptible for practical applications to neglect fitting of elements which are not really obtained from testing but from assumptions.

ILLUSTRATION

To illustrate the performance of TMP method, let us consider a uniform beam of 25 translational DOFs. The total length is 120 inches and it is equally spaced into 24 segments. The beam properties are A=.0974 sq. in., I=.0480 in^4., E=10^6 psi, and ρ=.0318 lb-sec^2/in^4. The boundary nodes are 1, 6, 13, 18, and 25 (Fig. 1). Heavisides step forcing functions are applied to three points of the beam, 5 lbs at both ends (nodes 1 and 25) and 10 lbs at the middle point (node 13). A nominal damping coefficient of 10% for the interior modal DOFs of C-B form is assumed in order to easily illustrate the contribution of damping. Two cases of damping values at boundary DOFs are considered, D_{bb}=0 and $D_{bb}\neq0$. For the case of $D_{bb}\neq0$, a set of damping value equivalent to 10% is applied when M_{bb} and K_{bb} are assumed to be an independent subsystem. Explicitly, a transformation is first performed to generalize the boundary DOFs alone into a subsystem. A subsystem damping of 10% is then obtained. Inverse transformation of the subsystem damping, the boundary damping matrix D_{bb} is thus defined. To simplify the analysis, no other substructure is coupled to the beam. Therefore, the problem is simply the transformations between C-B form and the generalized system.

Based on the material and geometric properties, the matrices of mass, stiffness, and discrete damping are established. Through the use of Eqs.(3-5*), structural responses are obtained. To verify the damping values actually used in TMP response analysis, Eq.(6) is applied to transform the TMP damping back to C-B coordinates. The diagonal elements of the converted matrix are then compared to the corresponding elements of the discrete damping. The results shown in Table 1 indicates that the converted damping are significantly different from the provided discrete damping. The maximum error is up to 23% in the 6th mode for the case without boundary damping. When the synthesized damping is applied, the maximum error of converted diagonal damping are less than 1% in all modes for both cases of D_{bb}=0 and $D_{bb}\neq0$. Therefore, the synthesized system damping are much more accurate than TMP damping when the discrete damping values are compared.

Despite the significant discrepancies between the provided discrete damping and the damping values actually used in the TMP method, the responses are in good agreement with the results of direct integrations of using the discrete damping. As shown in Table 2, the largest response error which happens to be at the negative value of node 6 is only over-estimated by 1.6% with respect to the

peak acceleration 1.672 g, for the case of $D_{bb} \neq 0$. The corresponding maximum error by using the synthesized system damping method is 2.9% at the negative value of node 18, for the case $D_{bb}=0$. It must be noted that if the errors are computed by using local values, the maximum errors become very large. They are respectively 11.2% for TMP and 20.3% for synthesized system damping methods, both at the negative value of node 18 for the case of $D_{bb} \neq 0$. However, due to ignorance of accumulated numerical error acquired by using these approximate methods, this way of numerical comparison may not be fair. Generally, the results obtained from both TMP and synthesized damping methods are about in the same degree of accuracy. TMP may be slightly more accurate than the synthesized damping in this illustration.

Nevertheless, the proposed approach provides room for future improvement that TMP method does not. One of the possible improvement in syntheses of system damping is to weigh the importance of certain particular DOFs by using participation factors of the associated forcing functions. Although formulations using the factors are yet to be derived, one can capture the concept by studying the correlations between system mode shapes and the distribution of forcing functions. For this purpose, the damping values at generalized DOFs must be considered. Table 3 shows that the values for both TMP and synthesized damping are fairly close for some modes, but are significantly different for others. This indicates that the responses by using TMP damping and synthesized damping may be significantly different, depending upon the frequency of the applied forcing function. For a set of three point loads applied to the beam, the distribution of the forcing function is close to the 5th mode if it is expanded into mode shapes of the beam. Explicitly, the forcing function is more sensitive to frequency 5.2 Hz of the 5th mode. The successive important frequencies are 23.5 Hz for the 9th mode, 54.4 Hz for the 13th mode, etc., since these mode shapes, as shown in Fig. 1 for the first 9 modes, are closer to the distribution of the applied forcing function. Using these modes, it is shown by Table 3 that the coefficients of both TMP and synthesized damping are fairly close. Therefore, the responses due to both methods are little different. It may be expected that structural responses become significantly different if the distribution of forcing functions coincides with a mode for which the damping coefficients in TMP and synthesized approaches are significantly different.

The results between the cases $D_{bb}=0$ and $D_{bb} \neq 0$ must also be noted. These results are independent of the methods of analysis. For the case of $D_{bb}=0$, Fig. 2 shows that the amplitude of oscillations are fairly uniform after the early time spikes. However, Fig. 3 for the case of $D_{bb} \neq 0$ reveals that the responses decay considerably at later time. Therefore, boundary damping is important to structural responses. Due to the lack of test data, it may be difficult to establish a perfect boundary damping. Until a better approach is available, a uniform subsystem damping of 1% or 2% in the form similar to that illustrated earlier for $D_{bb} \neq 0$ may be acceptable for practical applications.

DISCUSSIONS AND CONCLUSIONS

The purpose of this study is to synthesize a system damping matrix that may best simulate the true damping behavior of a structural system. Using a given discrete damping matrix, a new approach in synthesis of system damping by using Gaussian least square is proposed. The synthesized damping matrix is always a diagonal and is readily applicable to the TRD module in NASTRAN. As illustrated by a uniform beam subjected to three point step function forces, the synthesized damping are in excellent agreement with the provided discrete damping in C-B coordinates. The structural responses using the synthesized damping also correlate very well with those using direct integration. Therefore, the new approach is worthy of further investigation for developing an improved method which can best represent the true system damping.

Many possible syntheses can be made to upgrade the proposed method, depending upon the goal of an analysis. Specifically, a set of participation factors can be assigned to weigh a class of interest. Using the factors as a weighting function, a best fit can be performed for the interest of certain structural components. For instance, the damping values can be best estimated for certain DOFs that are closest to the modes and frequencies of forcing functions as explained earlier.

In addition to the potential of the proposed method in synthesizing system damping, several properties found from the illustration may be useful for future refinement of the method. (1) Variations of boundary damping may significantly influence structural responses. The influence is more expressive for late time than for early time responses. (2) Discrepancies between the provided discrete damping and the converted values of TMP and synthesized damping appear to be not an important factor to structural responses. It is known that this may not be a correct statement. Further study is required to determine the true correlations. (3) The 10% constant discrete damping in the C-B coordinates are different from those in the generalized coordinates. It is particularly significant in the low frequency modes.

ACKNOWLEDGEMENTS

REFERENCES

1. ROCKWELL NASTRAN THEORETICAL MANUAL, Level 17.500, Rockwell Int'l, M8700282, June 1979.
2. Craig, R. R., Bampton, M. C., "Coupling of Substructures for Dynamic Analysis," AIAA J., Vol. 7, July 1968, pp 1313-1319.
3. Johnson, E. W., "Effect of SSV Residual Model Damping and Fixed Interface SSV Component Damping on Coupled SSV/Cargo Element Systems," Martin Marietta Corp., MCR-85-2019, Dec. 1985.

4. Cao, T., Tengler, N, "JSC Analysis of Orbiter Seat/Floor
   Lift-off and Landing Loads Using Triple Matrix Product (TMP)
   Damping," JSC Loads and Structural Dynamics Branch, Sep. 1988,
   (unpublished).
5. Beliveau, J. G., Soucy, Y., "Damping Synthesis Using Complex
   Substructure Modes and A Hermitian System Representation," AIAA
   26th Structures, Structural Dynamics, and Material Conference,
   Paper No. 85-0785, 1985, pp. 581-586.
6. Chen, J. C., "Evaluation of Spacecraft Modal Test Methods," J.
   Spacecraft, AIAA, Vol. 24, No. 1, pp. 52-62.

Table 1.   COMPARISONS OF DAMPING VALUES FOR 10% DISCRETE DAMPING

MODE	DISCRETE DAMPING*	$D_{bb} = 0$		$D_{bb} \neq 0$	
		TMP	SYN.	TMP	SYN.
1	(.0423)	.0023	.0027	.0405	.0426
2	(.1306)	.0104	.0127	.1247	.1316
3	(.2000)	.0127	.0146	.1929	.1999
4	(.1518)	.0079	.0082	.1486	.1567
5	(.0271)	.0006	.0006	.0260	.0272
6	7.603	5.867	7.660	7.289	7.603
7	9.195	8.282	9.223	10.38	9.195
8	15.91	15.15	15.92	15.57	15.91
9	19.48	19.64	19.51	20.38	19.48
10	29.05	30.30	29.18	32.52	29.05
11	33.21	36.55	33.25	38.14	33.21
12	52.83	56.35	52.85	57.63	52.83
13	56.96	62.53	57.08	65.06	56.96
14	65.10	72.69	65.13	74.51	65.10
15	72.76	80.26	72.77	82.46	72.76
16	102.9	108.7	102.9	109.6	102.9
17	107.6	123.1	107.7	125.9	107.6
18	120.6	131.8	120.6	133.3	120.6
19	129.6	141.2	129.6	143.0	129.6
20	156.2	173.6	156.2	174.5	156.2
21	161.7	182.5	161.7	183.1	161.7
22	185.8	200.4	185.8	201.1	185.8
23	190.1	212.1	190.1	213.2	190.1
24	200.9	230.1	200.9	231.4	200.9
25	203.5	229.7	203.5	232.6	203.5

* Values in () are for the case $D_{bb} \neq 0$.

Table 2. COMPARISONS OF ACCELERATION RESPONSES FOR 10% DAMPING

ITEMS	NODAL NUMBER							
	1 (END)		6		13 (MIDDLE)		18	
	MIN	MAX	MIN	MAX	MIN	MAX	MIN	MAX
$D_{bb}=0$								
DIR. INT.	-.389	1.672	-.374	.481	-.259	1.672	-.263	.355
TRD-TMP	-.390	1.672	-.399	.471	-.260	1.672	-.282	.354
TRD-SYN.	-.387	1.672	-.414	.478	-.265	1.672	-.303	.354
$D_{bb}\neq 0$								
DIR. INT.	-.148	1.672	-.343	.412	-.174	1.672	-.242	.290
TRD-TMP	-.147	1.672	-.370	.412	-.174	1.672	-.269	.286
TRD-SYN.	-.153	1.672	-.389	.418	-.189	1.672	-.291	.290

Table 3. COMPARISONS OF TMP AND SYNTHESIZED DAMPING COEFFICIENTS (%) IN GENERALIZED COORDINATES FOR 10% DISCRETE DAMPING

| MODE	SYSTEM FREQ. (Hz)	$D_{bb} = 0$		$D_{bb} \neq 0$	
		TMP	SYN.	TMP	SYN.
1	0	-	-	-	-
2	0	-	-	-	-
3	.9675	.009	.001	9.90	10.1
4	2.657	.193	.146	9.44	10.1
5	5.191	.484	.536	9.55	9.98
6	8.550	12.3	16.7	14.0	15.0
7	12.73	16.5	17.5	18.3	13.9
8	17.71	14.1	15.1	14.2	15.3
9	23.49	14.9	13.9	15.1	13.9
10	30.06	13.5	13.2	13.9	12.2
11	37.41	14.5	12.6	14.9	12.4
12	45.51	11.2	10.5	11.3	10.5
13	54.36	12.5	11.4	12.9	11.1
14	63.91	12.9	11.3	13.2	11.3
15	74.13	13.4	11.9	13.6	12.0
16	84.94	10.6	10.1	10.7	10.1
17	96.25	12.1	10.4	12.4	10.3
18	107.9	11.7	10.7	11.8	10.8
19	119.7	12.1	11.3	12.2	11.3
20	131.3	11.1	9.99	11.2	9.99
21	142.4	12.0	10.5	12.0	10.5
22	152.4	10.5	10.1	10.5	10.0
23	161.2	11.8	10.4	11.8	10.4
24	167.9	11.6	9.99	11.7	9.99
25	172.1	11.1	10.2	11.8	10.2
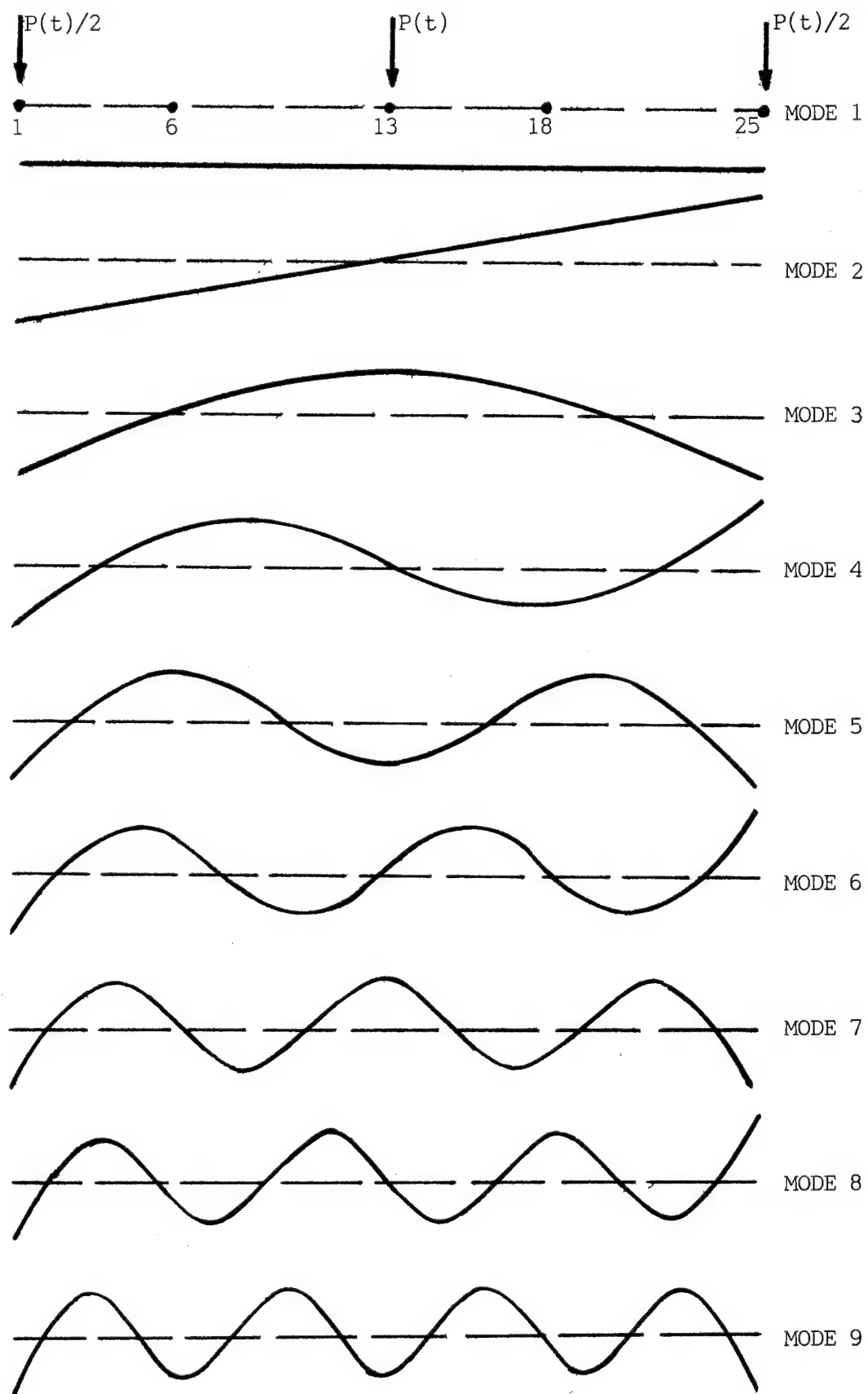
Fig. 1. MODE SHAPES OF FREE-FREE BEAM
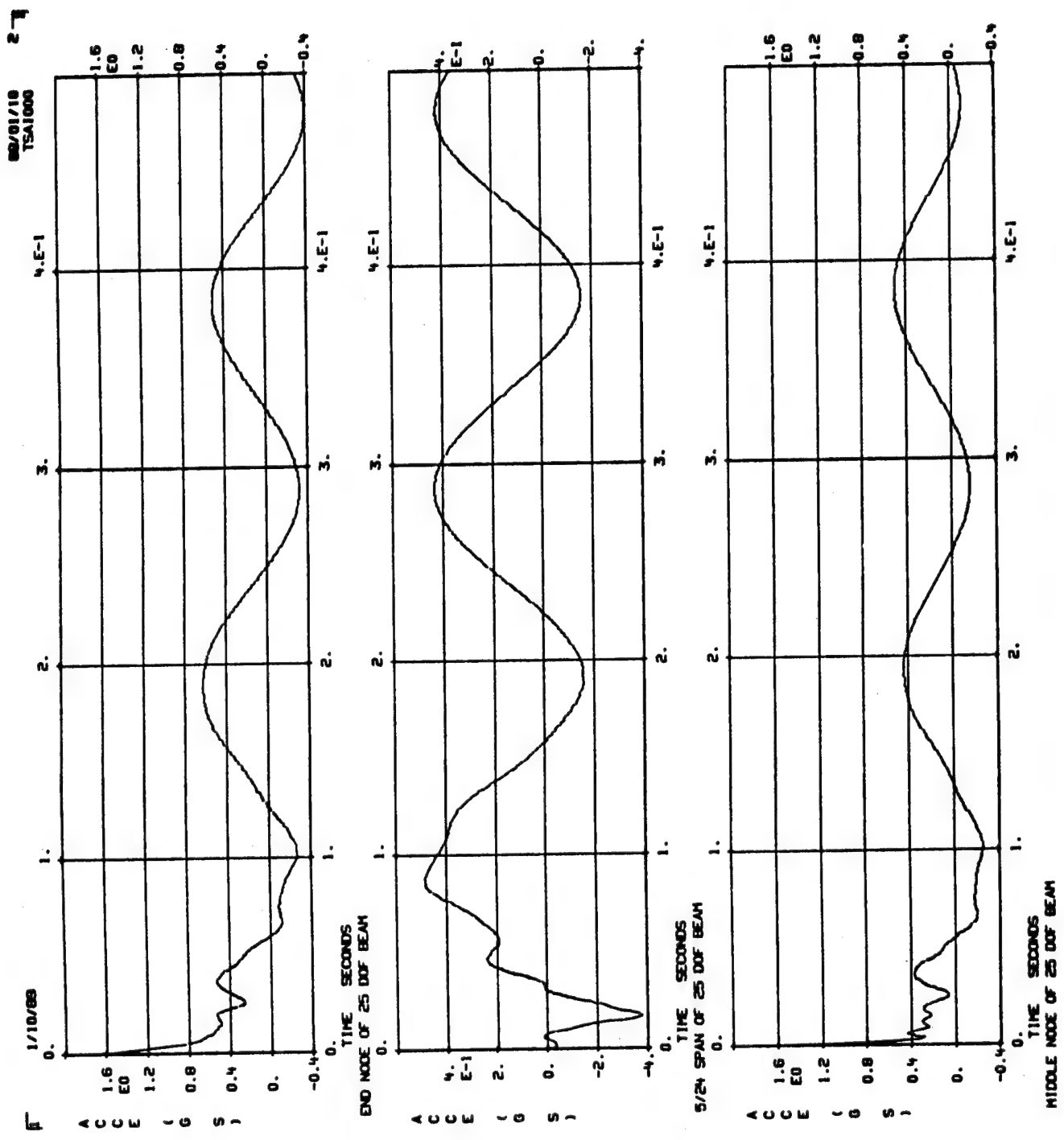
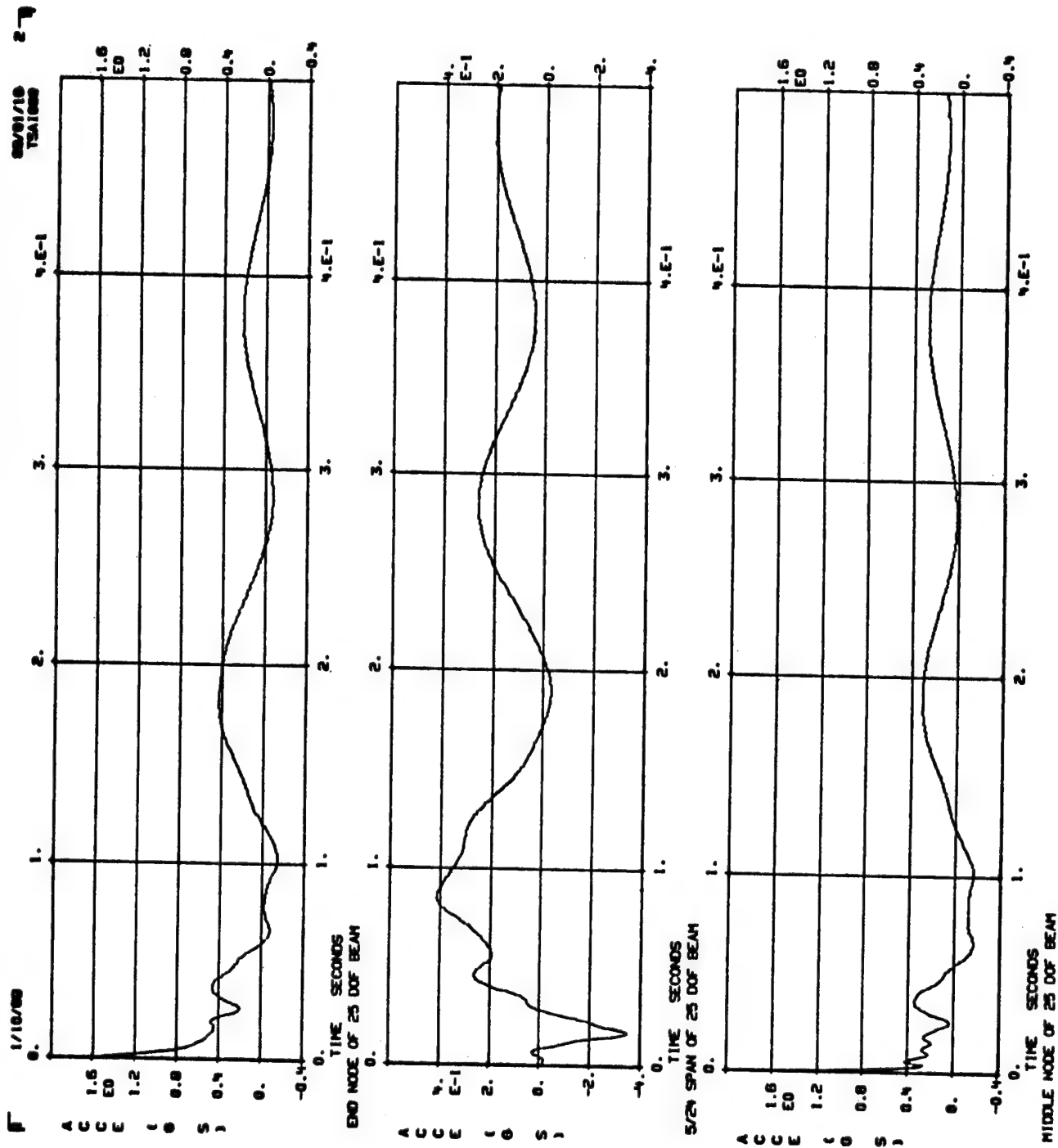Fig. 2. RESPONSE TIME HISTORY WITHOUT BOUNDARY DAMPING

Fig. 3. RESPONSE TIME HISTORY WITH BOUNDARY DAMPING

ON PASSIVE SPOT DAMPING ANOMALIES

by

Dr. Maurice I. Young
Consultant
Vigyan Research Associates, Inc.
Hampton, VA 23666-1325
Telephone: (804) 865-1400

ABSTRACT

Analysis and computation for several damping coupled, lumped parameter models of structural systems demonstrates that passive spot damping treatments become progressively less effective as the natural frequencies of dissimilar modes of vibration coalesce. In the limiting case of dissimilar modes with identical frequencies, an analytical solution is given demonstrating the anomaly of complete loss of damping in one damped mode and the doubling of the damping in another damped mode. These damped modes are shown to be linear combinations of the undamped ones with identical frequencies.

The analysis is extended to continuous structural members such as rectangular membranes and plates, where the anomaly of complete damping loss is again demonstrated. When the aspect ratios of these structural members are selected to yield differing modal patterns with identical natural frequencies, application of passive spot damping yields a pair of damped modes, where one has no damping and the other has twice the effective damping expected.

Finally, a numerical study employing the rectangular plate as an example is presented to quantify the efficacy of a passive spot damping treatment as a function of natural frequency separation. This is then contrasted with the effects of a pervasive damping treatment of the plate.

INTRODUCTION

Vibration control through spot damping treatments can sometimes produce the anomalous result that some of the "damped" modes either remain undamped or have more damping than anticipated. Several lumped parameter examples are presented demonstrating that this is most pronounced when dissimilar modes have the same natural frequency. A plate vibration example is also presented which shows that a spot damping treatment can fail [1,2,3] to damp certain dissimilar modes having the same natural frequency, while others have twice the damping expected. It is shown that frequency matching of damping coupled modes employing spot damping results in nodal and anti-nodal points at the point of application of the spot damping, and that this is the basis of the anomalous result.

ANALYSIS

Consider first two single degree of freedom oscillators of natural frequencies $\omega_1 = (k_1/m_1)^{1/2}$ and $\omega_2 = (k_2/m_2)^{1/2}$. Their displacements x_1 and x_2 are coupled by a dashpot of viscous damping rate c as shown in Figure 1. The coupled equations of motion are

$$m_1\ddot{x}_1 + c(\dot{x}_1 - \dot{x}_2) + k_1 x_1 = 0, \tag{1}$$

$$m_2\ddot{x}_2 + c(\dot{x}_2 - \dot{x}_1) + k_2 x_2 = 0. \tag{2}$$

Consider now the special case when $\omega_1 = \omega_2 = \omega$. Introducing the relative motion coordinate $y \equiv (x_1 - x_2)$ and the damping fraction $\zeta_1 \equiv (c/2m_1\omega_1)$ and $\zeta_2 \equiv (c/2m_2\omega_2)$, equations (1) and (2) can be combined to yield

$$\ddot{y} + 2(\zeta_1 + \zeta_2)\omega\dot{y} + \omega^2 y = 0. \tag{3}$$

Clearly the modal pattern $x_1 = x_2$ yields no relative motion across the dashpot and the coupled mode has the natural frequency ω and no damping. The modal pattern $x_1 = -x_2$, or $y = 2x_1$ also has the natural frequency ω, but the damping fraction $\zeta = \zeta_1 + \zeta_2$. As a second illustration, consider the damping coupled oscillations of the bouncing and pitching motions of the rigid body shown in Figure 2. The coupled equations of motion are

$$m\ddot{z} + c(\dot{z} + b\dot{\phi}) + kz = 0 \tag{4}$$

$$m\rho^2 \ddot{\phi} + cb(b\dot{\phi} + \dot{z}) + ka^2 \phi = 0. \tag{5}$$

When the radius of gyration ρ equals the spring offset distance a, the natural frequencies of bouncing and pitching are equal with $\omega = (k/m)^{1/2} = (a/\rho)(k/m)^{1/2}$. Introducing the variable $u \equiv (z + b\phi)$ which is the displacement at the dashpot, equations (4) and (5) can be combined to yield

$$\ddot{u} + 2(\zeta_\phi + \zeta_z)\omega\dot{u} + \omega^2 u = 0 \tag{6}$$

where $\zeta_\phi \equiv (b/\rho)^2(c/2m\omega)$ and $\zeta_z \equiv (c/2m\omega)$. As in the first example, when $u = (z + b\phi)$ is zero, there is an undamped oscillation at natural frequency ω. When $u = (z + b\phi)$ is not zero, the oscillation has the damping fraction $\zeta_u = \zeta_\phi + \zeta_z$. As a third example, consider the three degree of freedom, damping coupled oscillator shown in Figure 3. The three uncoupled natural frequencies are $\omega_u = (k_u/m)^{1/2}$, $\omega_v = (k_v/m)^{1/2}$, and $\omega_\phi = [(k_u d_u^2 + k_v d_v^2)/(m\rho^2)]^{1/2}$. Introducing $\tau \equiv \omega_u t$, $\zeta \equiv (c/2m\omega_u)$ and $^\prime \equiv d()/d\tau$, then the three damping coupled equations of motion in matrix format are

$$\begin{bmatrix} 1 & 0 & 0 \\ 0 & 1 & 0 \\ 0 & 0 & 1 \end{bmatrix} \begin{Bmatrix} u'' \\ v'' \\ \phi'' \end{Bmatrix} + 2\zeta \begin{bmatrix} \sin^2\alpha & \dfrac{\sin 2\alpha}{2} & \varepsilon\sin\alpha \\ \dfrac{\sin 2\alpha}{2} & \cos^2\alpha & \varepsilon\cos\alpha \\ \varepsilon\sin\alpha & \varepsilon\cos\alpha & \varepsilon^2 \end{bmatrix} \begin{Bmatrix} u' \\ v' \\ \phi' \end{Bmatrix}$$

$$+ \begin{bmatrix} 1 & 0 & 0 \\ 0 & (\omega_v/\omega_u)^2 & 0 \\ 0 & 0 & (\omega_\phi/\omega_u)^2 \end{bmatrix} \begin{Bmatrix} u \\ v \\ \phi \end{Bmatrix} = \begin{Bmatrix} 0 \\ 0 \\ 0 \end{Bmatrix} \qquad (6)$$

Consider the case of $(\omega_v/\omega_u) = 1$ when the horizontal and vertical motion natural frequencies are equal. The loss of damping anomaly can again be demonstrated: there is a modal pattern $|\bar{u},\ \bar{v},\ \bar{\phi}|$ corresponding to the pure imaginary eigenvalue $\lambda = j$, $j^2 = -1$. That is, the damping coupled mode occurs at the frequency $\omega = \omega_u$, but with no damping. Direct substitution in equation (6) yields the characteristic determinant

$$\begin{vmatrix} 1 & (2\zeta\cos\alpha)j & (2\zeta\varepsilon) \\ \cos\alpha & \{[(\omega_v/\omega_u)^2 - 1] + (2\zeta\cos^2\alpha)j\} & (2\zeta\varepsilon\cos\alpha)j \\ \varepsilon & (2\zeta\varepsilon\cos\alpha)j & \{[(\omega_\phi/\omega_u)^2 - 1] + (2\zeta\varepsilon^2)j\} \end{vmatrix} = 0 \quad (7)$$

Expanding and taking $(\omega_v/\omega_u)^2 = 1$, the determinant vanishes for $(\omega_\phi/\omega_u)^2 \neq 1$; the determinant also vanishes for $(\omega_\phi/\omega_u)^2 = 1$ and $(\omega_v/\omega_u)^2 \neq 1$. It does not vanish unless two of the three natural frequencies are equal.

As a final illustration of the spot damping anomaly, consider a simply supported, uniform rectangular plate as illustrated in Figure 4. A dashpot applies a concentrated damping force at the interior point $(\tilde{x},\tilde{y})$. The governing partial differential equation for free vibration follows, where D is the plate flexural rigidity, μ is the plate mass per unit area and d is the viscous damping constant per unit area for the dashpot at $(\tilde{x},\tilde{y})$.

$$D\nabla^4 W(x,y,t) + \mu\ddot{W}(x,y,t) + d\dot{W}(\tilde{x},\tilde{y},t) = 0. \qquad (8)$$

The undamped modal patterns and associated natural frequencies for the integers m and n, and for a plate aspect ratio $N = (a/b)$ are

$$\overline{W}_{mn}(x,y) = \sin(m\pi x/a)\ \sin(n\pi y/b) \qquad (9)$$

$$\omega_{mn}^2 = (\pi/a)^4 \, (m^2 + N^2 \, n^2)^2 \, (D/\mu) \tag{10}$$

Now consider the case where the differing modal patterns $\overline{W}_{mn}$ and $\overline{W}_{rs}$ have the same natural frequency. Then the plate aspect ratio N is related to the modal integers m, n, r and s by

$$N = \left[(r^2 - m^2)/(n^2 - s^2) \right]^{1/2} \tag{11}$$

Now consider the hypothesis that two of the damping coupled modes are

$$\overline{W}_{(+\nu)}(x,y) = \overline{W}_{mn}(x,y) + \nu\overline{W}_{rs}(x,y) \tag{12}$$

$$\overline{W}_{(-\nu)}(x,y) = \overline{W}_{mn}(x,y) - \nu\overline{W}_{rs}(x,y). \tag{13}$$

This hypothesis leads to the eigenvalue equation in λ

$$D\nabla^4\left[\overline{W}_{mn}(x,y) \pm \nu\overline{W}_{rs}(x,y)\right] + \mu\lambda^2\left[\overline{W}_{mn}(x,y) \pm \nu\overline{W}_{rs}(x,y)\right]$$

$$+ d\lambda\left[\overline{W}_{mn}(\tilde{x},\tilde{y}) \pm \nu\overline{W}_{rs}(\tilde{x},\tilde{y})\right] = 0. \tag{14}$$

Taking the parameter $\nu = \left[\overline{W}_{mn}(\tilde{x},\tilde{y})/\overline{W}_{rs}(\tilde{x},\tilde{y})\right]$ constrains the displacement at the dashpot location $(\tilde{x},\tilde{y})$ to be either an anti-node or a node point. In the case of an anti-node, the modal pattern

$$\overline{W}_{(+\nu)} = \left\{\overline{W}_{mn}(x,y) + \left[\overline{W}_{mn}(\tilde{x},\tilde{y})/\overline{W}_{rs}(\tilde{x},\tilde{y})\right]\overline{W}_{rs}(x,y)\right\} \tag{15}$$

has twice the effective damping constant since

$$\overline{W}_{mn}(\tilde{x},\tilde{y}) + \nu\overline{W}_{rs}(\tilde{x},\tilde{y}) = 2\overline{W}_{mn}(\tilde{x},\tilde{y}) \tag{16}$$

and $\overline{W}_{mn}(x,y)$ and $\overline{W}_{rs}(x,y)$ are mutually orthogonal functions despite their matching natural frequencies. This can be seen by multiplying equation (14) by $\overline{W}_{mn}(x,y)$ and integrating over the surface area of the plate. Noting that

$$D\nabla^4 \overline{W}_{mn}(x,y) = \mu\omega_{mn}^2 \overline{W}_{mn}(x,y) \tag{17}$$

the surface integration yields

$$\lambda_{(+\nu)}^2 + \left[(8d/\mu)\overline{W}_{mn}^2(\tilde{x},\tilde{y})\right]\lambda_{(+\nu)} + \omega_{mn}^2 = 0 \tag{18}$$

and

$$\zeta_{\substack{\text{effective} \\ (+\nu)}} = \left\{4(d/\mu)\left[\overline{W}_{mn}^2(\tilde{x},\tilde{y})/\omega_{mn}\right]\right\} \tag{19}$$

which is double that for $\overline{W}_{mn}(x,y)$ when the frequency for $\overline{W}_{rs}(x,y)$ does not match.

In the case of a nodal point at $(\tilde{x},\tilde{y})$, [4,5,6], $W_{(-\nu)} = \{W_{mn}(x,y) - \left[\overline{W}_{mn}(\tilde{x},\tilde{y})/\overline{W}_{rs}(\tilde{x},\tilde{y})\right]\overline{W}_{rs}(x,y)\}$ and $\lambda_{(-\nu)}^2 = -\omega_{mn}^2$, the modal pattern occurs with no damping.

It has been demonstrated that spot damping treatments can fail when dissimilar modes have the same natural frequency. A numerical analysis is now presented which reveals that as the natural frequencies of a rectangular plate depart from the normal spacing of dissimilar modes and coalesce, a progressive deterioration of the effective damping provided by spot damping treatments results.

PLATE NUMERICAL ANALYSIS

The governing partial differential equation for the plate is given in equation (8). A modal expansion of undamped modes is employed. That is taking

$$w(x,y,t) = \sum_{m,n=1}^{\infty} \overline{w}_{mn}(x,y)e^{\lambda t} \tag{20}$$

and employing the orthogonality relationships that

$$\int_0^b \int_0^a \overline{w}_{mn}(x,y)\overline{w}_{rs}(x,y)dxdy = 0 \tag{21}$$

for differing integer subscripts and

$$\int_0^b \int_0^a \overline{w}_{mn}^2(x,y)dxdy = \left(\frac{ab}{4}\right). \tag{22}$$

Truncating the modal expansion at N terms, the first N modes of undamped plate vibrations are damping coupled. Employing matrix notation with the generalized coordinates $q_1(t), q_2(t), \cdots, q_N(t)$, the governing matrix differential equation is as follows:

$$
\begin{bmatrix}
1 & 0 & \cdots & 0 \\
0 & 1 & \cdots & 0 \\
\vdots & \vdots & \ddots & \vdots \\
0 & 0 & \cdots & 1
\end{bmatrix}
\begin{Bmatrix}
\ddot{q}_1 \\
\ddot{q}_2 \\
\vdots \\
\ddot{q}_N
\end{Bmatrix}
+
\begin{bmatrix}
d_{11} & d_{12} & \cdots & d_{1N} \\
d_{21} & d_{22} & \cdots & d_{2N} \\
\vdots & & \ddots & \vdots \\
d_{N1} & d_{N2} & \cdots & d_{NN}
\end{bmatrix}
\begin{Bmatrix}
\dot{q}_1 \\
\dot{q}_2 \\
\vdots \\
\dot{q}_N
\end{Bmatrix}
$$

$$
+
\begin{bmatrix}
\omega_1^2 & 0 & \cdots & 0 \\
0 & \omega_2^2 & \cdots & 0 \\
\vdots & \vdots & \ddots & \vdots \\
0 & 0 & \cdots & \omega_N^2
\end{bmatrix}
\begin{Bmatrix}
q_1 \\
q_2 \\
\vdots \\
q_N
\end{Bmatrix}
=
\begin{Bmatrix}
0 \\
0 \\
\vdots \\
0
\end{Bmatrix} \tag{23}
$$

where ω_1^2, ω_2^2, $\cdots$, ω_N^2 are the undamped natural frequencies of the undamped plate corresponding to the rectangular plate modal patterns; they are arranged in ascending order of frequency; the damping matrix is symmetrical with

$$d_{ij} \equiv d_{mn,rs} \equiv \left(\frac{c}{ab}\right) \frac{\int_0^b \int_0^a \bar{w}_{mn}(\tilde{x},\tilde{y}) \bar{w}_{rs}(\tilde{x},\tilde{y}) dx dy}{\mu \int_0^b \int_0^a \bar{w}_{mn}^2(x,y) dx dy}, \qquad (24)$$

or

$$d_{ij} \equiv d_{mn,rs} \equiv \left[\frac{4c}{(ab)^2}\right] \bar{w}_{mn}(\tilde{x},\tilde{y}) \bar{w}_{rs}(\tilde{x},\tilde{y}). \qquad (25)$$

Introducing dimensionless time $\tau \equiv \omega_1 t$ and the reduced damping matrix entries $2\delta_{ij} \equiv (d_{ij}/\omega_1)$, the governing matrix differential equation becomes

$$\begin{bmatrix} 1 & 0 & \cdots & 0 \\ 0 & 1 & \cdots & 0 \\ \vdots & \vdots & \ddots & \vdots \\ 0 & 0 & \cdots & 1 \end{bmatrix} \begin{Bmatrix} q_1'' \\ q_2'' \\ \vdots \\ q_N'' \end{Bmatrix} + 2 \begin{bmatrix} \delta_{11} \delta_{12} & \cdots & \delta_{1N} \\ \delta_{12} \delta_{22} & \cdots & \delta_{2N} \\ \vdots & \ddots & \\ \delta_{1N} \delta_{2N} & \cdots & \delta_{NN} \end{bmatrix} \begin{Bmatrix} q_1' \\ q_2' \\ \vdots \\ q_N' \end{Bmatrix}$$

$$+ \begin{bmatrix} (\omega_1/\omega_1)^2 & 0 & \cdots & 0 \\ 0 & (\omega_2/\omega_1)^2 & \cdots & 0 \\ \vdots & \vdots & \ddots & \vdots \\ 0 & 0 & \cdots & (\omega_N/\omega_1)^2 \end{bmatrix} \begin{Bmatrix} q_1 \\ q_2 \\ \vdots \\ q_N \end{Bmatrix} = \begin{Bmatrix} 0 \\ 0 \\ \vdots \\ 0 \end{Bmatrix} \qquad (26)$$

A solution is sought in the form

$$\{q(t)\} = \{\bar{q}\} e^{\nu\tau} \qquad (27)$$

where

$$\nu \equiv (\lambda/\omega_1) \qquad (28)$$

Taking

$$(\omega_p/\omega_1)^2 = \eta_p^2, \qquad p = 1,2,\cdots,N \qquad (29)$$

the characteristic determinant follows as

$$\begin{vmatrix} \nu^2 + 2\delta_{11}\nu + \eta_1^2 & 2\delta_{12}\nu & \cdots & 2\delta_{1N}\nu \\ 2\delta_{12}\nu & \nu^2 + 2\delta_{22}\nu + \eta_2^2 & \cdots & 2\delta_{2N}\nu \\ \vdots & \vdots & \ddots & \vdots \\ 2\delta_{1N}\nu & 2\delta_{2N}\nu & \cdots & \nu^2 + 2\delta_{NN}\nu + \eta_N^2 \end{vmatrix} = 0 \qquad (30)$$

The influence of natural frequency separation is now evaluated by systematic-ally perturbing the plate aspect ratio N while preserving the plate area, with mass per unit area and flexural rigidity properties constant, with spot damping coupling the first nine modes. Since the reference aspect ratio N_o has yielded a frequency match and a complete loss of damping, a tabular relationship is now obtained which shows the influence of natural frequency proximity on the effective or virtual damping. This is shown below in Figure 5 in tabular format for several nominal damping levels ranging from 5% to 50% of critical in the fundamental plate mode, with the frequency match occurring in the fourth and fifth modes. It is seen that the loss of damping is almost complete over a significant range of frequencies above and below the match.

PLATE WITH PERVASIVE DAMPING

To contrast the foregoing spot damping case, now consider a uniform, simply supported rectangular plate with uniform or pervasive damping over its entire surface. The governing partial differential equation with equivalent viscous damping per unit area $d_o \equiv \left(\dfrac{c_o}{ab}\right)$ follows:

$$D\nabla^4 W(x,y,t) + \mu\ddot{W}(x,y,t) + d_o\dot{W}(x,y,t) = 0. \qquad (31)$$

Seeking the solution in the form

$$W(x,y,t) = \hat{W}(x,y)e^{\lambda t} \qquad (32)$$

$$D\nabla^4\hat{W}(x,y) + (\mu\lambda^2 + d_o\lambda)\hat{W}(x,y) = 0 \qquad (33)$$

Since

$$D\nabla^4\overline{W}_{mn}(x,y) = \mu\omega_{mn}^2\overline{W}_{mn}(x,y) \qquad (34)$$

for $d_o = 0$, the undamped case, it follows that the undamped modal functions also are solutions for the case of pervasive damping with the characteristic equation

$$\mu\lambda^2 + d_o\lambda + \mu\omega_{mn}^2 = 0, \qquad (35)$$

or

$$\left(\frac{\lambda}{\omega_{mn}}\right)^2 + \left(\frac{d_o/\mu}{\omega_{mn}}\right)\left(\frac{\lambda}{\omega_{mn}}\right) + 1 = 0. \qquad (36)$$

Since the effective pervasive viscous damping ratio for mode mn is given by

$$\zeta_{mn}\omega_{mn} = \left(\frac{d_o}{2\mu}\right), \tag{37}$$

a direct comparison of spot damping and pervasive damping can now be inferred. It is seen that barring frequency matching in the case of spot damping

$$\zeta_{mn}\omega_{mn} = \left(\frac{d}{2\mu}\right)\overline{W}_{mn}^2(\tilde{x},\tilde{y}). \tag{38}$$

Since $\overline{W}_{mn}^2(\tilde{x},\tilde{y})$ varies from zero to unity, the spot damping level per unit are required exceeds the pervasive damping level in the ratio

$$\left(\frac{d}{d_o}\right) = \overline{W}_{mn}^{-2}(\tilde{x},\tilde{y}), \tag{39}$$

providing that no two natural frequencies coalesce. Factoring in the influence of the distributed or pervasive damping over the entire plate area A = ab, the equivalent effective spot damping level follows as

$$d = d_o(ab)\overline{W}_{mn}^{-2}(\tilde{x},\tilde{y}) \tag{40}$$

to achieve the same fraction of critical damping in the mn-th mode.

CONCLUSION

Passive spot damping treatments are seen to be straightforward in concept, but potentially ineffective when neighboring, but differing modal patterns have natural frequencies that are close to one another. In the special case of matching natural frequencies the effective damping fraction is zero. This stems from the appearance of a nodal point at the spot damping point of application. In fact, the unusual nodal patterns [5] when frequency matches occur can render broader spot and localized damping treatments ineffectual also. Nevertheless, spot damping treatments are attractive in their simplicity compared to pervasive ones, providing true anti-nodal points of application can be found. This is difficult when frequency matches exist.

Acknowledgment

REFERENCES

[1] P. H. Geiger 1953 *Noise Reduction Manual*. University of Michigan Engineering Research Institute.

[2] D.I.G. Jones 1967 *Shock and Vibration Bulletin*, 36 (4), 9-24. Damping of Structures by Viscoelastic Links.

[3] M. I. Young 1989 *Journal of Sound and Vibration*. In press. Spot Damping Anomalies.

[4] R. Courant and D. Hilbert 1953 John Wiley and Sons, Inc. (301-302) *Methods of Mathematical Physics*.

[5] F. Pockels 1891 B. G. Teubner (76-85) *Uber Die Partielle Differentialgleichung* $\Delta u + k^2 u = 0$.

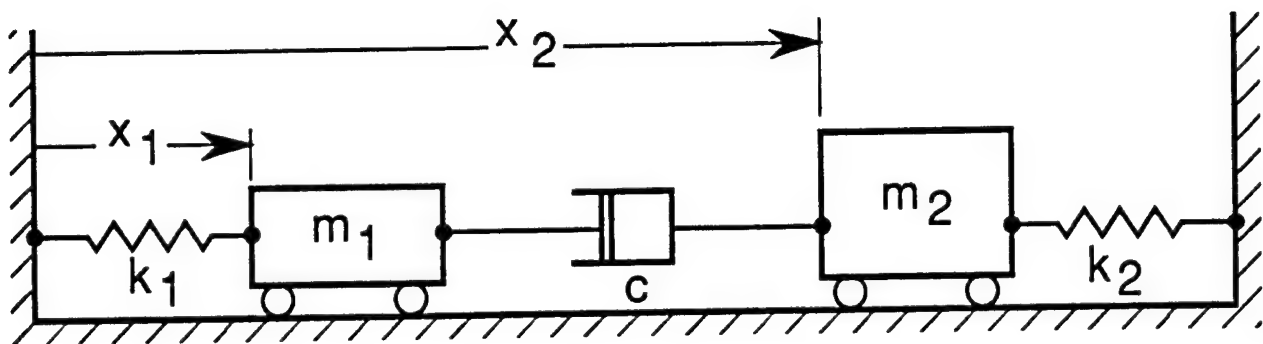[6] S. H. Crandall 1956 McGraw-Hill Book Co., Inc. (76-77) *Engineering Analysis: A Survey of Numerical Procedures*.

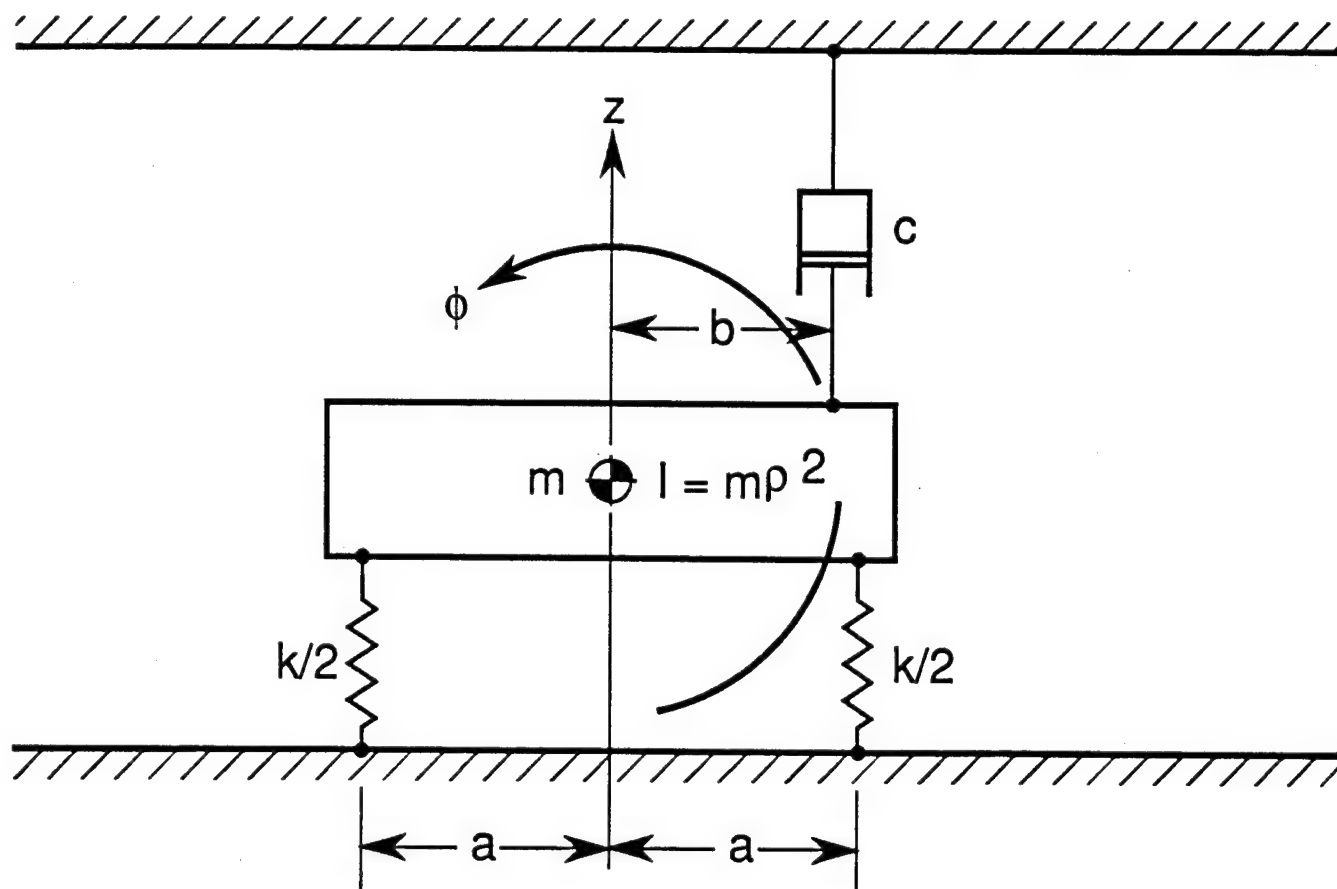Figure 1. Dashpot Coupled System with Two Degrees of Freedom.

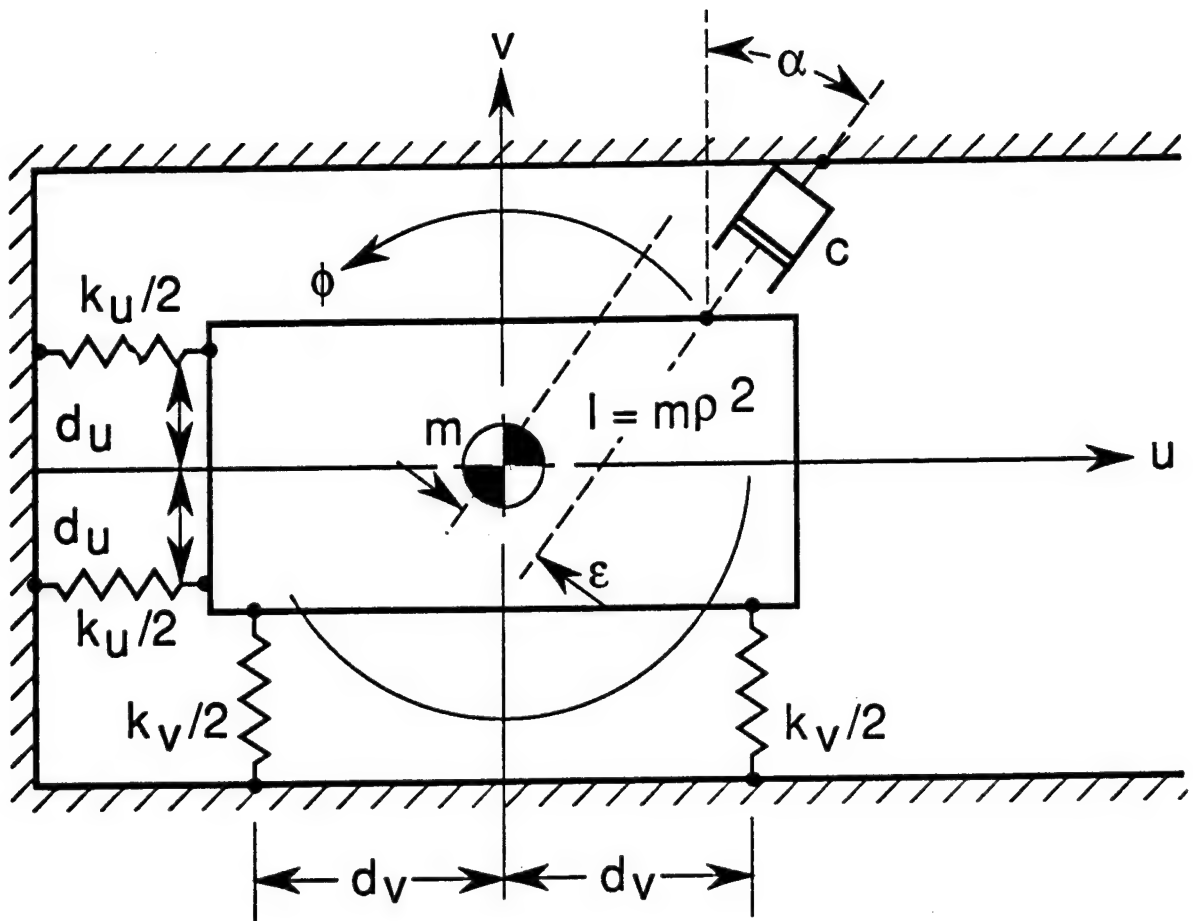Figure 2. Dashpot Coupled System with Bounce and Pitch Freedoms.

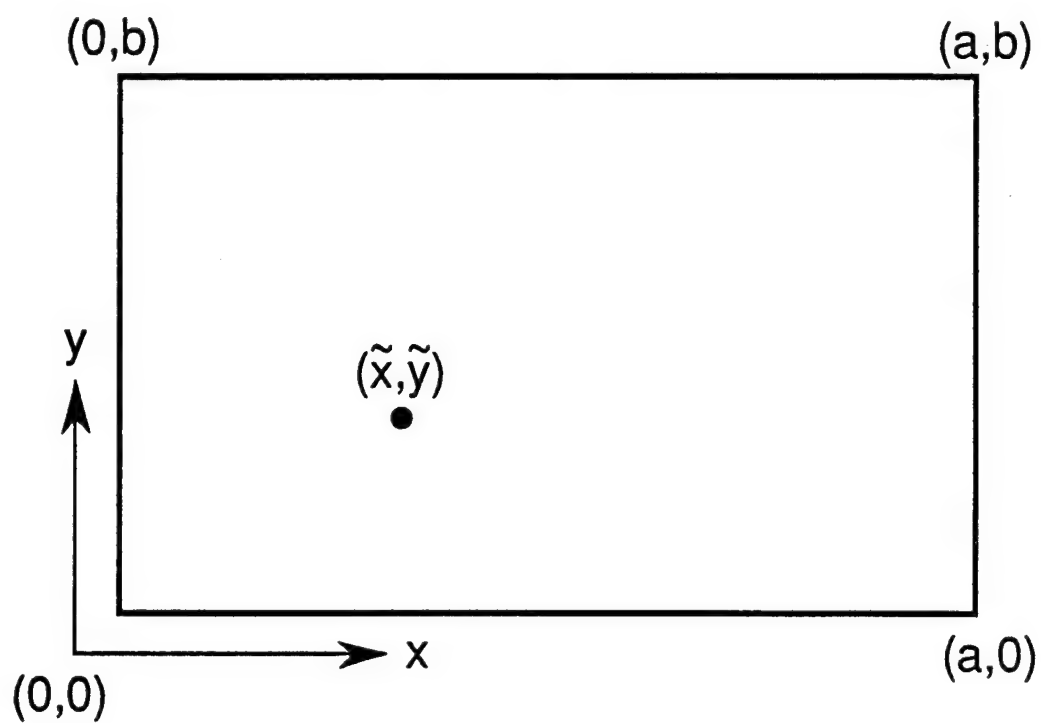**Figure 3.** Dashpot Coupled System with Three Degrees of Freedom.

Figure 4.   Simply Supported, Uniform Rectangular Plate
with Damper Force at $(\tilde{x},\tilde{y})$.

Table: $A = ab = 1.0$ Meters Squared; $\tilde{x}/u = \tilde{y}/b = (1/\pi)$

a	r	$N \equiv a/b \equiv a^2$	$\delta_{ref} = .05$	$\delta_{ref} = .10$	$\delta_{ref} = .25$	$\delta_{ref} = .50$
.65	0.5529	.4225	1.7005	3.3506	8.7111	12.2702
.70	0.6372	.4900	1.7019	3.3618	8.7960	10.2591
.75	0.7307	.5625	1.7029	3.3696	8.9389	0.2759
.80	0.8316	.6400	0.0423	0.0834	0.1856	0.2574
.83	0.8937	.6889	0.0387	0.0743	0.1392	0.1346
.85	0.9345	.7225	0.0357	0.0616	0.0726	0.0379
.86	0.9572	.7396	0.0325	0.0469	0.0328	0.0071
.87	0.9785	.7569	0.0224	0.0193	0.0045	0.0052
.88	0.9998	.7744	0.0000	0.0000	0.0001	0.0002
.89	1.0211	.7921	0.0205	0.0196	0.0160	0.0170
.90	1.0423	.8100	0.0287	0.0401	0.0404	0.0406
.91	1.0635	.8281	0.0306	0.0500	0.0632	0.0658
.93	1.1058	.8649	0.0309	0.0564	0.0942	0.1170
.95	1.1478	.9025	0.0302	0.0572	0.1097	0.1437

Figure 5

VIBRATION DAMPING PERFORMANCE -
WHAT WE SHOULD KNOW ABOUT IT

By:

John Chahine
and
Pranab Saha
of Kolano and Saha Engineers, Inc.
1899 Orchard Lake Rd., Suite 105
Pontiac, Michigan 48053-2610
Telephone: (313) 338-8510

ABSTRACT

The vibration damping performance of materials that are used in the automotive industry, are usually evaluated by either: (1) Geiger Thick-Plate Test Method, or (2) Complex Modulus Test Method. Both of these methods have certain limitations, though the second method is a superior one since it can measure the damping performance with temperature and frequency. This paper discusses the limitations of the way data is typically presented using this method and proposes a procedure for overcoming these limitations. This procedure allows for the rank-ordering of damping materials by composite damping properties obtained using different size Oberst bars.

Introduction

The Interior noise In a car has been of a concern for quite a while. In recent years It has become more Important due to the high demand of customer satisfaction. The trend now Is to have a better fuel economy car with lighter body panels (less total weight of the car), and still have very powerful engines. In this respect, the Interior noise concern Is becoming very Important. Also with unitized body constructions, the structure-borne noise due to vibration of the floor pan and other Interior body panels Is becoming Increasingly Important. One way to reduce this noise Is to treat vibrating panels with damping materials. These materialss will reduce the vibration of the panels and therefore reduce the structure-borne noise Inside the car. This paper discusses two different test methods that are currently used In the automotive Industry to evaluate the vibration damping performance of various materials. These are: Geiger thick-plate test method and complex modulus test method. The paper discusses the advantages and limitations of both test methods. Finally, a technique to rank order the performance of various damping materials, based on composite damping properties obtained by the complex modulus method, Is presented here.

Geiger Thick-Plate Test Method

The damping performance using this test method Is expressed In terms of decay rate. The decay rate Is a measure of dissipation of the vibrational energy of the damping material. The set-up consists of a 6 mm (1/4 Inch) thick and 500 mm by 500 mm (20 Inch by 20 Inch) steel plate which Is supported at 4 points along the plate's nodal line. It Is supported by Isolation mounts to minimize losses. The plate Is excited In its fundamental frequency mode (typically between 130 and 160 Hz) by an electromagnet at the center of the plate. The vibration Is detected by either an electromagnetic transducer, a small accelerometer, or even a microphone placed near the plate to measure the sound pressure caused by the plate. The damping performance Is determined by measuring the vibrational decay after the test plate Is excited and the excitation then suddenly removed. The results of the measurements are normalized to a frequency of 160 Hz. This method can be used for evaluating materials at several temperatures.

The advantages to the Geiger thick-plate test method are:

o Measurements are made at several temperatures.

o Provides data relatively quickly for rank ordering materials.

o Easy to Interpret data (units of dB/sec).

The disadvantages to this method are:

o Provides data at only one frequency.

o Does not provide a material property.

o Though the thick plate dimensions can be varied, the thickness
is usually much greater than the thickness of automobile
panels.

Complex Modulus Test Method

This method is sometimes called the Oberst Bar Method after H. Oberst. The
set-up consists of a thin metal bar to which the damping material is
bonded. This forms a composite bar which is also the test sample. The bar
is clamped at one end and free on the other end. The bar, using an
electromagnetic transducer, is excited with a random noise or a sweep-sine
wave to determine the resonant peak frequencies of the various modes of
vibration. The response of the bar is sensed by a pick-up transducer which
can be an electromagnetic transducer, a strain gauge or a small
accelerometer. The frequency response consists of several resonances which
are characteristic of the bar configuration. The half-power band width
(frequency difference between 3 dB down points from the resonant peak) of
each mode in the response spectrum is read (Figure 1). The damping
performance is expressed in terms of the composite loss factor (n_c). The
term, n_c, is computed from the measured data. The composite loss factor at
each resonant frequency is the ratio of the half-power band width (Δf) over
the resonant frequency (f) i.e., $n_c = {}^{\Delta f}/f$. With additional information
from testing the bare bar alone, the damping properties of the damping
material can also be computed.

The advantages of the complex modulus test method are:

o Measurements are made at several different frequency modes and
temperatures.

o Can compute material loss factor if bare bar is tested, in
addition to testing the composite bar. The material loss
factor allows one to predict the performance of the material in
an application.

o Rank order materials using composite loss factor if tests are
done with the same bare bar material type, size, and test
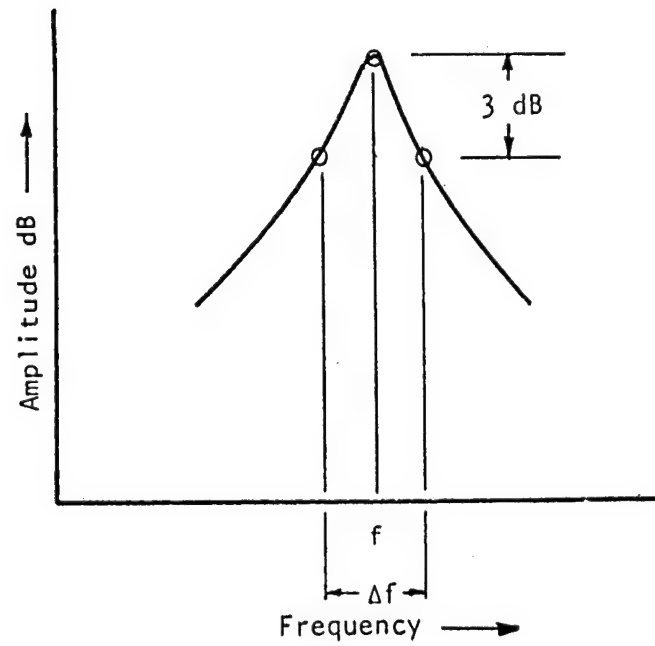configuration (free-layer, constrained layer, etc.).

Figure 1   Variables Used to Determine Loss
Factor of the Test Sample

The disadvantages to this test method are:

o Calculation for material damping properties can be laborious
   without a computer.

o To get meaningful results of material damping properties at a
   wide range of temperatures, more than one test configuration
   (free layer, constrained layer, etc.) may be needed.

Comparison of Composite Data

If a given number of damping materials were tested according to the complex
modulus test method, the performance of these materials can be rank-ordered
based on the composite loss factor. Time and effort to test the bare bar
and subsequently to compute the material damping properties would not be
necessary.

The use of rank-ordering materials by composite loss factor, however, has
its limitations. The problem arises when trying to compare damping
materials which were tested with different bar dimensions or
configurations. To overcome this problem, the first step would be to
compare damping materials by the material damping values.

The material damping properties can be estimated from composite damping
values if an assumption can be made. The assumption is that the modulus of
the bare bar is relatively constant over the temperature range and
frequency range of the damping test. By estimating a constant value for
the modulus of the bare bar (for example, the modulus of steel equals 20 $\times$
10^{10} Pa (29 $\times$ 10^6 psi)), the resonant frequencies of the bare bar can be
calculated and hence, the damping material properties. The estimate can be
improved if data is available on the change of the modulus of the bare bar
with temperature and frequency.

Once the material properties are computed for each damping material for a
comparison, there still exists the problem of discrete values at different
frequencies and perhaps different temperatures. This can, however, be
overcome with the use of the reduced-frequency nomogram technique[1]. It
should be noted that the purpose of this paper is not to show how the
reduced frequency technique works but to use reduced frequency technique to
rank-order damping performance without conducting extensive tests.
However, a brief description of the development of a reduced frequency
nomogram from discrete material property values follows below.

----

[1] Jones, D. I. G., *A Reduced-Temperature Nomogram for Characterization of
Damping Material Behavior*, The Shock and Vibration Bulletin, Bulletin 48,
Part 2, pp 13-22, (September 1978).

When the modulus of a material versus frequency is plotted for given
temperatures, what results is a series of curves as shown in Figure 2. If
each of these curves is shifted horizontally by a given factor, what then
results is a single continuous curve of modulus versus frequency made up
from the data of different temperatures. The same can be done for material
loss factor versus frequency data of different temperatures. The curves
obtained by this procedure are shown in Figure 3. The curves are
calculated by a curve fitting technique. This allows for the interpolation
of material damping properties between the discrete measured values at
temperatures and frequencies within the range of the test. The frequency
axis is on the right-hand-side and the temperature lines run diagonally.
To obtain the loss factor for a given frequency and temperature, (e.g.:
frequency 10 Hz and temperature T_8 in Figure 4), simply mark horizontally
from the frequency scale and diagonally along the temperature line to the
point of intersection. Then mark vertically to the loss factor curve and
read the values from the left-hand-side scale. The same can be done for
obtaining values of modulus at a given frequency and temperature from the
modulus curve of the nomogram.

To test the procedure of comparing composite damping properties for rank-
ordering materials tested with different bar sizes, two different complex
modulus tests were done. Rather than verifying the procedure by rank-
ordering two or more materials, it would be more appropriate to see if a
material would rank the same with itself when tested with two different bar
sizes. For this case, the same damping material was tested by the complex
modulus test method configured for free layer damping on one side of a thin
steel bar and on one side of a thick steel bar. The damping material was a
homogeneous material.

Having obtained the composite damping data, the modulus of steel was
estimated to be 20×10^{10} Pa (29×10^6 psi) and the material damping
properties were computed. The computed material damping properties
obtained with the thin steel bar were then compared with those of the thick
steel bar. This was done by first preparing a reduced frequency nomogram
for the material damping properties obtained by the use of the thin steel
bar (Figure 5). The curves from this nomogram were then overlaid on the
material damping property values of obtained using the thick steel bar
(Figure 6). As can be seen, the curves fit the second set of data
reasonably well. This proves that the damping material rank-ordered the
same with itself for both bar sizes when the composite damping data only
was provided.

Concluding Remarks

This paper discusses the advantages and limitations of two different
vibration damping test methods that are used in the automotive industry,
namely Geiger thick-plate test method and complex modulus test method. A
technique, based on the results of the complex modulus tests method, has
been discussed here to rank-order damping performance based on composite
loss factor data obtained by different size Oberst bars.

FREQUENCY (Log Scale)

LOSS FACTOR
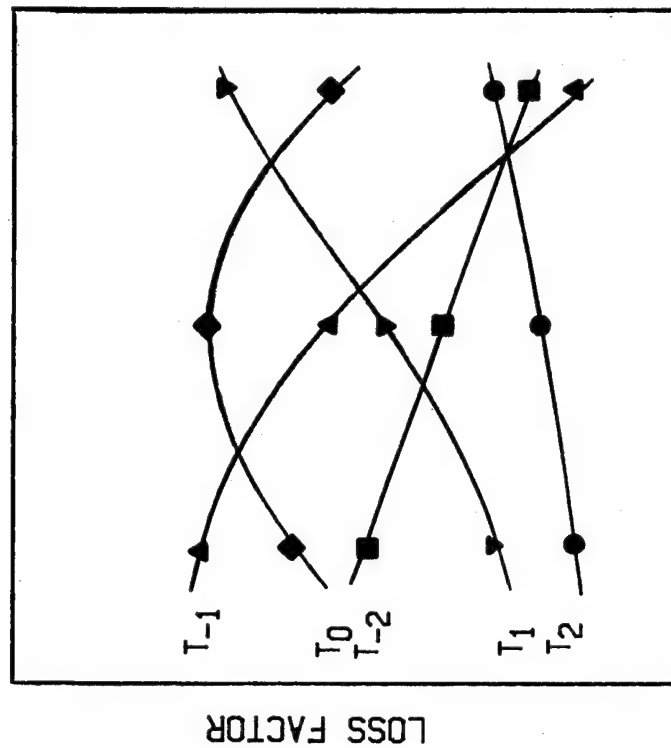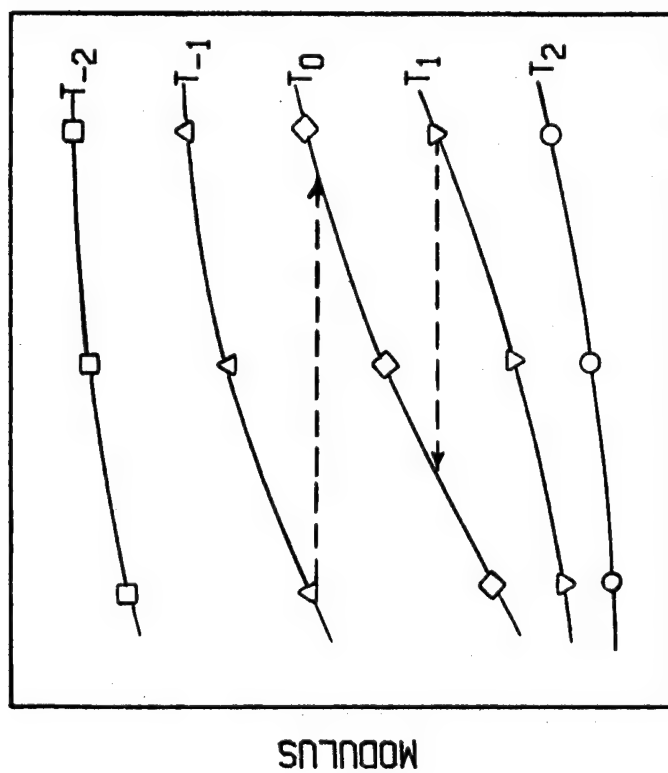
FREQUENCY (Log Scale)

MODULUS

Figure 2 Variation of Modulus and Loss Factor with Frequency and Temperature
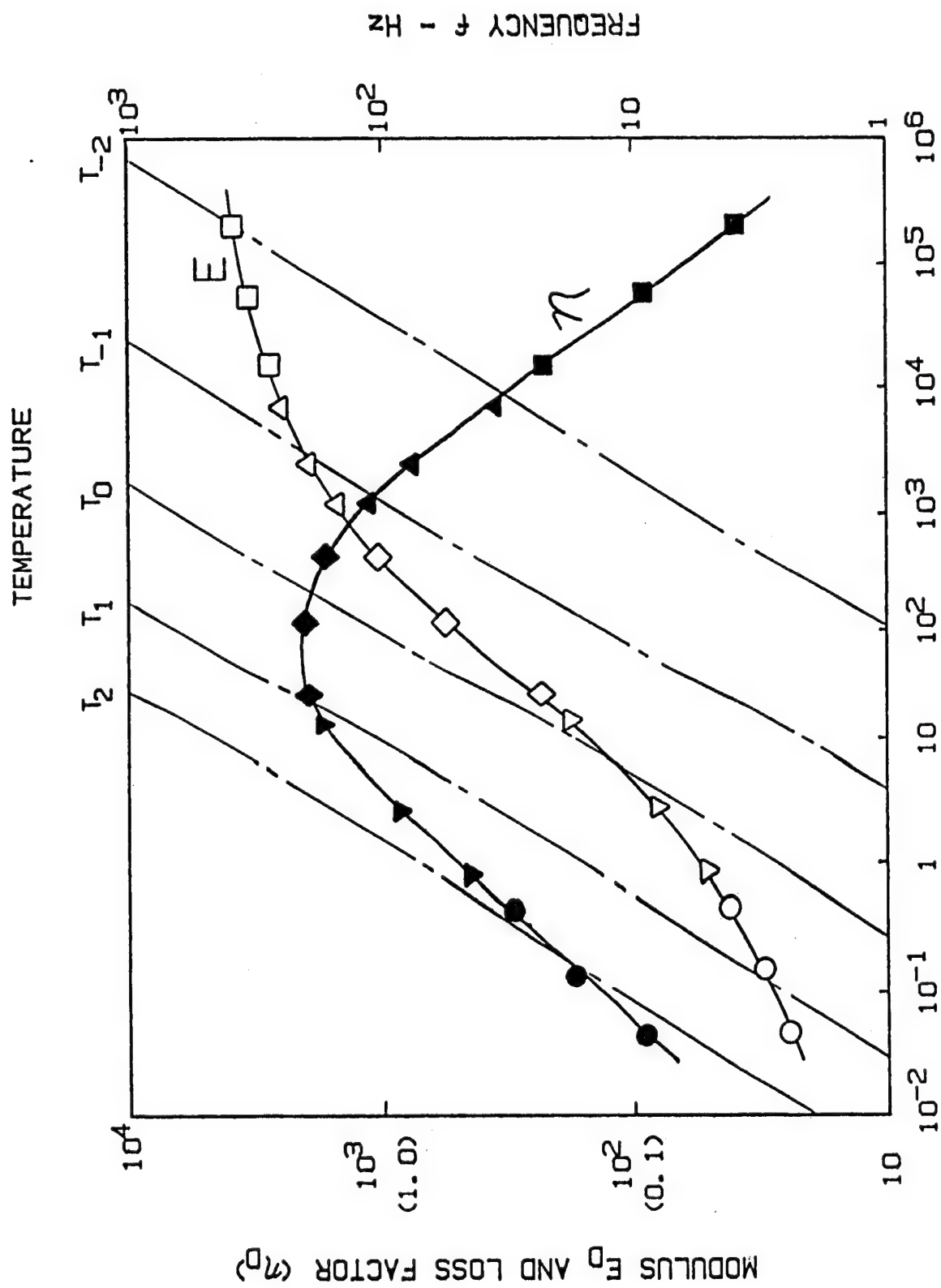
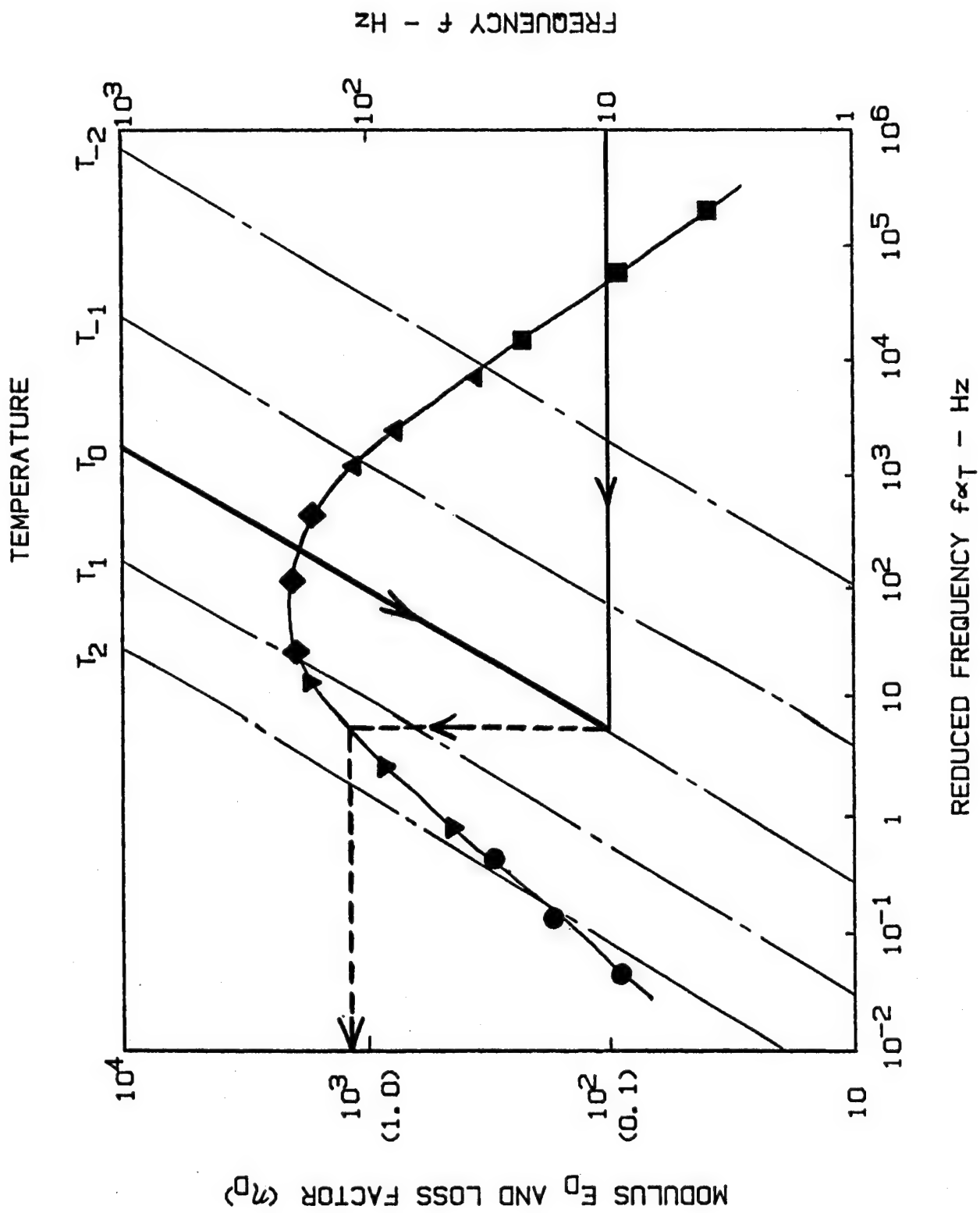Figure 3 A Typical Reduced Frequency Nomogram

Figure 4 Interpretation of Data from a Reduced Frequency Nomogram
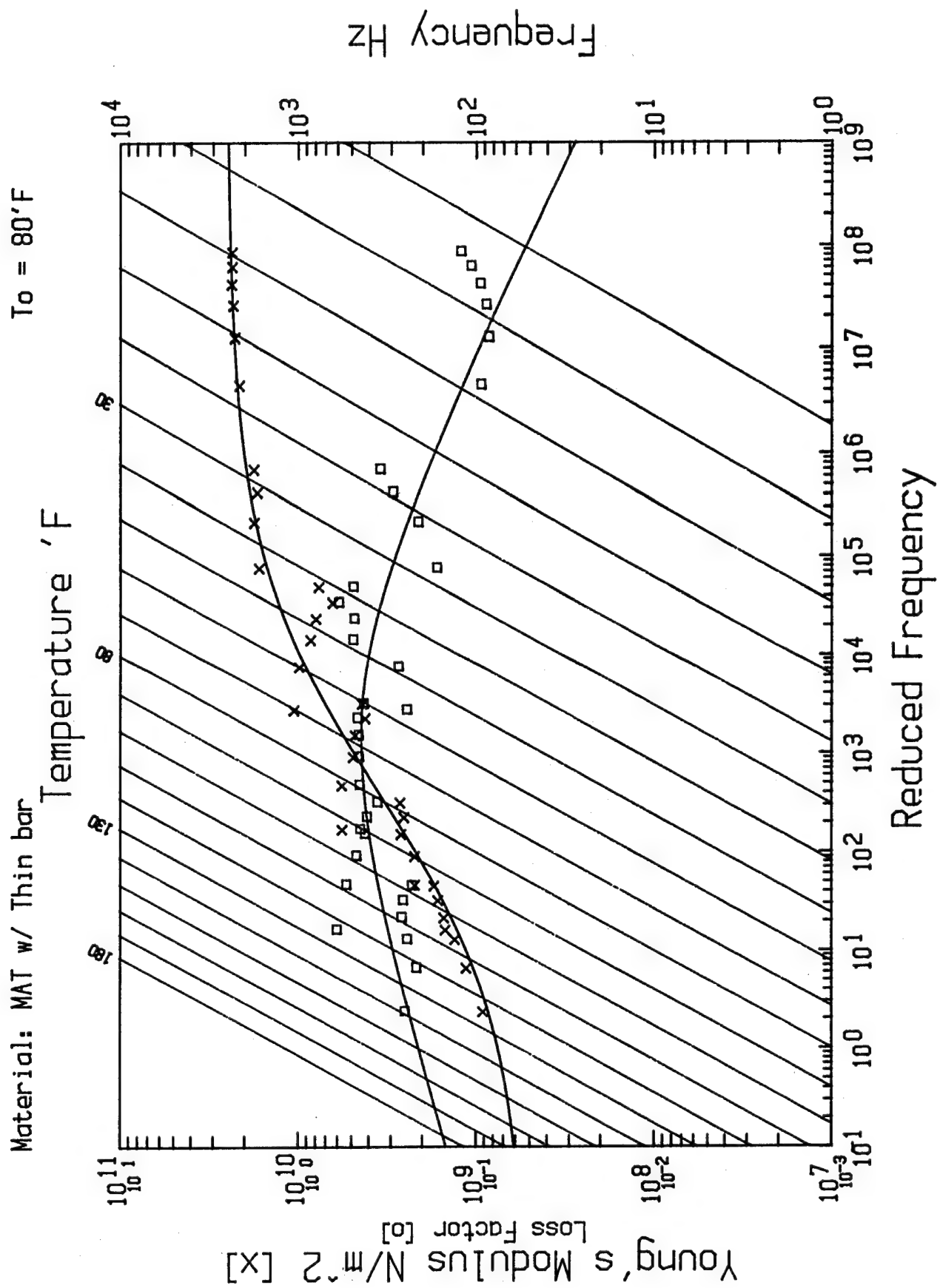
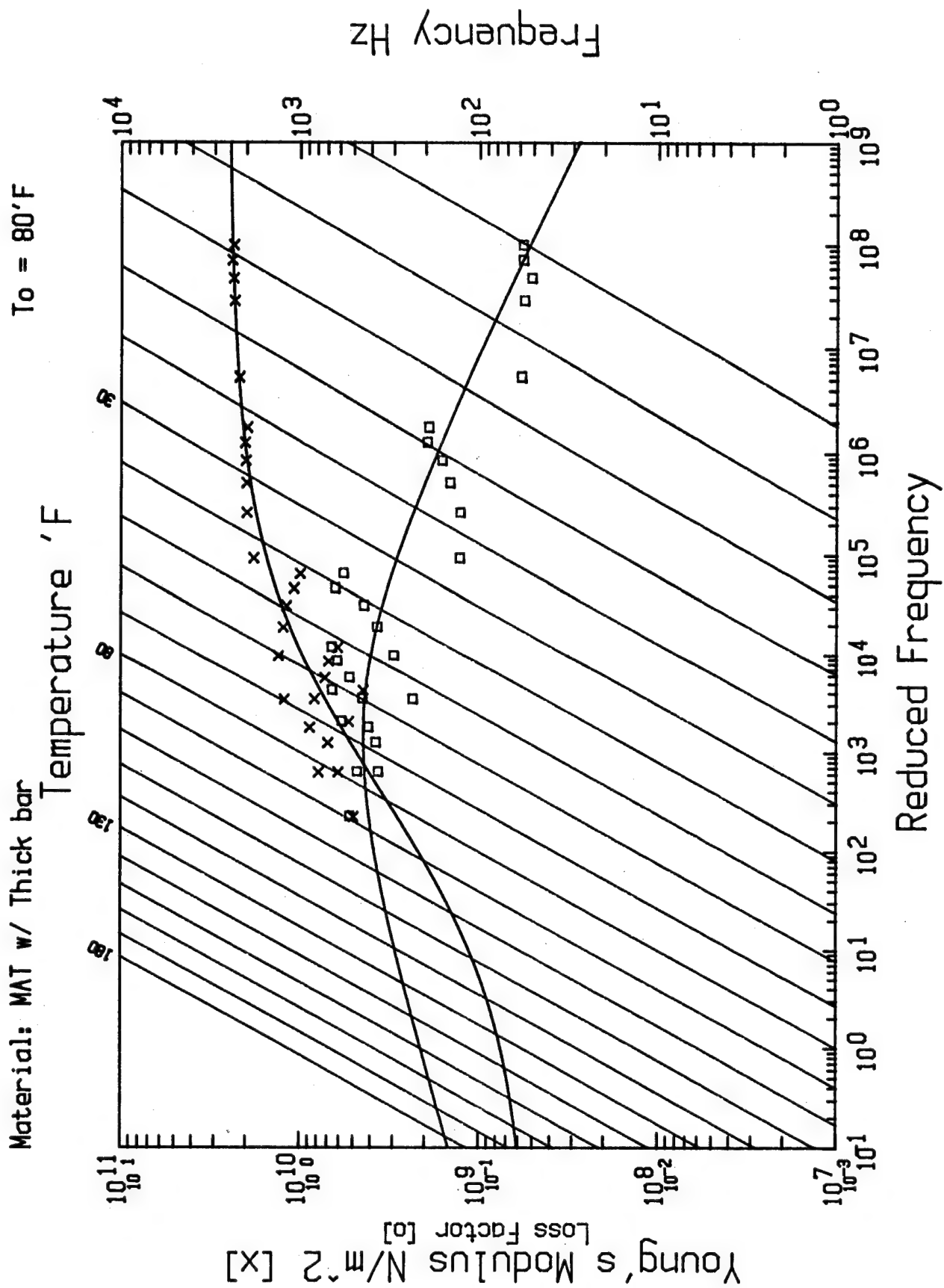Figure 5 Reduced Frequency Nomogram with Thin Bar

Figure 6   Reduced Frequency Nomogram with Thick Bar

DESCRIPTION OF STRUCTURAL DAMPING

L. Gaul, Professor
P. Klein, Lt. Col.
Institute of Mechanics
S. Kempfle, Dr.-Ing.
Institute of Mathematics
Department of Mechanical Engineering
University of the Federal Armed Forces Hamburg
Holstenhofweg 85
2000 Hamburg 70
Federal Republic of Germany
(040) 6541 - 2219

ABSTRACT

Structural damping is frequently approximated in frequency domain by the constant hysteretic damping model. Transient vibrations of a member with constant hysteretic damping lead to a noncausal precursor response [1, 2]. Noncausal response can be avoided by introducing actual measured frequency dependent stiffness and damping behaviour of material, or by introducing constitutive equations of differential operator type with classical derivatives (integer order) or generalized type (fractional order).

This paper recalls and generalizes constitutive equations of viscoelastic behaviour of materials and members in time and frequency domain.

Weak frequency dependence of actual viscoelastic material can be fitted with only few parameters by adopting the fractional derivative concept.
The impulse response function of an oscillator with fractional derivative damping model is integrated in the present paper by a new efficient technique using inverse Fourier transform. This requires a unique definition of the constitutive equation in frequency domain. The response in shown to fulfill causality requirement. Amplitude decay of the considered damping models are compared after selection of equivalent damping properties.

Fractional derivatives in constitutive equations

The elastic-viscoelastic correspondence principle replaces Hooke's law describing a linear elastic material by the corresponding equations of a viscoelastic material in time domain of differential operator type or hereditary integral type [3]. For a one dimensional state of stress Hooke's law $\sigma(t) = E\varepsilon(t)$ is replaced by the constitutive equation of differential operator type

$$\sum_{k=0}^{N} p_k \frac{d^k}{dt^k} \sigma(t) = \sum_{k=0}^{M} q_k \frac{d^k}{dt^k} \varepsilon(t) \tag{1}$$

or hereditary integral type

$$\sigma(t) = \int_{-\infty}^{t} E(t-\upsilon) \frac{d\varepsilon(\upsilon)}{dt} d\upsilon \tag{2}$$

Young's modulus E corresponds to the relaxation function $E(t)$ in equation (2). Thermorheological simple materials allow introducing the influence of space and time dependent temperature T on material behaviour by replacing the actual time t by a reduced time

$$\zeta(x,t) = \int_{0}^{t} \phi[T(x,\eta)]d\eta \tag{3}$$

This transformation is based on the shift function ϕ determined from experimental data [3]. As a generalization of the constitutive equation (1) with integer order derivatives in operators, fractional calculus can be used to respresent viscoelastic behaviour [4].

The derivative of fractional order α

$$\frac{d^\alpha \varepsilon(t)}{dt^\alpha} = D^\alpha \{\varepsilon(t)\} = \frac{1}{\Gamma(1-\alpha)} \frac{d}{dt} \int_{0}^{t} \frac{\varepsilon(t-\upsilon)}{\upsilon^\alpha} d\upsilon \quad 0 < \alpha < 1 \ , \tag{4}$$

defined with the gamma function $\Gamma(1-\alpha) = \int_{0}^{\infty} e^{-x} x^{-\alpha} dx$ is the inverse operation of fractional integration attributed to Riemann and Liouville [5].
Equation (1) with each integer order derivative being replaced by one of fractional order leads to

$$\sum_{k=0}^{N} p_k D^{\beta_k} \{o(t)\} = \sum_{k=0}^{M} q_k D^{\alpha_k} \{\varepsilon(t)\} \tag{5}$$

Although the defining relationship (4) appears complicated with respect to computations both Laplace and Fourier transforms reveal the useful results

$$L \left[D^{\alpha}\{x(t)\} \right] = s^{\alpha} L \left[x(t) \right] \tag{6}$$

$$F \left[D^{\alpha}\{x(t)\} \right] = (i\omega)^{\alpha} F \left[x(t) \right]$$

Harmonic functions of time such as $\varepsilon = \varepsilon^* exp\,(i\omega t)$ in steady state or the frequency domain of Fourier transform convert equations (2,5) with (6) to

$$o^*(\omega) = E^*(\omega) \varepsilon^*(\omega) \tag{7}$$

Complex modulus $E^*(\omega)$ with storage modulus $E'(\omega)$ loss modulus $E''(\omega)$ and loss factor $\eta(\omega) = E''(\omega)/E'(\omega)$

$$E^*(\omega) = \frac{\displaystyle\sum_{k=0}^{M} q_k (i\omega)^{\alpha k}}{\displaystyle\sum_{k=0}^{N} p_k (i\omega)^{\beta k}} = E'(\omega) + i E''(\omega) = E'(\omega)[1 + i\eta(\omega)] \tag{8}$$

is related to the relaxation function $E(t)$ in equation (2) by the inverse Fourier transform $E(t) = F^{-1}[E^*(\omega)/(i\omega)]$.

Complex moduli of several viscoelastic models and associated rheological models are compared in Fig. 1 with the corresponding storage and loss moduli.

A frequency parameter $a_0 = \omega/\omega_n$ with a scaling frequency ω_n has been introduced which leads to a nondimensional time $\tau = \omega_n t$ according to $a_0 \tau = \omega t$.
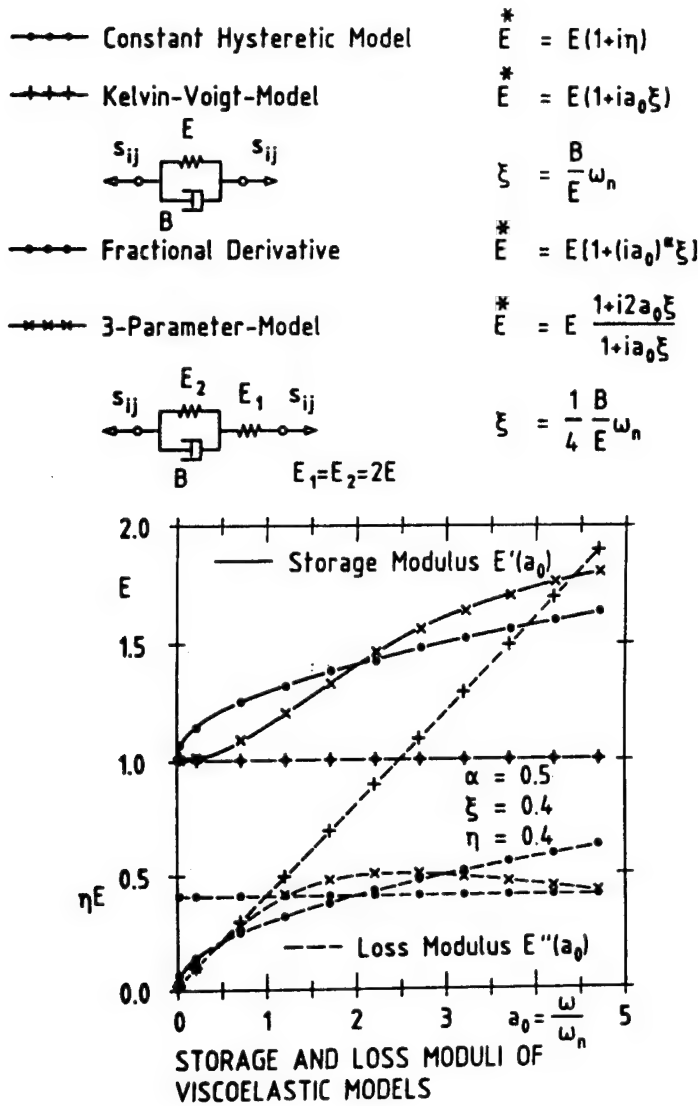
Fig. 1 Complex moduli, storage and
loss moduli of viscoelastic models

In a limited frequency band, the frequency independent, so called constant hysteretic damping model approximates experimental results. This damping model is frequently extended over the entire range of positive frequencies to yield the complex modulus

$$E^* = E(1 + i\eta) . \qquad (9)$$

Noncausal response occurs when results obtained with this model are transformed into the time domain [1, 2, 6, 7]. An analytical solution of the corresponding impulse response function of a SDOF oscillator is given in [1]. Noncausal response can be avoided by introducing actual measured frequency dependent stiffness and damping behaviour of material [2]. It is stated in the present paper, that noncausal response can be avoided by constitutive equations with fractional derivatives.

Damping models of a member

Transfer behaviour of a massless member in Fig. 2b is formulated by integrating equation (5) for a Kelvin-Voigt model (Fig. 1) with fractional derivative with respect to the volume of a member. This relates the force N to the tip displacement u in time domain

$$N(\iota) = k\,u(\iota) + c D^{\alpha}\{u(\iota)\} \quad 0 < \alpha < 1 \qquad (10)$$

and in frequency domain of Fourier transform
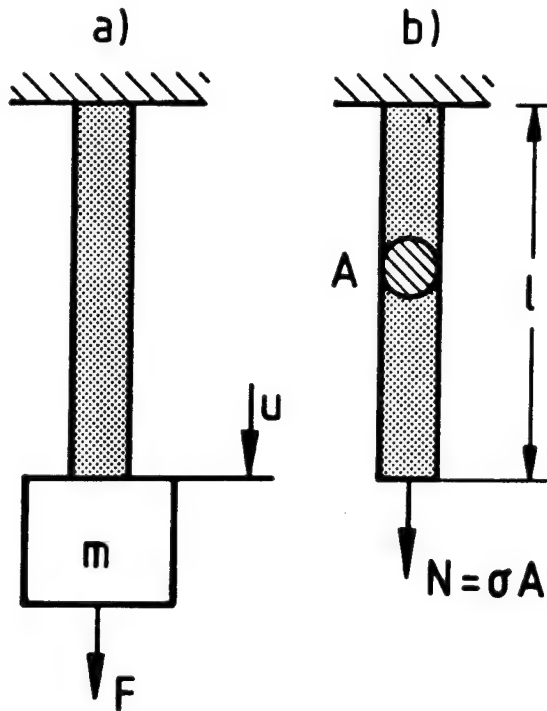
$$N^*(a_o) = k\{1 + \xi(ia_o)^a\} u^*(a_o) \tag{11}$$

with stiffness $k = EA/\ell$ and viscosity $\xi = c/k$, where $c = BA/\ell$. Constant hysteretic model (9) leads to

$$N^*(a_o) = k(1+i\eta) u^*(a_o) . \tag{12}$$

Both complex moduli of the member

$$k^*(a_o) = N^*(a_o)/u^*(a_o) = k'(a_o) + i k''(a_o) \tag{13}$$

(11, 12) do not as yet meet the requirements of a unique definition for the entire range of frequencies $-\infty < a_o < \infty$ of Fourier transform.

Unique definition of constitutive equations in frequency domain

Consider the term $(ia_o)^a a_o$, $a \in \mathbb{R}$ in equation (11) as a special case of the complex expression $\Omega^z \Omega$, $z \in \mathbb{C}$. A unique definition of $\Omega^z = \exp(zLn\Omega)$ is gained by restricting the arguments of $Ln\Omega$ to the principal values $-\pi < Im(Ln\Omega) < \pi$, leading to a branch cut along the negative real axis [8]. This definiton restricts the arguments

$$(ia_o)^a = R\exp(i\phi) \text{ to}$$

$$-a\pi \le \phi < a\pi \quad 0 < a < 1 . \tag{14}$$

Fig. 2 (a) SDOF oscillator (b) Massless member

Storage and loss moduli of the member in equation (11)

$$k'(a_o) = k\{1+\xi Re(ia_o)^a\}, \quad k''(a_o) = k \xi Im(ia_o)^a \tag{15}$$

have a unique definition with equation (14). A physical interpretation supports the choice of proper roots. The force $N^* exp\,(ia_o\tau)$, interpreted as a rotating vector in complex plane, causes the displacement $u^* exp\,(ia_o\tau)$ and has to be ahead with minimal phaseshift counterclockwise for positive frequencies $a_o > 0$, $exp\,(ia_o\tau)$, and clockwise for negative frequencies $a_o < 0$, $exp\,(-i|a_o|\tau)$. Negative frequencies occur in two sided Fourier transform. This condition is fullfilled by equation (14) and requires the well known extension of complex modulus (12) according to

$$k^* = k\,(1 + i\eta\,sgn\,a_o) \quad . \tag{16}$$

The fractional derivative of order $a = 1/2$ can be derived to be relevant for polymeric materials from molecular physics [4].

According to (14) we have to choose

$$(ia_o)^{1/2} = \sqrt{|a_o|/2}\;\begin{Bmatrix} 1+i, & a_o \geq 0 \\ 1-i, & a_o < 0 \end{Bmatrix} \tag{17}$$

and obtain the complex modulus

$$k^*(a_o) = \begin{cases} k\,(1 + \xi\sqrt{a_o/2} + i\xi\sqrt{a_o/2})\,, & a_o \geq 0 \\ k\,(1 + \xi\sqrt{|a_o|/2|} + i\xi\sqrt{|a_o|/2})\,, & a_o < 0 \end{cases} \tag{18}$$

Complex moduli (16, 18) contain storage moduli, which are even functions of frequency and loss moduli, which are odd functions of frequency

$$k'(a_o) = k'(-a_o),\;\; k''(a_o) = -k''(-a_o) \quad . \tag{19}$$

Impulse response function of a damped oscillator

Vibration response of the damped SDOF oscillator in Fig. 2a is calculated by Fourier transform, i.e. $u^*\,(a_o) = (1/\omega_n)\int^\infty_{-\infty} u(\tau)\,exp\,(-ia_o\tau)\,d\tau$, of Newtons equation of motion for mass m

$$m\,\omega_n^2\,u''(\iota) = F(\iota) - N(\iota) \quad , \tag{20}$$

where $(\;)' = d/d\tau$, $\omega_n = \sqrt{k/m}$. With Fourier transformed constitutive equation (11) of member, the frequency response function is given by

$$F(a_o): = \frac{k \, u^*(a_o)}{F^*(a_o)} = \frac{1}{1 - a_o^2 + \xi(ia_o)^a} \quad . \tag{21}$$

Transient response can be obtained from inverse Fourier transform.

Dirac unit impulse excitation $F(\tau) = \delta(\tau)$ o—• $F^*(a_o) = 1$ leads to the impulse response function $u(\tau) = h(\tau)$

$$f(\tau): = m\omega_n h(\tau) = \frac{1}{2\pi} \int_{-\infty}^{\infty} F(a_o)e^{ia_o\tau} \, da_o \quad , \tag{22}$$

which governs the response for an arbitrary force $F(\tau)$ by the Duhamel convolution integral

$$u(\tau) = \frac{1}{\omega_n} \int_{-\infty}^{\tau} h(t - \xi)F(\xi) \, d\xi \quad . \tag{23}$$

By contour integration of equations (21, 22) and theory of residue the authors calculated the familiar impulse response function of the undamped oscillator as

$$f(\tau) = \frac{1}{2\pi} \int_{-\infty}^{\infty} \frac{e^{ia_o\tau}}{1 - a_o^2} \, da_o = \begin{cases} \sin \tau, & \tau \geq 0 \\ 0, & \tau < 0 \end{cases} \quad . \tag{24}$$

A new efficient solution of the damped impulse response (22) is obtained by cutting the infinite integral in two intervals $-\infty > a_o \geq 0$ and $0 < a_o < \infty$ with associated unique definition of the integrand according to (17). Complex conjugate contributions lead to a real semiinfinite integral after reassembling

$$f(\tau) = \frac{1}{\pi} \int_0^{\infty} \frac{A(a_o) \cos(a_o\tau) + B(a_o) \sin(a_o\tau)}{A^2(a_o) + B^2(a_o)} \, da_o \quad , \tag{25}$$

where

$$A(a_o) = 1 - a_o^2 + \xi\sqrt{a_o/2}, \quad B(a_o) = \xi\sqrt{a_o/2} \quad . \tag{26}$$

The corresponding solution for the member with constant hysteretic damping in equation (16) requires substitution of (26) by

$$A(a_o) = 1 - a_o^2, \quad B(a_o) = \eta \quad [2] \quad . \tag{27}$$

Causality of impulse response function

Causal response of the damped oscillator due to the impulse excitation $F(\tau) = \delta(\tau)$ requires the system to be at rest $f(\tau) = 0$ for $\tau < 0$.

Causality of the transformation pair in equations (21, 23) $f(\tau)$ o—• $F(a_0)$ requires [9]

$$f(\tau) = \frac{2}{\pi} \int_0^\infty Re\, F(a_0) \cos(a_0 \tau)\, da_0 = -\frac{2}{\pi} \int_0^\infty Im\, F(a_0) \sin(a_0 \tau)\, da_0 \quad (28)$$

for $\tau > 0$. The abbreviations in equation (25) lead to

$$f(\tau) = \frac{2}{\pi} \int_0^\infty \frac{A(a_0) \cos(a_0 \tau)}{A^2(a_0) + B^2(a_0)}\, da_0 = \frac{2}{\pi} \int_0^\infty \frac{B(a_0) \sin(a_0 \tau)}{A^2(a_0) + B^2(a_0)}\, da_0 \quad (29)$$

for $\tau > 0$.

The sum of the two expressions in (29) for $\tau > 0$ lead to equation (25), whereas for $\tau < 0$ equations (29) assure causality $f(\tau) = 0$ when they are inserted in equation (25). A numerical proof of the causality requirement (29) is given in the present paper for the damping model with fractional derivative and abbreviations (26). This is why the simple equations (29, 26) govern the impuls response $h(\tau) = f(\tau)/(m\omega_n)$ after numerical integration.

A published solution of the problem at hand is based on Laplace transform and contour integration [10]. It requires numerical root finding of the denominator of equation (21). Besides the residues at these poles, there is a contribution to the solution from integration along the earlier mentioned branch cut segments that requires numerical integration of a seminfinite integral as well.

Causality condition (28) is violated with equations (27) corresponding to the constant hysteretic damping model. Precursor response $f(\tau)$ for $\tau < 0$ is discussed in [1, 2].

Numercial results of impulse response

Fig. 3 depicts the impulse response calculated from equations (25, 26) for positive and negative time $\tau = \omega_n t$. The response proves to be causal. Numerical integration of infinite integral converges rapidly.

No difference of impulse response was found when both simpler integrals (29) were integrated for $\tau > 0$. Negative time $\tau < 0$ characterizes the first integral (29)

as an even function of time, the second as an odd function of time. Parameters ξ weighting the fractional derivative of order $a = 1/2$ are chosen to be $\xi = \sqrt{2}/5$ and $\sqrt{2}/20$. Regarding equation (18), an increase of ξ does not only increase the damping but also stiffens the member according to $k(1 + \xi \sqrt{a_o/2})$. That is why stronger amplitude decay is associated with decreasing periods of zero crossing.
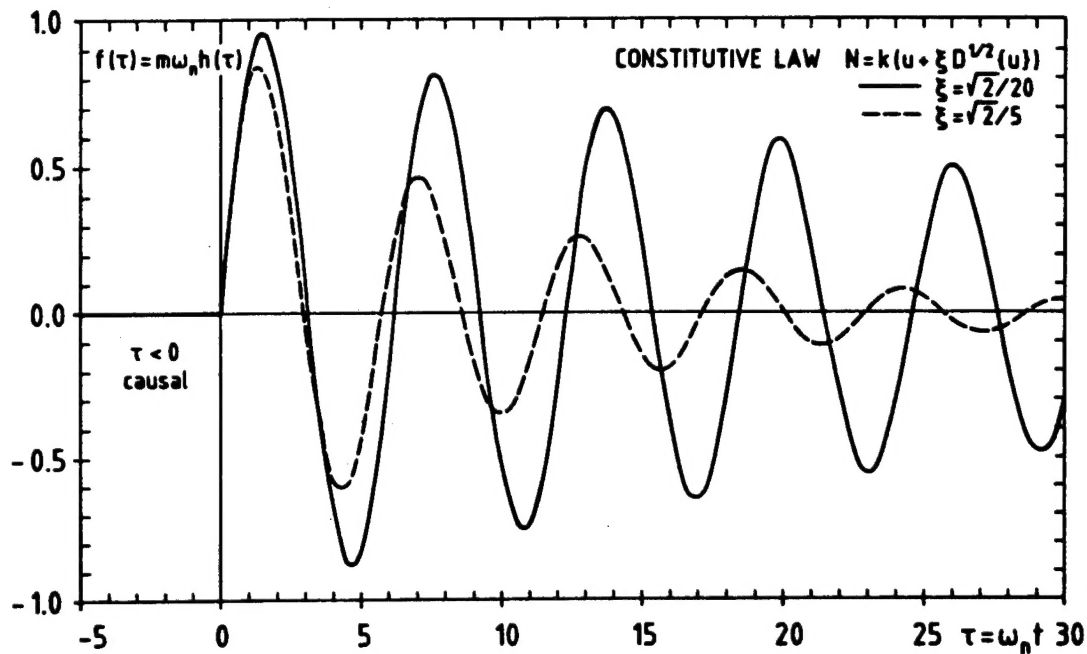

Fig. 3 Impulse response of oscillator with fractional derivative damping model

Impulse response for different damping models

Fig. 4 compares the impulse response functions corresponding to three damping models of Fig. 1:

– Constant hysteretic model [1]
– Kelvin-Voigt model with first oder derivative [1] and
– with fractional derivative of order 1/2

Equivalent loss factors have been chosen at $a_o = \omega/\omega_n = 1$ such that $\eta = a_o \xi$ (Kelvin-Voigt) $= \sqrt{a_o/2}\, \xi$ (Frac.Der.) $= 1/20$. This leads to nearly equal amplitude decay of all models, whereas the stiffening of the fractional derivative model decreases the periods of zero crossing.
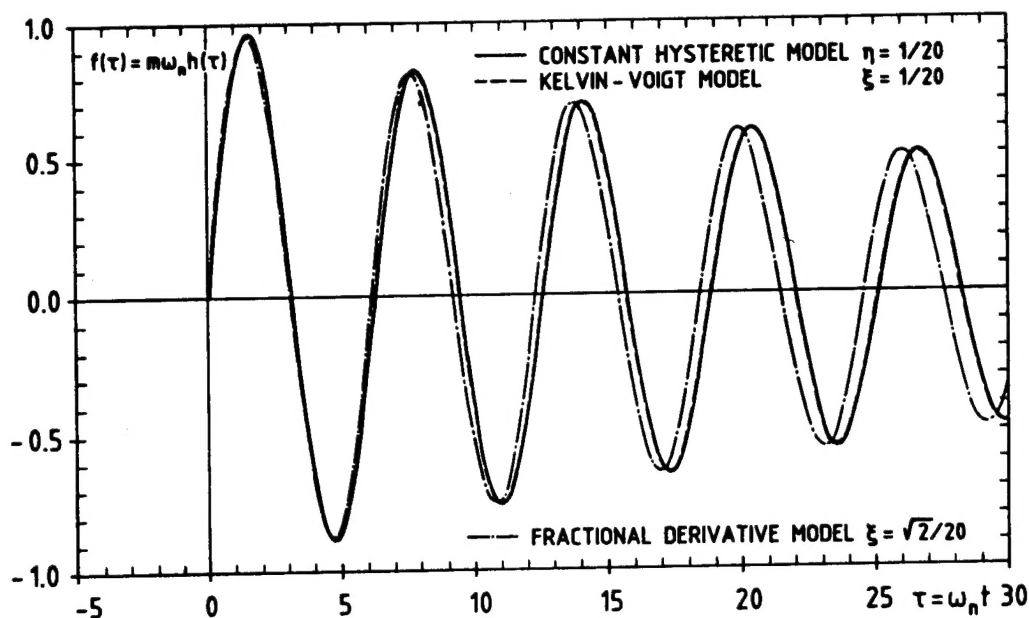
Fig. 4 Impulse response for different damping models

Acknowledgements

References

1. L. Gaul, S. Bohlen and S. Kempfle, Transient and forced oscillations of system with constant hysteretic damping, Mech. Res. Comm. Vol. 12 (4) pp. 187-201 (1985)

2. A. D. Nashif, D.I.G. Jones and J. P. Henderson, Vibration damping, John Wiley & Sons, New York, 1985

3. R. M. Christensen, Theory of viscoelasticity, Academic Press, New York, 1971

4. P. J. Torvik and D. L. Bagley, Fractional derivatives in the description of damping materials and phenomena, The Role of Damping in Vibration and Noise Control, ASME DE-5, pp. 125 - 135, 1987

5. B. Ross, Fractional calculus, Mathematics Magazine, 50 (3), pp. 115-122 (1977)

6. B.M. Fraeijs de Veubeke, Influence of internal damping on aircraft resonance, AGARD Manual on Elasticity, part 1, chapter 3 (1960)

7.   S. H. Crandall, Dynamic response of systems with structural damping, Air, Space and Instruments, Draper Anniversary Volume (S. Lees, ed.) McGraw-Hill Book., New York, pp. 183-193, 1963

8.   M.C. Gaer and L. A. Rubel, The fractional derivative and entire functions, Fractional Calculus and its Applications, Lecture Notes in Mathematics (A. Dold, B. Eckmann ed.) Vol. 457, Springer-Verlag, Berlin, pp. 171-206, 1975

9.   A. Papoulis, The fourier integral and its applications , McGraw-Hill Book Co., New York, 1962

10. R.L. Bagley and P.J. Torvik, A generalized derivative model for an elastomer damper, Shock and Vibration Bulletin, No. 49, Part 2, pp. 135-143 (1979)